Springer Proceedings in Physics 183

Olena Fesenko
Leonid Yatsenko *Editors*

Nanophysics, Nanophotonics, Surface Studies, and Applications

Selected Proceedings of the 3rd International Conference Nanotechnology and Nanomaterials (NANO2015), August 26-30, 2015, Lviv, Ukraine

Springer

Springer Proceedings in Physics

Volume 183

More information about this series at http://www.springer.com/series/361

The series Springer Proceedings in Physics, founded in 1984, is devoted to timely reports of state-of-the-art developments in physics and related sciences. Typically based on material presented at conferences, workshops and similar scientific meetings, volumes published in this series will constitute a comprehensive up-to-date source of reference on a field or subfield of relevance in contemporary physics. Proposals must include the following:—name, place and date of the scientific meeting—a link to the committees (local organization, international advisors etc.)—scientific description of the meeting—list of invited/plenary speakers—an estimate of the planned proceedings book parameters (number of pages/articles, requested number of bulk copies, submission deadline).

Olena Fesenko • Leonid Yatsenko
Editors

Nanophysics, Nanophotonics, Surface Studies, and Applications

Selected Proceedings of the 3rd International Conference Nanotechnology and Nanomaterials (NANO2015), August 26-30, 2015, Lviv, Ukraine

Springer

Editors
Olena Fesenko
Institute of Physics of National Academy of Sciences of Ukraine
Kiev, Ukraine

Leonid Yatsenko
Institute of Physics of National Academy of Sciences of Ukraine
Kiev, Ukraine

ISSN 0930-8989 ISSN 1867-4941 (electronic)
Springer Proceedings in Physics
ISBN 978-3-319-30736-7 ISBN 978-3-319-30737-4 (eBook)
DOI 10.1007/978-3-319-30737-4

Library of Congress Control Number: 2016946430

Printed on acid-free paper

This Springer imprint is published by Springer Nature
The registered company is Springer International Publishing AG Switzerland

Preface

This book highlights the most recent advances in nanoscience from leading researchers in Ukraine, Europe, and beyond. It features contributions from participants of the 3rd International Research and Practice Conference "Nanotechnology and Nanomaterials" (NANO-2015), held in Lviv, Ukraine, on August 26–29, 2015. This event was organized jointly by the Institute of Physics of the National Academy of Sciences of Ukraine, University of Tartu (Estonia), University of Turin (Italy), and Pierre and Marie Curie University (France). Internationally recognized experts from a wide range of universities and research institutes shared their knowledge and key results in the areas of nanocomposites and nanomaterials, nanostructured surfaces, microscopy of nano-objects, nano-optics and nanophotonics, nanoplasmonics, nanochemistry, nanobiotechnology, and surface-enhanced spectroscopy.

The book is divided into five sections: Part I is on *Nanoscale Physics*; Part II is on *Nanooptics and Photonics*; Part III is on *Nanostructured Interfaces and Surfaces*; Part IV is on *Nanochemistry and Biotechnology*; and Part V is on *Nanocomposites and Nanomaterials*.

Part I: Nanoscale Physics

In Chap. 1 (Gburski), the ultrathin one-atom-thick krypton layer between graphite surfaces has been studied using the molecular dynamics simulation method. Chapter 2 (Raczyński) focuses on the properties of 4-*n*-pentyl-4′-cyanobiphenyl molecules placed over a wall made of fullerene molecules. The authors of Chap. 3 (Raczyńska) present the results of a study of the nanoindentation of a phospholipid layer by carbon nanotubes of different diameters. In Chap. 4 (Raczyńska), the behavior of paracetamol molecules in clusters composed of 30 and 80 molecules was investigated over a wide range of temperatures. Chap. 5 (Krupa) focuses on the current-driven spin–orbit-mediated spin torque for the case of an arbitrary

magnetization orientation and a linear in momentum. In Chap. 6 (Gudyma), the authors examined the kinetics of transition in the light-induced spin-crossover system in contact with thermostat.

Part II: Nanooptics and Photonics

A study of the dynamics of pattern formation in a class of adsorption/desorption systems described by the reaction-Cattaneo model (with memory effects of the diffusion flux) is presented in Chap. 7 (Kharchenko). The authors of Chap. 8 (Los) apply their approach to the solution of the time-dependent Schrödinger equation in the case when a particle moves toward a rectangular, generally asymmetric well/barrier potential, which changes in the x (perpendicular to interfaces) direction and models the spin-dependent potential profile in magnetic nanostructures. Chapter 9 (Bulavinets) is devoted to modeling of absorption and scattering by multilayer nanoparticles of the form metal/semiconductor/metal and semiconductor/metal/semiconductor. The goal of the work described in Chap. 10 (Sartinska) is to synthesize and research the properties of boron nitride powder produced under the effect of concentrated light in a flow of nitrogen in a xenon high-flux optical furnace. In Chap. 11 (Smirnova), the authors investigated the dynamics of electron excitations in a plasmonic nanocomposite based on a polymer matrix with a periodic substructure of ordered silver nanoparticles.

Part III: Nanostructured Interfaces and Surfaces

In Chap. 12 (Stetsko), the complex method of chemical treatment and diffusive chrome plating is proposed as a novel approach to surface hardening, providing the required quality characteristics for machine parts and tools. Dispersion kinetics research on niobium and hafnium nanofilms of 100 nm of thickness deposited on the surface of samples from alumina ceramics, sapphire, and ZrO_2-based ceramics at vacuum annealing at 1300–1600 °C and different pauses in the range of 2–20 min is described in Chap. 13 (Gab). The aim of the investigations presented in Chap. 14 (Panko) is to reveal the colloid-chemical mechanisms and features of geomechanical and microbiologic processes aided by nanoparticles and nanostructures in carbonate-clay peloids and, relatedly, the establishment of biocolloid and colloid-chemical transformations with variations of colloid-chemical properties and biological activity of bottom sediments. The authors of Chap. 15 (Galaktionov) investigate the morphology of nanostructural anodic titanium. Chapter 16 (Martseniuk) is devoted to theoretical research into the properties in vacancies and divacancies of silicon. A few interesting examples emerging from the density functional theories for two-dimensional discorectangles are discussed in

Chap. 17 (Chrzanowska) together with the factors responsible for their structure. In Chap. 18 (Frolova), the authors present their study on the influence of ultrasonic treatment and contact non-equilibrium plasma on the ferritization process in Fe^{2+}–Ni^{2+}–SO_4^{2-}–OH^- system. Chapter 19 (Nasiedkin) presents a quantum chemical simulation of the formation of mono-vacancy defects on the single graphite sheet (graphene) as a result of carbon atom removal due to reaction with molecular oxygen in both basal-plane and edge positions, as well as clarification as to whether the defects at the graphite basal plane are associated with the original defect sites or can be formed as a result of oxidative removal of carbon atoms. In Chap. 20 (Nedolya), the effect of the position of impurity carbon atom and substitutional atoms of nickel on energy changes of iron subnanoclusters of face-centered cubic type was evaluated via molecular mechanics. Chapter 21 (Raks) focuses on obtaining robust superhydrophobic coatings based on conventional materials for the paint industry. The aim of Chap. 22 (Wiśniewska) is to determine the adsorption and stability mechanism in a colloidal system in which mesoporous zirconia nanoparticles are dispersed in the aqueous biopolymer solution.

Part IV: Nanochemistry and Biotechnology

Evolution of derma porosity during pre-tanning, tanning, retanning, and modifications with inorganic particles was investigated in Chap. 23 (Dzyazko) with techniques of standard contact porosimetry, transmission, and scanning electron microscopy. The authors of Chap. 24 (Savkina) focus on the cavitation process at a silicon surface. In Chap. 25 (Gburski), the authors embedded paracetamol molecules in high-density lipoprotein aggregate. The authors of Chap. 26 (Gburski) report the dynamics of homocysteine molecules embedded in high-density lipoprotein aggregate and compare the results with the free sample, where the homocysteine molecules were not surrounded by water. In Chap. 27 (Shevchenko), the authors present the result of their study of the physical properties of magnetic nanocomplexes consisting of ferromagnetic iron oxide nanoparticles or superparamagnetic iron oxide nanoparticles loaded with the antitumor drug doxorubicin. Chapter 28 (Nagirnyak) considers the influence of a range of parameters (process temperature, treatment duration, and type of precursor) on the composition and morphology of obtained tin(IV) oxide powders. Chapter 29 (Liapina) evaluates the possibility of using the additional reagents in preparation of a feedwater for extraction of sucrose from the beet slices. In Chap. 30 (Burlaka), the background and recent achievements of using carbon nanotubes as gene delivery vehicles are discussed. The authors of Chap. 31 (Nadtoka) investigate the photocatalytic properties of semiconductor dye-polymer films. The authors of Chap. 32 (Chumachenko) present the results of a study using previously characterized polymers as carrier/stabilization systems in experiments on antitumor photodynamic therapy in vitro and in vivo with chlorin e6 as a photosensitizing agent. The

gasification of an aqueous suspension of lignite from the Alexandria coalfield (Ukraine) under supercritical pressure was studied in Chap. 33 (Korzh). The problem of understanding genetic information coding is discussed from the perspective of the influence of amino acids and proline physical and structural properties in Chap. 34 (Shmeleva). In Chap. 35 (Stolyarchuk), amino-containing spherical particles were synthesized based on 1.2-bis(triethoxysilyl)ethane and 3-aminopropyltriethoxysilane using the modified Stöber method. The aim of Chap. 36 (Talankova-Sereda) is to investigate the influence of copper and cobalt nanoparticles on clonal microreproduction of *Mentha longifolia* plants received by method of isolated cells and tissue culture.

Part V: Nanocomposites and Nanomaterials

Chapter 37 (Kalinichenko) presents the authors' investigation into the formation of nanocomposites on a base of sludge biosolids and pH-sensitive acrylic hydrogel with immobilized bioelements as well as estimates for their efficacy for plant growth. Nanocomposites based on polyurethane/poly(2-hydroxyethyl methacrylate) multicomponent polymer matrix and nanofiller densil were created, and structure, thermodynamic miscibility, dynamic mechanical and physical-mechanical properties have been investigated in Chap. 38 (Karabanova). Chapter 39 (Perets) reveals how liquid dispersive media affect the degree of graphite nanoplatelet (GNP) surface modification and electric properties of GNP/epoxy nanocomposites depending on ultrasonic dispersion and ultraviolet/ozone treatment time. The influence of components on optical and photovoltaic properties of polymer nanocomposite films made of polymethine dyes at high concentrations is analyzed in Chap. 40 (Vertsimakha). Chapter 41 (Barbash) presents the determination of a suitable nanostructuring approach for the bleached softwood sulfate pulp by mechanochemical treatment, followed by a study of the optical characteristics (transparency in the visible spectrum range) and physical-mechanical properties (Young's modulus, tensile strength) of the obtained films. Chapter 42 (Galstyan) addresses the electrical and thermoelectrical properties of carbon nanotubes and their nanocomposite with polytetrafluorethylene and the relationship between the electrical conductivity and Seebeck coefficient. Chapter 43 (Gdula) is dedicated to iron oxides and their composites at the nanometer scale as biocompatible systems for biomedical applications. Chapter 44 (Gorban) considers the influence of modification by copper-containing complexes at a stage of hydrogel synthesis on surface state of nanoparticles and their organization in the structure of amorphous xerogel. Chapter 45 (Ivasyshyn) presents the results of a study of Ti_3AlC_2-based materials oxidized at 600 °C. The authors of Chap. 46 (Huczko) show how the self-propagating high-temperature synthesis route can be used to produce different carbon-related nanomaterials: silicon carbide

nanowires and few-layered graphene. Chapter 47 (Podhurska) is aimed at studying the physical and mechanical behavior of solid oxide fuel cell anode material during cyclic redox treatment depending on the treatment temperature as well as determining the responsible microstructural changes.

Kiev, Ukraine

Olena Fesenko
Leonid Yatsenko

Contents

Contributors

S.V. Alushkin National Technical University of Ukraine "Kyiv Polytechnic Institute", Kyiv, Ukraine

Ihor Astrelin National Technical University of Ukraine "Kyiv Polytechnic Institute", Kyiv, Ukraine

K.D. Babov Ukrainian Research Institute of Medical Rehabilitation and Balneology, Ministry of Health of Ukraine, Odessa, Ukraine

V.A. Barbash National Technical University of Ukraine "Kyiv Polytechnic Institute", Kyiv, Ukraine

M. Barczak Maria Curie Skłodowska University, Lublin, Poland

T.V. Basyuk V. Bakul Institute for Superhard Materials, NAS of Ukraine, Kiev, Ukraine

Yaroslav Blume Institute of Food Biotechnology and Genomics, National Academy of Sciences of Ukraine, Kyiv, Ukraine

Ya. Bobitski Lviv Polytechnic National University, Lviv, Ukraine

Faculty of Mathematics and Natural Sciences, University of Rzeszow, Rzeszow, Poland

O. M. Bondaruk Institute of Macromolecular Chemistry of National Academy of Sciences of Ukraine, Kiev, Ukraine

Valerii Bortyshevskii Institute of Bioorganic Chemistry and Petrochemistry of National Academy of Sciences of Ukraine, Kyiv, Ukraine

Yu. F. Bozbey G. V. Kurdyumov Institute for Metal Physics NASU, Kiev, Ukraine

Ye. M. Brodnikovskyi I. M. Frantsevich Institute for Problems of Materials Science of the NAS of Ukraine, Kyiv, Ukraine

Oleksii Brusylovets Departments of Physics and Chemistry, Taras Shevchenko National University of Kyiv, Kyiv, Ukraine

O.V. Buganov Institute of Physics, National Academy of Sciences of Belarus, Belarus, Belarus

T. Bulavinets Lviv Polytechnic National University, Lviv, Ukraine

A. Burlaka R.E. Kavetsky Institute of Experimental Pathology, Oncology and Radiobiology of the National Academy of Sciences of Ukraine, Kyiv, Ukraine

Olga Burlaka Institute of Food Biotechnology and Genomics, National Academy of Sciences of Ukraine, Kyiv, Ukraine

Levan Chkhartishvili Georgian Technical University, Tbilisi, Georgia

Tavadze Institute of Metallurgy & Materials Science, Tbilisi, Georgia

N. Chorna Chuiko Institute of Surface Chemistry NASU, Kyiv, Ukraine

Agnieszka Chrzanowska Institute of Physics, Kraków University of Technology, Kraków, Poland

V.A. Chumachenko Department of Chemistry, Taras Shevchenko National University of Kyiv, Kyiv, Ukraine

Andrzej Dąbrowski Department of Theoretical Chemistry, Maria Curie-Sklodowska University, Lublin, Poland

O.V. Danko Institute of Physics NAS Ukraine, Kiev, Ukraine

A. Dawid Institute of Physics, University of Silesia, Katowice, Poland

Tetiana Dontsova National Technical University of Ukraine “Kyiv Polytechnic Institute”, Kyiv, Ukraine

Peter Dulnev Institute of Bioorganic Chemistry and Petrochemistry, Kyiv, Ukraine

P.G. Dulnev Institute of Bioorganic Chemistry and Petrochemistry, Kyiv, Ukraine

Yuliya Dzyazko V.I. Vernadskii Institute of General and Inorganic Chemistry of the NAS of Ukraine, Kyiv, Ukraine

Liliya Frolova State University of Chemical Technology, Dnipropetrovsk, Ukraine

Krzysztof Górny Institute of Physics, University of Silesia, Katowice, Poland

I.I. Gab Frantsevich Institute for Problems of Materials Science of National Academy Sciences of Ukraine, Kyiv, Ukraine

D.A. Galaktionov Institute of Physics NAS Ukraine, Kiev, Ukraine

I.Ye. Galstian G. V. Kurdyumov Institute for Metal Physics NASU, Kiev, Ukraine

N. F. Gamaleia Laboratory of Quantum Nanobiology, R. E. Kavetsky Institute for Experimental Pathology, Oncology and Radiobiology, Kiev, Ukraine

Zygmunt Gburski Institute of Physics, University of Silesia, Katowice, Poland

Karolina Gdula Department of Theoretical Chemistry, Maria Curie-Sklodowska University, Lublin, Poland

Yu. P. Gomza Institute of Macromolecular Chemistry of National Academy of Sciences of Ukraine, Kiev, Ukraine

O. Gorban Donetsk Institute for Physics and Engineering After Named O.O. Galkin NAS of Ukraine, Kiev, Ukraine

S. Gorban Donetsk Institute for Physics and Engineering After Named O.O. Galkin NAS of Ukraine, Kiev, Ukraine

Iurii Gudyma Chernivtsi National University, Chernivtsi, Ukraine

Anatoliy Grebenyuk Chuiko Institute of Surface Chemistry of the National Academy of Sciences of Ukraine, Kiev, Ukraine

D.O. Grynko Institute of Semiconductor Physics NAS Ukraine, Kiev, Ukraine

Andrzej Huczko Laboratory of Nanomaterials Physics and Chemistry, Department of Chemistry, Warsaw University, Warsaw, Poland

A.D. Ivasyshyn Karpenko Physico-Mechanical Institute, NAS of Ukraine, Lviv, Ukraine

K.V. Kalinichenko Colloidal Technologies of the Natural Systems Department, F.D. Ovcharenko Institute of Biocolloidal Chemistry, National Academy of Sciences of Ukraine, Kiev, Ukraine

Paweł Karbowniczek Institute of Physics, Kraków University of Technology, Kraków, Poland

Dmitrii Kharchenko Institute of Applied Physics, National Academy of Sciences of Ukraine, Sumy, Ukraine

Vasyl Kharchenko Institute of Applied Physics, National Academy of Sciences of Ukraine, Sumy, Ukraine

M. Kharchenko Donetsk Institute for Physics and Engineering After Named O.O. Galkin NAS of Ukraine, Kiev, Ukraine

L.V. Karabanova Institute of Macromolecular Chemistry of National Academy of Sciences of Ukraine, Kiev, Ukraine

T. Konstantinova Donetsk Institute for Physics and Engineering After Named O. O. Galkin NAS of Ukraine, Kiev, Ukraine

V. Yu. Koda G. V. Kurdyumov Institute for Metal Physics NASU, Kiev, Ukraine

A.S. Kondratyuk L. V. Pisarzhevsky Institute of Physical Chemistry of the National Academy of Sciences of Ukraine, Kyiv, Ukraine

A.M. Korostil Institute of Magnetism NASU, Kyiv, Ukraine

Raisa Korzh Institute of Bioorganic Chemistry and Petrochemistry of National Academy of Sciences of Ukraine, Kyiv, Ukraine

V.G. Koshechko L. V. Pisarzhevsky Institute of Physical Chemistry of the National Academy of Sciences of Ukraine, Kyiv, Ukraine

B. D. Kostyuk Frantsevich Institute for Problems of Materials Science of National Academy Sciences of Ukraine, Kyiv, Ukraine

A.V. Kovalyova Zaporozhian National Technical University, Zaporozhye, Ukraine

I.G. Kovzun Institute of Biocolloid Chemistry Named After F. D. Ovcharenko, NAS of Ukraine, Kyiv, Ukraine

E. Kruchkov National Cancer Institute, Kyiv, Ukraine

M.M. Krupa Institute of Magnetism NASU, Kyiv, Ukraine

N.I. Kucenko Research Station of Medicinal Plants of Agroecology and Nature Management Institute, NAAS, Berezotocha, Poltavskiy, Ukraine

Magdalena Kurcz Laboratory of Nanomaterials Physics and Chemistry, Department of Chemistry, Warsaw University, Warsaw, Poland

N.V. Kutsevol Department of Chemistry, Taras Shevchenko National University of Kyiv, Kyiv, Ukraine

Kira Liapina E.O. Paton Electric Welding Institute, Kyiv, Ukraine

K.V. Liapina E.O. Paton Electric Welding Institute, Kyiv, Ukraine

O. Linnik Chuiko Institute of Surface Chemistry NASU, Kyiv, Ukraine

Victor Los Institute of Magnetism, National Academy of Sciences of Ukraine, Kiev, Ukraine

Mykola Los Institute of Magnetism, National Academy of Sciences of Ukraine, Kiev, Ukraine

S. Lukin R.E. Kavetsky Institute of Experimental Pathology, Oncology and Radiobiology of the National Academy of Sciences of Ukraine, Kyiv, Ukraine

National Technical University of Ukraine “Kyiv Polytechnic Institute”, Kyiv, Ukraine

Victoriya Lutz National Technical University of Ukraine “Kyiv Polytechnic Institute”, Kyiv, Ukraine

P.I. Lytvin Institute of Semiconductor Physics NAS Ukraine, Kiev, Ukraine

Artur Maksymov Chernivtsi National University, Chernivtsi, Ukraine

Advanced Material Research Institute, University of New Orleans, New Orleans, LA, USA

A.I. Marinin Problem Research Laboratory, National University of Food Technology, Kyiv, Ukraine

Ludmila MARTSENIUK Institute for Nuclear Researches, National Academy of Science of Ukraine, Kiev, Ukraine

Andrii Marynin National University of Food Technologies, Kyiv, Ukraine

Ludmila Matzui Departments of Physics and Chemistry, Taras Shevchenko National University of Kyiv, Kyiv, Ukraine

I.V. Melnyk Chuiko Institute of Surface Chemistry, Kyiv, Ukraine

Elena Mokrousiva Kyiv National University of Technology and Design of the MES of Ukraine, Kyiv, Ukraine

G. Yu. Mykhailova G. V. Kurdyumov Institute for Metal Physics NASU, Kiev, Ukraine

O.V. Myronyuk National Technical University of Ukraine “Kyiv Polytechnic Institute”, Kyiv, Ukraine

O. Nadtoka National Taras Shevchenko University of Kyiv, Kyiv, Ukraine

Svitlana Nagirnyak National Technical University of Ukraine “Kyiv Polytechnic Institute”, Kyiv, Ukraine

Y.V. Naidich Frantsevich Institute for Problems of Materials Science of National Academy Sciences of Ukraine, Kyiv, Ukraine

Dmytro Nasiedkin Chuiko Institute of Surface Chemistry of the National Academy of Sciences of Ukraine, Kiev, Ukraine

A.V. Nedolya Department of Applied Physics, Zaporizhzhya National University, Zaporizhzhya, Ukraine

S.D. Nesin Institute of Macromolecular Chemistry of National Academy of Sciences of Ukraine, Kiev, Ukraine

E.M. Nikipelova Ukrainian Research Institute of Medical Rehabilitation and Balneology, Ministry of Health of Ukraine, Odessa, Ukraine

Nadejda Nikolskaya A.N. Frimkon Institute of Physical Chemistry and Electrochemistry of the RAS, Moscow, Russia

G.N. Nikovskaya Colloidal Technologies of the Natural Systems Department, F. D. Ovcharenko Institute of Biocolloidal Chemistry, National Academy of Sciences of Ukraine, Kiev, Ukraine

M.M. Nishchenko G. V. Kurdyumov Institute for Metal Physics NASU, Kiev, Ukraine

L.V. Nosach Chuiko Institute of Surface Chemistry of National Academy of Sciences of Ukraine, Kiev, Ukraine

V.A. Oleinik Institute of Biocolloid Chemistry Named After F. D. Ovcharenko, NAS of Ukraine, Kyiv, Ukraine

Valentyn Olishevskyy National University of Food Technologies, Kyiv, Ukraine

V. Orel National Cancer Institute, Kyiv, Ukraine

O.P. Ostash Karpenko Physico-Mechanical Institute, NAS of Ukraine, Lviv, Ukraine

O.P. Ostash H. V. Karpenko Physico-Mechanical Institute of the NAS of Ukraine, Lviv, Ukraine

Iryna Ovsiienko Departments of Physics and Chemistry, Taras Shevchenko National University of Kyiv, Kyiv, Ukraine

A.V. Panko Institute of Biocolloid Chemistry Named After F. D. Ovcharenko, NAS of Ukraine, Kyiv, Ukraine

Yulia Perets Departments of Physics and Chemistry, Taras Shevchenko National University of Kyiv, Kyiv, Ukraine

Yaroslav Pirko Institute of Food Biotechnology and Genomics, National Academy of Sciences of Ukraine, Kyiv, Ukraine

Alexandr Pivovarov State University of Chemical Technology, Dnipropetrovsk, Ukraine

Yuri Plyuto Chuiko Institute of Surface Chemistry of the National Academy of Sciences of Ukraine, Kiev, Ukraine

A.N. Ponyavina Institute of Physics, National Academy of Sciences of Belarus, Belarus, Belarus

V. Ya. Podhurska H. V. Karpenko Physico-Mechanical Institute of the NAS of Ukraine, Lviv, Ukraine

O. Yu. Posudievsky L. V. Pisarzhevsky Institute of Physical Chemistry of the National Academy of Sciences of Ukraine, Kyiv, Ukraine

T.O. Prikhna V. Bakul Institute for Superhard Materials, NAS of Ukraine, Kiev, Ukraine

A.V. Prydatko National Technical University of Ukraine "Kyiv Polytechnic Institute", Kyiv, Ukraine

Yu. Prylutskyy Taras Shevchenko National University of Kyiv, Kyiv, Ukraine

Natalia Pushanko National University of Food Technologies, Kyiv, Ukraine

Violetta Raczyńska Institute of Physics, University of Silesia, Katowice, Poland

Przemysław Raczyński Institute of Physics, University of Silesia, Katowice, Poland

V.A. Raks Department of Analytical Chemistry, Faculty of Chemistry, Taras Shevchenko National University of Kyiv, Kyiv, Ukraine

A. Romanov National Cancer Institute, Kyiv, Ukraine

O. Rykhalskyi National Cancer Institute, Kyiv, Ukraine

Lina Sartinska Frantsevich Institute for Problems of Materials Science, National Academy of Sciences of Ukraine, Kyiv, Ukraine

Yu. M. Samchenko Colloidal Technologies of the Natural Systems Department, F.D. Ovcharenko Institute of Biocolloidal Chemistry, National Academy of Sciences of Ukraine, Kiev, Ukraine

I.A. Savchenko National Taras Shevchenko University of Kyiv, Kyiv, Ukraine

R.K. Savkina V. Lashkaryov Institute of Semiconductor Physics, NAS of Ukraine, Kyiv, Ukraine

A.I. Schurenko Taras Shevchenko National University of Kyiv, Kiev, Ukraine

A. Shevchenko G.V. Kurdyumov Institute for Metal Physics of the National Academy of Sciences of Ukraine, Kyiv, Ukraine

E.D. Shishko Laboratory of Quantum Nanobiology, R. E. Kavetsky Institute for Experimental Pathology, Oncology and Radiobiology, Kiev, Ukraine

E.A. Shkopinskij Zaporozhian National University, Zaporozhye, Ukraine

L.V. Shmeleva Departments of Theoretical Physics, Faculty of Physics, Taras Shevchenko National University of Kyiv, Kyiv, Ukraine

I.O. Shton Laboratory of Quantum Nanobiology, R. E. Kavetsky Institute for Experimental Pathology, Oncology and Radiobiology, Kiev, Ukraine

Ewa Skwarek Department of Radiochemistry and Colloid Chemistry, Maria Curie-Sklodowska University, Lublin, Poland

A.B. Smirnov V. Lashkaryov Institute of Semiconductor Physics, NAS of Ukraine, Kyiv, Ukraine

T.N. Smirnova Institute of Physics, National Academy of Sciences of Ukraine, Kiev, Ukraine

N. Smirnova Chuiko Institute of Surface Chemistry NASU, Kyiv, Ukraine

Michał Soszyński Laboratory of Nanomaterials Physics and Chemistry, Department of Chemistry, Warsaw University, Warsaw, Poland

Andrew Stetsko Ukraine Academy of Printing, Lviv, Ukraine

T.V. Stetsyuk Frantsevich Institute for Problems of Materials Science of National Academy Sciences of Ukraine, Kyiv, Ukraine

V.I. Stiopkin Taras Shevchenko National University of Kyiv, Kiev, Ukraine

N.V. Stolyarchuk Chuiko Institute of Surface Chemistry, Kyiv, Ukraine

A.D. Suprun Departments of Theoretical Physics, Faculty of Physics, Taras Shevchenko National University of Kyiv, Kyiv, Ukraine

Katarzyna Szewczuk-Karpisz Department of Radiochemistry and Colloid Chemistry, Faculty of Chemistry, Maria Curie-Sklodowska University, Lublin, Poland

Paweł Szroeder Institute of Physics, Faculty of Physics, Astronomy and Informatics, Nicolaus Copernicus University, Torun, Poland

T.E. Talankova-Sereda Medical college of Zaporozhian state medical university, Zaporozhye, Ukraine

S. A. Tikhomirov Institute of Physics, National Academy of Sciences of Belarus, Belarus, Belarus

Elena Tsepich State University of Chemical Technology, Dnipropetrovsk, Ukraine

Anatoliy I. Ukrainets National University of Food Technologies, Kyiv, Ukraine

Z.R. Ulberg Institute of Biocolloid Chemistry Named After F. D. Ovcharenko, NAS of Ukraine, Kyiv, Ukraine

Anatoliy I. Ustinov E.O. Paton Electric Welding Institute, Kyiv, Ukraine

A.I. Ustinov E.O. Paton Electric Welding Institute, Kyiv, Ukraine

B.D. Vasyliv H. V. Karpenko Physico-Mechanical Institute of the NAS of Ukraine, Lviv, Ukraine

O.D. Vasylyev I. M. Frantsevich Institute for Problems of Materials Science of the NAS of Ukraine, Kyiv, Ukraine

Ya. Vertsimakha Institute of Physics, NASU, Kyiv, Ukraine

Yurii Volfkovich A.N. Frimkon Institute of Physical Chemistry and Electrochemistry of the RAS, Moscow, Russia

E.P. Voronin Chuiko Institute of Surface Chemistry of National Academy of Sciences of Ukraine, Kiev, Ukraine

Ludmila Vovchenko Departments of Physics and Chemistry, Taras Shevchenko National University of Kyiv, Kyiv, Ukraine

Małgorzata Wiśniewska Department of Radiochemistry and Colloid Chemistry, Faculty of Chemistry, Maria Curie-Sklodowska University, Lublin, Poland

Olena Yakovenko Departments of Physics and Chemistry, Taras Shevchenko National University of Kyiv, Kyiv, Ukraine

I. Yaremchuk Lviv Polytechnic National University, Lviv, Ukraine

O.V. Yaschenko National Technical University of Ukraine "Kyiv Polytechnic Institute", Kyiv, Ukraine

Alla Yemets Institute of Food Biotechnology and Genomics, National Academy of Sciences of Ukraine, Kyiv, Ukraine

P.V. Yezhov Institute of Physics, National Academy of Sciences of Ukraine, Kiev, Ukraine

O. Zarechnaya L.M. Litvinenko Institute of Physical-Organic Chemistry and Coal Chemistry, Donetsk, Ukraine

M. Zabolotny Taras Shevchenko National University of Kyiv, Kyiv, Ukraine

O. Samchenko L.M. Litvinenko Institute of Physical-Organic Chemistry and Coal Chemistry, Donetsk, Ukraine

Yu. L. Zub Chuiko Institute of Surface Chemistry, Kyiv, Ukraine

Part I
Nanoscale Physics

Chapter 1
Depolarized Rayleigh Light Scattering in the Ultrathin Krypton Layer Between Graphite Surfaces: Computer Simulation

A. Dawid and Zygmunt Gburski

1.1 Introduction

First simulations of depolarized Rayleigh light scattering (DRLS) spectra concentrated on the small number of noble gas atoms grouped in the form of clusters [1–10]. Further development of computer technology allowed simulations of DRLS spectra in bulk noble gas samples [11–19]. The dynamics of fluids in a confined space has been increasingly studied in the recent years due to its potential applications in nanoelectronic devices, nanoscale molecule sensors [20], and gas storage devices. The interacting pair of rare gas atoms induces a short-lived dipole moment, which can be measured in the interaction-induced light scattering (depolarized Rayleigh) experiment. Depolarized Rayleigh light scattering spectrum is related to the polarizability anisotropy of colliding pairs of atoms. The polarizability anisotropy can be described by the dipole-induced dipole (DID) mechanism [21–24]. The DID interactions come from the fact that the incident light beam induces an oscillating dipole on the *i*th particle and this dipole generates an oscillating local field at the *j*th particle. The DRLS spectra of adsorbed noble gases differ from those obtained in pure noble gas samples [25–33]. There were also several studies of the argon adsorption on graphite surface. Earlier experimental studies [34] showed that adsorbed argon atoms form several layers over graphite surface. The phase transition in argon layer covered graphite surface has been also reported [35]. In this work we have calculated the depolarized Rayleigh light scattering many-body correlation function and its spectrum in ultrathin krypton layer located between two parallel graphite walls.

A. Dawid • Z. Gburski (✉)
Institute of Physics, University of Silesia, Uniwersytecka 4, 40-007 Katowice, Poland
e-mail: zygmunt.gburski@us.edu.pl

O. Fesenko, L. Yatsenko (eds.), *Nanophysics, Nanophotonics, Surface Studies, and Applications*, Springer Proceedings in Physics 183,
DOI 10.1007/978-3-319-30737-4_1

1.2 Simulation Details

The graphite walls are simulated as interacting sites without internal degrees of freedom. The walls did not move during the MD simulation; all atoms in graphite are fixed. It approximates bulk sample of graphite sheets. The interaction potential between krypton–krypton and krypton–carbon pairs is taken to be Lennard–Jones (LJ) potential with the usual form

$$V(r_{ij}) = 4\varepsilon_{ij}\left[\left(\frac{\sigma_{ij}}{r_{ij}}\right)^{12} - \left(\frac{\sigma_{ij}}{r_{ij}}\right)^{6}\right],$$

where r_{ij} is the distance between atoms and ε_{ij} and σ_{ij} are the LJ potential parameters listed in Table 1.1. The parameters between unlike atoms were calculated using Lorentz–Berthelot mixing rule [36]. Simulations were performed with the three-dimensional orthogonal periodic boundary conditions (PBC) using minimum image convention algorithm. The simulation cell was of the edge size $x = 28.31$ Å, $y = 25.73$ Å, and $z = 80$ Å. The size in z-direction was chosen so to fulfill the condition of minimum image convention. The classical equations of motion were integrated up to 1.5 ns by the velocity Verlet algorithm [37]. The integration time step used in simulation is 5 fs which ensures total energy conservation within 0.01 %. The average temperature was adjusted as desired by a process of velocities scaling using Berendsen algorithm [37]. The system was equilibrated for 10^6 MD steps. The total time of a single simulation was 1 ns. All simulations have been performed using our own simulation program RIGMD [38].

1.3 The DRLS Model

Although the DID mechanism is a two-body interaction, it gives rise to two-, three-, and four-body correlations contributing to the total intensity of scattered light. The pair anisotropy β_{ij} in the DID limit is $\beta_{ij}(t) = \sigma^3\left[3x_{ij}(t)z_{ij}(t)/r_{ij}^5(t)\right]$, where x_{ij} and z_{ij} are components of the separation vector $\boldsymbol{r_{ij}}$ between the ith and jth atoms. The depolarized Rayleigh spectrum is the Fourier transform of the polarizability anisotropy autocorrelation function $G(t)$, which for a monatomic sample of N atoms is $G(t) \propto \left\langle \sum_{i,j,k,l=1,i\neq j,k\neq l}^{N} \beta_{ij}(t)\beta_{kl}(0) \right\rangle$, where i, j, k, and l identify different atoms.

Table 1.1 Lennard–Jones potential parameters for argon

Atom	ε (meV)	σ (Å)
Carbon	2.412873	3.40
Krypton	14.391	3.633

The total correlation function $G(t)$ can be decomposed into pair, triplet, and quadruplet contributions $G(t) = G_2(t) + G_3(t) + G_4(t)$, where $G_2(t) \propto \left\langle \sum_{\substack{i,j=1,\\ i\neq j}}^{N} \beta_{ij}(t)\beta_{ij}(0) \right\rangle$, $G_3(t) \propto \left\langle \sum_{\substack{i,j,k=1,\\ i\neq j, i\neq k, j\neq k}}^{N} \beta_{ij}(t)\beta_{ik}(0) \right\rangle$, and $G_4(t) \propto \left\langle \sum_{\substack{i,j,k,l=1, i\neq j, i\neq k,\\ k\neq l, i\neq l, j\neq l, j\neq k}}^{N} \beta_{ij}(t)\beta_{kl}(0) \right\rangle$. The appropriate correlation functions were averaged over 10^4 time origins. The time gap between origins was equal 0.125 ps. The interaction-induced spectrum was calculated as the cosine Fourier transform of $G(t)$ function $I(\nu) = \int_{-\infty}^{\infty} \cos(2\pi\nu t) G(t) \mathrm{d}t$.

1.4 Results

The simulation of krypton layer between graphite slabs has been made using $N = 40$ atoms. The krypton atoms were initially uniformly distributed in XY plane parallel to the graphite sheets. The distance between graphite slabs was set to 9.36 Å. The estimated density of krypton atoms in this system is equal to 3.58 g/cm^3. The movement of krypton atoms in such system is restricted to XY-directions. The snapshot of our system is shown in Fig. 1.1. The collisions of krypton atoms are more probable in XY plane than in XZ plane perpendicular to the graphite walls (Fig. 1.1a). The incident light beam is set to be perpendicular to the graphite walls. Thin graphite walls are transparent to light that can interact with krypton layer in fluid form. We begin our analyzing of the result from the mean square displacement $\langle |\Delta r(t)|^2 \rangle$, where $\Delta r(t) = r(t) - r(0)$ and r is the position of krypton atom. The linear slope of the function $\langle |\Delta r(t)|^2 \rangle$ indicates the diffusion in the system, according to Einstein law. We have made our simulations of krypton layer in the temperature range from 60 to 320 K. The mobility of krypton atoms increases with increasing of the temperature in the system. We can observe that in Fig. 1.2. The shape of diffusion coefficient against temperature plot reveals a nonlinear behavior. The first jump (Fig. 1.2a) is so high that it is impossible to show both regions (Fig. 1.2a, b) on the same plot, without using logarithmic scale on y axis. The corresponding $\langle |\Delta r(t)|^2 \rangle$ functions show that for $T = 100.3$ K, we have almost constant function (the increase is very slow) (Fig. 1.3). The next mean square displacement function for $T = 117.1$ K is six times higher after 250 ps. This sudden increase of the diffusion coefficient can be interpreted as the phase transition between the system where atoms are oscillating around the same position (solid phase) and the system where the nearby atoms can interchange their positions (liquid phase). This phenomenon was observed also by visual inspection of the system. In the second region, we have also observed the sudden jump of the diffusion coefficient value

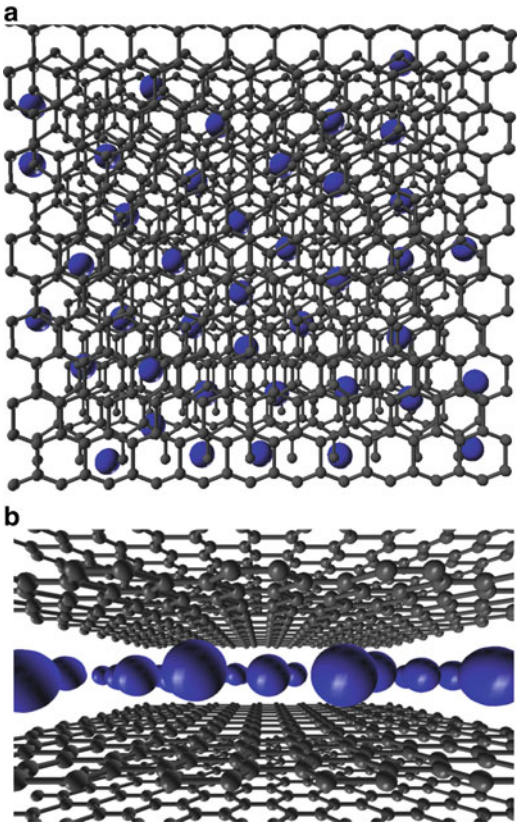

Fig. 1.1 An example of the instantaneous configuration of krypton atom layer between graphite walls; (**a**) projection XY, (**b**) projection XZ

(Fig. 1.2b). The corresponding mean square functions show that this happens between temperatures $T = 199.8$ K and $T = 220.0$ K (Fig. 1.4). After the temperature $T = 220$ K, the mobility of krypton atoms suggests that the system is in the gas-like phase. We begin the study of the DRLS by the decomposition of $G(t)$ correlation function into two-, three-, and four-body contributions. The calculated $G_2(t)$ function for several temperatures is shown in Fig. 1.5. At higher temperatures $T = 299.8$ K (room temperature), the $G_2(t)$ function decays to zero within 38 ps. It indicates fast movement of the particle in the system. The decay time increases with the lowering of the temperature. In the case of $T = 80.0$ K, the estimated decay time is equal to seconds. The opposite situation is in the plot of $G_3(t)$ function (Fig. 1.6). All $G_3(t)$ functions in this plot are negative and only function for $T = 299.8$ K rises to zero within 38 ps. The four-body correlation functions of krypton atoms between graphite slabs are shown in Fig. 1.7. The results are similar to those of $G_2(t)$ functions. The only difference is in absolute values of $G_2(t)$ and $G_4(t)$ functions. The complete polarizability anisotropy correlation functions reveal sudden decay within 1 ps (Fig. 1.8). This behavior of $G(t)$ functions can be explained by the so-called ballistic region, where first collisions occur. The low temperature

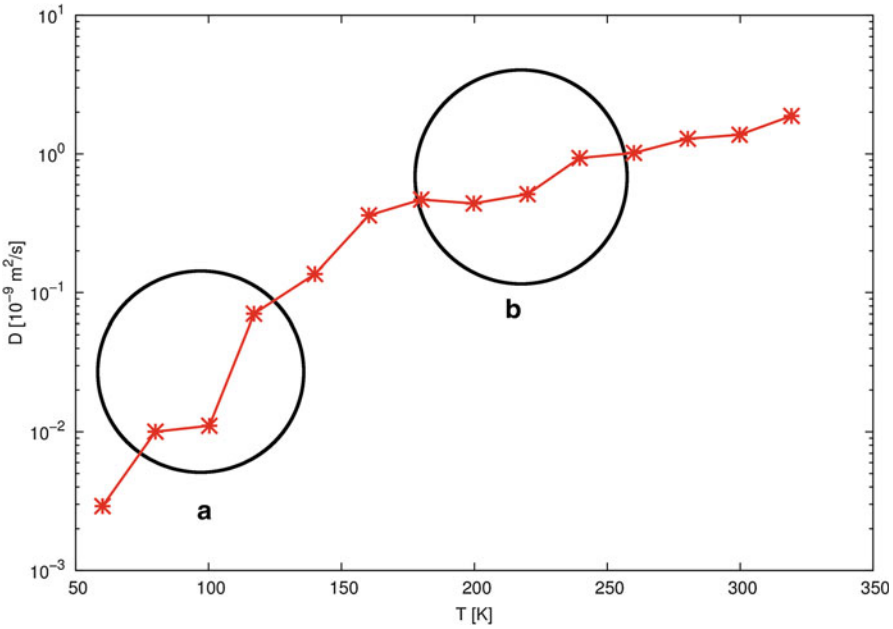

Fig. 1.2 The temperature dependence of diffusion coefficient of krypton atoms between graphite walls; (**a**) the solid–liquid and (**b**) liquid–gas phase transition region

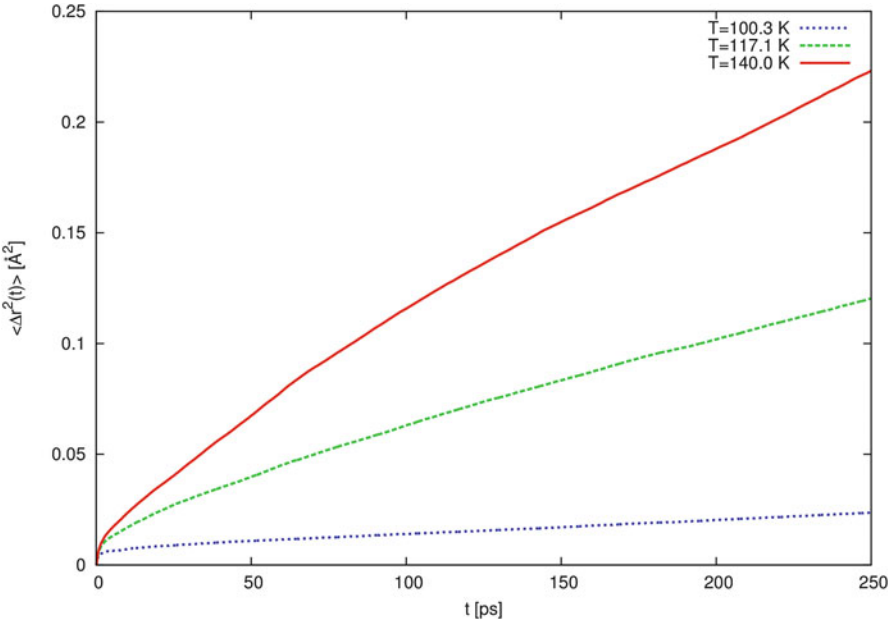

Fig. 1.3 The mean square displacement functions at three temperatures near solid–liquid phase transition region (Fig. 1.2a)

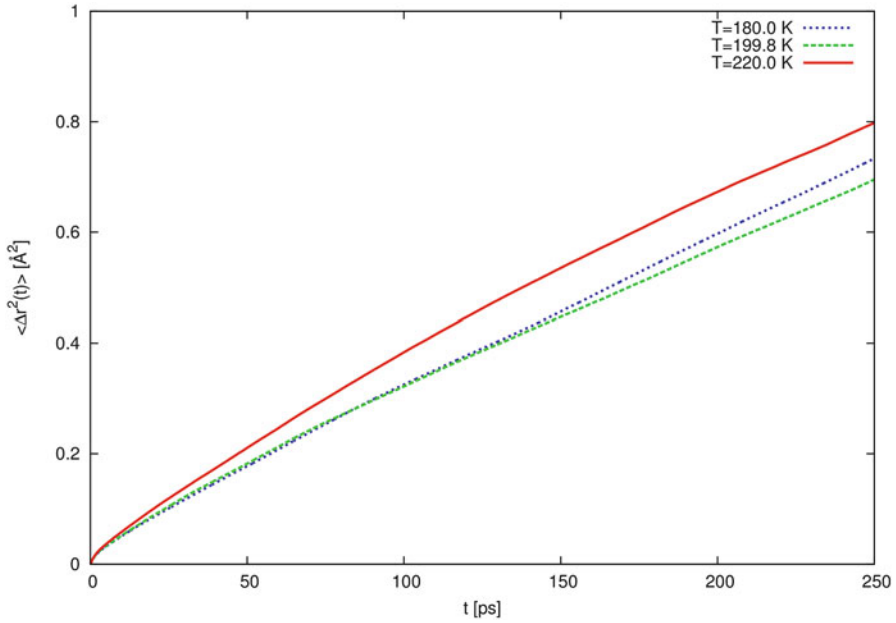

Fig. 1.4 The mean square displacement functions at three temperatures near liquid–gas phase transition region (Fig. 1.2b)

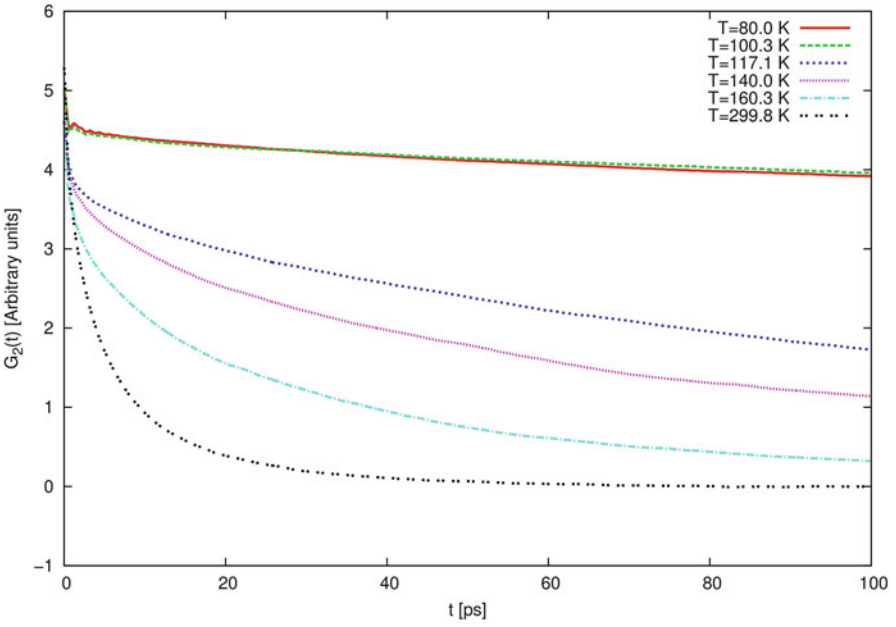

Fig. 1.5 The two-body contribution of total polarizability anisotropy correlation function of krypton atoms at several temperatures

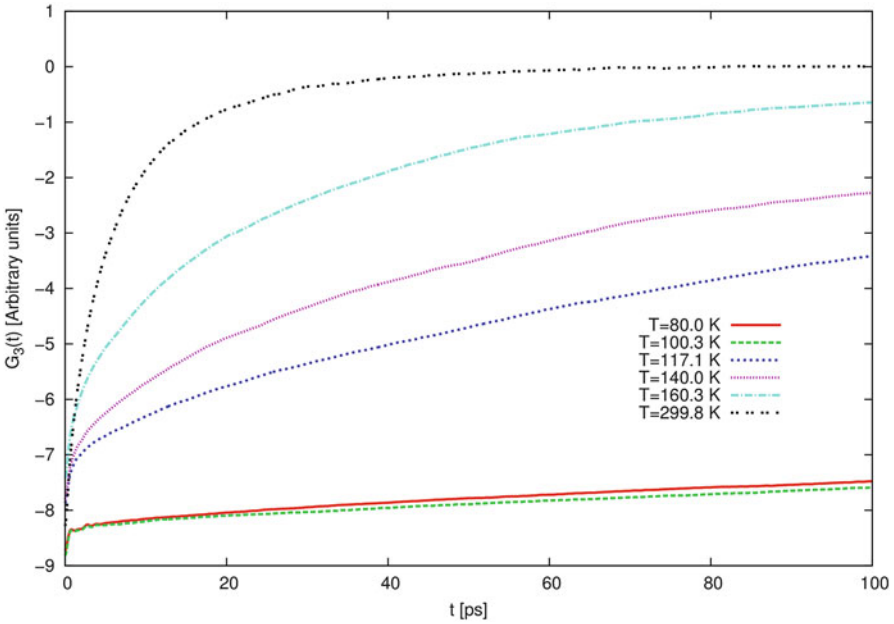

Fig. 1.6 The three-body contribution of total polarizability anisotropy correlation function of krypton atoms at several temperatures

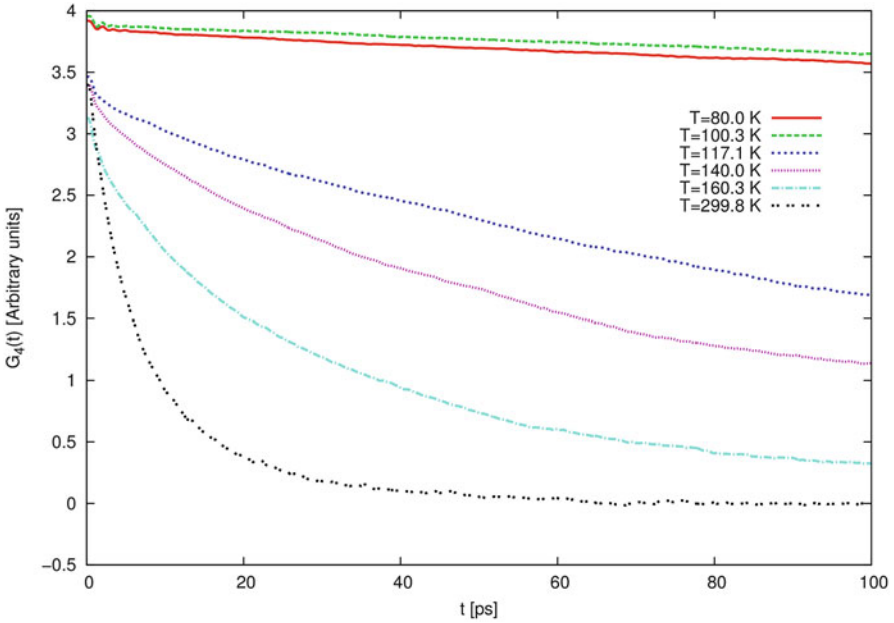

Fig. 1.7 The four-body contribution of total polarizability anisotropy correlation function of krypton atoms at several temperatures

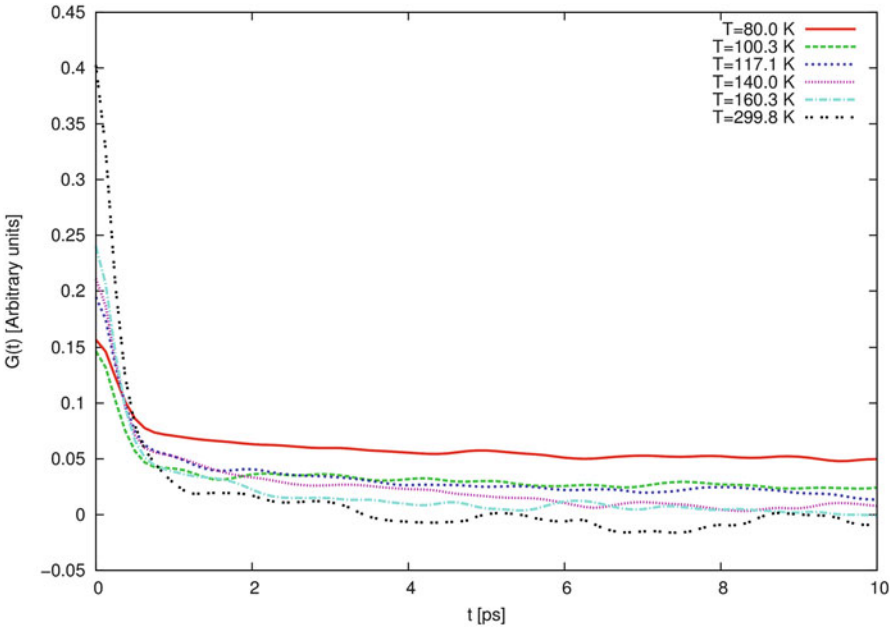

Fig. 1.8 The total polarizability anisotropy correlation function of krypton atoms at several temperatures

functions after that region take almost constant oscillating values. When the temperature increases, the faster decay of the $G(t)$ function is observed. The lower band wave number spectrum of the total intensity $I(\nu)$ shows that the higher value of $I(\nu)$ is for $\nu = 0$ cm^{-1} at the temperature $T = 80.0$ K (Fig. 1.9). Only one $I(\nu)$ function, simulated at $T = 299.8$ K, has maximum at $\nu = 3.8$ cm^{-1}. The intensity of spectra increases with the temperature.

1.5 Conclusions

The depolarized Rayleigh light scattering spectra of ultrathin krypton layer between parallel graphite walls strongly depend on temperature. DRLS intensity increases with the raising of temperature, in the observed wave number range. At the room temperature, the light scattering intensity takes the higher value at $\nu > 0$; it suggests that the system is in a gas-like phase. We have found the appearance of the phase transitions, solid–liquid and liquid–gas, by analyzing the diffusion process in the system studied. In this article we do not attempt to analyze the obtained computer simulation results in terms of theoretical model, because the theoretical treatment of depolarized Rayleigh light scattering in confined space is not yet developed. The preliminary computer simulations reported here may serve as the reconnaissance

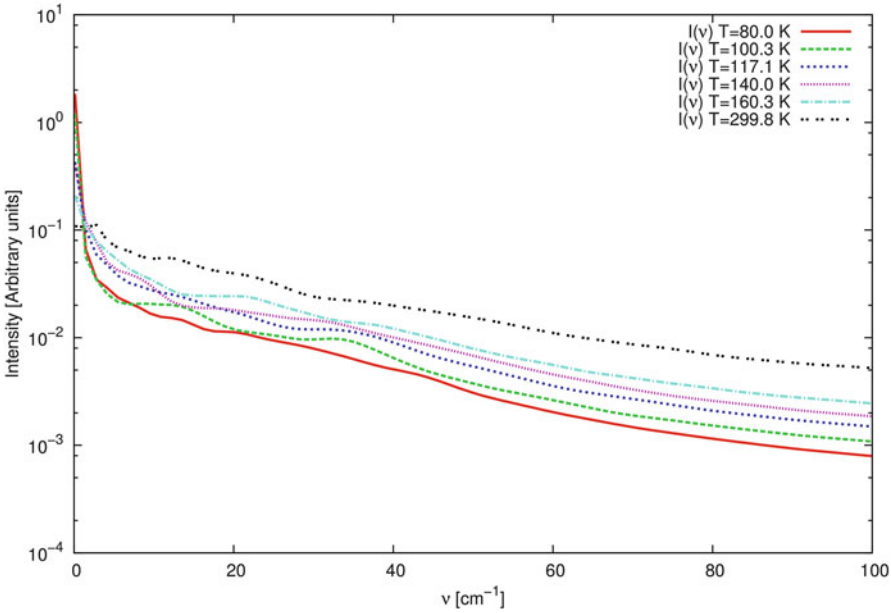

Fig. 1.9 The depolarized Rayleigh light scattering spectra of krypton atoms at several temperatures

for the future experimental and theoretical research of the collision induced light scattering in confined space and ultrathin layers.

References

1. Bhattacharya A, Chen B, Mahanti SD (1996) Structural dynamics of clusters near melting. Phys Rev E 53:R33–R36. doi:10.1103/PhysRevE.53.R33
2. Dawid A, Gburski Z (1997) Interaction-induced light scattering in Lennard–Jones argon clusters: computer simulations. Phys Rev A 56:3294–3296. doi:10.1103/PhysRevA.56.3294
3. Raczyński P, Dawid A, Gburski Z (2005) Depolarized light scattering in small fullerene clusters—computer simulation. J Mol Struct 744–747:525–528. doi:10.1016/j.molstruc.2004.12.064
4. Dawid A, Gburski Z (1998) Interaction-induced absorption in argon–krypton mixture clusters: molecular-dynamics study. Phys Rev A 58:740–743. doi:10.1103/PhysRevA.58.740
5. Piatek A, Dawid A, Gburski Z (2006) The existence of a plastic phase and a solid–liquid dynamical bistability region in small fullerene cluster (C60)7: molecular dynamics simulation. J Phys Condens Matter 18:8471. doi:10.1088/0953-8984/18/37/006
6. Dawid A, Gburski Z (1999) Interaction-induced light scattering in xenon clusters: molecular dynamics study. J Mol Struct 482–483:271–276. doi:10.1016/S0022-2860(98)00668-1
7. Barocchi F, Zoppi M, Proffitt MH, Frommhold L (1981) Determination of the collision-induced depolarized Raman light scattering cross section of the argon diatom. Can J Phys 59:1418–1420. doi:10.1139/p81-187

8. Dawid A, Gburski Z (2002) Interaction-induced absorption in liquid argon–xenon mixture cluster: MD simulation. J Mol Struct 614:177–182. doi:10.1016/S0022-2860(02)00243-0
9. Piatek A, Dawid A, Dendzik Z, Gburski Z (2006) Molecular dynamics (MD) simulation study of the liquid phase of small fullerene cluster (C-60)(7). J Mol Struct 792:82–85. doi:10.1016/j.molstruc.2006.01.054
10. Dawid A, Gburski Z (2002) Fluctuation of the interaction-induced polarizability anisotropy in fullerene cluster—MD study. J Mol Struct 614:183–187. doi:10.1016/S0022-2860(02)00245-4
11. Bucaro JA, Litovitz TA (1971) Rayleigh scattering: collisional motions in liquids. J Chem Phys 54:3846–3853. doi:10.1063/1.1675436
12. Dawid A, Raczynski P, Gburski Z (2014) Depolarised Rayleigh light scattering in argon layer confined between graphite plains: MD simulation. Mol Phys 112:1645–1650. doi:10.1080/00268976.2013.853111
13. Bancewicz T, Glaz W, Godet J-L, Maroulis G (2008) Collision-induced hyper-Rayleigh spectrum of H(2)-Ar gas mixture. J Chem Phys 129(12):124306. doi:10.1063/1.2981042
14. Dawid A, Gorny K, Wojcieszyk D et al (2014) Collision-induced light scattering in a thin xenon layer between graphite slabs—MD study. Spectrochim Acta A Mol Biomol Spectrosc 129:594–600. doi:10.1016/j.saa.2014.03.101
15. An S-C, Montrose CJ, Litovitz TA (1976) Low-frequency structure in the depolarized spectrum of argon. J Chem Phys 64:3717–3719. doi:10.1063/1.432684
16. Stassen H, Gburski Z (1994) Instantaneous normal-mode analysis of binary-liquid Ar–Kr mixtures. Chem Phys Lett 217:325–332. doi:10.1016/0009-2614(93)E1390-3
17. Gburski Z, Gray CG, Sullivan DE (1984) Lineshape in collision-induced absorption. Mori theory. Chem Phys Lett 106:55–59. doi:10.1016/0009-2614(84)87010-4
18. Kader MSAE (2002) The depolarized interaction-induced light scattering spectrum and ground state potential curve of gaseous argon. J Phys B: At Mol Opt Phys 35:4021–4032. doi:10.1088/0953-4075/35/19/306
19. Gburski Z, Zereda T (1980) Vibrational dephasing and intermolecular interactions in liquids. Acta Phys Pol A 57(3):447–454
20. Huang B, Li Z, Liu Z et al (2008) Adsorption of gas molecules on graphene nanoribbons and its implication for nanoscale molecule sensor. J Phys Chem C 112:13442–13446. doi:10.1021/jp8021024
21. Frommhold L (1994) Collision-induced absorption in gases. Cambridge University Press, Cambridge
22. Dawid A, Gburski Z (1997) Dynamical properties of the argon–krypton clusters: molecular dynamics calculations. J Mol Struct 410–411:507–511. doi:10.1016/S0022-2860(96)09512-9
23. Alder BJ, Beers JC, Strauss HL, Weis JJ (1979) Depolarized scattering of atomic fluids with variable polarizability. J Chem Phys 70:4091–4094. doi:10.1063/1.438032
24. Gburski Z (1985) Convergence of memory functions for the vibrational dephasing process in liquids. Chem Phys Lett 115:236–240. doi:10.1016/0009-2614(85)80687-4
25. Dawid A, Gburski Z (2003) Rayleigh light scattering in fullerene covered by a spherical argon film—a molecular dynamics study. J Phys Condens Matter 15:2399–2405. doi:10.1088/0953-8984/15/14/315
26. Kachel A, Gburski Z (1997) Chain formation in a model dipolar liquid: computer simulation study. J Phys Condens Matter 9:10095–10100. doi:10.1088/0953-8984/9/46/007
27. Dawid A, Gburski Z (2003) Interaction-induced light scattering in a fullerene surrounded by an ultrathin argon "atmosphere": molecular dynamics simulation. Phys Rev A 68:065202. doi:10.1103/PhysRevA.68.065202
28. Skrzypek M, Gburski Z (2002) Fullerene cluster between graphite walls—computer simulation. Europhys Lett 59:305–310. doi:10.1209/epl/i2002-00242-8
29. Dawid A, Dendzik Z, Gburski Z (2004) Molecular dynamics study of ultrathin argon layer covering fullerene molecule. J Mol Struct 704:173–176. doi:10.1016/j.molstruc.2004.01.065

30. Dendzik Z, Kośmider M, Dawid A, Gburski Z (2005) Interaction induced depolarized light scattering from ultrathin Ne film covering single-walled carbon nanotubes of different chiralities. J Mol Struct 744–747:577–580. doi:10.1016/j.molstruc.2004.12.049
31. Dendzik Z, Kośmider M, Dawid A et al (2005) Interaction-induced depolarized light scattering spectra of exohedral complexes of Ne and Ar with fullerenes and nanotubes. Mater Sci 23:457–466
32. Kosmider M, Dendzik Z, Palucha S, Gburski Z (2004) Computer simulation of argon cluster inside a single-walled carbon nanotube. J Mol Struct 704:197–201. doi:10.1016/j.molstruc.2004.02.050
33. Dawid A, Gburski Z (2007) Dielectric relaxation of 4-cyano-4-n-pentylbiphenyl (5CB) thin layer adsorbed on carbon nanotube—MD simulation. J Non-Cryst Solids 353:4339–4343. doi:10.1016/j.jnoncrysol.2007.02.072
34. Lamb AB, Ohl EN (1938) On the adsorption of gases by graphite. J Am Chem Soc 60:1287–1290. doi:10.1021/ja01273a003
35. Jura G, Criddle D (1951) Phase transitions of argon adsorbed on graphite. J Phys Chem 55:163–172. doi:10.1021/j150485a001
36. Allen MP, Tildesley DJ (1989) Computer simulation of liquids. Oxford University Press, New York
37. Rapaport DC (2004) The art of molecular dynamics simulation. Cambridge University Press, New York
38. Dawid A (2012) RIGid Molecular Dynamics (RIGMD)—simulation software. http://prac.us.edu.pl/~dawid/RIGMD/rigmdUS.php. http://prac.us.edu.pl/~dawid/RIGMD/rigmdUS.php

Chapter 2
Study of the Dynamics of 5CB Thin Layer Placed on the Fullerene Wall: Computer Simulations

Przemysław Raczyński and Zygmunt Gburski

2.1 Introduction

The properties of liquid crystals are still not fully explored, and they are intensively studied, also using MD technique [1–8]. These studies are motivated by the search for the materials suitable for the new generation of displays, and our research follows that line. In view of this, the combination of liquid crystals with a specific carbon nanostructure is the subject of our studies. The molecule 5CB, with the chemical formula $C_{18}H_{19}N$, was first synthetized from the series of n-cyanobiphenyls, an important group of mesogens. The aim of our research was to find a mesogen with the specific intention of using it in liquid crystal displays (LCD).

Nanostructures, such as graphene, nanotubes, or fullerenes, exhibit interesting physical properties [9–17], and they are still intensively studied. C60, called buckminsterfullerene, is the most famous and very carefully examined. It is the most common naturally occurring molecule of fullerenes' family, which can be found, for example, in soot.

In this work we describe the properties of the molecular system consisted of C60 and 5CB. Mesogen molecules were placed on the surface composed of two fullerene layers. This system was studied for a wide range of temperatures, from 240 to 390 K, for a thorough examination of the behavior of 5CB. The properties of mesogens placed on the surface consisted of fullerenes C60 are interesting for scientific reasons and potential applications.

P. Raczyński (✉) • Z. Gburski
Institute of Physics, University of Silesia, Uniwersytecka 4, 40-007 Katowice, Poland
e-mail: przemyslaw.raczynski@us.edu.pl

O. Fesenko, L. Yatsenko (eds.), *Nanophysics, Nanophotonics, Surface Studies, and Applications*, Springer Proceedings in Physics 183,
DOI 10.1007/978-3-319-30737-4_2

2.2 Simulation Details

All simulations were performed using NAMD 2.8 simulation code [18] and visualized in VMD [19].

The model of 5CB mesogen molecule has been adopted from the CHARMM-type united atom potential developed by Tiberio and co-workers [20]. C60 molecule has been modeled using all-atom potential described elsewhere [21, 22].

Interactions between the mesogens have been described using electrostatics and van der Waals forces modeled with coulombic and Lennard–Jones 12-6 potential, respectively. Cutoff was equal to 12 Å. Interactions between C60 and 5CB molecules have been described with van der Waals interactions modeled with Lennard–Jones 12-6 potential. Periodic boundary conditions were applied on x- and y-axes to treat fullerene surface as an infinite. Equations of motion were integrated using Brunger–Brooks–Karplus (BBK) scheme, implemented in NAMD, with the time step of integration equal to 0.5 fs.

All simulations were performed in NVT ensemble, for temperatures $T = 240$, 270, 300, 330, 360, and 390 K. Between successive temperatures, the system was slowly heated and, next, equilibrated for 1 ns. After that, the simulation runs when the data were collected were performed for 10 ns. To check the reproducibility, all runs were repeated.

We prepared "C60 surface" consisted of the two layers. Fullerenes in the layer adjacent to the mesogen molecules were not fixed. In the second C60 layer, two of the fullerene atoms were fixed.

2.3 Results

Figure 2.1 shows the snapshot of the instantaneous configuration of the studied system after all performed simulations. Some of the 5CB molecules tried to penetrate C60 surface by immersing themselves between fullerene molecules. This process is slight in the low temperatures studied, and it proceeds with the heating of the cluster because mesogen molecules become more mobile.

The process of increasing dynamics of 5CB molecules with the heating of the cluster can be observed in the mean square displacement $\left\langle |\Delta\vec{r}(t)|^2 \right\rangle$ plots of the center of mass of a single molecule. It can be also confirmed by evolution of the diffusion coefficient D: $\left\langle |\Delta\vec{r}(t)|^2 \right\rangle \approx 6Dt$.

Figure 2.2 shows the $\left\langle |\Delta\vec{r}(t)|^2 \right\rangle$ plots of the center of mass of 5CB. For the clarity only first 5 ns for the three different temperatures is shown. Table 2.1 shows obtained values of the diffusion coefficient D.

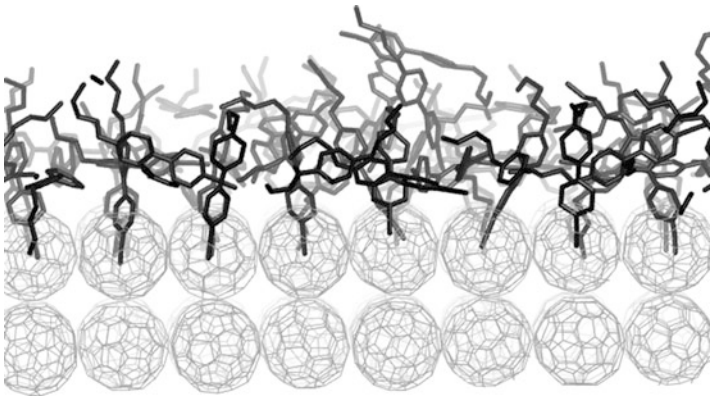

Fig. 2.1 The snapshot of the final configuration of the studied system

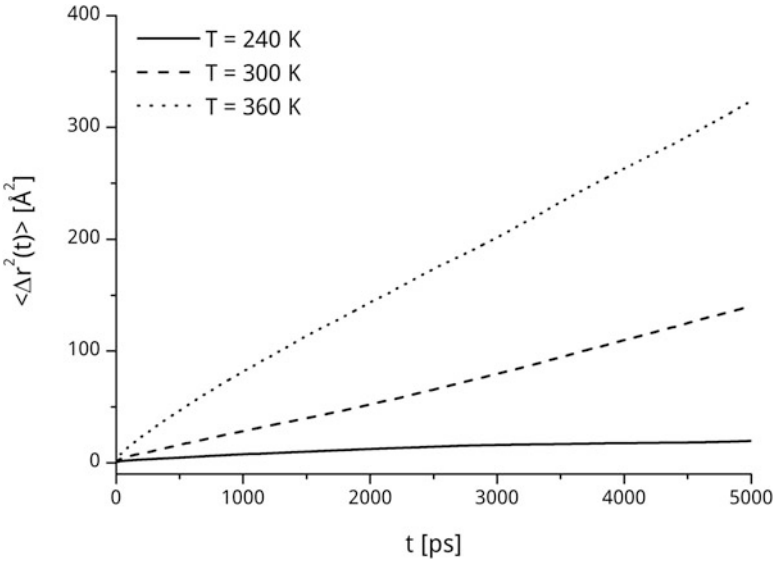

Fig. 2.2 The mean square displacement of the center of mass of 5CB molecule

Table 2.1 Obtained values of the diffusion coefficient D

T (K)	D (Å^2/ps)
240	0.002
270	0.003
300	0.007
330	0.011
360	0.021
390	0.033

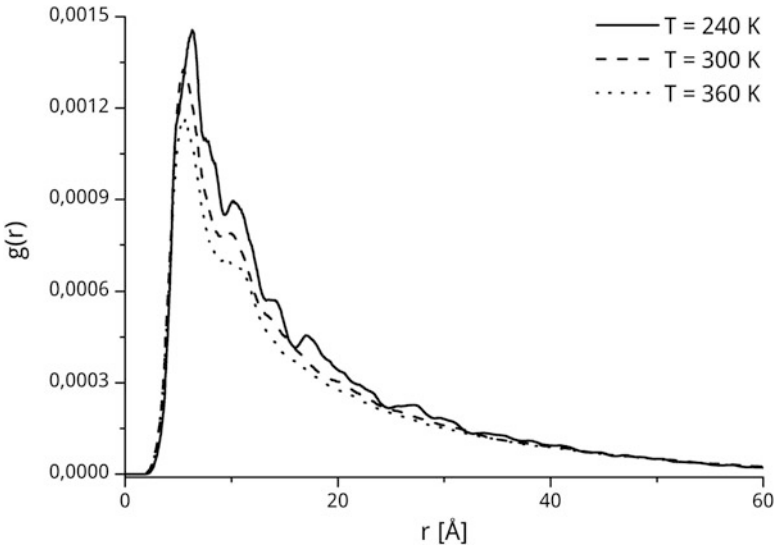

Fig. 2.3 The radial distribution function of the center of mass of 5CB molecule

The $\left\langle |\Delta\vec{r}(t)|^2 \right\rangle$ plots and related values of D show that the 5CB molecules became more mobile with an increasing of the temperature of the system.

The plot of $\left\langle |\Delta\vec{r}(t)|^2 \right\rangle$ for the lowest temperature studied is typical for the solid state. The shape of $g(r)$ for this temperature, shown in Fig. 2.3, confirms that 5CB molecules are in the solid state, because first and next peaks are sharp and clearly visible. The first peak of $g(r)$ function corresponds to the nearest neighbor distance, and next peaks reflect a distance to the further neighbors. Contrary to $g(r)$ at the lowest temperature, the next peaks at higher temperatures studied are not so much visible. Only the first and second peaks can be observed for the higher temperatures. The differences in $g(r)$ plots between the lowest and the highest temperatures indicate an occurrence of the phase transition.

To confirm this conclusion, the evolution of the Lindemann index δ_L is shown in Fig. 2.4, where the "jump" between 270 and 300 K is observed. This jump indicates the phase transition between these temperatures.

In the Fig. 2.3 one can observe small shift of the maximum of $g(r)$ plot for the first peak at the $T = 240$ K, comparing to the other temperatures. It means that the orientation at the lowest temperature differs from these at the higher. As we pointed earlier, the 5CB molecules tried to penetrate C60 surface at the higher temperatures. The shift is caused by an attempt to penetrate the fullerene wall by mesogen molecules, when they have higher kinetic energy. 5CB molecules are not able to destroy C60 surface because the interaction between fullerenes is strong.

We have also calculated the thermal activation of translational diffusion for the studied system, using the Arrhenius law:

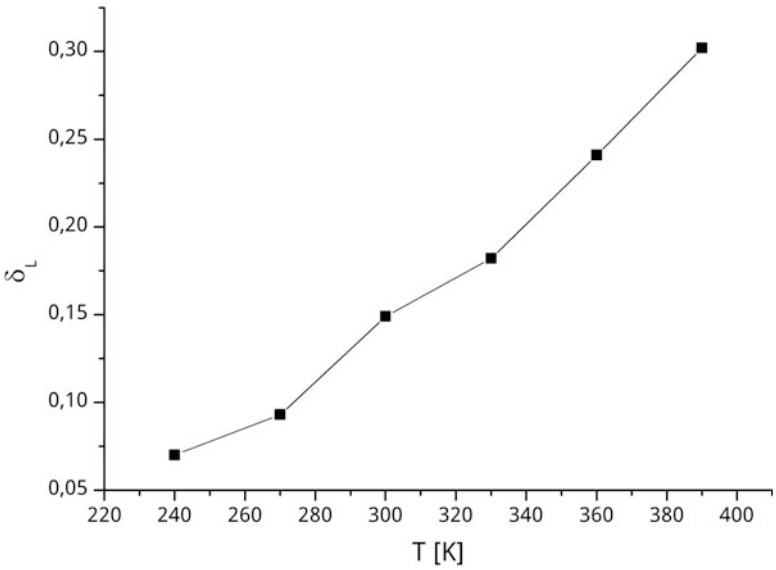

Fig. 2.4 The evolution of Lindemann index obtained for 5CB molecules

$$D = D_0 \exp\left(\frac{E_A}{k_B T}\right),$$

where k_B is the Boltzmann constant and E_A is the activation energy. Fitting data with the Arrhenius law allowed us to estimate the diffusion activation energy E_A, which is equal to 1799 K.

Figure 2.5 shows the values of the second-rank order parameter P_2, averaged over all time steps. The values of P_2 parameter diminish almost linearly with the heating of the cluster up to the temperature equal to 330 K. For the higher temperatures, the declines of the value of P_2 are practically unnoticeable.

2.4 Conclusions

5CB molecules tried to penetrate C60 surface by immersing themselves between fullerene molecules. This process proceeds with the heating of the system.

At the lowest temperature studied, the mesogen molecules are in the solid state. We have found that the phase transition occurs between $T = 270$ and 300 K.

The orientation of 5CB molecules differs in various temperatures. It is caused by an attempt to penetrate fullerene surface by liquid crystal molecules.

The behavior of 5CB molecules on the C60 surface was examined because it can be interesting for potential applications, for example, in nanotechnology.

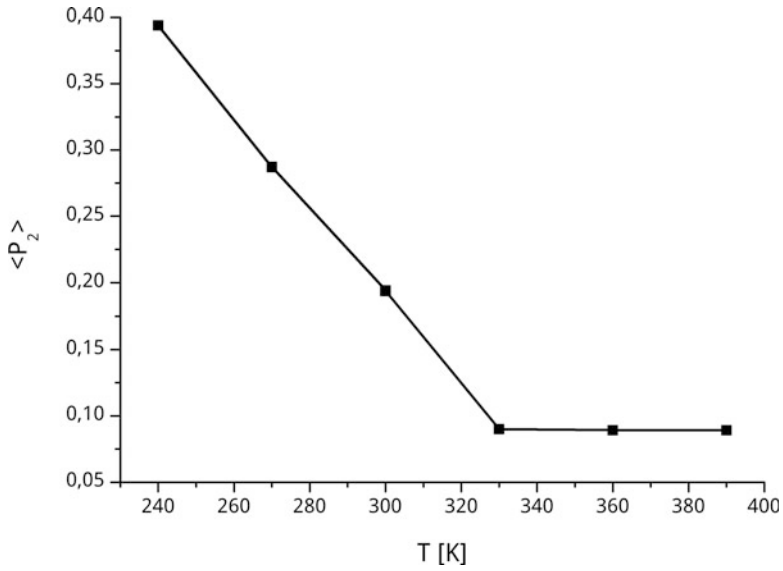

Fig. 2.5 The evolution of second rank order parameter obtained over all time steps, for 5CB molecules

References

1. Yan XQ, Lu YJ (2015) Mechanism of abnormally slow crystal growth of CuZr alloy. J Chem Phys 143:164503. doi:10.1063/1.4934227
2. Ewiss MAZ, Moawia F, Stoll B (2007) Molecular alignment of the 4-octyl-4′-cyanobiphenyl liquid crystal filled with SiO2. Liq Cryst 34:127–133. doi:10.1080/02678290601076213
3. Gwizdala W, Gorny K, Gburski Z (2008) Molecular dynamics and dielectric loss in 4-cyano-4-n-pentylbiphenyl (5CB) mesogene film surrounding carbon nanotube—computer simulation. J Mol Struct 887:148–151. doi:10.1016/j.molstruc.2007.12.045
4. Bag S, Maingi V, Maiti PK, Yelk J, Glaser MA, Walba DM, Clark NA (2015) Molecular structure of the discotic liquid crystalline phase of hexa-peri-hexabenzocoronene/oligothiophene hybrid and their charge transport properties. J Chem Phys 143:144505. doi:10.1063/1.4932373
5. Gwizdala W, Gorny K, Gburski Z (2011) The dynamics of 4-cyano-4-n-pentylbiphenyl (5CB) mesogen molecules located between graphene layers-MD study. Spectrochim Acta Mol Biomol Spectrosc 79:701–704. doi:10.1016/j.saa.2010.08.040
6. Shahinyan AA, Hakobyan PK, Arsenyan LH, Poghosyan AH (2012) The study of lyotropic liquid crystal structure using the molecular dynamics simulation method. Mol Cryst Liq Cryst 561:155–169. doi:10.1080/15421406.2012.687174
7. Gorny K, Raczynski P, Dendzik Z, Gburski Z (2015) Odd-even effects in the dynamics of liquid crystalline thin films on the surface of single walled carbon and silicon carbide nanotubes: computer simulation study. J Phys Chem C 119:19266–19271. doi:10.1021/acs.jpcc.5b05961
8. Stieger T, Schoen M, Mazza MG (2014) Effects of flow on topological defects in a nematic liquid crystal near a colloid. J Chem Phys 140:054905. doi:10.1063/1.4862953

9. Iijima S (1991) Helical microtubules of graphitic carbon. Nature 354:56–58. doi:10.1038/354056a0
10. Skrzypek A, Dendzik Z, Brol P, Gburski Z (2004) Cluster and layers of fullerene molecules between graphite planes. J Mol Struct 704:287–290. doi:10.1016/j.molstruc.2004.02.045
11. Tong L, Liu Y, Dolash BD, Jung Y, Slipchenko MN, Bergstrom DE, Cheng J-X (2012) Label-free imaging of semiconducting and metallic carbon nanotubes in cells and mice using transient absorption microscopy. Nat Nanotechnol 7:56–61. doi:10.1038/nnano.2011.210
12. Keren S, Zavaleta C, Cheng Z, de la Zerda A, Gheysens O, Gambhir SS (2008) Noninvasive molecular imaging of small living subjects using Raman spectroscopy. Proc Natl Acad Sci 105:5844–5849. doi:10.1073/pnas.0710575105
13. Dawid A, Gburski Z (2003) Rayleigh light scattering in fullerene covered by a spherical argon film—a molecular dynamics study. J Phys: Condens Matter 15:2399–2405. doi:10.1088/0953-8984/15/14/315
14. Welsher K, Sherlock SP, Dai H (2011) Deep-tissue anatomical imaging of mice using carbon nanotube fluorophores in the second near-infrared window. Proc Natl Acad Sci 108:8943–8948. doi:10.1073/pnas.1014501108
15. Delogu LG, Vidili G, Venturelli E, Ménard-Moyon C, Zoroddu MA, Pilo G, Nicolussi P, Ligios C, Bedognetti D, Sgarrella F, Manetti R, Bianco A (2012) Functionalized multiwalled carbon nanotubes as ultrasound contrast agents. Proc Natl Acad Sci 109:16612–16617. doi:10.1073/pnas.1208312109
16. Raczynski P, Dawid A, Gburski Z (2005) Depolarized light scattering in small fullerene clusters—computer simulation. J Mol Struct 744:525–528. doi:10.1016/j.molstruc.2004.12.064
17. Ali-Boucetta H, Kostarelos K (2013) Carbon nanotubes in medicine & biology—therapy and diagnostics. Adv Drug Deliv Rev 65:1897–1898. doi:10.1016/j.addr.2013.11.002
18. Phillips JC, Braun R, Wang W, Gumbart J, Tajkhorshid E, Villa E, Chipot C, Skeel RD, Kalé L, Schulten K (2005) Scalable molecular dynamics with NAMD. J Comput Chem 26:1781–1802. doi:10.1002/jcc.20289
19. Humphrey W, Dalke A, Schulten K (1996) VMD—visual molecular dynamics. J Mol Graph 14:33–38
20. Tiberio G, Muccioli L, Berardi R, Zannoni C (2009) Towards in silico liquid crystals realistic transition temperatures and physical properties for n-cyanobiphenyls via molecular dynamics simulations. ChemPhysChem 10:125–136. doi:10.1002/cphc.200800231
21. Hilder TA, Pace RJ, Chung S-H (2012) Computational design of a carbon nanotube fluorofullerene biosensor. Sensors 12:13720–13735. doi:10.3390/s121013720
22. D'Avino G, Muccioli L, Zannoni C (2015) From chiral islands to smectic layers: a computational journey across sexithiophene morphologies on C60. Adv Funct Mater 25:1985–1995. doi:10.1002/adfm.201402609

Chapter 3
Nanoindentation of DMPC Layer by Nanotubes of Various Diameters

Violetta Raczyńska, Przemysław Raczyński, Krzysztof Górny, and Zygmunt Gburski

3.1 Introduction

Phospholipid and cholesterol molecules are the essential components of a membrane of eukaryotic cells. The role of cell membrane, particularly its part called phospholipid bilayer, is to protect the cell interior from the outside environment [1–3]. The recent researches indicate nanotubes as the potential nanocontainers for delivering cargo (medicaments) to the living cells [4–9]. That is because several experiments show that the carbon nanotubes (CNTs) can penetrate the cell membrane and enter the interior of the cells [10–13]. Unfortunately, this mechanism is still not well known.

It is a challenging task to better understand the interactions between biomembranes and CNTs. There are only a few computer simulations of these systems [14–16]. However, either these simulations were not performed in fully atomistic way or only nanotube with one diameter was taken into account. In this work we make the next step to observe in details how carbon nanotubes can penetrate cell membrane. We prepared the model of one phospholipid layer consisting of DMPC (80 %) and cholesterol molecules (20 %) [2].

Recent studies have shown that carbon nanotube could be considered as a potential candidate for nanoscale vehicle, able to deliver cargo to the biological cell. From this point of view, it is a challenging task to appropriately choose the optimal diameter of a nanotube, to ensure the integrity of membrane during the penetration process and to deliver maximal possible cargo to the cell. Our studies allow to better understand the mechanism of penetration of the bilayer by CNTs with various diameters.

V. Raczyńska (✉) • P. Raczyński • K. Górny • Z. Gburski
Institute of Physics, University of Silesia, Uniwersytecka 4, 40-007 Katowice, Poland
e-mail: vraczynska@gmail.com

O. Fesenko, L. Yatsenko (eds.), *Nanophysics, Nanophotonics, Surface Studies, and Applications*, Springer Proceedings in Physics 183,
DOI 10.1007/978-3-319-30737-4_3

3.2 Simulation Details

All fully atomistic simulations were performed with NAMD 2.8 simulation code [17–22] and visualized with VMD 1.8.7 [23]. Phospholipid layer consisted of 120 DMPC (1,2-dimyristoyl-*sn*-glycero-3-phosphocholine) and 25 cholesterol molecules. Above the lipid heads (about 9 Å), the single-walled carbon nanotube was placed. From the bottom, the layer was underpinned by fixed graphene sheet to prevent shifting of the layer by nanotube. Cholesterol and DMPC were modelled using CHARMM 27 force field [24]. CHARMM-based force field was also employed for CNTs [25].

First, the model of the lipid layer was prepared and equilibrated for 2 ns to obtain the initial configurations of molecules. Afterwards, the CNT was added and the system was equilibrated for 2 ns again. During these processes, CNT was held fixed. Next, the CNT started to be pushed towards the layer.

The steered molecular dynamics (SMD) method was used to push CNT inside the layer. Springs were added between the most distant (from the layer) rings of CNT carbon atoms, and imaginary points were moving with constant velocity perpendicularly to the layer surface. Force constant was set to 10 kcal mol^{-1} Å^{-2} for each spring.

Three different pulling velocities were studied: 0.5, 1.5 and 2.5 m/s. Four nanotubes with different diameters were embedded into the layer ($d \approx 9.5$, 13.5, 16 and 20 Å). The physical variables studied (force, work and potential of mean force (PMF)) were obtained from ten independent simulation runs. During runs the system was controlled by means of Langevin thermostat. All simulations were performed in NVT ensemble, at physiological temperature $T = 310$ K. The periodic boundary conditions were applied to the layer (x and y axis). The molecules forming the layer are oriented with their heads towards CNT. The snapshot of the initial configuration (before start of the nanoindentation process) of the system with CNT with diameter 16 Å is shown in Fig. 3.1a.

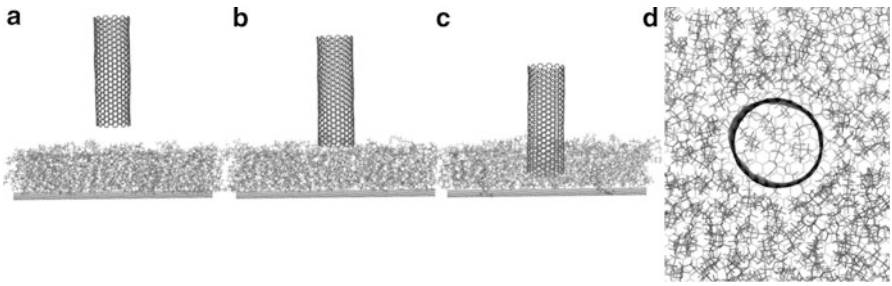

Fig. 3.1 The snapshot of the layer penetration by CNT with diameter $d = 16$ Å and with pulling velocity $v = 0.5$ m/s, for three penetration depths d: (**a**) first simulation step, (**b**) CNT reaches lipid layer, (**c**) and (**d**) CNT pressed apart phospholipid backbones and moves along hydrocarbon chains

3.3 Results

Figure 3.1 shows the snapshot of next stages of the nanoindentation process with the pulling velocity $v = 0.5$ m/s.

Figure 3.1a shows the system with carbon nanotube of diameter $d = 16$ Å and the layer after equilibration process but before the start of nanoindentation. Figure 3.1b shows CNT reaching the lipid layer and Fig. 3.1c shows one end of CNT between DMPC and cholesterol tails. Figure 3.1d shows the same moment of simulation run as Fig. 3.1c, but it is a view from the top. It is not clearly visible in Fig. 3.1c, d but we have checked that one of the DMPC molecules is inside CNT and another one is pushed by CNT. Another DMPC and cholesterol molecules were pressed apart laterally by the nanotube.

Figure 3.1 shows that the molecules (DMPC or cholesterol) which form the layer can fit inside CNT; however, it is possible in the case of three nanotubes with the largest diameter $d = 13.5$, 16 and 20 Å. In the case of CNT with the smallest diameter $d = 9.5$ Å, we did not observe molecule inside CNT in any simulation run.

We have also calculated the total force F required to push CNT into phospholipid layer. Figure 3.2 shows two examples of average forces (calculated from each independent run), for the nanotube with diameter $d = 13.5$ and 20 Å, as a function of the indentation depth z. Zero on the x-axis corresponds to moment when CNT reaches DMPC heads.

Force required to perform indentation is of the order of nanonewtons. The maximal value of the force F increases with increasing pulling velocity and is the highest for the highest speed studied, $v = 2.5$ m/s. Initially, CNT spreads DMPC polar heads and moves between them. During this motion the force gradually grows.

When CNT reaches the level of DMPC hydrophobic chains, the force grows rapidly because large amount of it is required to move apart glycerol backbone. This moment of passing CNT through layer corresponds to maximal value of the force. Next, when the nanotube starts its shifting through hydrocarbon chains, the force begin to diminish.

We have not observed any differences between the forces required for nanoindentation taking into account the various diameters of the applied CNTs. As an example, Fig. 3.3 shows the force required for the highest nanoindentation speed and for all nanotubes studied. The lack of differences is mainly due to the fact that the nanotube practically in each simulation run pushes lipid molecules, but CNTs with larger diameter do not push a larger number of lipid molecules than those with smaller diameter. Note that CNT barges DMPC heads (not tails), so relatively very few molecules are oriented in a way enabling pushing. On the other hand, in the case of nanotubes with larger diameter, only a few lipids are located inside the nanotube, so it is not necessary to push a larger number of molecules by CNTs with larger diameter. This is the cause of no significant differences between the values of average force required to pierce phospholipid layer.

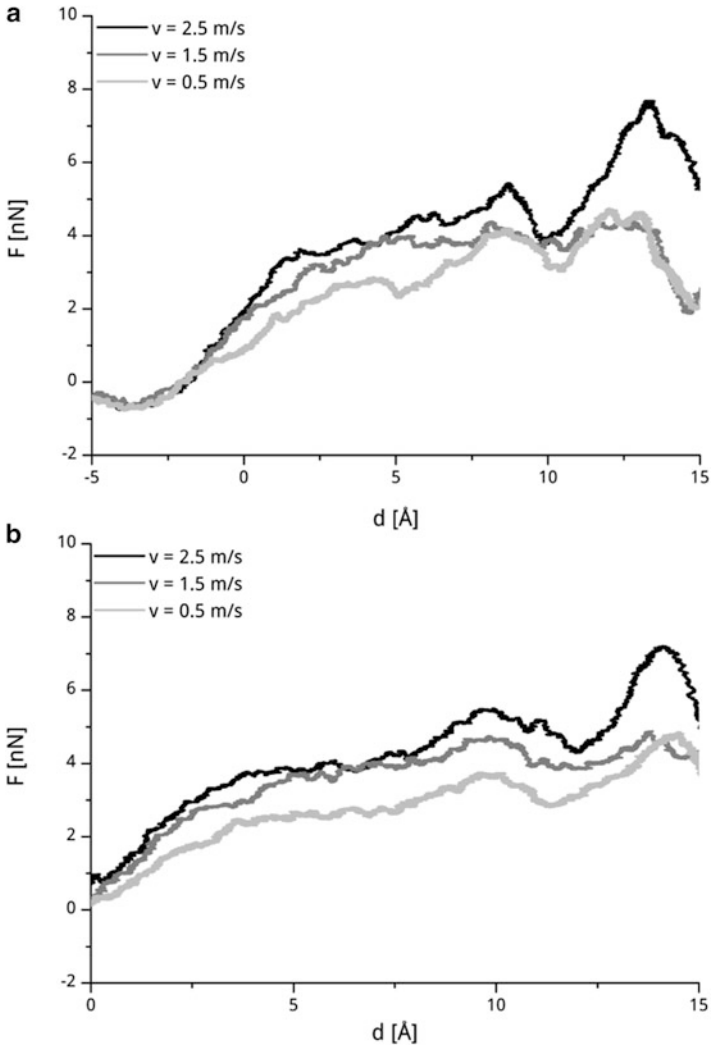

Fig. 3.2 The average force required to pierce phospholipid layer versus penetration depth for CNTs with diameters $d = 16$ Å (**a**) and $d = 20$ Å (**b**)

Figure 3.4 shows the average work performed when the CNTs were pushed through the layer. The work was calculated using equation

$$W(d) = \int_{d_0}^{d} F(z)\,\mathrm{d}z,$$

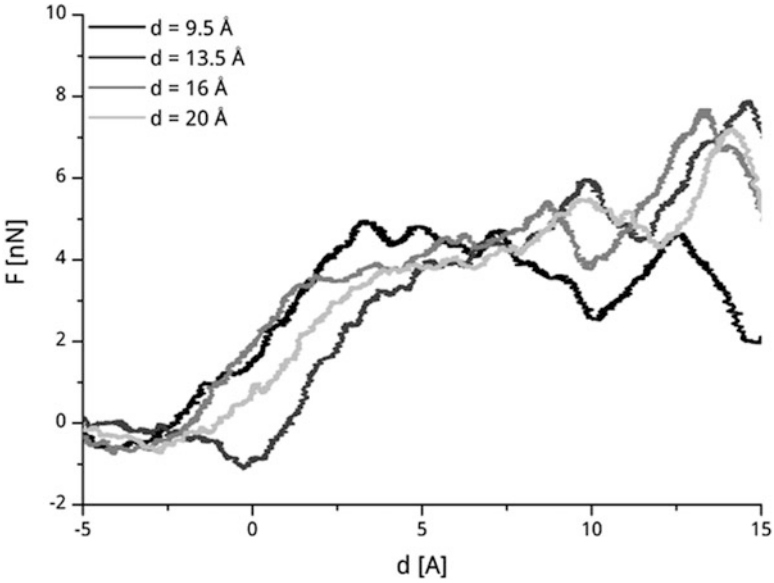

Fig. 3.3 Comparison of average force required for pulling the CNT with different diameters through phospholipid layer versus indentation depth and for the highest speed $v = 2.5$ m/s

where the force F is a function of indentation depth d and d_0 is the initial location of carbon nanotube.

In Fig. 3.4, we present examples of work for CNTs with diameters $d = 7$ and $d = 13.5$ Å.

The average work required to pierce phospholipid layer is the largest for the largest nanoindentation speed and the smallest for the smallest speed. For the largest and medium speeds, the plots are located close to each other which means that the average work required to push CNT through the layer is similar. The differences are more significant comparing these speeds with the smallest, because its plots are not located in the immediate vicinity.

We have also calculated potential of mean force (PMF) using Jarzynski equality [26, 27]:

$$\exp^{-\Delta F/kT} = \exp^{-W/kT},$$

where ΔF is the change of free energy of the system, W is the work done over the system, k is the Boltzmann constant and T is the temperature of the system in the equilibrium state or the temperature of the heat reservoir with which the system was thermalized before the process took place. PMF was calculated with second-order cumulant expansion:

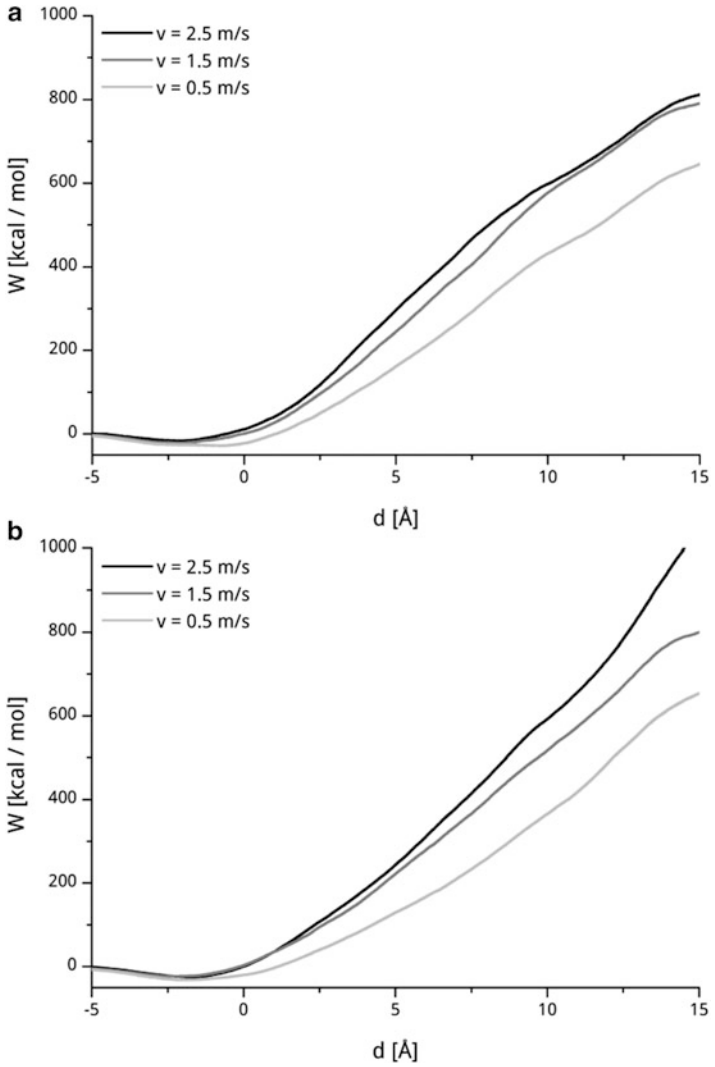

Fig. 3.4 The average work required to pierce phospholipid layer versus penetration depth for CNTs with diameters $d = 9.5$ Å (**a**) and $d = 16$ Å (**b**)

$$\Delta F(t) = \langle W(t) \rangle - \frac{1}{2kT} \left(\left\langle W(t)^2 \right\rangle - \langle W(t) \rangle^2 \right).$$

Figure 3.5 presents the comparison between PMF curves for all speeds and for CNTs with diameter $d = 10$ and 15 Å.

It can be observed that for both nanotubes, the free energy barrier decreases with decreasing of the pulling velocity. With the indentation depth, the values of PMF increase until the nanotube reaches massive and densely packed phospholipid

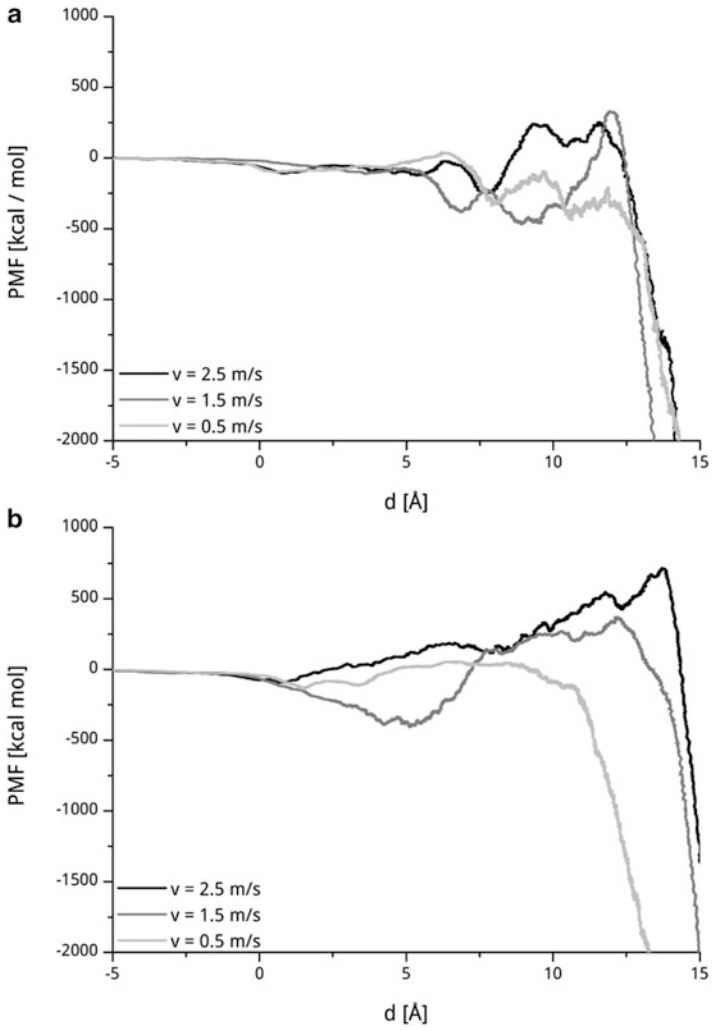

Fig. 3.5 The potential of mean force (PMF) versus penetration depth for CNTs with diameters $d = 13.5$ Å (**a**) and $d = 20$ Å (**b**)

backbones and tails. The values of PMF are relatively small when the CNTs are moving through loosely packed lipid tails. In case of the smallest speed, CNTs barge lipids gently, comparing to the others.

3.4 Conclusions

A series of computer simulations concerning the nanoindentation of lipid layer by CNTs with various diameters was performed using SMD method. Our simulations show that nanotube can pierce through the layer. We do not notice significant differences in the nanoindentation process regarding CNT diameters, but there are changes with regard to the indentation speed. The force, work and potential of mean force needed to pierce the layer diminish with the reduction of the indentation speed.

Our findings allow better understanding of the interactions between CNTs and membranes that might be helpful for future real-life experiments using carbon nanotubes as the indenters.

References

1. Alberts B (2008) Molecular biology of the cell. Garland Science, New York
2. Sperelakis N (2012) Cell physiology sourcebook essentials of membrane biophysics. Elsevier/AP, Amsterdam
3. Nelson DL, Cox MM, Lehninger AL (2013) Lehninger principles of biochemistry. W.H. Freeman, New York
4. Kam NWS, Liu ZA, Dai HJ (2006) Carbon nanotubes as intracellular transporters for proteins and DNA: an investigation of the uptake mechanism and pathway. Angew Chem Int Ed Engl 45:577–581. doi:10.1002/anie.200503389
5. Losic D, Simovic S (2009) Self-ordered nanopore and nanotube platforms for drug delivery applications. Expert Opin Drug Deliv 6:1363–1381. doi:10.1517/17425240903300857
6. Bhirde AA, Patel V, Gavard J, Zhang G, Sousa AA, Masedunskas A, Leapman RD, Weigert R, Gutkind JS, Rusling JF (2009) Targeted killing of cancer cells in vivo and in vitro with EGF-directed carbon nanotube-based drug delivery. ACS Nano 3:307–316. doi:10.1021/nn800551s
7. Sokol M, Dawid A, Dendzik Z, Gburski Z (2004) Structure and dynamics of water—molecular dynamics study. J Mol Struct 704:341–345. doi:10.1016/j.molstruc.2004.02.048
8. Heister E, Neves V, Lamprecht C, Silva SRP, Coley HM, McFadden J (2012) Drug loading, dispersion stability, and therapeutic efficacy in targeted drug delivery with carbon nanotubes. Carbon 50:622–632. doi:10.1016/j.carbon.2011.08.074
9. Gburski Z, Górny K, Raczynski P (2010) The impact of a carbon nanotube on the cholesterol domain localized on a protein surface. Solid State Commun 150:415–418. doi:10.1016/j.ssc.2009.12.005
10. Porter AE, Gass M, Bendall JS, Muller K, Goode A, Skepper JN, Midgley PA, Welland M (2009) Uptake of noncytotoxic acid-treated single-walled carbon nanotubes into the cytoplasm of human macrophage cells. ACS Nano 3:1485–1492. doi:10.1021/nn900416z
11. Raffa V, Ciofani G, Nitodas S, Karachalios T, D'Alessandro D, Masini M, Cuschieri A (2008) Can the properties of carbon nanotubes influence their internalization by living cells? Carbon 46:1600–1610. doi:10.1016/j.carbon.2008.06.053
12. Debouzy JC, Crouzier D, Flahaut E (2010) Hydrophobic double walled carbon nanotubes interaction with phopholipidic model membranes: 1H-, 2H-, 31P NMR and ESR study. Environ Toxicol Pharmacol 30:147–152. doi:10.1016/j.etap.2010.05.002

13. Obataya I, Nakamura C, Han S, Nakamura N, Miyake J (2005) Nanoscale operation of a living cell using an atomic force microscope with a nanoneedle. Nano Lett 5:27–30. doi:10.1021/nl0485399
14. Wallace EJ, Sansom MSP (2008) Blocking of carbon nanotube based nanoinjectors by lipids: a simulation study. Nano Lett 8:2751–2756. doi:10.1021/nl801217f
15. Raczynski P, Gorny K, Pabiszczak M, Gburski Z (2013) Nanoindentation of biomembrane by carbon nanotubes—MD simulation. Comput Mater Sci 70:13–18. doi:10.1016/j.commatsci.2012.12.031
16. Raczyński P, Górny K, Dawid A, Gburski Z (2014) Delivery of nitric oxide to the interior of mammalian cell by carbon nanotube: MD simulation. Arch Biochem Biophys 554:6–10. doi:10.1016/j.abb.2014.04.014
17. Phillips JC, Braun R, Wang W, Gumbart J, Tajkhorshid E, Villa E, Chipot C, Skeel RD, Kalé L, Schulten K (2005) Scalable molecular dynamics with NAMD. J Comput Chem 26:1781–1802. doi:10.1002/jcc.20289
18. Kale L, Skeel R, Bhandarkar M, Brunner R, Gursoy A, Krawetz N, Phillips J, Shinozaki A, Varadarajan K, Schulten K (1999) NAMD2: greater scalability for parallel molecular dynamics. J Comput Phys 151:283–312. doi:10.1006/jcph.1999.6201
19. Frenkel D, Smit B (2001) Understanding molecular simulation: from algorithms to applications, 2nd edn. Academic Press, Orlando, FL
20. Gburski Z (1985) Convergence of memory functions for the vibrational dephasing process in liquids. Chem Phys Lett 115:236–240. doi:10.1016/0009-2614(85)80687-4
21. Rapaport DC (2004) The art of molecular dynamics simulation. Cambridge University Press, New York
22. Gwizdala W, Górny K, Gburski Z (2008) Molecular dynamics and dielectric loss in 4-cyano-4-n-pentylbiphenyl (5CB) mesogene film surrounding carbon nanotube—computer simulation. J Mol Struct 887:148–151. doi:10.1016/j.molstruc.2007.12.045
23. Humphrey W, Dalke A, Schulten K (1996) VMD: visual molecular dynamics. J Mol Graph Model 14:33–38. doi:10.1016/0263-7855(96)00018-5
24. MacKerell AD Jr, Banavali N, Foloppe N (2000) Development and current status of the CHARMM force field for nucleic acids. Biopolymers 56:257–265. doi:10.1002/1097-0282(2000)56:4<257::AID-BIP10029>3.0.CO;2-W
25. Alexiadis A, Kassinos S (2008) Molecular simulation of water in carbon nanotubes. Chem Rev 108:5014–5034. doi:10.1021/cr078140f
26. Jarzynski C (1997) Nonequilibrium equality for free energy differences. Phys Rev Lett 78:2690–2693. doi:10.1103/PhysRevLett.78.2690
27. Jarzynski C (1997) Equilibrium free-energy differences from nonequilibrium measurements: a master-equation approach. Phys Rev E 56:5018–5035. doi:10.1103/PhysRevE.56.5018

Chapter 4
The Study of Properties of Paracetamol Clusters: MD Simulations

Violetta Raczyńska and Zygmunt Gburski

4.1 Introduction

Paracetamols' chemical name is *N*-acetyl-*p*-aminophenol or acetaminophen. It is a readily available, over-the-counter antipyretic and analgesic compound, and it is very often used to treat mild to moderate pain or fever. It is rapidly and completely metabolized to form inactive metabolites, which can be easily eliminated from body [1, 2]. Paracetamol and other biologically important compounds are now intensively studied [3–14].

Our studies were performed using molecular dynamics (MD) simulations technique. It is a frequently used method applied for a wide range of research, including paracetamol systems [15–28].

Here, we present and discuss obtained results for a small paracetamol clusters consisted of 30 or 80 molecules, since MD simulations of paracetamol clusters have not been reported so far. The size of the clusters was selected in a way that in the bigger cluster, an internal core was developed. We compare obtained results for these clusters with the bulk sample, composed of 600 paracetamol molecules placed inside the cubic simulation cell. Several temperatures, ranging from 100 to 600 K, were taken into account. The temperature interval was equal to 50 K.

Our fully atomistic studies will be helpful to better understand intermolecular interactions between these one of the most used molecules, in the context of human health.

V. Raczyńska (✉) • Z. Gburski
Institute of Physics, University of Silesia, Uniwersytecka 4, 40-007 Katowice, Poland
e-mail: vraczynska@gmail.com

O. Fesenko, L. Yatsenko (eds.), *Nanophysics, Nanophotonics, Surface Studies, and Applications*, Springer Proceedings in Physics 183,
DOI 10.1007/978-3-319-30737-4_4

4.2 Materials and Methods

All simulations were performed using molecular dynamics method. The initial configurations of all systems were obtained from the series of NVT simulations (2×10^6 time steps). In the case of the bulk sample to obtain the initial configurations, we also included NPT simulations with the assumption of the atmospheric pressure (1 atm).

All simulations, where the data were collected, were performed in NVT ensemble for 20 ns and with the time step equal to 1 fs (2×10^7 time steps).

The paracetamol molecules were modeled with CHARMM36 force field [29, 30].

The system composed of 600 molecules was simulated with periodic boundary conditions. The initial size of the cubic box, where the molecules of paracetamol were located, was equal to $5.2 \times 5.2 \times 5$ nm.

MD simulations were performed with NAMD 2.8 program [31, 32] and visualized in VMD [33].

4.3 Results

The instantaneous configurations of all simulated systems, at the closest to the physiological temperature studied, $T = 300$ K, are shown in Fig. 4.1.

In the clusters, the molecules keep together and are arranged in this way that the systems adopt the energetically favorable, spherical shape. In the system composed of $n = 80$ molecules, some of them formed an inner core. In the smallest system, the number of molecules is too small to form the core, and in the largest, with periodic boundary conditions, each acetaminophen is surrounded by other molecules.

One of the calculated observables is the mean square displacement $\left\langle |\Delta\vec{r}(t)|^2 \right\rangle$, where $< \Delta\vec{r}(t) > = < \vec{r}(t) - \vec{r}(0) >$ and $\vec{r}$ is the position of the center of mass of single molecule. Figure 4.2a, b, c show the temperature dependence of the mean square displacement of the center of mass of paracetamol for all systems studied.

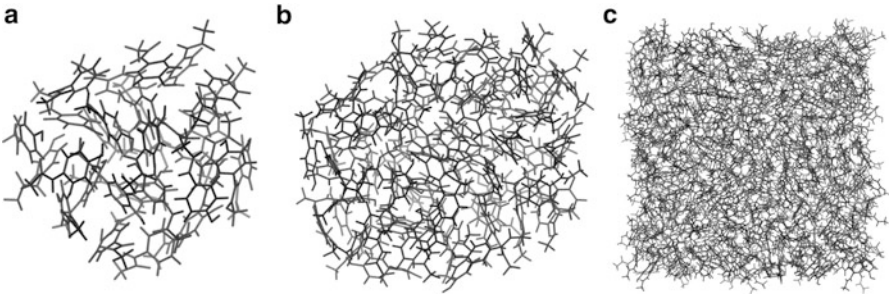

Fig. 4.1 The instantaneous configurations of the system consisted of (**a**) $n = 30$, (**b**) $n = 80$, (**c**) $n = 600$ (bulk sample) paracetamol molecules, at $T = 300$ K

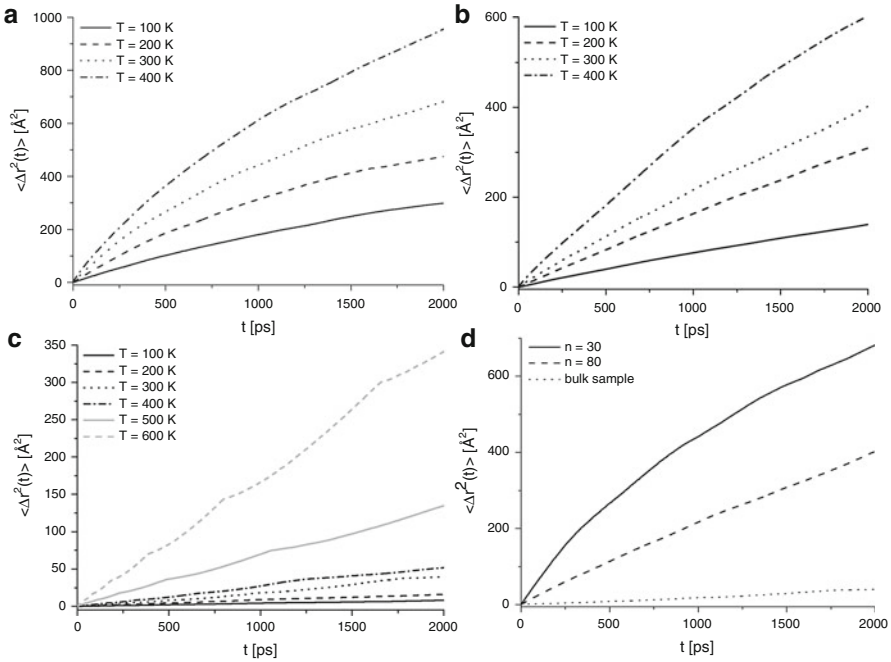

Fig. 4.2 The mean square displacement of the center of mass of paracetamol: (**a**) the temperature dependence for the cluster composed of $n = 30$ molecules, (**b**) the temperature dependence for the cluster composed of $n = 80$ molecules, (**c**) the temperature dependence for the bulk sample, (**d**) the comparison between the smaller and the larger cluster and the bulk sample at $T = 300$ K

Figure 4.2d shows the comparison of $\left\langle |\Delta \vec{r}(t)|^2 \right\rangle$ between smaller and larger clusters and bulk sample. To increase the clarity of presented data, only first 2 ns, containing the linear part of the $\left\langle |\Delta \vec{r}(t)|^2 \right\rangle$, is shown.

The plots of the $\left\langle |\Delta \vec{r}(t)|^2 \right\rangle$ in Fig. 4.2a–c show that the dynamics of molecules increase with the heating of the system and they are more mobile and move relatively faster.

The plots of the mean square displacement for the clusters are shown only to $T = 400$ K, whereas for the bulk sample is shown up to $T = 600$ K. The clusters started to vaporize at $T = 500$ K, so the plots for the highest temperatures are not shown (the clusters vaporize earlier). As one could expect, the smaller cluster vaporized faster ($T = 500$ K) than the larger one.

Figure 4.2d shows strong differences in dynamics between all simulated systems. Although the data in the figure are presented for only one temperature ($T = 300$ K), these differences can be observed at each temperature studied. These differences are even more pronounced when one will take into account obtained values of translational diffusion coefficient D: $\left\langle |\Delta \vec{r}(t)|^2 \right\rangle \approx 6Dt$. These values, calculated from the linear part of $\left\langle |\Delta \vec{r}(t)|^2 \right\rangle$ slope, are equal to

$D = 0.11$ Å^2/ps for the smaller cluster, $D = 0.042$ Å^2/ps for the larger cluster, and $D = 0.0024$ Å^2/ps for the bulk sample. The value of D, at $T = 300$ K, for the bulk sample is an order of magnitude lower that for the larger cluster and two orders of magnitude lower that for the smaller cluster. The dynamics of acetaminophen molecules is the highest in the smaller cluster where the inner-cluster core does not exist. In contradiction to other systems, all of the molecules in this cluster have large accessible volume to move. This facilitates their motions within accessible volume. The dynamics of molecules in the bulk sample can be compared to these forming an internal core of the cluster. They are surrounded from all sides by other molecules; this causes that they have limited volume to move—their dynamics is slower. In the cluster composed of $n = 80$ molecules, some of them form an inner core of the cluster, and some of them are located in the outer shell. Hence, the dynamics of the molecules in this system is less vigorous than in the smaller cluster but still higher than in the bulk sample.

The radial distribution function of the center of mass of paracetamol is shown in Fig. 4.3. The arrangement of the figure is similar to Fig. 4.3, but for clarity, only two temperatures ($T = 100$ K and $T = 400$ K) are shown in Fig. 4.2a–c.

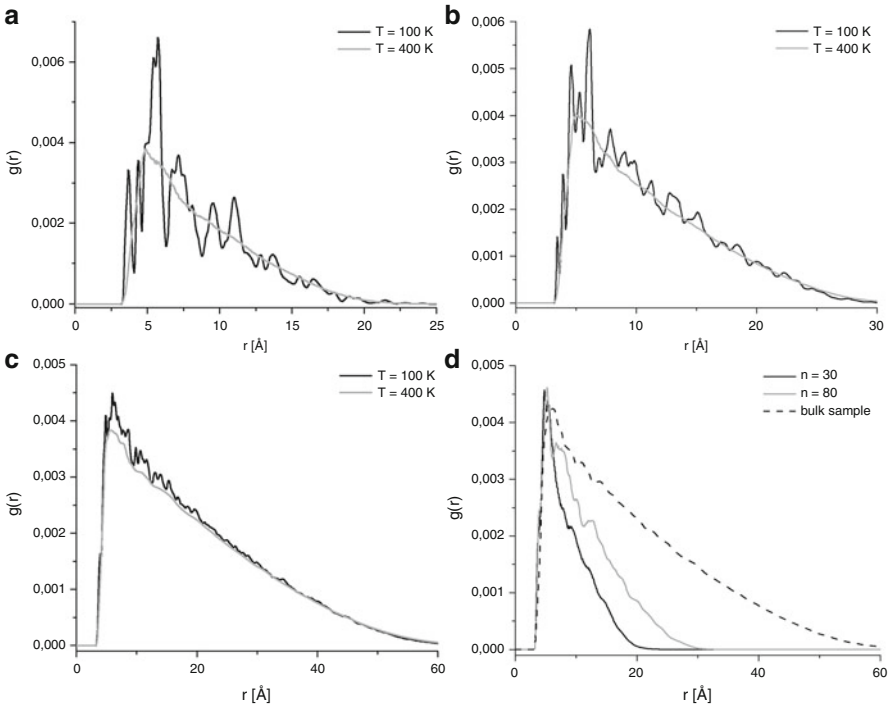

Fig. 4.3 The radial distribution function $g(r)$ of the center of mass of paracetamol: (**a**) the temperature dependence for the cluster composed of $n = 30$ molecules, (**b**) the temperature dependence for the cluster composed of $n = 80$ molecules, (**c**) the temperature dependence for the bulk sample, (**d**) the comparison between the smaller and the larger cluster and the bulk sample at $T = 300$ K

Distinct differences can be observed in Fig. 4.3a, b. The plots of $g(r)$ curves for larger and lower temperature presented vary. The shape of the curves indicates that at $T = 100$ K the clusters are in different phases than at $T = 400$ K. At $T = 100$ K, clearly visible peaks, characteristic for condensed phase, appear. At $T = 400$ K, there is only one maximum, indicating the distance to the nearest neighbors. The shape of $g(r)$ plot is similar to these, which are characteristic for the liquid state, so the clusters are in liquid phase at this temperature. This conclusion is confirmed by the $\left\langle |\Delta \vec{r}(t)|^2 \right\rangle$ plots.

The shape of the curves in Fig. 4.3c (for the bulk sample) allows to conclude that, as before, the paracetamol is in one phase at $T = 100$ K and in the another (softer, liquid like) at $T = 400$ K.

From Fig. 4.3d, the size of the cluster might be estimated. The size of the smaller cluster is equal to 22 Å, and the size of the cluster composed of the $n = 80$ molecules is equal to 31 Å. Moreover, all of the systems are in the same phase.

4.4 Conclusions

Two clusters composed of $n = 30$ and $n = 80$ molecules and the bulk sample of paracetamol were studied in a wide range of temperatures (from $T = 100$ K up to $T = 600$ K).

There are strong differences in mobility of the molecules in the studied systems. The most mobile are molecules in the smaller cluster composed of $n = 30$ paracetamol molecules. The least mobile are molecules in the bulk sample, where they have a very limited volume to move.

The molecules in the studied systems are in the condensed state at $T = 100$ K and in the liquid state at $T = 400$ K. Above this temperature clusters vaporize at $T = 500$ K.

Our studies might be helpful to understand the dynamics of biologically important paracetamol molecules in medium-size clusters.

References

1. Dar AI, Saxena RC (2013) Novel herbs for liver disorders: paracetamol induced hepatotoxicity and its herbal remedy. LAP LAMBERT Academic Publishing, Saarbrücken
2. Prescott LF (1996) Paracetamol (Acetaminophen): a critical bibliographic review. CRC Press, London
3. Pacifici GM, Allegaert K (2015) Clinical pharmacology of paracetamol in neonates: a review. Curr Ther Res Clin Exp 77:24–30. doi:10.1016/j.curtheres.2014.12.001
4. Gburski Z, Raczynski P (2010) Influence of carbon nanotube on cholesterol lodgment: molecular dynamics simulation. Rev Adv Mater Sci 23:64–69

5. Teng Y, Fan L, Dai Y, Zhong M, Lu X, Kan X (2015) Electrochemical sensor for paracetamol recognition and detection based on catalytic and imprinted composite film. Biosens Bioelectron 71:137–142. doi:10.1016/j.bios.2015.04.037
6. Mendez-Albores A, Tarin C, Rebollar-Perez G, Dominguez-Ramirez L, Torres E (2015) Biocatalytic spectrophotometric method to detect paracetamol in water samples. J Environ Sci Health A Tox Hazard Subst Environ Eng 50:1046–1056. doi:10.1080/10934529.2015.1038179
7. de Fays L, Van Malderen K, De Smet K, Sawchik J, Verlinden V, Hamdani J, Dogne J-M, Dan B (2015) Use of paracetamol during pregnancy and child neurological development. Dev Med Child Neurol 57:718–724. doi:10.1111/dmcn.12745
8. Raczynski P, Dawid A, Gburski Z (2007) Molecular dynamics (MD) in homocysteine nanosystems—computer simulation. Biomol Eng 24:577–581. doi:10.1016/j.bioeng.2007.08.011
9. Brozek W, Hassler N, Varga F, Klaushofer K, Paschalis EP (2012) Effect of bisphosphonates on gene expression of fibroblasts cultured in the presence of homocysteine. Bone 51:S8–S8. doi:10.1016/j.bone.2012.08.021
10. Huang C, Zhang L, Wang Z, Pan H, Zhu J (2011) Endothelial progenitor cells are associated with plasma homocysteine in coronary artery disease. Acta Cardiol 66:773–777. doi:10.2143/AC.66.6.2136962
11. Raczynski P, Gorny K, Samios J, Gburski Z (2014) Interaction between silicon–carbide nanotube and cholesterol domain. A molecular dynamics simulation study. J Phys Chem C 118:30115–30119. doi:10.1021/jp505532f
12. Phillips MC (2013) Thematic review series: high density lipoprotein structure, function, and metabolism new insights into the determination of HDL structure by apolipoproteins. J Lipid Res 54:2034–2048. doi:10.1194/jlr.R034025
13. Fielding C, Fielding P (1995) Molecular physiology of reverse cholesterol transport. J Lipid Res 36:211–228
14. Gburski Z, Górny K, Raczynski P (2010) The impact of a carbon nanotube on the cholesterol domain localized on a protein surface. Solid State Commun 150:415–418. doi:10.1016/j.ssc.2009.12.005
15. Xu X-T, Tang F-L, Xue H-T, Yu W-Y, Zhu L, Rui Z-Y (2015) Molecular dynamics simulations of void shrinkage in gamma-TiAl single crystal. Comput Mater Sci 107:58–65. doi:10.1016/j.commatsci.2015.05.007
16. Volz SG, Chen G (1999) Molecular dynamics simulation of thermal conductivity of silicon nanowires. Appl Phys Lett 75:2056–2058. doi:10.1063/1.124914
17. Raczynski P, Dawid A, Dendzik Z, Gburski Z (2005) Dielectric relaxation in water–cholesterol mixture cluster: molecular dynamics simulation. J Mol Struct 750:18–21. doi:10.1016/j.molstruc.2005.03.036
18. Yamakov V, Wolf D, Phillpot SR, Gleiter H (2002) Grain-boundary diffusion creep in nanocrystalline palladium by molecular-dynamics simulation. Acta Mater 50:61–73. doi:10.1016/S1359-6454(01)00329-9
19. Berneche S, Roux B (2000) Molecular dynamics of the KcsA K+ channel in a bilayer membrane. Biophys J 78:2900–2917
20. Gorny K, Dendzik Z, Raczynski P, Gburski Z (2012) Dynamic properties of propylene glycol confined in ZSM-5 zeolite matrix—A computer simulation study. Solid State Commun 152:8–12. doi:10.1016/j.ssc.2011.10.020
21. Skoulidas AI, Sholl DS (2005) Self-diffusion and transport diffusion of light gases in metal-organic framework materials assessed using molecular dynamics simulations. J Phys Chem B 109:15760–15768. doi:10.1021/jp051771y
22. Borodin O (2009) Polarizable force field development and molecular dynamics simulations of ionic liquids. J Phys Chem B 113:11463–11478. doi:10.1021/jp905220k

23. Freddolino PL, Liu F, Gruebele M, Schulten K (2008) Ten-microsecond molecular dynamics simulation of a fast-folding WW domain. Biophys J 94:L75–L77. doi:10.1529/biophysj.108.131565
24. Dendzik Z, Kosmider M, Raczynski P, Piatek A (2007) Interaction induced absorption of rare gas mixtures physisorbed on nanotubes and fullerenes—computer simulation study. J Non-Cryst Solids 353:4586–4590. doi:10.1016/j.jnoncrysol.2007.03.042
25. Greiner M, Elts E, Schneider J, Reuter K, Briesen H (2014) Dissolution study of active pharmaceutical ingredients using molecular dynamics simulations with classical force fields. J Cryst Growth 405:122–130. doi:10.1016/j.jcrysgro.2014.07.046
26. Nademi Y, Iranagh SA, Yousefpour A, Mousavi SZ, Modarress H (2014) Molecular dynamics simulations and free energy profile of paracetamol in DPPC and DMPC lipid bilayers. J Chem Sci 126:637–647. doi:10.1007/s12039-013-0556-x
27. Lim W, Feng YP, Liu XY (2005) Molecular dynamics simulation of paracetamol molecules ordering around glycogen. Phys Rev E 71:051604. doi:10.1103/PhysRevE.71.051604
28. Ohlsson A, Shah PS (2015) Paracetamol (acetaminophen) for prevention or treatment of pain in newborns. Cochrane Database Syst Rev 6:CD011219. doi:10.1002/14651858.CD011219.pub2
29. Vanommeslaeghe K, Hatcher E, Acharya C, Kundu S, Zhong S, Shim J, Darian E, Guvench O, Lopes P, Vorobyov I, Mackerell AD Jr (2010) CHARMM general force field: a force field for drug-like molecules compatible with the CHARMM all-atom additive biological force fields. J Comput Chem 31:671–690. doi:10.1002/jcc.21367
30. Yu W, He X, Vanommeslaeghe K, MacKerell AD (2012) Extension of the CHARMM general force field to sulfonyl-containing compounds and its utility in biomolecular simulations. J Comput Chem 33:2451–2468. doi:10.1002/jcc.23067
31. Phillips JC, Braun R, Wang W, Gumbart J, Tajkhorshid E, Villa E, Chipot C, Skeel RD, Kalé L, Schulten K (2005) Scalable molecular dynamics with NAMD. J Comput Chem 26:1781–1802. doi:10.1002/jcc.20289
32. Kale L, Skeel R, Bhandarkar M, Brunner R, Gursoy A, Krawetz N, Phillips J, Shinozaki A, Varadarajan K, Schulten K (1999) NAMD2: greater scalability for parallel molecular dynamics. J Comput Phys 151:283–312. doi:10.1006/jcph.1999.6201
33. Humphrey W, Dalke A, Schulten K (1996) VMD: visual molecular dynamics. J Mol Graph Model 14:33–38. doi:10.1016/0263-7855(96)00018-5

Chapter 5
Electric-Driven Magnetization Dynamics of Multilayer Nanostructures

A.M. Korostil and M.M. Krupa

5.1 Introduction

The phenomenon of spin-transfer torque has attracted increasing attention due to its potential applications in spintronic devices. This phenomenon occurs in spin-valve structures composed of two ferrimagnetic layers separated by a nonmagnetic one. A transverse (perpendicular to the layers) charge current through the device produces a flow of spin-polarized conduction electrons from the fixed layer into the free layer. This causes a direct transfer of angular momentum from the spin-polarized flowing electrons to the local magnetization of the free layer, resulting in a torque that may produce magnetization reversal or steady-state precessions with frequencies in the microwave range. This spin-transfer mechanism allows nanomagnets to be manipulated without magnetic fields, and it is the subject of extensive research for new applications in nonvolatile memory technology and radio-frequency oscillators. Up to now, the majority of investigations on the spin-transfer-driven excitations have been performed on planar spin-valve nanopillar or nanocontact structures in which a noncollinear configuration of the magnetic structure is required.

However, spin torque phenomena may also be present in collinear spin valves composed of two ferromagnetic contacts separated by a two-dimensional electron gas with spin–orbit coupling. Even in a single, uniformly magnetized ferromagnetic layer, when spin–orbit interaction is present, an in-plane current can induce a spin torque on the magnetization of the layer without the need for noncollinear ferromagnetic configuration of the structure. Here, we investigate the current-driven

A.M. Korostil (✉) • M.M. Krupa
Institute of Magnetism NASU, Vernadsky Str., 36b, Kyiv 03142, Ukraine
e-mail: amand@rambler.ru

O. Fesenko, L. Yatsenko (eds.), *Nanophysics, Nanophotonics, Surface Studies, and Applications*, Springer Proceedings in Physics 183,
DOI 10.1007/978-3-319-30737-4_5

spin–orbit-mediated spin torque for the case of an arbitrary magnetization orientation and a linear in momentum.

5.2 Characteristic Features of Current-Driven Magnetization

The interrelation between the spin-polarized current and magnetization in magnetic multilayer nanostructures, permitting their mutual control, constitutes the basis of the operation of novel nano-devices with properties of a magnetic random-access memory (MRAM), magnetic logic, and coherent microwave radiation sources that present considerable fundamental and application interest [1–6]. The operation of these devices relies on the spin-polarized current-induced magnetization switching together with tunnel magnetoresistance effect and the like-induced magnetization precession [1–3].

The electric control of the magnetization in the mentioned magnetic nanostructures occurs through the exchange interaction between the spin current and localized spins of the controlled magnetization. This interaction generates the torque of the magnetization causing its switching or precession [3, 4, 7–12]. The magnitude of the torque is directly dependent on the degree of the spin polarization and its formation mechanism, which must provide the passage of the spin current into the region of the controlled magnetization.

The spin polarization of the input electric current in the magnetic nanostructures can be produced by the effective bias field of the *s*-*d*-exchange interaction in the magnetic layer acting as a spin polarizer. The spin polarization occurs as the result of the spin splitting of the electron band spectrum on the two branches with and without their intersection by the Fermi level that corresponds to two- and single-channel conductions of the electrons with different spin projections relatively to the magnetization. In the usual two-channel case, the majority electrons with the spin projection parallel to the magnetization occupy the one conduction channel, and the minority electrons with the spin projection antiparallel to the magnetization occupy the another conduction channel. This results in the incomplete spin polarization of the electric current. In the single-channel case, which is realized for magnetic semimetals (Fig. 5.1), the conduction electrons with the fixed spin projection occupy only one conduction band because electron spins become like directed and the spin polarization of the electric current becomes complete (Fig. 5.1).

The impact of the control electric current on the magnetization occurs through the exchange interaction between the corresponding spin-polarized current and the controlled localized spins. The passage of the spin-polarized current into the controlled magnetic nanolayer causes the spin torque exerting the magnetization switching or precession.

In the mentioned case, the transfer electron charges into the controlled magnetic layer results in thermal losses and increase of a power consumption. This imposes

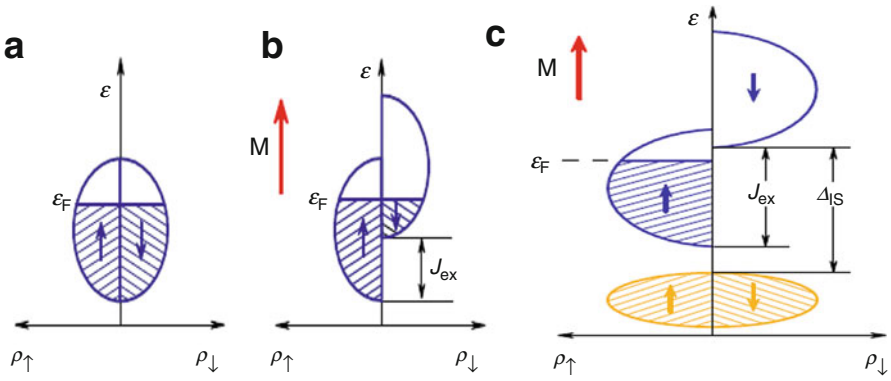

Fig. 5.1 Scheme of the spin splitting of the band spectrum caused by the exchange interaction J_{ex}, where $\rho_\uparrow$ and $\rho_\downarrow$ are the densities of electron states with different spin projections ($\uparrow$, $\downarrow$) and **M** is the magnetization vector: (**a**) and (**b**) non- and ferromagnetic metals; (**c**) magnetic semimetals

restrictions on contact sizes, which have to provide the threshold density of the spin current subject to the condition that the electric current does not exceed the value of an electrical breakdown. These problems can be avoided by the utilizing the spin–orbit interaction for the spin polarization. In this case, the exchange interaction of the spin current with the localized spins is provided without passage of the charge current in the magnetic nanolayer [1, 2, 7].

The spin–orbit interaction in the two-dimensional systems with of the broken structure inversion symmetry, known as the Rashba spin–orbit interaction [1–3], is realized in the interfaces of the magnetic nanostructures with two-dimensional electron properties and an interfacial potential drop. In a single-electron approximation, this interaction, within a constant multiplier, is described by the two-dimensional expression for a quasi-relativistic correction [2]. Taking into account the electric field $\boldsymbol{E} = E_z \cdot \boldsymbol{z}$ along growth direction z, the corresponding Rashba Hamiltonian can be represented as

$$H_R = \boldsymbol{B}_R \boldsymbol{\sigma}, \quad \boldsymbol{B}_R = \left(\frac{\alpha_R}{\hbar}[\boldsymbol{z} \times \boldsymbol{p}]\right), \tag{5.1}$$

where $\alpha_R \sim E_z$ is the Rashba parameter, $\boldsymbol{B}_R$ is the effective Rashba magnetic field which is dependent on the electron momentum $\boldsymbol{p}$ and σ is the vector of the Pauli spin matrices. Equation 5.1 describes the characteristic properties of the Rashba spin–orbit interaction, although in realistic systems, the broken inversion symmetry causes distorts of the free electron wave functions near the atomic nuclei and, consequently, it changes in spin–orbit interaction [2]. Due to (5.1), the effective Rashba field $\boldsymbol{B}_R$ exerts the spin precession of the conduction electrons. In addition, one leads to the symmetric spin splitting of the single-electron dispersion along the conduction electron momentum that experimentally observed in interfaces of magnetic nanostructures [2] (see Fig. 5.2).

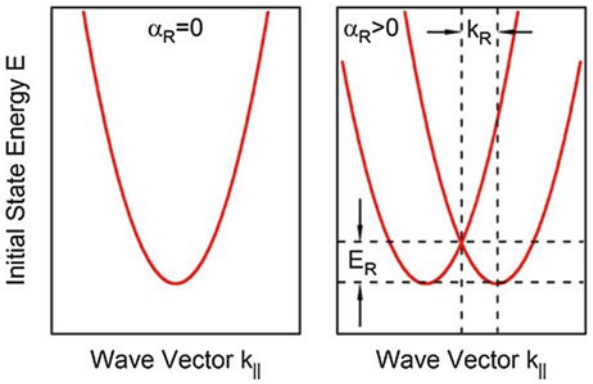

Fig. 5.2 The dispersions of the two-dimensional electron gas before (on the *left*) and after (on the *right*) the Rashba spin–orbit interaction causing the spin splitting along the planar momentum vector $k_{||}$; a_R is the Rashba parameter, and k_R is the offset away from $k_{||} = 0$ of the spectral curves relative to the initial position

The spin-polarized electric current lies in the plane of the magnetic layer, and one does not pass in the normal direction. Its intersection with the localized magnetization occurs through *s-d*-exchange interaction of the form $H_{sd} = J_{sd}\boldsymbol{S} \cdot \sigma$, where $J_{sd} \sim J_c$, where J_c is the input electric current, and $\boldsymbol{S}$ is the localized spin. Thereby, the change of the input electric current results in the corresponding change of the magnetization. The application of an electric field along the vector $\boldsymbol{z}$ results in changes of the Rashba parameter and magnetization dynamics. However, the last is restricted only by the magnetization switching.

The spin polarization of the electric current can be caused by the spin Hall effect, in which the passage of the electric current through heavy metal (for instance, Pt, Ta) with the strong spin–orbit interaction exerts the spin-dependent transverse deviation of the electric current and the transverse pure spin current. The spin orientation of the latter is perpendicular to the electric current and the interface normal. The electric current lies in the plane of the adjacent heavy metal nanolayer and do not pass into the magnetic nanolayer. This avoids the mentioned constraints on contact sizes in the magnetic nanostructure and leads to reduction of the threshold current densities and the energy consumption.

The rise of the additional transverse momentum component $\boldsymbol{p}_{\sigma\perp}$ in the spin Hall effect is proportional to the derivative with respect to the momentum $\boldsymbol{p}$ of the spin–orbit interaction $H_{so} = \beta[\nabla V \times \boldsymbol{p}]\boldsymbol{\sigma}$, i.e., $\boldsymbol{p}_{\sigma\perp} \sim \beta[\boldsymbol{\sigma} \times \nabla V]$. From the solutions of the Schrödinger Hamiltonian with the spin–orbit interaction, it follows that the action of the latter on the conduction electrons is equivalent to the action of the effective spin-dependent Lorentz force $\boldsymbol{F}_\sigma \sim [\boldsymbol{v} \times \boldsymbol{B}_\sigma]$ (where $\boldsymbol{v}$ is the electron velocity and $\boldsymbol{B}_\sigma$ is the spin-dependent effective magnetic field). The effective field $\boldsymbol{B}_\sigma$ causes the transverse deviation of the electric current with generation of the transverse spin current in the spin Hall effect. The charge current passes along the heavy metal nanolayer, and the generated spin current passes into the controlled magnetic layer where the exchange interaction through the torque changes the magnetization dynamics causing the magnetization switching or precession. Depicted in Fig. (5.3) is the scheme of the generation spin current and its influence on the magnetization in the magnetic nanolayer.

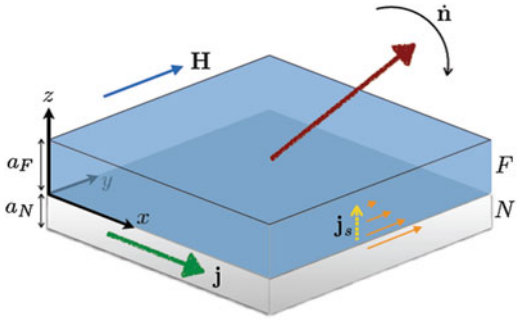

Fig. 5.3 The spin Hall effect of the spin–orbit conversion of the input electric current $\boldsymbol{j}$ in the transverse spin current $\boldsymbol{j}_S$ with the spin polarization denoted by arrows along the y axis in the two-layered magnetic nanostructure. The latter is composed of the bottom layer made of heavy normal metal (N) and the strong spin–orbit interaction and the upper ferromagnetic layer (F). The spin current exerts on the dynamics of magnetization **n** of the magnetic layer; **H** is external magnetic field

5.3 Spin Torques Due to Electric-Driven Magnetization

The impact of the spin-polarized electric current on the magnetization dynamics in the transition metal-based magnetic nanolayer is described in the framework of the *s-d* model. In this model, the exchange interaction occurs between itinerant electrons of *sp* type with the spin $\boldsymbol{s}=(\hbar/2)\sigma$ and localized electrons of *d* type with the spin $\boldsymbol{S_d}$ (5.2). The states of this system are described by the Hamiltonian

$$H = \left(\frac{\boldsymbol{p}^2}{2m} + V(\boldsymbol{r})\right) - J_{sd}(\boldsymbol{s}\cdot\boldsymbol{S_d}) + \frac{1}{mc^2}[\nabla V \times \boldsymbol{p}]\boldsymbol{s} \tag{5.2}$$

where the term separated by bracket is the kinetic and potential energies, the second term is the *s-d*-exchange interaction with the *s-d*-exchange constant J_{sd}, and the third term is the spin–orbit interaction. Introducing the spinor wave functions $\Psi(\boldsymbol{r},t)$, the local spin density of itinerant electrons $\boldsymbol{m} = \Psi^*(\boldsymbol{r},t)\,\boldsymbol{s}\,\Psi(\boldsymbol{r},t)$, and local spin current density $\boldsymbol{J}_s = -(\hbar/m)[\Psi^*(\boldsymbol{r},t)\boldsymbol{s}\,\nabla_r\Psi^*(\boldsymbol{r},t)]$ and performing a quantum-mechanical averaging, expression (5.2) can be transformed to the form

$$H = \left(\frac{\boldsymbol{p}^2}{2m} + V(\boldsymbol{r})\right) - J_{\mathrm{ex}}(\boldsymbol{m}\cdot\boldsymbol{M}) + \frac{1}{mc^2} < [\nabla V \times \boldsymbol{p}]\,\boldsymbol{s} > \tag{5.3}$$

where $\boldsymbol{M}$ is the unit vector of the localized magnetization. From the Hamiltonian (5.3), the spin density continuity equation for the carriers can be deduced. This together with the Landau-Lifshitz-Gilbert equation for the magnetization result in the system

$$\begin{aligned}\frac{d\boldsymbol{m}}{dt} &= \nabla J_s - \frac{J_{\text{ex}}}{\hbar}\boldsymbol{M}\times\boldsymbol{m} + \frac{1}{mc^2} < [\nabla V \times \boldsymbol{p}] \times \boldsymbol{s} >, \\ \frac{d\boldsymbol{M}}{dt} &= -\gamma \boldsymbol{M}\times\boldsymbol{H} + \alpha \boldsymbol{M}\times\frac{d\boldsymbol{M}}{dt} + \frac{J_{\text{ex}}}{\hbar}\boldsymbol{M}\times\boldsymbol{m},\end{aligned} \tag{5.4}$$

where $\boldsymbol{H}$ is the effective field, γ is the gyromagnetic ratio, and α is the Gilbert damping. The last term is the current-induced spin torque $\boldsymbol{T}$. Assuming a uniformly magnetized nanolayer ($\nabla J_s = 0$) in the steady-state condition, the out-of-equilibrium torque on the magnetization is directly proportional to the spin density of conduction electrons:

$$\boldsymbol{T} = \frac{J_{\text{ex}}}{\hbar}\boldsymbol{M}\times\boldsymbol{m} = \frac{1}{mc^2} < [\nabla V \times \boldsymbol{p}] \times \boldsymbol{s} > \tag{5.5}$$

The spin torque due to (5.5) depends on the electric field, the exchange interaction, and spin–orbit interaction. Without the latter, the Fermi surfaces of majority and minority bands are for the carrier spins pointing parallel and antiparallel to the magnetization. When applying an electric field, the Fermi surface of each band is shifted, but the amount of spins in excess is exactly balanced by the amount of lacking spins. The net spin density generated by the Fermi surface shift for both spin populations is then zero, i.e., there is no nonequilibrium spin density and thus the spin torque is zero.

If there is only spin–orbit interaction but without exchange interaction between the background magnetization and the itinerant spins, the Fermi surfaces are two spheres with the spin direction perpendicular to the electron momentum. When the electric field displaces the Fermi surfaces in the direction of the current, each band gains a net spin density with an opposite sign. Since these two Fermi spheres have different radii, the total spin density is thus finite. However, these electric field-induced spin densities do not exert a torque on the local magnetization due to the absence of the exchange interaction.

Thus, one needs both spin–orbit interaction and the exchange interaction to generate the current-driven spin torque. The Rashba spin–orbit interaction produces the nonequilibrium spin density proportional to the current density, and the exchange interaction couples the electron spin density with the local magnetization.

It is interesting to compare the spin torque with the conventional spin-transfer torque (STT). First of all, the spin-transfer torque comes from the absorption of the transverse spin current by the magnetization, and thus it requires a noncollinear magnetization configuration in the direction of the spin current (e.g., spin-valve structures or domain walls). The electrical current must flow perpendicular to the plane of the layers. In general, the STT possesses two components, referred to as in plane and out of plane. The former generally dominates the latter and directly competes with the damping torque. Consequently, the STT induces magnetization switching [13, 14] as well as steady high-frequency magnetic precessions [15]. The present spin–orbit-induced spin torque is created by the intrinsic (or extrinsic, in

case of impurity-induced SOI) spin–orbit coupling in the nonequilibrium condition, and thus it does not involve the transfer of the conduction electron spin to the magnetization. Then, this torque exists for a uniformly magnetized single layer with the current applied in the plane of the layer and acts as an effective field. Since the torque does not compete with the damping, it cannot excite current-driven steady magnetization precessions.

References

1. Zutic L, Fabian J, Das Sarma S (2004) Spintronics: fundamentals and applications. Rev Mod Phys 76:323
2. Manchon A, Koo HC, Nitta J, Frolov SM, Duine RA (2015) New perspective for Rashba spin–orbit coupling. Nat Mater 36:871
3. Sinova J, Valenzuela S, Wunderlich J, Back CH, Jungwirth T (2015) Spin Hall effects. Rev Mod Phys 87:1213
4. Manchon A, Zhang S (2009) Theory of spin torque due to spin–orbit coupling. Phys Rev B79:094422
5. Zhang S (2009) Theory of spin torque due to spin-orbit coupling. Phys Rev B79:094422
6. Manchon A, Zhang S (2009) Theory of spin torque due to spin-orbit coupling. Phys Rev B79:094422
7. Liu RH, Lim WL, Urazdin S (2015) Control of current-induced spin–orbit effects in a ferromagnetic heterostructure by electric field. Phys Rev B89:220409
8. Ando K, Takahashi S, Harii K, Sasage K, Ieda J, Maekawa S, Saitosh E (2008) Electric manipulation of spin relaxation in a film using spin-Hall effect. Phys Rev Lett 101:036601
9. Tserkovnyak J, Bender SA (2014) Spin Hall phenomenology of magnetic dynamics. Phys Rev B90:014428
10. Liu L, Moriyama T, Ralph DC, Buhram RA (2011) Spin-torque ferromagnetic resonance induced by the spin Hall effect. Phys Rev Lett 106:036601
11. Liquao LL, Pai CF, Tsen HV, Ralph DC, Buhrman RA (2012) Spin-torque switching with the giant spin Hall effect of Tantalum. Science 336:555
12. Volkov NV (2012) Spintronics: manganite-based magnetic tunnel structures. Phys Usp 55:250
13. Katine JA, Albert FJ, Buhram RA, Myers EB, Ralph DC (2000) Current-driven magnetization reversal and spin-wave excitation in Co/Cu/Co pillars. Phys Rev B8:3149
14. Slonczewski JC (1996) Current-driven excitation of magnetic multilayers. J Magn Magn Mater 159:L1
15. Kiselev SL, Sankey JC, Krivorotov IN, Emly NC, Schoelkopf TJ, Buhrman RA, Ralph DC (2003) Microwave oscillations of a nanomagnet driven by a spin-polarized current. Nature 425:380

Chapter 6
Phenomenological Models of Photoinduced Transition in Spin-Crossover Materials

Iurii Gudyma and Artur Maksymov

6.1 Introduction

In the last decades the interest in the synthetic molecular magnets has been increased due to their application as multifunctional materials with tuning properties. Among molecular magnetic materials especial attention deserves the spin-crossover complexes which may have considerable application in the contemporary nanoelectronics and spintronics. The spin-crossover phenomenon was discovered by L. Cambi in 1931 [1]. It was observed in the coordination complexes with the octahedral symmetry with central situated transition metals ion with $d^4 - d^7$ electronic configuration. In these materials spin state can change from the low-spin (LS) state to the high-spin (HS) one with increase in temperature or action of external stimuli such as light irradiation, pressure, and magnetic field [2–4]. Changes of magnetic and electrical properties as well as color give to the scientists the confidence that it is possible to use these materials as the memory storage, optical displays, or multifunctional sensors [2].

For the first time studies of the spin transition in synthetic iron (II)-based spin-crossover had been performed by König and Madeja in the 1967s [5]. Their extensive magnetic and Mössbauer spectroscopic studies on synthetic complexes

Iu. Gudyma (✉)
Chernivtsi National University, Kotsubynski Str., Nr. 2, Chernivtsi 58012, Ukraine
e-mail: yugudyma@gmail.com

A. Maksymov
Chernivtsi National University, Kotsubynski Str., Nr. 2, Chernivtsi 58012, Ukraine

Advanced Material Research Institute, University of New Orleans, 2000 Lakeshore Drive, New Orleans, LA 70148, USA
e-mail: maxyartur@gmail.com

O. Fesenko, L. Yatsenko (eds.), *Nanophysics, Nanophotonics, Surface Studies, and Applications*, Springer Proceedings in Physics 183,
DOI 10.1007/978-3-319-30737-4_6

gave the explanation of the nature of spin transition in some of the first iron (II) spin-crossover complexes.

Since the moment of discovering the spin-crossover phenomenon, the temperature controlled transition was in the focus of interest [6]. The interesting points of the thermally activated interconversion between LS and HS states are related to the relative simple way of its detection and possibility to obtain large hysteresis loop. The disadvantages of transition of this kind lie in low switching rate between the state and small quantum efficiency. Nevertheless, the recent entropy studies of spin-crossover system with two order parameters reported in [7] increase the attractiveness of temperature induced spin-crossover transition.

A discovery in 1984 of the photoinduced phase transition (PIPT) [8] from LS to HS [known as the light-induced excited spin-state trapping (LIESST)] in a Fe (II) complex generated a lot of scientific literature devoted to this field of research in this way emphasizing the heightened interest to the transitions of this kind. The ability to have the ultrafast light-controlled devices of the nanoscopic size looks very promising and it can considerably contribute to the applications of spin-crossover compounds. The main advantage of light-induced transition among the others possible for spin-crossover compounds (temperature-induced, by pressure action, magnetic field, and others) lies in the highest interconversion rate between the HS and LS states supported by quantum efficiency very close to 1.

The light-induced kinetics based on competition between photoexcitation and relaxation gives birth to various hysteresis under light [2], as the light-induced thermal hysteresis [LITH] or the light-induced optical hysteresis [LIOH] [9]. The transitions from the one side to the other in the vicinity of such hysteresis can be induced by interactions with the environment. This interaction that leads to nonlinear stochastic kinetic is typically described by a thermal noise [10–12]. The role of noise and its spectral compositions may be crucial for nonstationary behavior of nonequilibrium system, especially during phase transition of different kind [13, 14].

The nonlinear stochastic behavior of a system with external periodic driving force represents important precondition for stochastic resonance phenomena. Stochastic resonance is a cooperative phenomenon arising from the interplay between deterministic and random dynamics in a nonlinear system wherein the coherent response to a deterministic monochromatic signal can be enhanced by the presence of an optimal amount of noise [15, 16]. The importance of the stochastic resonance phenomenon in noise driven system is related to emphasizing the efficient role of noise that can have new possibility for practical application especially in data-secured telecommunication systems.

In the present chapter is examined the kinetics of transition in the light-induced spin-crossover system in contact with thermostat. The theoretical analysis supported by numerical calculations was performed on macroscopic phenomenological model described by Langevin kinetics with corresponding Fokker–Planck formalism. The provided studies are organized as follows: in the second section we examined the macroscopic kinetics driven by relaxation term, reflecting the temperature dependent transition. We began with the white noise action avoiding the consideration of its time correlation, which is the simplest way to describe the nonequilibrium stochastic behavior. Then we put the focus on the system with

non-Markovian stochastic processes by considering the non-zero noise autocorrelation time. This is more realistic description of the system contacting with environment. The third section is devoted to the detailed examination of stochastic resonance as a potential possibility of experimental detection of stochastic behavior and practical applications of noise driven nonlinear systems.

6.2 Macroscopic Kinetics of Photoinduced Spin-Crossover System

6.2.1 Stochastic Kinetic Driven by Relaxation Term

The successful attempts to describe the dynamics of a system being in contact with an environment playing a role of the heat bath are based on the concept of the Langevin equation. Such approach may be used for any system in that each process has, in fact, its time scale. Then, all degrees of freedom can be decomposed into slow and fast degrees of freedom. One selects some relevant degrees of freedom and treats the rest as a bath in form of additive noise. System has two distinct mechanism for time evolution—regular motion and random or disorganized motion. The random forces induced by environment are correlated on a very small time scale compared to the characteristic relaxation time for the system, around a locally stable state. Thereby the evolution of spin-crossover system perturbed by noise can be described by a one-variable nonlinear Langevin equation, written in terms of transition rates.

Applied force can be written in the alternative form

$$f(n_H) = -\frac{\partial U_\beta(n_H)}{\partial n_H}, \tag{6.1}$$

where the dynamic potential U_β is defined as a Lyapunov function and depends on the HS fraction n_H and fixed parameter β. The dynamic potential may be defined as

$$U_\beta(n_H) - U_\beta(n_H^g) = -\int_0^{n_H} f(x)dx \tag{6.2}$$

and the potential U_β satisfies inequalities

$$\begin{array}{rcll} U_\beta(n_H) & \geq & 0 & \text{non} - \text{negativity} \\ \int \exp\left[-U_\beta(n_H)\right] dn_H & < & \infty & \text{normability.} \end{array} \tag{6.3}$$

Here $U_\beta(n_H^g)$ is the global minimum of $U_\beta(n_H)$ corresponding to the stable state of the system. The similar approach exploiting conception of dynamic potential was previously used in [10, 17, 18] and recently in [19].

The presence of a noise component can unexpectedly modify the behavior of the corresponding deterministic (noiseless) equation, therefore it must be described in Langevin approximation as follows:

$$\frac{dn_H}{dt} = f(n_H) + \xi(t), \tag{6.4}$$

where $\xi(t)$ indicates the noise induced by the environment.

The Langevin equation represents the direct noisy driving of the stochastic dynamics of the relevant variable n_H and describes the dynamics of a system in the presence of an interaction with environment (similar to model A in critical phenomena, see [20, 21]). The stability of the high-spin states in spin-crossover compounds with respect to the influence of the external thermal white noise has been first studied in [10]. The detailed theoretical analysis of the nonlinear kinetics in spin-crossover solids under cross-correlated noises was provided in paper [22].

An idealized treatment assumes the random force in Eq. (6.4) $\xi(t)$ as a white Gaussian noise with zero means and a zero-ranged correlation functions $\xi(t)\xi(t+\Delta t) = 2\varepsilon^2\delta(\Delta t)$, where ε is the noise strength. Equation (6.4) with the mentioned correlation function completely defines the evolution of the system. For white noise case Eq. (6.4) represents the mathematical fact that

$$n_H(t+\Delta t) = n_H(t) + f(n_H)\Delta t + \int_0^{\Delta t} \xi(s)ds \tag{6.5}$$

and may be computed in the limit of $\Delta t \to 0$.

In general the noise represents the hierarchical coupling of the system to the heat bath. In terms of generalized functions, the Gaussian white noise is a derivative of the Wiener process. Therefore, one can show that the Fokker–Planck equivalent of Eq. (6.4) in Stratonovich's interpretation, defining the evolution of the system transition probability, is given in [23]

$$\frac{\partial P(n_H,t)}{\partial t} = -\frac{\partial}{\partial n_H}[f(n_H)P(n_H,t)] + \frac{\partial^2}{\partial n_H^2}P(n_H,t), \tag{6.6}$$

where $P(n_H,t)$ is the probability distribution function, defined so that the value $P(n_H,t)dn_H$ is the probability to find a diffusive particle in the position n_H at time t. In the case of the natural or instantly reflected boundary condition the probability flux does not exist. The steady state solution of Eq. (6.6) is easily found to be

$$P_{st} = N \cdot \exp\left[\int_0^{n_H} \frac{f(y)}{\varepsilon^2}dy\right], \tag{6.7}$$

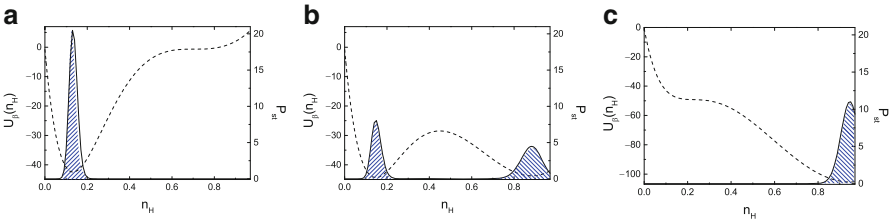

Fig. 6.1 The evolution of dynamic potential $U_\beta(n_H)$ (*solid lines*) and corresponding probability distribution function $P_{st}(n_H)$ (*dash dot lines*) for various self-acceleration coefficients α. The additive noise intensity is $\varepsilon = 0.01$

where N is a normalization constant. The simplest way to analyze the stochastic dynamics of the system expressed by Eq. (6.4) is to take the Boltzmann–Gibbs form of the stationary probability function

$$P_{st} \sim \exp(-U_\beta(n_H)/\varepsilon^2). \tag{6.8}$$

The extremes of potential $U_\beta(n_H)$ correspond to the stationary fixed points of system dynamics. For a bistable system, the probability distribution has two maxima which correspond to the steady states.

Figure 6.1 presents bistable ranges for values of α leading to bistable behavior for the control parameter of the systems $\beta = 0.081$ which gives two equivalent depth of potential wells. This bistability appears for $\alpha \leq 4.8$ (a) and disappears for $\alpha \geq 5.7$ (c). Part (b) is for $\alpha = 5.14$ and indicates to the equalization of two peaks of probability distribution function and satisfies coexistence conditions for both states. This case answers the equilibrium point where half of the low-spin fractions cross the potential barrier and become the high-spin ones. Further increase of α leads to the formation of another metastable state situated in opposite side from the last one. Here parts (a) and (c) correspond to the spinodal points identified as the values of a above (a) and below (c) which $U_\beta(n_H)$ develops a local non-zero minimum.

6.2.2 *Kinetics with Non-Markovian Stochastic Processes*

In the simplest form, the evolution of a spin-crossover system perturbed by noise can be described by a one-variable nonlinear equation, written in terms of transition rates as is given by Eq. (6.4). The presence of a noisy term can modify in an unexpected way the behavior of the corresponding deterministic (noiseless) equation; this is why it must be described in Langevin approach at the least. In a previous work [10], it was studied the stability of the high-spin states in spin-crossover compounds with respect to the influence of the external thermal white noise.

Recently [22], the state diagrams of the spin-crossover system have been built for the interplay between parametric and additive noise using the concept of a Gaussian white noise with zero correlation time. But a real noise has a finite (perhaps small, but not zero) correlation time. In this case, the hypothesis of white noise, although suitable for a general description of the process, does not explore all the possibilities of a real noise.

Now we assume that $\xi(t)$ describes the realistic noise sources with a finite correlation time. The noise $\xi(t)$ is considered stationary and Gaussian distributed with zero mean and correlation function

$$\xi(t)\xi(t+\Delta t) = \Phi(\Delta t). \tag{6.9}$$

The spectral density given by the Fourier transform of the correlation function is frequency dependent, hence the term "colored noise." In our study, an exponential correlation function $\Phi(\Delta t) = (1/\tau)\exp(-\Delta t/\tau)$ has been used, with τ describing the time scale. Videlicet τ is the noise correlation time. This time-correlated noise is the Ornstein–Uhlenbeck process, which can describe the behavior of the system in a better approach to the physical reality.

The time-correlated noise with this correlation function implies two-dimensional Markovian process, i.e.,

$$\dot{n_H} = f(n_H) + \xi(t) \tag{6.10}$$

$$\dot{\xi} = -\xi/\tau + (\sigma/\tau)\varepsilon(t), \tag{6.11}$$

where $\dot{n_H}$, $\dot{\xi}$ means the derivative of n_H and ξ with respect of t. For the concerned system, the noise intensity σ indicates the amplitude of the instantaneous fluctuations during the change of the high-spin fraction. These fluctuations represent the cumulative effects of many weakly coupled environmental degrees of freedom.

In Eq. (6.11), $\varepsilon(t)$ is the white Gaussian noise with zero mean and correlation function

$$\varepsilon(t)\varepsilon(t+\Delta t) = 2\delta(\Delta t). \tag{6.12}$$

In the absence of noise (faster variable), the deterministic dynamics is given by

$$\begin{aligned} \dot{n_H} &= f(n_H) + \xi(t), \\ \dot{\xi} &= -\xi/\tau. \end{aligned} \tag{6.13}$$

The Equation. (6.13) has three fixed points at $\xi(t) = 0$: two locally stable fixed points (stable nodes) and an unstable fixed point (saddle point). In Fig. 6.2 we show several trajectories calculated for various correlation times.

The separatrix dividing the two basins of attraction is indicated by a dotted line. The system starting at the left stable node will reach the right stable node only after

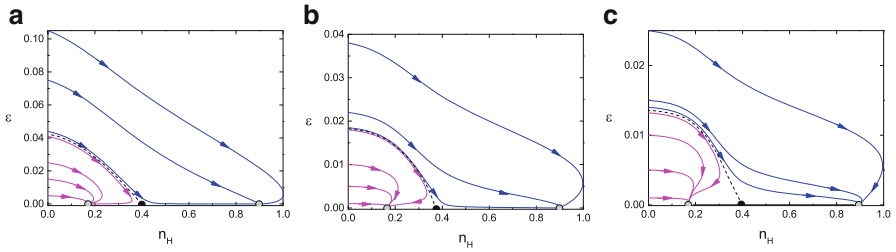

Fig. 6.2 Bistable flow diagram with $\tau = 10$ (**a**), $\tau = 30$ (**b**), $\tau = 50$ (**c**). The *arrow lines* show evolution of the system to the stable states. The *dotted lines* are separatrixes, which divide two basins of attraction

having crossed the separatrix under the noise. As described in paper [24] for small correlation times, the actual escape takes place at large values of $\xi(t)$. At $\varepsilon = 0$ on the line are located three fixed points (two empty semicircles indicate the stable nodes, filled semicircle—the saddle point) which correspond to a completely deterministic case. When increasing the noise, the stationary states shift to smaller values. If coloration of noise augments, then this shift becomes more significant and nonlinear. Taking into account the scaling of flow diagrams in Fig. 6.2, we can also see that with τ increasing, the system moves rapidly toward the separatrix and then relaxes to the corresponding stable fixed points.

In the following, we derived the kinetic equation of spin-crossover system driven by Ornstein–Uhlenbeck noise. For this we eliminate the variable $\xi(t)$ in Eqs. (6.10), (6.11) and make a scaling of the time variable according to $\widehat{t} = t\tau^{-1/2}$. This then yields

$$n_H + \gamma(n_H, \tau)\dot{n_H} - f(n_H) = \sigma\varepsilon\left(\tau^{1/2}\widehat{t}\right) \tag{6.14}$$

where $\gamma(n_H, \tau) = \tau^{-1/2} - \tau^{1/2} f'(n_H)$. In regions of n_H space for which $\gamma(n_H, \tau) > 0$, the nonlinear damping approaches infinity both for the $\tau \to 0$ and $\tau \to \infty$. Neglecting the velocity variations (i.e., $n_H = 0$), we find that the non-Markovian flow in combined Eqs. (6.10), (6.11) is approximated by a truly one-dimensional Markovian process. According to a "unified colored-noise approximation" [25], a set of Eqs. (6.10) and (6.11) reduces to an equation that is linear in $\dot{n_H}$, but nonlinear in n_H. The result is a stochastic differential equation with a multiplicative Markovian noise

$$\dot{n_H} = \gamma^{-1}(n_H, \tau) f(n_H) + g(n_H, \tau)\varepsilon(\widehat{t}), \tag{6.15}$$

where the noise amplitude $g(n_H, \tau) = \tau^{-1/4}\sigma\gamma^{-1}(n_H, \tau)$ and $\varepsilon(\widehat{t})\varepsilon(\widehat{t} + \Delta\widehat{t}) = 2\delta(\Delta\widehat{t})$. Master equation in the form (6.15) can be used for kinetic studies of nonequilibrium spin-crossover systems driven by colored noise in the same way as spin-crossover systems under influence of multiplicative white noise [22, 26].

6.3 Noise Driven Resonance Phenomena in Photoinduced Spin-Crossover System

In the system with additive noise action, the transition between its states is possible, but it is a very rare event unless the values of intensity of additive noise are comparable or larger than the height of the potential barrier. It can be shown that an external weak periodic modulation is introduced in the system, the transition between the system states may occur with some regularity for the values of noise intensity lower than potential barrier height, i.e., the stochastic resonance takes place [15, 16]. We presuppose that the external periodic modulation on the experiment is possible to introduce at least in two different ways: through irradiation of the sample by additional modulated source of light or to carry out the modulation through applied pressure. In this case the system dynamics may be described in the following way:

$$\frac{dn_H}{dt} = -\frac{dU(n_H)}{dn_H} + A\cos\left(\frac{2\pi}{T}t + \phi_0\right) + \xi(t), \tag{6.16}$$

where A is the amplitude of periodic signal; T is its period and ϕ_0 is the initial phase. The arbitrary phase ϕ_0 can be choose equal to zero. The model (6.16) with zero mean of stochastic process $\xi(t)$ and non-zero autocorrelation function $\xi(t)\xi(t') = 2\varepsilon^2\delta(t - t')$ describes the overdamped Brownian motion in the bistable asymmetric potential subject to a small periodic forcing.

The evolution of the system with dynamic periodically forcing potential driving by additive noise may be described by the linear Fokker–Planck equation for the probability density, which in the Stratonovich interpretation is the following [27, 28]

$$\frac{\partial P(n_H, t)}{\partial t} = \widehat{L}P(n_H, t) - \frac{\partial}{\partial n_H}A\cos\left(\frac{2\pi}{T}t\right)P(n_H, t) \tag{6.17}$$

with the Fokker–Planck operator

$$\widehat{L} = -\frac{\partial}{\partial n_H}\left(-U'_{n_H}(n_H)\cdot\right) + \varepsilon^2\frac{\partial^2}{\partial n_H^2}\cdot \tag{6.18}$$

Here, dots indicate where to put the objects upon which the operator acts, while U'_{n_H} represents first derivative of dynamic potential on n_H. The value of $P(n_H, t)dt$ is the probability to find the spin-crossover system described by the kinetic equation (6.16) in the position of phase space n_H at time t. Since the period T is relatively large, there is enough time for the system to reach the local equilibrium during this period. In this case will be valid the adiabatic limit [29], when the signal frequency is much slower than the characteristic relaxation time and for the double-well

system this is the time for probability within one well to equilibrate. One should be expected that a quasi-state regime will be established. Then the probability distribution of spin-crossover system states is given by the quasi-steady solution of Fokker–Planck equation (6.17), which for additive noise driven system is found to be

$$P_{st}(n_H, t) = N\exp\left[-\frac{-U(n_H) + A\cos\left(\frac{2\pi}{T}t\right)n_H}{\varepsilon^2}\right], \tag{6.19}$$

where N is the normalization constant. If the control parameters of the system are chosen in such a way that leads to a bistable behavior, the probability distribution gives two peaks that coincide with the minima of dynamic potential corresponding to the LS and HS state.

The analysis of stochastic resonance phenomenon was carried out by the signal-to-noise ratio (SNR), what was found as the ratio of first Fourier component in the power spectral density of resulting signal at the angular frequency $\omega = 2\pi/T$ to the level of the background noise at the same frequency according to the standard definition

$$SNR = \frac{\int_{\omega-\Delta\omega}^{\omega+\Delta\omega} S(z)dz}{\int_{\omega-\Delta\omega}^{\omega+\Delta\omega} S_N(z)dz}. \tag{6.20}$$

Here S is the spectral power of resulting signal in neighborhood of the frequency ω, whereas S_N is the spectral power of noise level at the same frequency. Qualitatively, power spectral density $S(\omega)$ may be described as the superposition of a background power spectral density $S_N(\omega)$ and a structure of delta spikes centered at $\omega = (2n+1)\frac{2\pi}{T}$ with $n = 0, \pm 1, \pm 2 \ldots$. The studying of SR phenomenon by SNR lies in its increasing for periodically modulated system with random noise, relative to that observed with no externally injected noise. Therefore the SNR measures how much the system output contains the input signal frequency ω. The ways to define SNR for the systems with different dynamic potential are considered in [30].

For our system the SNR was found as a result of stochastic experiment by finding the averaged Fourier transform over ensemble of simulated stochastic trajectories. This scheme of calculating SNR is more close to the experimental ones [31–34].

6.3.1 Stochastic Resonance Driven by White Noise

As previously was shown the evolution of spin-crossover system may be described through the dynamic potential in terms of Lyapunov function [10, 22, 26, 35]. The various kinetic properties of LS and HS species of spin-crossover compounds lead to the asymmetrization of system potential from which also may be clearly seen the

diverse response on external perturbation of physical fields for stable and metastable states [35]. In this context the problem of stochastic resonance can reveal very interesting and important properties for nonlinear spin-crossover systems. The LIESST long-lived metastable HS states have been observed for numerous number of Fe(II) spin-crossover systems [36]. The carried out simulations presented here are for the parameters that more corresponds to $[Fe(ptz)_6](BF_4)_2$ but generally may also be applied for a wide range of Fe(II) spin-crossover systems.

For studying the SR phenomena we focus on the spin-crossover system with photoinduced transitions that is characterized by the dynamic potential with the same depth of the potential wells obtained for the light intensity $\beta = 0.081$ shown in Fig. 6.3a. This value of β with self-acceleration factor $\alpha = 5.14$ was chosen for all carried out calculations in this section. The positions of LS state ($n_H = 0.15$) and HS state ($n_H = 0.88$) are asymmetric relative to the unstable point of dynamic potential ($n_H = 0.45$). Thus, although the depths of potential wells are the same, the dynamic potential cannot be regarded as completely symmetric one. Even if our potential shows the equiprobable transition between the states the asymmetric behavior of the system is still preserved.

Besides the action of control field, we add the small external periodic signal that modulates the system potential. Depending on the phase of the periodic signal a system state may change from stable to metastable, and vice-versa, as shown in Fig. 6.3b. The chosen amplitude of periodic force is insufficient to overcome the potential barrier defined by the value of control parameter $\beta = 0.081$ and does not provide the transitions between the states, i.e., the deterministic system oscillates around its steady LS state or HS state, depending on initial position of the system, with the period T of harmonic force.

The situation cardinally differs for the system with additive noise. The nonstationary dynamics of the system with periodic forcing and noise action is described by Eq. (6.16). This stochastic differential equation may be solved numerically by using Heuns methods [26, 37]. The Heuns algorithm is based on the second-order Runge–Kutta type method, and integrates the stochastic equation (6.16) by following recursive formula:

$$\begin{aligned} n_H(t+h) &= n_H(t) + \frac{h}{2}[F(n_H(t)) + F(y(t))] + \varepsilon\sqrt{\frac{h}{2}}u(t), \\ y(t) &= n_H(t) + F(n_H(t))h + \varepsilon\sqrt{2h}u(t). \end{aligned} \tag{6.21}$$

Here, $F(n_H) = f(n_H) + A\cos(\frac{2\pi}{T}t)$ is the force derived from the bistable potential; h is integration time step; $u(t)$ represent the Gaussian distributed random number with variance one obtained by Box–Muller algorithm and a pseudo-random-number generator [38].

We characterize the SR phenomenon by SNR (6.20) obtained from numerical simulations carried out over an ensemble of 100 sample trajectories with 100,000 time steps everyone. The resulting SNR of the system was found as average of SNR for each trajectory calculated by Eq. (6.21) with initial condition $n_H(0) = 1$. Due to

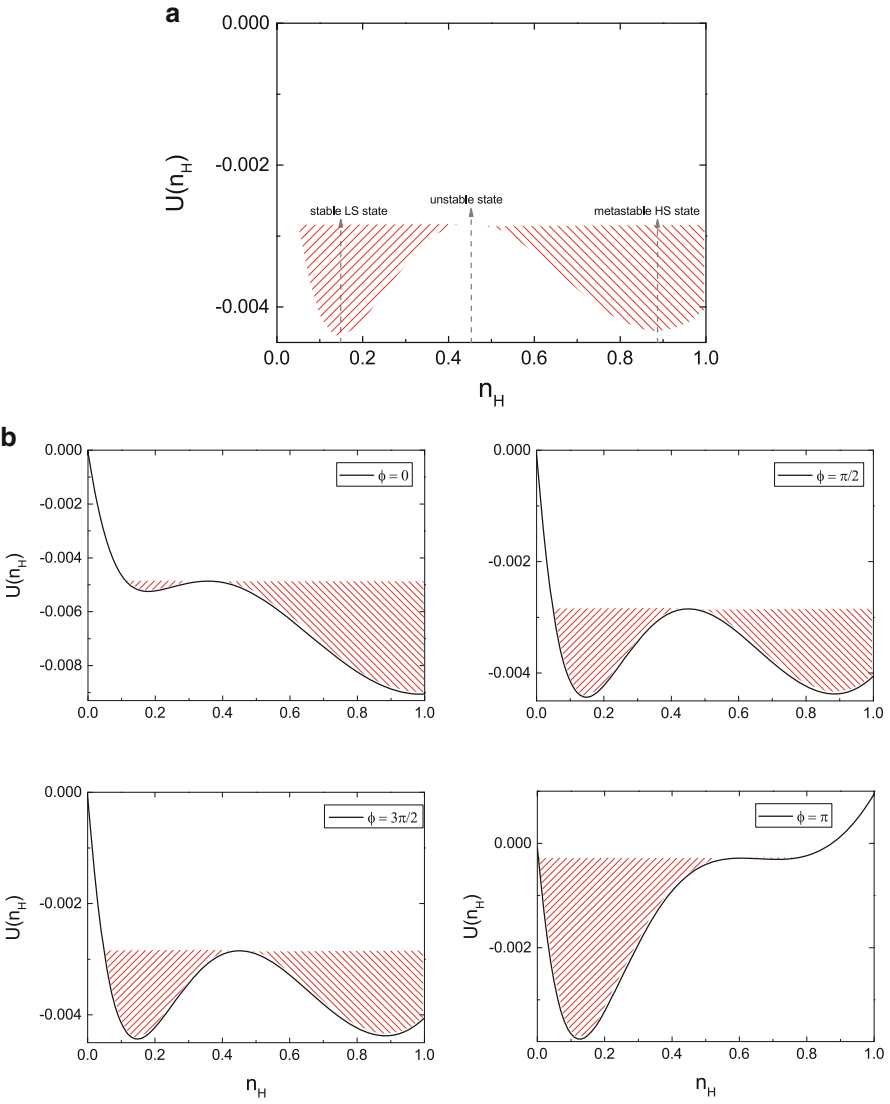

Fig. 6.3 The deterministic dynamic potential (**a**) and its changes by periodic forcing signal with the amplitude A = 0.005 (**b**). Hereinafter the other parameters of periodic signal are $T = 10,000$ and $\phi_0 = 0$

unequal states response on external perturbation the system is sensitive to the choice of initial value for numerical simulations. For the sake of completeness of ongoing processes we initialize the simulations of system kinetics from more sensitive HS potential well. In order to determine the resonance noise strength with the increasing of the amplitude of periodic signal for our spin-crossover

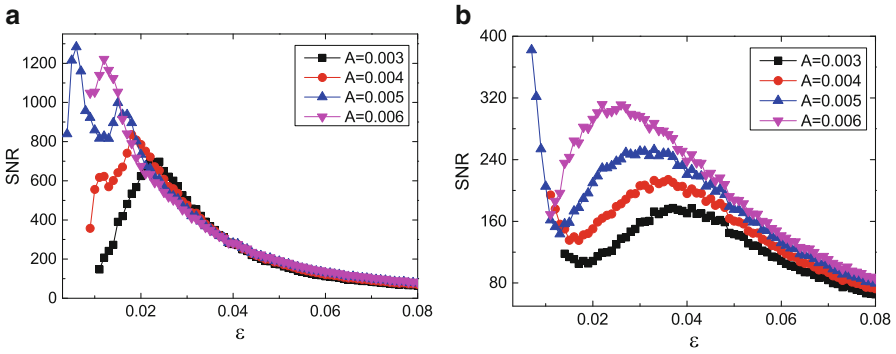

Fig. 6.4 The SNR versus additive noise intensity for the period of harmonic signal $T = 10,000$ (**a**) and $T = 1000$ (**b**)

system, we perform the SNR for some fixed values of periodic modulation amplitude and two different frequencies defined here by period of harmonic signal. The results are presented in Fig. 6.4a, b.

As we can see from the plots the behavior of SNR is quite different as one for classic symmetric double-well potential where single peak in SNR curve is observed due to equality of noise intensities enough for escape from each state. In the case of our bistable asymmetric spin-crossover system for the specific range of periodic amplitude two resonance noise intensity is observed (see Fig. 6.4a). The apparition of second peak in the SNR curve has been previously shown in the paper [39] for the periodically forced system under simultaneous influence of additive and multiplicative noise. In the mentioned work the asymmetrization of system dynamic potential is the result of multiplicative noise action and is the main reason of such behavior. More sophisticated theory of phenomenon based on noise-induced transition and SR is known as double stochastic resonance [40]. This term emphasizes that additive noise causes a resonance-like behavior in the structure, which in its own turn is induced by multiplicative noise.

In our case two peaks in the SNR curve arise from different potential barrier height for LS and HS metastable phase of dynamic potential and is a consequence of system behavior described by Fig. 6.4a from [35]. The additive noise influence is similar to the action of temperature in thermodynamic equilibrium systems and leads to the effective reducing of the depths of potential wells together with its barrier height. The slope of potential well for HS state undergoes more drastic change in comparison with one for LS state. The resonance intensity for the lower noise value corresponds to the escape from HS metastable state [41]. Due to higher potential barrier of LS state the value of this intensity is not enough for reverse transition. With further increasing of noise intensity the transitions between LS and HS states take place [41]. Thereby another peak for higher noise intensity is observed where more favorable conditions for transitions are realized. Thus there is a window of amplitude values of periodic signal where two peaks in SNR dependence are observed. For the periodic amplitude lower than

$A = 0.003$ and higher than $A = 0.005$, only one resonance intensity is observed, but the system dynamics for the each case is different. For low periodic amplitudes the peak on SNR curve which corresponds to small noise intensity cannot be observed due to the fact that its value is merged with the background ones. The background effects are also the reason of losing this peak with increasing the frequency of periodic signal, as is shown in Fig. 6.4b. This is characteristic for all amplitudes despite the fact that the behavior of stochastic trajectories is similar to the case with lower frequency. For high periodic amplitude the metastable state is not realized and the behavior of spin-crossover system is similar to the one for monostable overdamped system [28].

6.3.2 Stochastic Resonance Driven by Colored Noise

For the real spin-crossover compounds, the noise spectrum may have a large bandwidth but finite, i.e., the noise are colored. When an additive stochastic term is colored, the evolution equation of system becomes untractable unless some assumptions are made. We consider here the simplest case of colored noise which is Ornstein–Uhlenbeck (OU) process [42, 43]. Now the system dynamics may be described by the following equation:

$$\frac{dn_H}{dt} = -\frac{dU(n_H)}{dn_H} + A\cos\left(\frac{2\pi t + \phi_0}{T}\right) + \eta(t), \tag{6.22}$$

where the noisy relaxation process $\eta(t)$ satisfies the stochastic differential equation:

$$\frac{d\eta(t)}{dt} = -\frac{1}{\tau}\eta(t) + \frac{\varepsilon}{\tau}\xi(t), \tag{6.23}$$

with the autocorrelation time of noise τ representing the degree of noise coloration. The Ornstein–Uhlenbeck (OU) process $\eta(t)$ with constant intensity ε^2 has an exponential correlation function in the following form:

$$\left\langle \eta(t)\eta(t') \right\rangle = \frac{\varepsilon^2}{\tau}\exp\left(-\frac{|t - t'|}{\tau}\right). \tag{6.24}$$

The autocorrelation time is also related to the cutoff frequency characteristic to the Lorentzian power spectrum of OU noise:

$$S_\eta(\omega) = \frac{2\varepsilon^2}{\tau^2\omega^2 + 1}. \tag{6.25}$$

The correlation of white stochastic term ξ, with zero mean, between times t and $t^{'} > t$ is $\xi(t)\xi(t^{'}) = 2\delta(t^{'} - t)$. If we replace the term $\eta(t)$ in Eq. (6.23) by its expression (6.22) one obtains the following general form of kinetic equation for system dynamics:

$$\tau \frac{dn_H^2}{dt^2} + \gamma(n_H, \tau)\frac{dn_H}{dt} - F(n_H) = \varepsilon\xi(t). \tag{6.26}$$

This is the equation of motion of the stochastic nonlinear oscillator. For the system with simultaneous action of periodic force and noise the nonlinear damping function reads

$$\gamma(n_H, \tau) = 1 - \tau\left(\frac{df(n_H)}{dn_H} - \frac{2\pi}{T}A\sin\left(\frac{2\pi}{T}t\right)\right). \tag{6.27}$$

Using the mathematical tools for calculating SNR as in previous subsection, we found the dependence of SNR on colored-noise intensity for the system dynamics described by Eq. (6.26). Sample results are shown in Fig. 6.5 for $A = 0.003$ at fixed values of autocorrelation time τ for different frequencies of harmonic signal.

The system behavior on colored-noise action causes the special dependence of SNR on noise intensity which differs from the ones obtained for the system with white noise. For the chosen modulation amplitude and low τ only one peak in SNR dependence is observed, but with increase of τ the second peak arises (see Fig. 6.5a). The appearance of second peak for small ε is related to the intrawells transition of the system. For the system with colored noise the increasing of frequency increases the role of background effects similarly to the white noise case and for small ε the corresponding resonant peak is not observed for all autocorrelation time τ shown in Fig. 6.5b. In this case the double-peak behavior may be characterized by the minimum of SNR curves which correspond to the noise

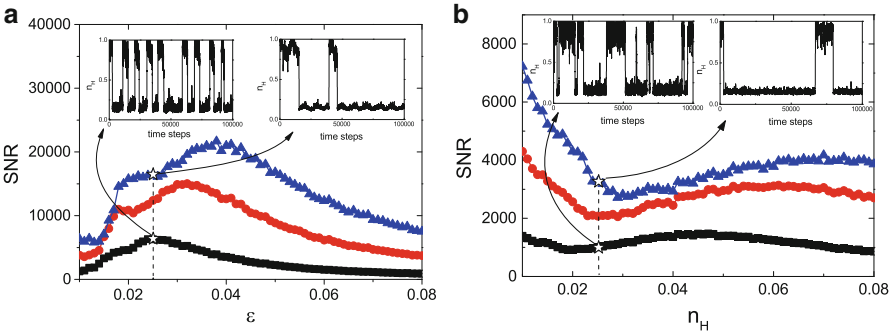

Fig. 6.5 The changes of SNR with the increasing of the colored-noise intensity for periods of the signal $T = 10,000$ (**a**) and $T = 1000$ (**b**). The modulation amplitude is $A = 0.003$. Here the curve marked by *squares* (*black online*) is for $\tau = 10$; *circles* (*red online*) are for $\tau = 30$, *triangles* (*blue online*) are for $\tau = 50$. The *insets* show the sample trajectories for the noise intensity $\varepsilon = 0.025$

intensity enough for transition from HS to LS state with minimal possible passage time, but still small for back transition to HS state. This minimal value of SNR is provided by minimal oscillations amplitude of stochastic trajectories due to their location in LS state. As we can see from Fig. 6.5 the difference between resonant noise value is increased with frequency increasing due to peaks shifting with asymmetric rate toward lower and higher noise values, respectively.

The increase of τ shifts both peaks of SNR curve toward larger values of noise intensity and the SNR rise for all noise values is observed. These risings are related to the cutoff of power spectrum, which lead to lower contribution of noise in value of SNR. It may clearly be observed from (6.24) and (6.25). According to Eq. (6.25), for large values of autocorrelation time it is need the larger value of noise intensity to observe the SR phenomenon. In the insets of Fig. 6.5 are shown two sample trajectories calculated for $\tau = 10$ and $\tau = 50$ and for the noise intensity $\varepsilon = 0.025$ which corresponds to resonance intensity of SNR obtained for $\tau = 10$, but this is not maintained for $\tau = 50$.

6.4 Conclusion

Spin-crossover compounds have attracted our attention for reasons of their various future applications that are not limited as data storage, processing, visualization, or communication systems, especially if the molecules of these compounds can be optically switched.

The response of the spin-crossover system to mutual influence of additive and multiplicative Gaussian white noises as well as the influence of realistic non-Markovian colored noise has been investigated. The examination of noise driven photoinduced transition in spin-crossover system is based on a simple phenomenological model describing photoexcitation and relaxation in spin-crossover compounds where the noise is described as an action of heat bath. The mathematical framework for study of stochastic kinetics of a PIPT in spin-crossover compounds was based on the Langevin equation and steady solution of the Fokker–Planck equation. The system behavior was described by nonequilibrium (dynamic) potential in terms of Lyapunov functions for the deterministic case and by stochastic Fokker–Planck potential in the noise case action. For the system with noise action, the Langevin equation that describes the particle dynamics in the Stratonovich sense was derived for white and colored-noise action. For the colored-noise action it was derived the flow diagrams showing evolution of the system to the stable states. The separatrix which divides two basins of attraction describes the spinodal line between HS and LS phase. It was shown that the transition in spin-crossover solids is very sensitive to noise influence.

The stochastic resonance phenomena arising in noise driven spin-crossover system with periodic modulation also have been the focus of interest. Based on the numerical simulation of the Langevin kinetic equation with a periodic

modulating signal, we have analyzed the SNR ratio in the case of white- and colored-noise actions.

The specific asymmetric dynamic potential of the spin-crossover system leads to unusual behavior during the stochastic resonance phenomenon. The different responses of the LS and HS states to the external actions generate two peaks in SNR ratio curves which correspond to various resonant noise intensity. The double-peaks behavior of the system is clearly observed only for a specific range of modulation amplitude. Similar behavior is observed in systems with colored-noise action, but it is influenced by the noise autocorrelation time. The increasing of noise autocorrelation time generates the shifting of SNR ratio peaks, which correspond to the intrawells and interwells transitions, toward a higher noise intensity but with different shifts.

It is important to note that the concepts proposed in this chapter may be also applied for other real bistable systems described in terms of dynamic potential.

Acknowledgements The work at University of New Orleans was supported by the National Science Foundation under the NSF EPSCoR Cooperative Agreement No. EPS-1003897 with additional support from the Louisiana Board of Regents.

References

1. Cambi L, Gagnasso A (1931) Iron dithiocarbamates and nitrosodithiocarbamates. Atti Accad Naz Lincei 13:809–813
2. Gütlich P, Goodwin HA (eds) (2004) Spin crossover in transition metal compounds I–III. Springer, Berlin
3. Gudyma Iu, Enachescu C, Maksymov A (2015) Kinetics of nonequilibrium transition in spin-crossover compounds. In: Fesenko O, Yatsenko L (eds) Nanocomposites, nanophotonics, nanobiotechnology, and applications. Springer, Cham, p. 375–401
4. Gudyma Iu, Maksymov A, Ivashko V (2015) Spin-crossover nanocrystals and ising model. In: Fesenko O, Yatsenko L (eds) Nanoplasmonics, nano-optics, nanocomposites, and surface studies. Springer, Cham, p 165–192
5. König E, Madeja K (1967) 5T2-1A1 Equilibria in some iron(2)-bis (1, 10-phenanthroline) complexes. Inorg Chem 6:48–55
6. Kahn O (1993) Molecular magnetism. VCH, New York
7. Gudyma Iu, Ivashko V, Linares J (2014) Diffusionless phase transition with two order parameters in spin-crossover solids. J Appl Phys 116:173509
8. Decurtins S, Gütlich P, Köhler CP, Spiering H, Hauser A (1984) Light-induced excited spin state trapping in a transition-metal complex: the hexa-1-propyltetrazole-iron (II) tetrafluoroborate spin-crossover system. Chem Phys Lett 105:1–4
9. Gudyma Iu, Maksymov A (2012) Optically induced switching in spin-crossover compounds: microscopic and macroscopic models and their relationship. Appl Opt 51:C55–C61
10. Gudyma Yu, Semenko O (2004) Nonequilibrium kinetics in spin-crossover compounds. Phys Status Solidi B 241:370–376
11. Gudyma Yu, Ivans'kii B (2006) Behavior of asymmetric bistable system under influence of cross-correlated noises. Mod Phys Lett B 20:1233–1239
12. Gudyma AIu, Gudyma IuV (2010) Noise-induced collective regimes of complex system in contact with a random reservoir. Physica A 389:667–672

13. Gudyma IuV, Maksymov AIu, Miyashita S (2011) Noise effects in a finite-size Ising-like model. Phys Rev E 84:031126
14. Gudyma Iu, Maksymov A, Enachescu C (2014) Phase transition in spin-crossover compounds in the breathing crystal field model. Phys Rev B 89:224412
15. Gammaitoni L, Hänggi P, Jung P, Marchesoni F (1998) Stochastic resonance. Rev Mod Phys 70:223–287
16. McDonnell MD, Stocks N, Pearce C, Abbott D (2012) Stochastic resonance. Cambridge University Press, Cambridge
17. Boukheddaden K, Shteto I, Hoô B, Varret F (2000) Dynamical model for spin-crossover solids. I. Relaxation effects in the mean-field approach. Phys Rev B 62:14796–14805
18. Boukheddaden K, Shteto I, Hoô B, Varret F (2000) Dynamical model for spin-crossover solids. II. Static and dynamic effects of light in the mean-field approach. Phys Rev B 62:14806–14817
19. Varret F, Boukheddaden K, Chong C, Goujon A, Gillon B, Jeftic J, Hauser A (2007) Light-induced phase separation in the $[Fe(ptz)_6](BF_4)_2$ spin-crossover single crystal. Europhys Lett 77:30007
20. Hohenberg PC, Halperin BI (1977) Theory of dynamic critical phenomena. Rev Mod Phys 49:435–479
21. Ma S-K (2000) Modern theory of critical phenomena. Westview Press, Boulder
22. Gudyma IuV, Maksymov AIu (2010) Theoretical analysis of the states of spin-crossover solids under cross-correlated noises. Physica B 405:2534–2537
23. Horsthemke W, Lefever R (1984) Noise-induced transitions. Springer, Berlin
24. Hänggi P, Jung P, Marchesoni F (1989) Escape driven by strongly correlated noise. J Stat Phys 54:1367–1380
25. Jung P, Hänggi P (1987) Dynamical systems: a unified colored-noise approximation. Phys Rev A 35:4464–4466
26. Gudyma Iu, Maksymov A (2011) High spin metastable state relaxation of spin-crossover solids driven by white noise. J Phys Chem Solids 72:73–77
27. Fox RF, Lu Y-N (1993) Analytic and numerical study of stochastic resonance. Phys Rev E 48:3390–3398
28. Evstigneev M, Reimann P, Pankov V, Prince RH (2004) Stochastic resonance in monostable overdamped system. Europhys Lett 65:7–12
29. McNamara B, Wiesenfeld K (1989) Theory of stochastic resonance. Phys Rev A 39:4854–4869
30. Mitaim S, Kosko B (1998) Adaptive stochastic resonance. Proc IEEE 86:2152–2183
31. Douglass JK, Wilkens L, Pantazelou E, Moss F (1993) Noise enhancement of information transfer in crayfish mechanoreceptors by stochastic resonance. Nature 365:337–340
32. Dunn T, Guerra DN, Mohanty P (2009) Noise color and asymmetry in stochastic resonance with silicon nanomechanical resonators. Eur Phys J B 69:5–10
33. Tweten DJ, Mann BP (2014) Experimental investigation of colored noise in stochastic resonance of a bistable beam. Physica D 268:25–33
34. Abbaspour H, Trebaol S, Morier-Genoud F, Portella-Oberli MT, Deveaud B (2014) Stochastic resonance in collective exciton-polariton excitations inside a GaAs microcavity. Phys Rev Lett 113:057401
35. Gudyma Iu, Maksymov A, Dimian M (2013) Stochastic kinetics of photoinduced phase transitions in spin-crossover solids. Phys Rev E 88:042111
36. Hauser A (1991) Intersystem crossing in Fe(II) coordination compounds. Coord Chem Rev 111:275–290
37. Miguel MS, Toral R (2000) Stochastic effects in physical systems. In: Tirapegui E, Martinez J, Tiemann R (eds) Instabilities and nonequilibrium structures VI. Kluwer Academic, Dordrecht, p 35–130
38. Box GEP, Muller ME (1958) A note on the generation of random normal deviates. Ann Math Stat 29:610–611

39. Jia Y, Yu S-N, Li J-R (2000) Stochastic resonance in a bistable system subject to multiplicative and additive noise. Phys Rev E 62:1869–1878
40. Zaikin AA, Kurths J, Schimansky-Geier L (2000) Doubly stochastic resonance. Phys Rev Lett 85:227–231
41. Gudyma Iu, Maksymov A, Dimian M (2014) Stochastic resonance in bistable spin-crossover compounds with light-induced transitions. Phys Rev E 90:052135
42. Hanggi P, Jung P (1995) Colored noise in dynamical systems. Adv Chem Phys 89:239–326
43. Gudyma Iu, Maksymov A, Enachescu C (2010) Decay of a metastable high-spin state in spin-crossover compounds: mean first passage time analysis. Eur Phys J B 78:167–172

Part II
Nanooptics and Photonics

Chapter 7
Nano-Sized Pattern Formation in Nonequilibrium Adsorptive Systems with Interacting Adsorbate

Dmitrii Kharchenko and Vasyl Kharchenko

7.1 Introduction

Nano-sized patterning in thin films attains an increasing interest from theoretical and practical viewpoints due to usage of nano-sized objects in new electronic devices and, generally, in opto-electronics. A manipulating with atomic sizes allows one to manufacture new materials with exceptional functionality such as giant magnetoresistance [1], tunable optical emission [2], high efficiency photovoltaic conversion [3], and ultralow thermal conductivity [4]. These advantages of new materials are used in magnetoresistive sensors, memory devices, quantum dot lasers, and detectors which can be exploited at quantum communications.

As far as industrial applications of nano-sized patterns have become more and more complex it is of great scientific and technological interest to understand a role of main mechanisms governing and controlling nanostructured thin films growth. A modeling texture formation and their evolution are of primary importance in the study of thin film growth. By exploiting different technics for deposition one can use effectively mechanisms for nano-sized islands growth (adsorption/desorption, diffusion, and interaction of adatoms) leading to formation of different types of patterns. During last few decades it was shown experimentally and by theoretical modeling that nano-sized objects can be produced at vapor or ion-beam deposition [5–8], ion-beam sputtering [9–13], molecular beam epitaxy [14–20].

Nowadays in adsorption–desorption processes when material can be deposited from the gaseous phase, a development of experimental methods including scanning tunneling microscopy, field ion microscopy serves as a technique to monitor chemical

D. Kharchenko (✉) • V. Kharchenko
Institute of Applied Physics, National Academy of Sciences of Ukraine, 58 Petropavlovskaya St., 40000 Sumy, Ukraine
e-mail: dikh@ipfcentr.sumy.ua; vasiliy@ipfcentr.sumy.ua

O. Fesenko, L. Yatsenko (eds.), *Nanophysics, Nanophotonics, Surface Studies, and Applications*, Springer Proceedings in Physics 183,
DOI 10.1007/978-3-319-30737-4_7

reactions in real time on metal surfaces. It was shown that adsorbed atoms can arrange into islands/clusters of nanometer range on adsorbed monoatomic layer. Such experimental methods allow one to study formation of clusters or islands of adsorbed molecules/atoms [21] having a linear size of nanometer range [22–26]. Nanometer islands were observed experimentally in Si/Si(100) [27], the same were found at deposition of Ge on Si [28], metallic elongated islands were observed at deposition of Cu on Pd(110) [29] and at deposition of Ag on Cu(110) [30]. It was shown that adsorbate clusters are governed by a formation of dimers and their reconstructions [31] representing nonequilibrium chemical reactions. Nanometer-sized vacancy islands organized in a perfect triangular lattice were observed when a single monolayer of Ag was exposed on Ru(0001) surface at room temperature [32].

These experimental observations have initiated theoretical studies of surface pattern formation. During last decades it was shown that the continuous approach related to reaction–diffusion models is able to study dynamics of adsorptive system on wide range of time scales and consider dynamics of pattern formation on length scales from nano- to micro-meters. This approach was successfully applied to study surface nano-size patterns in reaction–diffusion systems (see, for example, [33–42]).

In this work we aim to study the dynamics of pattern formation and selection processes at vapor deposition by taking into account relaxation of the diffusion flux and introducing stochastic source satisfying fluctuation–dissipation relation. Studying the behavior of islands as clusters of adsorbate in deterministic system we will show that their average size behaves in the oscillatory manner. By considering overdamped stochastic system we will show that an increase in internal noise intensity leads to decrease in the linear size of adsorbate clusters and to transition to chaotic configuration. It will be shown that stationary nano-sized adsorbate islands emerging during the system evolution can be controlled by the rates of chemical reactions and interaction strength of adsorbate.

7.2 Model

We will consider a model of interacting adsorbate where only one class of particles is possible. Following references [33–38, 42] we introduce the scalar field $x(\mathbf{r}, t) \in [0, 1]$ describing dynamics of the local coverage at surface, where t is the time variable, $\mathbf{r} = \{x, y\}$ is the space coordinate. The local coverage $x = x(\mathbf{r}, t)$ is defined as the quotient between the number of adsorbed particles in a cell of the surface and the fixed number of available sites in each cell. From theoretical viewpoint an evolution of the field variable $x = x(\mathbf{r}, t)$, let say coverage for adsorption/desorption systems, is governed by the reaction–diffusion equation of the form

$$\partial_t x = f(x) - \nabla \cdot \mathbf{J}. \tag{7.1}$$

The term $f(x)$ stands for local dynamics and describes birth-and-death or adsorption–desorption processes; the flux $\mathbf{J}$ represents the mass transport.

Let us consider, initially, components of the reaction term $f(x)$ in detail. It incorporates adsorption and desorption terms together with nonequilibrium chemical reactions. Adsorption processes are characterized by a constant k_a and a partial pressure p of the gaseous phase. Moreover, adsorption is only possible to the free sites. It means that the adsorption rate is $k_a p(1 - x)$. Adsorption rate can be defined through the adsorption energy E_a, temperature T measured in energetic units, and frequency factor ν as $k_a = \nu e^{-E_a/T}$. Desorption processes occur with a rate $k_d = k_d^0 \exp(U(\mathbf{r})/T)$, where $k_d{}^0$ is the desorption rate for noninteracting particles, $U(\mathbf{r})$ gives contribution due to strong local bond (substratum-mediated interactions). Desorption rate $k_d^0 = \nu e^{-E_d/T}$ relates to the life time scale of adatoms $\tau_d = [k_d^0]^{-1}$, where E_d is the desorption energy. Therefore, the desorption processes are defined by a contribution $- k_d x$. Introducing this term we admit that only substratum-mediated interactions are possible. In such a case this term describes desorption of adatom into gaseous phase. Adsorption and desorption processes are equilibrium reactions, whereas nonequilibrium ones relate to interactions of adatoms with formation of dimers, associates, resulting to a decrease in separated adatoms concentration. Nonequilibrium chemical reactions responsible to a formation of dimers can be described by a rate $- k_r x^2$, where k_r is the constant.

The total flux $\mathbf{J}$ is a sum of both ordinary diffusion flux $(-D_0 \nabla x)$ and flow of adsorbate $(-(D_0/T)x(1 - x)\nabla U)$. Here the multiplier $x(1 - x)$ denotes that the flux is only possible to the $(1 - x)$ free sites. Hence, the total flux can be written as

$$\mathbf{J} = -D_0 M(x) \left[\frac{\nabla x}{M(x)} + \frac{1}{T} \nabla U \right], \tag{7.2}$$

where the Cahn mobility $M(x) = x(1 - x)$ is introduced. Formally the total flux can be rewritten as follows: $\mathbf{J} = -D_0 M(x) \nabla \frac{\delta \mathscr{F}}{\delta x}$, where $\mathscr{F}$ is the total mesoscopic free energy functional. As was shown in [33–35, 42, 43] the mesoscopic free energy is of the form

$$\mathscr{F} = \int d\mathbf{r}[x \ln(x) + (1 - x)\ln(1 - x)] - \frac{1}{2T} \iint d\mathbf{r} d\mathbf{r}' x(\mathbf{r}) u\left(\mathbf{r} - \mathbf{r}'\right) x\left(\mathbf{r}'\right), \tag{7.3}$$

where for interacting potential $U(r)$ one assumes [34]: $U(\mathbf{r}) = -\int d\mathbf{r}' u(\mathbf{r} - \mathbf{r}') x(\mathbf{r}')$. Here $- u(r)$ is the binary attraction potential for two adsorbate particles separated by the distance r, it is of symmetrical form, i.e., $\int d\mathbf{r} \mathbf{r}^{2n+1} u(\mathbf{r}) = 0$, $n = 1, \ldots, \infty$.

Following reference [35] as a simple approximation for the interaction potential, we choose the Gaussian profile $u(r) = \frac{2\varepsilon}{\sqrt{4\pi r_0^2}} \exp\left(-r^2/4r_0^2\right)$, where ε is the interaction strength, r_0 is the interaction radius. Assuming that x does not vary significantly within the interaction radius, one can estimate

$$\int \mathrm{d}\mathbf{r}^{'} u\left(\mathbf{r}-\mathbf{r}^{'}\right) x\left(\mathbf{r}^{'}\right) \simeq \int \mathrm{d}\mathbf{r}^{'} u\left(\mathbf{r}-\mathbf{r}^{'}\right) \sum_{n} \frac{\left(\mathbf{r}-\mathbf{r}^{'}\right)^{n}}{n!} \nabla^{n} x(\mathbf{r}), \tag{7.4}$$

and for terms up to the fourth order one gets $\int u(r)x(r)\mathrm{d}r = 2\varepsilon x$, $\frac{1}{2!}\int u(r)r^2\nabla^2 x(r)\mathrm{d}r = 2\varepsilon r_0^2\nabla^2 x$, $\frac{1}{4!}\int u(r)r^4\nabla^4 x(r)\mathrm{d}r = \varepsilon r_0^4\nabla^4 x$.

Therefore, using notation $\varepsilon = \varepsilon/T$ one arrives at the mesoscopic free energy functional

$$\mathscr{F} = \int \mathrm{d}\mathbf{r}\left[-\frac{\varepsilon}{2}x^2 + x\ln x + (1-x)\ln(1-x) - \frac{\varepsilon}{2}x(1+r_0^2\nabla^2)^2 x\right]. \tag{7.5}$$

and the total flux is defined by the free energy (7.5).

Next, it will be more convenient to measure time in units k_d, introduce the diffusion length $L_d = \sqrt{D_0/k_d}$ and dimensionless rates $\alpha = k_a p/k_d$, $\beta = k_r/k_d$. Therefore, the reaction term takes the form $f(x) = \alpha(1-x) - xe^{-2\varepsilon x} - \beta x^2$ and the system is described by two length scales, where $r_0 \ll L_d$.

As far as real systems (molecules, atoms) have finite propagation speed one should take into account memory (correlation) effects, assuming

$$\mathbf{J} = -L_d \int_0^t \mathrm{d}t' \mathscr{M}(t,t';\tau_J)\nabla \frac{\delta \mathscr{F}}{\delta x(\mathbf{r},t')}, \tag{7.6}$$

where $\mathscr{M}(t,t^{'})$ is the memory kernel. Taking it in the exponential decaying form $\mathscr{M}(t,t^{'}) = \tau_J^{-1} M(x(\mathbf{r},t^{'}))\exp(-|t-t^{'}|/\tau_J)$, where τ_J is the flux relaxation time instead of one equation for the coverage we get a system of two equations:

$$\partial_t x = f(x) - L_d\nabla\cdot\mathbf{J}\,; \tau\partial_t\mathbf{J} = -\mathbf{J} - L_d M(x)\nabla\frac{\delta\mathscr{F}}{\delta x}, \tau = \tau_J k_d. \tag{7.7}$$

At $\tau_J \to 0$ the asymptotic $M(t,t^{'}) = \delta(t-t^{'})$ leads to the Fick law $\mathbf{J} = -L_d M(x)\nabla \delta\mathscr{F}_{tot}/\delta x$ with an infinite propagation. The equivalent equation for the coverage takes the form

$$\begin{aligned} &\tau\partial_{tt}^2 x + \gamma(x)\partial_t x = \varphi(x,\nabla), \quad \gamma(x) \equiv 1 - \tau f^{'}(x); \\ &\varphi(x;\nabla) \equiv f(x) + L_d^2\nabla\cdot[\nabla x - \varepsilon M(x)(\nabla x + \nabla\mathscr{L}_{SH}x)], \quad \mathscr{L}_{SH} = (1+r_0^2\nabla^2)^2. \end{aligned} \tag{7.8}$$

To study a class of real systems one should take into account the corresponding fluctuations obeying fluctuation–dissipation relation. To that end we introduce the corresponding stochastic source in ad hoc form and instead of deterministic equation (7.8) one arrives at a stochastic equation of the form

$$\tau\partial_{tt}^2 x + \gamma(x;\tau)\partial_t x = \varphi(x,\nabla) + g(x;\tau)\xi(\mathbf{r},t), \tag{7.9}$$

where $g^2(x;\tau) = \gamma(x;\tau)$ in order to satisfy the fluctuation– dissipation relation and the random force ξ is the white Gaussian noise with zero mean and correlation $\langle\xi(\mathbf{r},t)\xi(\mathbf{r}',t')\rangle = 2\sigma^2\delta(\mathbf{r}-\mathbf{r}')\delta(t-t')$. Here the noise intensity σ^2 is reduced to the bath temperature, in our case it relates to the gaseous phase temperature.

7.3 Pattern Selection in Deterministic System

In this section we are aimed to describe deterministic dynamics of pattern formation and selection processes in a class of reaction-Cattaneo systems given by Eq. (7.7). We will study an oscillatory dynamics of pattern formation in such class of models with chemical reactions governed by adsorption/desorption processes. It will be shown that in reaction-Catteneo system pattern selection processes are realized. Studying behavior of islands size as clusters of dense phase we will show that averaged island size behaves itself in oscillatory manner.

Let us initially consider stationary homogeneous system states in the deterministic limit $\sigma^2 = 0$. The corresponding phase diagram is shown in Fig. 7.1a. Outside the cusp the system is monostable: at small α (before the cusp) the system is in low density state x_{LD}, whereas at large α the high density state x_{HD} is realized. In the cusp the system is bistable. Nonequilibrium chemical reactions governed by the rate β shift the whole phase diagram and shrink the domain where the system is bistable. Here possible values for x related to the uniform states decrease whereas critical values for ε become larger; if β grows, then critical values for α decrease.

It is known that systems with memory effects admit pattern selection processes at fixed set of the system parameters [44–46]. These processes can be observed at early stages of the system evolution where linear effects are essential. Therefore, pattern selection can be studied considering stability of statistical moments, reduced to the averaged filed and/or structure function as the Fourier transform of a two-point correlation function for the coverage. As far as fourth order contribution in the interaction potential $u(r)$ is not essential at small $r_0 \ll L_d$, next we consider a case where $\int u(r)x(r)\mathrm{d}r \simeq 2\varepsilon(1 + r_0^2\nabla^2)x$, neglecting ${r_0}^4\nabla^4 x$.

Averaging Eq. (7.8) over initial conditions and taking $\langle x\rangle - x_0 \propto e^{\mathrm{i}}(\omega t - kr)$ one gets the dispersion relation of the form

$$\omega(k)_{\mp} = -\frac{\mathrm{i}\gamma(x_0)}{2\tau} \mp \left[\frac{L_d^2k^2(1-2\varepsilon M(x_0)(1-r_0^2k^2)) - f'(x_0)}{\tau} - \frac{\gamma^2(x_0)}{4\tau^2}\right]^{1/2}.$$

One can see that $\omega(k)$ can have real and imaginary parts, i.e., $\omega(k) = \Re\omega(k) \pm \mathrm{i}\Im\omega(k)$. The component $\Re\omega(k)$ is responsible for oscillatory solutions, whereas $\Im\omega(k)$ describes stability of the solution $\langle\delta x_{\mathbf{k}}(\omega)\rangle$. Analysis of

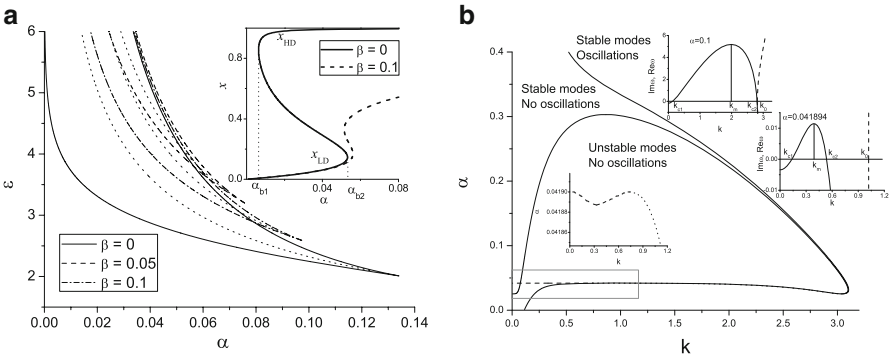

Fig. 7.1 (**a**) Phase diagram for homogeneous system in the parameter plane (α, ε). Dependencies $x(\alpha)$ in insertion are obtained at $\varepsilon = 4$. (**b**) Stability diagram at $\varepsilon = 5$, $\tau = 0.5$, and $\beta = 0.1$. Dependencies of $\Im\ \omega(k)$ and $\Re\ \omega(k)$ are shown as *solid* and *dashed lines* in insertions at $\alpha = 0.1$ and $\alpha = 0.041894$ related to high density and low density phases

both $\Re\omega(k)$ and $\Im\omega(k)$ allows us to set a threshold for a wavenumber where oscillatory solutions are possible. Moreover, it gives a wavenumber for the first unstable solution. From the obtained dispersion relations it follows that at $k = k_0$ satisfying equation $k_0^2\big(1 - 2\varepsilon M(x_0)\big(1 - r_0^2 k_0^2\big)\big) = \frac{1}{L_d^2}\left[f^{'}(x_0) + \frac{\gamma^2(x_0)}{4\tau}\right]$ two branches of the dispersion relation degenerate. The unstable mode appears at $k = k_c$ obtained from the equation $L_d^2 k_c^2(1 - 2\varepsilon M(x_0)(1 - r_0^2 k_c^2)) = f^{'}(x_0)$. From the dispersion relation $\omega(k)$ one can find the most unstable mode k_m as a solution of the equation $\mathrm{d}\Im\omega/\mathrm{d}k = 0$. It coincides with first unstable mode when only one nonzeroth solution of the equation $\Im\ \omega(k) = 0$ emerges.

Using obtained relations one can calculate a diagram indicating spatial stability of homogeneous states to inhomogeneous perturbations. The corresponding diagram is shown in Fig. 7.1b. Here domain of unstable modes with respect to inhomogeneous perturbations is bounded by solid and dash thick curves. The solid curve relates to high density phase, whereas dash line corresponds to low density phase; dot line addresses to unstable homogeneous stationary state. When we increase the adsorption rate α from zeroth value the first unstable mode emerges at large k and is possible only for high density phase. There is a small domain for α where spatial instability of the low density phase is possible (see insertion of $\alpha(k)$ at small α and k). Wave numbers related to these unstable modes in both low- and high density phases are observed in fixed interval $k \in [k_{c1}, k_{c2}]$. The thin solid line in Fig. 7.1b denotes critical values k_o where oscillatory solutions $\langle x(k,t)\rangle$ are possible. The domain of unstable modes with respect to inhomogeneous perturbations is limited by large values for α. It means that instability of high density phase is possible only in fixed interval for adsorption rate values.

Considering properties of pattern selection we need to find dynamical equation for the structure function $S(\mathbf{k}, t)$ as the Fourier transform of the two-point correlation function $\langle \delta x(\mathbf{r}, t)\delta x(\mathbf{r}^{'}, t)\rangle$ and study its behavior at small times. To that end we

obtain the linearized evolution equation for the Fourier components $\delta x_{\mathbf{k}}(t)$ and $\delta x_{-\mathbf{k}}(t)$ and compute $S(\mathbf{k},t) = \langle \delta x_{\mathbf{k}}(t)\delta x_{-\mathbf{k}}(t)\rangle$. The corresponding dynamical equation takes the form

$$\tau\partial_{tt}^2 S(\mathbf{k},t) + \gamma(x_0)\partial_t S(\mathbf{k},t) = 2\Big\{f^{'}(x_0) - L_d^2 k^2(1 - 2\varepsilon M(x_0)(1 - r_0^2 k^2))\Big\}S(\mathbf{k},t).$$

Analytical solution can be found assuming $S(\mathbf{k},t) - S_0 \propto \exp(-i\varpi(\mathbf{k})t)$, where

$$\varpi(k)_{\pm} = -\frac{\mathrm{i}\gamma(x_0)}{2\tau} \pm \left[\frac{2\big(L_d^2 k^2(1 - 2\varepsilon M(x_0)(1 - r_0^2 k^2)) - f^{'}(x_0)\big)}{\tau} - \frac{\gamma^2(x_0)}{4\tau^2}\right]^{1/2}.$$

As in the previous case $\Im\varpi$ is responsible for stability of the system, whereas $\Re\varpi$ relates to pattern selection processes.

To make a quantitative study next we use numerical simulations. To perform numerical simulations of the process of vapor deposition one can use two different lattices with square and triangular symmetries. A presentation of spatial operators onto a square grid can be exploited to modelize processes of surface alloying in metal-on-metal growth for crystalline systems with cubic symmetry, for example, Ag on Cu(110) (see [30, 47, 48]). To modelize pattern formation in systems having the hexagonal symmetry, for example, Zr, Zn, Ru in the plane (0001), one should use the corresponding presentation of spatial operators on the triangle lattice [49]. It leads to a formation of islands with more symmetrical shape, comparing to ones on square lattice (see detailed discussion in [48]).

In our study all simulations were done on the lattice with triangular symmetry of the linear size $L = 256\Delta x$ with periodical boundary conditions and a mesh size $\Delta x = 0.5$; $\Delta t = 0.00025$ is the time step. In the case of the triangular/hexagonal symmetry there are three wave vectors separated by $2\pi/3$ angles. We consider the case when $L_d = 40r_0$ and the total size of the system is $L = 12.8L_d$. As initial

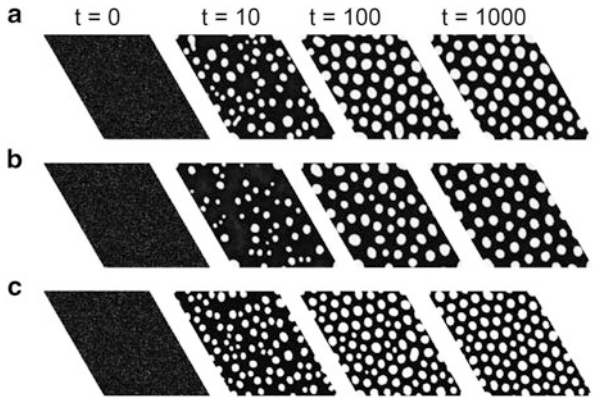

Fig. 7.2 Typical snapshots of the system evolution at different system parameters: (**a**) $\tau = 0.0$, $\varepsilon = 3.0$; (**b**) $\tau = 0.1$, $\varepsilon = 3.0$; (**c**) $\tau = 0.1$, $\varepsilon = 4.0$. Other parameters are: $\alpha = 0.1$, $\beta = 0.1$, $\sigma^2 = 0.0$, $\rho_0 = 0.25$

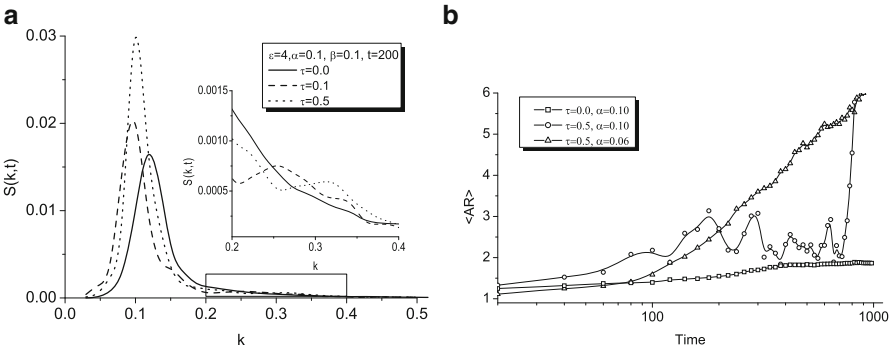

Fig. 7.3 (**a**) Structure function dynamics for different values of the diffusion flux relaxation time τ at $t = 200$. (**b**) Dynamics of the averaged aspect ratio. System parameters are: $\alpha = 0.1$, $\beta = 0.1$, $\varepsilon = 4$

conditions we take: $\langle x(\mathbf{r},0)\rangle = 0$, $\langle(\delta x(\mathbf{r},0))^2\rangle = 0.1$. Typical evolution of the system with different values for τ, ε, and α is shown in Fig. 7.2.

Comparing rows (a) and (b) in Fig. 7.2 it follows that at elevated τ related to the field dependent mobility γ^{-1} the number of adsorbate islands decreases. With an increase in ε (an effective decrease in the temperature) one arrives at the structure with large number of islands having small sizes [see row (c)].

Let us consider dynamics of the structure function at different values for τ shown in Fig. 7.3a. To calculate $S(k,t)$ we have used fast Fourier transformation procedure. Let us start with the simplest case of $\tau = 0$ (see solid line in Fig. 7.3a). Here only major peak of $S(k,t)$ is realized that is related to period of islands. There is smooth behavior of the structure function tails. During the system evolution the peak is shifted toward stationary value of the island size; its height increases (islands become well defined and boundaries between dense and diluted phases become less diffusive). In the case $\tau \neq 0$ we get one major peak at small wave number and additional peaks at large k. Emergence of such minor peaks means formation of other patterns (patterns with other periods). In the course of time an amplitude of such satellite peaks decreases that means pattern selection processes when the system selects one most unstable mode characterized by the major peak whose height increases. This oscillatory behavior of the structure function at large wave numbers is well predicted by the linear stability analysis [47].

To prove that islands can oscillatory change their sizes we compute an averaged aspect ratio $\langle AR\rangle = \langle R_x/R_y\rangle$, where R_x and R_y are sizes of an island in x- and y-direction, respectively. From the obtained dependencies shown in Fig. 7.3b it follows that for pure dissipative system deviations from the straight line are small and may be considered as fluctuations in R_x and R_x values. At $\tau \neq 0$ and small ε oscillations in $\langle AR\rangle$ are well pronounced. Such oscillations in lateral and longitudinal sizes of islands mean that at some fixed time interval most of the islands grow in one direction whereas in other direction their size decreases, in next time interval

these two directions are changed. When this scenario is repeated one gets an oscillation picture of island size growth.

7.4 Patterning in Overdamped Stochastic System

This section is devoted to study stochastic effects related to fluctuation–dissipation relation in pattern formation process at vapor deposition. We will deal with the Langevin equation (7.9).

As was shown in [48, 50–53] the correct transition to overdamped limit is achieved by using standard effective potential method [54]. It results to effective Langevin equation of the form

$$\partial_t x = \frac{1}{\gamma(x)}\left[\varphi(x,\nabla) - \frac{\sigma^2}{2}\frac{\partial_x \gamma(x;\tau)}{\gamma(x;\tau)}\right] + \frac{1}{\sqrt{\gamma(x;\tau)}}\xi(\mathbf{r},t). \tag{7.10}$$

Here, as far as τ is small but nonzero quantity a dynamics of the averaged field x can be governed by τ even in overdamped limit.

An equation for the first statistical moment reads

$$\partial_t \langle x\rangle = \frac{\varphi(x,\nabla)}{\gamma(x;\tau)} - \sigma^2 \frac{\partial_x \gamma(x;\tau)}{\gamma^2(x;\tau)}. \tag{7.11}$$

Considering deviation of the coverage filed from stationary value x_0 related to homogeneous steady state one can find that in the linear analysis averaged fluctuation can be described as $\langle \delta x\rangle \equiv \langle x\rangle - x_0 = \langle \delta x(0)\rangle e^{\lambda(\kappa)\tilde{\tau}} e^{i\kappa r}$ where $\kappa = kL_d$. Here the time variable $\tilde{t}$ is measured in units $\gamma(x_0;\tau)$, $\rho_0 \equiv r_0/L_d$. The corresponding

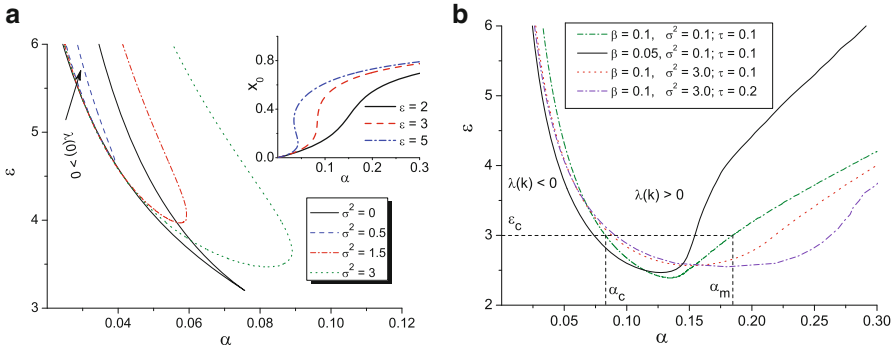

Fig. 7.4 Phase diagram for linear stability analysis of the uniform state to (**a**) homogeneous perturbations at $\tau = 0.1$ and $\beta = 0.1$; and (**b**) inhomogeneous perturbations at different system parameters

increment is $\lambda(\kappa) = \lambda(0) - \kappa^2[1 - \varepsilon M(x_0)(1 + (1 - \rho_0^2\kappa^2)^2)]$, where $\lambda(0) = \partial_x f|_{x_0} + \frac{\tau\sigma^2}{\gamma(x_0;\tau)}\partial^3_{xxx} f|_{x_0}$.

From stability diagram shown in Fig. 7.4a it is seen that in the noiseless case the instability domain for homogeneous perturbations with $\lambda(0) > 0$ is bounded by solid lines. In this domain the system is bistable: at small α (before the left solid line) one has the low density state, whereas at large α only the high density state is realized; in the cusp low- and high density states are separated by unstable state. Dependencies of the stationary coverage x_0 on adsorption coefficient at different values of the interaction strength ε and $\beta = 0.1$, $\tau = 0.1$, $\sigma^2 = 0.0$ are shown in the insertion in Fig. 7.4a. Introducing fluctuations with small intensity one can find that this domain shrinks essentially. Increasing the noise intensity we get an emergence of the instability domain; at large σ^2 it has large size compared to the noiseless case due to a positive contribution of the second term in $\lambda(0)$.

Instability of the system states due to inhomogeneous perturbations are characterized by $\lambda(k) > 0$. Dependencies $\varepsilon(\alpha)$ illustrating domain of spatial instability are shown in Fig. 7.4b at different system parameters. From the obtained dependencies bounding the domain with $\lambda(k) > 0$ it follows that pattern formation in the system is possible in reentrant manner when at fixed ε one can vary the adsorption coefficient α: at small and large values α no patterning is possible, whereas spatial structure of adsorbate is realized in a window $\alpha \in [\alpha_c, \alpha_m]$. It follows that fluctuations extend an

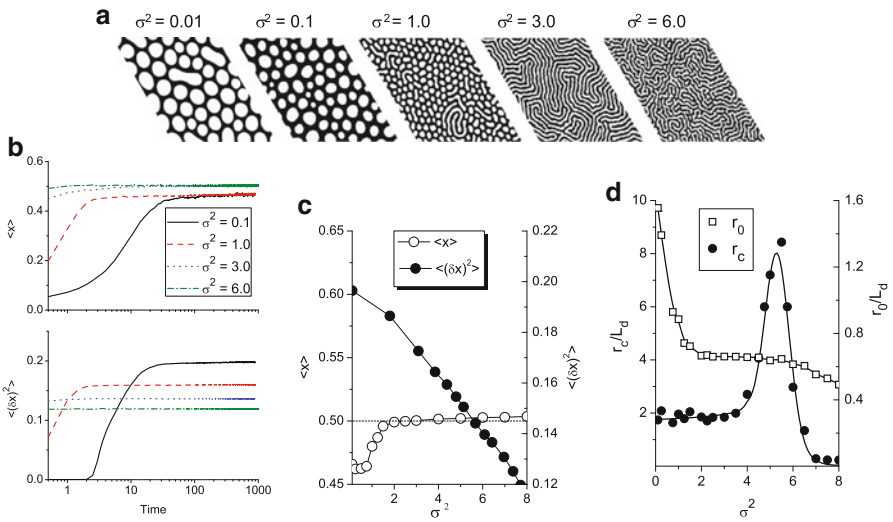

Fig. 7.5 (**a**) Typical snapshots of the surface pattern at $t = 10^3$ and different values of the noise intensity. (**b**) Evolution of the averaged coverage field $\langle x \rangle$ and the dispersion $\langle (\delta x)^2 \rangle$ at different noise intensity σ^2. (**c**) Stationary values for the averaged coverage field and its dispersion *versus* σ^2. (**d**) Averaged period of patterns $\langle r_0 \rangle$ and correlation radius $\langle r_c \rangle$ *versus* noise intensity σ^2 in stationary limit. Main system parameters are: $\alpha = 0.1$, $\varepsilon = 4$, $\beta = 0.05$, $\tau = 0.1$

interval for α where spatial instabilities are possible. The same effect is observed at elevated τ.

Next we will perform numerical simulations of the pattern formation process according to scheme presented above. We use the Milshtein algorithm to satisfy the Stratonovich interpretation for the Langevin equation (7.10). In Fig. 7.5a we show typical snapshots of the surface pattern in stationary limit at different values of the noise intensity σ^2. It follows that with an increase in noise intensity the size of adsorbate islands decreases (compare snapshots at $\sigma^2 = 0.1$ and $\sigma^2 = 1$). At large noise intensity islands of adsorbate are organized into strips via labyrinthine structure (see snapshot at $\sigma^2 = 3$). With further increasing the noise intensity such strips desorganize into islands changing their shape constantly and as a results no stationary structures are possible (see snapshot at $\sigma^2 = 6$).

To illustrate properties of adsorbate structures formation we compute averaged values, $\langle x \rangle$ and $\langle (\delta x)^2 \rangle$. From protocols shown in Fig. 7.5b it follows that if the noise is added into the system dynamics the averaged coverage $\langle x \rangle$ rapidly attains the stationary state. The dispersion $\langle (\delta x)^2 \rangle$ at initial stages at nonzero σ^2 grows faster than in the noiseless case. It means that internal fluctuations accelerate destabilization of the initial state $x = 0$.

In Fig. 7.5c we present dependencies for quantities $\langle x \rangle$ and $\langle (\delta x)^2 \rangle$ averaged over large time interval when the system attains the stationary state versus noise intensity. Here the average coverage increases with σ^2 meaning that the system is in dense phase. At large noise intensity one has $\langle x \rangle \simeq 0.5$ that indicates formation of mixed state. The quantity $\langle (\delta x)^2 \rangle$ monotonically decreases with σ^2 meaning transition to the so-called disordered configuration when atoms can be adsorbed or desorbed with the same probability.

To make detailed analysis of such phase transition one can consider behavior of stationary two-point correlation function $C(r) = \langle x(0)x(r) \rangle$ at different noise intensities. Numerical data for $C(r)$ can be approximated by function $C(r) \propto e^{-r/\langle r_c \rangle} \sin(2\pi r/\langle r_0 \rangle)$, where $\langle r_0 \rangle$ and $\langle r_c \rangle$ related to period of patterns and correlation radius, respectively. Dependencies $\langle r_0 \rangle(\sigma^2)$ and $\langle r_c \rangle(\sigma^2)$ are shown in Fig. 7.5d. It is seen that $\langle r_0 \rangle$ monotonically decays with the noise intensity. The physically interesting quantity $\langle r_c \rangle$ manifests more complicated behavior: $\langle r_c \rangle(\sigma^2)$ has well-pronounced peak meaning transition to chaotic configurations when the quantity $\langle x \rangle$ monotonically attains the value 1/2.

7.5 Statistical Properties

In this section we pay our attention to study statistical properties of localized nanostructures in overdamped stochastic reaction-Cattaneo model. It will be shown that a linear size of adsorbate islands depends essentially on rates for chemical reactions, interaction strength, and intensity of internal fluctuations. Typical snapshots of the corresponding surface structures at different values of

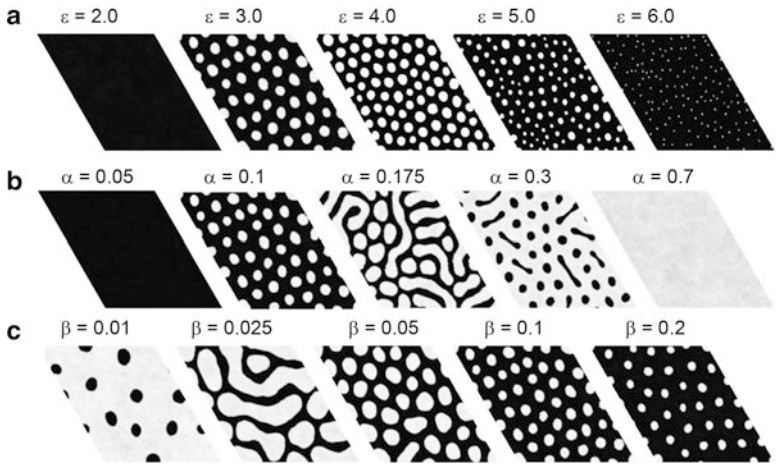

Fig. 7.6 Typical snapshots of the surface patterns at $t = 10^3$ and different values of the system parameters at $\rho_0 = 0.25$: (**a**) $\alpha = 0.1$, $\beta = 0.1$, $\tau = 0.1$, $\sigma^2 = 0.1$; (**b**) $\beta = 0.1$, $\varepsilon = 3$, $\tau = 0.1$, $\sigma^2 = 0.1$; (**c**) $\alpha = 0.1$, $\varepsilon = 3$, $\tau = 0.1$, $\sigma^2 = 0.1$

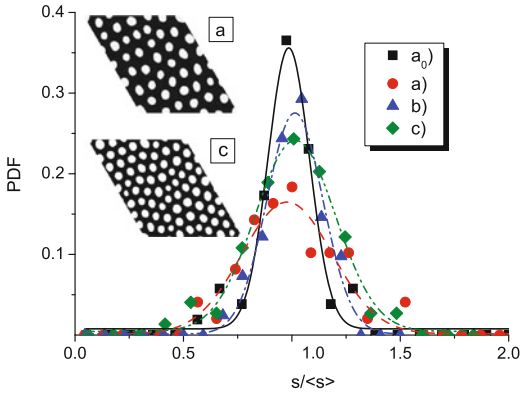

Fig. 7.7 Stationary probability density functions (*PDF*) of adsorbate islands area $s/\langle s\rangle$ at different system parameters: (a_0) $\tau = 0.0$, $\varepsilon = 3.0$, $\sigma^2 = 0.0$; (*a*) $\tau = 0.0$, $\varepsilon = 3.0$, $\sigma^2 = 0.1$; (*b*) $\tau = 0.1$, $\varepsilon = 3.0$, $\sigma^2 = 0.1$; (*c*) $\tau = 0.1$, $\varepsilon = 4.0$, $\sigma^2 = 0.1$. Other parameters are: $\beta = 0.1$, $\alpha = 0.1$, $\rho_0 = 0.25$

the main parameters illustrating a surface microstructure change are shown in Fig. 7.6 in the stationary limit.

From Fig. 7.6a it follows that at $\varepsilon < \varepsilon_c$ no adsorbate islands can be formed. An increase in ε leads to formation of separated stationary adsorbate clusters. Large ε promotes formation of large amount of small-size islands. Considering an influence of the adsorption rate α (see Fig. 7.6b) one finds a morphology change of the surface pattern: at small α the system is homogeneous; an increase in α promotes formation of separated adsorbate islands; at elevated α the structure of vacancy islands in adsorbate matrix is observed; at large α the system is totally homogeneous. Considering an influence of the parameter β responsible for the rate of nonequilibrium reactions one should stress that a condition $\beta \neq 0$ is necessary for formation of stationary structures. According to results shown in Fig. 7.6c it follows that at small

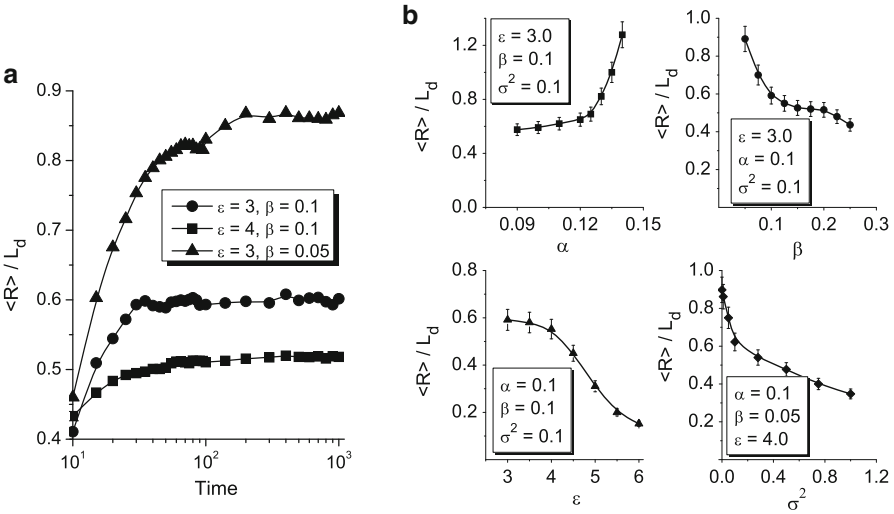

Fig. 7.8 (**a**) Time dependencies of the mean radius of adsorbate islands at $\alpha = 0.1$, $\sigma^2 = 0.1$, $\tau = 0.1$. (**b**) Dependencies of the radius of separated spherical adsorbate islands *versus* system parameters at $\tau = 0.1$

β and fixed other control parameters one gets a structure with separated vacancy islands. An increase in β leads to transition to a structure of adsorbate islands. An influence of the noise intensity onto pattern formation was discussed in previous section in detail.

Next, let us study stationary distribution functions *PDF* of adsorbate islands over area of islands $s/\langle s\rangle$, where $\langle s\rangle$ is the mean adsorbate island area at different set of the system parameters shown in Fig. 7.7. Here numerical results are shown by symbols; approximations characterized by maximal determination coefficient with χ^2-test are shown by curves. It is seen that at $\tau = 0$ (in stochastic case it relates to additive noise contribution) obtained data can be well approximated by the Gaussian distribution, centered in the vicinity $\langle s\rangle$ (see curve a_0). The noise action smears the distribution function (cf. curves a_0 and a). By taking $\tau \neq 0$ (see curves with triangles and diamonds in Fig. 7.7) the corresponding distribution does not change its form and remains Gaussian. A position of the corresponding peak is shifted toward $s > \langle s\rangle$.

To determine the characteristic size of separated islands we compute the corresponding mean radius $\langle R\rangle$ of spherical islands. Time dependencies of $\langle R\rangle$ measured in units L_d are shown in Fig. 7.8a at different system parameters. From the obtained data it follows that at large time scales we arrive at stationary picture where island sizes remain constant. The growth law of island sizes is very complicated and cannot be approximated by single exponential or power-law functions. At elevated ε (cf. curves with filled circles and squares) an island size growth is delayed essentially. Comparing curves with different β (cf. curves with filled circles and triangles) one finds that due to small rate of nonequilibrium reactions islands

grow with extremely large speed and in stationary case attain sizes compared with the diffusion length L_d.

Stationary dependencies of $\langle R \rangle$ *versus* the main system parameters are shown in Fig. 7.8b. It is seen that separated islands are characterized by $\langle R \rangle < L_d$. Estimation for the diffusion length $L_d \sim 10^{-6} \div 10^{-7}$ m gives $\langle R \rangle \sim 10^{-7} \div 10^{-8}$ m. According to the obtained results one can conclude that the radius of nano-size adsorbate islands can be controlled by variation in the pressure of gaseous phase (the adsorption rate α), temperature/interaction energy of adsorbate ε, annihilation rate β, and the noise intensity σ^2. At elevated adsorbate interaction energy and large nonequilibrium reaction rate adsorbate islands are characterized by $\langle R \rangle \sim 20 \div 100$ nm [49]. An increase in the noise level leads to formation of islands with small sizes.

7.6 Conclusions

We have studied the dynamics of adsorbate islands formation during vapor deposition by using the generalized approach including the persistent motion of particles having the finite speed at initial stages and the diffusion kinetics at final ones. We have introduced nonequilibrium chemical reactions responsible for formation of complexes and fluctuation source responsible for dissipation processes. By studying deterministic system it was found that during system evolution, pattern selection processes are realized. We have shown that the possible oscillatory regimes for islands formation are realized at a finite propagation speed related to the nonzero relaxation time for the diffusion flux.

Dynamics of pattern formation of the adsorbate in stochastic system was studied in overdamped limit. It was found that a transition from a well-spatially organized stationary pattern to a chaotic pattern is realized. Comparing both deterministic and stochastic cases we have found that the internal fluctuation source accelerates the transition to a spatially ordered configuration at small intensities and delays aggregation of islands; at large intensities it leads to formation of a smaller number of islands due to its organizations into a strip pattern. A further increase in fluctuations destroys the stationary pattern. Phase transition between ordered and chaotic phases is described in terms of stationary averaged coverage filed, its dispersion, and the corresponding correlation radius, which manifests enhancement of coverage fluctuations. Considering the two-point correlation function it was shown that in the vicinity of such a phase transition point the correlation radius of the adsorbate exhibits a well-pronounced peak that reflects above the fluctuations' increase.

Statistical properties of arranged islands of adsorbate are studied by distribution functions over island size analysis and dependence of a characteristic size versus control parameters reduced to adsorption/desorption rate, interaction energy of adsorbate, nonequilibrium chemical reactions rate, and an intensity of corresponding fluctuations. It is shown that distribution function of adsorbate

islands over areas (squares) is characterized by Gaussian-like form and it remains invariant with variation in main system parameters. We have found that the linear size of adsorbate islands is of nanometer range. It increases with an increase in the adsorption rate. An increase in interaction strength or rate of nonequilibrium reactions, or noise intensity leads to decrease in the linear size of adsorbate islands.

Our results can be used to describe the formation of nano-islands at processes of condensation from the gaseous phase. Even though we have considered a general model where the relaxation time τ_J for the diffusion flux is small, but a nonzero value, one can say that the condensation processes with the formation of metallic islands can be described in the limit $\tau_J/\omega_D^{-1} \lesssim 10^{-3}$ (here ω_D is the Debye frequency), whereas the nano-islands formation with $\tau_J/\omega_D^{-1} \sim 10^{-1} \div 10^{-2}$ is possible for soft matter condensation (semiconductors, polymers, etc).

References

1. Hirota E, Sakakima H, Inomata K (2002) Giant magneto-resistance devices. Springer, Berlin/Heidelberg
2. Warburton RJ, Schäflein C, Haft D et al (2000) Nature 405:926
3. Shah A, Torres P, Tscharner R et al (1999) Science 285:692
4. Zhao L, Lo S, Zhang Y et al (2014) Nature 508:373
5. Wadley HNG, Zhou X, Johnson RA et al (2001) Prog Mater Sci 46:329
6. Sree Harsha KS (2006) Principles of physical vapor deposition of thin films. Elesevier, Amsterdam
7. Perotto G, Bello V, Cesca T et al (2010) Nucl Instrum Methods Phys Res B 268:3211
8. Bernas H (2010) Nucl Instrum Methods Phys Res B 268:3171
9. Bradley RM, Harper JME (1988) J Vac Sci Technol A 6(4):2390
10. Karmakar P (2013) Nanostructures in thin films by keV ion beams. In: Som T, Kanjilal D (eds) Nanofabrication by ion-beam sputtering. Taylor & Francis Group, Boca Raton
11. Lian J, Zhou W, Wei QM et al (2006) Appl Phys Lett 88:093112
12. Kharchenko DO, Kharchenko VO, Lysenko IO et al (2010) Phys Rev E 82:061108
13. Kharchenko VO, Kharchenko DO (2011) Condens Matter Phys 14(2):23602
14. Venables JA, Spiller GDT, Hanbücken M (1984) Rep Prog Phys 47:399
15. Pimpinelli A, Villian J (1998) Physics of crystal growth. Cambridge University Press, Cambridge
16. Caflisch RE (2006) Proceedings of the international congress of mathematicians, Madrid, p 1419
17. Kharchenko DO, Kharchenko VO, Lysenko IO (2011) Phys Scr 83:045802
18. Kharchenko DO, Kharchenko VO, Zhylenko TI et al (2013) Eur Phys J B 86(4):175
19. Kharchenko DO, Kharchenko VO, Kokhan SV (2014) Condens Matter Phys 17:33004
20. Kharchenko VO, Kharchenko DO, Dvornichenko AV (2015) Eur Phys J B 88:3
21. Zambelli T, Trost J, Wintterlin J, Ertl G (1996) Phys Rev Lett 76:795
22. Gorodetskii V, Lauterbach J, Rotermund HA, Block JH, Ertl G (1994) Nature 370:276
23. Kern K, Niehus H, Schatz A et al (1991) Phys Rev Lett 67:855
24. Parker TM, Wilson LK, Condon NG, Leibsle FM (1997) Phys Rev B 56:6458
25. Brune H, Giovannini M, Bromann K, Kern K (1998) Nature 394:451
26. Clark PG, Friend CM (1999) J Chem Phys 111:6991
27. Mo YM, Swartzentruber BS, Kariotis R et al (1989) Phys Rev Lett 63:2393
28. Cirlin GE, Egorov VA, Sokolov LV, Werner P (2002) Semiconductors 36(11):1294–1298

29. Bucher JP, Hahn E, Fernandez P, Massobrio C, Kern K (1994) Europhys Lett 27:473
30. Besenbacher F, Nielsen LP, Sprunger PT (1997) Surface alloying in heteroepitaxial metal-on-metal growth. In: King DA, Woodruff DP (eds) The chemical physics of solid surfaces, Chap. 6. Elsevier, Amsterdam, p 207
31. Brune H (1998) Surf Sci Rep 31:121–229
32. Pohl K, Bartelt MC, de la Figuera J et al (1999) Nature 397:238
33. Mikhailov A, Ertl G (1994) Chem Phys Lett 238:104
34. Batogkh D, Hildebrant M, Krischer F, Mikhailov A (1997) Phys Rep 288:435
35. Hildebrand M, Mikhailov AS, Ertl G (1998) Phys Rev E 58:5483(11)
36. Mangioni SE, Wio HS (2005) Phys Rev E 71:056203
37. Mangioni SE (2010) Physica A 389:1799
38. Casal SB, Wio HS, Mangioni S (2002) Physica A 311:443
39. Wolgraef D (2002) Physica E 15:33
40. Wolgraef D (2003) Physica E 18:393
41. Wolgraef D (2004) Int J Quantum Chem 98:248
42. Hildebrand M, Mikhailov AS, Ertl G (1998) Phys Rev Lett 81:2602(4)
43. Hildebrand M, Mikhailov AS (1996) J Phys Chem 100:19089
44. Kharchenko D, Kharchenko V, Lysenko I (2011) Cent Eur J Phys 9(3):698
45. Lecoq N, Zapolsky H, Galenko P (2009) Eur Phys J Spec Top 177:165
46. Galenko PK, Kharchenko D, Lysenko I (2010) Physica A 389:3443
47. Kharchenko VO, Kharchenko DO, Kokhan SV et al (2012) Phys Scr 86:055401
48. Kharchenko VO, Kharchenko DO (2012) Phys Rev E 86:041143
49. Kharchenko VO, Kharchenko DO, Dvornichenko AV (2014) Surf Sci 630:158
50. Miguel MS, Sancho JM (1980) J Stat Phys 22:605
51. Sancho JM, Miguel MS, Dürr D (1982) J Stat Phys 28(2):291
52. Van Kampen NG (1992) Stochastic processes in physics and chemistry. North–Holland, Amsterdam
53. Olemskoi AI, Kharchenko DO, Knyaz' IA (2005) Phys Rev E 71:041101
54. Shapiro VE (1993) Phys Rev E 48:109

Chapter 8
Kinetics of Transmission Through and Reflection from Interfaces in Nanostructures

Victor Los and Mykola Los

PACS: 03.65.Nk, 03.65.Xp, 72.25.Mk, 73.21.Ac, 85.75.-d

8.1 Introduction

The time-dependent aspects of reflection from and transmission through a potential step/barrier/well have recently acquired relevance not only in view of renewed interest in the fundamental problems of measuring time in quantum mechanics (see [1, 2]) but also due to important practical applications of the newly emerged field of nanoscience and nanotechnology. Rectangular potential barriers/wells may often satisfactorily approximate the one-dimensional potential profiles in layered magnetic nanostructures (with sharp interfaces). In such nanostructures, the giant magnetoresistance (GMR) [3] and tunneling magnetoresistance (TMR) [4, 5] effects occur. These effects, which stem, particularly, from quantum mechanical spin-dependent electrons tunneling through potential barriers or their reflection from potential wells, have led to very important commercial applications of spintronic devices. For stationary states, these quantum mechanical phenomena easily follow from matching the plane waves and their derivatives at the potential steps. However, the development of high-speed devices, based on tunneling structures in semiconductors, and of ultrafast spectroscopy of semiconductors and semiconductor nanostructures (see, e.g., [6]) has brought new urgency to the understanding, in particular, of the time-dependent properties of particle scattering by potential barriers/wells.

V. Los (✉) • M. Los
Institute of Magnetism, National Academy of Sciences of Ukraine, 36-b Vernadsky Blvd., 03142 Kiev, Ukraine
e-mail: victorlos@mail.ru

O. Fesenko, L. Yatsenko (eds.), *Nanophysics, Nanophotonics, Surface Studies, and Applications*, Springer Proceedings in Physics 183,
DOI 10.1007/978-3-319-30737-4_8

The time-dependent picture of the mentioned processes in a realistic situation, when a particle, originally localized outside the potential well/barrier, moves towards the potential and experiences scattering at the potential steps, is much more involved as compared to the conventional stationary case. In order to describe these time-dependent processes, the corresponding time-dependent Schrödinger equation with a rectangular potential should be solved, which is a rather difficult problem. The solution to the time-dependent Schrödinger equation can be obtained with the help of the spacetime propagator (Green function), which has been conveniently calculated by the path-integral method. The list of exact solutions for this propagator is very short. For example, there is an exact solution to the spacetime propagator by the path-integral method in the one-dimensional square barrier case obtained in [7], but this solution is very complicated, implicit, and not easy to analyze.

Recently, we have suggested a multiple scattering theory (MST) approach [8–10] for the calculation of the energy-dependent Green function (resolvent) based on the effective energy-dependent potentials [8], which are responsible for reflection from and transmission through the potential step. Then, the spacetime propagator is obtained by the energy integration of the spectral density matrix (discontinuity of the energy-dependent Green function across the real energy axis).

In this paper, we apply our approach to the solution of the time-dependent Schrödinger equation in the case when a particle moves towards a rectangular, generally asymmetric well/barrier potential, which changes in the x (perpendicular to interfaces) direction and models the spin-dependent potential profile in magnetic nanostructures. The obtained solution provides exact analytical expressions for the wave function $\psi(\mathbf{r}, t)$ in the spatial regions before, inside and after the potential with account for the backward-moving terms caused by the negative momentum components of the initial wave function. The corresponding probability densities $|\psi(x,t)|^2$ are analyzed and numerically visualized for a Gaussian initial wave packet with special attention to the counterintuitive quantum contribution of the backward-moving wave packet components (see [11, 12]) and the potential asymmetry. The obtained results pave the foundation to the kinetic theory of nanostructures.

8.2 Propagator for the Schrödinger Equation

We consider a particle moving towards the following asymmetric one-dimensional rectangular potential of the width d placed in the interval $(0 < x < d)$

$$V(x) = [\theta(x) - \theta(x-d)]U + \theta(x-d)\Delta, \tag{8.1}$$

where $\theta(x)$ is the Heaviside step function, and the potential parameter U can acquire positive (barrier) as well as negative (well) values. With the potential (8.1) we can model the spin-dependent potential profile of three layers made of nonmagnetic

spacer (metallic or insulator) sandwiched between two magnetic (infinite) layers. Spin-dependence of the potential (8.1) is defined by the parameter Δ via the electron spectrum in different magnetic layers as

$$\begin{aligned} &k^0_<(E;\mathbf{k}_{||}) = k(E;\mathbf{k}_{||}), k^d_>(E;\mathbf{k}_{||}) = k_\Delta(E;\mathbf{k}_{||}), \\ &k(E;\mathbf{k}_{||}) = \sqrt{\frac{2m}{\hbar^2}E - \mathbf{k}^2_{||}}, k_\Delta(E;\mathbf{k}_{||}) = \sqrt{\frac{2m}{\hbar^2}(E-\Delta) - \mathbf{k}^2_{||}}, \\ &k^0_>(E;\mathbf{k}_{||}) = k^d_<(E;\mathbf{k}_{||}) = k_u(E;\mathbf{k}_{||}), k_u(E;\mathbf{k}_{||}) = \sqrt{\frac{2m}{\hbar^2}(E-U) - \mathbf{k}^2_{||}}, \end{aligned} \tag{8.2}$$

where $k^0_{>(<)}(E;\mathbf{k}_{||})$ and $k^d_{>(<)}(E;\mathbf{k}_{||})$ are the perpendicular-to-interfaces (located at $x=0$ and $x=d$) components of the particle wave vector $\mathbf{k}$ to the right ($>$) or to the left ($<$) of the corresponding interface, while $\mathbf{k}_{||}$ is the parallel-to-interfaces component of an electron wave vector, which is conserved for the sharp interfaces under consideration. The two-dimensional vector $\mathbf{k}_{||}$ defines the angle of electron incidence at the interface.

From the particle propagation point of view, the partial reflection from and transmission through a potential inhomogeneity may be explained by the quantum mechanical rules of computing the probabilities of different events. These rules represent the quantum mechanical generalization of the Huygens–Fresnel principle and were introduced by Feynman as the path-integral formalism [13]. It states that a wave function of a single particle moving in a perturbing potential $V(\mathbf{r},t)$ may be presented as

$$\psi(\mathbf{r},t) = \int d\mathbf{r}' K(\mathbf{r},t;\mathbf{r}',t_0)\psi(\mathbf{r}',t_0). \tag{8.3}$$

The propagator $K(\mathbf{r},t;\mathbf{r}',t_0)$ is the probability amplitude for the particle's transition from the initial spacetime point $(\mathbf{r}',t_0)$ to the final point $(\mathbf{r},t)$ by means of all possible paths. It provides the complete information on the particle's dynamics and resolves the corresponding time-dependent Schrödinger equation.

Thus, the problem is to find the propagator $K(\mathbf{r},t;\mathbf{r}',t_0)$ for the given potential $V(\mathbf{r},t)$. In some cases, for example, when the potential is quadratic in the space variable, the kernel $K(\mathbf{r},t;\mathbf{r}',t_0)$ may be calculated exactly. In the case when the potential changes smoothly enough, a quasi-classical approximation can be employed. It is not, however, the case for the singular potential (8.1).

According to [8], the time-dependent retarded (operator) propagator $K(t;t') = \theta(t-t')\exp\left[-\frac{i}{\hbar}H(t-t')\right]$ can be calculated with the use of the following: definition

$$K(t;t') = \theta(t-t')\frac{i}{2\pi}\int_{-\infty}^{\infty} e^{-\frac{i}{\hbar}E(t-t')}[G(E+i\varepsilon) - G(E-i\varepsilon)]dE, \varepsilon \to +0, \tag{8.4}$$

where

$$G(E) = \frac{1}{E - H} \tag{8.5}$$

is the resolvent operator, E stands for the energy, and H is the Hamiltonian of the system under consideration. Correspondingly, $G(E \pm i\varepsilon) = G^{\pm}(E)$ defines the retarded (G^{+}) or the advanced (G^{-}) Green function.

We are looking for the spacetime propagator $K(\mathbf{r}, t; \mathbf{r}', 0) = < \mathbf{r}|K(t;0)|\mathbf{r}' >$, defining the probability amplitude for a particle's transition from the initial point $(\mathbf{r}', 0)$ to the final destination $(\mathbf{r}, t)$ in the presence of the potential (8.1). For the considered geometry, it is convenient to present the r-representation of the Green function with the Hamiltonian H, $G(\mathbf{r}, r'; E) = < \mathbf{r}| \frac{1}{E-H} |\mathbf{r}' >$, as follows:

$$G(\mathbf{r}, \mathbf{r}'; E) = \frac{1}{A} \sum_{\mathbf{k}_{||}} e^{i\mathbf{k}_{||}(\boldsymbol{\rho} - \boldsymbol{\rho}')} G(x, x'; E; \mathbf{k}_{||}), \tag{8.6}$$

where $\boldsymbol{\rho} = (y, z)$ is a two-dimensional parallel-to-interface vector and A is the area of the interface. Thus, the problem is reduced to finding the one-dimensional Green function $G(x, x'; E; \mathbf{k}_{||})$ dependent on the conserved particle energy and parallel-to-interface component of the wave vector. In the following calculation of this function we will suppress for simplicity the dependence on the argument $\mathbf{k}_{||}$, which will be recovered at the end of calculation.

We showed in [8] that the Hamiltonian corresponding to the energy-conserving processes of scattering at potential steps can be presented as

$$\begin{aligned} H &= H_0 + H_i(x; E), \\ H_i(x; E) &= \sum_s H_i^s(E) \delta(x - x_s). \end{aligned} \tag{8.7}$$

Here, $H_i(x; E)$ describes the perturbation of the "free" particle motion (defined by $H_0 = -\frac{\hbar^2}{2m} \frac{\partial^2}{\partial \mathbf{r}^2}$) localized at the potential steps with coordinates x_s (in the case of the potential (8.1), there are two potential steps at $x_s = 0$ and $x_s = d$)

$$
\begin{aligned}
H^s_{i>}(E) &= \frac{i\hbar}{2}[v^s_>(E) - v^s_<(E)],\\
H^s_{i<}(E) &= \frac{i\hbar}{2}[v^s_<(E) - v^s_>(E)],\\
H^s_{i><}(E) &= \frac{2i\hbar v^s_>(E)v^s_<(E)}{[\sqrt{v^s_>(E)} + \sqrt{v^s_<(E)}]^2},
\end{aligned}
\tag{8.8}
$$

where $H^s_{i>(<)}(E)$ is the reflection (from the potential step at $x = x_s$, $s \in \{0, d\}$) potential amplitude, the index $>(<)$ indicates the side on which the particle approaches the interface at $x = x_s$: right $(>)$ or left $(<)$; $H_{i><}{}^s(E)$ is the transmission potential amplitude, and the velocities $v^s_{>(<)}(E) = \hbar k^s_{>(<)}(E)/m$, $[k^s_{>(<)}(E)$ are given by (8.2)]. Note that the perturbation Hamiltonian $H_i{}^s$'s dependence on $\mathbf{k}_{||}$ (which is omitted for brevity) comes from Eq. (8.2).

In the case of the rectangular potential (8.1), the perturbation expansion of the retarded Green function $G^+(x, x'; E)$ for different source (given by x') and destination (determined by x) areas of interest is presented by the infinite series of multiple scattering events expressed in terms of the two-step effective Hamiltonian (8.7) and the one-dimensional retarded Green function $G^+_0(x, x'; E)$ corresponding to a free particle moving in constant potential $V(x) = 0$ or $V(x) = U$ (or Δ) (see, e.g., [14])

$$
\begin{aligned}
G^+_0(x, x'; E) &= \frac{m}{i\hbar^2 k(E)}\exp[ik(E)|x - x'|], V(x) = 0,\\
G^+_0(x, x'; E) &= \frac{m}{i\hbar^2 k_{u(\Delta)}(E)}\exp[ik_{u(\Delta)}(E)|x - x'|], V(x) = U(\text{or}\Delta),
\end{aligned}
\tag{8.9}
$$

where the wave numbers are determined by (8.2). The multiple scattering series can be summed up resulting in the following scattering t-matrix (at the step located at $x = x_s$)

$$
\begin{aligned}
T^s(E) &= H^s_i(E) + H^s_i(E)G_0(x_s, x_s; E)H^s_i(E) + \ldots\\
&= \frac{H^s_i(E)}{1 - G_0(x_s, x_s; E)H^s_i(E)},
\end{aligned}
\tag{8.10}
$$

where $H_i{}^s(E)$ and the interface Green function $G_0(x_s, x_s; E)$ are defined differently for reflection and transmission processes [8]: the step-localized effective potential is given by Eq. (8.8) and the retarded Green functions at the interface for the considered reflection and transmission processes are, correspondingly,

$$G^{+}_{0>(<)}(x_s, x_s; E) = 1/i\hbar v^{s}_{>(<)}(E)$$
$$G^{+}_{0><}(x_s, x_s; E) = 1/i\hbar\sqrt{v^{s}_{>}(E)v^{s}_{<}(E)} \tag{8.11}$$

in accordance with (8.9).

As a result of this approach we obtain (for more details see [10, 15])

$$G^{+}(x, x^{'}; E) = \frac{m}{i\hbar^2\sqrt{kk_\Delta}}e^{ik_\Delta(x-d)}t(E)e^{-ikx^{'}}, x^{'} < 0, x > d,$$
$$G^{+}(x, x^{'}; E) = \frac{m}{i\hbar^2\sqrt{kk_\Delta}}e^{-ikx}t(E)e^{ik_\Delta(x^{'}-d)}, x^{'} > d, x < 0,$$
$$G^{+}(x, x^{'}; E) = \frac{m}{i\hbar^2\sqrt{kk_u}}[e^{ik_u x}t^{'}(E)e^{-ikx^{'}} + e^{-ik_u x}r^{'}(E)e^{-ikx^{'}}], x^{'} < 0, 0 < x < d,$$
$$G^{+}(x, x^{'}; E) = \frac{m}{i\hbar^2\sqrt{kk_u}}[e^{-ikx}t^{'}(E)e^{ik_u x^{'}} + e^{-ikx}r^{'}(E)e^{-ik_u x^{'}}], x < 0, 0 < x^{'} < d,$$
$$G^{+}(x, x^{'}; E) = \frac{m}{i\hbar^2 k}[e^{ik|x-x^{'}|} + r(E)e^{-ik(x+x^{'})}], x < 0, x^{'} < 0, \tag{8.12}$$

where the transmission and reflection amplitudes are defined as

$$t(E) = \frac{4\sqrt{kk_\Delta}k_u e^{ik_u d}}{d(E)}, t^{'}(E) = \frac{2\sqrt{kk_u}(k_\Delta + k_u)}{d(E)}, r^{'}(E) = \frac{2\sqrt{kk_u}(k_u - k_\Delta)e^{2ik_u d}}{d(E)},$$
$$r(E) = \frac{(k - k_u)(k_\Delta + k_u) - (k + k_u)(k_\Delta - k_u)e^{2ik_u d}}{d(E)},$$
$$d(E) = (k + k_u)(k_\Delta + k_u) - (k - k_u)(k_\Delta - k_u)e^{2ik_u d}. \tag{8.13}$$

Equations (8.12) and (8.13) generalize the results obtained in [10, 15] on the case of the asymmetric rectangular potential (8.1). Using the same approach, it is not difficult to obtain the Green function $G^{+}(x, x^{'}; E)$ for other areas of arguments x and $x^{'}$. The transmission probability $|t(E)|^2$ through and reflection probability $|r(E)|^2$ from the asymmetric potential (8.1) can be easily found from Eq. (8.13).

In accordance with the obtained results for Green functions, we will consider the situation when a particle, given originally by a wave packet localized to the left of the potential area, i.e., at $x^{'} < 0$, moves towards the potential (8.1). We also choose $\Delta \geq 0$, which corresponds to the case when, e.g., the spin-up electrons of the left magnetic layer ($x^{'} < 0$) move through the nonmagnetic spacer to the right magnetic layer ($x > d$) aligned either in parallel ($\Delta = 0$) or antiparallel ($\Delta > 0$) to the left magnetic layer.

From Eq. (8.12) we see that $G^{+}(x,x^{'};E) = G^{+}(x^{'},x;E)$, and, therefore, the advanced Green function $G^{-}(x,x^{'};E) = \left[G^{+}(x^{'},x;E)\right]^{*} = \left[G^{+}(x,x^{'};E)\right]^{*}$ (see, e.g., [14]). Thus, the transmission amplitude (8.4) is determined by the imaginary part of the Green function and can be written as

$$K(x,t;x^{'},t_0) = -\theta(t-t_0)\frac{1}{\pi}\int\limits_{-\infty}^{\infty} dE e^{-\frac{i}{\hbar}E(t-t_0)}\mathrm{Im}G^{+}(x,x^{'};E). \tag{8.14}$$

Formulas (8.12)–(8.14) present the exact solution for the particle propagator in the presence of the potential (8.1) in terms of integrals (over E) of elementary functions for a given angle ($\mathbf{k}_{||}$) of a particle's arrival at the potential (8.1). It can be shown that the energy interval ($-\infty \div \hbar^2\mathbf{k}_{||}^2/2m$) does not contribute to the propagation of the particles through the potential well/barrier region. From Eqs. (8.2), (8.12), and (8.13) we see that the dependence of the Green function on E and $\mathbf{k}_{||}$ comes in the combination $E - \hbar^2\mathbf{k}_{||}^2/2m$, and, therefore, it is convenient to shift to this new energy variable, which is the perpendicular-to-interface component of the total particle energy. It then follows from (8.12)–(8.14) that for the new energy variable the energy interval ($-\infty \div 0$) does not contribute to the propagator (8.14).

It is easy to verify that the integration over E and $\mathbf{k}_{||}$ [according to (8.6)] of the first term in the last line of (8.12) results in the known formula for the spacetime propagator for a freely moving particle

$$K_0(\mathbf{r},t;\mathbf{r}^{'},t_0) = \theta(t-t_0)\left[\frac{m}{2\pi i\hbar(t-t_0)}\right]^{3/2}\exp\left[\frac{im(\mathbf{r}-\mathbf{r}^{'})^2}{2\hbar(t-t_0)}\right], x<0, x^{'}<0. \tag{8.15}$$

The obtained results for the particle propagator completely resolve [by means of Eq. (8.3)] the time-dependent Schrödinger equation for a particle moving under the influence of the rectangular potential (8.1) for the given initial wave function $\psi(\mathbf{r}^{'},t_0)$.

8.3 Time-Dependent Probability Density of Finding a Particle in Different Spatial Regions

Using Eqs. (8.3), (8.6), (8.12), and (8.14), we can present the wave function in different spatial regions at $t > t_0$ as

$$\psi(\mathbf{r},t) = \psi_{>}(\mathbf{r},t) + \psi_{<}(\mathbf{r},t). \tag{8.16}$$

Here

$$\begin{aligned}
\psi_{>}(\mathbf{r},t) &= \frac{1}{\sqrt{2\pi\hbar}}\int_0^\infty dE e^{-\frac{i}{\hbar}E(t-t_0)}\frac{1}{\sqrt{v_\Delta(E)}}t(E)e^{ik_\Delta(E)(x-d)}\psi_{>}(E;\boldsymbol{\rho},t), x > d,\\
\psi_{<}(\mathbf{r},t) &= \frac{1}{\sqrt{2\pi\hbar}}\int_0^\infty dE e^{-\frac{i}{\hbar}E(t-t_0)}\frac{1}{\sqrt{v^*_\Delta(E)}}t^*(E)e^{-ik^*_\Delta(E)(x-d)}\psi_{<}(E;\rho,t), x > d,\\
\psi_{>}(\mathbf{r},t) &= \frac{1}{\sqrt{2\pi\hbar}}\int_0^\infty dE e^{-\frac{i}{\hbar}E(t-t_0)}\frac{1}{\sqrt{v_u(E)}}\left[t'(E)e^{ik_u(E)x} + r'(E)e^{-ik_u(E)x}\right]\psi_{>}(E;\rho,t), 0 < x < d,\\
\psi_{<}(\mathbf{r},t) &= \frac{1}{\sqrt{2\pi\hbar}}\int_0^\infty dE e^{-\frac{i}{\hbar}E(t-t_0)}\frac{1}{\sqrt{v^*_u(E)}}\left[t'^*(E)e^{-ik^*_u(E)x} + r'^*(E)e^{ik^*_u(E)x}\right]\psi_{<}(E;\rho,t), 0 < x < d,\\
\psi_{>}(\mathbf{r},t) &= \frac{1}{\sqrt{2\pi\hbar}}\int_0^\infty dE e^{-\frac{i}{\hbar}E(t-t_0)}\frac{1}{\sqrt{v(E)}}\left[e^{ik(E)x} + r(E)e^{-ik(E)x}\right]\psi_{>}(E;\rho,t), x < 0,\\
\psi_{<}(\mathbf{r},t) &= \frac{1}{\sqrt{2\pi\hbar}}\int_0^\infty dE e^{-\frac{i}{\hbar}E(t-t_0)}\frac{1}{\sqrt{v(E)}}\left[e^{-ik(E)x} + r^*(E)e^{ik(E)x}\right]\psi_{<}(E;\rho,t), x < 0
\end{aligned} \tag{8.17}$$

and $\mathbf{r} = (x,\boldsymbol{\rho})$. The wave function in the E-representation $\psi_{>(<)}(E;\boldsymbol{\rho},t)$ is related to its k-representation $\psi_{>(<)}[k(E);\rho,t)]$ as

$$\psi_{>}(E;\rho,t) = \frac{1}{\sqrt{2\pi\hbar v(E)}}\psi_{>}[k(E);\rho,t], \psi_{<}(E;\rho,t) = \frac{1}{\sqrt{2\pi\hbar v(E)}}\psi_{<}[k(E);\rho,t],$$

$$\psi_{>}[k(E);\rho,t] = \int d\rho' K(\boldsymbol{\rho},t;\rho',t_0)\int dx' e^{-ik(E)x'}\psi(x',\rho',t_0),$$

$$\psi_{<}[k(E);\boldsymbol{\rho},t] = \int d\rho' K(\boldsymbol{\rho},t;\rho',t_0)\int dx' e^{ik(E)x'}\psi(x',\rho',t_0),$$

$$K(\boldsymbol{\rho},t;\rho',t_0) = \frac{1}{A}\sum_{\mathbf{k}_{||}}\exp\left[-\frac{i}{\hbar}\frac{\hbar^2\mathbf{k}^2_{||}}{2m}(t-t_0)\right]e^{i\mathbf{k}_{||}(\boldsymbol{\rho}-\rho')} = \frac{m}{2\pi i\hbar(t-t_0)}\exp\left[-\frac{(\boldsymbol{\rho}-\rho')^2 m}{2i\hbar(t-t_0)}\right], \tag{8.18}$$

where $K(\boldsymbol{\rho}, t; \boldsymbol{\rho}', t_0)$ is the "free" propagator in the parallel-to-interface (y, z) plane [see (8.6) and (8.15)].

To be definite, we assume that for positive energies $k(E) = \sqrt{2mE/\hbar^2} > 0$ and, therefore, $\psi_>[k(E); \boldsymbol{\rho}, t]$ is related to the component of the initial wave function $\psi(x', \boldsymbol{\rho}', t_0)$ corresponding to propagation to the right along the x axis, and, accordingly, $\psi_<[k(E); \boldsymbol{\rho}, t]$ represents propagation to the left. When the potential $V(x) \neq 0$, integration over x' in (8.18) is restricted to the negative semispace ($x' < 0$), as it follows from the expression (8.12) for the particle propagator.

The result, given by Eqs. (8.16), (8.17), and (8.18), indicates that, generally, the contribution of the wave function, originated at $t = t_0$ to the left of the potential (8.1) ($x' < 0$), to the wave function in the region of the potential ($0 < x < d$) and to the right of it ($x > d$) comes at $t > t_0$ from both: the components moving to the right, $\psi_>$, and to the left, $\psi_<$. This rather paradoxical result follows from the fact that if the initial wave packet has the nonnegligible negative momentum components (restricted to a half-line in the momentum space), the corresponding spatial wave function is different from zero in the entire x-region $(-\infty, \infty)$, interacting with the potential even at $t < t_0$, and is thus modified by this interaction (see also [11, 16]). As a result, the backward-moving components contribute to the behavior of the wave function at $t > t_0$ in the spatial regions to the right of the original wave packet localization.

Consequently, the probability density of finding a particle in the spacetime point $(\mathbf{r}, t)$, $|\psi(\mathbf{r}, t)|^2$ is determined by the forward- and backward-moving terms, as well as their interference:

$$|\psi(\mathbf{r}, t)|^2 = |\psi_>(\mathbf{r}, t)|^2 + |\psi_<(\mathbf{r}, t)|^2 + 2\mathrm{Re}\psi_>(\mathbf{r}, t)\psi_<^*(\mathbf{r}, t). \tag{8.19}$$

Equations (8.17)–(8.19) generally resolve the problem of finding a particle in the spatial region of interest at time t for a given initial wave function $\psi(\mathbf{r}', t_0)$. These equations can be used for numerical modeling of the corresponding probability density in the different spacetime regions (see below) and for determining some characteristics of the particle dynamics under the influence of the potential (8.1).

In order to estimate the actual contribution of the backward-moving and interference terms to the obtained general formulas, we should consider a physically relevant situation as to the initial wave packet. Let us consider the case when the moving particles are associated with a wave packet which is initially sufficiently well localized to the left of the potential (8.1). Thus we now consider the problem for a particular case of the initial state corresponding to the wave packet

$$\psi\left(\mathbf{r}', t_0\right) = \frac{1}{(2\pi\sigma^2)^{3/4}} \exp\left[-\frac{(\mathbf{r}' - \mathbf{r}_i)^2}{4\sigma^2} + i\mathbf{k}_i\mathbf{r}'\right], x_i < 0, k_i > 0, \tag{8.20}$$

located in the vicinity of $\mathbf{r}_i = (x_i, \boldsymbol{\rho}_i)$ and moving in the positive x direction with the average momentum $\mathbf{p}_i = \hbar\mathbf{k}_i$, $k_i = k_x > 0$ ($\mathbf{k}_i = (k_i, \mathbf{k}_{||}^i)$, $\mathbf{r}' = (x', \boldsymbol{\rho}')$). Thus, we consider a general situation, when a particle, associated with the wave packet (8.20), comes to the potential (8.1) from the left with the positive perpendicular-to-interface momentum component $\hbar k_i > 0$ at the angle defined by the parallel-to-interface momentum component $\hbar\mathbf{k}_{||}^i$. Now, we can perform integration over spatial variables x', $\boldsymbol{\rho}'$, as it follows from (8.18) and (8.20).The result is

$$\begin{aligned}
&\psi_>(E;\boldsymbol{\rho},t) = C_{||}(\boldsymbol{\rho},t)\psi_>(E), \psi_<(E;\boldsymbol{\rho},t) = C_{||}(\boldsymbol{\rho},t)\psi_<(E),\\
&\psi_>(E) = \frac{1}{\sqrt{\pi\hbar v(E)}}(2\pi\sigma^2)^{1/4} e^{i[k_i - k(E)]x_i} e^{-[k_i-k(E)]^2\sigma^2},\\
&\psi_<(E) = \frac{1}{\sqrt{\pi\hbar v(E)}}(2\pi\sigma^2)^{1/4} e^{i[k_i + k(E)]x_i} e^{-[k_i+k(E)]^2\sigma^2},\\
&C_{||}(\boldsymbol{\rho},t) = \sqrt{\frac{2}{\pi}}\frac{m\sigma}{i\hbar(t-t_0)+2m\sigma^2}\exp[-\frac{(\boldsymbol{\rho}-\boldsymbol{\rho}_i - 2i\mathbf{k}_{||}^i\sigma^2)^2 m}{2i\hbar(t-t_0)+4m\sigma^2}] e^{i\mathbf{k}_{||}^i\boldsymbol{\rho}_i} e^{-(\mathbf{k}_{||}^i\sigma)^2},
\end{aligned} \tag{8.21}$$

where the factor $C_{||}(\boldsymbol{\rho},t)$ defines the dependence on the parallel-to-interface components of the vectors involved. Thus, the forward- and backward-moving components of the wave function $\psi_{>(<)}(\mathbf{r},t)$ (8.17) for the initial wave packet (8.20) reduce to the one-dimensional integral over energy E with the energy-dependent functions $\psi_{>(<)}(E)$ and the common factor $C_{||}(\boldsymbol{\rho},t)$.

We note that

$$\int d\boldsymbol{\rho}\left|C_{||}(\boldsymbol{\rho},t)\right|^2 = 1, \tag{8.22}$$

and, therefore, the total probability density of finding a particle in the given spacetime point (x,t)

$$\begin{aligned}
|\psi(x,t)|^2 &= \int d\rho|\psi(\mathbf{r},t)|^2\\
&= |\psi_>(x,t)|^2 + |\psi_<(x,t)|^2 + 2\mathrm{Re}\psi_>(x,t)\psi_<^*(x,t),
\end{aligned} \tag{8.23}$$

as it follows from (8.19), and the functions $\psi_{>(<)}(x,t)$ are determined by Eq. (8.17) where $\psi_{>(<)}(E;\rho,t)$ is replaced with $\psi_{>(<)}(E)$ [see (8.21)].

A physically relevant situation occurs when the initial wave function is well localized within the $x<0$ half-line because the propagator transmits this function from the $x' < 0$ region to the $x>0$ or $x<0$ regions. It can be shown that when the condition

$$\left|\frac{x_i}{2\sigma}\right| \gg 1 \tag{8.24}$$

holds, the tail of the initial wave packet (8.20) is very small near the arrival point $x = 0$.

Generally, both the $\psi_>(\mathbf{r},t)$ and $\psi_<(\mathbf{r},t)$ components contribute to the probability density $|\psi(\mathbf{r},t)|^2$ [see (8.19)]. We can also assume that

$$k_i\sigma \gg 1, \tag{8.25}$$

which implies that the perpendicular-to-interface momentum dispersion $\hbar/2\sigma$ is much smaller than the corresponding characteristic momentum $p_i = \hbar k_i$, or, equivalently,

$$\frac{\hbar^2}{2m\sigma^2} \ll E_\perp, E_\perp = \frac{\hbar^2 k_i^2}{2m} = E_i - \frac{\hbar^2 \mathbf{k}_{||}^{i2}}{2m}, \tag{8.26}$$

i.e., the energy dispersion $\hbar^2/8m\sigma^2$ is much smaller than the perpendicular component $E_\perp$ of the incident particle energy $E_i = (\hbar^2/2m)(k_i^2 + \mathbf{k}_{||}^{i2})$. Then one can see from (8.17) and (8.21) that in the case when condition (8.25) holds, the contribution of the backward-moving term $\psi_<(\mathbf{r},t)$ to the probability density is significantly smaller than that of the forward-moving term $\psi_>(\mathbf{r},t)$, and, therefore, in the first approximation the former can be neglected. Thus, the backward-moving term $\psi_<(\mathbf{r},t)$ is not essential in the quasi-classical approximation when both inequalities (8.24) and (8.25) are satisfied and, therefore, the particle scattering at the potential (8.1) associated with the wave packet (8.20) is characterized by a well-defined location relative to the potential and well-defined momentum. However, if the inequality (8.25) [or (8.26)] is violated (e.g., it may happen when the particle with the given energy E_i arrives at the interface $x = 0$ at an angle significantly different from the perpendicular-to-interface one, i.e., $\mathbf{k}_{||}^i$ is not small), then both the forward- and backward-moving components of the wave function (8.17) equally contribute to the probability density $|\psi(\mathbf{r},t)|^2$. In this case the quasi-classical approximation is not relevant and the particle is associated with the well-localized wave packet which has the broad perpendicular-to-interface momentum (energy) distribution.

8.4 Numerical Modeling

We will consider the probability density $|\psi(x,t)|^2$ (8.23). It is convenient to shift to dimensionless variables. As seen from (8.17), there is a natural spatial scale d, an energy scale $E_d = \hbar^2/2md^2$ (the energy uncertainty due to particle localization

within a barrier of width d), and a corresponding time scale $t_d = \hbar/E_d$. Thus, we introduce the scaled variables $\tilde{E} = E/E_d$, $\tilde{U} = U/E_d$, $\tilde{\Delta} = \Delta/E_d$, $\tilde{E}_\perp = E_\perp/E_d$, $E_\perp = \hbar^2 k_i^2/2m$, $\tilde{t} = t/t_d$, $\tilde{t}_0 = t_0/t_d$, $\tilde{\sigma} = \sigma/d$, $\tilde{x} = x/d$, $\tilde{x}_i = x_i/d$. Then, using (8.17) and (8.21) (with $C_{||}(\boldsymbol{\rho}, t) = 1$), we can obtain the wave function

$$\psi(\tilde{x}, \tilde{t}) = \psi_>(\tilde{x}, \tilde{t}) + \psi_<(\tilde{x}, \tilde{t}), \tilde{t} > \tilde{t}_0, \tag{8.27}$$

in the dimensionless variables for the different spatial regions defined in (8.17).

The conditions (8.24) and (8.26) read in the dimensionless variables, correspondingly,

$$|\tilde{x}_i| \gg 2\tilde{\sigma}, \tilde{E}_\perp \gg 1/\tilde{\sigma}^2. \tag{8.28}$$

In the limiting case, when the second inequality (8.28) holds, the forward-moving terms $\psi_>(\tilde{x}, \tilde{t})$ in Eq. (8.27) give the main contribution to the total wave function, i.e., $\psi(\tilde{x}, \tilde{t}) \approx \psi_>(\tilde{x}, \tilde{t})$. Also, the integrals over energy in $\psi_>(\tilde{x}, \tilde{t})$ can be asymptotically evaluated at $\lambda = \tilde{E}_i \tilde{\sigma}^2 \gg 1$ due to the fact that the contribution to these integrals mainly comes from the energy region $\tilde{E} \approx \tilde{E}_\perp$. In this case, the wave functions $\psi_>(\tilde{x}, \tilde{t})$ reduce (in the first approximation with $\frac{1}{\tilde{E}_\perp \tilde{\sigma}^2} \ll 1$) to the stationary (for $\tilde{E} = \tilde{E}_\perp$) results, oscillating with time as $\exp[-i\tilde{E}_\perp(\tilde{t} - \tilde{t}_0)]$.

The time dependence of the probability density $|\psi(x,t)|^2$ exhibits itself only when there is a sufficient momentum dispersion, as follows from Eq. (8.17) and (8.21). On the other hand, a sufficient momentum dispersion, when $\tilde{E}_\perp \tilde{\sigma}^2 \sim 1$, leads to a nonnegligible counterintuitive contribution of the backward-moving components of the wave packet to $|\psi(x,t)|^2$. The spacetime evolution of the scattering process can be visualized by numerical evaluation of the probability density $\left|\psi(\tilde{x}, \tilde{t})\right|^2$ of finding the particle in the scaled spacetime point $(\tilde{x}, \tilde{t})$. We will focus on the influence of the wave packet backward-moving components and the potential asymmetry parameter Δ on the particle dynamics.

To make the dynamics of the wave packet more particle-like, we accept the condition of the narrow wave packet, $\tilde{\sigma} < 1$, and put $\tilde{t}_0 = 0$. For an electron and the potential width $d = 10^{-7}$ cm (1 nm), the characteristic energy $E_d \sim 3 \cdot 10^{-2}$ ev and the characteristic time $t_d \sim 2 \cdot 10^{-14}$ s. In accordance with the accepted conditions, we will posit $\tilde{E}_\perp = 10^2$, $\tilde{x}_i = -10$, and $\tilde{\sigma} = 1/3$ or $\tilde{\sigma} = 0.1$. We choose $\tilde{U} = 10$ in the case of a potential barrier (over-barrier transmission), and $\tilde{U} = -10^2$ for a potential well. We will compare two cases: $\tilde{\sigma} = 1/3$, when the second inequality (8.28) is satisfied and the backward-moving positive energies components of the initial wave packet are not essential, and $\tilde{\sigma} = 0.1$, when their contribution matters. The dimensionless time interval $\tilde{t} = 0.1 \div 1.5$ is chosen from a simple estimation for the average scaled time t_i/t_d that it takes a particle with the initial energy $\tilde{E}_\perp$

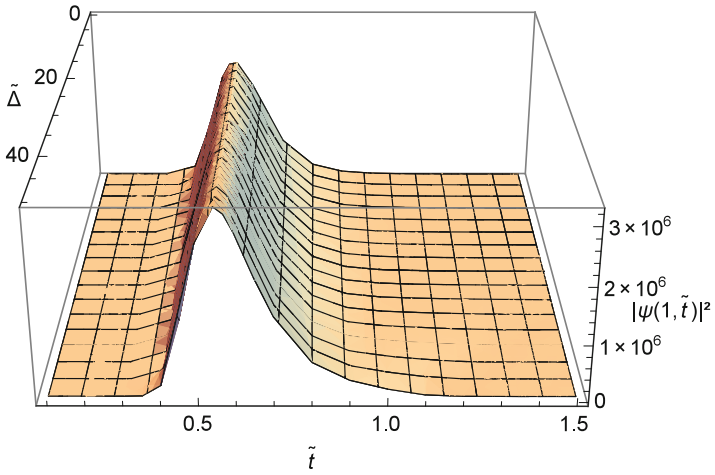

Fig. 8.1 Probability density distribution $|\psi(1,\tilde{t})|^2$ on the *right-hand side* of the barrier as a function of time and asymmetry parameter $\tilde{\Delta}$ for the narrow energy distribution of the initial wave packet ($\tilde{\sigma} = 1/3$)

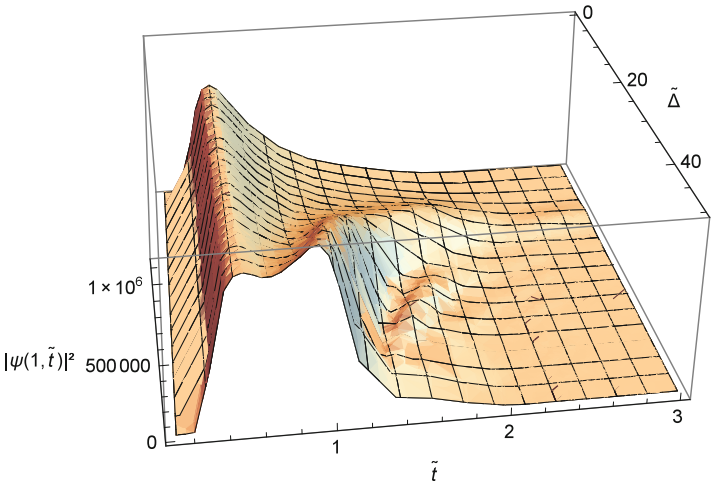

Fig. 8.2 Probability density $|\psi(1,\tilde{t})|^2$ as a function of $\tilde{t}$ and $\tilde{\Delta}$ for the broad energy distribution of the initial wave packet ($\tilde{\sigma} = 0.1$)

$= 10^2$ to reach the potential starting from the point $\widetilde{x}_i = -10$: $t_i/t_d = |x_i|m/\hbar k_i t_d = |\widetilde{x}_i|/2\sqrt{\widetilde{E}_\perp} = 1/2$.

Figure 8.1 shows the probability density $\left|\psi(\widetilde{x},\widetilde{t})\right|^2$ of finding the particle at $\widetilde{x} = 1$, i.e., on the right-hand side of the barrier (8.1) ($\widetilde{U} > 0$), as a function of $\widetilde{t}$ and $\widetilde{\Delta}$ changing from $\widetilde{\Delta} = 0$ to $\widetilde{\Delta} = \widetilde{E}_\perp/2$ when $\widetilde{\sigma} = 1/3$. Figure 8.2 shows the same function for $\widetilde{\sigma} = 0.1$. We see that in the case when the contribution of the backward-

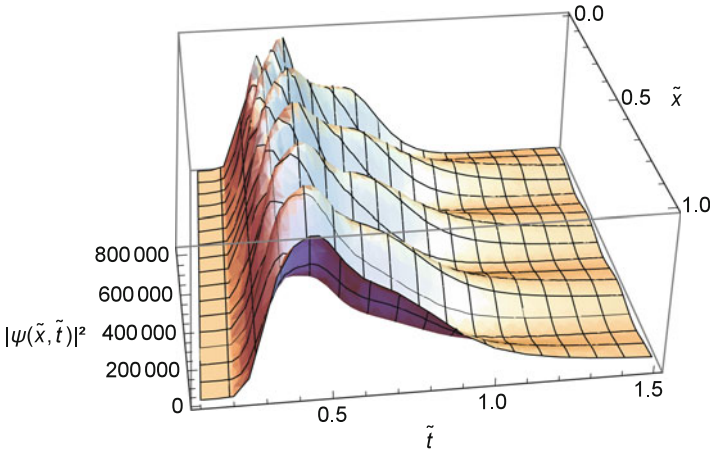

Fig. 8.3 Probability density $|\psi(\tilde{x},\tilde{t})|^2$ inside the symmetric well ($\tilde{\Delta} = 0$) for the broad energy distribution of the initial wave packet ($\tilde{\sigma} = 0.1$)

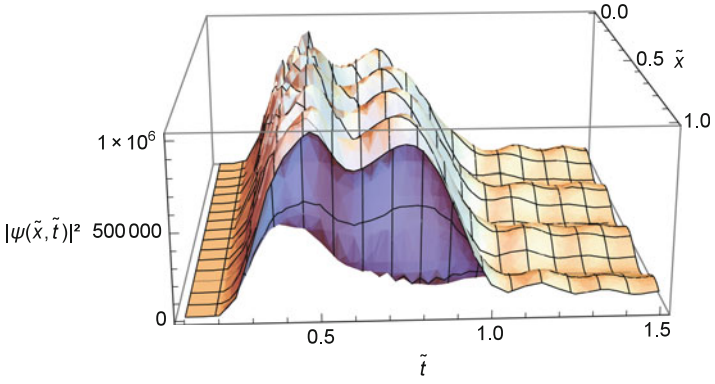

Fig. 8.4 Probability density $|\psi(\tilde{x},\tilde{t})|^2$ inside the asymmetric well ($\tilde{\Delta} = 50$) for $\tilde{\sigma} = 0.1$

moving components of the wave packet is important ($\widetilde{\sigma} = 0.1$), the time distribution of finding the particle beyond the barrier $\left|\psi(1,\widetilde{t})\right|^2$ for the asymmetric potential is essentially different from that for the symmetric one: Beginning from the value of the asymmetry parameter $\widetilde{\Delta} \approx 20$, this distribution becomes more broad and pronouncedly nonmonotonic for $\widetilde{\Delta} > 20$.

For the case of a potential well with $\widetilde{U} = -10^2$, we numerically evaluated $\left|\psi(\widetilde{x},\widetilde{t})\right|^2$ inside the well ($\widetilde{x} = 0 \div 1$) for the case of the broad energy distribution of the initial wave packet ($\widetilde{\sigma} = 0.1$) and the asymmetry parameter $\widetilde{\Delta} = 0$ and $\widetilde{\Delta} = \widetilde{E}_{\perp}/2 = |\widetilde{U}|/2$. Figure 8.3 shows the interference pattern inside the well which differs sufficiently from the stationary square cosine type picture (for $\Delta = 0$). It is seen that the amplitude of this pattern grows with time from zero to the

maximum value (reached approximately at $\widetilde{t} = 0.5$) and then again diminishes to zero, thereby showing the finite time during which a particle exists in the well region before leaving it either for the region before ($\widetilde{x} < 0$) or beyond ($\widetilde{x} > 1$) the well. We also see that the interference pattern of $\left|\psi(\widetilde{x},\widetilde{t})\right|^2$ is more structured in space and time. These changes in the probability density distribution result from the influence of the backward-moving components of the wave function $\psi_<(\widetilde{x},\widetilde{t})$, which is essential for the considered case of sufficient energy dispersion ($\widetilde{E}_\perp\widetilde{\sigma}^2 = 1$). In Fig. 8.4, we see the influence of the asymmetry parameter ($\widetilde{\Delta} = 50$) on that probability density $\left|\psi(\widetilde{x},\widetilde{t})\right|^2$ inside the asymmetric well. The calculated distribution exhibits a very structured and pronouncedly nonmonotonic interference pattern in space and time compared with that displayed in Fig. 8.3.

8.5 Summary

We have exactly resolved the time-dependent Schrödinger equation for a particle in the presence of a one-dimensional rectangular asymmetric well/barrier potential (8.1). Aside from being related to the fundamental issues of quantum mechanics, the obtained results can also be important for the kinetic theory of nanostructures, where the considered rectangular potential (8.1) is often used to model the potential profile in the magnetic nanostructures utilized, e.g., in spintronics devices. The obtained solution (a particle wave function) gives the time-dependent picture of the particle's transport through the spin-dependent well/barrier spacer potential of these nanostructures. The solution is generally the sum of the forward- and backward-moving terms, which take into account that the initial wave packet, confined to the restricted spatial area and representing a particle moving towards a potential, contains both the positive and negative momentum components. These wave function components are expressed in terms of integrals of elementary functions over the semi-bounded energy range $E = 0 \div \infty$. Thus, the probability density $|\psi(x,t)|^2$ of finding a particle in the spacetime point (x,t), when it initially was located in some spatial region and moved in some direction, is generally defined by the probability density corresponding to the wave component moving in this direction $|\psi_>(x,t)|^2$ as well as by the probability densities related to the backward-moving component $|\psi_<(x,t)|^2$ and the interference of both $2\mathrm{Re}[\psi_>(x,t)\psi_<^*(x,t)]$.

For the case of the initial Gaussian wave packet, we have shown that the contribution of the backward-moving component to the probability density $|\psi(x,t)|^2$ is small when the initial packet is characterized by a narrow energy (momentum) distribution, which is characteristic of the quasi-classical approximation for a transport phenomenon. For the extra narrow energy distribution, this situation actually corresponds to the stationary case with no energy dispersion. Thus, the transmission through and reflection from the potential well/barrier can be

described as a function of time only when the momentum (energy) dispersion of the initial wave packet is essential (accordingly, the wave packet spatial localization is narrow). But in this case the counterintuitive (non-classical) contribution of the backward-moving components of the wave packet should be accounted for. This rather paradoxical quantum mechanical result reveals itself in the problems connected to measuring time in the quantum mechanical effects.

Using the exact result for $|\psi(x,t)|^2$, we have numerically plotted the time distribution of finding the particle beyond the barrier ($U>0$), $|\psi(1,t)|^2$ and found that, when the contribution of the backward-moving wave packet components is important (broad wave packet energy distribution), the influence of the potential asymmetry can be essential (Figs. 8.1 and 8.2). Plotting $|\psi(x,t)|^2$ in the well ($U<0$) region, we showed that the backward-moving components of the wave packet fundamentally change the probability density, when the initial wave packet is broad enough in the energy (momentum) space, and the asymmetry of the potential well adds more to the structure of this spacetime distribution (Figs. 8.3 and 8.4).

References

1. Muga JG, Mayato RS, Egusquiza IL (eds) (2008) Time in quantum mechanics, vol. 1. Lecture notes in physics, vol 734. Springer, Berlin
2. Muga JG, Ruschhaup A, del Campo A (eds) (2009) Time in quantum mechanics, vol. 2. Lecture notes in physics, vol 789. Springer, Berlin
3. Baibich MN, Broto JM, Fert A, Van Dau FN, Petroff F, Etienne P, Creuzet G, Friederich A, Chazelas J (1988) Phys Rev Lett 61:2472
4. Julliere R (1975) Phys Lett A 54:225
5. LeClair P, Moodera JS, Meservay R (1994) J Appl Phys 76:6546
6. Shah J (1999) Ultrafast spectroscopy of semiconductors and semiconductor nanostructures. Springer, Heidelberg
7. Barut AO, Duru IH (1988) Phys Rev A 38:5906
8. Los VF, Los AV (2010) J Phys A Math Theor 43:055304
9. Los VF, Los AV (2011) J Phys A Math Theor 44:215301
10. Los VF, Los MV (2012) J Phys A Math Theor 45:095302
11. Baute AD, Egusquiza IL, Muga JG (2001) J Phys A Math Theor 34:4289
12. Baute AD, Egusquiza IL, Muga JG (2002) Int J Theor Phys Group Theory Nonlinear Opt **8**:1. *quant-ph*/0007079
13. Feynman RP, Hibbs AR (1965) Quantum mechanics and path integrals. McGraw-Hill, New York
14. Economou EN (1979) Green's functions in quantum physics. Springer, Berlin
15. Los VF, Los NV (2013) Theor Math Phys 177(3):1706
16. Muga JG, Brouard S, Snider RF (1992) Phys Rev A 46:6075

Chapter 9
Modeling Optical Characteristics of Multilayer Nanoparticles of Different Sizes for Applications in Biomedicine

T. Bulavinets, I. Yaremchuk, and Ya. Bobitski

9.1 Introduction

In recent years, nanotechnology found wide application in different areas of physics, chemistry, biology, and medicine. High achievements in the synthesis of nanoparticles [1, 2] and their optical characteristics caused interest to use plasmon nanostructures in photonics [3] and later for biomedical applications [4]. Nanoobjects have huge potential for applications in diagnosis, prevention, hygiene, and therapy, particularly for high-quality images of organs and drug delivery to cancer cells [5–11]. The main advantages of nanoparticles used in medicine are their nontoxicity, biocompatibility, ability to biodegradation, or excretion from the body naturally [12]. The noble metal nanoparticles have gained more attention to research in biomedicine due to their uniquely optical, chemical, and biological properties [13–16]. These particles are able to effectively absorb and scatter radiation on a specified wavelength.

Recent research has shown that nanoobjects, which consist of thin metal shell on base of silicon dioxide or titanium dioxide, can be effectively used for targeted delivery of drugs. The working range of the wavelength can significantly expand and shifted it to the certain region using such nanoshells. This is achieved by choice of their size, shape, and materials [17]. These nanosystems absorb infrared radiation

T. Bulavinets (✉) • I. Yaremchuk
Lviv Polytechnic National University, S. Bandery Str., 12, 79013 Lviv, Ukraine
e-mail: tetiana.o.protalchuk@lpnu.ua

Ya. Bobitski
Lviv Polytechnic National University, S. Bandery Str., 12, 79013 Lviv, Ukraine

Faculty of Mathematics and Natural Sciences, University of Rzeszow, Pigonia Str. 1, 35959 Rzeszow, Poland

O. Fesenko, L. Yatsenko (eds.), *Nanophysics, Nanophotonics, Surface Studies, and Applications*, Springer Proceedings in Physics 183,
DOI 10.1007/978-3-319-30737-4_9

that is safe for humans; however, it leads to local heating of particles [18] and destroyed only sick cells leaving healthy intact.

However, work [19] indicated that obtaining plasmon resonance in nanoshells for the wavelength range, which coincide with a window transparency of biological tissue, is not easy. Moreover, value of absorption decreased if peak of absorption is shifted to long-wavelength region.

This work is devoted to modeling of absorption and scattering by multilayer nanoparticles of type metal/semiconductor/metal and semiconductor/metal/semiconductor. In this study, we examine the effect of nanoparticle size and core-shell ratio on the plasmon resonance shifts for biomedical applications.

9.2 Theoretical Justification

9.2.1 Mathematical Model

There are various methods to obtain qualitative assessment of optical property nanoshells. Algorithm of calculation of two-layer nanoparticles is described in works [20, 21]. However, it is needed to develop algorithm of calculation of nanoparticles with more than two layers. Thus, the principle of dipole equivalence approach (Fig. 9.1) was used to calculate the cross sections of absorption and scattering by nanoshells.

Dipole equivalence principle is to determine the equivalent medium permittivity of multilayer particle using their polarization.

The calculation of dielectric constant is performed in step-by-step sequence. Firstly, the equivalent average permittivity ε_1 of the homogeneous sphere is calculated as follows:

$$\alpha_1 = a_1^3 \frac{\varepsilon_1 - \varepsilon_m}{\varepsilon_1 + 2\varepsilon_m}, \tag{9.1}$$

where a_1 is the radius of the core.

In the next step, we suppose that in a particle with ε_1, a_1 is surrounded by a cover layer of radius a_2 with permittivity ε_2 (Fig. 9.1a). To find the polarization of such

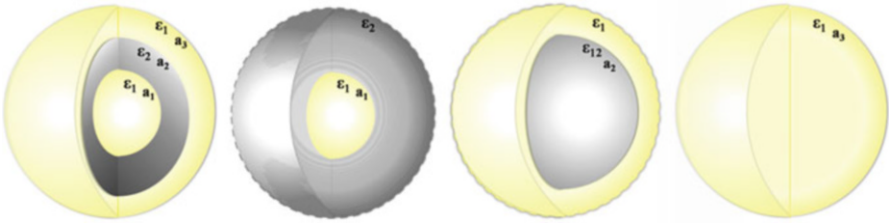

Fig. 9.1 The scheme of the principle of dipole equivalence

particle, put the initial particle in the environment ε_2 and surrounded imaginary sphere of radius a_2 (see Fig. 9.1b).

Then, the imaginary shell of the homogeneous sphere was replaced by equivalent permittivity ε_2 (see Fig. 9.1c) with equal dipole moment of the particle shown in Fig. 9.1b.

As a result, the equivalent permittivity ε_2 can be expressed as follows:

$$a_1^3 \frac{\varepsilon_1 - \varepsilon_2}{\varepsilon_1 + 2\varepsilon_2} = a_2^3 \frac{\varepsilon_1 - \varepsilon_2}{\varepsilon_2 + 2\varepsilon_2}, \tag{9.2}$$

where a_2 is the radius of the first shell.

Replacing the new particle (Fig. 9.1c) in the original environment of ε_m (Fig. 9.1d), we obtained the same physical situation in Fig. 9.1a, d. Thus, the dipole moments are the same and the polarization can be written as:

$$\alpha_2 = a_2^3 \frac{\varepsilon_2 - \varepsilon_m}{\varepsilon_2 + 2\varepsilon_m} \tag{9.3}$$

Detailed description of calculation of absorption and scattering cross section of nanoparticles and two-layer nanoshells is given in [22].

It is needed to calculate the electrostatic polarization α_0 for calculations of the absorption and scattering of small nanoparticles with the radius a in a homogeneous environment ε_m (Fig. 9.2). Electrostatic polarization is expressed using dielectric permittivity ε as follows:

$$\alpha_0 = a^3 \frac{\varepsilon - \varepsilon_m}{\varepsilon + 2\varepsilon_m} \tag{9.4}$$

Extinction coefficient $C_{ext} = C_{abs} + C_{sca}$ of nanoparticles is determined by absorption (C_{abs}) and scattering (C_{sca}) cross sections as follows:

$$C_{abs} = \frac{12\pi k}{a^3} \frac{\varepsilon_m \mathrm{Im}(\varepsilon)}{|\varepsilon - \varepsilon_m|^2} |\alpha|^2, \tag{9.5}$$

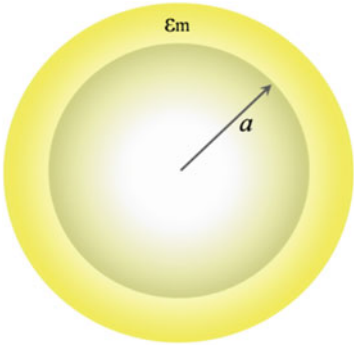

Fig. 9.2 The spherical metal nanoparticle with radius a in the environment with permittivity ε_m

$$C_{\text{sca}} = \frac{8\pi}{3} k^4 |\alpha|^2, \tag{9.6}$$

where $k = \frac{2\pi\varepsilon_{\text{m}}^{1/2}}{\lambda^2}$ is the wave number in the surrounding media ε_{m}.

Renormalized polarization is given by:

$$\alpha = \frac{\alpha_0}{1 + \varphi(\kappa a) a^{-3} \alpha_0}, \tag{9.7}$$

where the function $\varphi(\kappa a)$ takes into account the effects of radiation attenuation and is defined as:

$$\varphi(\kappa a) = 2 + 2(i\kappa a - 1)\exp(i\kappa a) \cong -(\kappa a)^2 - i\frac{2}{3}(\kappa a)^3. \tag{9.8}$$

Based on the calculations described above, the algorithm of modeling the absorption and scattering cross sections of three- and four-layer spherical nanoshells was developed.

The renormalized polarization of three-layer nanoshells is as follows:

$$\alpha_{23} = \frac{\varepsilon_3 - \varepsilon_2}{\varepsilon_3 + 2 \cdot \varepsilon_2} \tag{9.9}$$

Then, equivalent permittivity can be written as:

$$\varepsilon_{23} = \varepsilon_2 \cdot \frac{1 + 2 \cdot f_{23} \cdot \alpha_{23}}{1 - 2 \cdot f_{23} \cdot \alpha_{23}} \tag{9.10}$$

where

$$f_{23} = \frac{a_2^3}{a_3^3}.$$

The average polarization can be expressed as follows:

$$a_3 = a_3^3 \cdot \frac{\varepsilon_{23} - \varepsilon_{\text{m}}}{\varepsilon_{23} + 2 \cdot \varepsilon_{\text{m}}} \tag{9.11}$$

As a result, calculation of absorption (C_{abs}) and scattering (C_{sca}) cross sections of the three-layer nanoshells is performed using the next equations:

$$C_{\text{abs}} = \frac{12\pi k}{a_3^3} \frac{\varepsilon_{\text{m}} \text{Im}(\varepsilon_{23})}{(\text{Re}(\varepsilon_{23}) - \varepsilon_{\text{m}})^2} |\alpha_3|^2 \quad C_{\text{sca}} = \frac{8\pi}{3} k^4 |\alpha_3|^2. \tag{9.12}$$

Absorption (C_{abs}) and scattering (C_{sca}) cross sections of four-layer spherical nanoshells can be written as follows:

$$C_{abs} = \frac{12\pi k}{a_4^3} \frac{\varepsilon_m \mathrm{Im}(\varepsilon_{34})}{(\mathrm{Re}(\varepsilon_{34}) - \varepsilon_m)^2} |\alpha_4|^2 \quad C_{sca} = \frac{8\pi}{3} k^4 |\alpha_4|^2. \tag{9.13}$$

9.3 Materials

It is known that in medicine nanoobjects are used that consist of a thin shell of noble metals which coat the semiconductor (core/shell).

The nanoparticles of noble metals have unique optical, chemical, and biological properties. They are characterized by one or more resonance peaks in the visible and near-infrared spectrum.

These peaks are due to the localized plasmon resonance metal nanoparticles which are caused by coherent collective oscillations of free electrons. Oscillating electric fields of a light ray propagating near a nanoparticle interact with the free electrons causing a concerted oscillation of electron charge that is in resonance with the frequency of visible light. These resonant oscillations are known as surface plasmons. This behavior makes the metal nanoparticle one of the most important objects of modern nanobiotechnology [23].

The nanoparticles of noble metals Au, Ag, and Cu are found widely used in medicine as antibacterial and anticancer drugs due to their low oxidative ability [21, 24].

The unique physical and chemical, biological, biochemical, and pharmacological properties, such as inertness, stability, biocompatibility, effects on organs, and low cytotoxicity, caused the considerable interest to nanoparticles of Au. It is known that nanogold has a high affinity for (-SH) groups, which opens up opportunities for a combination of gold nanoparticles with various molecules (including macromolecules) by chemical interaction with the surfaces. Such nanoparticles can be used as vectors for targeted delivery of anticancer, anti-inflammatory, and antimicrobial agents, as well as contrast agents which are more effective than conventional drugs based on iodine derivatives of compounds [25].

Nanostructured gold has properties that appear only at the nanoscale. These properties are mainly related to a large number of superficial atoms. This is caused by a large ratio of surface area to volume ratio of nanoparticles. They include characteristics of surface plasmon resonance, a giant (surface-reinforced) Raman scattering, and high catalytic and chemical activity. Gold nanoparticles are able to intensively absorb light in the visible spectrum with a maximum absorption for 520–550 nm and reflect light with an intensity, which is orders of magnitude higher than the intensity of radiation many known dyes used for diagnostic purposes, while on excellent from last, there is no effect discoloration. At the same time, gold

nanoparticles strongly absorb waves of some length with subsequent conversion of light energy into thermal. The wavelength at which the observed surface plasmon resonance much depends on the shape, size, and chemical nature of nanoparticles [23].

Dielectric permittivity of metal can be expressed as follows:

$$\varepsilon = \varepsilon_1 + i\varepsilon_2, \tag{9.14}$$

where the real ε_1 and imaginary ε_2 parts dielectric permittivity of respectively.

Dielectric permittivity of gold nanoparticles was used from [27]. Dispersion curves were extrapolated by six-order polynomial to fit the measured data as follows:

$$\varepsilon_1 = 17.52725 - 204.5352 \cdot \lambda + 864.83314 \cdot \lambda^2 - 1693.86081 \cdot \lambda^3 + \\ +1518.72674 \cdot \lambda^4 - 653.4475 \cdot \lambda^5 + 107.79912 \cdot \lambda^6 \tag{9.14a}$$

$$\varepsilon_2 = -23.88814 + 252.00399 \cdot \lambda - 773.16362 \cdot \lambda^2 + 1071.59139 \cdot \lambda^3 - \\ -745.10009 \cdot \lambda^4 + 255.43663 \cdot \lambda^5 - 34.11917 \cdot \lambda^6 \tag{9.14b}$$

Fitted measured data are presented in Fig. 9.3.

In medicine silicon dioxide (SiO_2) is often chosen as materials of nanoshells. Silicon dioxide is actively researched as a carrier for protein molecules. SiO_2 nanoparticles have a large active surface, are chemically and thermally stable, have aqueous suspensions, and are relatively inert in the surrounding media. Moreover, silicon nanoparticles exhibit therapeutic properties due to their ability to bind pathogenic substances of protein naturally and do not contribute to the development of microorganisms. They are optically transparent and can act as an insulator, protecting the contents of the capsule on surrounding influences. The nanoparticles of silicon are actively used in research for drug delivery, visualization, and diagnostics. SiO_2 nanoparticles affect the cell viability, causing oxidative stress, impaired cell cycle, and apoptosis. However, they show a negative effect on dopaminergic neurons and have neurotoxicity [26].

Dielectric permittivity nanoparticle SiO_2 ε is used for calculation from [28] and is written as follows:

$$n^2 = \frac{0.665721 \cdot \lambda^2}{\lambda^2 - 0.060^2} + \frac{0.503511 \cdot \lambda^2}{\lambda^2 - 0.106^2} + \frac{0.214792 \cdot \lambda^2}{\lambda^2 - 0.119^2} + \frac{0.539173 \cdot \lambda^2}{\lambda^2 - 8.792^2} + \\ + \frac{1.807613 \cdot \lambda^2}{\lambda^2 - 19.70^2} + 1 \tag{9.15}$$

Dielectric permittivity of SiO_2 on wavelength is presented in Fig. 9.4.

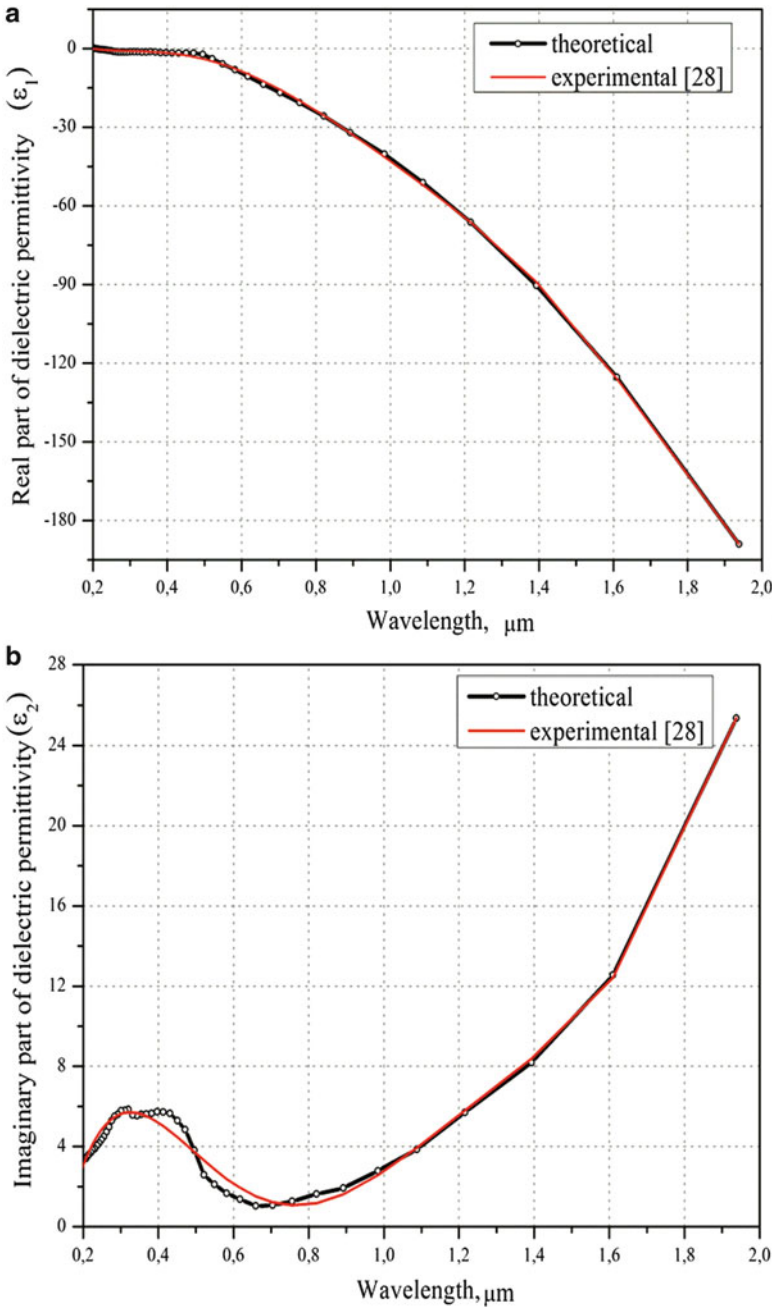

Fig. 9.3 Comparison of theoretical and experimental curves of real (a) and imaginary (**b**) parts of dielectric permittivity Au

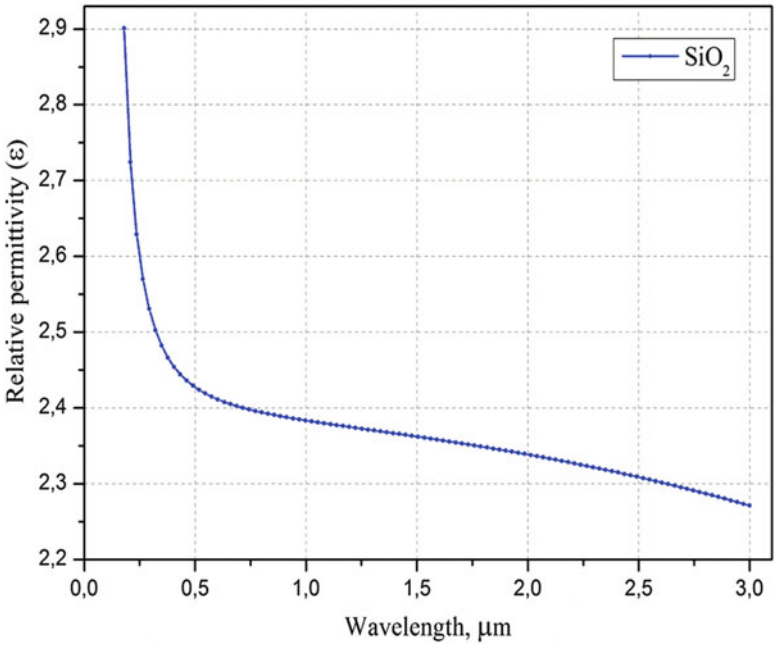

Fig. 9.4 Dielectric permittivity SiO_2 on wavelength

9.4 Results and Discussion

Calculation of optical parameters of two- and three-layer nanoshells was carried out using dipole principle of equivalence to assess the effectiveness of plasmon resonance for application in biomedicine.

Firstly, absorption (Fig. 9.5a) and scattering (Fig. 9.5b) cross sections of nanoparticle Au with radius $a_1 = 20$ nm were calculated.

As shown in Fig. 9.5, maximum absorption and scattering of such nanoparticles is at the wavelength $\lambda = 0.44$ μm. It does not allow to use Au nanoparticles in medicine, since the window transparency biological tissue is in the range 850–1100 nm.

It is known that nanoshells are used to shift of plasmon peak to working range of wavelengths. We propose to use nanoshells which consist of metal core (Au) with radius $a_1 = 20$ nm and semiconductor shell (SiO_2) with radius $a_2 = 70$ nm as shown in Fig. 9.6.

It is easy to see from Fig. 9.6 that compared with nanoparticle Au, absorption (Fig. 9.6a) and scattering (Fig. 9.6b) peaks of the nanoshell Au-SiO_2 not only shifted to long-wavelength region of the spectrum, but also their maximum value is increased.

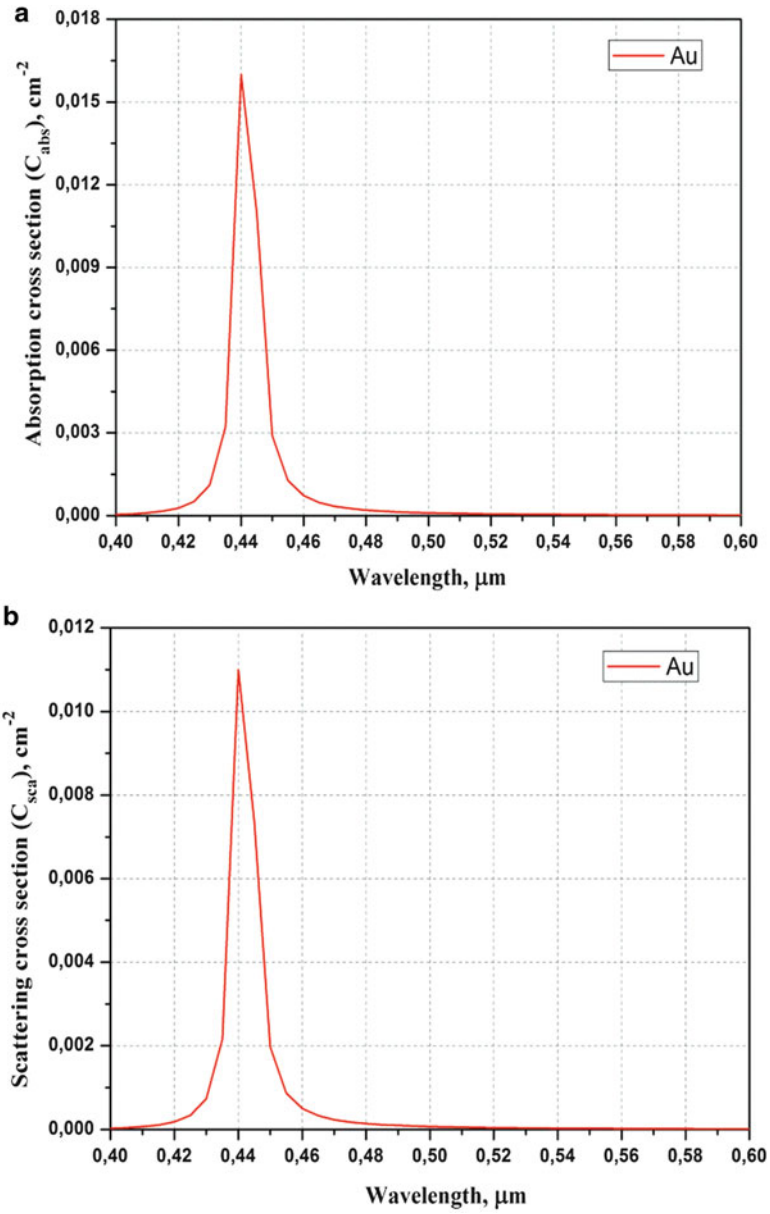

Fig. 9.5 Cross section of absorption (**a**) and scattering (**b**) radiation of nanoparticle Au with $a_1 = 20$ nm

Figure 9.7 presents the results of the calculation of the absorption (Fig. 9.7a) and scattering (Fig. 9.7b) cross section of the three-layer nanoshell (thickness of the shell $d_3 = 5$ nm). Au is used as a third layer.

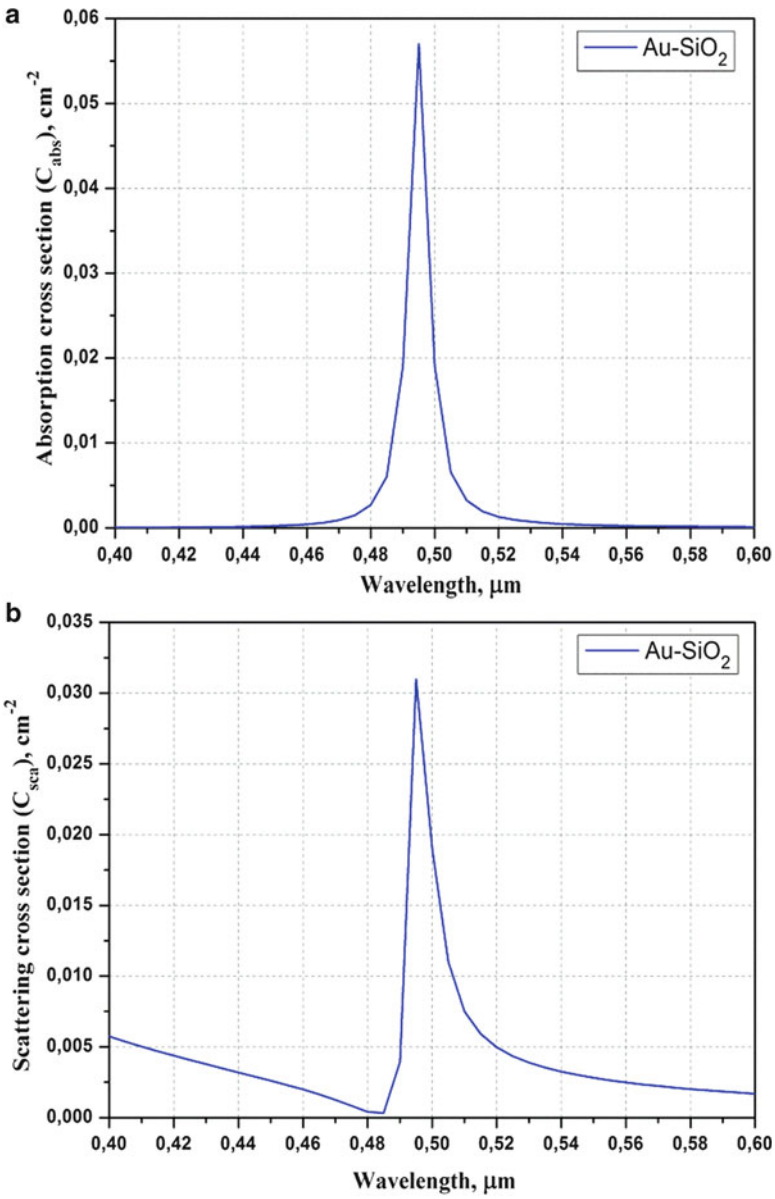

Fig. 9.6 Cross section of absorption (**a**) and scattering (**b**) radiation of nanoshell Au-SiO_2 with $a_1 = 20$ nm and $a_2 = 70$ nm

Results in Fig. 9.7 indicate that such nanoshell effectively absorb radiation which is safe for humans (in this case $\lambda = 0.90$ μm). The maximum values of absorption and scattering cross sections are much higher than shown in Figs. 9.5 and 9.6.

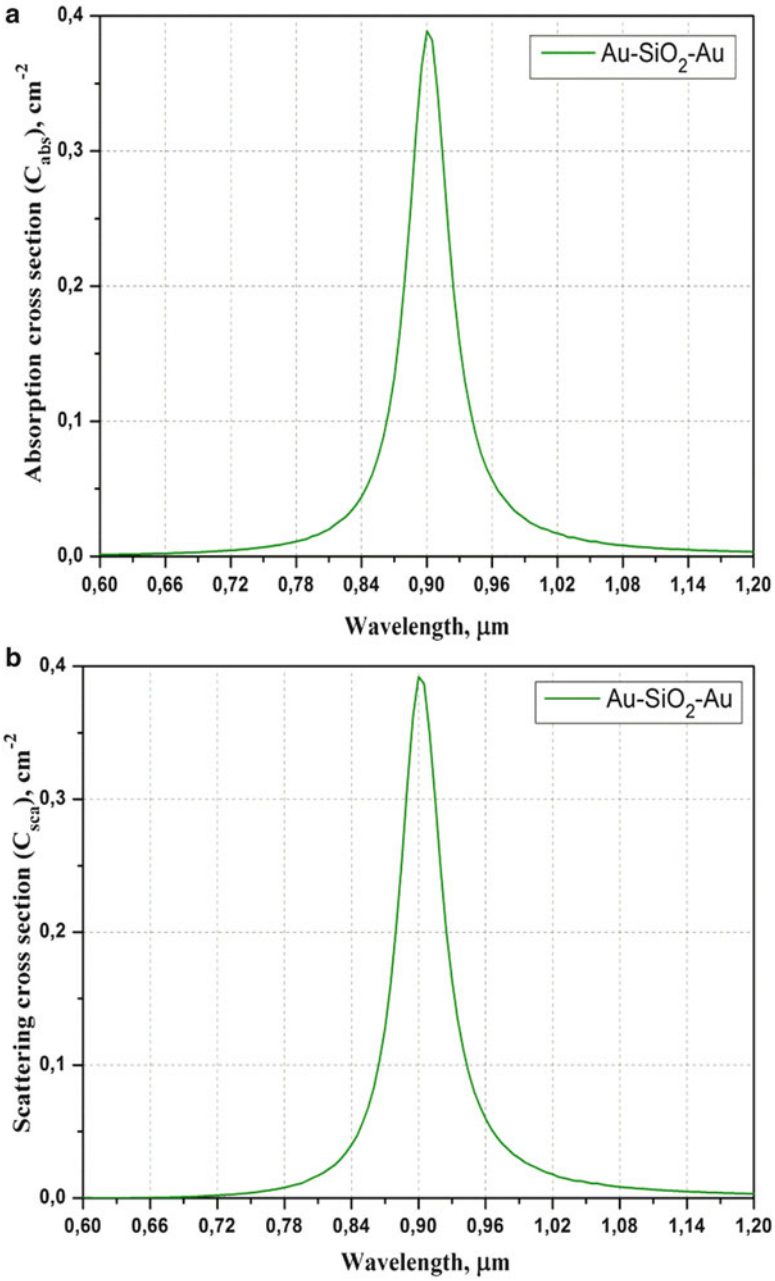

Fig. 9.7 Cross section of absorption (**a**) and scattering (**b**) radiation of nanoshell Au-SiO_2-Au with $a_1 = 20$ nm, $a_2 = 70$ nm, $a_3 = 75$ nm

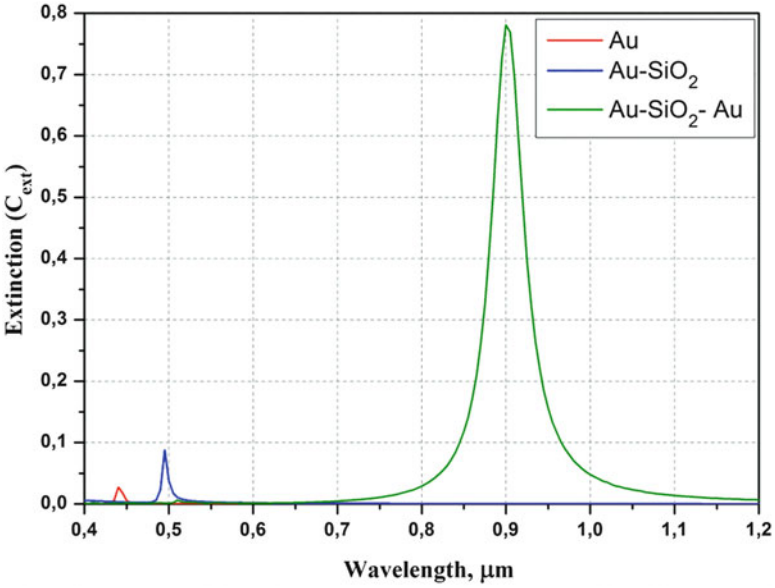

Fig. 9.8 Extinction nanoshell Au-SiO_2-Au with $a_1 = 20$ nm, $a_2 = 70$ nm, $a_3 = 75$ nm

Figure 9.8 shows the comparison of the value of extinction cross sections of each calculated layer of the nanoshell Au-SiO_2-Au.

Maximum extinction of the three-layer nanoshell for these radii (Fig. 9.8) is in the window transparent biological tissue. This makes it possible to use such nanosystems for biomedical applications.

Using two-layer nanoparticle type of semiconductor/metal, it is possible to achieve appearance of the plasmon resonance in the desired wavelength range 850–1100 nm [19]. However, in comparison with the two layer, using three-layer nanoshells with greater accuracy allows them to manipulate the optical characteristics and peak position of the absorption and scattering spectrum of wavelengths.

It is studied that the value of peak absorption and scattering decreases with their shift in the long-wavelength region of the spectrum. In other words, the deeper the infrared region shifts absorption peak of nanoparticles, the more energy is required for its local heating.

As shown in Fig. 9.9, in comparison with SiO_2-Au [19], nanoshell Au-SiO_2-Au much more efficiently absorbs radiation at the same wavelength and thus requires less energy for heating. Extinction coefficient of three-layer nanoshell at the wavelength 0.96 μm more than 2.5 times the extinction bilayer.

Dependences of absorption cross section of nanoshells Au-SiO_2-Au with different radii of the upper layer a_3 on the wavelength are presented in Fig. 9.10.

Obtained results showed that the absorption cross section of nanoshells is extremely sensitive to changes in size and more precisely to the ratio of the radii of the second and third shells a_2/a_3. Figure 9.10 shows that the change in the relative

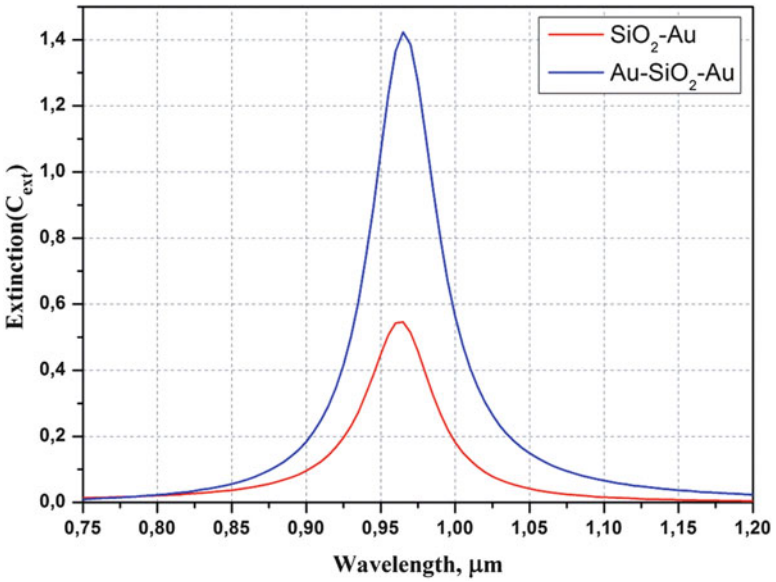

Fig. 9.9 Extinction two- and three-layer nanoshell on the wavelength

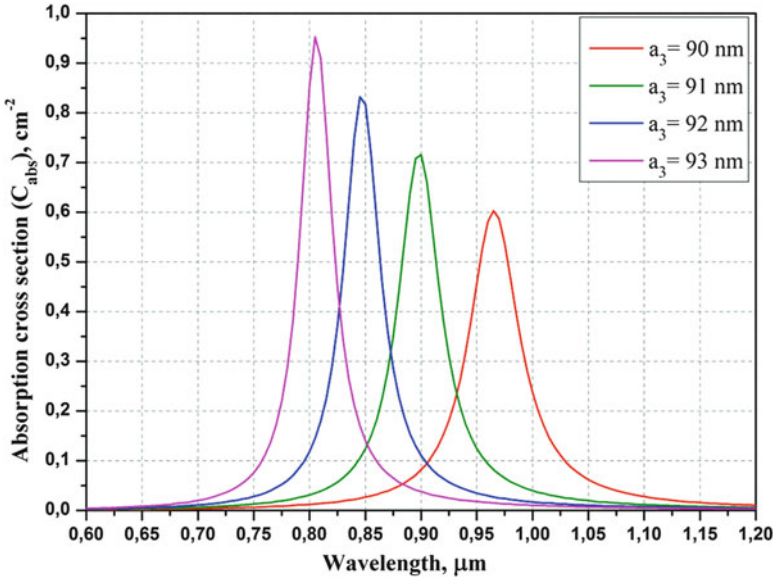

Fig. 9.10 Cross section of absorption of nanoshell Au-SiO_2-Au with $a_1 = 20$ nm and $a_2 = 85$ nm

a_3 to a_2 in 1 nm leads to a sharp displacement the peak absorption to the long-wavelength region of the spectrum. This opens up new possibilities for the use of multilayer nanoshells.

9.5 Conclusions

The calculations of the absorption and scattering cross sections of multilayer spherical metal nanoshells using the principle of dipole equivalence have been conducted.

It is shown that usage of multilayer nanoparticles allows getting peak of plasmon resonance in a safe for human spectrum of wavelength without significant loss in the value of intensity. Three-layer nanoshells more efficiently absorb radiation at the same wavelength than the two-layer nanoshells. Therefore, they require less energy for local heating, which greatly simplifies their practical use.

Moreover, obtained results have shown that multilayer nanoshell is extremely sensitive to changes in their geometrical parameters. It opens new possibilities for the use of multilayer nanoshells in different areas of science and technology.

References

1. Burda C, Chen X, Narayanan R, El-Sayed MA (2005) Chemistry and properties of nanocrystals of different shapes. Chem Rev 105:1025 (and references therein)
2. Katz E, Willner I (2004) Integrated nanoparticle-biomolecule hybrid systems: synthesis, properties, and applications. Angew Chem Int Ed Engl 43:6042 (and references therein)
3. Maier SA, Kik PG, Atwater HA, Meltzer S, Harel E, Koel BE, Requicha AG (2003) Local detection of electromagnetic energy transport below the diffraction limit in metal nanoparticle plasmon waveguides. Nat Mater 2:229–232
4. Shafer-Peltier KE, Haynes CL, Glucksberg MR, Van Duyne RP (2003) Toward a glucose biosensor based on surface-enhanced Raman scattering. J Am Chem Soc 125:588
5. Yelin D, Oron D, Thiberge S, Moses E, Silberberg Y (2003) Multiphoton plasmon-resonance microscopy. Opt Express 11:1385
6. Wang Y, Xie X, Wang X, Ku G, Gill KL, O'Neal DP, Stoics G, Wang LV (2004) Photoacoustic tomography of a nanoshell contrast agent in the in vivo rat brain. Nano Lett 4:1689
7. Sokolov K, Follen M, Aaron J, Pavlova I, Malpica A, Lotan R, Richards-Kortum R (2003) Real-time vital optical imaging of precancer using anti-epidermal growth factor receptor antibodies conjugated to gold nanoparticles. Cancer Res 63:1999
8. El-Sayed IH, Huang X, El-Sayed MA (2005) Surface plasmon resonance scattering and absorption of anti-EGFR antibody conjugated gold nanoparticles in cancer diagnostics: applications in oral cancer. Nano Lett 5:829
9. Hayat MA (1989). In: Colloidal gold: principles, methods and applications, vol 1. Academic Press, San Diego
10. Hirsch LR, Stafford RJ, Bankson JA, Sershen SR, Rivera B, Price RE, Hazle JD, Halas NJ, West JL (2003) Nanoshell-mediated near-infrared thermal therapy of tumors under magnetic resonance guidance. Proc Natl Acad Sci U S A 100:13549

11. Loo C, Lowery A, Halas N, West J, Drezek R (2005) Immunotargeted nanoshells for integrated cancer imaging and therapy. Nano Lett 5:709
12. Chernousova S, Epple M (2012) Nanoparticles in medicine. Nanosyst Nanomater Nanotechnol 10(4):667–685 (in Russian)
13. Dykman LA, Bogatyrev VA, Shchyogolev SY, Khlebtsov NG (2008) Gold nanoparticles: synthesis, properties and biomedical applications. Nauka, Moscow, p 319 (in Russian)
14. Chow PE (ed) (2010) Gold nanoparticles: properties, characterization and fabrication. Nova Science, New York, p 343
15. Vazhnycha OM, Bobrova NO, Gancho OV, Loban GA (2014) Nanoparticles of silver: antibacterial and antifungal properties. Pharmacol Drug Toxicol 2(38):3–11 (in Russian)
16. Kim JS, Kuk E, Yu KN et al (2007) Antimicrobial effects of silver nanoparticles. Nanomedicine 3(1):95–101
17. Khlebtsov NG (2008) Optics and biophotonics of nanoparticles with plasmon resonance. Quant Electron 38(6):504–529
18. Rfsler A, Vandermeulen GW, Klok HA (2001) Advanced drug delivery devices via self-assembly of amphiphilic block copolymers. Adv Drug Deliv Rev 53:95–108
19. Loo C et al (2004) Nanoshell-enabled photonics-based imaging and therapy of cancer. Technol Cancer Res Treat 3(1):33–40, ISSN 1533-0346
20. Hamilton RF, Wu N, Porter D et al (2009) Particle length-dependent titanium dioxide nanomaterials toxicity and bioactivity. Part Fibre Toxicol 6:35
21. Kreibig U, Vollmer M (1995) Optical properties of metal clusters. Springer, Berlin
22. Khlebcov NG (2008) Optics and biophotonics of nanoparticles with plasmon resonance (review). Quant Electron 38(6):504–529 (in Russian)
23. Chekman IS, Pryskoka AO (2010) Nanogold and gold nanocoatings: the state of research, prospects for application in medicine. Ukrainian Med J 2(76):37–43 (in Russian)
24. Lee J, Mahendra S, Alvarez PJJ (2010) Nanomaterials in the construction industry: a review of their applications and environmental health and safety considerations. ACS Nano 4:3580
25. Sotiriou C, Pusztai L (2009) Gene-expression signatures in breast cancer. N Engl J Med 360:790–800
26. Wu J, Wang C, Sun J et al (2011) Neurotoxicity of silica nanoparticles: brain localization and dopaminergic neurons damage pathways. ACS Nano 5(6):4476–4489
27. Johnson PB, Christy RW (1972) Optical constants of the noble metals. Phys Rev B 6:4370–4379
28. Radhakrishnan T (1951) Further studies on the temperature variation of the refractive index of crystals. Proc Indian Acad Sci 31:22–34

Chapter 10
Effect of Concentrated Light on Boron Nitride Nanostructures Formation

Lina Sartinska and Levan Chkhartishvili

10.1 Introduction

Being suitable for both conducting and non-conducting materials, the heating under concentrated light demonstrates numerous advantages due to versatility, rapid heating and cooling rates, ability to adjust temperature profile along each axis, maximum operating temperatures, and environmental adaptability. Moreover, the light energy is one of cleanest energy sources available. Light or solar energy is virtually unlimited and can be concentrated to provide directly high-temperature process heat. Based on significant research work, advantages of the use of concentrated solar radiation for substituting fossil and electrical energy in energy-intensive production has also been demonstrated [1, 2]. Variation in solar intensity poses challenges of repeatability in performance assessment of solar thermal systems in outdoor conditions, leading to the development of indoor laboratories incorporating simulative sunlight to conduct endothermic processes. The most convenient tool for solar thermal research in indoor conditions is a high-flux solar simulator capable of providing an artificial source of concentrated radiation with a spectral distribution approaching to solar one [3]. The solar simulator is a unique facility that allows much flexibility and control over experiments for attaining reproducible results and examining various facets of solar processes at high temperatures (up to 3000 K) and high heating rates (up to 1000 K/s). In general, solar simulators employ various

L. Sartinska (✉)
Frantsevich Institute for Problems of Materials Science, National Academy of Sciences of Ukraine, 3 Krzhyzhanivsky Str., Kyiv 03680, Ukraine
e-mail: linasartinska@yahoo.com

L. Chkhartishvili
Georgian Technical University, 77 Kostava Ave., Tbilisi 0175, Georgia

Tavadze Institute of Metallurgy & Materials Science, 15 Kazbegi Ave., Tbilisi 0160, Georgia

O. Fesenko, L. Yatsenko (eds.), *Nanophysics, Nanophotonics, Surface Studies, and Applications*, Springer Proceedings in Physics 183,
DOI 10.1007/978-3-319-30737-4_10

types of lamps to imitate the sun such as xenon arc lamps, argon arc lamps, metal halide lamps, high-pressure sodium vapor lamps, mercury vapor lamps, and incandescent spotlights [4]. The most common solar simulators usually are those based on xenon arc lamps.

h-BN is a synthetic chemical compound containing boron and nitrogen atoms with layered structure. The in-plane atoms are linked through covalent bonds, while the out-of-plane layers are bonded by weak interactions, providing anisotropic properties. BN displays a large band gap and offers the lowest density ($d = 2.26$ g cm^{-3}) among non-oxide ceramics. It proposes relatively good thermal stability in air and vacuum, high thermal conductivity, good thermal shock resistance, high electrical resistance, a low dielectric constant and loss tangent, microwave transparency, non-toxicity, and easy machinability [5, 6].

Many studies have been reported on BN nanomaterials and nanostructures such as nanotubes, bundled tubes, nanocorns, nanohorns, nanocapsules, nanoparticles, BN clusters, and BN metallofullerenes, which are expected to be useful as electronic devices, field-effect transistors, high heat-resistant semiconductors, insulator, lubricants, nanowires, magnetic nanoparticles, gas storage materials, and optoelectronic applications including ultraviolet light emitters [7]. Theoretical calculations on BN nanomaterials such as nanotubes, cluster-included nanotubes, BN clusters, BN metallofullerenes, cluster solids, nanohorns, and hydrogen storage have also been carried out for prediction of the properties [8–10]. By controlling a size, morphology, and compositions, these structures are expected to show various properties. Observation of the process of nanostructures formation during heating under concentrated light due to versatility, rapid heating and cooling rates, and high operating temperatures allows controlling the nanostructures properties in a wide range.

10.2 Methodology

Platelet graphite-like fine-grained powder of boron nitride (h-BN) and three boron powders with different grain sizes of 0.05, 0.20, and 2.00 μm were used as initial [3, 11, 12]. The origin powder of h-BN is textured on 002 with impurity of B_2O_3. The mean size of h-BN platelets is about ~0.3 μm, their thickness ~0.01 μm. Commercial boron of 0.05 μm mean grain size is mostly amorphous boron with negligible content of β-rhombohedral phase. Boron powder of 0.20 μm mean grain size contains β-tetragonal boron phase due to stabilization effect of the tetragonal α-$B_{49.94}C_{1.82}$ impurity. Boron powder of 2.00 μm mean grain size is a β-rhombohedral boron with negligible quantity of the amorphous boron phase.

h-BN initial powder was annealed at 800 °C for 1 h in order to increase the chemical stability.

Heating of initial compacted powders was performed on a high-flux optical furnace (Fig. 10.1a) with xenon sources of exposure (Fig. 10.1b) “Crystal M” in a flow of nitrogen. A quartz chamber (Fig. 10.2) was used for the process of BN

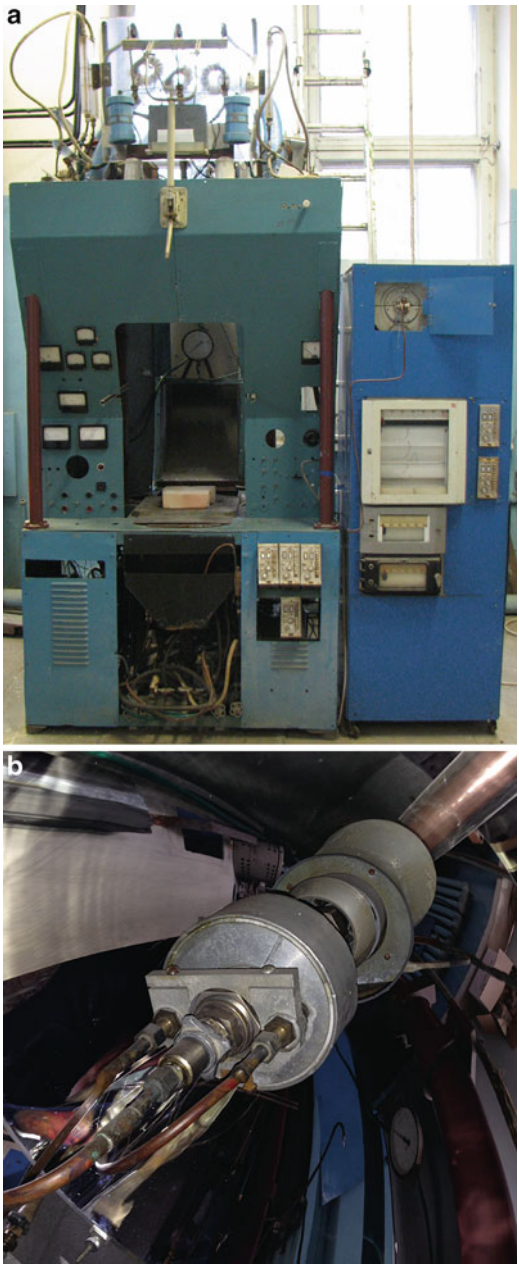

Fig. 10.1 The high-flux optical furnace (**a**) and xenon arc lamp with ellipsoidal reflector (**b**)

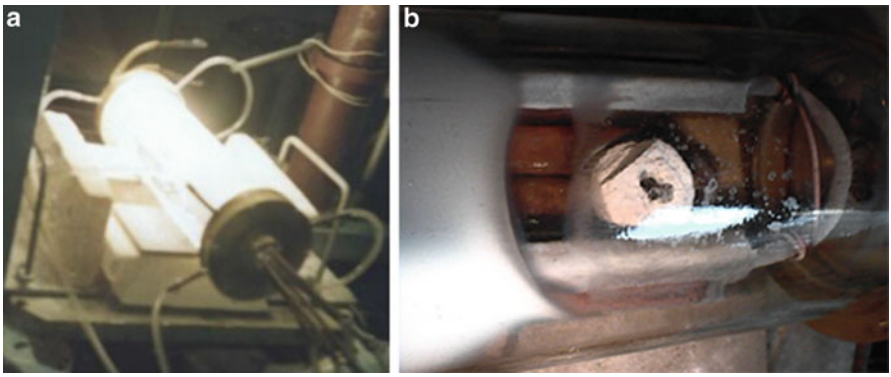

Fig. 10.2 A quartz chamber with compacted sample of initial h-BN powder during experiment (**a**) and after heating (**b**)

nanostructures formation. An experimental sketch and procedure were presented anywhere in [3, 11, 13]. A compacted sample of initial h-BN powder was placed on a copper water-cooling screen of the quartz chamber, which was positioned in the center of a focal zone of three xenon emitters. Sublimation and evaporation of h-BN were carried out at the low density of energy in focal zone of setup ~0.7×10^4 kW/m^2 (Fig. 10.2a). Time of the experiment was 30 min.

The chamber was flowed by purified and dried nitrogen under pressure ~1.2 atm. The nitrogen was purified from oxygen by copper chips at 500 °C. Pellets of KOH made drying of nitrogen from water. Produced nanostructures precipitated on copper screens and on the surface of a quartz chamber near reaction zone (Fig. 10.2b).

Laser treatment of the compacted samples was performed also on setup "Quantum—15" with a quantum optical generator based on yttrium–aluminum garnet (YAG), wavelength $\lambda = 1.06$ μm, pulse duration $\tau = 5 \times 10^{-3}$ s, pulse energy $W_n = 8.5$ J, and power density of laser radiation in the range of $P = 10^2$–10^5 W/cm^2 in a chamber.

Initial powders and produced BN nanostructures were examined by optical and transmission electron microscopy (TEM). Scanning electron microscopy (SEM) "Superprobe 733" ("JEOL," Japan) and a DRON-3.0-type (CuKα radiation) diffractometer were used for research. Raman spectroscopy was performed with a Dilor XY-800 spectrometer in micro configuration. Excitation beam of Ar + ion or Kr + ion lasers was used. It was applied 514.5 and 488 nm wavelengths of the Ar + laser and a 647 nm line of the Kr + laser. No dependence on the excitation wavelength was observed. The spectra were taken in backscattering geometry at room temperature. Fourier transform infrared (FTIR) absorption spectra were recorded by Nicolet 6700—FTIR spectrometer (Thermo Scientific). It is the most important and widely used tool for characterizing BN. FTIR analysis is a straightforward, nondestructive, and rapid technique that can be done in either reflection or transmission.

10.3 Process of Nanostructures Formation from h-BN

It is known that the presence of a liquid phase in the process of nanostructures formation from the initial graphite-like h-BN is very important [11, 13]. Based on visual observation of h-BN transformation to nanostructures under concentrated light heating, "gaseous model" was proposed [11, 13]. Therefore, structure and properties of produced nanostructures will be considered from the point of view of this model for the formation and growth of nanostructures.

Concentrated light heating of h-BN sample in different setups ("Crystal M" and "Quantum 15") results in melting and decomposition of h-BN simultaneously with vaporizing of nitrogen from a surface. Boron and boron oxides compose this surface layer [11]. Melted zone with small droplets (Fig. 10.3a, b) and a crater with large droplets were formed at the lowest or higher density of energy, respectively (Fig. 10.3c), because of bad wetting ability of h-BN.

Careful investigation of obtained droplets has demonstrated that their surface consists from triangular plates [14, 15] of 10–80 μm stacked together (Fig. 10.4). Plates are shiny on the outer surface, but matte black on the inner surface. It is perhaps because once the shell has sealed itself, neither any gas can escape nor can be contaminated by impurities of nitrogen in the chamber. They are slightly enriched boron (Fig. 10.4a). Small particles on the surface of a droplet are BN plates, which oxidized due to small size (Fig. 10.4b).

High-temperature gradients in a flow of dried and purified nitrogen lead to formation of complicated threadlike structures, which are consisted of dendrites (Fig. 10.5a, b), nanowires (Fig. 10.5c), and nanotubes (Fig. 10.5d) mostly formed around the crater (Fig. 10.3c). However, decreasing the density of energy after melting can promote their growth on the melted surface in the center of a spot (Fig. 10.3a).

"Gaseous model" for nanotubes formation and growth suggests effect of gas output during boiling melted boron on their nucleation in the form of bubble [11, 13]. This fact has found its confirmation in direct observation of boron nitride

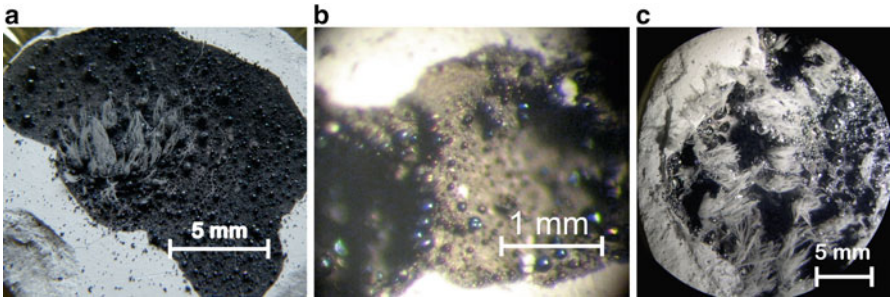

Fig. 10.3 Surface of compacted sample of h-BN after heating in a high-flux optical furnace "Crystal M" (**a**, **c**) and on laser setup "Quantum 15" (**b**) at the lowest (**a**, **b**) and higher density of energy (**c**)

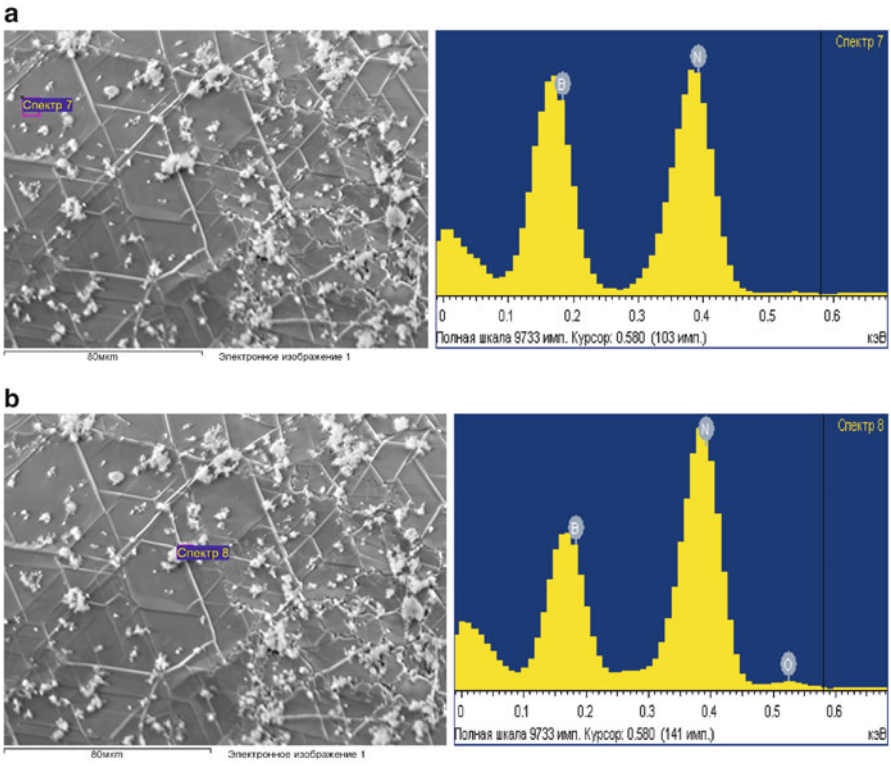

Fig. 10.4 SEM image and element composition of the surface of droplet (**a**) and particle on its surface (**b**)

nanocage growth by molecular beam nitriding and liquid-like motion of Fe–B nanoparticles [16]. It was demonstrated that the growth of a BN shell around an Fe–B nanoparticle, followed by strain-induced ejection of Fe–B globs, and the subsequent formation of a second shell connected to the first [16]. Beside Fe, Zr, Hf, Ta, W, Nb, and La can be good catalytic metals for synthesis of BN nanotubes [17]. We observed the same process of structure nucleation for nanowires and nanotubes at high temperatures without any catalyst [11, 13]. Since the temperatures in a high-flux optical furnace is much higher, the rate of strain-induced ejection of boron globs/bubble-enriched nitrogen is very high. Therefore, instead of nanocage growth, we can observe the growth of nanowires from globs of melted boron (Fig. 10.5c) and nanotubes from bubbles (Fig. 10.5d) inside a shell.

The size of produced BN nanotubes is limited by binding energy ~23 eV/mol for single-layer boron nitride which is in good agreement with binding energy data available for BN multilayered structures [18]. Calculated corrected binding energy of the ultra-large-radius tube is predicted as 22.95 eV. Previous quasi-classical calculations (but in tight-binding approximation) performed for BN isolated plane sheet have given the binding energy 23.00 eV/mol, which coincides in order of

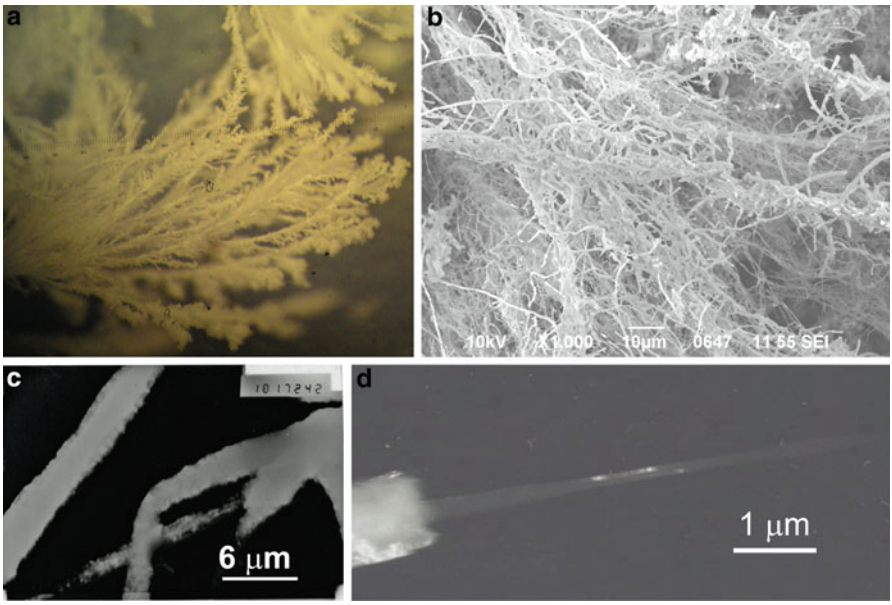

Fig. 10.5 Optical (**a**) and SEM (**b**, **c**, **d**) image of dendritic crystals at low (**a**) and high magnification (**b**), nanowires (**c**), and nanotubes (**d**)

magnitude with this interval and agrees very well with result obtained for large tubes [18].

The next stage of heating results in dendritic crystal formation due to the supersaturated nitrogen vapor on the surface of sample. It is known that dendritic crystals can form from growth instabilities that occur when the growth rate is limited by the rate of diffusion of atoms to the interface. In the latter case, there must be a concentration gradient from the supersaturated vapor (in our case) to the concentration in equilibrium with the crystal at the surface. Any protuberance that develops is accompanied by steeper concentration gradients at its tip. This increases the diffusion rate to the tip. In opposition to this is the action of the surface tension tending to flatten the protuberance and setting up a flux of solute atoms from the protuberance out to the sides. However, overall, the protuberance becomes amplified. This process occurs repeatedly until a dendrite is produced. Concentration in equilibrium at the surface of dendritic BN crystals takes place when the surface of the molten boron is saturated with nitrogen that was confirmed by the results of electron microscopic studies (Fig. 10.6). Moreover, nitrogen content is much higher than boron in values of BN in the central part of crystals (Fig. 10.6a). Stoichiometric values of nitrogen and boron in upper (Fig. 10.6b) and lower (Fig. 10.6c) parts of dendritic BN crystals are occurring in the presence of oxygen (1–3 %).

X-ray diffraction pattern of dendritic BN crystals has demonstrated their crystalline structure with a big percentage of disorder (Fig. 10.7). The most intensive peaks may be attributed to hexagonal boron nitride formation, boron-rich tetragonal

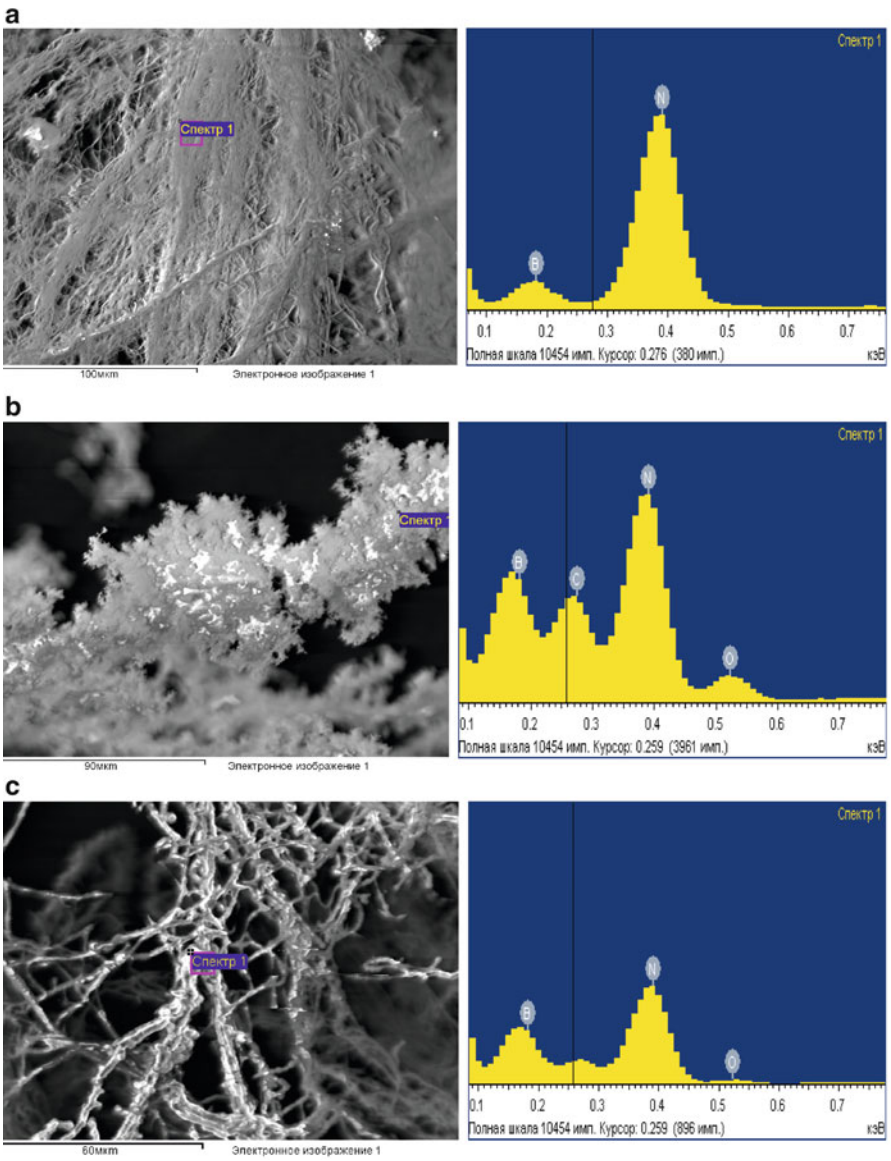

Fig. 10.6 SEM image and element composition of the central part of dendritic crystals with highest nitrogen content (**a**), lower (**b**) and upper part of dendritic crystals (**c**)

$B_{25}N$ and $B_{51.2}N$ phases, and small quantity of cubic BN. The peak at 26° which corresponds to the (002) diffraction peak of h-BN [19] is very intense but broaden. Therefore, dendritic BN crystals are not so crystalline compared to initial nanosized h-BN powder [3, 11]. Their shell consists on a number of textured phases and

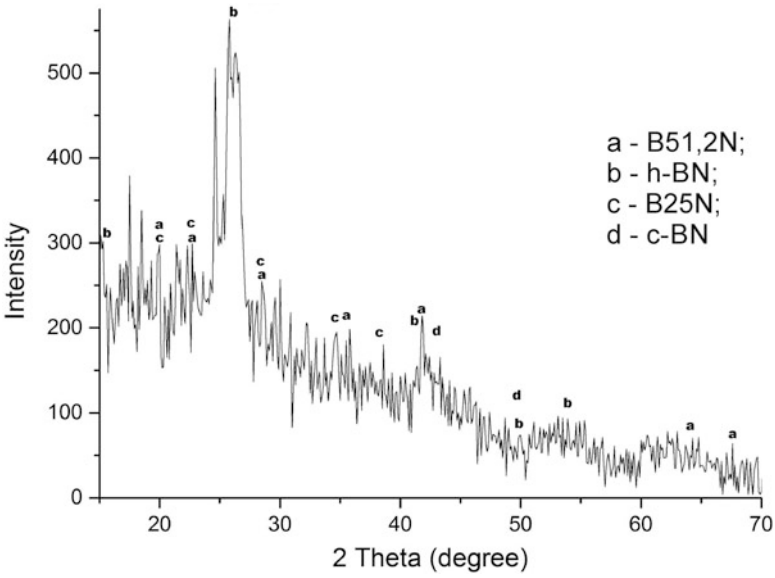

Fig. 10.7 X-ray diffraction pattern of dendritic BN crystals

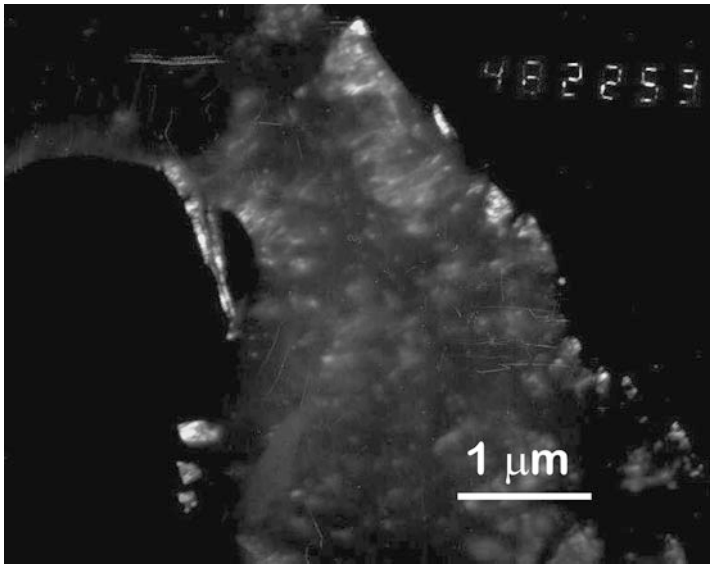

Fig. 10.8 TEM image of the surface of dendritic BN crystals

amorphous phase, which may be attributed to nanopolycrystalline structure of BN. This fact has found its confirmation in TEM research of the surface of dendritic BN crystals (Fig. 10.8), electron diffraction study [11], and Raman spectroscopy (Fig. 10.9).

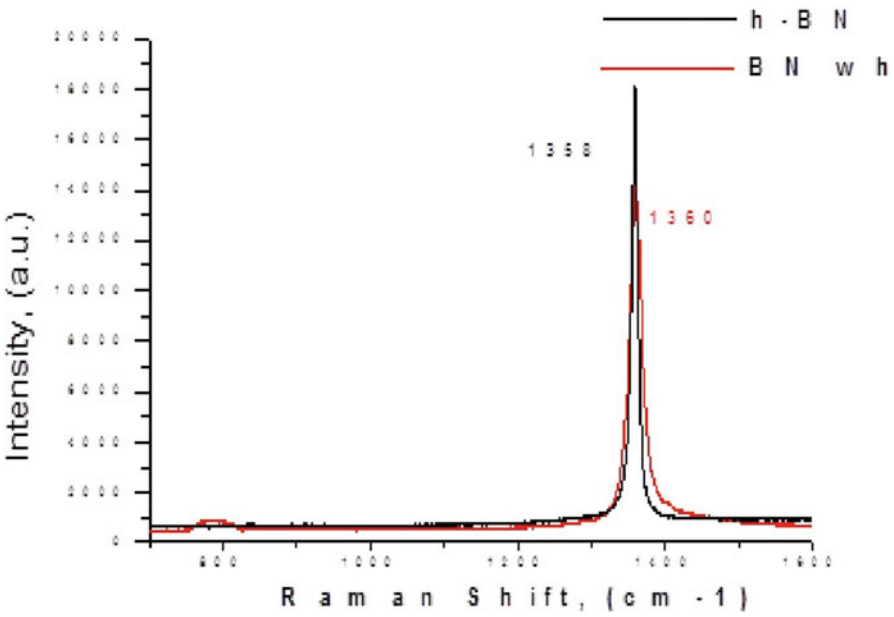

Fig. 10.9 Raman spectra of initial h-BN powder and synthesized BN dendritic crystals (whiskers)

The dominant feature of the Raman spectra for dendritic BN crystals is a peak at 1360 cm^{-1} that corresponds to E_{2g} phonon mode of h-BN in agreement with a peak at 1358 cm^{-1} for initial h-BN. This BN characteristic peak is analogous to the G peak in graphene and occurs at 1366–1368 cm^{-1} usually [20–22]. A half-width of peaks for h-BN and dendritic BN crystals is 11 and 21 cm^{-1}, respectively. Compared to an infinitely long system with periodic boundary conditions like h-BN, the force constant for dendritic crystals could not be reduced because of size effects. Given that the dendritic crystals have a broader size distribution, the force constants, which are size dependent, will also have a broader distribution, which in turn leads to a larger frequency range. Some presence of oxygen (Fig. 10.6b, c) results in a negligible peak at 790–800 cm^{-1} for dendritic BN crystals, which can be considered as boric acid. No peak in the visible Raman spectra can be attributed to BN nanotubes. All observed modes are due to nanopolycrystalline structure of shell or contaminants with oxygen.

Besides dendrites (Fig. 10.5a, b), nanowires (Fig. 10.5c), and nanotubes, the resulting powder undoubtedly consists from boron nitride films (Fig. 10.10) as a result of some bubbles bursting [13]. During TEM study, an electron beam significantly affected on these films enabling the electrification charge on the surface. They quickly change their position and size or disappear at all. Thickness of films, their composition and charge stability together with density of energy of the electron result in quality of TEM image.

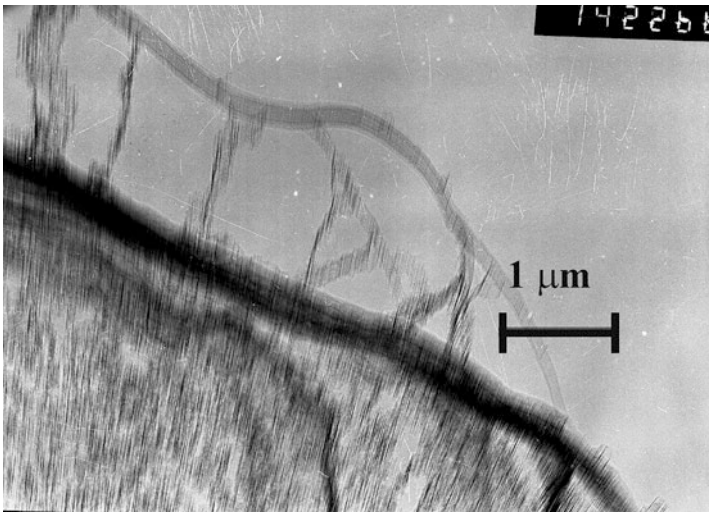

Fig. 10.10 TEM image of boron nitride films

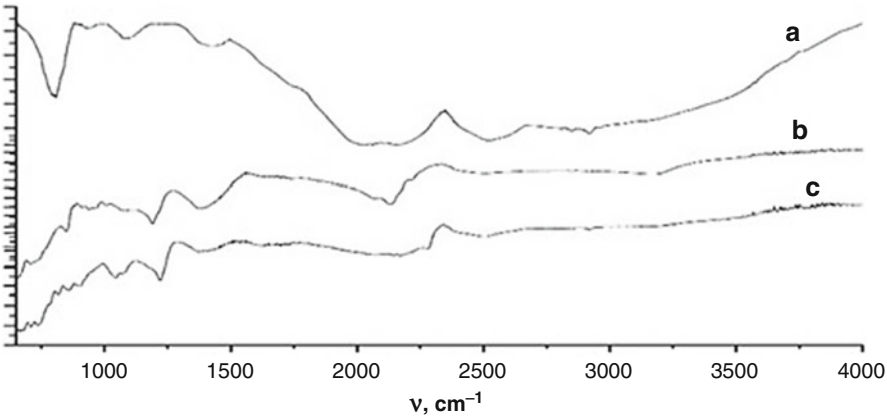

Fig. 10.11 FTIR spectra of initial boron powders of mean sizes: (**a**) 0.05 μm, (**b**) 0.20 μm, and (**c**) 2.00 μm

10.4 Process of Nanostructures Formation from Boron

Complex molecules have many bonds; therefore, their Fourier transform infrared spectra are complicated. Vibrational FTIR spectra of initial boron powders are simple enough and indicate the main characteristics of their chemical bonds on the surface (Fig. 10.11). The vibrational FTIR spectrum of boron powder of a mean grain size of 0.05 μm has CH = CH out-of-plane bending and C–OH stretching

vibrations of 750 and 990 cm^{-1}, respectively. This powder is a little bit different from the others due to high surface activity and its ability to form new compounds (Fig. 10.11). A FTIR spectra of boron powders of a mean grain sizes of 0.20 and 2.00 μm are very close, despite the difference in phase composition and presence of carbon impurity [12].

Interesting to underline that all FTIR spectra of the initial h-BN and boron powders of different mean sizes have demonstrated absence of a band of hydrogen with a wave number of 3197 cm^{-1}, which indicates specific defects and defective structures [23].

Direct synthesis of BN using initial boron powders with mean sizes of 0.05, 0.20, and 2.00 μm [12] in flow of nitrogen containing H_2O as impurity resulted in platelike, equiaxed, and filmlike structures of different sizes [12]. Boron powders of mean size of 0.05 and 2.00 μm formed a mostly platelike BN of 0.50, 0.50, and 0.60 μm mean sizes, respectively. However, the most active boron powder with 0.05 μm mean size stimulates a filmlike structure formation about 4.00 μm^2 area as well [12]. The presence of carbon impurity in boron powder of mean size 0.20 μm results in formation of equiaxed nanosized powders of the smallest mean size 0.30 μm.

All produced BN powders have a very strong band of hydrogen with wave number of 3184–3197 cm^{-1} that indicates defective structures formed during rapid heating and cooling rates. These defects provide the suitable trapping sites for hydrogen storage and consequently affect the hydrating properties of produced nanostructured powders [23]. The vibration at 2510–2517 cm^{-1} can be ascribed to stretching B–H vibrations [12].

Powders produced from pure boron have the same aspect ratio ~5 like presented in [24]. Proposed in [24] model gives for specific surface a value, which significantly exceeds that from globular model. Therefore, the deviation of the particle shape from the sphere substantially increases surface-specific area of nanopowdered BN.

10.5 Synthesis By-Products

Alongside the formation of h-BN nanostructures, during the synthesis in a high-flux optical furnace, there are formed the significant amounts of different phases: structural modifications of boron and boron-rich systems stabilized with nitrogen and other impurities. This statement is based on our present results, as well as results obtained in previous works [3, 11–13].

In some regards, the similar situation was observed in [25]. Namely, B/N shell structures of chemical composition BN_x with boron excess ($x << 1$) contaminated with carbon were synthesized in the process of melting of a boron-rich material in a boron nitride crucible with the nitrogen source in the form of high-purity pressed boron nitride rods, which held up the crucible. The obtained material was found to be conductive despite the fact that all the boron nitrides of stoichiometric chemical

composition BN are insulators. “Metallic” boron nitride was modeled as a mixture of structural modifications of semiconducting boron and boron carbide heavily doped with nitrogen. First principle calculations performed within the quasi-classical approximation proved that nitrogen impurities, accommodated in large crystallographic voids characteristic of all-boron and boron-rich crystalline lattices, create donor electron states inside the conduction band and then lead to the local “metallization” of chemical bonds in these initially covalently bonded structures [25].

10.6 Summary and Outlook

In this chapter, the investigations of the direct synthesis of boron nitride nanostructures under concentrated light were presented. The importance of high temperatures and high-temperature gradients for nanowire and nanotubes formation was highlighted.

The goal of the research was to understand the process of new boron nitride nanostructures formation with desired dimensionality. Through a detailed investigation on the structures and properties of new boron nitride nanomaterials, it was targeted at advance understanding of the unique boron chemistry and physics in the nanoscale.

References

1. Meyers RA (ed) (2012) Encyclopedia of sustainability science and technology. Springer, New York. doi:10.1007/978-1-4419-0851-3
2. Ahmad SQS, Hand RJ, Wieckert C (2014) Use of concentrated radiation for solar powered glass melting experiments. Sol Energy 109:174–182
3. Sartinska LL et al (2008) Transformation of fine-grained graphite-like boron nitride induced by concentrated light energy. Mater Chem Phys 109:20–25
4. Sarwar J, Georgakis G, LaChance R, Ozalp N (2014) Description and characterization of an adjustable flux solar simulator for solar thermal, thermochemical and photovoltaic applications. Sol Energy 100:179–194
5. Paine RT, Narula CK (1990) Synthetic routes to boron nitride. Chem Rev 90:73–91
6. Moussa G et al (2014) Nanostructured boron nitride: from molecular design to hydrogen storage application. Inorganics 2:396–409
7. Oku T (2013) Synthesis, atomic structures adn properties of boron nitride nanotubes. In: Suzuki S (ed) Nanotechnology and nanomaterials “physical and chemical properties f carbon nanotubes”, ISBN 978-953-51-1002-6, Published: February 27, 2013 under CC BY 3.0 license. doi: 10.5772/51968
8. Rubio A, Corkill JL, Cohen ML (1994) Theory of graphitic boron nitride nanotubes. Phys Rev B 49:5081–5084
9. Chkhartishvili L (2009) Boron nitride nanosystems of regular geometry. J Phys Conf Ser 176:1–17

10. Chkhartishvili L, Murusidze I (2012) Relative stability of BN nanotubes. Solid State Sci 14:1664–1668
11. Sartinska LL (2011) Catalyst-free synthesis of nanotubes and whiskers in an optical furnace and a gaseous model for their formation and growth. Acta Mater 59:4395–4403
12. Sartinska LL et al (2015) Effect of moisture on the properties and structure formation of BN under concentrated light. Eur Chem Bull 4:165–168
13. Sartinska LL (2015) Surface modification to test 'gaseous model' for BN nanotubes formation under the concentrated light and its application for graphene. Superlattice Microst 85:392–400
14. Bao K et al (2009) Synthesis of highly crystalline rhombohedral BN triangular nanoplates via a convenient solid state reaction. J Solid State Chem 182:925–931
15. Wang L, Hang R, Xu Y, Guo C, Qian Y (2014) From ultrathin nanosheets, triangular plates to nanocrystals with exposed (102) facets, a morphology and phase transformation of sp2 hybrid BN nanomaterials. RSC Adv 4:14233
16. Yeadon M et al (2003) Direct observation of boron nitride nanocage growth by molecular beam nitridation and liquid-like motion of Fe-B nanoparticles. J Mater Chem 13:2573
17. Narita I, Oku T (2003) Synthesis of boron nitride nanotubes by using NbB2, YB6 and YB6/Ni powders. Diam Relat Mater 12:1912–1917
18. Chkhartishvili L, Murusidze I (2010) Molar binding energy of zigzag and armchair single-walled boron nitride nanotubes. Mater Sci Appl 1:223–246
19. Hao X et al (2002) The effect of temperature on the synthesis of BN nanocrystals. J Cryst Growth 241:124–128
20. Gorbachev RV et al (2011) Hunting for monolayer boron nitride: optical and Raman signatures. Small 7:465–468
21. Arenal R et al (2006) Raman spectroscopy of single-wall boron nitride nanotubes. Nano Lett 6:1812–1816
22. Liu F et al (2014) Cheap, gram-scale fabrication of BN nanosheets via substitution reaction of graphite powders and their use for mechanical reinforcement of polymers. Sci Rep 4:1–8
23. Moon OM, Kang B-C, Lee S-B, Boo J-H (2004) Temperature effect on structural properties of boron oxide thin films deposited by MOCVD method. Thin Solid Films 464–465:164–169
24. Цагарейшвили ОА, Л С et al (2015) Расчет удельной поверхности нанокристаллических порошков: гексагональный нитрид бора. Наноструктурное материаловедение
25. Becker R et al (2015) 'Metallic' boron nitride. Eur Chem Bull 4:8–23

Chapter 11
Time-Dependent Absorption Spectra of 1D, 2D Plasmonic Structures Obtained by the Ordering of Ag Nanoparticles in Polymer Matrix

T.N. Smirnova, P.V. Yezhov, S.A. Tikhomirov, O.V. Buganov, and A.N. Ponyavina

11.1 Introduction

Novel materials based on transparent polymer matrix with embedded noble metal nanoparticles (NPs) have been a subject of intense research in recent years since they possess specific optical and electronic properties caused by the quantum-size effect and surface plasmon excitation [1–4]. Spatial ordering of metal-containing nanocomposites makes it possible to create metal NPs-polymer gratings and photonic crystals which may find applications in photonics as nonlinear optical elements, diffractive elements with ultrahigh spectral dispersion or effective laser cavities [4–10].

Noble metal NPs exhibit intensive absorption bands in the visible region due to localized surface plasmon (SP) excitation. Exposure to the ultra-short light pulses near plasmon absorption band creates a strongly non-equilibrium ensemble of charge carriers in the metal NP. Because of the limited size of the NPs, electron dynamics in them differs considerably from the one in the bulk material and follows laws defined by the properties of the individual metal NP as well as their environment and spatial arrangement [11–17]. It is known that ordering of the NPs with a sub-wavelength periodicity can affect the heating and cooling of electron gas in the NPs, for example, [17, 18].

T.N. Smirnova (✉) • P.V. Yezhov
Institute of Physics, National Academy of Sciences of Ukraine, Prospect Nauki 46, Kiev 03680, Ukraine
e-mail: smirnova@iop.kiev.ua; yezhov@iop.kiev.ua

S.A. Tikhomirov • O.V. Buganov • A.N. Ponyavina
Institute of Physics, National Academy of Sciences of Belarus, Pr. Nezavisimosti, 68, Minsk 220072, Belarus
e-mail: tikhomirov@imaph.bas-net.by; bouganov@imaph.bas-net.by; ponyavina@imaph.bas-net.by

O. Fesenko, L. Yatsenko (eds.), *Nanophysics, Nanophotonics, Surface Studies, and Applications*, Springer Proceedings in Physics 183,
DOI 10.1007/978-3-319-30737-4_11

In our work we investigated the dynamics of electron excitations in plasmonic nanocomposites with a periodic substructure of ordered Ag-NPs in a polymer matrix. The use of photopolymerizable nanocomposite materials opens the possibility to create sub-micrometer periodic distribution of NPs in polymer matrix by a simple one-step holographic method.

Organic polymers as the matrices for plasmonic NP have several advantages over solid non-organic matrices, in particular, glasses. Besides a high flexibility of structure and properties, polymers exhibit excellent homogeneity and easy processability as compared to glasses.

11.2 Fabrication of Periodic Structures by Holographic Method

Two main approaches are usually used for the creation of periodical polymer–metal NPs structures by holographic method. According to the first approach, ex situ prepared NPs are introduced in photopolymer mixture and then photopolymerization in an interference pattern is carried out. The photocurable composites containing ex situ prepared metal NPs possess high absorption in visible spectral range that prevents the use of vis-emissive laser sources for holographic recording and limits the concentration of NPs in the matrix material. Periodic distribution of metal NPs in polymer matrix can also be obtained by in situ formation of NPs upon exposure to an interference pattern. We have proposed an original method of formation of periodic polymer–metal NPs structures (Fig. 11.1) [19].

The initial composite for holographic patterning is a homogeneous mixture containing monomers, photoinitiator of radical polymerization and metal precursor solution. During the first step, photopolymerization in the interference pattern, a stable volume polymer–metal precursor grating is formed. Reduction of the precursor and formation of metal NPs occur mainly during the stage of photo- or

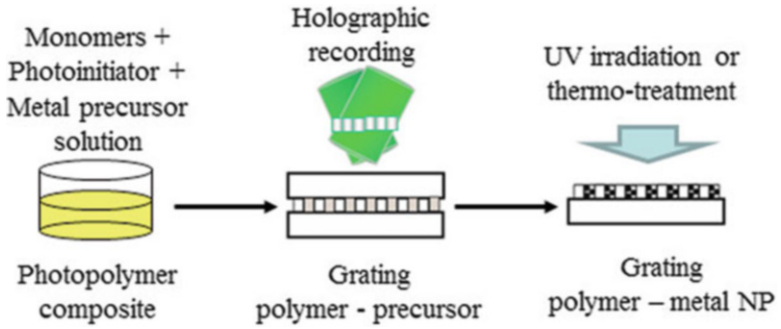

Fig. 11.1 In situ method of polymer–metal NPs structures fabrication

thermo-processing. The proposed method has the following advantages: holographic photopolymerization can be carried out in a vis spectral range since the solution of the precursor of gold or silver absorbs light in the spectral range < 350 nm; NP concentration in the final structure can be increased compared to the ex situ method; the long-term stability of the grating is provided by the irreversible periodical redistribution of the components during the holographic recording that avoids the fixation step.

The proposed optimal composition includes two copolymerized monomers that form a cross-linked polymer network and solutions of $AgNO_3$ in acetonitrile as an Ag NPs precursor. Photoinitiating system (Camphorquinone and Michler's ketone) is added to the syrup to provide the sensitivity in the spectral range of 440–500 nm. The reactive layers for the holographic patterning were prepared by sandwiching a drop of the initially liquid composite between two glass slides separated by spacers of proper thickness which is then exposed to the interference pattern. Typical thickness of the layer was ca. 10–20 μm.

A conventional two-beam interference scheme based on the Ar-ion laser operating at $\lambda_{rec} = 488$ nm was used for holographic recording of the one-dimensional (1D) Bragg structures of $\Lambda = 0.9$ μm and 0.38 μm periods (samples 1D1 and 1D2). Two-dimensional (2D) distributions of silver NPs in polymer film can be obtained by exposing to the interference pattern formed by three (for hexagonal 2D-H structures) or four (for quadratic 2D-Q structures) laser beams.

In order to obtain a system of three or four interfering beams from a single collimated laser beam we used a diffractional beam-splitter based on highly efficient Bragg gratings whose period and line inclination assures formation of the structures with a period of real space lattice of about 370–380 nm.

The mechanism of grating formation in the composites, comprising monomer and metal precursor was studied in [19]. It was established that during photopolymerization in the periodic light pattern both main components, the monomer and the metal precursor solution, take part in the irreversible photo-induced mass-transfer, providing the stability of the resulting structure. The precursor solution is forced out from the forming polymer network and is mostly located in the regions of the structure corresponding to low-intensity areas of the interference pattern. Full polymerization of the composite leads to formation of a high-efficient volume structure consisting of periodic polymer and metal precursor containing regions. Subsequent thermal treatment of the grating intensifies evaporation of the solvent and selective reduction of silver salt to Ag NPs in the areas of the film containing metal precursor.

Figure 11.2 shows AFM microscopy images of 2D-H (hexagonal) (a) and 2D-Q (b) (quadratic) structures with a period of real space lattice of about 370 nm. More clear regions correspond to the polymer phase. Silver NPs are concentrated in darker regions. The particle density was not modulated periodically along the layer thickness.

The periodic distribution of the NPs in the polymer matrix was directly confirmed by TEM measurements of the 1D grating (Fig. 11.3). It can be seen that the spherical NPs with average particle diameter of 5 nm are periodically distributed in polymer film.

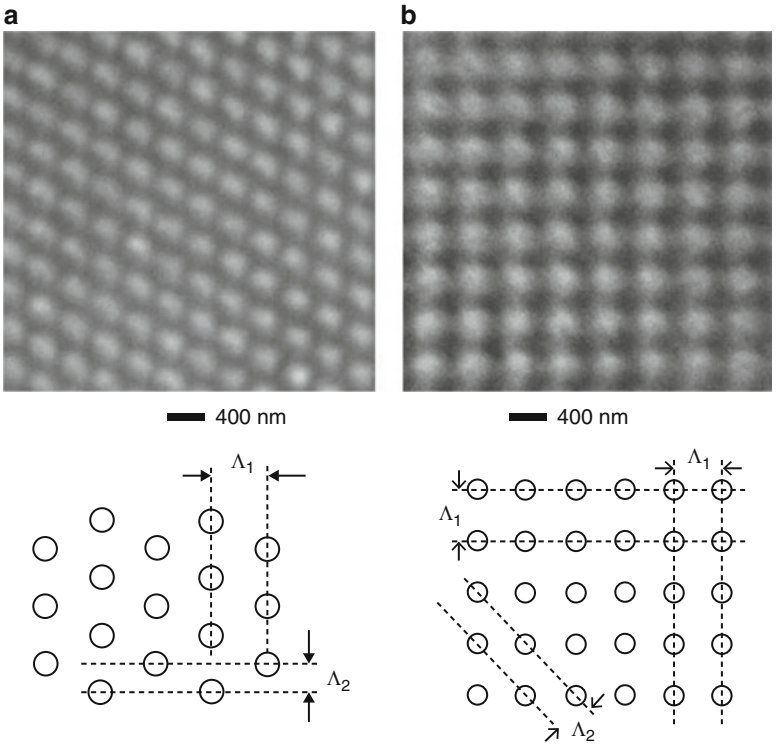

Fig. 11.2 AFM microscopy images of 2D-H (**a**) and 2D-Q (**b**) structures with a period of the real space lattices: $\Lambda_1 \approx 375$ nm, $\Lambda_2 \approx 216$ nm for 2D-H and $\Lambda_1 \approx 370$ nm, $\Lambda_2 \approx 262$ nm for 2D-Q structures

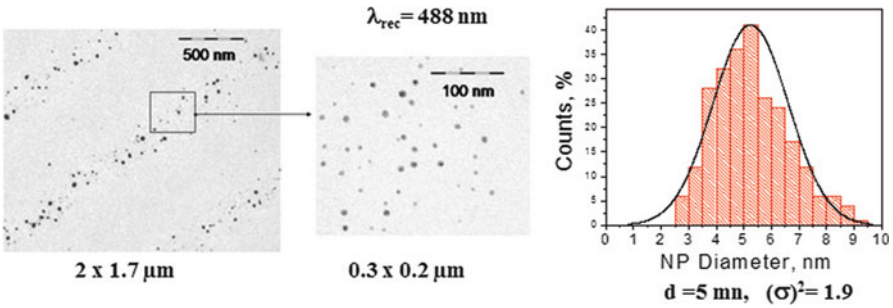

Fig. 11.3 TEM image of the grating ($\wedge = 900$ nm) after post-processing, and the histogram of Ag-NP diameter distribution

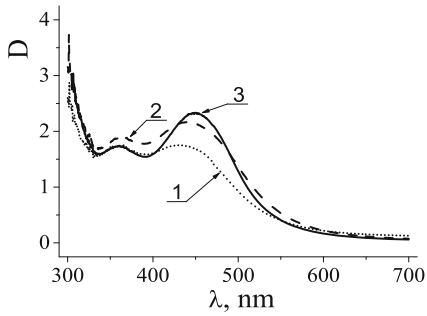

Fig. 11.4 Absorption spectra of the layers with 1D- and 2D-ordered structures of Ag-NPs: 1D (1), 2D-Q, quadratic lattice (2), 2D-H, hexagonal lattice (3)

The formation of the Ag NPs in the 1D and 2D structures is also confirmed by the changes in the absorption spectra of the gratings. Figure 11.4 shows stationary absorption spectra of 1D- and 2D-periodic structures obtained with the same metal precursor concentration. The band at 450 nm corresponds to SP absorption; at 360 nm —to photoinitiator (Michler's ketone) absorption. Curves 2 and 3 are the optical spectra of 2D periodic structures with different ordering of the particles, 2D-Q and 2D-H, respectively. A slight long-wavelength shift of the SP band maximum is observed as the complexity of the structure increases from 1D to 2D-Q and 2D-H.

Also, the optical density at the SP peak maximum slightly increases as the structure symmetry changes. These spectral changes can be caused by the increase of NPs size and concentration that are due to a different precursor location and NP synthesis conditions. This hypothesis requires further experimental confirmation.

11.3 Spectral-Kinetic Measurements

The dynamics of transient absorption was studied by the known pump-probe method using a femtosecond spectrometer including an original femtosecond pulse generator based on Ti:Sa laser with pulsed synchronous pumping [20]. Samples were excited at $\lambda = 395$ nm using the second harmonic of laser oscillations. Pulse duration was approximately 140 fs. Output pulse energy was changed from 1 to 10 μJ at 1 kHz repetition rate. At pulse energy of 10 μJ pulse power was ca. 7×10^7 W and pulse intensity was ca. 3.5×10^{11} W/cm^2. The femtosecond supercontinuum was used as a probe radiation. In order to reduce the noise caused by instability of supercontinuum, the probe radiation was split into two beams, the probe (I_{prob}) and reference (I_{ref}). Transient spectra are characterized by a change of optical density ΔD that was calculated using the formula: $\Delta D_{\Delta t}(\lambda) = \log(T_0/T)$, where $T = I_{prob}/I_{\text{ref}}f$ and $T_0 = I^0_{prob}/I_{\text{ref}}f^0$ are intensity ratios of probe and reference pulses passing through the sample with and without excitation; Δt is the delay time between the excitation and probe pulses. Differential spectra $\Delta D_{\Delta t}(\lambda)$ of 1D and 2D ordered structures with Ag-NPs were studied near SP band for different excitation regimes.

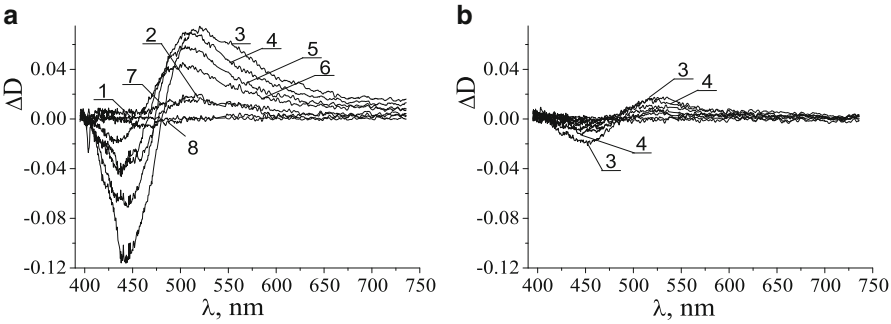

Fig. 11.5 Differential absorption spectra of 1D1 with 1D-ordered Ag-NPs at exciting pulse energy 10 (**a**) and 1 μJ (**b**); delay time $\Delta t = 1.0$ (1), 0 (2), 0.3 (3), 1.0 (4), 1.8 (5), 3.0 (6), 10 (7), and 100 ps (8); $\lambda_{pump} = 400$ nm

11.4 Results and Discussion

As an example, Fig. 11.5 shows differential spectra at two excitation energies for the sample with 1D-ordered Ag-NPs with a period of 0.9 μm. Analysis of the shape of plasmon band and its evolution during and after pump pulse excitation has shown that it bleached and broadened under the influence of a powerful illumination.

In the vicinity of initial plasmon peak the induced bleaching was observed while optical density increased on the wings of plasmon band. These processes are reversible and explained by the heating of electron gas in metal NPs under the influence of the powerful laser excitation. Electrons lose energy in the initial time interval mainly through electron–electron, electron–surface, and electron–phonon scattering. Induced changes of the optical density and broadening of the absorption spectra increased with increasing pump intensity for all studied structures. These transformations of differential absorption spectra of 1D plasmonic structures coincide with the ones observed in spectra of composites with chaotic distribution of NPs, for example, [15, 16].

However our investigations have shown that electron dynamics in excited organized structures differed in a number of features. Figure 11.6 demonstrates transient optical density spectra of a 1D-structure at different pump energies and 1 ps delay time.

Inset shows the optical density dependency on pump impulse energy for 440 nm probing impulse, close to the SP peak maximum in the corresponding stationary spectrum. Linear optical density decrease is observed with the increase of pump power. Furthermore, in addition to "bleaching" of SP at certain delay times, weak splitting of the absorption band is observed at the maximum pump power. Band splitting was observed in glasses, doped with silver, gold, and copper NPs. This phenomenon was explained by laser-induced anisotropy of matrix. The splitting can appear due to optical Kerr effect and enhancement of electric field at

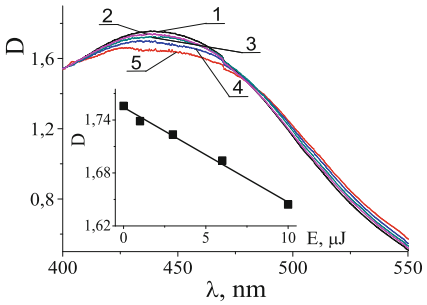

Fig. 11.6 Influence of exciting pulse energy on optical density of 1D-ordered structure 1D2 near the SPRA maximum; delay time $\Delta t = 1$ ps; stationary spectrum (1), E = 1 (2), 3 (3), 6 (4), and 10 μJ (5); in the inset, optical density at $\lambda = 440$ nm as a function of exciting pulse energy

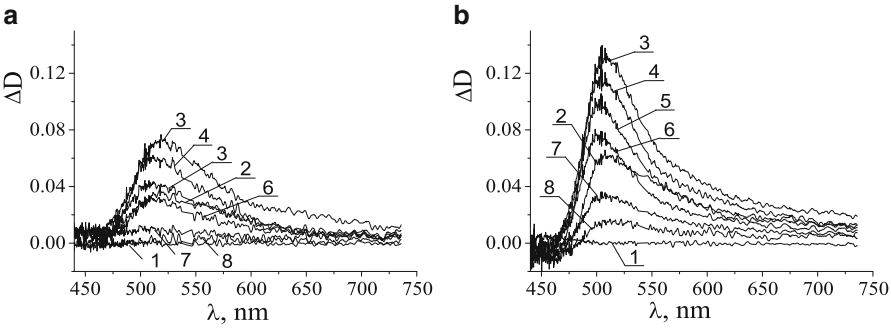

Fig. 11.7 Differential spectra of polymer films with 1D-ordered (**a**) and 2D-ordered 2D-H (**b**) Ag-NPs: exciting pulse energy 10 J; delay time $\Delta t = 1.0$ (1), 0 (2), 0.3 (3), 1.0 (4), 1.8 (5), 3.0 (6), 10 (7), and 100 ps (8)

the surface of metal NPs similar to splitting in anisotropic shape (elliptical) NPs or spherical NPs incorporated into anisotropic matrix [16]. It is important to note that pumping power necessary to induce splitting is one order of magnitude higher than used in our experiment. Moreover, dynamics of induced changes depends on the polarization of probing beam, while our experiments didn't show such a dependency. Absorption band splitting may occur as well due to laser-induced modification of NPs: their shape becomes elongated and their orientation is determined by the polarization and power of incident impulse. Such processes may be caused by interactions between electron photoemission effect, photoionization of NPs, and their coalescence (see, for example, [21–23]. Therefore ultrafast dynamics of these processes as well as possible contribution of the matrix need to be deeply studied for correct interpretation of the observed reversible SP band splitting.

The induced changes of transient spectra in the range of 450–700 nm at constant pump energy grew even stronger as the structure became more complicated. As an example, Fig. 11.7 shows differential spectra of 1D1 ($\Lambda = 0.38$ μm) and 2D-H ($\Lambda_1 = 0.37$ μm).

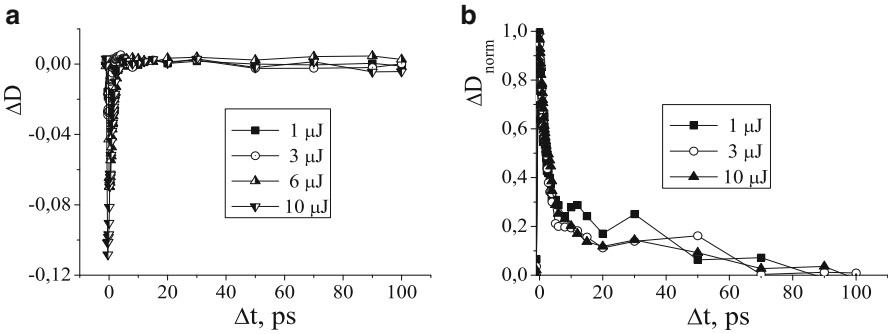

Fig. 11.8 Optical density kinetics for 1D-structure in the vicinity of induced bleaching ($\lambda = 450$ nm, $\tau_1 = 1.3$ ps) (**a**) and absorption ($\lambda = 520$ nm, $\tau_1 = 1.8$ ps) (**b**)

It may be assumed that the increase of symmetry order of the system and decrease of the NP placement period favors manifestation of collective effects when electron subsystem is excited by powerful laser radiation. They may be furthermore promoted by the presence of metal NPs in the nodes of 2D lattices.

Temporal evolution of electron gas characteristics in NPs can be described by studying kinetics of induced bleaching and induced absorption measured in maxima of plasmon peak and of induced absorption, respectively (Fig. 11.8). It was found that both induced processes demonstrate double-exponential decay, in which fast component (τ_1) reflects energy transfer from electron gas to lattice and slow component (τ_2) corresponds to energy transfer to polymer matrix. It can be seen that the induced changes of the optical density relax in an oscillating manner.

It is known that oscillations are acoustic breathing modes excited by the rapid heating of particle lattice after a powerful laser excitation (see [15, 21] and the references therein). In contrast to the measured electron–phonon relaxation times for Au NPs that increase with increasing pump power [15] in our case the values of τ_1 are power independent in both spectral regions. A significant growth of τ_1 (almost 1.5 times) is observed as well for $\lambda_{pr} = 520$ nm as compared to $\lambda_{pr} = 450$ nm. The opposite effect was observed in [11] for Cu-NPs of 10 nm diameter. As the pump energy increased from 2.139 eV ($\lambda \approx 650$ nm) to 2.255 eV ($\lambda \approx 580$ nm, practically the Cu-NP SP band maximum) relaxation time increased approximately 1.5 times. The relaxation time was independent of detuning from the SP maximum for Cu-NPs with 15 nm diameter. The authors explain this by competition of two processes: interaction of electron subsystem with plasmons excited by probing beam and generation of plasmons from electron–hole pairs that is stimulated by surface polarization. The role of the second process increases with decreasing NP size. It is possible that the differences of kinetics for Ag-NPs in our case may be related to significant detuning of the SP band from the spectral range of inter-band absorption as well as by the presence of matrix absorption band with 360 nm maximum.

Table 11.1 Characteristic relaxation times in induced absorption band maximum for holographic films with 1D- and 2D-ordered Ag-NPs

Structure	1D1	1D2	2D-Q	2D-H
type	$\Lambda = 900$ nm	$\Lambda = 380$ nm	$\Lambda_1 = 370$ nm	$\Lambda_1 = 375$ nm
τ_1[a], ps	1.1	1.8	2.7	2.7
τ_2, ps	12	16	131	141

[a]The accuracy of fitting is$\Delta\tau/\tau < 5\%$

Analysis of the obtained spectral-kinetic data indicates that relaxation times in the vicinity of induced absorption increase significantly as the symmetry varies from 1D to 2D-Q and 2D-H structures (Table 11.1).

At $\lambda_{pr} = 520$ nm and excitation energy of 10 J relaxation time $\tau_1 = 1.1$ ps for 1D1 and 2.7 ps for 2D-H structure. The decay time τ_2 is 16 ps for 1D structure and is an order of magnitude higher, 140 ps, for 2D-H structure. We will note that the electron excitation relaxation time was 1.6–2 ps for disordered systems of silver NPs (Ag-NPs) that were synthesized in situ in photopolymer films [24]. Thus, it can be seen that sub-wavelength ordering of Ag-NPs affects the decay constants of the induced changes in the SP spectra.

11.5 Conclusion

We have presented the main results of our experimental investigations of electron excitation dynamics in ordered plasmonic structures. We found out that the change of period and symmetry of the structure significantly influences the values of induced changes of intensity and shape of plasmonic band as well as relaxation times of electron subsystem. The change of symmetry of the structure from 1D to 2D-Q (quadratic) and 2D-H (hexagonal) leads to the enhancement of induced absorption and increase of relaxation times of electron subsystem, determined at the maximum of induced absorption. The relaxation time increases 1.5 times for electron–electron and approximately an order of magnitude for phonon–phonon interactions.

In the studied structures Ag-NPs are synthesized from metal precursor in the matrix after structure formation. Change of the size of regions where precursor is localized may alter the conditions of NPs formation and, respectively, alter their shape and size thus strongly influencing the electron excitation dynamics in ordered nanocomposites. It can be also assumed that the decrease of inter-particle distance stimulates the manifestation of collective effects upon excitation of the electron subsystem by a powerful laser radiation. Our further research will be aimed at confirmation of the stated assumptions.

Acknowledgements This work was supported by the grant of the Target Comprehensive Program of Fundamental Research of National Academy of Science of Ukraine “The Fundamental Problems of Creation of New Nanomaterials and Nanotechnologies” (Project 3/15-H).

References

1. Kreibig U, Vollmer M (1995) Optical properties of metal cluster. Berlin, Springer
2. Nicolais L, Carotenuto G (2005) Metal-polymer nanocomposites. Wiley, New Jersey
3. Gonela F, Mazzoldi P (2000) Handbook of nanostructured materials and nanotechnology, vol 4. Academic, New York
4. Shalaev V (2002) Optical properties of nanostructured random media. Springer, Berlin
5. Dyachenko PN, Miklyaev YuV (2007) One-dimensional photonic crystal based on nanocomposite of metal nanoparticles and dielectric. Opt Mem Neural Netw 16:198–203
6. Ditlbacher H, Krenn JR, Schider G, Leitner A, Aussenegg FR (2002) Two-dimensional optics with surface plasmon polaritons. Appl Phys Lett. doi: 10.1063/1.1506018
7. Rai K, Fontecchio A (2005) Holographically phase separated gold/nanoparticle films. In: APS march meeting. American Physical Society. Available via The Smithsonian/NASA Astrophysics Data System. http://meetings.aps.org/link/BAPS.2005.MAR.L30.2. Cited 21 March 2005
8. Busch K, Lölkes S, Wehrspohn RB, Fall H (2004) Photonic crystals: advances in design, fabrication, and characterization. Wiley, Weinheim
9. Mikhailov V, Elliott J, Wurtz G, Bayvel P, Zayats AV (2007) Dispersing light with surface plasmon polaritonic crystals. Phys Rev Lett. doi: 10.1103/PhysRevLett.99.083901
10. Stehr J, Grewett J, Shimdler F, Sperling R, von Plessen G, Lemmer U, Lupton JM, Klar TA, Feldman J, Holleitner AW, Forster M, Scherf UA (2003) Low threshold polymer laser based on metallic nanoparticle gratings. Adv Mater 15:1726–1729
11. Bigot J-Y, Halté V, Merle J-C, Daunois A (2000) Electron dynamics in metallic nanoparticles. Chem Phys 251:181–203
12. Link S, El-Sayed MA (2003) Optical properties and ultrafast dynamics of metallic nanocrystals. Annu Rev Phys Chem. doi: 10.1146/annurev.physchem.54.011002.103759
13. EahS S-K, Jaeger HM, Scherer NF, Lin X-M, Wiederrecht GP (2004) Femtosecond transient absorption dynamics of close-packed gold nanocrystal monolayer arrays. Chem Phys Lett. doi:10.1016/j.cplett.2004.01.056
14. Sonnichsen C, Franzl T, Wilk T, von Plessen G, Feldmann J (2002) A nanoscale optical biosensor: sensitivity and selectivity of an approach based on the localized surface plasmon resonance spectroscopy of triangular silver nanoparticles. Phys Rev Lett. doi:10.1021/ja020393x
15. Link S, El-Sayed MA (2000) Shape and size dependence of radiative, non-radiative and photothermal properties of gold nanocrystals. Int Rev Phys Chem. doi:10.1080/01442350050034180
16. Dmitruk I, Blonskiy I, Pavlov I, Yeshchenko O, Alexeenko A, Dmytruk A, Korenyuk P, Kadan V, Zubrilin N (2010) Optically induced anisotropy of surface plasmons in spherical metal nanoparticles. Phys Rev B. doi:10.1103/PhysRevB.82.033401
17. Lamprecht B, Schider G, Lechner RT, Ditlbacher H, Krenn JR, Leitner A, Aussenegg FR (2000) Metal nanoparticle gratings: influence of dipolar particle interaction on the plasmon resonance. Phys Rev Lett. doi:10.1103/PhysRevLett.84.4721
18. Tikhomirov SA, Buganov OV, Ponyavina AN, Yezhov PV, Kokhtich LM, Smirnova TN (2014) Transient absorption spectra of photopolymeric films with a periodic silver-nanoparticle substructure. J Appl Spectrosc. doi:10.1007/s10812-014-0006-7
19. Smirnova TN, Kokhtych LM, Kutsenko AS, Sakhno OV, Stumpe J (2009) The fabrication of periodic polymer/silver nanoparticle structures: *in situ* reduction of silver nanoparticles from precursor spatially distributed in polymer using holographic exposure. Nanotechnology. doi:10.1088/0957-4484/20/40/405301
20. Blokhin AP, Gelin MF, Buganov OV, Dubovskii A, Tikhomirov SV, Tolstorozhev GB (2003) Collisional relaxation of the optically induced dichroism of complex molecules in a gas. J. Appl. Spectrosc. 70:66–77

21. Unal A, Stalmashonak A, Graener H, Seifert G (2009) Time-resolved investigation of laser-induced shape transformation of silver nanoparticles. Phys Rev B. doi:http://dx.doi.org/10.1103/PhysRevB.80.115415
22. Seifert G, Stalmashonak A, Hofmeister H, Haug J, Dubiel M (2009) Laser-induced, polarization dependent shape transformation of Au/Ag nanoparticles in glass. Nanoscale Res Lett 4:1380–1383
23. Stalmashonak A, Seifert G, Graener H (2007) Optical three-dimensional shape analysis of metallic nanoparticles after laser-induced deformation. Opt Lett. doi:10.1364/OL.32.003215
24. Tikhomirov SA, Buganov OV, Ponyavina AN, Smirnova TN, Yezhov PV, Kokhtich LM (2012) Transient absorption spectra of photopolymeric films with a periodic silver-nanoparticle substructure. In: Paper of the 9th international scientific conference laser physics and optical technologies LFIOT-2012 [in Russian]. Grodno Gos. University, Grodno, 30 May–2 June 2012

Part III
Nanostructured Interfaces and Surfaces

Chapter 12
Composite Coatings Formed by Complex Methods of Surface Hardening

Andrew Stetsko

12.1 Introduction

The chemical heat treatment of surfaces of machine parts is an effective method for generating appropriate surface-hardened layers [1]. To change these characteristics, another technological effect can be applied simultaneously or sequentially with chemical–thermal treatment [2, 3]. This provides a comprehensive treatment of hardened surface layers' required parameters.

Objective: To develop a new method of surface hardening, providing the required quality characteristics of machine parts and tools.

12.2 Materials and Methods

To harden a surface or restore machine parts, a complex method of chemical treatment and plating diffusion is offered [4–8]. It is prepared first by deposition on the surface of renewable details of Ni-Co-P chemical coating in defined aqueous solution formulations and adopted by diffusion chromium plating modes. As a result of recovery on the workpiece, a surface diffusion layer is formed. Its structure (depending on the mode of the applied method) consists of several zones, which are working with the external composite zone, which reaches 250 μm. During the recovery process, universal equipment available in the workplace is used in the complex method.

A. Stetsko
Ukraine Academy of Printing, Mendeleeva Str., 4, Apt. 4, Lviv 79005, Ukraine
e-mail: andrew73@ukr.net

O. Fesenko, L. Yatsenko (eds.), *Nanophysics, Nanophotonics, Surface Studies, and Applications*, Springer Proceedings in Physics 183,
DOI 10.1007/978-3-319-30737-4_12

Table 12.1 Composition of Chemical Sedimentation Recipes

Chemical Element	#1	#2	#3	#4	#5
$CoCl_2$ (g/L)	–	15	15	30	–
$NiCl_2$ (g/L)	–	30	30	30	–
$Na_3C_6H_5O_7$ (g/L)	84	100	100	80	–
NaH_2PO_2 (g/L)	30	20	60	10	25
NH_4Cl (g/L)	–	50	50	50	50
$CoCO_3$ (g/L)	7	–	–	–	–
$CoSO_4$ (g/L)	–	–	–	–	30
$NiSO_4$ (g/L)	15	–	–	–	30
CH_3COONa (g/L)	–	–	–	–	100
H_2SO_4 (g/L)	15	–	–	–	–
NH_4Cl (mL)	90	60	60	60	50

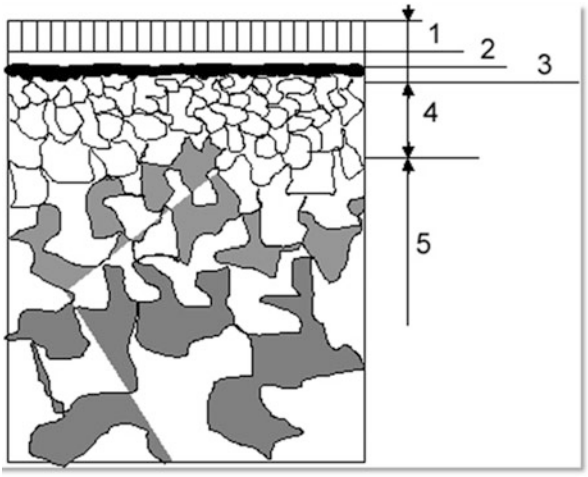

Fig. 12.1 The structure of the diffusion layer after diffusion saturation Cr: *1*—chromium carbides in solid solution Cr in α-Fe; *2*—solid solution Cr in α-Fe; *3*—eutectoid layer; *4*—without carbon layer; *5*—inner part

Chemical treatment (Table 12.1) is applied to the surface details of the preliminary machining, and is followed by cleaned, degreased, chemical deposition in an aqueous solution of a particular recipe. Due to the increased chemical deposition load the process lasts 45 min. The obtained result is a Ni-Co-P amorphous-type chemical coating with thickness of 8–12 μm.

Chemical–thermal treatment—diffusion plating is carried out at a temperature of 1050 °C. The detail is placed in a retort with a powder mixture of ferrochrome, aluminum oxide, and ammonium chloride and a consumable sealed gate. To form the desired diffusion layer structure, isothermal aging at 700 or 800 °C with a duration of 1 or 1.5 h is used.

Compared with the traditional chrome diffusion, which is made up of hardened layers of thickness 15–30 μm, consisting of chromium carbides $Cr_{23}C_6$ and Cr_7C_3, after a complex method of chemical treatment and recovery the chrome diffusion layer is formed by diffusion (Fig. 12.1), which for medium and high carbon steels

contains four zones: a composite outer zone consisting of columnar chromium carbide matrix Cr solid solution in α-Fe thickness of 100–250 μm and integrated microhardness of 11–15 GPa; an area solid solution of chromium in αFe 10–50 μm thickness and microhardness of 4.5 GPa; an eutectoid zone thickness of 10–30 μm and microhardness 4 GPa; and a carbonless zone thickness of 100–180 μm and 1.4–1.6 GPa microhardness for the ferritic component and core parts. Composite structure zones can significantly increase the relaxation life because of the accumulation in the course of internal microstresses in the soft phase—solid solution of chromium in αFe, at a time when the main burden will perceive a solid phase—grain columnar chromium carbide high hardness (up to 18 GPa).

12.3 Discussion

Particular attention to the diffusion layers is obtained on a complex method of steel. With the implementation of regimes the complex method of chemical treatment and plating diffusion of 5-h diffusion in chrome and 1050 °C 1-h isothermal holding at 700 °C we get the steel reinforced layer, which consists of four main zones (Fig. 12.2). The outdoor composite zone 1 (thickness 100 μm), consists of packages transkrystal micrograin chromium carbides. At the same time, there are grain

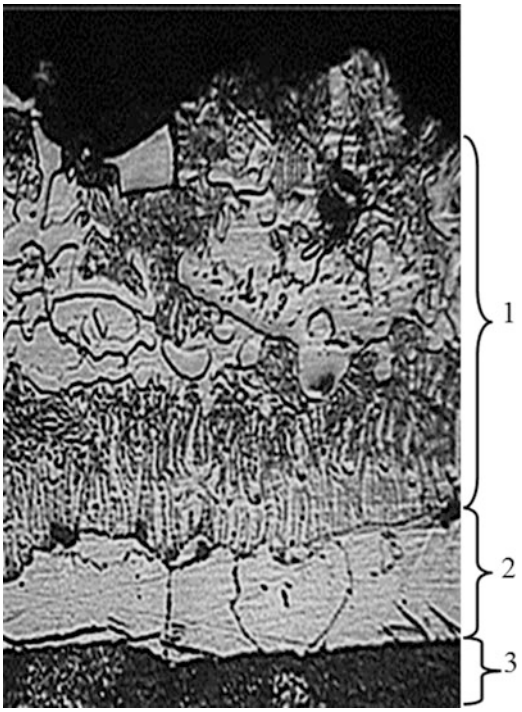

Fig. 12.2 The microstructure of hardened diffusion layer of chemical Ni-Co-P coating for recipe №2 and for the diffusion Cr modes: isothermal holding 1 h at 700 °C, diffusive saturation Cr 5 h at a temperature of 1050 °C magnification ×600

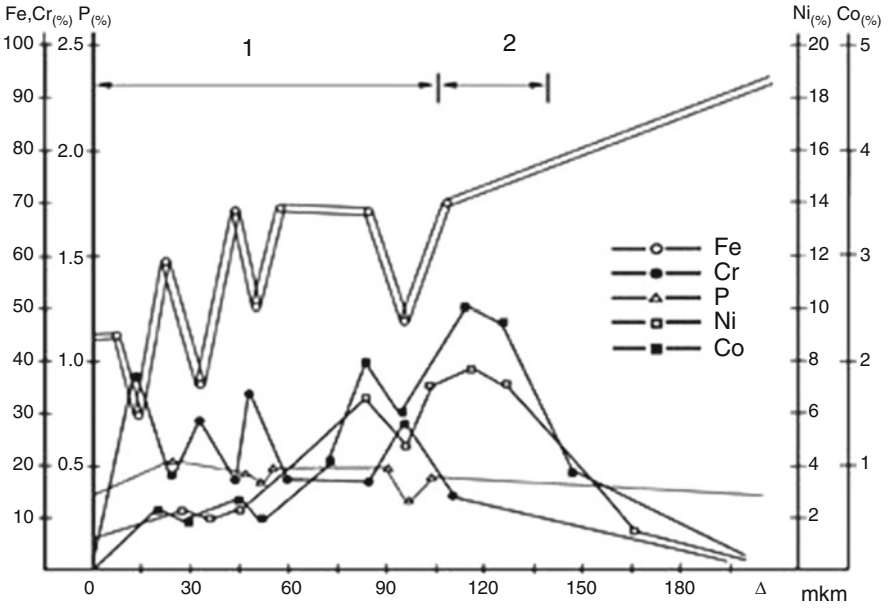

Fig. 12.3 Diffusion concentration distribution of element diffusion layer of hardened diffusion layer of chemical Ni-Co-P coating for recipe №2 and for the diffusion Cr modes: isothermal holding 1 h at 700 °C, diffusive saturation Cr 5 h at a temperature of 1050 °C

carbide inclusions, which are mainly located at the physical surface (closer to the source of chromium).

Phase analysis conducted on these samples showed the presence of chromium carbides Cr_7C_3 here and αFe (Table 12.1).

Schedule diffusion element distribution indicates the presence of a large number of Ni-Co-P in the zone 2 solid solution of chromium in αFe (Fig. 12.3), indicating active diffusion processes. Peak bursts of chromium content and, accordingly, a sharp drop in the concentration of other elements in these areas indicate the presence of colonies formed in the carbide composite zone.

Microhardness integrated composite samples of zone 1 are equal to 11 GPa (Fig. 12.4). Here you can see colonies of solid carbide micrograins. There micrograin carbide forms colonies in the source material.

After a comprehensive restoration parts made of steel with 0.45 % C with chemical coating, 7-h diffusion chrome (at 1050 °C), and isothermal holding hour (with 800 °C) the morphology develops a diffusion layer composite zone structure (Fig. 12.5).

The composite layer 1, a thickness of 250 μm, is a typical developed network stretched to the physical surface of carbide grains, which are placed in a matrix of a solid solution of chromium in αFe. On the border of zone 2, these grains fused into a continuous strand of carbides. It is interesting that the carbide grains do not completely permeate zone 1 and 30–50 μm do not reach the physical surface. The integrated composite microhardness zone is 12 GPa (Fig. 12.6).

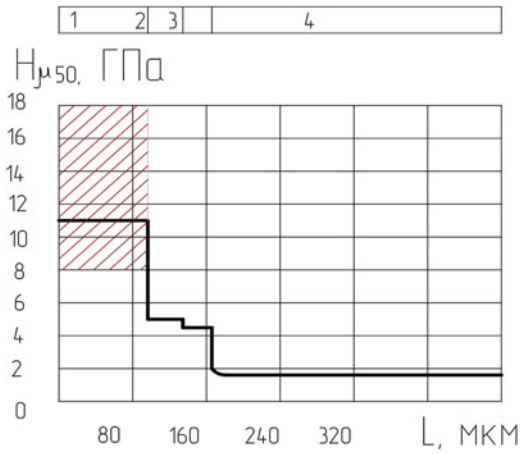

Fig. 12.4 Hardness of hardened diffusion layer of chemical Ni and Co coating for recipe №2 and for the diffusion Cr modes: isothermal holding 1 h at 700 °C, diffusive saturation Cr 5 h at a temperature of 1050 °C

Fig. 12.5 The microstructure of hardened diffusion layer of chemical Ni-Co-P coating for recipe №3 and for the diffusion Cr modes: isothermal holding 1 h at 800 °C, diffusive saturation Cr 7 h at a temperature of 1050 °C; magnification ×600

Schedule distribution diffusion elements (Fig. 12.6) confirm that the surface area of a solid solution of chromium in αFe, in which the diffusion element concentration stabilizes, and peaks (above 50 %) of the concentrations of chromium (under falling concentration in these areas of other elements) by depth location carbide grains (Table 12.2). The zone 2 homogeneous solid solution of chromium in αFe content is characterized by high values of Ni (10 %) and Co (up 3 %). Thickness zone 2 is on average 25–40 μm. Obviously, the nickel pushes carbon from the

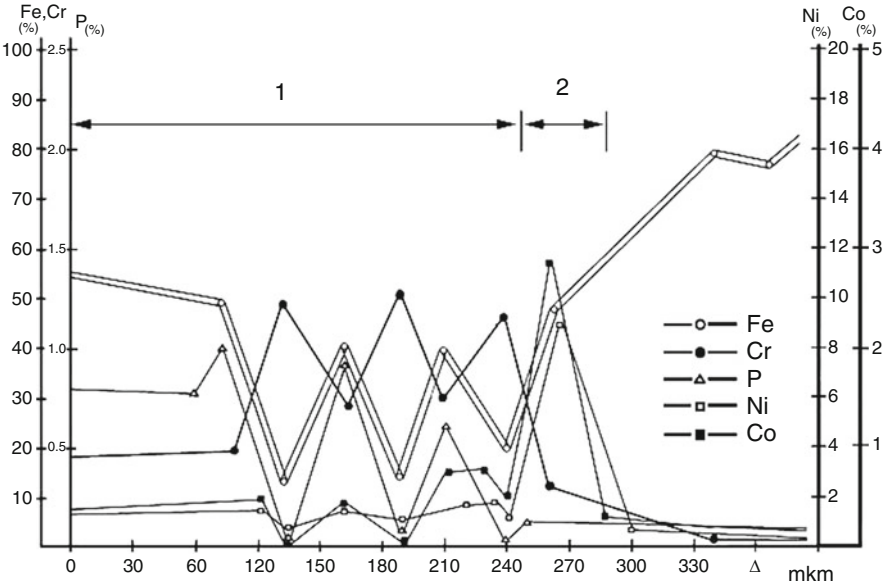

Fig. 12.6 Hardness of hardened diffusion layer of chemical Ni-Co-P coating for recipe №3 and for the diffusion Cr modes: isothermal holding 1 h at 800 °C, diffusive saturation Cr 7 h at a temperature of 1050 °C

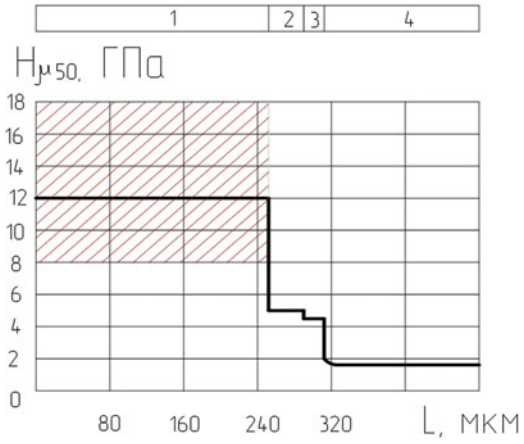

Fig. 12.7 Diffusion concentration distribution of element diffusion layer of hardened diffusion layer of chemical Ni-Co-P coating for recipe №3 and for the diffusion Cr modes: isothermal holding 1 h at 800 °C, diffusive saturation Cr 7 h at a temperature of 1050 °C

subsurface zone, and the formation of elongated carbide grains is observed, which are located on the border zones 1 and 2 toward the physical surface (Table 12.3).

The presence of the complex method of chemical treatment and the effect of the liquid metal phase, which occurs as a result of this, and isothermal holding allows a reinforcing ply to develop at a fairly great depth. The composite zone

Table 12.2 Phase analysis of hardened diffusion layer of chemical Ni-Co-P coating for recipe №3 and for the diffusion Cr modes: isothermal holding 1 h at 800 °C, diffusive saturation Cr 7 h at a temperature of 1050 °C

#	2Θ	*d*	Phase
1	56,75	2,41	Unidentified
2	65,3	2,12	Cr_7C_3
3	66,8	2,08	Unidentified
4	68,8	2,027	αFe (110)
5	88,9	1,625	Unidentified
6	105,8	1,43	αFe (002)
7	110,9	1,391	Unidentified
8	151,9	1,181	Cr_7C_3
9	155,8	1,171	αFe (112)
10	159,8	1,163	Cr_7C_3

Table 12.3 Phase analysis of hardened diffusion layer of chemical Ni-Co-P coating for recipe №3 and for the diffusion Cr modes: isothermal holding 1 h at 800 °C, diffusive saturation Cr 7 h at a temperature of 1050 °C

#	2Θ	*d*	Phase
1	44,4	2,56	Unidentified
2	55,1	2,09	Unidentified
3	74,2	1,606	Unidentified
4	89,1	1,381	Unidentified
5	145,3	1,051	αFe (002)

1 layer, which in detail friction pairs is working, reaches 250 μm, providing an increased service life.

Phase analysis was performed on this sample twice through large unidentified peaks, indicating the complex state of the presence of a stress-hardened layer,. But there is definitely the availability of a large number of Cr_7C_3 and αFe.

The diffusion layer on the steel with 1.0 % C (Fig. 12.8), obtained after a complex method of implementation mode recovery is 7 h diffusion plating (with 1050 °C), the previous hour isothermal holding (at 800 °C) with chemical treatment, characterized by a high volume content of chromium carbide grains in composite zone 1. These grains are elongated to the physical surface shape, and on the border with the zone 2 forming solid carbide with chromium carbide grains, fused together. There is a visually observed difference between these types of grains, according to the elongated grain carbide—a $Cr_{23}C_6$, and carbide fused together—Cr_7C_3 (Table 12.4). The integrated composite microhardness zone 1 reaches 15 GPa (Fig. 12.9).

Some graphics division diffusion elements (Fig. 12.10), which is the depth that reflects zone 1, shows a fairly even content diffusion of elements with small vibrations, and only in the end zone; at the location of a solid carbide colony an increase in chromium content (50 %) was noticed, and accordingly a decrease in concentrations of other elements. Content diffusion elements in zone 1 are relatively high and there is stable zone thickness (excluding solid carbide locations near the boundaries of zone 2). Homogeneous zone 2 Cr in solid solution Feα is characterized by unstable thickness, and in places very close to zone 1 and/or

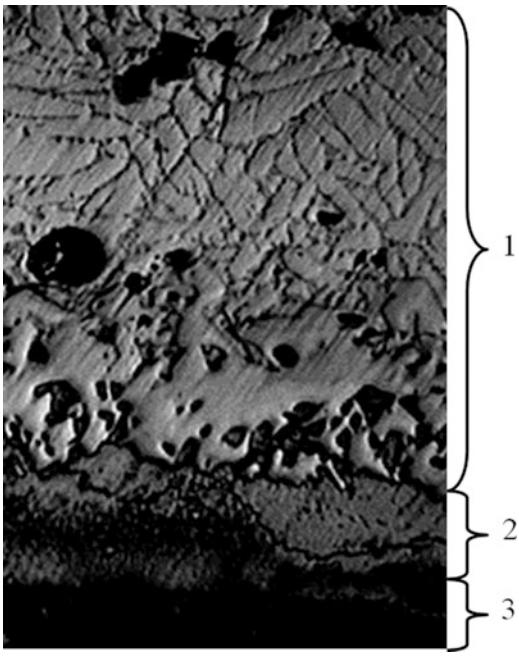

Fig. 12.8 The microstructure of hardened diffusion layer on the steel U10 of chemical Ni-Co-P coating for recipe №4 and for the diffusion Cr modes: isothermal holding 1 h at 800 °C, diffusive saturation Cr 7 h at a temperature of 1050 °C; magnification ×600

Table 12.4 Phase analysis of hardened diffusion layer of chemical Ni-Co-P coating for recipe №4 and for the diffusion Cr modes: isothermal holding 1 h at 800 °C, diffusive saturation Cr 7 h at a temperature of 1050 °C

#	2Θ	*d*	Phase
1	65,5	2,12	Cr_7C_3
2	67	2,075	γFe
3	68,8	2,027	αFe (110)
4	79,1	1,8	γFe
5	85,1	1,69	Unidentified
6	91,2	1,603	Unidentified
7	105	1,44	αFe
8	125,7	1,29	Unidentified
9	128,8	1,27	γFe
10	148	1,19	Unidentified
11	154	1,17	αFe (112)

zone 3. This model has a maximum content of Ni and Co in zone 2 (about 18 % Ni and Co 3 %).

After the restoration of the complex by chemical processing and diffusion plating on steel with 1.0 % C in us, just as the steel with 0.45 % C, characterized traced all areas, including eutectoid zone 3. This difference appears to HCS. Phase analysis, carried out twice showed that this layer presented chromium carbides Cr_7C_3, $Cr_{23}C_6$, and α- and γ-iron.

Chart distribution diffusion elements (Ni, Co, P), shown in Figs. 12.3, 12.6, and 12.10, placed their increased concentration between the grains of chromium

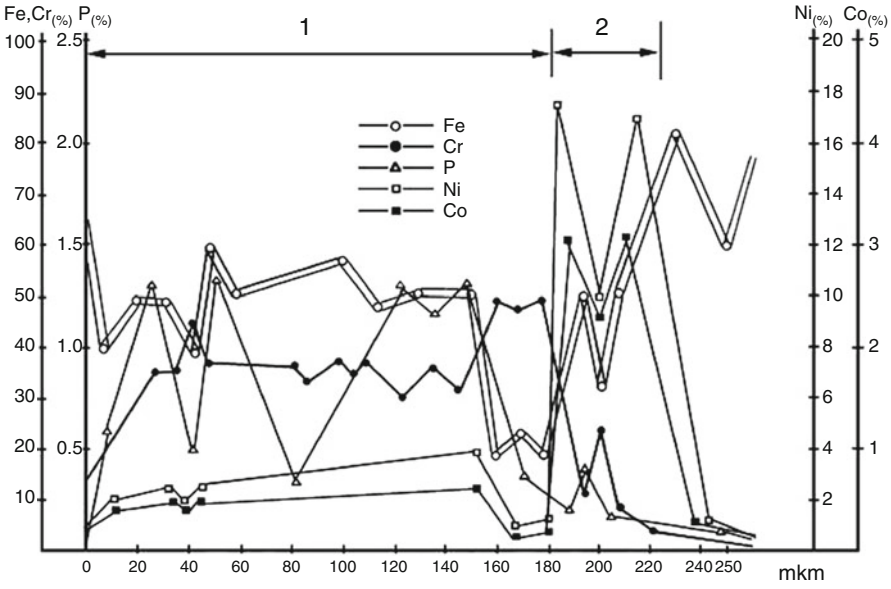

Fig. 12.9 Hardness of hardened diffusion layer of chemical Ni-Co-P coating for recipe №4 and for the diffusion Cr modes: isothermal holding 1 h at 800 °C, diffusive saturation Cr 7 h at a temperature of 1050 °C

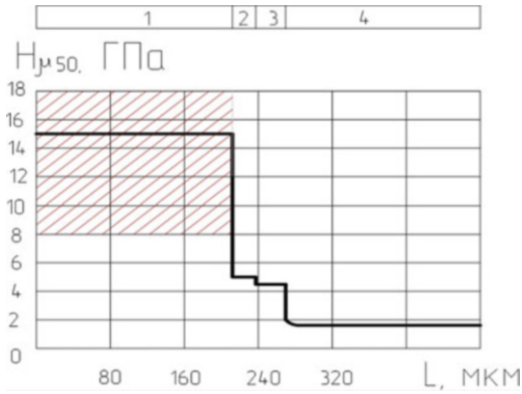

Fig. 12.10 Diffusion concentration distribution of element diffusion layer of hardened diffusion layer of chemical Ni-Co-P coating for recipe №4 and for the diffusion Cr modes: isothermal holding 1 h at 800 °C, diffusive saturation Cr 7 h at a temperature of 1050 °C

carbides. For example, Ni, which despite increased strength and ductility simultaneously increases, the material is observed to increase it to 10 %. Thus, the carbide grains such as "wrapped" plastic material (Ni), which is well able to relax internal stresses that occur when the parts are working, which increases the life of the parts, constitute the refurbished complex method of chemical processing and diffusion plating.

12.4 Conclusion

Implementation of the complex chemical processing method and diffusion plating to restore the machine parts enables gets diffusion layers that are different in structure, thickness, and hardness.

The optimal method for recovering chemical processing machine parts is made of structural steel with 0.3–0.6 % C. On manufactured or remanufactured parts that are made of steel 45, diffusion layers, the composite thickness of the outer zone reaches 250 μm, and the integral microhardness of 12 GPa. The phase composition composite zone consists of chromium carbides $Cr_{23}C_6$, Cr_7C_3, and α-Fe (002).

The complex method of chemical treatment and plating diffusion can restore parts made of high carbon steel. The diffusion layer has a composite zone of highly integrated microhardness (about 15 GPa) and thickness to 200 μm with tightly spaced carbide grains. The phase composition composite zone consists of chromium carbides $Cr_{23}C_6$, Cr_7C_3, and αFe (002).

Parts that are made of steel with 0.3–0.6 % C operating under dynamic loads should recover in modes that provide 5-h diffusion of chromium hour isothermal holding at 700 °C. This enables restored diffusion layers, the outer composite area of which consists of fine whiskers of chromium carbides in a Cr matrix solid solution in αFe about 100 μm thick and integral microhardness to 11 GPa. The phase composition of such layers are chromium carbides Cr_7C_3, αFe (110), and αFe (002).

References

1. Lampman S (1991) Introduction to surface hardening of steels, heat treating. In: ASM handbook, vol 4. ASM International, Novelty, OH, pp 259–267
2. Kulka M, Pertek A (2003) Characterization of complex (B + C + N) diffusion layers formed on chromium and nickel-based low-carbon steel. Appl Surf Sci 218(1–4):114–123
3. Murali M, Sambathkumar M, Saravanan MSS (2014) Micro structural and mechanical properties of AA 7075/Tio_2 in situ composites. Univers J Mater Sci 2(3):49–53
4. Stetsko A (2013) Technological support resource of manufactured and remanufactured parts, Monograph, Lviv, p 240. ISBN 978-966-2739-29-9
5. UA 110046, C23C 8/70, C23C 10/32, 10 Nov 2015
6. UA 109285, C23C 10/32, C23C 22/62, C23C 22/05, C23C 10/02, 10 Aug 2015
7. UA 109283, C23C 10/32, C23C 22/62, C23C 22/05, C23C 10/02, 10 Aug 2015
8. UA 108895, C23C 22/62, C23C 10/18, C23C 10/32, C23C 10/38, C23C 10/40, 25 Jun 2015

Chapter 13
Influence of Annealing in Vacuum on Kinetics of Dispersion–Coagulation of Niobium and Hafnium Nanofilms Deposited onto Oxide Materials

I.I. Gab, T.V. Stetsyuk, B.D. Kostyuk, and Y.V. Naidich

13.1 Introduction

Joining of ceramics and other nonmetallic materials (sapphire, single crystals, etc.) with metals by brazing using metal brazes or by pressure welding using deformable metal gaskets is widely used in modern technology. For obtaining secure joints, nonmetallic materials are often coated with films of various metals [1–3]. A special role in joining such different materials is played by adhesively active metals such as titanium, zirconium, niobium, hafnium, etc. These metals are either included as a part of the braze or used as a coating, in particular in the form of thin films on the materials' surfaces to be joined. These metals show good adhesion properties both with other metals and with a number of nonmetals and also provide good spreading of molten metal brazes and interaction at the interface "braze–solid joined surfaces." In most cases, for brazing nonmetallic materials with metals, titanium is used [4–8], but niobium and hafnium may also be used for this purpose because these metals are of considerable interest for obtaining with their help of a number of high-temperature joints of nonmetallic compounds with metals [9–16].

Promising is the use of hafnium and niobium in the form of thin films, such as nanofilms, making it possible to develop technology to produce precise and durable joints of dissimilar materials with very fine solder joints.

Since, during brazing or pressure welding, metalized parts to be joined must be heated to high temperatures (1300–1600 °C), the study of the processes of dispersion–

I.I. Gab (✉) • T.V. Stetsyuk • B.D. Kostyuk • Y.V. Naidich
Frantsevich Institute for Problems of Materials Science of National Academy Sciences of Ukraine, 3, Krzhyzhanovskogo st., Kyiv 03142, Ukraine
e-mail: gab@ipms.kiev.ua

O. Fesenko, L. Yatsenko (eds.), *Nanophysics, Nanophotonics, Surface Studies, and Applications*, Springer Proceedings in Physics 183,
DOI 10.1007/978-3-319-30737-4_13

coagulation to take place with heating of metal thin film coating is not only of scientific interest but also of practical importance in the development of new technological modes of nonmetallic materials joining. The study of the processes taking place during annealing of niobium and hafnium nanofilms deposited onto oxide materials and annealed in vacuum up to 1600 °C is the aim of the present work.

13.2 Materials and Experimental Methods

Niobium and hafnium films 100 nm thick were deposited onto the alumina ceramics, artificial leucosapphire (hereinafter—sapphire), and ceramics based on zirconia. These films were deposited by electron-beam sputtering onto the well-polished surfaces of the oxide substrates $4 \times 3 \times 1$ mm [2]. Surface roughness R_z was equal to $0.03 \div 0.05$ μm. The polished surfaces of the substrates were degreased with acetone and alcohol, heated in air at 1200 °C for 2 h, and then annealed in vacuum better than 2×10^{-3} Pa at the same temperature for 1 h.

Metal nanofilm thickness (100 nm) was selected based on the consideration that these films are continuous and covering completely the oxide surfaces having a good adhesion to them and providing good braze spreading [2]. Thicker films are able to delaminate due to the presence of residual stresses as a result of growth stresses during the multilayer deposition and as a result of the large difference in thermal coefficient of linear expansion of films' metals and substrates' materials. Films were deposited for 10–15 min onto substrates which temperature was about 100 °C, and the films' thickness was measured with a special device, the sensitive element of which is a quartz sensor. The films were deposited onto all substrates under the same conditions, and their quality was controlled by metallographic microscope XJL-17. Annealing of the sputtered samples was carried out in a vacuum chamber at different time intervals (from 2 up to 20 min) at different temperatures (1300–1600 °C) in vacuum not worse than 2×10^{-3} Pa.

The annealed samples were studied using scanning electron microscopes NeoScope JCM-5000 and ZEISS EVO SO XVP and atomic force microscope Nanoscope IIIa with photomicrographs obtained. Using these photomicrographs, percentages of metal film islet areas to the entire surface of samples were calculated by planimetric weighing method, i.e., through the weight of the images of the elements of metalized coatings at the sample surface cut out from photomicrographs [17]. The experimental data were processed graphically which has demonstrated the dependence of the sample surface areas coated with niobium and hafnium films on the annealing parameters (temperature, time).

13.3 Results and Discussion

The starting films of both metals at all the three oxides' surfaces were continuous without any significant defects, and photographs made using a scanning electron microscope show only a uniform dark gray field. After annealing of these films in a

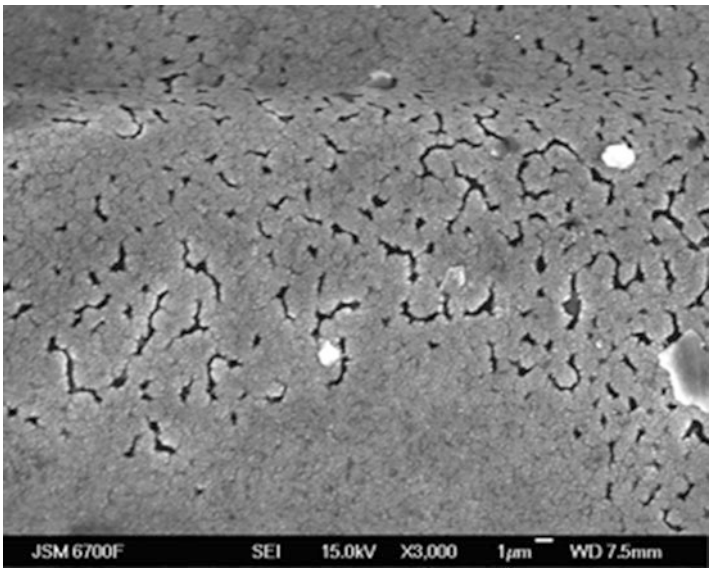

Fig. 13.1 Niobium film of 100 nm in thickness deposited onto sapphire and annealed in vacuum under 1400 °C for 20 min (× 3000)

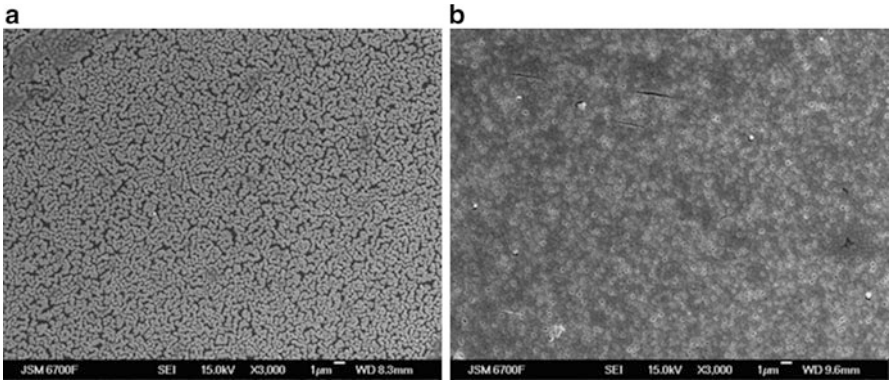

Fig. 13.2 Metal films of 100 nm in thickness deposited onto oxides and annealed in vacuum under 1500 °C for 5 min (× 3000): (**a**) niobium film onto sapphire, (**b**) hafnium film onto Al_2O_3 ceramics

vacuum 2×10^{-3} Pa at 1300 °C for 20 min, all the films showed no change, and only as a result of annealing at 1400 °C for 20 min, it was possible to observe films cracking (Fig. 13.1). With the increase of the annealing temperature up to 1500 °C, the films' dispersion process acceleration was found since, after 5 min of exposure, the films were markedly dispersed (Fig. 13.2) and, after 20 min of annealing, niobium films were substantially disintegrated into individual rather large conglomerates and fragments (Fig. 13.3) covering about 50 % of the original area of metal

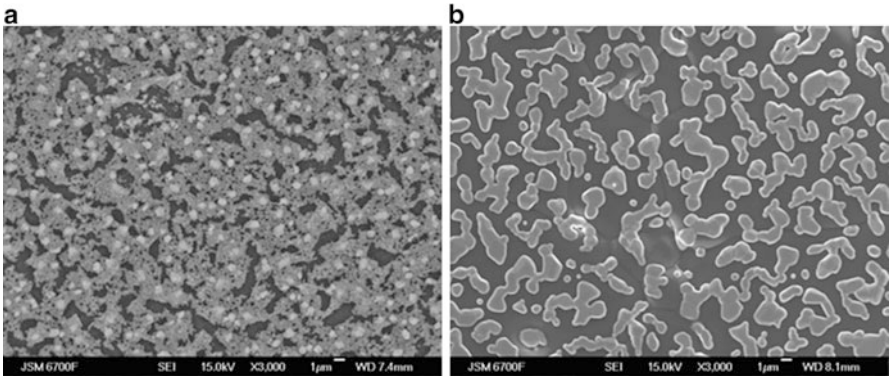

Fig. 13.3 Metal films of 100 nm in thickness deposited onto oxides and annealed in vacuum under 1500 °C for 20 min (× 3000): (**a**) niobium film onto sapphire, (**b**) niobium film onto Al_2O_3 ceramics, and (**c**) hafnium film onto sapphire

coatings (Fig. 13.4), while the disintegration of hafnium nanofilms was slower and, after 20 min exposure, their fragments covered about 80 % of the oxide substrates' surfaces (Fig. 13.5) which can be obviously explained by hafnium's greater affinity to oxygen versus niobium.

Further increase of the annealing temperature up to 1600 °C intensified significantly the process of the films' dispersion leading to a complete disintegration of the films into separate aggregates covering only 40 ÷ 50 % of the original substrate surface in the case of niobium coating (Figs. 13.4 and 13.6a, b) and 50 ÷ 60 % in the case of hafnium one (Figs. 13.5 and 13.6c, d). At the same time, along with the films' dispersion, reverse process is presumably possible, namely, coagulation occurring through the merger of small films' fragments to form larger ones, as it can be seen at the photographs made by an atomic force microscope (Fig. 13.6b, d). This process may occur probably due to the surface diffusion of metals.

Some differences in behavior of the kinetic curves at the graphs, as well as differences in the areas covered by the broken films' fragments of the same metal at the different oxides' surfaces, can be explained by the different nature and state of the oxide surfaces onto which the metal films were deposited. For example, the surface of the sapphire which is a single crystal of alumina is homogeneous without any extraneous matter and substantially nonporous unlike surfaces of aluminum oxide and zirconium oxide ceramics containing a number of additives including oxides of yttrium, calcium, etc. and also having a sufficient number of micropores which are not able to retain the metal films' fragments during annealing. This leads to the fact that, at the nonporous and homogeneous sapphire surface, the area covered by broken films' fragments is somewhat larger compared with one at the other investigated ceramic surfaces.

Since metallization of the oxides by adhesion-active metals including niobium and hafnium is applicable for the subsequent brazing of these materials with the molten metal brazes or for pressure welding, some practical recommendations can be made based on the results obtained on the kinetics of the dispersion of these films.

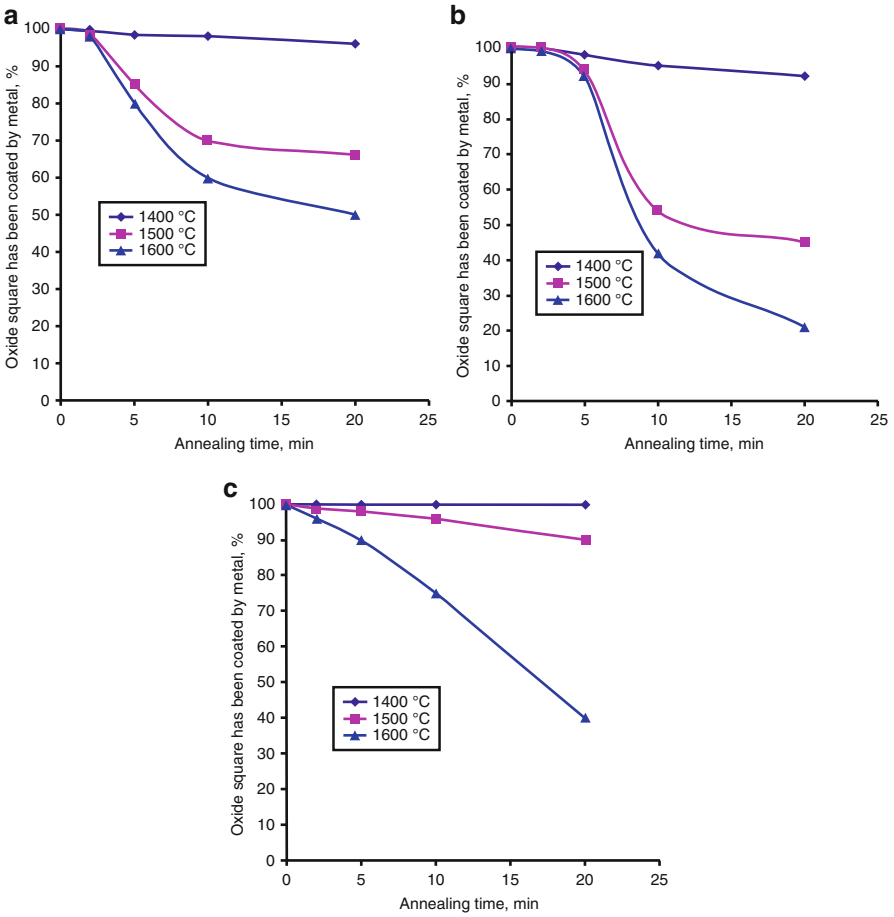

Fig. 13.4 Dependence of oxide square coated by niobium from annealing time under various temperatures (1400–1600 °C): (**a**) sapphire, (**b**) Al_2O_3 ceramics, and (**c**) ZrO_2 ceramics

Based on these data, we can recommend hafnium and niobium coatings for subsequent brazing of all three oxides at temperatures up to 1400 °C within the range of exposures at these temperatures $2 \div 20$ min.

If it is necessary to braze metalized products at higher temperatures, it will be helpful to reduce the brazing process time, i.e., to use the time when the fragments of metallization layer comprise at least 70 % of the brazed surface. In particular, when using a niobium coating on sapphire and zirconia surfaces at 1500 °C, soldering process time should not exceed 10 min, and the use of hafnium coating on all three oxides can extend this process up to 20 min.

With the use of these guidelines, in particular, experimental joints were obtained of the polished sapphire discs (15 mm diameter) metalized by niobium film (100 nm

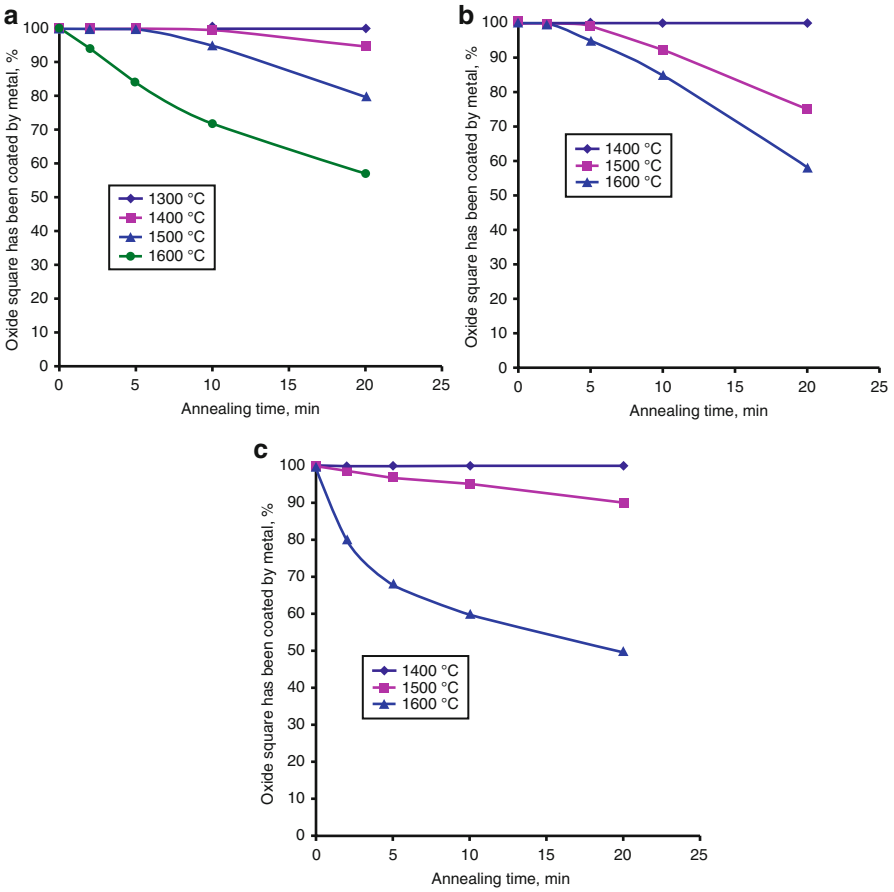

Fig. 13.5 Dependence of oxide square coated by hafnium from annealing time under various temperatures (1300–1600 °C): (**a**) sapphire, (**b**) Al_2O_3 ceramics, and (**c**) ZrO_2 ceramics

thick) by nickel braze at 1500 °C for 10 min. The shear strength of the soldered joint was 210 MPa.

During brazing at 1600 °C, hafnium coating on all three oxides' surfaces can provide processing time up to 10 min and niobium coating only up to 5–7 min.

13.4 Conclusions

The kinetics of dispersion–coagulation during annealing in vacuum of niobium and hafnium nanofilms deposited onto oxide materials was investigated. It was found that these films show a little change in their structure during annealing up to 1400 °C, and with further annealing temperature rise, the films' disintegration

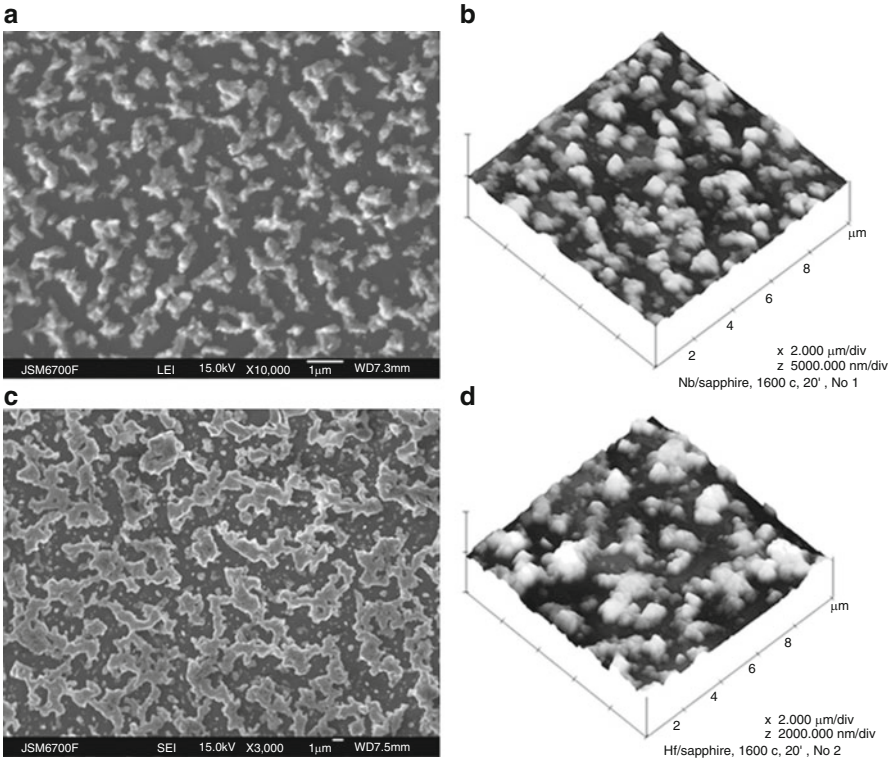

Fig. 13.6 Metal film of 100 nm in thickness deposited onto sapphire and annealed at 1600 °C for 20 min in vacuum has been investigated using scanning microscopy (a, **c**) and atomic force microscopy (**b**, **d**): (**a**, **c**) niobium, (**c**, **d**) hafnium

process is intensified substantially. Such disintegration process at the different oxides' surfaces has approximately the same pattern and is almost completed during 20 min of annealing with simultaneous coagulation of small films' fragments into larger conglomerates. Intensity of niobium films dispersing for all studied oxides is slightly higher compared to the hafnium ones due to the different affinity of these metals to oxygen.

As a result of the behavior study of niobium and hafnium films deposited onto alumina ceramic, sapphire, and zirconium oxide ceramics and annealed in vacuum at high temperatures, these films can be recommended for use in high-temperature brazing without process duration limit at 1500 °C for hafnium coating at all oxides' surfaces and for niobium coating at zirconia and sapphire surfaces, but for niobium coating at the alumina surface, brazing process time is desirable to be limited to 5–7 min.

At 1600 °C, brazing duration for these three oxides metalized by both metals is desirable to be limited to 5–7 min.

References

1. Naydich YV, Gab II, Stetsyuk TV, Kostyuk BD (2012) The kinetics of coagulation and dispersion during annealing Ag nanofilms deposited on oxide materials. J Technol Mech Eng 4:35 (in Russian)
2. Naydich YV, Gab II, Kostyuk BD, Stetsyuk TV, Kurkova DI, Dukarov SV, Kulikovskiy VY, Onoprienko AA (2006) The study of the structural and the capillary characteristics of the metal nanofilms deposited on oxide materials. J Nanostruct Mater Sci 1:31 (in Ukrainian)
3. Naydich YV, Gab II, Kostyuk BD, Stetsyuk TV, Kurkova DI, Dukarov SV (2006) Investigation of the structure, morphology and wetting by metals for metal nanofilms deposited on the surface of aluminum oxide in order to obtain welded and brazed joints materials on its basis. J Tech Mech Eng 4:13 (in Russian)
4. Naydich YV (1972) Contactnie yavlenia v metallicheskih rasplavah. Naukova Dumka, Kiev (in Ukrainian)
5. Nikolas M (1974) Physical aspect of liquid metals. Ingenierus Blad 53(2):139
6. Harding FL, Rossington DR (1970) Wetting of ceramic oxides by molten metals under ultrahigh vacuum. J Am Ceram Soc 53(2):87
7. Rhee SK (1971) Wetting ceramic by liquid metals. J Am Ceram Soc 54(7):332
8. Metelkin II, Pavlov MA, Pozdeeva NV (1977) Svarka keramiki s metallami. Metallurgia, Moscow (in Russian)
9. Melnikov VV, Eremeev SV, Kulkova SE (2011) Investigation of films adhesion of niobium on the differently oriented surfaces of α-Al_2O_3. J Tech Phys 81(10):114 (in Russian)
10. Qiao-ying T, Lai-fei C, Li-tong Z (2004) Infiltration bonding C/SiC composite and niobium [J]. J Aviat Mater 24(1):53
11. Masaaki N, Tohru S, Ikuo O (1998) Bonding behavior between niobium and reaction-sintered SiC. Trans JWRI 17(2):67
12. Shalz ML, Dalgleish BJ, Tomsia AP, Cannon RM, Glaeser AM (1994) Ceramic joining III. Bonding of alumina via Cu/Nb/Cu interlayers. J Mater Sci 29(14):3678
13. Marks RA, Sugar JD, Glaeser AM (2001) Ceramic joining IV. Effects of processing conditions on the properties of alumina joined via Cu/Nb/Cu interlayers. J Mater Sci 36(23):5609
14. Marks RA, Chapman DR, Danielson DT, Glaeser AM (2000) Joining of alumina via copper/niobium/copper interlayers. Acta Mater 48(18):4425
15. Gab II, Zhyravlev VS, Kurkova DI, Stetsyuk TV, Naydich YV (1997) Contact interaction of oxide materials with refractory metals with high-temperature solid phase pressure welding. J Powder Metall 7–8:69 (in Ukrainian)
16. Karakozov ES, Kotelkin IS, Matveev GN et al (1968) The formation mechanism of the compound at the solid state welding of ceramics from Al with Nb. J Phys Chem Mater Treat 3:123 (in Russian)
17. Naydich YV, Gab II, Kostyuk BD, Stetsyuk TV, Kurkova DI, Dukarov SV (2007) Investigation of the ceramic materials connection processes (soldering) using metal nanofilms. J Rep Natl Acad Sci Ukr 35:97

Chapter 14
Colloid-Chemical Modification of Peloids with Nano- and Microparticles of Natural Minerals and Their Practical Use

A.V. Panko, I.G. Kovzun, Z.R. Ulberg, V.A. Oleinik, E.M. Nikipelova, and K.D. Babov

14.1 Introduction

Clay-carbonate ferrous peloids, having a large constant practical importance in medicine, balneology, and cosmetology, attract the researchers' attention for many years [1–11]. In particular, such peloids involve enormous deposits of bottom sediments of seas and oceans, for example, the Black Sea deposit of clay-carbonate sapropelic sediments. Colloid-chemical properties of such peloids have been studied insufficiently [12, 13] or on model materials [4, 6].

Clay-carbonate sludge sea sediments, similar to peloids from estuaries and salinas, are polydispersed polymineral compositions of biocolloid origin. They are formed following perennial geomechanical, biocolloid, geochemical, and nanochemical transformations aided with microorganisms and microalgae, salt aqueous, and air media, under influence of complex physicochemical, colloid-chemical, and biochemical processes. Depending on combination of exposure to external factors, such processes can be accompanied with micro- and nanostructured transformation of mineral and organic peloid base. For example, it was supposed that at intensive peloid stirring number of nanoparticles, there is increased and decreased at-rest state in accordance with established [14] occurrence of nanochemical dispersion of artificial suspensions of clay mineral and calcium carbonate opposite to isothermal distillation effect. Processes in clay minerals

A.V. Panko (✉) • I.G. Kovzun • Z.R. Ulberg • V.A. Oleinik
Institute of Biocolloid Chemistry Named After F. D. Ovcharenko, NAS of Ukraine, 42, Ak. Vernadskogo Blvd., Kyiv 03680, Ukraine
e-mail: wiz@list.ru

E.M. Nikipelova • K.D. Babov
Ukrainian Research Institute of Medical Rehabilitation and Balneology, Ministry of Health of Ukraine, 6, Lermontovskiy Lane, Odessa 65014, Ukraine

O. Fesenko, L. Yatsenko (eds.), *Nanophysics, Nanophotonics, Surface Studies, and Applications*, Springer Proceedings in Physics 183,
DOI 10.1007/978-3-319-30737-4_14

[15, 16] and hydration dispersion processes of heat-treated clays up to nanoparticles [17] can considerably influence on bioactivity of peloids. At the same time mechanisms of peloid formation, in particular influence of geomechanical, physicochemical, and microbiological transformations on them, are not investigated enough [12, 13, 18].

Therefore, the aim of current investigations was in specifying colloid-chemical mechanisms and features of geomechanical and microbiological processes aided with nanoparticles and nanostructures in carbonate-clay peloids and in relationship establishment of biocolloid and colloid-chemical transformations with variations of colloid-chemical properties and biological activity of bottom sediments.

14.2 Principles of Physicochemical Geomechanics and Mechanisms of Nano- and Microparticle Formation in Ferrioxide-Silicate Clay-Carbonate Rock and Peloids

Geological rock transformations with nano- and microparticle formation precede peloid generation in natural conditions, accompanied by formation of nano- and microparticles and studied by physicochemical geomechanics (FCGM). According to [19], FCGM is an independent boundary section of a science using methods of physicochemical mechanics for analysis of geological processes.

As far as water is mandatory component of rocks being in polydispersed state and subjected to mechanical stresses and liquid media, the role of water in mechanochemical rock processes is exceptional. Rocks and peloids are dispersed mostly according to siloxane bonds' hydrolytic fracture mechanism [20]:

$$\equiv \mathrm{Si} - \mathrm{O} - \mathrm{Si} \equiv + \mathrm{HOH} \rightarrow \equiv \mathrm{Si} - \mathrm{OH} + \mathrm{HO} - \mathrm{Si} \equiv \qquad (14.1)$$

Reaction (14.1) is accelerated influenced by mechanical stresses, which by turn leads to relieving of dispersion crack formation even in occurrence of water traces [19–21]. Crack bond fracture frequency on its top and its velocity growth (V) depends on applied mechanical stress (P):

$$V = V_0 \exp\left[-(U_0 - \gamma P)/RT\right]; \quad V_0 \approx \nu_0 \qquad (14.2)$$

where ν is the Debye resonance frequency, γ the activation volume including overstrain factor $(c/b)^{1/2}$, c the crack size, b the crystal lattice parameter, U_0 the process activation energy when $P = 0$, R the gas constant, and T the temperature.

On initial stages the process of follow-up mechanical dispersion starts from reaction (14.1) and formation of at least nano-crack in accordance with (14.2). Then, in accordance with Gibbs-Smith condition [20], grain boundary between crystals A and B is being replaced by liquid C:

$$\sigma_{GG} > \sigma_{AC} + \sigma_{BC} \tag{14.3}$$

where σ is surface tension at gas-grain boundary (σ_{GG}), A and C boundary (σ_{AC}), and B and C boundary (σ_{BC}).

The dispersion process goes continuously and is being described by linear-parabolic equation:

$$AL + BL^2 = t \tag{14.4}$$

where A and B are coefficients and t is time for edge of liquid layer intrusion into crack tip that will move to distance L from liquid source.

Linear part of (14.4) is being described by crystallization pressure (PCR) growth kinetic:

$$A = \delta RT / D_{SL} c_0 P_{CR} w \tag{14.5}$$

where δ is the grain mean size, R the gas constant, T the temperature, D_{SL} the coefficient of grain matter diffusion in liquid, c_0 its mole fraction concentration, and w the molar volume.

Parabolic part of (14.4) is being determined by process limiting liquid by viscous flow in gap (10–100 nm) between grains. Using Poiseuille equation for coefficient B from (14.4) gives the following expression [20]:

$$B = 12\eta / \delta P_{CR} \tag{14.6}$$

where η is the liquid viscosity.

Value $1/B$ is considered as effective (conditional) diffusion coefficient, and it exceeds solid body diffusion coefficient to many degrees. Hence, it follows that such hydrolytic splitting processes run rather quickly. Experimentally it was proven that in porous bodies, which include clays, the realization of such processes needs only 10–20 h [21]. And polycrystalline feature of porous structures supposes particle formation of different sizes, including nano- and microparticles, at that. Similar processes run in marine peloid sediments at high-pressure conditions in large depths and in zones of natural gas and organic-clay sediment bedding.

Apart from examined silicate system fracture process, the process of spontaneous (chemical) dispersion under influence of water and aqueous solutions can be possible [20]. Kinetics of geological processes herewith is also obeyed to (14.4), (14.5), and (14.6). Latter experimental and theoretical analysis of the mechanism from chemical dispersion and physicochemical point of view showed [21] that dispersion process may be over in few hours for porous silicate rock at applied external mechanical action. Alkalescent medium of aqueous solutions enables it, and process kinetics is submitted to equation:

$$(S - S_0)^2 = kt \tag{14.7}$$

where S_0 is the initial specific surface of dispersed material.

Chemical processes in alkalescent medium, which is typical for most peloids, may run along with reaction (14.1) in accordance with scheme:

$$\begin{gathered} nAl_2O_3 \cdot mSiO_2 \cdot kH_2O + 4MOH + (k-2)H_2O \rightarrow \\ \rightarrow M_2O \cdot nAl_2O_3 \cdot kH_2O + M_2O \cdot mSiO_2 \cdot kH_2O \end{gathered} \tag{14.8}$$

Then products of reaction (14.8) react in the following scheme:

$$\begin{gathered} M_2O \cdot nAl_2O_3 \cdot kH_2O + M_2O \cdot mSiO_2 \cdot kH_2O \rightarrow \\ \rightarrow M_2O \cdot nAl_2O_3 \cdot mSiO_2 \cdot kH_2O + 2MOH + (k-1)H_2O \end{gathered} \tag{14.9}$$

Crystalline hydrate formed in the nano-crack by reaction (14.9) has bigger volume than initial product in the reaction (14.8). Therefore, formed crystallization pressure promotes rupture (chemical wedging) of the crack, and external mechanical force accelerates the process. Water, entering the extended crack mouth up to micro-sizes, also provides for adsorption reduction of strength (Rehbinder effect) and dispersion of initial alumosilicate (clay) material up to nano- and microparticles. Aqueous alkaline solution formed by scheme (14.9) is participated again in remained solid matter chemical wedging by scheme (14.8). This process runs similar to the case of liquid-phase penetration through intergranular bounds, but quicker. Laboratory studies showed few hours shall be sufficient for its finalization for porous material or few weeks for dense rock [21].

Naturally, described physicochemical processes may run not only in rocks and disperse clay-carbonate peloid compositions at natural conditions but also at conditions of their practical application.

Along with physicochemical processes, microorganism-aided biocolloid, biological, and biochemical processes are being activated in disperse mineral systems (peloids) [22]. The latter provides for formation of organic clay-carbonate structures, which is as living organisms dying off enrich peloids with carbonate material, mostly in a form of calcite [18]. Dispersion of carbonates up to nano- and microparticles is aided by carbon dioxide from air through intermediate formation of calcium bicarbonate [18, 21].

Thus, most of peloids represent themselves as concentrated pasty aqueous suspensions of nano- and microparticles of clays, carbonates, and organic matter, formed by microorganisms' vital activity and physico-mechanical geological processes. It's quite obvious that superfine clays and carbonates, as well as microorganisms, establish a complex of specific therapeutic peloid properties during these physico-mechanical geological processes [1, 2, 4, 7, 8, 12, 13, 18]. Thus, the mechanisms of such processes should be studied in more details, especially concerning nano- and microparticles of clays and carbonates.

14.3 Materials and Investigation Methods

Poorly studied deep-water clay-carbonate silts taken from 2020 m depth in western part of the Black Sea have been used as investigation material. Silts from six sampling points were mixed for their composition homogenizing and kept in closed glass jars. Well-studied peloids from Kuyalnik Estuary (nearby Odessa, Ukraine) were taken as comparison sample. Bentonite from Cherkassy deposit (Dashukovka, Ukraine) enriched by elutriation in distilled water for separation of layered structure montmorillonite mineral able to disperse up to 30–40 nm particles was used. Montmorillonite aqueous suspension also was stored in closed glass jars. One part of montmorillonite was dried and burned in air atmosphere at 500–600 °C, and the other part was milled up to 0–63 μm particle sizes, mixed with precursor (lignin), and burned without access for air until formation of nanoporous sorbent by method described in [23].

Burned samples were milled in porcelain ball mill at ratio of material/balls/water = 1:1.5:0.45 with the presence of chemical additives which form nanoclusters and nanoparticles [21].

Chemically pure soda and calcium chloride were used for obtaining artificial calcite nanoparticles [14].

Sampling from jars for investigation of micro- and nanoparticle influence on variation of colloid-chemical and medico-biological properties was made by "cutting ring" method using sterile glass tube with 10 mm inner diameter. Peloid samples for analysis were mixed with sterile tap water.

Investigations of the materials were made by XRD, EMI, thermogravimetric, rheological, chemical, and sedimentometric methods, as well as with medico-biological methods described in [18].

14.4 Experimental Results and Their Discussion

14.4.1 Physicochemical Properties and Chemical Composition of the Black Sea Peloids

Main results for definition of physicochemical indexes of marine deep-water bottom silts are produced in Table 14.1. There are also indicated comparative data for silts of shallow water Kuyalnik coastal salt lake. Deep-sea silts are dark-gray and black plastic and well-spread muds with hydrogen sulfide smell. They have alkaline reaction of medium. Negative values of Eh redox potential indicate dominance of reduction processes in such bottom sediments. Water mass concentrations in them are within value limits acceptable for silt peloids (25–75 %). They are also characterized by high shear stress and plasticity providing for better peloid bonding with human skin. Pollution of deep-sea bottom sediments with particles

Table 14.1 Main physicochemical indexes of the Black Sea bottom sediments

Indexes	Black Sea sampling points				Kuyalnik Estuary
	1	2	3	4	
1. pH of liquid phase	7.35	7.52	7.40	7.05	7.20
2. Redox potential	−165	−175	−150	−105	−227
3. Humidity, wt%	64.21	51.19	71.25	77.04	58.1
4. Volume weight, g/cm^3	1.30	1.50	1.23	1.20	1.47
5. Adhesiveness, Pa	833	971	944	555	833
6. Shear stress limit, Pa	490	552	674	484	491
7. Concentration of particles bigger than 250 μm, %	0.067	0.036	0.042	0.013	0.61
8. Specific heat capacity, kJ/kg K	2.99	2.55	3.23	3.43	0.59
9. Concentration of H_2S, %	0.023	0.024	0.016	0.030	0.17
10. Concentration of C_{org}, %	2.02	0.96	3.34	3.26	2.06
11. Concentration of particles bigger than 1 μm, %	2.28	2.47	2.31	2.48	265
12. Concentration of particles less than 100 nm, %	0.36	0.39	0.41	0.25	0.34

bigger than 250 μm in diameter is negligible. Nano- and microparticle content is small too. Organic carbon C_{org} content is typical for silt peloids (1–5 %).

Investigation of physicochemical peloid characteristics has shown that main mass of soluble salts is represented by chloride ions (0.92 %) and a sum of potassium and sodium cations (0.53 %). Main components of calcium magnesia structure are calcium carbonate (9.19 %) and phosphate (0.39 %). Solid structure base of coarse-dispersion complex includes also particles exceeding 1 μm containing crystals of salts; gypsum cuts; remains of plants and living substance microcosm, in particular carbonate remains of Foraminifera (Fig. 14.1b); as well as microorganisms [18]. Increased carbonate concentrations in sediments depend on content of Foraminifera remains and, to a lesser extent, on carbonate setting out from mud solution during diagenesis process.

Fine-dispersed part of peloids, or their colloidal complex, containing nano- and microparticles of less than 1 μm in diameter, consists of decayed organic matter and mineral substance including iron sulfides, silicic acid, layered smectite clay minerals, etc. Mineral origin substances prevail at composition of hydrophilic colloid complex. Among them nanodispersed and colloid-dispersed clay minerals, hydrates of iron sulfides, hydrotroilite, and iron oxides are the most influential upon their viscosity.

According to obtained X-ray and chemical analysis and data analysis shown in Fig. 14.1 and at [18], marine peloids contain quartz (7.3–14.9 %), calcium and magnesia carbonates (15.2–26.5 %), and clay minerals—hydromica, kaolinite, glauconite, montmorillonite (40–70 %), and amphoteric silica (0.1–4.0 %). Spectral analysis of selected spots during peloid SEM imaging showed a presence of carbonates, oxides of silicon, aluminum, iron, and also sulfides in broad concentration ranges.

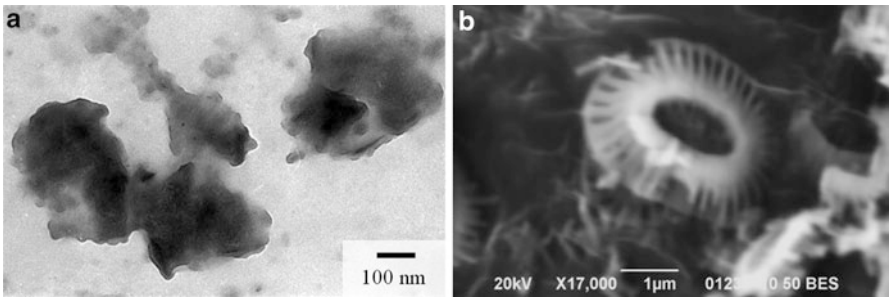

Fig. 14.1 SEM images of different Black Sea peloid fractions

14.4.2 Microbiological Investigations

Along with other components, peloids contain microorganisms (Fig. 14.1b) contacting to micro- and nanoparticles ([18] and Fig. 14.2). Following metabolism processes they form deep decay products of organic and inorganic substrates. The latter substantially determines biocolloid properties of peloids. At that, natural process of peloid formation goes on for the period from few years to many centuries at big depth in strict selective conditions of aerobic and microaerophilic medium with high content of salts. Microbiocenosis, consisting of different microorganism group representatives formed at such conditions, adapts to a common existence as autonomic object controlling the following processes basic for all types of natural mediums:

- Decay of organic matter with saprophytic and other microorganisms with formation of carbon dioxide or methane, hydrogen sulfide, and ammonia in anaerobic conditions
- Sulfate reducing with formation of hydrogen sulfide in anaerobic conditions
- Transformation of nitrogen compounds by ammonification (protein hydrolysis with formation of ammonia)
- Denitrification by anaerobic process of nitrogen compound reduction up to oxide/protoxide and free nitrogen
- Nitrification following ammonia oxidation to nitrites and then to nitrates in aerobic conditions
- Reduction or oxidation of ferric and magnesia compounds by different aerobic and anaerobic microorganisms

Different ecotrophic group microorganism concentrations in peloids of Kuyalnik Estuary (initial, used after therapeutic mud application and after their regeneration) are presented in Table 14.2. Opportunistic microorganisms (*E. coli* bacteria and *Staphylococcus*) have not been revealed in samples. pH indexes of initial sample (7.4), used (6.8), and after regeneration (7.3) testify of peloid ability to recover its physicochemical properties.

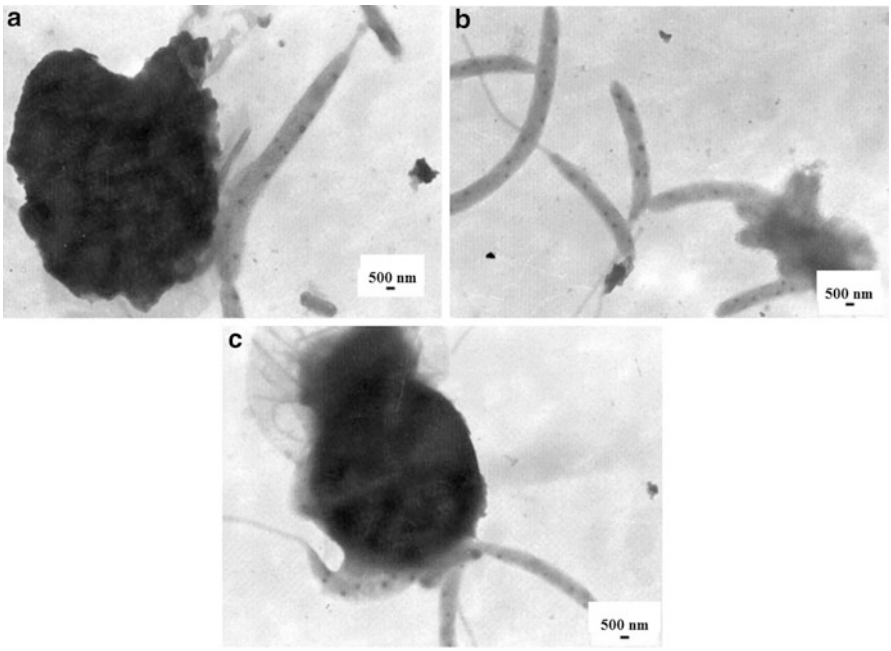

Fig. 14.2 SEM images of microorganisms in clay-carbonate peloid composition

Table 14.2 Microorganism concentration in peloids (CFU/cm^3)

Type of microorganism (bacteria)	CFU/cm^3 in peloids		
	Initial	Used	After regeneration
1. Cellulose fermenting			
–Aerobic	10^3	10^4	10^3
–Anaerobic	10^1	10^1	10^1
2. Butyric acid	10^4	10^2	10^4
3. Denitrifying	10^2	10^2	10^2
4. Sulfate reducing	10^4	10^2	10^4
5. Nitrifying	10^6	10^5	10^6
6. Methane producing	10^7	10^6	10^7
7. Iron oxidizing	3×10^6	1×10^6	3×10^6
8. Ammonification			
–Aerobic	10^6	10^2	10^6
–Anaerobic	10^2	10^2	10^2
9. Fat decomposing	10^2	10^2	10^2
10. Sulfur oxidizing	10^4	10^4	10^4

Saprophytic microorganism concentration dynamics of peloids during their regeneration under 20 cm of brine is shown in Fig. 14.3. The aforesaid data displays that saprophyte count increases up to values in initial peloids during incubation.

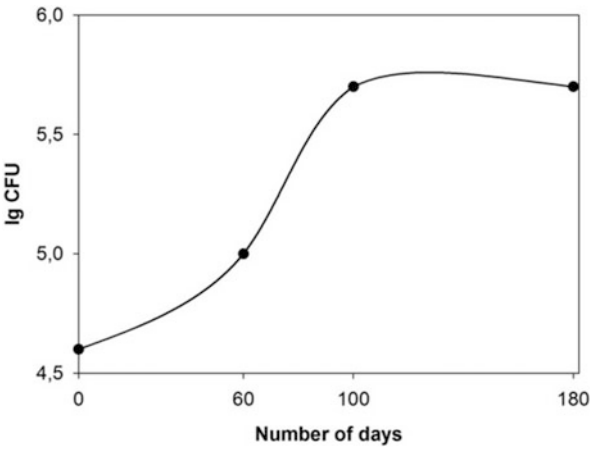

Fig. 14.3 Dynamics of microbiological composition changing during regeneration process of preliminary used peloids

Regeneration process is completed after 100 days of exposition. *E. coli* bacteria die within 9 days of incubation after its doping in peloids.

Tested peloids relate to high-bactericide ones. This property preserves also in peloids after their regeneration.

Thus, peloid lost properties can be restored by regeneration for its further use in therapeutic practice. Peloids are self-purified from pathogenic and opportunistic microflora intruded into them during their application and storage. Other peloid properties restore at regeneration too (organic matter content, catalase activity, concentration of hydrogen sulfide, sulfate and hydrocarbonate ions, medium activity).

14.4.3 Influence of Nanodispersed Inorganic Additives on Balneological Peloid Activity

Obtained results show that the Black Sea bottom sediments, which undoubtedly exist in other seas and oceans, have unique therapeutic properties according to common pelagic sediment formation mechanism [24]. However, influence of external factors, including their modification with bioactive clays and calcium carbonate, is not studied well enough [12, 13, 18].

Natural bentonitic clay from Dashukovka deposit (Ukraine) was used as clay nano- and microadditives. It was thermally treated for hydrophobization at 600 °C before its addition into peloid samples. It was needed for receiving the nano- and microparticles at further contact of thermo-treated bentonite with aqueous medium [23]. Sizes of formed nanoparticles are within 20–100 nm limits (Fig. 14.4). Physiologic investigations of peloid compositions with nanomaterials were made by estimation of different healthy animal (white Wistar rat) organism systems' response to biological activity of these compositions. Peloid and peloid

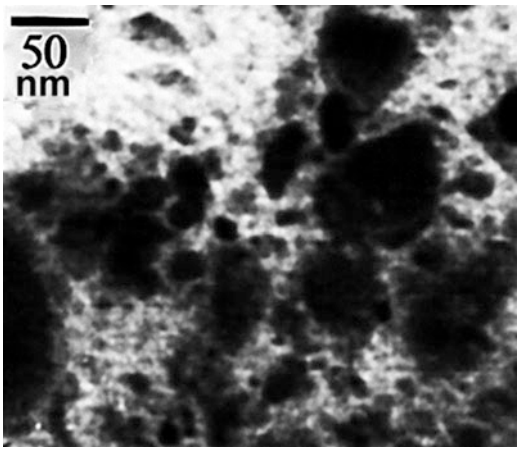

Fig. 14.4 SEM image of burnt bentonite nanoparticles at 600 °C

composition influence on the central nervous system (CNS) and liver were tested by sodium thiopental solution injection into abdominal cavity of animals with 0.75 mg of dry substance to 100 g of body mass dosage. Falling asleep time (in minutes) after barbiturate injection was measured for influence on CNS characterization. Medication sleep period characterizes antitoxic liver ability. Compositions were applied on animals by inserting their tails into tested suspensions with 40 ± 1 °C for 2 h.

Data in Fig. 14.5 shows skin-resorptive influence of natural bentonites in peloid composition on intact animal CNS and liver functional state. So, adding of 5 and 10 % of bentonite into peloids has practically no effect the falling asleep time and sleep duration while performing metabolic test with barbiturates. It indicates that also there is no negative influence of such composition on the CNS and liver. Increasing bentonite concentration up to 15 or 5 % addition of saponite clay into peloid composition decreases metabolic liver processes. It can be proved by metabolic sleep duration increasing in animals during thiopental test. CNS functional state remains almost the same.

Thus, the investigation gives reasons to believe that colloid-chemical properties of up to 5 % natural bentonite clays' additions into peloids have almost no influence on balneological characteristics of peloid compositions. Therefore, influence of bentonite clay hydrophilic nanoparticles is small too.

Investigation of thermally treated hydrophobitized bentonite clay at 600 °C influence to peloid biological activity (Fig. 14.6) showed that its 5 and 10 % addition substantially changes composition balneological characteristics. Influence on CNS remains almost the same, but antitoxic liver ability increases which can be seen by medication sleep duration decrease to three times for 5 % of bentonite and to 1.9 times for 10 % of bentonite. Medication sleep duration decreases to 3.7 times for 5 % of bentonite and to 2.2 times for 10 % of bentonite in case of preliminary mechanochemical grinding of burnt bentonite in ball mill for an hour.

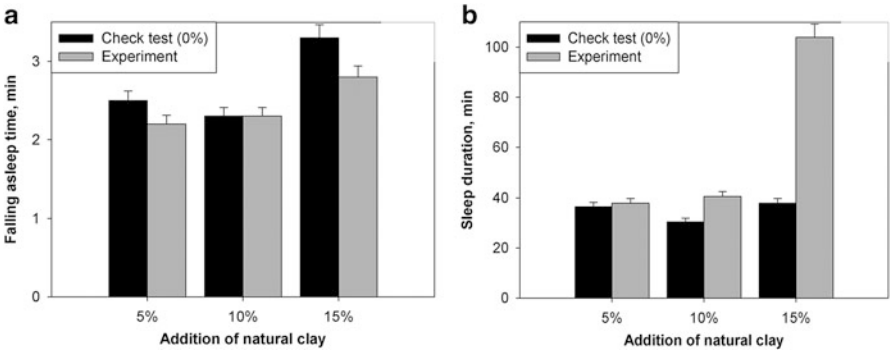

Fig. 14.5 Falling asleep time (**a**, min) and sleep duration (**b**, min) of intact animals for 5, 10, and 15 % natural clay addition into peloids

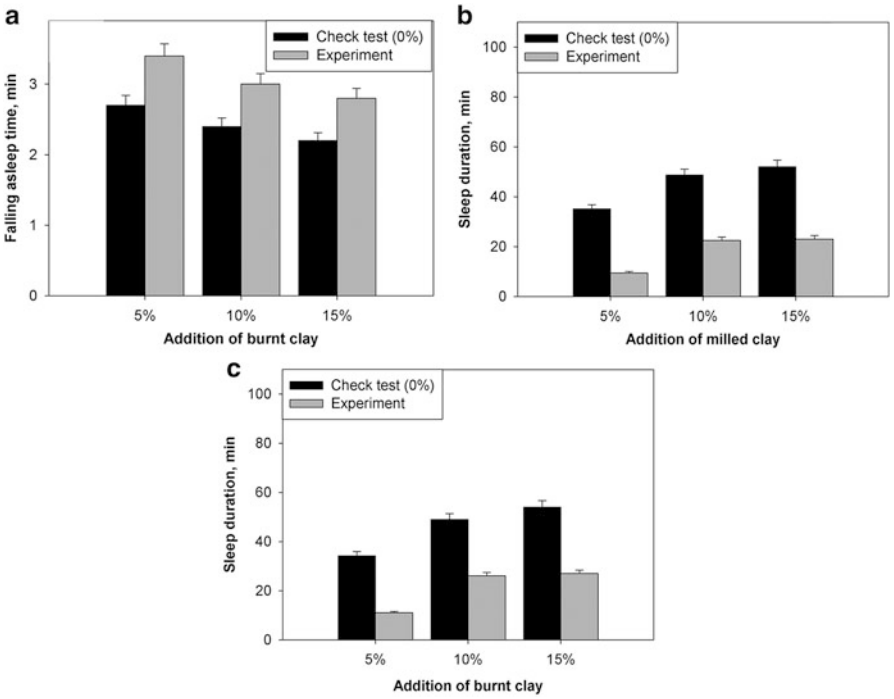

Fig. 14.6 Influence of burnt at 600 °C (**a**, **b**) and dispersed in ball mill (**c**) bentonite on falling asleep time (**a**, min) and on medication sleep duration (**b**, **c**, min) of intact animals

Addition of 5, 10, and 15 wt% of chemically precipitated calcium carbonate (Fig. 14.7) into peloids showed that CNS functional state isn't changed, but antitoxic liver ability increases to two to three times.

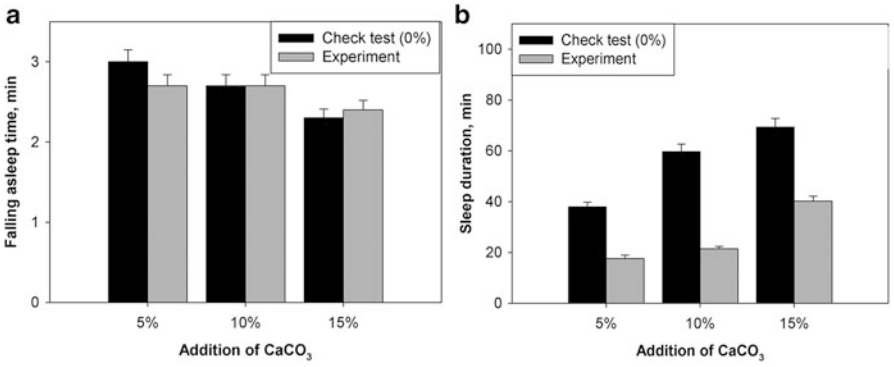

Fig. 14.7 Calcium carbonate nanoparticle influence on falling asleep time (**a**, min) and medication sleep duration (**b**, min) of intact animals

However, such results were obtained for peloid compositions and artificially added calcium carbonate containing nanoparticles. According to [14] their role is being diminished as far as clay-carbonate compositions are being aged in quiescent state due to flowing of isothermal distillation process in them. At the same time, in opened dissipative systems (mixing conditions), the effect of nanochemical dispersion of microparticles up to nanoparticles can be observed in the presence of dissolved NaCl in disperse medium and carbon dioxide from air medium. The latter can be described by generalized scheme (Fig. 14.8).

It follows from the scheme (Fig. 14.8) that while applying the intensive mixing, we can disperse carbonate microparticles contained in natural salt peloids up to nanoparticles in accordance with mechanism of nanochemical dispersion in intensive mixing conditions and further recondensation in quiescent state [14]. Really, rheological investigations on model composition contained 90 % of montmorillonite clay and 10 % of microdispersed calcium carbonate displayed substantial changing of peloid suspension parameters after its intensive mixing (Figs. 14.7 and 14.9).

Testing of real peloid suspensions after their mixing for 10 h showed that their biological activity, within measurement error limits, corresponds to data received for artificially prepared peloid composition (Fig. 14.7).

The aforesaid results prove that, while mixing, mechanism of carbonate microparticle nanochemical dispersion is affected by mechanochemical processes promoting its realization, which in fact influences the colloid-chemical properties and balneological activity of peloids.

Additional investigations of bioactivity and anti-inflammatory action of peloids with nanoadditives to intact animals and in ovalbumin arthritis modeling conditions, as well as in spa-resort practice, showed that composition application of prophylactic course is accompanied with significant therapeutic effect conditioned by improvement of inflammatory metabolic and immune rates, as well as by the increase of glucocorticoid background in an organism.

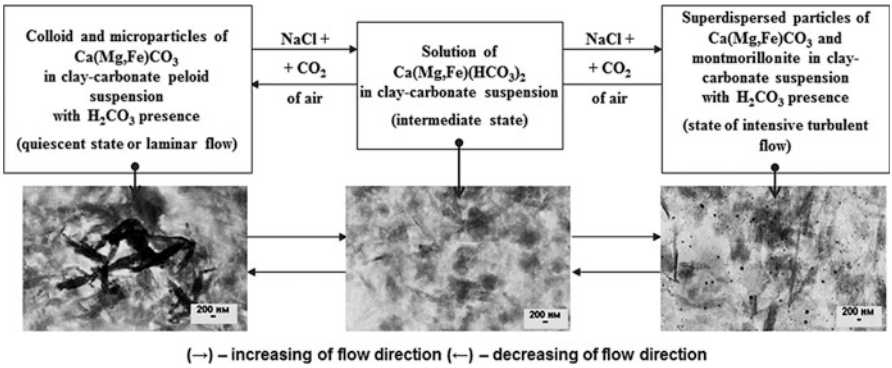

Fig. 14.8 Scheme of nanochemical dispersion of clay-carbonate suspensions and inverse isothermal distillation process

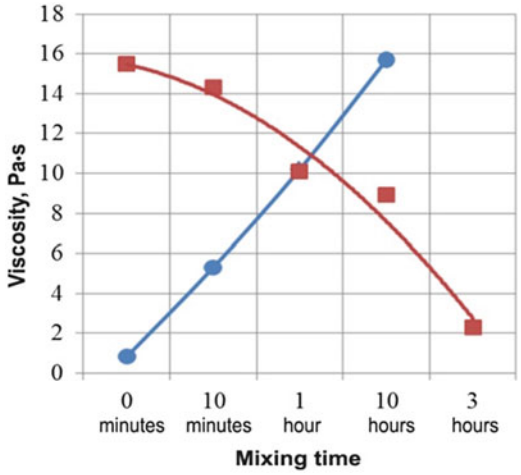

Fig. 14.9 Dependence of 50 % clay-carbonate brine suspension effective viscosity on mixing time: *filled circle* in mixing conditions, *filled square* in quiescent state

14.5 Conclusions

Investigations of physicochemical and microbiological properties and analysis of obtained laboratory and practical data prove that peloid microbiocenosis of Black Sea deep-water bottom sediments is the formation having the ability for self-purification and regeneration of its composition. High content of nitrifying and iron-oxidizing aerobic bacteria in tested peloids indicates behavior of quite active oxidation processes enriching environment with proteases, catalases, other ferments, and bioactive substances. When estimating the peloid antimicrobial effect for *E. coli* (added directly into peloid suspension with infective dose of 10^6 CFU/cm ^{3}) showed that tested bottom sediments are high-bactericide ones, and they can be recommended as remedy for series of diseases.

Following the investigation it was determined that additives of natural hydrophilic bentonites into peloids have not practically influenced on biological activity and, therefore, doesn't worsen balneal characteristics of peloid compositions. At the same time up to 15 % concentrations of burnt bentonites and calcite substantially improve peloid balneal activity.

These results testify that increasing nanoparticle quantities in peloids following introduction of burnt bentonite and calcium carbonate additives shall potentiate the peloids balneological activity, probably at the expense of increased sorption and ion-exchange ability of calcite nanoparticles and burnt dehydrated clay minerals in bentonite composition. At the same time, the formation of nanoparticles in natural bentonite is being inhibited, and that doesn't improve biological activity of system.

Following the completed investigation and analysis of collected data about colloid-chemical and nanochemical transformations of clay-carbonate structures [12, 14, 18], it was shown that the presence of nanoparticle in clay-carbonate peloids containing saline water (brine) and CO_2 from air can substantially affect the colloid-chemical properties and balneological activity of peloid compositions. Correlation has been determined between nanochemical transformations, colloid-chemical properties, and balneal activity in dependence of the fact that such compositions are in quiescent state, for example, when applied on animal's skin (thermodynamically isolated system) or at intensive mixing conditions.

References

1. Bergaya F, Theng BKG, Ladaly G (eds) (2011) Handbook of clay science. Elsevier, Amsterdam
2. Cara S, Carcangiu G, Padalino G, Palomba M, Tamanini M (2000) The bentonites in pelotherapy: chemical, mineralogical and technological properties of materials from Sardinia deposits (Italy). Appl Clay Sci 16:117–124
3. Carretero MI (2002) Clay minerals and their beneficial effects upon human health: a review. Appl Clay Sci 21:155–163
4. Carretero MI, Pozo M, Sánchez C, García F, Medina JA, Bernabé JM (2007) Behavior of saponite and montmorillonite bentonites with sea water during maturation processes for pelotherapy. Appl Clay Sci 36:161–173
5. Gamiz E, Martin-Garcia JM, Fernandez-Gonzalez MV, Delgado G, Delgado R (2009) Influence of water type and maturation time on the properties of kaolinite–saponite peloids. Appl Clay Sci 46:117–123
6. Gomes C, Silva J (2001) Beach sand and bentonite of Porto Santo Island: potentialities for applications in geomedicine. O Liberal, Câmara de Lobos-Madeira, Portugal
7. Legido JL, Medina C, Mourelle ML, Carretero MI, Pozo M (2007) Comparative study of the cooling rates of bentonite, sepiolite and common clays for their use in pelotherapy. Appl Clay Sci 36:148–160
8. Sánchez CJ, Parras J, Carretero MI (2002) The effect of maturation upon the mineralogical and physicochemical properties of illitic–smectitic clays for pelotherapy. Clay Miner 37:457–464
9. Tateo F, Agnini C, Carraro A, Giannossi ML, Margiotta S, Medici L, Finizio FE, Summa V (2010) Short-term and long-term maturation of different clays for pelotherapy in an alkaline-sulphate mineral water (Rapolla, Italy). Appl Clay Sci 50:503–511

10. Viseras C, Aguzzi C, Cerezo P, Lopez-Galindo A (2007) Uses of clay minerals in semi-solid health care and therapeutic products. Appl Clay Sci 36:37–50
11. Williams L, Haydel S, Giese R, Eberl D (2008) Chemical and mineralogical characteristics of French green clays used for healing. Clay Clay Miner 56:437–452
12. Panko AV, Ablets EV, Kovzun IG, Protsenko IT, Ulberg ZR, Nikipelova EM (2014) Biocolloid nanoparticle influence of $CaCO_3$ on medicoendoecological peloid properties. In: Proceedings of the 5th International Conference on Carpathian Euroregion, Berehovo, Ukraine, 26–28 March 2014
13. Olejnik VA, Panko AV, Nikipelova EM, Alekseenko NA, Kovzun IG (2012). Influence of nanomaterials on biological activity of marine pelagic sediments (peloids). In: Proceedings of NAP 1: 02NNBM16
14. Kovzun IG, Kovalenko IM, Protsenko IT (2007) Influence of dispersed $CaCO_3$ on the viscosity of montmorillonite suspensions containing NaCl. Colloid J 69:312–318
15. Balek V, Malek Z, Ehrlicher U, Gyoryova K, Matuschek G, Yariv S (2002) Emanation thermal analysis of TIXOTON (activated bentonite) treated with organic compounds. Appl Clay Sci 21:295–302
16. Lee H-C, Lee T-W, Lim YT, Park OO (2002) Improved environmental stability in poly (p-phenylene vinylene)/layered silicate nanocomposite. Appl Clay Sci 21:287–293
17. Kovzun IG, Protsenko IT (1994) Hydrophilicity of disperse carbon-silicate compositions and carbonaceous materials. Colloid J 56:712–714
18. Fesenko O, Yatsenko L (eds) (2015) Nanoplasmonics, nano-optics, nanocomposites and surface studies. Springer, Amsterdam
19. Pertsov NV, Kogan BS (1981) Fiziko-himicheskaja geomechanika. In: Fiziko-himicheskaya mehanika i liofilnost dispersnyih system, vol 13. Naukova dumka, Kyiv, pp 53–65
20. Pertsov NV, Kogan BS (1984) Fiziko-himicheskaya mehanika i liofilnost dispersnyih system. In: Fiziko-himicheskaya mehanika i liofilnost dispersnyih system, vol 16. Naukova dumka, Kyiv, pp 71–78
21. Kovzun IG, Pertsov NV (2010) Colloid-chemical processes of contact self-organization in alkaline silicate composites and their relation to formation of nanosized surface structures (chapter 19). In: Starov VM (ed) Nanoscience. Colloidal and interfacial aspects. CRC Press, London, pp 523–568
22. Prokopenko VA, Kovzun IG, Ulberg ZR (2014) The creative potential of scientific discovery. Her Natl Acad Sci Ukr 10:52–61
23. Sholudko DP, Kovzun IG, Protsenko IT, Panko AV, Zubkova VA (2010) Strukturnyie osobennosti sorbenov na osnove alyumosilikatov, modifitsirovannyih nanouglerodnyimi produktami termoraspada organicheskih prekursorov. Mater Sci Nanostruct 4:83–103
24. Govorin IA (2007) Allochthonous bacteria in the ecosystem “Marine environment—aquatic organisms—bottom sediment”. (A review). Hydrobiol J 43(4):48–58

Chapter 15
Anodic Nanostructuring of Titanium Oxide

A.I. Schurenko, V.I. Stiopkin, D.A. Galaktionov, O.V. Danko, P.I. Lytvin, and D.O. Grynko

15.1 Introduction

The goal of this work is to discover the technological factors in the systematic research of the morphology of nanostructural anodic titanium. The morphology was investigated with SEM and ASM techniques. Anodic oxidation of titanium film accompanied with molar volume expansion brings significant mechanical stress. That is why we pay attention to crystallinity, adhesion, and the inner stress of source titanium film which was deposited by magnetron sputtering. Unlike anodic aluminum oxide, anodic titanium oxide is resistant in alkaline solution, is more durable mechanically, and has higher heat resistance. Prospective usage of nanostructural anodic titanium oxide would be quasi-ordered cheap templates, membranes, nanostructure medium for chemosorption of specific molecules, nanofilter manufacture, optical and semiconductor devices, and nanosensors.

The actuality of this research is defined by the potential application of a nanostructured layer of titanium oxide. A comparison of potential of uses of solid layers of titanium oxide with the potential of a nanostructured layer of titanium oxide shows that they have different fields of application. The latest is used for

A.I. Schurenko • V.I. Stiopkin
Taras Shevchenko National University of Kyiv, Kiev, Ukraine

D.A. Galaktionov (✉) • O.V. Danko
Institute of Physics NAS Ukraine, Kiev, Ukraine
e-mail: glukxy@gmail.com

P.I. Lytvin • D.O. Grynko
Institute of Semiconductor Physics NAS Ukraine, Kiev, Ukraine

O. Fesenko, L. Yatsenko (eds.), *Nanophysics, Nanophotonics, Surface Studies, and Applications*, Springer Proceedings in Physics 183,
DOI 10.1007/978-3-319-30737-4_15

nanosensorics, for creation of nanomaterial, and for photoelectrochemical processes. At the same time solid layers of titanium oxide are widely used in classical optics and as qualitative dielectric layers in classical electronics [1, 2].

It is important to compare nanostructured titanium oxide and widely used anodic aluminum oxide [3]. Indeed these techniques have similar technologies and similar materials. The essential distinction is first of all defined by the chemical properties of these materials. Anodic aluminum oxide dissolves both in alkaline and acid etchants [4, 5]. Although titanium oxide dissolves only in strong acid containing fluoride ions. In comparison with anodic aluminum oxide, titanium oxide is more mechanically durable and can withstand heavy traffic without destruction. It can be very useful in forming membranes. In titanium oxide it is possible to get another type of surface symmetry of channels. Also the prospect of using long-lived surface states in the bandgap is very interesting. Such effects don't show themselves brightly in aluminum oxide [4].

15.2 Film Fabrication and Characterization Techniques

TiO_2 films are formed in two stages: magnetron sputtering of titanium is done in the first stage. Glass, quartz, and silicon have been used as a substrate. In the second stage anodic oxidation in the acid solution is done. This process is carried out under potentiostat conditions and the characteristic time of etching is a couple of minutes.

AFM is used for measuring the nanoparticle height and measurements of topography used by SEM images. The accuracy of AFM is conditioned by the precision of setting the needle position. During small motions the highest accuracy of the positioning is ensured by the piezooptic drive. If a large area of the experimental surface is scanned, the accuracy decreases. Also the limitation, which is caused by the geometry of the needle, is significant. The narrow deep channels are not available for detailed research using the AFM method. With the help of SEM, it is possible to receive more information about the surface. On basis of 2D topology and the AFM data, one can analyze the geometry of the deep channels [6].

15.3 Results

During anodic oxidation, the titanium film in the acid part AB corresponds to the formation of a solid dielectric film, and in point of fact, it is the process of charging the capacitor (Fig. 15.1).

One of the capacitor plates is the titanium film and the other is an electrolyte, which is adjacent to the titanium oxide film. If the electrolyte contains no fluoride ions, then the oxidation process stops here. If the process contains some amount of fluoride ions, then channel irritation begins and the curve has the typical AD form.

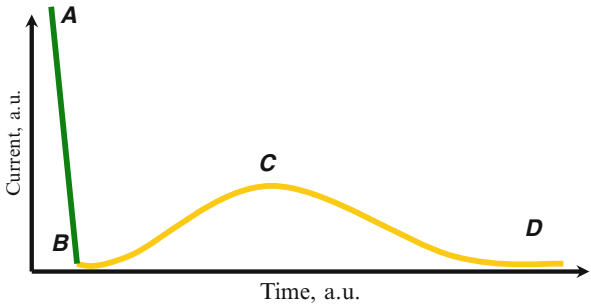

Fig. 15.1 *ABCD* parts of titanium oxide etching process

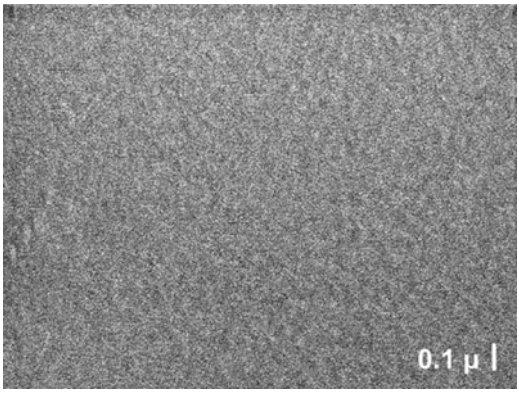

Fig. 15.2 Morphology of the evaporated titanium by magnetron sputtering by SEM

Channel etching takes place on the part BC. On the CD channel part irritation and forming separately staying pillars or the sponge material formation takes place.

Many factors have an effect on this curve form. There is a concentration of fluoride ions, electrolyte temperature, substrate material, and other factors. Our approach is to estimate points ABC with every factor combination. Then we renormalize the experimental data to the normalized curve. Only after that can we characterize the structure of the material by the placement of particular samples on the curve (Fig. 15.2).

The morphology of the titanium evaporated by magnetron sputtering has been explored by both SEM and AFM techniques. There are neither crystallites nor other formations on the surface. It is an homogeneous structure.

There are three junction points on Fig. 15.3 of the surface morphology and the figure shows their position on the curve. Near the point A on the curve relief accounts for about 5 nm (Fig. 15.3a). Then etching channels begin and on the next picture (Fig. 15.3b), relief accounts for about 30 nm. Then it increases up to more than 100 nm (Fig. 15.3c).

Research on the scanning electron microscope at two representative points allows us to understand that in reality formation of the nanochannels and their subsequent irritation is going on. The typical size for the wall of the channel is

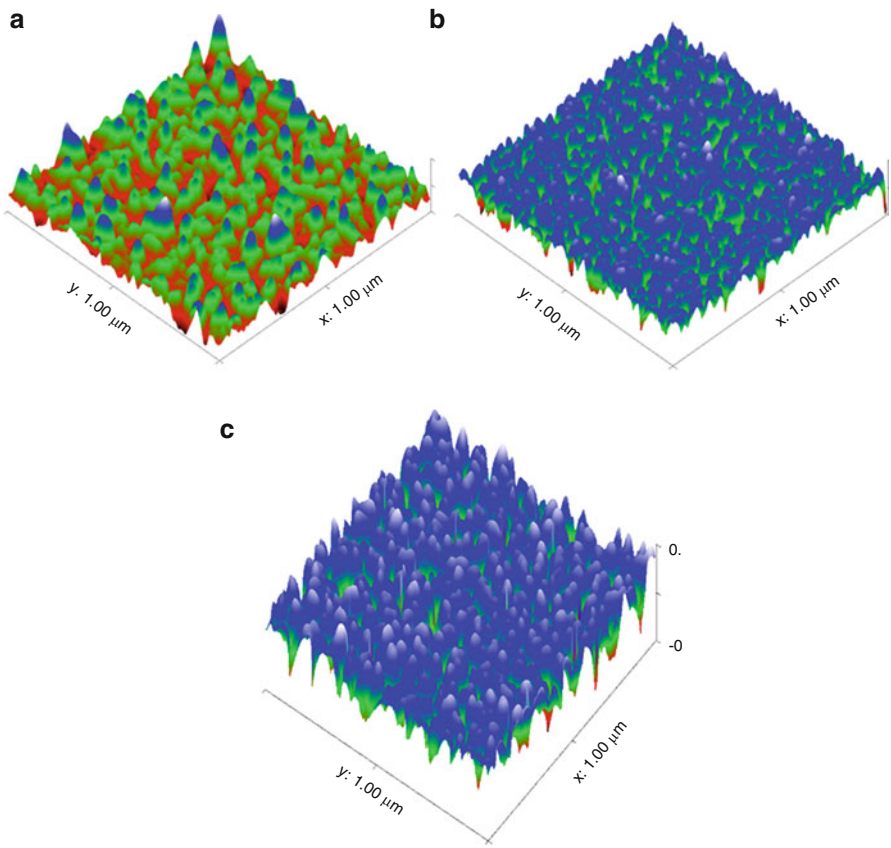

Fig. 15.3 AFM data for three junction points

about 60 nm and it becomes thinner during irritation. According to our data, the median value is 30 nm.

The image of a two-dimensional Fourier transform (Fig. 15.4c, d) shows the isotropy of material along the surface. There is some typical spacing of vials. In our experiments the size of the vials and the typical size of the structure varied within tens of nanometers. The valuation of the channels' diametrical structure, which is formed in the film, is essential. We can see separate channels, and it can be seen that the depth of the vials is about 300 nm, whereas the thickness of the whole film is 700 nm. The depth of the channels is the typical quantity. It has small statistical straggling. In this case, the vials do not reach the surface of the substrate.

On this sample the etching was carried out at an angle of 4° with the help of the ions' argon beam, which fits making a precision slice. We observe this structure at an angle of 50° (Figs. 15.5 and 15.6).

There is typical spacing of the structure of about 60 nm. In the foreground, we can see the ordered strip of channels, which we can describe by the correlated

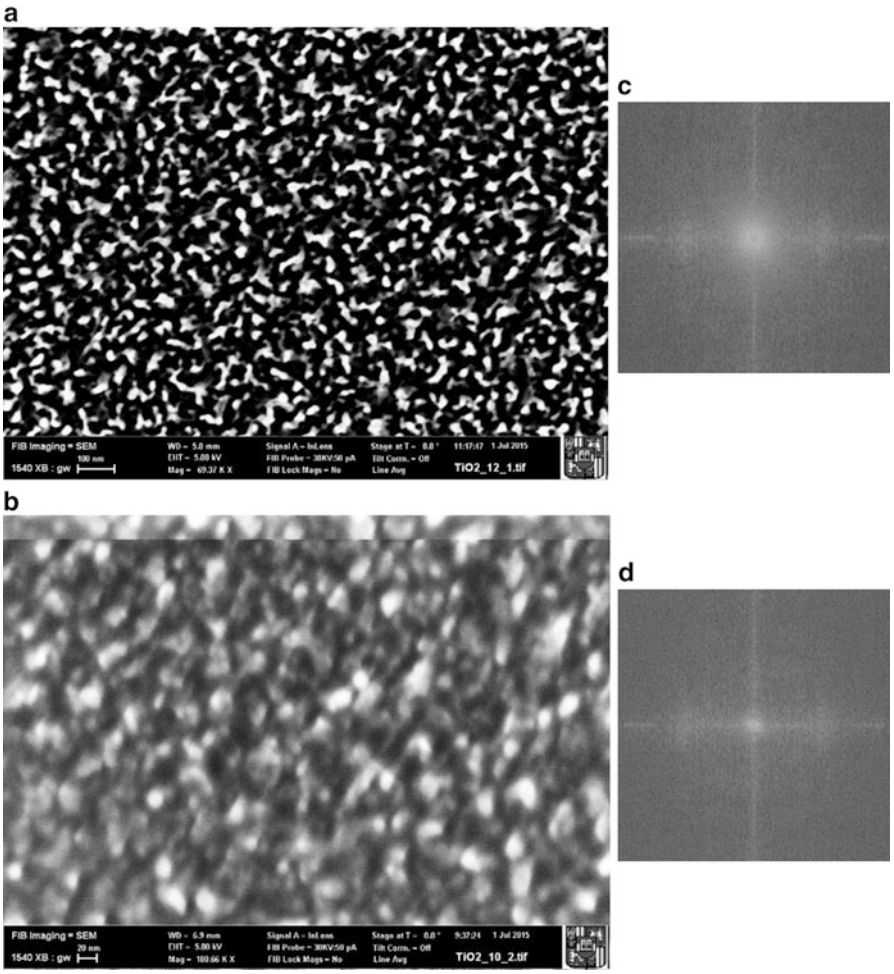

Fig. 15.4 SEM data for two junction points (**a**, **b**) and FTT of them (**c, d**), in order

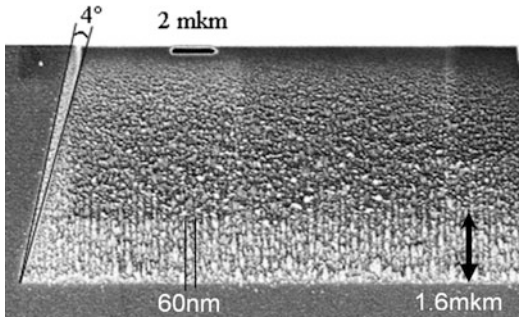

Fig. 15.5 TiO_2 sample: the etching at an angle 4° with the help of ion argon beam

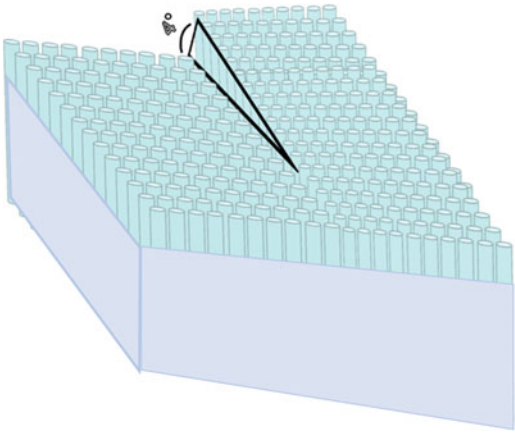

Fig. 15.6 Simple example for view of slice

channel position This can also be seen with the two-dimensional Fourier transform, where the typical degree is present. This representation shows that the correlation length conforms to both sizes and mutual positions of the channels and is 1.6 μm. In the background we can see a dark stripe with considerably less level of noise which fits that the flatness section etching is lower than the bottom of the channels. Channels have limited depth as we have already seen on the previous slide and their depth is ordered.

Therefore, we developed a finished technological process of getting the nanostructured layers of titanium oxide. Nanostructured titanium oxide forms by anodic oxidation with fluoride ions. The typical nanochannel size is tens of nanometers and the depth of the channels can reach 500 nm. Further irritation of these channels makes separately staying pillars or sponge material formation. We are expecting that using nanostructure titanium oxide, which is formed in guided processes self-organization, will make it possible to create a new level of integration in contemporary nanosensor devices.

15.4 Analysis

Applications of nanostructured continuous layer of anodic titanium oxide: UV protection optical filter, pigh-n optical layer for interference structures, low-k dielectric layer for electronics, diffusion barrier layer for electronics, antiscratching hard layer, protective antimoisture, antioxidation and chemical layer.

Applications of nanostructured layer of anodic titanium oxide:

- UV absorber and diffuser
- sorbent
- catalyst support

- electrochemical acceptor
- photoacceptor, nonlinear optical material
- quasiperionic templates for nanotechnology
- nanomembranes

The essential peculiarity of the process of anodic oxidation of titanium arises in titanium mechanical stress. The reason is easy to understand while comparing the molar volume of titanium and titanium oxide. The volume of titanium oxide is more than twice as big as the volume of titanium. That means that during anodic oxidation, the film of titanium and titanium oxide, which is formed on the surface, has very big tensile/internal stress. Discharging of this stress can be in two ways: swelling of the surface (that doesn't satisfy us because of exfoliation of the film) and by etching of the titanium oxide film [1].

To avoid this effect, we should obtain maximal adhesion of the substrate to deposit titanium films. Technologically by magnetron sputtering with the additional heating of the substrate it is possible to attain growth of the diffusion process.

Nevertheless, internal stress, which arises in the structure TiO_2 on titanium, is the fundamental and important peculiarity of the process of formation of nanostructured titanium oxide [7, 8]. If we want to get reproducibility of the results and ordered structures on the surface, we should take steps to decrease unwanted mechanical stresses, which can be caused by crystallites in the film of titanium, additional phase impurity, and other such phenomena (Fig. 15.7).

Our approach is that we estimated points ABC with every factor combination. Then we renormalized experimental data to the normalized curve. Only after that

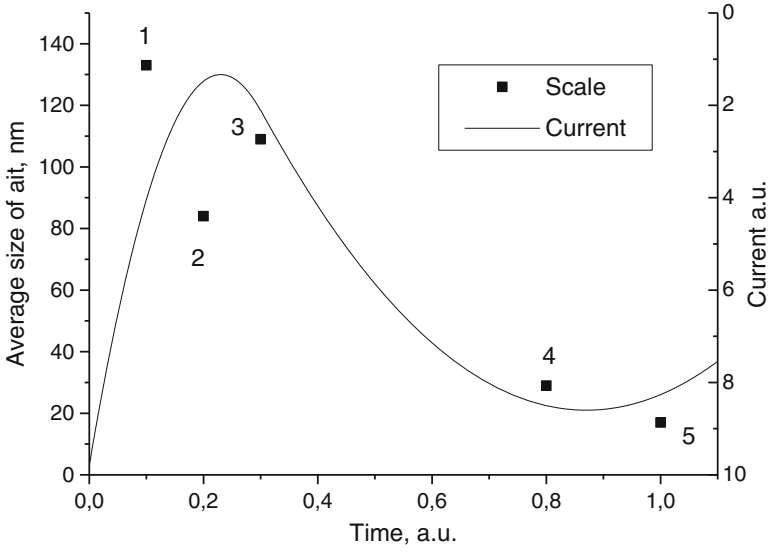

Fig. 15.7 Average size of ait TiO_2 during etching: (*1*) Fig 15.3a, (*2*) Fig. 15.3b, (*3*) Fig. 15.3c, (*4*) Fig. 15.4a, (*5*) Fig. 15.4c

we could characterize the structure of the material by the placement of particular samples on the curve.

15.5 Conclusions

The morphology of anodic titanium oxide depends a great deal on electrolyte composition. In the absence of fluoride ions in a side electrolyte on the titanium film surface, a solid protection layer of titanium oxide is formed. The surface structure of vial-type nanochannels arises at the time of electrochemical oxidation of titanium film in the acid solution with fluoride ions. The morphology of anodic nanostructured titanium oxide was investigated.

Injection of fluoride ions and some other supplements in the electrolyte leads to the formation of a quasi-ordered system of nanochannel grating. In our experiments the nanochannel diameter was 30–150 nm with a distance of 60–100 nm and height up to approximately 500 nm. Further etching of film forms nanopillars and sponge.

We worked out the approach to the problem of comparing the data, which were received in different experiments. We assume that in all experiments, the principle, which describes the curve of the etching, is the same. On this assumption, enumerating and further comparison of the points is done.

Acknowledgment We are very grateful to our Austrian colleagues for an opportunity to do detailed research at Johannes Kepler University Linz.

References

1. Diebold U (2003) The surface science of titanium dioxide. Surf Sci Rep 48:53–229
2. Park J, Lee T, Kang M (2008) Growth, detachment and transfer of highly-ordered TiO_2 nanotube arrays: use in dye-sensitizes solar cells. Chem Commun 25:2867–2869
3. Hu G, Zhang H, Di W, Zhao T (2009) Study on wet etching of AAO template. Appl Phys Res 1 (2):78–82
4. Gopal K, Oomman K, Paulose M, Grimes A (2005) Transparent highly ordered TiO_2 nanotube arrays via anodozation of titanium thin films. Adv Funct Mater 15:1291–1296
5. Troyon M, Lei HN, Wang Z, Shang G (1998) A scanning microscope combined with a scanning electron microscope for multidimensional dataanaysis. Scanning Microsc 12(1):139–148
6. Jarosz M, Kapusta-Kolodziej J, Jaskula M, Sulka GD (2015) Effect of different polishing methods on anodic titanium dioxide formation. J Nanomater 2015:295126
7. Paulose M, Shankar K, Varghese K, Gapal K, Grimes A (2006) Application of highly-ordered TiO_2 nanotube arrays in heterojunction dye-sensitized solar cell. J Phys D Appl Phys 39 (12):2498–2503
8. Ruan C, Paulose M, Oomman K, Gopal K, Grimes A (2005) Fabrication of highly ordered TiO_2 nanotube arrays using an organic electrolyte. J Phys Chem B 109(33):15754–15759

Chapter 16
About the Possibility of Quantum Interference Transitions and Entanglement in Vacancies and Divacancies of Silicon

Ludmila MARTSENIUK

16.1 Introduction

The nanostructures, which are formed in materials of solid state or in alive organisms, are the quantum objects on which all formalism of quantum theory is distributed.

E. Shrodinger in the famous work «the Modern situation in quantum mechanics» [1], issued as far back as 1935, in connection with discussion between A. Einstein and N. Bohr about the nature of the phenomena described by quantum mechanics, emphasized that the entanglement makes the essence of quantum mechanics.

The physics of the entangled states, which has arisen as a result of the realization of pre-visions of E. Shrodinger and other prominent researchers, has opened wide perspectives for researches and for practical applications in the field of quantum and informative technologies; in studying the functioning of nanostructures of alive objects.

Exceptionally important material for practical applications is silicon. Technology of growing of the perfect monocrystal silicon is well-developed; the comprehensive studying of its properties and the influences of various factors and radiative technologies on its parameters is carried out that has allowed receiving the materials on the basis of silicon with controllable characteristics for various areas of practical use.

Particular interest presently in connection with large-scale works on creation of quantum computers present the use of silicon as material for making on the basis of

L. MARTSENIUK
Institute for Nuclear Researches, National Academy of Science of Ukraine, Prospect Nauky 47, Kiev 03680, Ukraine
e-mail: prolisok77@yandex.ua

O. Fesenko, L. Yatsenko (eds.), *Nanophysics, Nanophotonics, Surface Studies, and Applications*, Springer Proceedings in Physics 183,
DOI 10.1007/978-3-319-30737-4_16

devices for quantum information technology: memory cells, elements of the quantum informative systems.

It appeared that the defects, entered into silicon in the radiating way, can be perspective of the decision of such tasks. The particular interest present such nanostructures, as vacancies and divacancies, artificially carried in silicon at an irradiation, and also the cluster structures.

Depending on the character of irradiation, such cluster systems, the main composition of which is formed by the silicon divacancies can appear in a single-crystal silicon. Such clusters bring substantial local distortions of field characteristics of the basic material that allows them to be to some extent in the shielded state from the field fluctuations. Presumably, different quantum effects, including entangling between the separate elements of cluster, can show up for such structures, that determine some parameters of cluster stability to external influences. Interference transitions are possible also between the near power states of cluster elements, especially at low temperatures.

Development of technology of artificial introduction of various radiating defects and clusters, including vacancies and divacancies, with the subsequent annealing of an irradiated material has led to creation of materials with the increased radiating stability that is very important for the creation of silicon detectors, the devices working in conditions of increased radiation.

By virtue of development of such technology the radiating defects are widely and comprehensively investigated.

It appeared that some radiation defects possess the properties of bistability that can open for them the prospects of the practical use as switching elements, having two stable states, and devices with memory cells at creation of devices of the quantum information systems. Vacancies and divacancies relate to such defects (a vacancy is bistable at low temperatures). These defects are interesting yet and in that relation, that they are structures with the Yahn-Teller stabilization.

In the submitted work, the literary data on experimental researches of properties of vacancies and divacancies silicon are analyzed. It is first shown, that for these defects under certain conditions (radiations, supply of the electric impulses or influences of photonic radiation) there can be some quantum effects, including quantum interference transitions between the states of minimums of adiabatic energy.

It specifies on the prospects of the use of materials on the basis of silicon with the radiation defects of type: vacancies and divacancies, artificially entered in them, in the devices of quantum information technology.

16.2 Vacancies and Divacancies in Silicon: The Literary Data

Radiation defects in silicon arise at an irradiation of a material by particles with various energies. Various radiating technologies are used for this purpose: ionic implantation, transmutation doping; the radiations by the charged particles

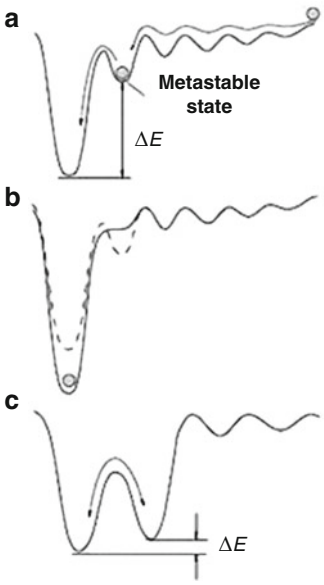

Fig. 16.1 The schematic image of configuration diagrams for metastable and (**a**), (**b**) bistable defects, (**c**) [3]

(by protons, electrons, ions) or neutral particles (by neutrons, γ-quantums) with the subsequent annealing of a material. Each of these methods has the advantages and the features of introduction in a material of radiation defects [2].

The development of technology of defects, introduction of and the studying of their properties have led to detection of some interesting features of radiation defects. It appeared that for some of them such qualities are revealed, as meta- or bistability, the Yahn-Teller effect can show up on them, they can be the centers with negative correlation energy.

In accordance with [3], the defects unstable at normal conditions are named the metastable defects. The configuration diagram, reproducing dependence of defect energy on some generalized coordinates of a lattice usually has some local minimums, as it is shown in Fig. 16.1, taken from [3].

The difference of energies of the basic and secondary minimums ΔE can exceed the energy of thermal fluctuations kT. It leads to reorganization of a configuration of defect (as shown in Fig. 16.1b) at which the non-basic states disappear. If $\Delta E \leq kT$, defect disappears or is united with the other defect.

A vacancy of silicon at room temperatures is not a bistable defect.

A vacancy was first entered in p-type silicon at a low-temperature irradiation, and it disappears at subsequent annealing of the material in a temperature interval 150–180 K. In n-type silicon it was not possible directly to observe vacancy [4] though it was possible to judge about its presence on an increase of concentration of the secondary defects.

As have been shown in the researches, vacancy can be in four charging states (V^+, V^0, V^-, V^{2-}).

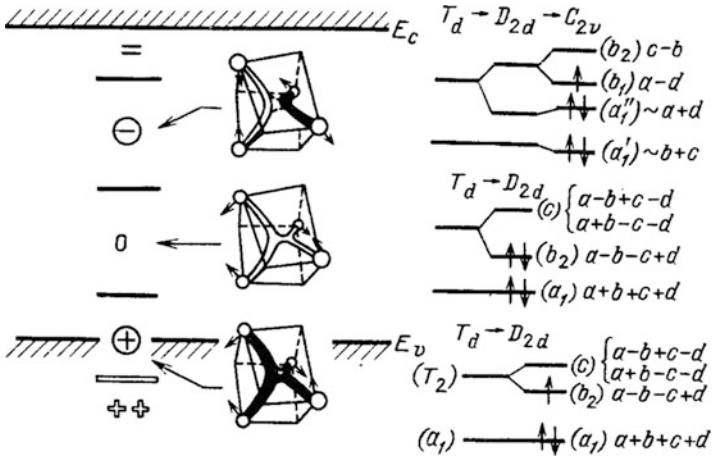

Fig. 16.2 Models and electronic structure of charge states of vacancies of silicon [4]

At the moment of formation, orbital a_1 (singlet) and t_2 (triplet) corresponds to the undistorted vacancy with symmetry T_d. Orbitals are filled by the electrons from torn off connections of the nearby atoms. So, for a charging state V^+ of vacancy, two electrons fill a_1-orbital, and the third—t_2-orbital (Fig. 16.2).

The attaching of the electron brings splitting of the t_2 orbital to change the configuration of defect because of the Yahn-Teller effect. Here the effect of Yahn-Teller shows up as a reduction of symmetry $T_d \to D_{2d} \to C_{2v}$ for $V^{2+} \to V^+$, $V^0 \to V^-$, [4].

The presence of negative correlation energy can be explained by means of the Yahn-Teller effect for a multicharge defect, to which a vacancy and divacancy in silicon pertain.

Yahn-Teller effect expressed in that [5], that at the analysis of molecular compounds or crystalline systems, the effects related to vibron interactions of atoms are revealed. Such vibrations exist even at a zero temperature, as by virtue of the uncertainty principle their energy $h\nu_0/2$ (energy of zero fluctuations) cannot be equal to zero.

In accordance with the adiabatic approaching, a difference between the masses of atoms and electrons is great enough to approximately suppose that the electrons can be inertialess (adiabatically) and follow the displacement of atoms. Within the framework of such a model, it is supposed that the atoms move in some average potential created by all electrons. Such approximation in some cases is not acceptable and does not describe the effects connected with the vibration interactions. At such an interaction, the electronic states change (at displacement of atoms) and there can be a mixing of the electronic states.

In connection with such phenomenon an author [5] specifies: «vibration mixing of the electronic states is an important starting point at the analysis of origin of

molecularproperties, resulting in the series of the new phenomena and laws. The Yahn-Teller effect can be considered as a case of the vibration mixing».

For the systems with the degenerate electronic states the Yahn-Teller effect will be, that for any polyatomic system always there will be such oscillatory state of nucleus, at which energy of the degenerate state of electrons falls down, and the minimum on a potential surface is displaced to position the characteristic for the system with lower symmetry [3, 5]. Thus, the potential surface can have some minima.

At splitting of the degenerate electronic states between the levels corresponding to these states, can occur the interference transitions which are found out in infrared spectrum, or at research of thin structure of optical spectra.

At enough transparent barriers dividing the minimums of the potential surfaces, the tunnel transitions can be carried out between the proper states. If a barrier between minima is high enough the system, having got in one of minima, can be in it a long time. The static Yahn-Teller effect will be shown for such system. The Dynamic effect corresponds to that variant, when the barrier appears transparent enough for tunneling, and the system will periodically be both in one or in other the minimums.

The row of phenomena is linked with Yahn-Teller effect in the crystalline systems, for example, the arising of the structural phase transitions. This effect shows up in the biological systems; with it even links the origin of superconductivity in the doped fullerene Co_{60} [6].

The interesting feature of vacancy appeared in the inverse position of levels that means that defect is the center with negative correlation energy.

The essence of the phenomenon of the inversion of levels for a multicharge center to which the divacancy belongs, consists in that, the Yahn-Teller splitting of levels is turned out more than the energy of repulsion of levels because of coulomb interaction at attaching of electron. The last leads to the change of position of a level in the forbidden zone to a zone of conductivity owing to coulomb repulsing.

So, it appeared that the position of level $E(+/++) = 0.13$ eV is deeper than of the level $E(0/+) = 0.05$ eV. Transition from V^{2+} into V^0 at the inverse location of levels takes place with emission of two holes $V^{2+} \rightarrow V^+ + h^+ \rightarrow V_0^0 + 2h^+$ simultaneously, as a hole at the state $E(0/+)$ is linked weaker, than in $E(+/++)$, i.e., V^+ —metastable [5].

Figure 16.3 taken from [4] illustrates the position of levels of the ordinary multicharge center and the center with negative correlation energy.

As specified in this work [4] with reference to [7] probability that a vacancy can capture n electrons, it is possible to find on a formula

$$p(n) = \frac{\exp\{-[E(n) - n\mu]/kT\}}{\sum_{n'} \exp\{-\left[E\left(n'\right) - n'(\mu)\right] \backslash kT}$$

where: $n = 0, 1, 2$ for V^{2+}, V^+, V^0, correspondingly.

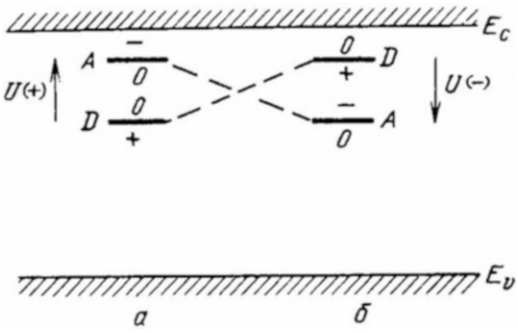

Fig. 16.3 The schematic image of a normal (a) and an inverse (**b**) locations of the levels of defect [4]

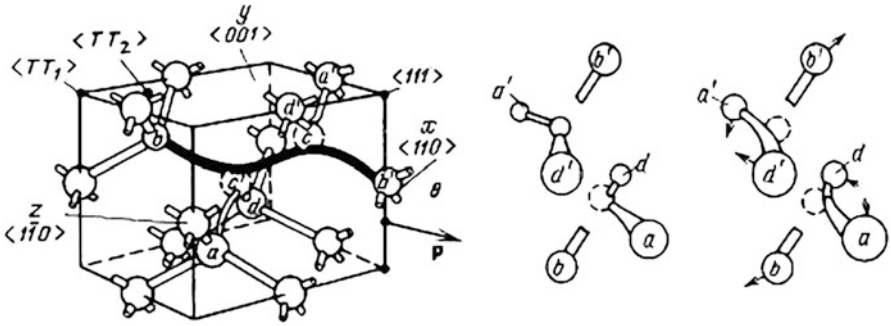

Fig. 16.4 The model of divacancy before the Yahn-Teller splitting.[4]

Thus, unlike the general formula of statistics, in which $E(n)$—the power position of the proper charge state of defect, in the expression of $p(n)$, $E(n)$ includes the energy of Yahn-Teller distortion additionally, i.e., the sum of change of the energy of electronic and the atomic subsystems of defect.

As pointed in [3], the existence of two stable (E_n and E_{n+2}) and of one unstable state is the common property of defects with negative correlation energy. For a low temperature «the system, as a rule, showed the properties of bistability», [3]. Thus, it is possible to assume that some charging states of divacancies at low temperature can be bistable defects.

Unlike of vacancy, divacancy is appeared as the defect, stable at room temperature.

As well as vacancy, divacancy is the center with negative correlation energy.

The calculations carried out by the author of [2], showed that it is the bistable center at room temperature for all charge states.

Divacancies are generated in silicon at irradiation of material by electrons with energy in diapason from 1.5 to 4.5 MeV.

The model of divacancy is presented in Fig. 16.4, taken from [4].

In [2] the electronic structure of divacancy is calculated at the (0, ± 1) charge states.

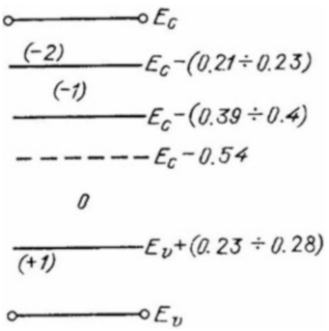

Fig. 16.5 The energies of levels corresponding to various charging states of divacancy of silicon [4]

According to [2, 4], the levels between charge states, which define the energy of divacancy, correspond to the next positions at forbidden zone:

$$\begin{aligned} E(2+/-) &= E_c - 0.23\,\text{eV} \\ E(-/0) &= E_c - (0.43-0.41)\,\text{eV} \\ E(0/+) &= E_v + (0.23-0.25)\,\text{eV}. \end{aligned}$$

Both the charge states of divacancy is paramagnetic, is what is conditioned by the presence of unpaired electron at the open electron shell, therefore at the joining of electrons, the not-paramagnetic states V_2^0 and V_2^- arise. The levels $E_v + 0.25\,\text{eV}$, $E_c - 0.4\,\text{eV}$ correspond to paramagnetic state V_2^+, V_2^-. Thus, the divacancy brings the three levels proper to four charging states: V_2^+, V_2^0 V_2^- and V_2^{2-}, Fig. 16.5, [4]

In accordance with the model, presented in [4], Fig. 16.4, at the beginning of arising, the two vacant neighboring lattice sites $c\,u\,c'$ are situated between the six broken bindings of atoms a', b', c' and a, b, c. The symmetry of such undistorted center is D_{3d}. After that the orbitals: $a-d$, $a'-d'$ and $b-b'$ are filling up by the electrons. On orbital $b-b'$ for divacancy V_2^+ the one electron is placed, and for V_2^- —three electrons. The first four electrons are filling the singlet states, and at filling of open shell (doublet), because of Yahn-Teller effect, its splitting occurs.

The unfilled shell is forming by the orbital ε_u and at small distortion (displacement of atoms), which match to lowering of symmetry $D_{3D} \rightarrow C_{2h}$, the component of distortion E_g corresponds to it. In [2] it is shown that for divacancy the Yahn-Teller effect has the two-mode character, and is present in the vibratory tie of an electronic orbital doublet with the resonant r and coupling p modes of the distortion. In accordance with [2]: «the coupling mode p is responsible for the approaching of a pairs of atoms 2–3 and 5–6 and formation of weak covalent bonds between the atoms 1 and 4. Resonance mode r is responsible for the five-coordinate state of atoms 1–4, the weak bonds of which are resonates» (Fig. 16.6, taken from [2]).

In [2] it is revealed that not everyone distortion leads to downturn of dimension of an open shell and only distortion E_g, lowering symmetry up to C_{2h}, appeared as the Yahn-Teller distortion. The calculation curves of multiplex structures of divacancies resulted as shown in Fig. 16.7, [2].

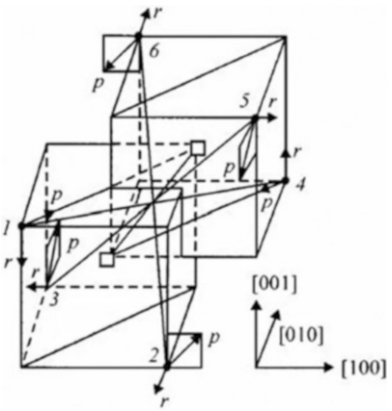

Fig. 16.6 The disposition of divacancy at the encirclement of silicon atoms. Atoms are described by the circlets, the divacancy—by the squares [2]

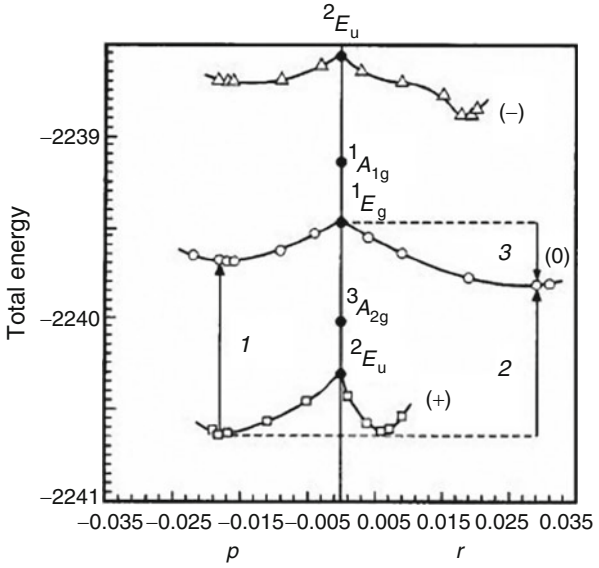

Fig. 16.7 The multiplex structure of the charge states of divacancy at dependence on two-mode distortion of Yahn-Teller [3]

In Fig. 16.7, the terms of totally symmetrical configurations designate by the dark circles, the energy of the basic states depending on the distortions designated by the light circles. The direct (1) and indirect (2) transitions between the charge states, the energy of Yahn-Teller stabilization (3) for the neutral states are shown by arrows.

Thus, the calculations which have been carried out [2] have confirmed the two-well character of a surface of potential energy of divacancy in the three charge states. According to the carried-out in [2] calculations, the energy of Yahn-Teller stabilization is equal 0.34 eV; the differences between absolute and metastable minima of adiabatic energies is 0.16 eV for V_2^- (r—mode of the distortion of basic station)), 0.07 eV for V_2^0 (r—mode) and 0.03 eV for V_2^+ (p—mode).

16.3 The Interference Phenomena in the Quantum Systems

16.3.1 The Superposition's States in Quantum Systems

The interference of waves in classical physics is the phenomenon, most typical of monochromatic waves with close lengths of waves. This phenomenon follows from a principle of superposition of wave oscillations, described in classic physics (in optics, radio physics); in accordance to it, at superposition of two waves, with close frequencies, the amplitudes of waves are summed up.

For quantum systems also take place, the interferential phenomena. The possibility of their existence is defined by a principle of the superposition of quantum system, which is one of the basic principles of quantum theory [8].

This principle consists in the following:

1. If the system can be in any state described by functions Ψ_1 and Ψ_2, it can be in a state as thus:

$$\Psi = \alpha\Psi_1 + \beta\Psi_2 \tag{16.1}$$

   where α and β are any complex numbers, not depending on time.
2. At multiplication of wave function of quantum states on any complex number, the new wave function will describe the same states.

It is necessary to specify for the system of identical particles, those states which satisfy conditions of the symmetry of system [8]that are allowable only. The superposition of quantum states has essential differences from superposition of the waves described by classical physics. One of them consists of those, that its consequence is the possibility of existence of the system in a state named by the superposition state, for which there is no analogue in classical physics.

So, if a particle can be with certain probability in the states Ψ_1 and Ψ_2 with impulses p_1 and p_2, then in the superposition state, described (Eq. 16.1), an impulse is the indefinite quantity.

One of the examples of the superposition state can by the state of proton in the system of hydrogen bonds of molecules of water that determines the many features of properties of this substance, primary for all alive. Quantum systems with the degenerate states, split in the magnetic field, or because of Yahn-Teller effect, can also pass to the superposition state.

For the quantum systems having the close energy states, the interference transitions can show up at their superposition [9, 10]. Here we will analyze the interference transitions for two quantum states with a small energy gap between them.

Let's consider, at first, the stationary states without affixment to some system of coordinates. Let some degenerate states be described by functions Ψ_1 and Ψ_2. Let's assume, that these conditions can also be described by functions φ_1 and φ_2. Passing to them is the turn in Hilbert space.

If the disturbance removing degeneration is entered, then the already selected system of coordinates appears. Now wave functions of states will become:

$$\Psi_1 = \Psi_1(0)\exp\left(i\frac{E_1}{\hbar}t\right)$$
$$\Psi_2 = \Psi_2(0)\exp\left(i\frac{E_2}{\hbar}t\right) \tag{16.2}$$

The states described by function (16.1) already will not be stationary. If a disturbance is absent, the states described by functions φ_1 and φ_2 are stationary. If the disturbance is present, the stationary states will be the states which correspond to the conserved quantities, i.e., to quantities, the operators of which commute with the Hamiltonian $\hat{H}$. And it is already defined by the symmetry of a field.

The interferential transitions are characteristic both for the individual atoms and the molecular systems, for particles (for example, for k_1, k_2 -mesons) and for various defective systems of monocrystal objects. Special interest represents such extremely important material for the industry, as silicon.

16.3.2 The Consideration of the Literary Data on Vacancy and Divacancy in Silicon from a Standpoint of Existences of Quantum Superposition States

From the brief review of properties of radiating defects—vacancy and divacancy—carried out here follows, that for them the phenomena of interference transitions must arise between both the split's electronic levels of degenerate states and between the states of minimums of adiabatic potential surfaces.

Vacancy at low temperatures can behave as a bistable defect. It means that if in the configuration diagram there are some minima, divided by a barrier, in such a system there can be the tunnel's splitting, and the tunnel transitions occur. The character of such transitions will depend on the height of barrier and from a temperature. Because with the increase of temperature a vacancy disappears, it is possible that pulsations from the probable tunnel transitions accelerate this process. Thus, at the increase of temperature the defect of vacancy type shows up already as unstable. On the other hand, the interference transitions will be characteristic of electrons, situated on the levels, splitting by virtue of Yahn-Teller effect. States, proper to the electronic system of the degenerate states will be non-stationary.

Unlike of vacancy, the divacancy is a defect having stable characteristics at normal temperature and by virtue of it is investigated well enough.

As specified higher, at forming of divacancy takes place the orbital filling by the electrons from torn off bonds, and the spatial reorientation of the divacancy with the lowering of degree of symmetry. Two modes—resonance r and coupling p,—correspond to small distortion $D_{3d} \rightarrow C_{2h}$.

The double degenerate electronic states are split. For all charge states as have shown calculations of work [2], is revealed the two-well's character of multiplex structures of divacancies.

In accordance with the calculation values [2], the height of barrier between minimums of divacancy for every charge state does not exceed the value of 0.34 eV (pointer 3 on рис.7). Such value of height of a potential barrier of divacancy in pure silicon specifies the relative stability of divacancy to thermal fluctuations. Such stability is promoted also by that factor that in the field of its formation there is a strong distortion of a lattice of a crystal, which can additionally shield it from external kT- influence. But it does not mean that between the proper minima there cannot be tunnel transitions.

Thus, it appears that the divacancy represents the quantum system which should be described from a position of possible superposition transitions between two possible statuses. Taking into account that the position of minimums is shifted on 0.07 eV for V_2^0 (r-mode) and 0.03 eV for V_2^+ (p-mode), for these charge states, the tunnel transitions, in principle, are possible; however a probability of finding of the system in each of these nonequivalent minimums in the absence of external influence should differ.

It is possible to suppose also that for V_2^- (position of its minimum is shifted on 0.16 eV,—the r- mode distortions of basic state) such transitions will be mainly blocked because a difference in the position of minimums here is greater, than for V_2^0—and V_2^+- states of the defect.

The situation can change essentially at any insignificant distortions of a lattice or at changes of structure of the atoms surrounding the areas of divacancy, and also due to feeding of voltage impulses on these areas. Another way of external influence is possible also, that means that it is possible to manage these states. It opens the ways for the use of such defects as cells with two possible states in the devices of quantum informative systems.

Both the transitions between minimums of adiabatic surfaces and the superposition states of the split levels of opened electron shells it is possible to describe from position of interference transitions in the quantum systems with two states. We shall use for the description of such transitions in bistable defects (vacancy and divacancy in silicon) the same approach, that was developed and in [10].

With the position of theory of such transitions, if there are two any stationary states Ψ_1 and Ψ_2 with close energy w_1 and w_2, proper to operator W, than between these states the transitions are possible, and the system Ψ describing such state is non-stationary:

$$\Psi = \alpha_1 \Psi_1 e^{i\omega_1 t} + \alpha_2 \Psi_2 e^{i\omega_2 t} \tag{16.3}$$

where α_1, α_2—the complex numbers: $a_1 = |a_1| e^{i\delta_1}$ and $a_2 = |a_2| e^{i\delta_2}$ which satisfy the condition: $|\alpha_1|^2 + |\alpha_2|^2 = 1$.

If in quality of such systems to take the bistable defect having two minimums on a surface of potential energy, the position of system in one of the minima Ψ_1 or Ψ_2,

at non-transparent barrier, will correspond to a stationary state. In that case if the barrier appeared transparent for tunneling, the system passes to the stationary state, described by the Eq. (16.3). As pointed in [10], instead of "the non-coherent mix of two stationary states we deal here with their superposition, adequate to some non-stationary state."

In this respect, the remark of the author [5] about the dependence of the measurement results of some parameters of bistable defect corresponding to the tunnel transitions, from the methods of measurement must be qualified, as it does not correspond to the quantum reality of superposition states and relate to the classic approach.

If besides the wave functions Ψ_1 and Ψ_2 to introduce the orthonormal functions φ_1 and φ_2 are as follows:

$$\varphi_1 = \frac{\Psi_1 + \Psi_2}{\sqrt{2}}, \quad \varphi_2 = \frac{\Psi_1 - \Psi_2}{\sqrt{2}}, \tag{16.4}$$

then they will describe too, the superposition state of our system. Really:

$$\Psi = \frac{\alpha_1 e^{i\omega_1 t} + \alpha_2 e^{i\omega_2 t}}{\sqrt{2}}\varphi_1 + \frac{\alpha_1 e^{i\omega_1 t} - \alpha_2 e^{i\omega_2 t}}{\sqrt{2}}\varphi_{21}. \tag{16.5}$$

Here the functions φ_1 and φ_2 proper to some other operator E having the eigenvalue ε_1, ε_2.

In such case the probabilities that the systems take on values w_1 и w_2 will be determined by coefficients α_1, α_2,—and takes on values ε_1, ε_2 by sizes $p_1 p_2$:

$$\begin{aligned} p_1 &= \frac{1}{2}\left\{|a_1|^2 + |a_2|^2 + 2|a_1||a_2| \cos(\Omega t + \delta)\right. \\ p_2 &= \frac{1}{2}\left\{|a_1|^2 + |a_2|^2 - 2|a_1||a_2| \cos(\Omega t + \delta)\right. \end{aligned} \tag{16.6}$$

where: $\Omega = \omega_1 - \omega_2$, $\delta = \delta_1 - \delta_2$.

Thus, if the probabilities of being in one of the states Ψ_1 or Ψ_2, determined by the coefficients α_1, α_2 do not depend on time, then for the $p_1 p_2$ such dependence is present and determined by Eq. (16.6). Thus for $|\alpha_1| = |\alpha_2| = 1/2$, the transitions will be most brightly expressing. The absence of energy gap between the minima of the potential energy on the surface of potential energy (for case of a bistable defect) corresponds to such a case.

In common case the coefficients α_1, α_2 depend from the time and Eq. (16.1) is decided by the method of perturbation theory.

In that case, if not dependent on time wave functions Ψ_1 and Ψ_2 to choose as basic states of system, the equation for any states of system will be written down as follows:

$$\Phi = \beta_1(t)\Psi_1 + \beta_2(t)\Psi_2 \tag{16.7}$$

Such equation can be applied to the descriptions of the behavior of bistable defects.

For the bistable defect, the static Jahn-Teller effect will correspond to the case, when a barrier is practically opaque, or the positions of minima differ enough substantially, to which a considerable difference of modulus of coefficients α_1, α_2 (Eq. 16.3) corresponds. The system will be for a long time in one of minima.

The dynamic effect is realized for the transparent-enough barriers. Thus the tunnel split of levels [4] described by functions φ_1 and φ_2 is found out.

The system passes on to the non-stationary state.

The period of passage (or a beating) between states is defined [8, 11] by an exponent of transparency of barrier:

$$D = \mathrm{e}^{-\frac{2}{\hbar}\int_a^b \sqrt{2m(U-E)}\mathrm{d}x} \tag{16.8}$$

As pointed in [2], the multiplex structure of divacancy in all of its charge states as a function from two-mode distortion has two-well character. For many mode systems, as shown in [4], it is possible so to pick up coordinates, that the type of surface of potential energy will be of quality such as in the one-mode task, where the vibronic effects are revealed only in one mode. It considerably simplifies the analysis of such system.

The Jahn-Teller effect leads to splitting of levels corresponding to states φ_1, φ_2, on a value $\Delta E = \varepsilon_2 - \varepsilon_1$.

In accordance with [5, 8, 9] the level's splitting means that the states Ψ_1, Ψ_2 are already not stable and in the system, the beats with the frequency of $f = \Delta E/\hbar$ arise.

The system makes the tunnel transitions between the minima of adiabatic potential. The transition time τ is inversely proportional to the size of a tunnel splitting. Demonstrably such transitions can be considered as pulsing deformations, since the position of system (of the defect or of the molecular system) in each minimum corresponds to the certain deformation, or the certain displacement of atoms.

Because of $\Delta E \ll \hbar\omega$ (ΔE—the value of tunnel splitting) the frequency of pulsing (beatings) movement of atoms is much smaller than the frequency of some possible vibrations $\hbar\omega$ in a deformed state.

The beating must be appeared on the resonant frequencies, inherent only for divacancies. The excitation of crystal on such frequencies probably, will allow manipulating by some parameters of divacancy that is important to practical applications.

As pointed in [5], for Jahn-Teller's systems there is an effect of the strengthening, shown in that the small deforming disturbances can significantly strengthen the distortions, inherent to the system. Some of such effects can be found out only in presence of the external distorting indignations. Therefore may be rational too, the

entering of some type of defects in silicon by means of the proper treatment of silicon material.

We will mark that the interference transitions take place and between the states of split levels of electron. The splitting of the degenerating levels corresponds to change of symmetry of systems, at which in a system the selected directions appear.

The various vibrations of atomic systems in common case are also not independent and between the different vibration states also may be the interferential transitions.

It is necessary also to suppose that the superposition states are present and in the clusters formations which include the different defects, and such states in a considerable extent determine the entangling of its elements and, as a result, the parameters of their stability.

16.4 Conclusion

On the basis of literary information, the descriptions of such defect of silicon, as vacancies and divacancies, are analyzed. These types of defects are entered in silicon at a radiating irradiation.

For divacancy in all its charge states, the adiabatic potential has two minimums, divided by a high quantum barrier (the height of barrier is more kT), that provides to it stability at room temperatures.

Besides, as follows from literary data, the rather high value of energy of Jahn-Teller stabilization is found out, (0.34 eV for a neutral state), that testifies the presence of the strong vibronic bond. At an opaque barrier the system is in a stationary state in one of the minima of adiabatic energy.

At a transparent-enough barrier, the system already is not stationary and the tunnel transitions between the minimums of potential energy are possible. The splitting of a level of a stationary state corresponds to this case and the frequency of transitions is inversely proportional to a size of tunnel splitting.

At such characteristics of divacancy at a transparent-enough barrier, the tunnel transitions between minima of adiabatic surfaces are possible

Such transitions can be considered as pulsing deformations since the position of the system in each minimum corresponds to the certain displacement of atoms. Frequency of the pulsing (beating) movements of a divacancy is much smaller than frequencies of some possible vibrations in the deformed state.

Also, it is shown, that for the divacancies, as quantum systems, can be shown the interferential transitions at all levels of the quantum organization of such systems,—at levels of the interactions connected with vibronic fluctuations, electronic interactions; with quantum correlations between the bistable states.

The results submitted in the present work can find application for further theoretical developments, and be taken into account at constructing of some devices of the quantum informative systems.

References

1. Schrodinger E (1935) Natural sciences. In: Modern situation in quantum mechanics, vol 23. pp 807–812, 823–828, 844–849 (on German)
2. Moliver SS (1999) Method of the opened shell for the electronic structure of divacancy of silicon. Phys Solid State 41(3):404–410 (in Russian)
3. Mukashev BN, Abdulin KA, Gorelkinskiy YV (2000) The metastable and bistable defects in silicon. Successes Phys Scy 170(2):143–155 (in Russian)
4. Vavilov VS, Kiselev VF, Mukashev BN (1990) In: The defects in silicon and on its surface. Nauka, Moscow, 211 p (in Russian)
5. Bersuker IB (1987) In: The Jahn-Teller effect and vibronic interaction in modern chemistry. Plenum, New York, 343 p (in Russian)
6. Loktev VM, Pashitskii EA (1992) The Jahn-Teller effect in the molecules of C60, as possible reason of superconductivity of a doped fullerite. J Exp Theor Phys Lett 55(8):465–468 (in Russian)
7. Kock AFR, Roksnoer PJ, Boonen PGT (1973) Semiconductor Silicon. In: Huff HR, Burgers R (eds) 2nd International Symposium on Silicon Materials Science and Technology. Electrochemical Society, New York, pp 83–94
8. Davydov AS (1973) In: The quantum mechanics. Nauka, Moscow, 703 p (in Russian)
9. Feynman R, Leyton R, Sands M (1966) In: Feynman's lectures on physics. Addison–Wesley, Reading, MA, 271 p (in Russian)
10. Podgoretskiy MI, Khrustalev OA (1963) About some interference phenomena in quantum transitions. Successes Phys Scy LXXXI(2):217–247 (in Russian)
11. Shpolskiy EV (1974) In: The atomic physics. Nauka, Moscow, 447 p (in Russian)

Chapter 17
Surface Pattern Formation in 2D System of Liquid Crystalline Molecules

Agnieszka Chrzanowska and Paweł Karbowniczek

17.1 Introduction

Two-dimensional structures occur in many areas of science and technology. They are important, for instance, in studying properties of thin layers of liquid crystals, adsorption of nanomolecules on solid surfaces [1–3], surfacial arrangement of nano and colloidal particles [4] or, also, behavior of vibrated granular materials on the plane [5–7]. Understanding molecular and thermodynamical factors that influence the shape of surface patterns may help in governing the directed self-assembling processes and also in tailoring surface patterns with anisotropic nanoparticles that are so much important in technology, mostly for applications in photoelectronic industry.

Hard spherocylinders are one of the most popular models used to study the above-mentioned anisotropic formations [8–12]. It finds its applications especially for real colloidal and nanoscopic systems that are composed of hard elongated rodlike molecules. It has been found, mainly by the Monte Carlo simulations, that spherocylinders of a sufficiently large length of the molecule can form nematic as well as smectic liquid crystalline phases. For shorter molecules upon increasing the density the system of spherocylinders transforms directly into the solid phase. The resulting phase diagram is rich (see Fig. 2 in [13]) and the equation of state strongly depends on the length-to-width aspect ratio of the considered spherocylinders.

The density functional theories (DFT) (for instance, [14–23]), which are widely used for description of nematic as well as smectic phases, underestimate the density

A. Chrzanowska (✉) • P. Karbowniczek
Institute of Physics, Kraków University of Technology, ul. Podchorążych 1,
30-084 Kraków, Poland
e-mail: achrzano@usk.pk.edu.pl

O. Fesenko, L. Yatsenko (eds.), *Nanophysics, Nanophotonics, Surface Studies, and Applications*, Springer Proceedings in Physics 183,
DOI 10.1007/978-3-319-30737-4_17

(or temperature) dependencies, since they are performed only within the framework of the second virial approximation. Fortunately, semiempirical scalings like the Parsons and Lee scaling [24] can help to improve the accuracy of prediction of the accurate phase transition points.

One can expect that the richness of the spherocylinders anisotropic properties can be mirrored on the properties of two-dimensional spherocylinders—discorectangles. In this case the density functional theories are also more tractable due to the reduced dimension of the integrals present in the theory. Relatively easily, it is also possible to extend the DFT description to the case of a binary mixture of particles of different lengths and widths, which may lead even to a broader spectrum of interesting results.

In view of the need to understand and control the surface pattern formations a few interesting examples emerging from the DFT theory for two-dimensional discorectangles will be here discussed together with the factors responsible for their structure.

The paper is organized as follows. Section 17.2 provides the basis of the Onsager theory adjusted to the smectic geometry for the case of a two-dimensional smectic liquid crystal with a simplifying assumption of perfect alignment. Section 17.3 gives the results and Sect. 17.4 is the summary.

17.2 Onsager Theory

We consider a system of perfectly aligned discorectangles (two-dimensional spherocylinders) of length L and width σ, as in Fig. 17.1. In such a system, by changing values of L and σ one can obtain different shapes of particles ranging from discs, through discorectangles of different length-to-width ratio L/σ, till infinitely thin needle like objects. Upon increasing density the particles may arrange themselves into layers whose positional order will depend on the particles parameter L. Mixing particles with different geometrical parameters may result even in richer scenarios of arrangement. One can also obtain phase separation. The emerging structures are the result of competition between excluded volume of the particles, orientational entropy, and mixing entropy.

According to the Onsager theory [25, 26] the state of a given particle is described by the function ρ, which, in general, is the probability to find a particle at the point $\mathbf{r}$ and having the orientation Ω. ρ is normalized to the number of particles N and can be obtained by solving the self-consistency equations

$$\log\rho_i = \int (e^{-\beta U_{ij}} - 1)\rho_j d(j), \tag{17.1}$$

where $d(j) \equiv d\mathbf{r}d\Omega$ and U_{ij} is the interparticle potential acting between the molecule i and j. $(e^{-\beta U_{ij}} - 1)$ is the so-called Mayer function. This equation formally results from the minimization of the free energy.

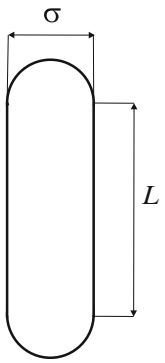

Fig. 17.1 Geometry of a discorectangle

For perfectly aligned particles, which can arrange themselves along Y direction the self-consistency equations can be transformed into the form with only one-dimensional integral

$$\log f_i = -d_{\mathrm{Ons}} \int_{-\infty}^{+\infty} V_{ij}^{excl} f_j dy_j. \tag{17.2}$$

V^{excl} is here an excluded area which comes from the Mayer function averaged along the X direction in the case of hard bodies, d_{Ons} is the density, (we will call it the Onsager density) and f is the distribution function normalized to unity as

$$\frac{1}{S_d} \int f dy = 1, \tag{17.3}$$

where S_d is the characteristic length of the periodic structure. The exact value of S_d is being obtained due to minimum of the free energy with respect to the periodicity values (see [3, 27]).

In the case of a binary mixture of the particles of A and B type, the self-consistency equations transform into the set

$$\begin{aligned} logf_A &= -x_A d_{\mathrm{Ons}} \int_{-\infty}^{+\infty} V_{AA}^{excl} f_A dy_A - x_B d_{\mathrm{Ons}} \int_{-\infty}^{+\infty} V_{AB}^{excl} f_B dy_B \\ logf_B &= -x_B d_{\mathrm{Ons}} \int_{-\infty}^{+\infty} V_{BB}^{excl} f_B dy_B - x_A d_{\mathrm{Ons}} \int_{-\infty}^{+\infty} V_{AB}^{excl} f_A dy_A \end{aligned} \tag{17.4}$$

where x_A and x_B are fractions of the particles A and B type, respectively [28, 29].

Introducing exact values of V^{excl} for discorectangles into the Onsager theory and solving self-consistency equations, one obtains density distributions, energies, and layer thicknesses for different types of layer arrangement and different components A and B. A few characteristic examples of surface patterns that can be foreseen from this theory are given in the next section. These results have been obtained using the algorithm originated in [30] and adapted for the above case as given in [27].

To obtain realistic densities in what follows the Parsons Lee scaling [31] based on the scaled-particle theory equation of state

$$d_{Ons} = \left[-\ln(1-\eta) - \frac{1}{1-\eta} \right] /2 \tag{17.5}$$

has been used. $\eta = \widetilde{d}\, v_0$ is here the packing fraction, where $\widetilde{d}$ is the rescaled density and v_0 is the proper volume of the particle. In the case of a binary mixture of particles A and B the effective proper volume is given by

$$v_0 = x_A(L_A\sigma_A + \pi\sigma_A^2/4) + x_B(L_B\sigma_B + \pi\sigma_B^2/4); \tag{17.6}$$

The predictions based on the above rescaled density $\widetilde{d}$ are consistent with the predictions of the hard spheres theories [32] and also have been found to be very close to the outcome of the Monte Carlo simulations for many different mesogenic molecules within the range of the liquid crystalline regime [13].

17.3 Results

The system, on the basis of which different two-dimensional structures will be presented, is made from the particles described only by two geometrical parameters like in Fig. 17.1.

The first structure we are going to present is for a system of the particles of the same kind.

In Fig. 17.2 the density profiles for a system built from discorectangles of $L = 0.5$ and $\sigma = 0.1$ are given for a set of the packing fractions. For $\eta = 0.6015$ ($d_{\mathrm{Ons}} = 21$) one observes here an onset of the layer formation with a well-recognized smectic structure with multiple regular peaks, yet the nonzero parts of the whole profile indicate that there are particles within the entire volume of the system. The lowest parts are still at the level of 0.5. For higher values of packing fractions $\eta = 0.6143$ ($d_{\mathrm{Ons}} = 22$) and $\eta = 0.6378$ ($d_{\mathrm{Ons}} = 24$) the probability to find a particle with its center position in between the smectic layers decreases. At the same time the peaks denoting smectic layers are getting more pronounced, increasing their heights, yet being almost of the same width. There is also observed a slight change in the width of the layer thickness S_d. Upon increasing density (and packing fraction) this width diminishes. The profile for the highest value of $\eta = 0.6954$

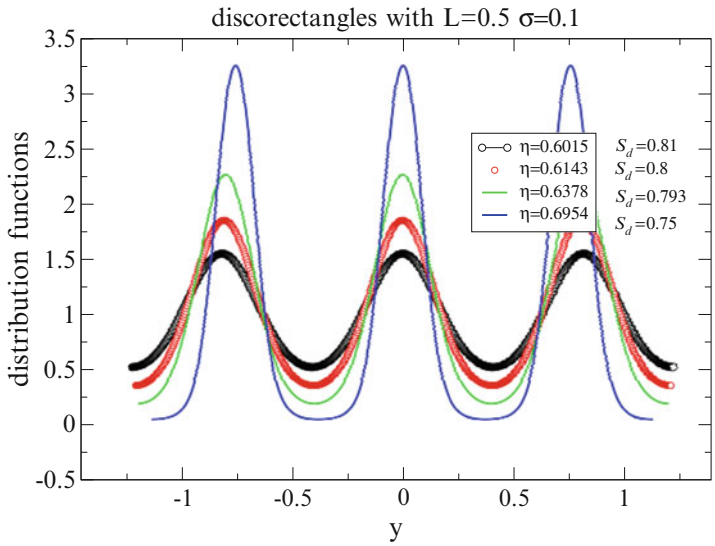

Fig. 17.2 Density profiles (distribution functions from the Onsager theory) for a smectic phase for a system built from the discorectangles of length $L = 0.5$ and width $\sigma = 0.1$ obtained for different values of the packing fraction

($d_{\mathrm{Ons}} = 30$) shows that there are almost no particles in between the layers. Note, however, that this curve may not be real in the sense that for such packing fractions the phase may not be smectic but already solid. On the basis of the Onsager theory it is not possible to judge about the transition to the solid phase. Also Parsons scaling is not valid for solid or hexatic phases. This curve is presented here for a comparison purpose.

An artistic view of the smectic layers is given in Fig. 17.3.

In Fig. 17.4 an example of the density profiles for a binary mixture of thin and thick discorectangles is given. The thin particles are 10 times thinner. According to these results the smectic layers contain both types of the particles and the system is fully miscible. The peaks of the thicker particles are higher and thinner than the profiles corresponding to the thinner particles which can be also found, to some degree, at any position also in between the layers.

The situation becomes different if we mix rodlike particles and discs, like in Fig. 17.5. Here one observes apparent phase separation into layers rich in discs and layers rich in discorectangles. Hence, subsequent layers, whose position is given by subsequent peaks, are completely of different type. It is possible, however, to imagine that the discs can be present also within the layer of the rodlike particles—probably in the form of a column of discs. Probability is not high, yet it is noticeably nonzero. Such a phase separation is realized because of the packing frustration that will be present if the system is forced to mix. As a result of this frustration demixing occurs.

An artistic view of the layer phase separation process is given in Fig. 17.6.

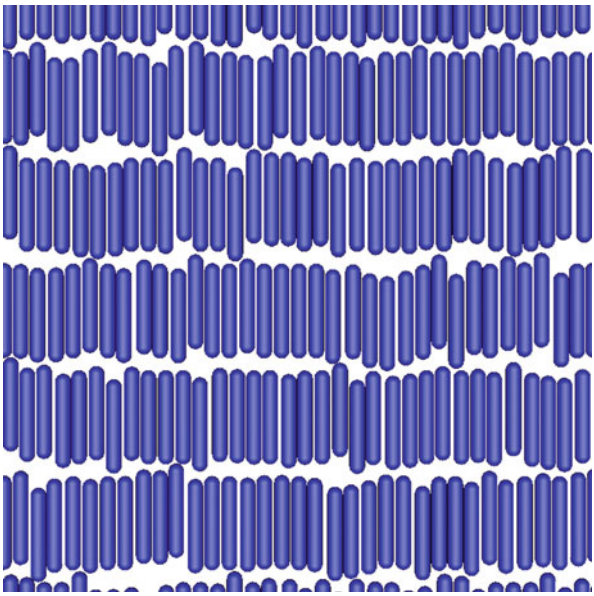

Fig. 17.3 An artistic view of the smectic system

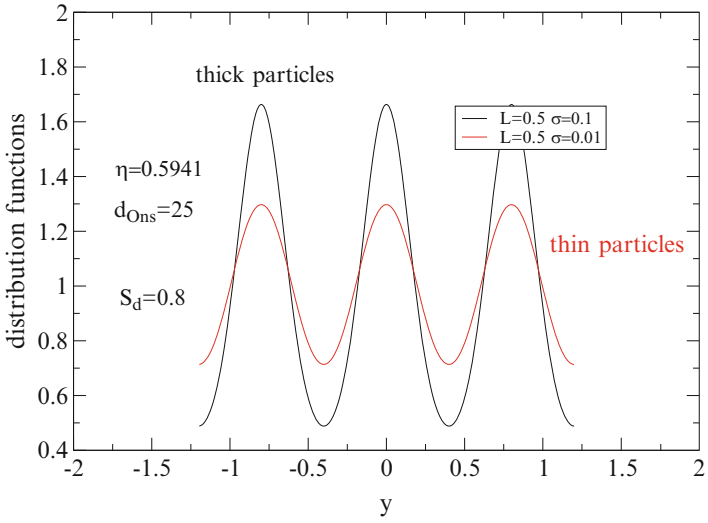

Fig. 17.4 Density profiles (distribution functions from the Onsager theory) for a smectic phase for a system built from the thin and thick particles of the same length $L_A = L_B = 0.5$ but for different widths $\sigma_A = 0.1$ and $\sigma_B = 0.01$; the packing fraction is $\eta = 0.5941$ and the compositions are $x_A = 0.8$ and $x_B = 0.2$

Tendencies to demix between different fluid phases have already been observed in mixtures where constituent particles are of different sizes, for instance in the system of hard squares of different sizes [33]. This effect is present when the size ratio of the constituent particles is sufficiently large. In the 3D case of a mixture

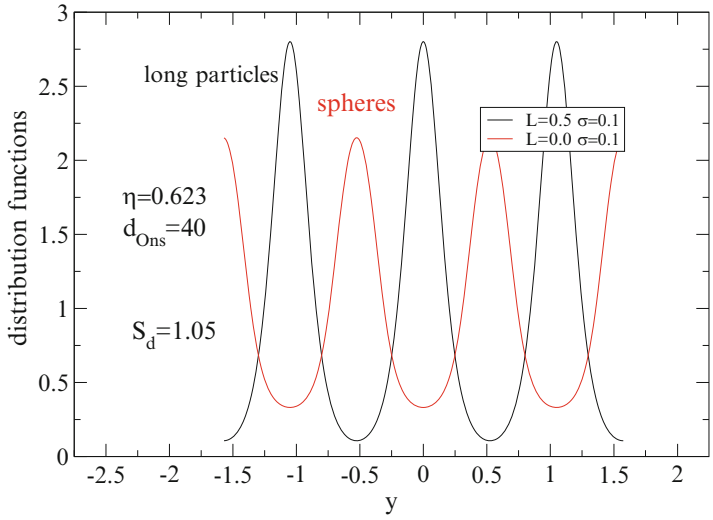

Fig. 17.5 Density profiles (distribution functions from the Onsager theory) for a smectic phase for a system built from discorectangles with $L_A = 0.5$, $\sigma_A = 0.1$ and spheres of the diameter $\sigma_B = 0.1$; the packing fraction is $\eta = 0.623$. Apparent phase separation is observed with layers made purely from spheres and layers made from discorectangles

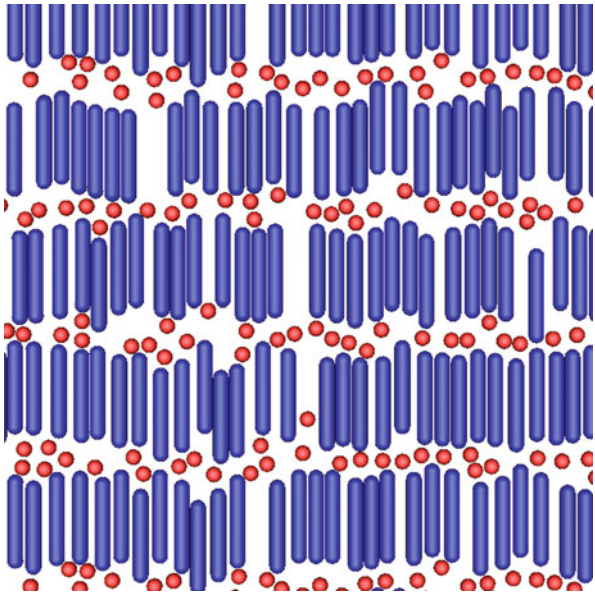

Fig. 17.6 An artistic view of the rod disc mixture

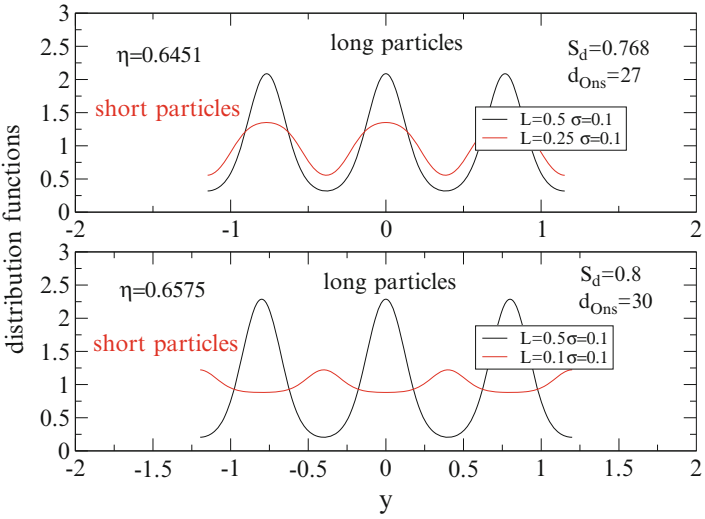

Fig. 17.7 Density profiles (distribution functions from the Onsager theory) for a smectic phase for a system built from the long and short particles of the same thickness $\sigma_A = \sigma_B = 0.1$ but for different lengths. The compositions used are $x_A = 0.8$ and $x_B = 0.2$. The *upper panel* is for $L_A = 0.5$ and $L_B = 0.25$ with the density fraction equal to $\eta = 0.6451$ and density $d_{\text{Ons}} = 27$ and the *lower panel* is for $L_A = 0.5$ and $L_B = 0.1$ with the packing fraction equal to $\eta = 0.6575$ and the Onsager density $d_{\text{Ons}} = 30$. In the latter case a partial phase separation occurs

made of hard spheres and parallel hard spherocylinders it has been even found that the layered phases exhibit an enhanced stability as compared to spherocylinders of the same kind [34].

Demixing can be also obtained for a mixture of rodlike particles with different lengths, like in Fig. 17.7. Here the particles are of the same width $\sigma_A = \sigma_B = 0.1$, but different lengths. In the upper panel of Fig. 17.7 when $L_A = 0.5$ and $L_B = 0.25$ the system is fully miscible, the peaks describing position of the A and B particles are in the same place. However, in the case from the lower panel when discorectangles B are short ($L_B = 0.1$) one observes partial demixing. Shorter particles are still present within the layers of longer particle, yet the tendency is observed to build a separate layer in between the longer particles rows. An interesting conclusion occurs from a comparison of the lower and upper panels: the partial phase separation occurs when the length of the shorter particles becomes commensurate with the space between long particles layers.

17.4 Summary

A two-dimensional system of hard discorectangles has been studied in purpose to explore the possibility to obtain controlled nanopatterned surfaces. Changing the shape parameters like the particles length or thickness a rich scenario of possible

patterns is observed together with the phase separation for the case of a binary mixture of discorectangles and spheres. Visualization of the discussed structures has been given. The resultant patterns come from the competition between excluded volume, orientational entropy, and mixing entropy.

The presented results may also serve as a guide for directed self-assembly patterns of nanoparticles on surfaces as well as a reference model for the granular spherocylinders on a vibrated plane. The analysis has been performed under the assumption of perfect alignment.

Acknowledgements This work was supported by DS Grant no F-1/46212015/DS of Institute of Physics of Kraków University of Technology.

References

1. Gong J-R, Wan L-J (2005) Two-dimensional assemblies of banana-shaped liquid crystal molecules on HOPG surface. J Phys Chem B 109:18733–18740
2. Martínez-González JA, Varga S, Gurin P, Quintana-H J (2012) Spontaneously bended nematic and antiferroelectric smectic structures of banana-shaped hard particles in two dimensions. EPL 97:26004p1–26004p6
3. Karbowniczek P, Cieśla M, Longa L, Chrzanowska A (submitted to *Liquid Crystals*)
4. Sau TK, Murphy CJ (2005) Self-assembly patterns formed upon solvent evaporation of aqueous cetyltrimethylammonium bromide-coated gold nanoparticles of various shapes. Langmuir 21:2923–2929
5. Narayan V, Menon N, Ramaswamy S (2006) Nonequilibrium steady states in a vibrated-rod monolayer: tetratic, nematic, and smectic correlations. J Stat Mech: P01005, 1–17
6. Herrmann HJ, Luding S(1998) Modeling granular media on the computer. Cont Mech Therm 10:189–231
7. Lee J (1994) Heap formation in two-dimensional granular media J Phys A Math Gen 27:L257–L262
8. Veerman JAC, Frenkel D (1990) Phase diagram of a system of hard spherocylinders by computer simulation. Phys Rev A 41:3237–3244
9. Polson JM, Frenkel D (1997) First-order nematic-smectic phase transition for hard spherocylinders in the limit of infinite aspect ratio. Phys Rev E 56:R6260–R6263
10. Stroobants A, Lekkerkerker HNW, Frenkel D (1986) Evidence for smectic order in a fluid of hard parallel spherocylinders. Phys Rev Lett 57:1452–1455
11. A. Stroobants, Lekkerkerker HNW, Frenkel D (1987) Evidence for one-, two- and three-dimensional order in a system of parallel hard spherocylinders. Phys Rev A 36:2929–2945
12. Veerman JAC, Frenkel D (1991) Relative stability of columnar and crystalline phases in a system of parallel hard spherocylinders. Phys Rev A 43:4334–4343
13. Bolhuis P, Frenkel D (1997) Tracing the phase boundaries of hard spherocylinders Phys Rev E 106: 666–687
14. Poniewierski A, Sluckin TJ (1992) Density Functional Theory of Liquid Crystal Phases. Mol Cryst Liq Cryst 212:61–75
15. Poniewierski A, Holyst R (1998) Density functional theory for nematic and smectic A ordering of hard spherocylinders. Phys Rev Lett 61:2461–2464
16. Graf H, Löwen H (1999) Density functional theory for hard spherocylinders: phase transitions in the bulk and in the presence of external fields. J Phys Condens Matter 11:1435–1452
17. Velasco E, Mederos L, Sluckin TJ (1996) Molecular theory of smectic C liquid crystals. Liq Cryst 20:399–410

18. Kyu T, Chiu HW, Kajiyama T (1997) Induced smectic phase in a nematic liquid crystal mixture. Phys Rev E 55:7105–7110
19. Govind AS, Madhusudana NV (2001) A simple molecular theory of smectic-C liquid crystals. EPL 55:505–511
20. Huang CC, Dumrongrattana S (1986) Generalized mean-field model for the smectic-A-chiral-smectic-C phase transition. Phys Rev A 34:5020–5026
21. A. V. Emelyanenko AV, Khokhlov AR (2015) Density-functional theory of inhomogeneous systems of hard spherocylinders. J Chem Phys 142:204905–204917
22. Velasco E, Mederos L, Sullivan DE (2000) Density-functional theory of inhomogeneous systems of hard spherocylinders. Phys Rev D 62:3708–3718
23. Pająk G, Osipov MA (2013) Unified molecular field theory of nematic, smectic-A, and smectic-C phases. Phys Rev E 88:012507–012519
24. Martínez-Ratón Y, Velasco E (2008) Nonuniform liquid-crystalline phases of parallel hard rod-shaped particles:From ellipsoids to cylinders J Chem Phys 129:0549071–0549079
25. Evans R (1979) The nature of the liquid-vapour interface and other topics in the statistical mechanics of non-uniform, classical fluids. Adv Phys 28:143–200
26. Onsager L (1949) The effect of shape on the interaction of colloidal particles. Ann NY Acad Sci 51:627–659
27. A. Chrzanowska, Still in preparation
28. Chrzanowska A (1998) Bicritical points in a nematic rod-disk mixture. Phys Rev E 58:3229–3236
29. Chrzanowska A (2013) Bifurcation analysis of a two-dimensional binary mixture of hard needles. Acta Phys Pol B 44:91–105
30. Chrzanowska A (2003) Application of Gaussian quadratures to density functional (df) theories of confined liquid crystals. J Comp Phys 191:265–281
31. Varga Sz, Szalai I (2000) Parsons-Lee theory and a simulation-based study of two-dimensional hard-body fluids. J Mol Liq 85:11–21
32. Helfand E, Frisch HL, Lebowitz JL (1961) Theory of the two- and one-dimensional rigid sphere fluids. J Chem Phys 34:1037–1042
33. de las Heras D, Martínez-Ratón Y, Velasco E (2007) Demixing and orientational ordering in mixtures of rectangular particles. Phys Rev E 76:0317041–03170411
34. Dogic Z, Frenkel, D Fraden S (2000) Enhanced stability of layered phases in parallel hard spherocylinders due to addition of hard spheres. Phys Rev E 62:3925–3933

Chapter 18
Non-equilibrium Plasma-Assisted Hydrophase Ferritization in Fe^{2+}–Ni^{2+}–SO_4^{2-}–OH^- System

Liliya Frolova, Alexandr Pivovarov, and Elena Tsepich

18.1 Introduction

Development of technologies for the production of ferromagnetic nanoparticles with spinel structure has been of considerable interest to researchers for many years [1–6]. The reason lies in the growing scope. The list of traditional fields of consumption such as radio engineering and household appliances is now complemented by extensive use in medicine. This demands the quality of ferrites to be improved. The problem can be solved by the use of hydrophase technologies instead of traditional high-temperature ones [7]. There are such methods to obtain it: electrolysis of aqueous salt solutions, sol–gel, and the use of microemulsions and coprecipitation from aqueous and nonaqueous media.

Promising but poorly understood methods of intensification of technological processes are ultrasonic treatment, contact non-equilibrium plasma, hydrothermal treatment, and microwave treatment [8–15]. Ultrasound mixing is usually used after the heat treatment [16]. The works [17–21] study the effect of various intensifying factors (heating, homogenization, radiolysis) on the properties of nickel ferrites.

Depending on the parameters of the contact non-equilibrium plasma can change the speed of the processes taking place between multiple heterogeneous environments and thus change the phase and morphological composition of the products obtained. The contact non-equilibrium plasma offers enhanced opportunities over solution chemistry for synthesis new nanomaterials and tailoring their functional properties. There has recently been increasing interest in the contact non-equilibrium plasma in water because of their potential applications for

L. Frolova (✉) • A. Pivovarov • E. Tsepich
State University of Chemical Technology, Prospect Gagarin, 8,
49005 Dnipropetrovsk, Ukraine
e-mail: Frolova_L.A@mail.ru

O. Fesenko, L. Yatsenko (eds.), *Nanophysics, Nanophotonics, Surface Studies, and Applications*, Springer Proceedings in Physics 183,
DOI 10.1007/978-3-319-30737-4_18

chemical technologies. Among them there are environmental tasks and materials processing. One of the major advantages of underwater plasma is that it combines different effects, including radical species $OH^{\cdot}$, $O^{\cdot}$, $HO_2^{\cdot}$, **etc**., molecular species H_2O_2, O_2, O_3, etc., ultraviolet radiation, electric field, and shock waves, in a single process [17, 18]. The synergy between these effects is usually believed to provide a higher efficiency than traditional chemical treatment methods.

This synthesis technique does not need any added oxidizing and/or capping agents and only requires a water-based solution with the different precursor. Contact non-equilibrium plasma is used to synthesize nickel ferrite without using any oxidizing or capping agents.

The aim of this study was to investigate the effect of contact non-equilibrium plasma processing on ferritization process in Fe^{2+}–Ni^{2+}–SO_4^{2-}–OH system, their comparative analysis and choice of optimal conditions.

Earlier in our work [20, 21] we carried out studies of their impact. Impact mechanisms are very important and are still hot topics for discussion.

This paper studies the choice of optimum ferritization modes using the method of experiment design, which makes it possible to obtain the relation between the input parameters and the response function and to find the optimal parameters for the process.

18.2 Experimental

The suspension was obtained by pouring and continuous stirring of appropriate mixture of sulfate solutions with the required cation ratio, as in ferrite, and a concentrated precipitant solution. It is treated by contact non-equilibrium plasma. Equipment and methodology are presented in detail in our works [17, 18].

The concentration of Ni^{2+} in the obtained samples was assessed complexometrically—iron cations—by potassium permanganate and dichromate method. To monitor the reaction progress, the reactor was provided with an electrode system including a glass electrode ECL 43-07 to measure pH, platinum electrode to measure oxidation potential, and comparative electrode EVL-1 M3. Temperature control was performed with a thermostat.

All precipitates were washed until a negative sulfate ion reaction occurs. After precipitation the suspension was left for 48 h in the mother liquor. After extraction the precipitate was magnetically separated. The washed and filtered precipitants were dried at 100 °C.

Relative magnetic characteristics were determined by the method described in [18].

Ferritization degree was calculated on the basis of magnetic flux density saturation growth.

The end of the process was determined according to changes in the system redox potential and oxidation time until constant value potential was obtained.

Table 18.1 Factors influencing ferritization process

Factor	Name	Dimension	Value	
			Max	Min
X_1	pH		11.0	8.0
X_2	Temperature	°C	24	50
X_3	Processing time	Min	0	8

The major effects and interaction between the main factors can be estimated using $A = X_1 * X_2$ (1) $B = X_2 * X_3$ (2) $C = X_1 * X_3$ (3)

Dry powder phase content was determined by X-ray diffraction (XRD) (DRON-2.0, Cu-Kα-radiation).

Solution electron microscopy with X-ray microanalysis was performed with device Remmy-102 (SELMI, Ukraine). Crystallite average size was assessed with a help of Debye-Scherrer method.

Based on experiments conducted, we selected ferritization, initial pH of the solution, processing time or CNR, and the temperature of the process as the main technological parameters influencing the process. The following values of factors are proposed as boundary conditions (Table 18.1).

18.3 Results and Discussion

Currently known are the factors that allow to adjust both the phase composition of the precipitants and the size of the produced particles (the initial solution concentration, the sequence of fluid draining, the ratio of reactants, etc.). Ferritization speed, which can be regulated in different ways can also be one of these factors.

In works, it was found that the shape and size of the nickel ferrite particles depend substantially on the production technology.

A typical pattern X-ray diffraction obtained with a help of contact non-equilibrium plasma is shown in Fig. 18.1. The diffractograms shown in Fig. 18.1 correspond to the nickel ferrite with various degrees of crystallinity.

The structure shown in Fig. 18.2 indicates that peak widths and their intensity in the spectra of two samples significantly differ.

Calculated crystallite sizes show that samples obtained by contact non-equilibrium plasma treating are smaller (b)—41.1 nm.

XRD and SEM photograph comparison enables to obtain information about the size of particles and their morphology. The size of nickel ferrite particle is obtained by the use of contact non-equilibrium 1–200 μm.

Conducting the research with a help of experimental design techniques, ferritization degree value performed as a response function (y_1), which characterizes the degree of conversion. Model calculation and subsequent optimization were performed using STATSGRAPHICS 7.0 (Table 18.2).

The correlation of the ferritization degree and the above-mentioned factors at contact non-equilibrium plasma processing is adequately described by the equation:

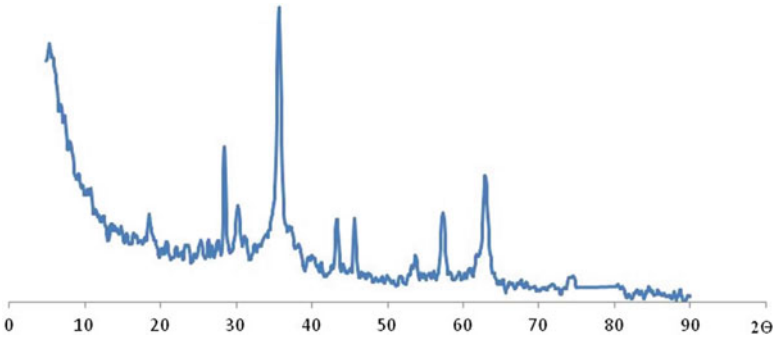

Fig. 18.1 Radiographs nickel ferrite powder-assisted NEP

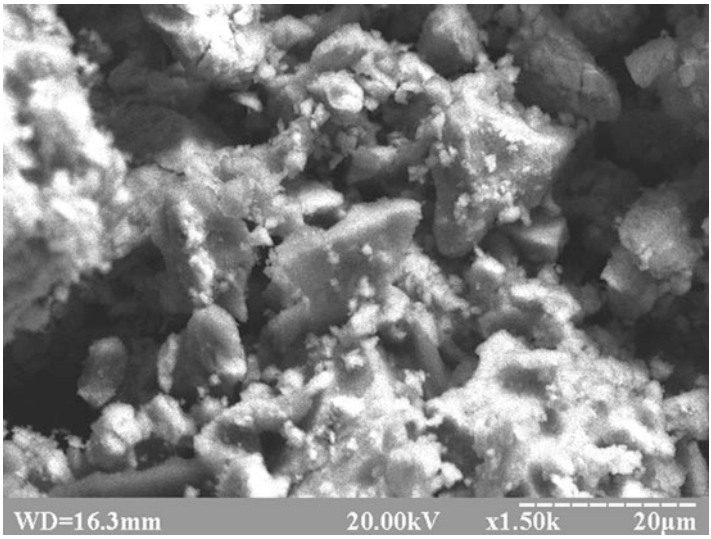

Fig. 18.2 Photomicrographs of nickel ferrite powders

Table 18.2 Results of the full factorial experiment

No.	pH	Temperature, °C	Time, min	Conversion degree, %
1	11	50	8	98.99
2	8	50	8	44.71
3	11	24	8	58.82
4	8	24	8	29.41
5	11	50	0	37.65
6	8	50	0	0
7	11	24	0	11.76
8	8	24	0	0

$$Y_2 = 35.29 + 16.76x_1 + 10.29x_2 + 22.94x_3 + 6.47x_1x_2 + 3.82x_1x_3 + 4.41x_3x_2 \quad (18.1)$$

In the given range of factors, high ferritization degree is obtained. When exposed to contact non-equilibrium plasma, the greatest effect has processing time and initial pH. For low pH, the shorter processing time is, the less is ferritization effect. On the other hand, if the pH is high, the longer contact non-equilibrium plasma processing time provides greater ferritization. The effect of factors x_1 and x_3 is shown in Fig. 18.3. Figure 18.3a shows that low factor value leads to lesser

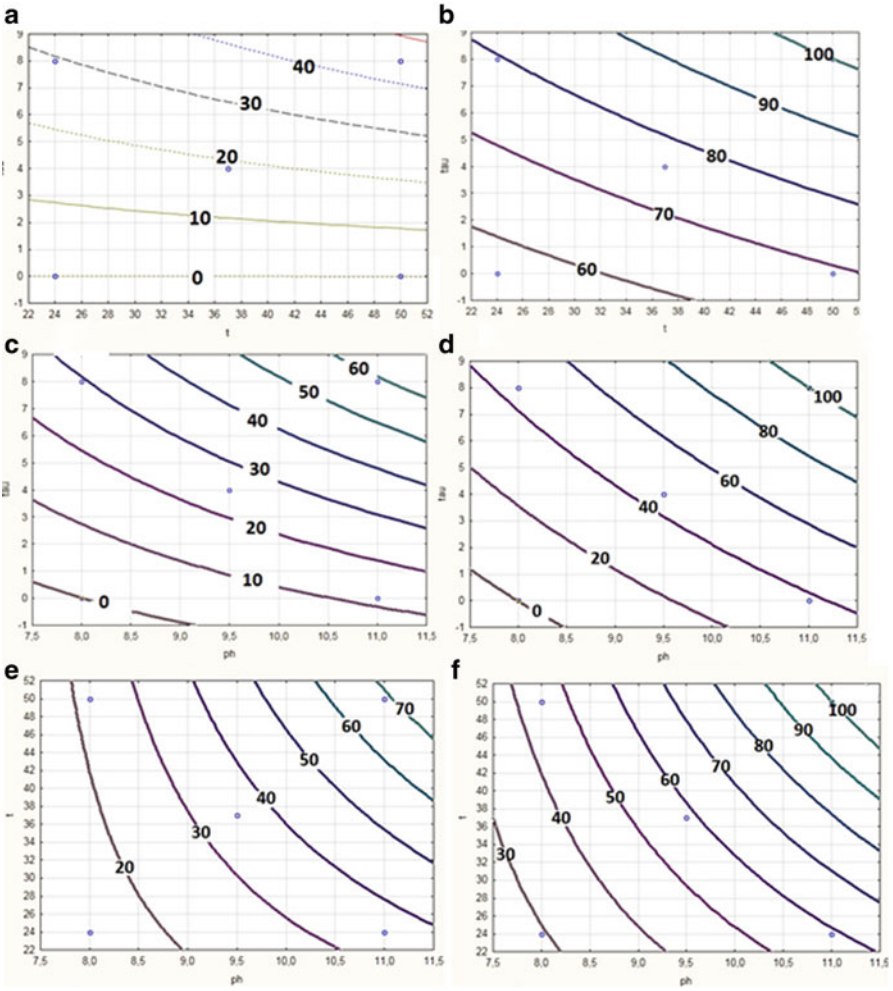

Fig. 18.3 Contour lines showing degree of ferritization under the influence of contact non-equilibrium plasma in different coordinates

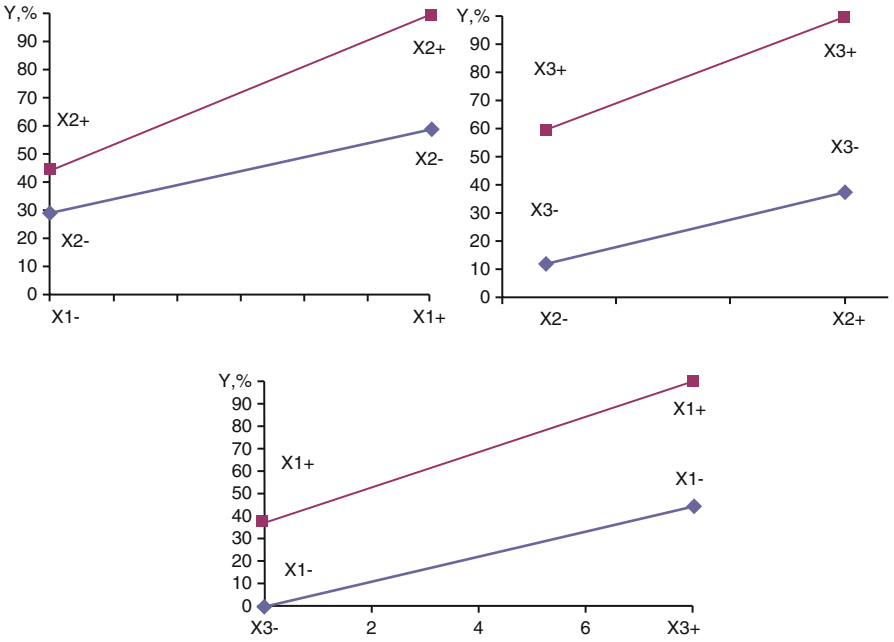

Fig. 18.4 The mutual influence of different factor effects (**a**) A ($x_3 = 8$ min), (**b**) The effect of ($x_1 = 11$), the effect of in C ($x_2 = 50$ °C)

conversion degree. The effect of treatment time and temperature is presented in Fig. 18.3b, c. Conversion degree grows together with the increase in temperature. Interpretation of double effect can be different. Figure 18.4 shows correlation A, B, and C.

$$1-\alpha = f(\tau, t) \quad \text{pH} = 7, \quad 2-\alpha = f(\tau, t) \quad \text{pH} = 11, \quad 3-\alpha = f(\tau, \text{pH})\, t = 24\,^{\circ}\text{C},$$

$$4-\alpha = f(\tau, \text{pH})\, t = 50\,^{\circ}\text{C}, \quad 5-\alpha = f(t, \text{pH})\, \tau = 4\,\text{min}, \quad 6-\alpha = f(t, \text{pH})\, \tau = 8\,\text{min}$$

The curves in Fig. 18.4c are almost parallel, which indicates the same effect of processing time at different pH values.

The biggest difference in angle of slope tangent can be observed in Fig. 18.4a, describing the joint effect of factors x_1 and x_2.

18.4 Conclusion

We studied the methods of hydrophase ferritization by means of contact non-equilibrium plasma processing. Also, we studied the influence of the key factors in the nature of the final product on the basis of full factorial experiment.

The advantage of this approach lies the provision of complex information about the conditions necessary to obtain final product with given characteristics by conducting a limited number of experiments. The results of experiment show that ferritization degree varies mainly depending on initial pH, temperature, and processing time. It was also found that contact non-equilibrium plasma processing provides higher ferritization degree.

On the basis of X-ray diffraction and microscopic analysis revealed the disperse and phase composition of the and the precipitate and its dependence on the conditions of preparation.

The powder obtained with a help of contact non-equilibrium plasma processing has more crystallinity and is finer.

References

1. Dumitrescua AM, Samoilaa PM, Nicab V, Dorofteic F, Iordana AR, Palamarua MN (2013) Study of the chelating/fuel agents influence on $NiFe_2O_4$ samples with potential catalytic properties. Powder Technol 243:9–17
2. Hong W, Da H, Jie S, Kebin L (2014) Intensification of levofloxacin sono-degradation in a US/H_2O_2 system with Fe_3O_4 magnetic nanoparticles. Chinese J Chem Eng. Available online 14 Nov 2014
3. Mohaia I, Gála L, Szépvölgyia J, Gubiczab J, Farkasc Z (2007) Synthesis of nanosized zinc ferrites from liquid precursors in RF thermal plasma reactor. J Eur Ceram Soc 27 (2–3):941–945
4. Guin D, Baruwati B, Sunkara VM (2005) A simple chemical synthesis of nanocrystalline AFe_2O_4 (A = Fe, Ni, Zn): an efficient catalyst for selective oxidation of styrene. J Mol Catal A: Chem 242(1–2):26–31
5. Fatemi DJ, Harris VG, Browning VM, Kirkland JP (1998) Processing and cation redistribution of MnZn ferrites via high-energy ball milling. J Appl Phys 83:6767–6769
6. Yi X, Yitai Q, Jing L et al (1995) Hydrothermal preparation and characterization of ultrafine powders of ferrite spinels MFe_2O_4 (M = Fe, Zn and Ni). Mater Sci Eng 34(1):L1–L3
7. Kong LB, Zhang TS, Ma J, Boey F (2008) Progress in synthesis of ferroelectric ceramic materials via high-energy mechanochemical technique. Prog Mater Sci 53:207–322
8. Pradeep A, Priyadharsini P, Chandrasekaran G (2008) Production of single phase nano size $NiFe_2O_4$ particles using sol–gel auto combustion route by optimizing the preparation conditions. Mater Chem Phys 112(2):572–576
9. Chen DH, He XR (2001) Synthesis of nickel ferrite nanoparticles by sol–gel method. Mater Res Bull 36:1369–1377
10. Baykal A, Kasapoglu N, Koseoglu Y, Toprak MS, Bayrakdar H (2008) CTAB-assisted hydrothermal synthesis of $NiFe_2O_4$ and its magnetic characterization. J Alloys Compd 464 (1–2):514–518
11. Goldman A (1993) Modern ferrite technology. Marcel Dekker, New York
12. Alarifi A, Deraz NM, Shaban S (2009) Structural, morphological and magnetic properties of $NiFe_2O_4$ nano-particles. J Alloys Compd 486(1–2):501–506
13. Shi Y, Ding J, Liu X, Wang J (1999) $NiFe_2O_4$ ultrafine particles prepared by co-precipitation/ mechanical alloying. J Magn Magn Mater 205(2–3):249–254
14. Salavati-Niasari M, Davar F, Mahmoudi T (2009) A simple route to synthesize nanocrystalline nickel ferrite ($NiFe_2O_4$) in the presence of octanoic acid as a surfactant. Polyhedron 28 (8):1455–1458

15. Maaz K, Karim S, Mumtaz A, Hasanain SK, Liu J, Duan JL (2009) Synthesis and magnetic characterization of nickel ferrite nanoparticles prepared by co-precipitation route. J Magn Magn Mater 321(12):1838–1842
16. Kavas H, Kasapoglu N, Baykal A, Kaseoglu Y (2009) Characterization of $NiFe_2O_4$ nanoparticles synthesized by various methods. Chem Pap 63(4):450–455
17. Frolova LA, Pivovarov AA, Baskevich AS (2014) Structure and properties of nickel ferrites produced by glow discharge in the Fe^{2+}–Ni^{2+}–SO_4^{2-}–OH^- system. Russ J Appl Chem 87 (8):1054–1059
18. Frolova LA, Pivovarov AA (2015) Investigation of conditions for ultrasound_assisted preparation of nickel ferrite. High Energy Chem 49(1):10–15
19. Frolova LA, Shapa NN (2011) Technology of extraction manganese compounds from the discharge water of metallurgical enterprises with the use of ultrasound. Metall Min Ind 3 (6):65–69
20. Kodama RH, Berkowitz AE, Foner S (1996) Surface spin disorder in $NiFe_2O_4$ nanoparticles. Phys Rev Lett 77(2):394–397
21. Nawale AB, Kanhe NS, Patil KR, Bhoraskar SV, Mathe VL, Das AK (2011) Magnetic properties of thermal plasma synthesized nanocrystalline nickel ferrite ($NiFe_2O_4$). J Alloy Compd 509(12):4404–4413

Chapter 19
The Nature of Carbon Vacancies Initiating Graphite Oxidation

Dmytro Nasiedkin, Yuri Plyuto, and Anatoliy Grebenyuk

19.1 Introduction

The microstructure of macrocrystalline natural graphite still remains controversial and not fully understood although it has been the subject of scientific investigation for longer than a century. To a great extent, this concerns graphite surface reactivity and its capability to oxidation [1, 2].

With very pure, highly graphitised materials, many investigators regard the graphite basal planes as virtually inactive at lower temperatures [3]. Basal-plane attack can occur at any temperature, however, if foci are provided by vacancies, dislocations and other imperfections.

The early studies of Thomas et al. [4, 5] demonstrated the anisotropy of the natural graphite surface to oxidation. It appeared that at 800 °C the rate of graphite surface oxidation was 26 times greater in the direction parallel than perpendicular to the basal plane. Hence, the edge carbon atoms are more reactive sites than those in the basal plane. Two types of edge sites (zigzag and armchair) exist at the terminations of the basal plane. The detailed optical studies of the oxidation of graphite crystals at 846 °C showed the reaction rate of the zigzag face to be about 1.20 times more rapid than that of the armchair face.

A systematic kinetic study of the oxidative etching in dry air of graphite basal planes of highly oriented pyrolytic graphite along the *a* and *c* directions at temperatures up to 950 °C was undertaken using the scanning tunnelling microscopy experiments [6]. It was found that thermal oxidation of graphite at 550–950 °C leads to pit formation by layer-by-layer etching of the carbon layer. Oxidation at

D. Nasiedkin (✉) • Y. Plyuto • A. Grebenyuk
Chuiko Institute of Surface Chemistry of the National Academy of Sciences of Ukraine, General Naumov Str. 17, Kiev 03164, Ukraine
e-mail: nasiedkindm@gmail.com

O. Fesenko, L. Yatsenko (eds.), *Nanophysics, Nanophotonics, Surface Studies, and Applications*, Springer Proceedings in Physics 183,
DOI 10.1007/978-3-319-30737-4_19

temperatures below 875 °C produces circular pits of uniform size that are formed at the sites of point defects. At temperatures above 875 °C, in contrast, pit formation occurs via etching at both defected and basal-plane carbon atoms. For the oxidation of graphite at temperatures above 875 °C, CO rather than CO_2 may be a major product of the vertical etch reaction because basal-plane carbons can be extracted by oxygen atoms.

It has been shown using the extended Hűckel molecular orbital method and cluster models [7] that lattice atomic vacancies on graphite surface (with one to several C atoms missing) create an enhancement of the charge density in the atoms directly surrounding them, implying their enhanced chemical reactivity. This partial electronic density enhancement, which is interpreted as dangling bonds, can cause an increase in the oxidation rate of graphite basal plane. By comparative STM and AFM study, the vacancy-induced enhancement of the partial charge density of states at the carbon atoms near the vacancy was observed [8]. The charge enhancement can occur over tens of the surrounding carbon atoms for multiatom vacancy.

In recent years, very much attention was paid to theoretical mimicking the vacancies formation [9] and their experimental creation and HREM observation [10]. Unfortunately, the present views on the origin of carbon vacancies are contradictory.

The aim of this work is the quantum chemical simulation of the formation of the mono-vacancy defects on the single graphite sheet (graphene) as a result of carbon atom removal due to reaction with molecular oxygen in both basal-plane and edge positions and clarification if the defects at graphite basal plane are associated with the original defect sites or can be formed as a result of oxidative removal of carbon atoms.

19.2 Computational Method

The analysis of electronic and thermochemical properties of single graphite sheet (graphene) models was performed using the Firefly QC package [11] which is partially based on the GAMESS (US) [12] source code. The density functional theory (DFT) at the B3LYP level was used. The dispersion interactions were taken into account within DFTD methodology [13]. Because of primary interest to comparative effects, the 3–21G(d,p) valence-split basis set expanded with polarisation functions that shortens computing time was used [14].

The criteria for convergence of the optimisation procedure were RMS/maximum values of 0.00003/0.00010 hartree/bohr or hartree/rad and 0.003/0.01 bohr or rad for force and displacement, respectively. The self-consistent field (SCF) energies, enthalpies and Gibbs free energies of singlet or triplet ground states were determined and are reported in kJ/mol (1 hartree = 2625.5 kJ/mol). Geometry optimisation and vibrational frequency calculations were carried out in all cases.

The Gibbs free energy (ΔG) values for single graphite sheet (graphene) models were calculated at definite temperatures using ideal gas, rigid rotor, harmonic

normal mode approximations and the pressure $P = 101.325$ kPa as the sum of electronic energy, zero point energy and energy contributions of vibrational, rotational and translational movements. For this purpose, vibrational spectra of the models were calculated via the search for the total energy second derivative tensor.

19.3 Results and Discussion

The graphite basal plane was simulated by $C_{42}H_{16}$ cluster model composed of 14 benzene rings and was previously adopted for investigation [15–17]. At cluster boundaries, the edge carbon atoms are terminated by hydrogen atoms following the standard procedure typical for covalent materials. The models were constructed using information about r(C–C) = 1.40 Å and r(C–H) = 1.08 Å bond length in benzene obtained from the literature [18].

To create the mono-vacancy defects, one carbon atom is individually removed at two different positions from pristine graphite sheet (Fig. 19.1a) resulting in C atom vacancy defect at the central part of the basal plane (Fig. 19.2b) and with C atom vacancy defect at the edge of the basal plane (Fig. 19.1c).

The initial optimised $C_{42}H_{16}$ cluster model (Fig. 19.1a) has singlet ground state and the energy of −1601.58655 hartree. The central part of the initial $C_{42}H_{16}$ cluster model (Fig. 19.2a) consists of practically regular hexagons with bond lengths of 1.411–1.429 Å and angles of 120°. This corresponds to the experimentally observed C–C bond lengths of 1.42 Å in the natural graphite [19–21]. At the edge region of the initial $C_{42}H_{16}$ cluster model (Fig. 19.3a), the practically regular hexagons with bond lengths varying from 1.372 to 1.431 Å and almost angles of 120° are observed.

The removal of carbon atom from the central region of the basal plane results in $C_{41}H_{16}$ cluster (Fig. 19.1b) having a triplet ground state and total energy of −1563.40667 hartree (in comparison, the respective singlet state has the energy of only −1563.36043 hartree). Both five- and seven-membered rings of carbon

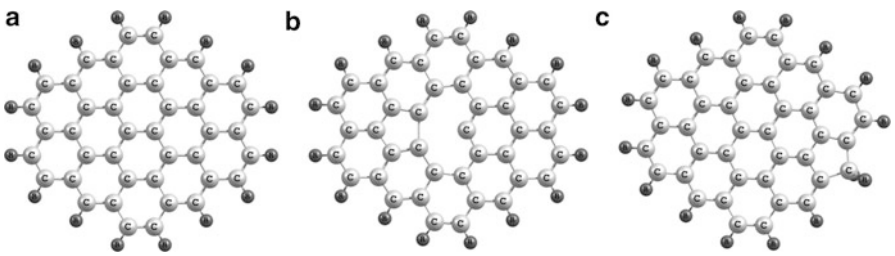

Fig. 19.1 Optimised structures and total energy values: (**a**)—$C_{42}H_{16}$ cluster model (−1601.58655 hartree); (**b**)—$C_{41}H_{16}$ cluster model with basal-plane mono-vacancy defect (−1563.40667 hartree); (**c**)—$C_{41}H_{16}$ cluster model with edge mono-vacancy defect (−1563.64501 hartree)

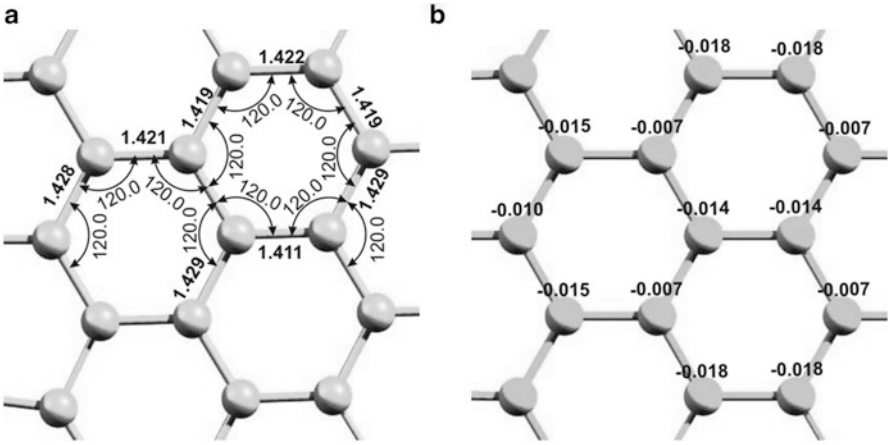

Fig. 19.2 Geometric parameters (**a**) and charge distribution (**b**) of the central region of optimised $C_{42}H_{16}$ cluster model

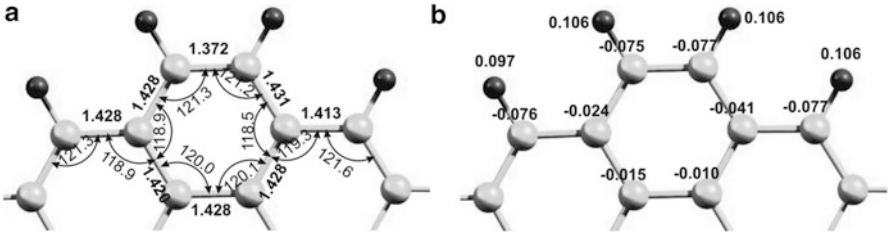

Fig. 19.3 Geometric parameters (**a**) and charge distribution (**b**) of the edge region of the optimised $C_{42}H_{16}$ cluster model

atoms are formed (so-called non-hexagonal region) which were experimentally observed [22]. This deformed structure (Fig. 19.4a) has the bond lengths varying from 1.353 to 1.812 Å and angles from 100 to 147°. Mono-vacancy of similar structure appeared to be energetically most stable in carbon nanotubes [23].

In case of carbon atom removal from the edge boundary of the basal plane (Fig. 19.1c), a more stable structure with a singlet ground state and total energy of −1563.64501 hartree is formed. This gives a system of almost regular hexagons (with C–C bond length from 1.385 to 1.412 Å) conjugated with a five-membered rings of carbon atoms (with two elongated 1.574 and 1.576 Å C–C bonds) terminated by CH_2 group (Fig. 19.5a).

It appears that that the optimised $C_{41}H_{16}$ cluster model with the edge defect is for 0.23834 hartree (625.8 kJ/mol) more stable than that containing basal-plane mono-vacancy defect.

Previous DFT calculations [24] reveal the possibility of the presence of defects in the graphene lattice that appear due to combinations of non-hexagonal rings. The

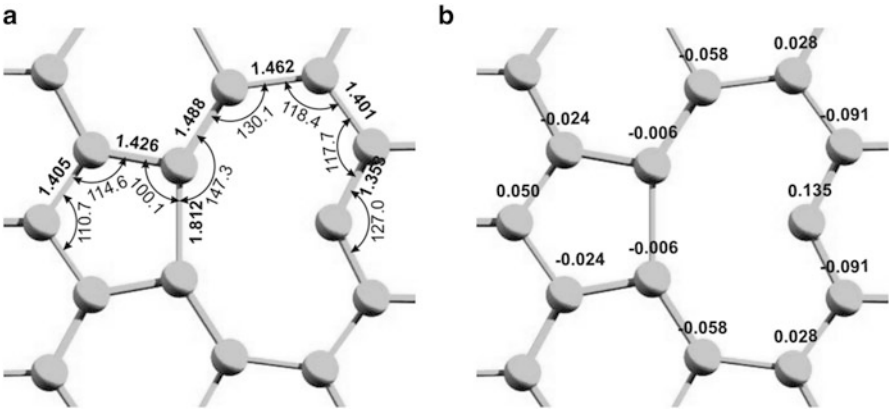

Fig. 19.4 Geometric parameters (**a**) and charge distribution (**b**) of the central region of optimised $C_{41}H_{16}$ cluster model with basal-plane mono-vacancy defect

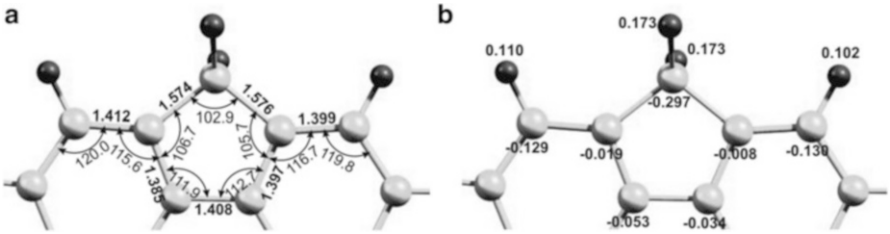

Fig. 19.5 Geometric parameters (**a**) and charge distribution (**b**) of the edge region of the optimised $C_{41}H_{16}$ cluster model with edge mono-vacancy defect

atoms in the neighbourhood of a vacancy rearrange to reduce the number of dangling bonds. Incomplete hexagons transform into irregular pentagons, and the atoms surrounding the vacancy rebond into a large vacancy ring containing N_{ring} atoms. The bond lengths in the vacancy ring vary between 1.42 and 1.80 Å and thus are up to 30 % longer than those in perfect graphene. This reflects that the interatomic bonds in the vacancy ring are strained and weaker than those between carbon atoms in a pure sp^2 hybridisation. The atomic relaxations at defects consequently result in the formation of motifs, which are combinations of non-hexagonal rings.

Although charge distribution in graphene varies from atom to atom [14, 25], the missing of carbon atoms from the pristine graphene structure results in substantial changes in bonding charge distribution [26, 27]. Therefore, in order to characterise the electron density distribution, the Mulliken charges of the atoms of each optimised cluster model were calculated. Their values for carbons and hydrogen atoms are shown in Figs. 19.2b, 19.3, 19.4 and 19.5b.

The Mulliken atomic net charges at C atoms in the central part of the initial $C_{42}H_{16}$ cluster model (Fig. 19.2b) are small (vary from −0.007 to −0.018 eu). In

contrast, the edge C–H bonds (Fig. 19.3b) are slightly polarised (−0.075 eu on C atom and +0.106 eu on H atoms). This corresponds to their experimentally observed higher reactivity at graphite edges [5].

An opposite situation is observed for defect areas of the considered models. In the case of $C_{41}H_{16}$ cluster model with basal defect vacancy (Fig. 19.4b), the two-coordinated carbon atom bears a considerable positive charge (+0.135 eu). The carbon atom of the residual CH_2 group in the case of vacancy defect formation at the edge (Fig. 19.5b) bears the negative charge (−0.297 eu), whereas the neighbouring hydrogen atoms are positively charged (+0.173 eu). High reactivity of defective single graphite sheet (graphene) with respect to oxygen is well documented [5].

The energy of the basal-plane and edge mono-vacancy defect formation as the result of C atom removal from single graphite sheet (graphene) as CO_2 molecule upon oxidation was calculated following the reaction:

$$C_{42}H_{16} + O_2 \rightarrow C_{41}H_{16} + CO_2 \uparrow .$$

The total energy values of the above-mentioned $C_{42}H_{16}$ and $C_{41}H_{16}$ cluster models mimicking pristine and defected graphene as well as those for O_2 (triplet state, −149.48199 hartrees) and CO_2 (singlet state, −187.52384 hartrees) molecules were used in order to calculate the energy effects of the reaction:

$$\Delta E(\text{react}) = E_{\text{tot}}(C_{41}H_{16}) + E_{\text{tot}}(CO_2) - E_{\text{tot}}(C_{42}H_{16}) - E_{\text{tot}}(O_2).$$

The formation of the edge mono-vacancy defect appeared to be energetically favourable due to reaction energy effect of −0.10031 hartrees (−263 kJ/mol).

In contrast, in the case of basal-plane mono-vacancy defect formation, the respective energy is equal to +0.13803 hartrees (+362 kJ/mol) and the considered process is energetically unfavourable.

To understand how the basal-plane and edge mono-vacancy defect formation as the result of C atom removal from single graphite sheet (graphene) depends on the temperature, the Gibbs free energy (ΔG) of the corresponding reaction was calculated in the temperature interval from 300 to 1200 K:

$$\Delta G(\text{react}) = \Delta G(C_{41}H_{16}) + \Delta G(CO_2) - \Delta G(C_{42}H_{16}) - \Delta G(O_2).$$

From Fig. 19.6, one can see that the reaction of edge mono-vacancy defect formation is energetically favourable since the Gibbs free energy is negative (from −267 to −281 kJ/mol). In contrast, the reaction of basal-plane mono-vacancy defect formation is energetically unfavourable as the Gibbs free energy remains positive (from +337 to +314 kJ/mol) in all temperature interval.

The obtained results agree well with the available experimental data which demonstrate the anisotropy of the natural graphite surface to oxidation [4–6]. As the removal of carbon atom from graphite basal plane is energetically unfavourable, the obtained results give us an opportunity to come to the conclusion that defects at

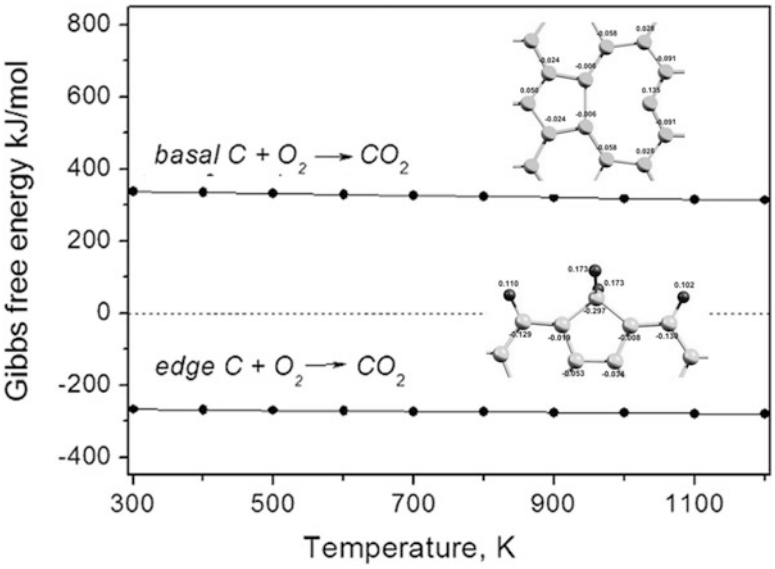

Fig. 19.6 Temperature dependence of Gibbs free energy (ΔG) for the reactions simulating the formation of basal-plane and edge mono-vacancy defects

graphite basal planes responsible for oxidation are associated with the original defect sites and cannot be formed as a result of oxidative removal of carbon atoms.

19.4 Conclusions

The formation of the edge mono-vacancy defect on the single graphite sheet (graphene) due to carbon atom reaction with oxygen appeared to be energetically favourable with energy effect of −263 kJ/mol. In contrast, in the case of basal-plane mono-vacancy defect formation, the respective energy is positive and equal to +362 kJ/mol and the considered process is energetically unfavourable. Similarly, in the temperature interval of 300–1200 K, the reaction of edge mono-vacancy defect formation is energetically favourable since the Gibbs free energy is negative (from −267 to −281 kJ/mol), while the reaction of basal-plane mono-vacancy defect formation is energetically unfavourable as the Gibbs free energy remains positive (from +337 to +314 kJ/mol). The obtained results agree well with the available experimental data which demonstrate the anisotropy of the natural graphite surface to oxidation and confirm that defects at graphite basal plane are most likely associated with the original defect sites and cannot be formed as the result of the removal of carbon atoms due to oxidation with molecular oxygen.

References

1. Badenhorst H, Focke W (2013) Comparative analysis of graphite oxidation behaviour based on microstructure. J Nucl Mater 442:75–82
2. Badenhorst H (2014) Microstructure of natural graphite flakes revealed by oxidation: limitations of XRD and Raman techniques for crystallinity estimates. Carbon 66:674–690
3. Essenhigh RH (1981) Fundamentals of coal combustion. In: Elliott MA (ed) Chemistry of coal utilization, 2nd suppl., Ch. 19. Wiley, New York, pp 1153–1312
4. Thomas JM, Jones KM (1964) Kinetic anisotropy in the oxidation of graphite. J Nucl Mater 11:236–239
5. Thomas JM (1965) Microscopic studies of graphite oxidation. In: Walker PL Jr (ed) Chemistry and physics of carbon, vol 1. Marcel Dekker, New York, pp 122–202
6. Hahn JR (2005) Kinetic study of graphite oxidation along two lattice directions. Carbon 43:1506–1511
7. Lee KH, Lee HM, Eun HM, Lee WR, Kim S, Kim D (1994) The electronic structure of lattice vacancies on the STM image of a graphite surface. The electronic structure of lattice vacancies on the STM image of a graphite surface. Surf Sci 321:267–275
8. Hahn JR, Kang H, Song S, Jeon IC (1996) Observation of charge enhancement induced by graphite atomic vacancy: a comparative STM and AFM study. Phys Rev B 53:R1725–R1728
9. Skowron ST, Lebedeva IV, Popov AM, Bichoutskaia E (2015) Energetics of atomic scale structure changes in graphene. Chem Soc Rev 44:3143–3176
10. Yamada Y, Murota K, Fujita R, Kim J, Watanabe A, Nakamura M, Sato S, Hata K, Ercius P, Ciston J, Song CY, Kim K, Regan W, Gannett W, Zettl A (2014) Subnanometer vacancy defects introduced on graphene by oxygen gas. J Am Chem Soc 136:2232–2235
11. Granovsky AA Firefly version 8.1.0. http://classic.chem.msu.su/gran/firefly/index.html
12. Schmidt MW, Baldridge KK, Boatz JA, Elbert ST, Gordon MS, Jensen JH, Koseki S, Matsunaga N, Nguyen KA, Su S, Windus TL, Dupuis M, Montgomery JA (1993) General atomic and molecular electronic—structure system. J Comput Chem 14:1347–1363
13. Grimme S, Antony J, Ehrlich S, Krieg H (2010) A consistent and accurate ab initio parametrization of density functional dispersion correction (DFT-D) for the 94 elements H-Pu. J Chem Phys 132:154104/1–154104/19
14. Silva-Tapia AB, García-Carmona X, Radovic LR (2012) Similarities and differences in O_2 chemisorption on graphene nanoribbon vs. carbon nanotube. Carbon 50(3):1152–1162
15. Ruuska H, Pakkanen TA (2003) Ab initio model study on a water molecule between graphite layers. Carbon 41:699–706
16. Abe S, Nagoya Y, Watari F, Tachikawa H (2010) Structures and electronic states of water molecules on graphene surface: a density functional theory study. Jpn J Appl Phys 49:06GJ13-1–06GJ13-3
17. Wang C, Xiao B, Ding Y (2012) Role of hydrocarbon radicals CH_x ($x = 1, 2, 3$) in graphene growth: a theoretical perspective. ChemPhysChem 13:774–779
18. Baba M, Kowaka Y, Nagashima U, Ishimoto T, Goto H, Nakayama N (2011) Geometrical structure of benzene and naphthalene: ultrahigh-resolution laser spectroscopy and *ab initio* calculation. J Chem Phys 135(5):054305
19. Bernal JD (1924) The structure of graphite. Proc R Soc Lond A 106:749–773
20. Nelson JB, Riley DP (1945) The thermal expansion of graphite from 15 °C to 800 °C: part I. Experimental. Proc Phys Soc 57:477–486
21. Kincaid BM, Meixner AE, Platzman PM (1978) Carbon *K* edge in graphite measured using electron-energy-loss spectroscopy. Phys Rev Lett 40(19):1296–1299
22. Meyer JC, Kisielowski C, Erni R, Rossell MD, Crommie MF, Zettl A (2008) Direct imaging of lattice atoms and topological defects in graphene membranes. Nano Lett 8(11):3582–3586
23. Berber S, Oshiyama A (2006) Reconstruction of mono-vacancies in carbon nanotubes: atomic relaxation vs. spin polarization. Physica B 376–377:272–275

24. Carlsson JM, Scheffler M (2006) Structural, electronic, and chemical properties of nanoporous carbon. Phys Rev Lett 96:046806-1–046806-4
25. Banerjee S, Bhattacharyya D (2008) Electronic properties of nano-graphene sheets calculated using quantum chemical DFT. Comp Mater Sci 44:41–45
26. Warner JH, Lee G-D, He K, Robertson AW, Yoon E, Kirkland AI (2013) Bond length and charge density variations within extended arm chair defects in graphene. ACS Nano 7 (11):9860–9866
27. Kheirabadi N, Shafiekhani A (2013) The ground state of graphene and graphene disordered by vacancies. Physica E 47:309–315

Chapter 20
Conditions of Spontaneous Growth of Iron Subnanocluster: The Influence of Impurity Atoms

A.V. Nedolya

Abbreviations

fcc	Face-centered cubic
CIS	Central (octahedral) interstitial site
PB	Potential barrier
SIS	Surface interstitial site

20.1 Introduction

It is known, a new phase grows from a nucleation centre formed in local volume and has interface [1–3]. This process includes the formation of crystallization centers and their further growth with the formation of grains of the crystalline phase, limited by surfaces that correspond with the Gibbs–Curie principle and Wulff theorem [4–7].

Typically, the crystallization process occurs below the equilibrium temperature of phases. This process is not only related to changes in the volume component of the Gibbs free energy (ΔG_v) but also strongly depends on the characteristics of the boundary surface of the newly formed crystalline particles. The change in free energy is associated with the formation of the surface (ΔG_σ); it is positive and counteracts the phase transition process [8]. In addition, it is associated with the energy change due to the deformation of nuclei during the phase transformation (ΔG_d), which is essential to the formation of a new crystalline phase inside an

A.V. Nedolya (✉)
Department of Applied Physics, Zaporizhzhya National University, 66 Zhukovsky Str., 69600 Zaporizhzhya, Ukraine
e-mail: avnedolya@hotmail.com

O. Fesenko, L. Yatsenko (eds.), *Nanophysics, Nanophotonics, Surface Studies, and Applications*, Springer Proceedings in Physics 183,
DOI 10.1007/978-3-319-30737-4_20

existing solid phase. All these components are included in the general expression for free energy:

$$\Delta G = -\Delta G_\nu + \Delta G_\sigma + \Delta G_\mathrm{d} \tag{20.1}$$

But in the case of the formation of clusters with a size corresponding to that of the unit cell, usually, it uses the molecular-kinetic approach, rather than a statistical approach, by which the size of the critical nucleus is determined from the condition of equality of opposing streams of atoms with respect to any surface of this kind of nanocrystal [9, 10]. Most of researches apply to the investigation of the nucleation processes for clusters of larger sizes [11, 12].

Note that crystal formation is possible without large supersaturation, for example, as a result of physical changes in the local volume caused by the presence of soluble elements because of nano- and microsegregation [13, 14], owing to a concentration gradient during accelerated crystallization. These processes can be viewed as changes in the nearest environment of certain atoms, which, under favorable conditions, lead to further ordering of phases. These physical changes in the local volume could be stimulated for further crystal formation in multicomponent systems under the influence of the impurities.

Recent research indicates the possibility of spontaneous emergence of clusters without a nucleus, growth, and self-organization of cluster groups into the crystal [15, 16].

Now the study of the initial stage of formation of a new crystalline phase is problematic because of the transience of the process, although the existence of clusters in melt [17–20], in liquid [21, 22], or even in gaseous phases is confirmed [23–26]. Therefore, modeling of such processes from first principles is the actual problem that attracts special attention in the research of possible configurations and shapes of nanocrystals of the condensed phase [27, 28], the existence and shape changes of which are specified by certain conditions and the sizes of clusters [29–33].

A spontaneous crystallization process can be carried out only when reduced total free energy of the system is decreasing:

$$\Delta G = \Delta U + p\Delta V - T\Delta S < 0 \tag{20.2}$$

where T is the *constant* temperature, p *constant* pressure, U internal energy of the system, S entropy, and V volume.

For a spontaneous process in an isolated system, it is necessary that $\Delta S > 0$. Taking into account the initial moment of formation of a new phase, a nucleus volume does not change; the condition (20.2) simplifies to

$$\Delta U < T\Delta S \tag{20.3}$$

where ΔS at a fixed temperature can be attributed among other things also to changes in the nuclear symmetry group. A change in the internal energy ΔU thus

should not be significant or even be negative, which is typical for the surface layers of the new phase. For small isolated groups of atoms, the inequality (20.3) can be changed, taking into account the statistical nature of entropy:

$$\Delta u < \frac{kT}{n} \ln \frac{N_2}{N_1} \tag{20.4}$$

where $\Delta u = \frac{\Delta U}{n}$ is the change of specific energy, n is the number of atoms in the cluster, and N_1, N_2 are the number of possible states of the atomic group changing initial central position (1) to final surface position (2) of the atom, respectively.

20.2 Method

Energy preconditions of the formation of a new crystalline phase in a small atomic group of based Fe-Ni-C (15 atoms) that was similar to the fcc elementary cell, using molecular mechanics method, were stimulated. Such a system was considered to be approximately quasi-stable and quasi-isolated. The type of lattice selected related to the fact that all Fe atoms located on the surface and their substitution for Ni atoms minimally affect the energy change of the system, which simplifies the interpretation of the calculation results.

The calculations were carried out from the first principles using the MM+ algorithm [34, 35] and taking into account the potential impact of atoms and Lennard–Jones potential [36, 37] by the molecular mechanics method [38] using the numerical solution of Newton's equations of motion for atoms that fit the model crystal lattice. The interaction of atoms with each other via potential fields is assigned empirically. Potential energy, among other things, also depends on:

1. The length of connections—potential harmonic connection
2. The potential of the valence angle bond
3. Potential harmonic cosine bond
4. The potential of flat groups and pseudo torsion angles
5. Electrostatic interaction potential of charged atoms, and the like.

For the numerical integration of the equations, a finite-difference scheme approximation, according to the Störmer–Verlet method [39, 40], was used.

To determine the possible positions of nickel atoms, they were numbered for convenience (Table 20.1). An analysis of the nickel atom's positions was held on the grounds of symmetry of the crystal and on the results of calculations of internal energy of the system from the first principles after changing the atomic coordinates. All calculations were carried out at $T = 300$ K. For convenience, the lattice parameter was set equal to $a_\gamma = 0.36$ nm.

The position of the carbon atom in a central octahedral interstitial site (CIS) of the cluster was chosen as a zero of path length (L) .

Table 20.1 Notation conventions for positions of atoms of Fcc atomic group

Coordinates	[[011]]	[[001]]	[[101]]	[[111]]	[[010]]	[[000]]	[[100]]
Position	1	2	3	4	5	6	7
Coordinates	[[110]]	[[½ ½ 1]]	[[0 ½ ½]]	[[½ 0 ½]]	[[½ ½ ½]]	[[½ 1 ½]]	[[½ ½ 0]]
Position	8	9	10	11	12	13	14

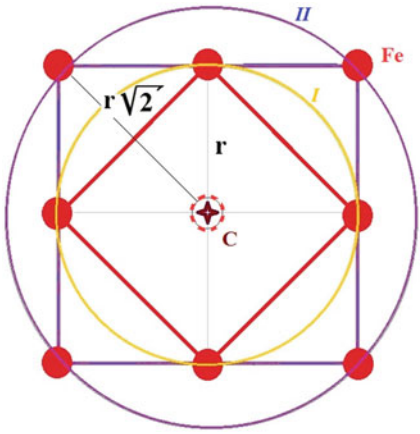

Fig. 20.1 Scheme of virtual coordination spheres of an fcc cluster; in the center is the carbon atom

The calculation was carried out mainly qualitatively with comparison of the energy change ΔU, which was determined in millielectron-volt per atom (meV/atom).

20.3 Result and Discussion

20.3.1 The Case of One Ni Atom

Carbon Atom Located in a Central Octahedral Interstitial Site

One atom of nickel affects the atomic group energy if located in either the first or second cluster surrounding the carbon atom (Fig. 20.1). The nickel atom, which is in the first clustered environment (I), can take positions marked with the numbers from one to eight corresponding to plane type (002) and, in the second (II), from 9 to 14, corresponding to plane type (111; Table 20.2).

The change of energy of the cluster is possible due to the size differences of Fe and Ni atoms. The energy of an atomic group is different when substituted for the iron atom on nickel atoms in the first (I) and second (II) carbon-clustered environment: the dependence has various inclination angles (Fig. 20.2).

Table 20.2 Cluster energy at different positions of carbon and nickel atoms where numbering is done: N_0 by symmetry, N_1 by Δ_1 criteria, N_2 by Δ_2 criteria, N_3 by Δ_3 criteria

C in CIS	N_0	$U\left(\frac{\text{meV}}{\text{atom}}\right)$	$\Delta_1\left(\frac{\text{meV}}{\text{atom}}\right)$	Equivalent points	N_1	$\Delta_2\left(\frac{\text{meV}}{\text{atom}}\right)$	N_2	$\Delta_3\left(\frac{\text{meV}}{\text{atom}}\right)$	N_3
1 ÷ 8	*I*	3018	427	1 = 4	*a*	481	*a*	909	*a*
			457	2 = 3 = 5 = 8	*b*	397	*b*	854	*bd*
			458	6 = 7	*b*	397	*b*	855	*bd*
9 ÷ 14	*II*	2787	462	9 = 13	*b*	400	*b*	862	*bd*
			506	10 = 12	*c*	318	*cd*	824	*c*
			534	11 = 14	*d*	315	*cd*	849	*bd*

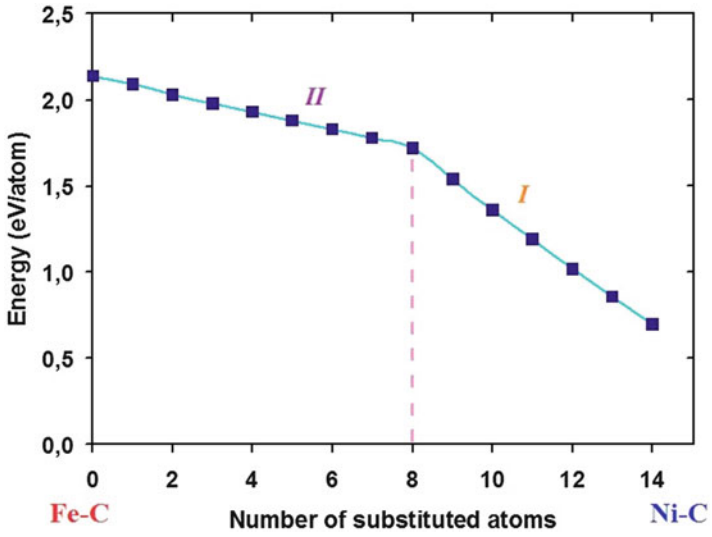

Fig. 20.2 Energy of the fcc cluster of system Fe–C with sequential displacement of atoms Fe by atoms of Ni: *0*—meets all the atoms of iron; *14*—all nickel atoms

Also, the calculations indicate the existence of a potential barrier (PB) for the carbon atom that moves to the surface in the direction <011> and which is 48 % higher for the system Ni–C compared with Fe–C (Fig. 20.3a). This can be explained by the difference between the sizes of the octahedral hole that forms atoms of iron and nickel.

Estimations of atomic group energy changes were based on three criteria at the change of the position of the carbon atom from the central octahedral interstices in the direction of type <011> to the unfinished surface octahedral site (SIS) on the middle of the edge of cube:

$$\begin{aligned} \Delta_1 &= U_{\text{PB}} - U_{\text{CIS}}, \\ \Delta_2 &= U_{\text{CIS}} - U_{\text{SIS}}, \end{aligned} \tag{20.5}$$

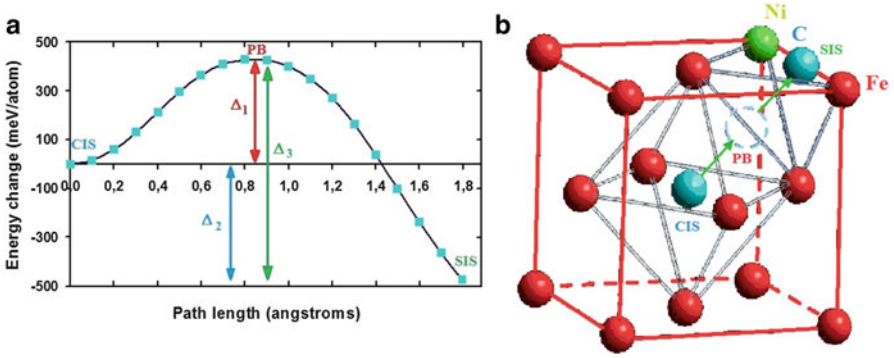

Fig. 20.3 Energetic evaluation criteria of the fcc cluster of system Fe–Ni–C (**a**) when changing the position of the carbon atom from the central octahedral interstitial site to the surface in the direction <011> (**b**)

$$\Delta_3 = U_{\mathrm{PB}} - U_{\mathrm{SIS}} = \Delta_1 + \Delta_2$$

where

Δ_1 = increment of the energy of cluster on the potential barrier
Δ_2 = gain of energy of cluster under the impact of the surface
Δ_3 = energy advantage on the surface compared to the position at the potential barrier
U_{CIS} = cluster energy when the carbon atom is located in the central octahedral interstitial site
U_{PB} = cluster energy when a carbon atom is in the maximum potential barrier
U_{SIS} = cluster energy when the carbon atom is on the surface in the unfinished octahedral interstitial site

Because the energy of a subnanocluster is significantly reduced, the movement of the carbon atom to the surface is possible. The change in the position of the nickel atom between the first and second carbon environment in the cluster differs by 8 %, but the change of the position of the carbon atom significantly has an impact to the energy change of the fcc cluster: at the position of a maximum potential barrier, the energy of the cluster increased by 20.5 % and in the octahedral interstitial site on the surface—vice versa—decreased by 23 %. This is due to the change of the central symmetry of the subnanocluster, when the carbon atom is located in the center, to the axial symmetry, when the carbon atom moved to the direction <011>.

Calculations were made of atomic group energy changes by criteria $\Delta_{1,2,3}$ for every possible position of nickel atoms despite such a small impact of the position of nickel atoms on the energy of the considered atomic group. To demonstrate the calculation results, three main positions of the carbon atom in this cluster were chosen: CIS, PB, and SIS (Fig. 20.3b).

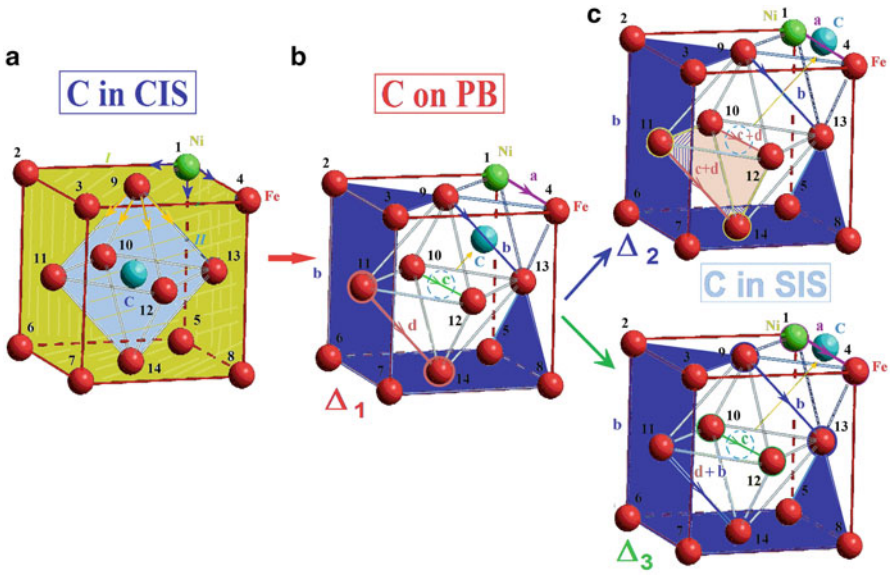

Fig. 20.4 Changes of equivalent positions of the Ni atom of the cluster that was estimated by the criteria Δ_1, Δ_2, and Δ_3 at different positions of the carbon atom: in the case when the carbon atom was in the central octahedral interstitial site (**a**), on the maximum of the potential barrier (**b**), and on the surface (**c**)

The Carbon Atom Located on the Potential Barrier

At the unstable position of the carbon atom at the potential barrier maximum (dashed area in Fig. 20.3b), a gain of energy of the cluster Δ_1 was estimated. Calculations indicate the existence of four possible values of the potential barrier height which must overcome the carbon atom to continue its movement to the surface depending on the position of atom Ni. Equivalent positions (states) of the Ni atom by those criteria were provisionally designated as (*a*) the position *1* or *4* (purple); (*b*) Ni atom in positions *2*, *3*, *5* ÷ *9*, and *13* (blue); (*c*) Ni atom at position *10* or *12* (*green*); and (*d*) Ni atom at position *11* or *14* (*brown*; Fig. 20.4b). The entry in Table 20.2, similar to the *11* = *14*, means that the position of the nickel atom in *11* or *14* in the cluster has the same value Δ_1.

Within the equivalent states, the change of the Ni atom's position had a small influence on the energy increment of the fcc cluster; the difference was less than 1 %. Between the different states (marked by different symbols), the gain of energy by changing the position of atoms Ni differed by 5 ÷ 10 %, in line with the change in energy of 0.4 ÷ 1.6 eV. Estimation of the potential barrier height shows that in the case of the Ni atom in position *1* or *4* (*a*), it was the lowest and was ~ 6.4 eV and, in the configuration *11* = *14*, the biggest, ~ 8 eV (*d*).

Thus the nickel atom's position in the fcc lattice of Fe–Ni–C significantly (20 %) affects the height of the energy barrier on the path of the carbon atom moving to the surface. The reduction of height of the potential barrier for the

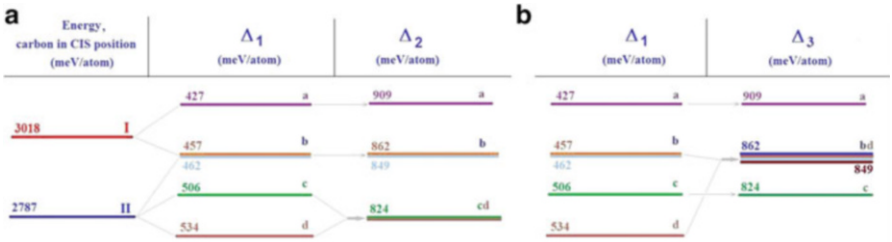

Fig. 20.5 Scheme of changes of energy of the fcc cluster when changing positions of one atom Ni and atom C which was estimated by Δ_1 criteria, (**a**) by Δ_2 criteria, (**b**) by Δ_3 criteria

carbon atom creates energetically favorable preconditions for the motion of carbon atoms to the surface in the direction of the nickel atoms. It corresponds to condition (20.3), the least significant change ΔU. The energy of the more stable position of the carbon atom on the edge of the unfinished surface octahedral interstitial site (SIS) was evaluated, because the carbon atom position at the maximum of the potential barrier is unstable.

The Carbon Atom on the Surface

The energy state of the fcc subnanocluster of the Fe–Ni–C system also depends on the position of the nickel atom, when the carbon atom is located on the surface. In this case, the evaluation of changes in energy was carried by two criteria: relative to the central position of the carbon atom by Δ_3 and relative to the potential barrier by Δ_3. In both cases, the change is consistent with $\Delta U < 0$.

Evaluation by the parameter Δ_2 showed the existence of three different values: *a*, *b*, *cd*, due to consolidation values of levels *c* and *d* (Fig. 20.4c on the top). When evaluating Δ_3 were only *a*, *bd* and *c* values due to approximation of values *b* and *d* (Fig. 20.4c, bottom).

Schematic changes of equivalent positions of the nickel atom in accordance with the position of the carbon atom are presented in Fig. 20.5a by Δ_2 and in Fig. 20.5b by Δ_3. Our analysis shows that it is energetically more advantageous for the carbon atom to choose the direction of movement to the surface, corresponding to the lowest energy loss (14 %) and the largest energy gain (30 %), that is, the configuration of nickel atom *a* ($1 = 4$). This also means that at such position of the nickel atom, the potential barrier is the smallest and the energy difference $\Delta U < 0$ is the most profitable.

Thus, discreteness of changes of energy depending on the arrangement of nickel and carbon atoms in the fcc subnanocluster was discovered. This is due to the change of symmetry of the fcc cluster that meets the condition of spontaneity of the process ($\Delta S > 0$), as well as the individual properties of atoms. Such processes can be determined for the formation of a new phase and correspond to

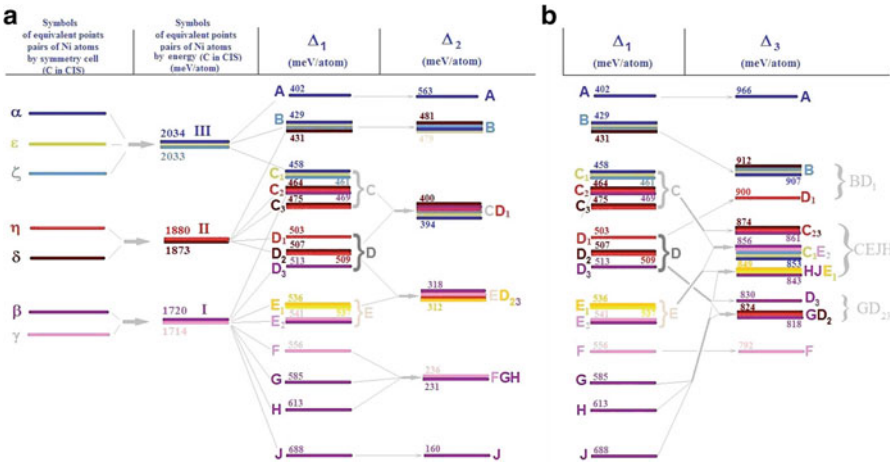

Fig. 20.6 Scheme of changes of energy of the fcc cell when changing positions of the pair of atoms Ni and atom C compared to the Δ_1 criteria, (**a**) by Δ_2 criteria, (**b**) by Δ_3 criteria

the thermodynamic conditions of its sustainable growth because the state with minimum surface energy is energetically favorable for the adhesion of new atoms.

The possible growth process of a new phase can be carried out in stages: (1) first, there should be established configuration conditions in the arrangement of solvent atoms that meet minimum energy costs to change the symmetry in the system ($\Delta S > 0$); (2) as a result, the impact of the surface that minimizes the energy of the cluster and meets the condition of spontaneity of the process ($\Delta U < 0$) becomes more significant; and (3) it promotes a certain accumulation of additional atoms near the surface, significantly increases the volume of the phase, and so on.

Then the process is repeated with new energy conditions for the gradual growth of the cluster or the formation of new, combining individual atomic groups in a new crystalline phase up to the establishment of balance.

20.3.2 The Case of Two Ni Atoms

Carbon Atom in the Center of the Cell

In the case when the fcc atomic group contains two atoms of nickel, the energy picture becomes more complex as shown in Fig. 20.6.

According to the symmetry of the crystal, there can be seven different configurations, if the carbon atom is located in the center of the cluster, which can be conventionally described as α, β, γ, δ, ε, ζ, and η (Table 20.3). Record *1,2 = 1,4* means that the position of a pair of atoms of nickel in positions *1* and *2* is the same as the symmetry of the positions of pairs *1* and *4*. However, calculations of the

Table 20.3 Lattice energy at different positions of the carbon atom and nickel atoms pair, where the numbering is done: N_0 by symmetry, N_1 by energy

Equivalent points pair of Ni at C in CIS	N_0	$U\left(\frac{\text{meV}}{\text{atom}}\right)$	N_1
1,2 = 1,4 = 2,3 = 3,4 = 1,5 = 5,8 = 4,8 = 5,6 = 6,7 = 7,8 = 2,6 = 3,7	α	2034	III
9,13 = 9,10 = 9,12 = 9,11 = 11,14 = 12,14 = 13,14 = 10,14 = 10,11 = 10,13 =	β	1720	I
= 12,13 = 11,12			
9,14 = 11,13 = 10,12	γ	1714	I
1,13 = 4,13 = 5,13 = 8,13 = 1,9 = 4,9 = 2,9 = 3,9 = 2,11 = 3,11 = 6,11 = 7,11 = 6,14 =	δ	1880	II
= 7,14 = 5,14 = 8,14 = 2,10 = 1,10 = 6,10 = 5,10 = 3,12 = 4,12 = 7,12 = 8,12			
1,3 = 2,4 = 1,8 = 4,5 = 5,7 = 6,8 = 1,6 = 2,5 = 3,8 = 4,7	ε	2033	III
1,7 = 4,6 = 2,8 = 3,5	ζ	2033	III
6,13 = 7,13 = 5,11 = 8,11 = 1,11 = 4,11 = 2,13 = 3,13 = 6,12 = 5,12 = 2,12 = 1,12 =	η	1873	II
= 7,10 = 8,10 = 3,10 = 4,10 = 3,14 = 4,14 = 2,14 = 1,14 = 6,9 = 7,9 = 5,9 = 8,9			

energy of the cluster in all possible positions of pairs of atoms of nickel (deviation of 0.4 %) showed that there are only three possible configurations: *I*, *II*, and *III*.

Configuration *I* contains all variants of the location of two atoms of nickel on the octahedra (the first sphere of the carbon environment). Configuration *II* contains all the variants of locations of nickel atoms, where one of them is on the outer part of the cube (second sphere) and the other is on the octahedra (first sphere). Configuration *III* displays all variants of positions of the pair of nickel atoms at the vertices of the outer part of the cube of the fcc cluster (second sphere of carbon atom environment). The difference between the energy values of all configurations is *I–II*—8.8 %; *I–III*—18.6 %; and *II–III*—8.6 %.

Estimation of Growth of Energy Δ_1

In the case of two atoms of nickel, the number of possible different values of energy by Δ_1 criteria is increased to nine, which can be conditionally described as levels *A*, *B*, *C*, *D*, *E*, *F*, *G*, *H*, and *J*, when the carbon is in the potential barrier area (Fig. 20.6a). Small differences in the values of Δ_1, which did not exceed 2.5 %, gave reason to split certain levels into sublevels: *C*—C_1, C_2, C_3; *D*—D_1, D_2, D_3; and *E*—E_1, E_2. The difference between adjacent levels ranged from 4 to 12 %, and the maximum difference between the most remote levels was 71 %.

The biggest potential barrier height corresponded to the configuration of a pair of nickel atoms *2,14* = *3,14* and occurred with an increase of energy of 83 %. The lowest barrier height was for configuration *1,4* where energy increased by almost 48 %. That is, at nickel atom positions *1,4*, energy conditions for the carbon atom's drift toward a smaller height of potential barrier are the best [41].

Thus, due to the asymmetric arrangement of substitutional impurities of atoms that could arise by chance, there are favorable conditions for energy drift of interstitial impurity atoms to the surface. This creates additional conditions for the further growth of the nanocluster by changing its energy state.

Estimation of Energy Gain Δ_2 and Energy Advantage Δ_3

The carbon atom exit on the surface on the SIS significantly changes the picture of changes of atomic group energy: the number of possible values of Δ_2 depending on the position of a pair of nickel atoms is reduced to six due to the merger of levels and sublevels and formation of new configurations: *A*, *B*, CD_1, ED_{23}, *FGH*, and *J* (Fig. 20.6b).

The difference between the adjacent groups of values Δ_2 was $18 \div 48$ %. The maximum difference between the most distant values reached 253 %. Within the levels, the energy difference did not exceed $0.6 \div 2.3$ %. The highest value Δ_2 for the carbon atom corresponded to configuration *A* of a pair of nickel atoms *1,4* (Fig. 20.7), which formed a local group together with the carbon atom on the edge of the cluster. The lowest value Δ_2 corresponded to configuration *J* (*2,14* = *3,14*) on

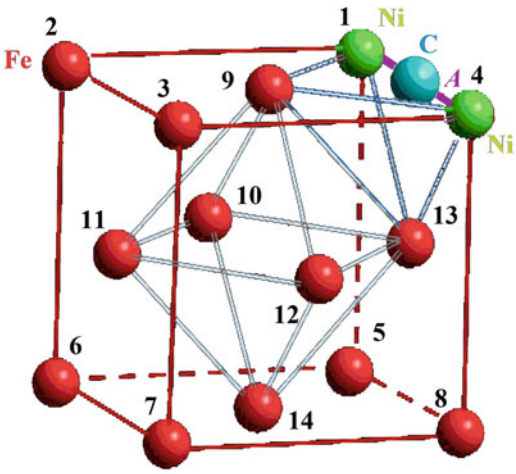

Fig. 20.7 Energetically advantageous configuration of a pair of nickel atoms at positions *1,4* with the carbon atom on the surface

the opposite side of the carbon atom. Thus there is a significant energy gain in the direction of motion of the carbon atom to the surface of the fcc cluster, where the pair of nickel atoms is located.

Evaluation of energy changes by Δ_3 criteria shows that there is a merger of levels and sublevels of energy changes into the broad bands of values BD_1, $CEJH$, and GD_{23}, although the configurations of F and A are unchanged (Fig. 20.6b). The difference between adjacent groups of values Δ_3 ranged from 1.5 to 5.6 %. Δ_3 values inside the group were in the range $1.3 \div 3.5$ %. The maximum change of Δ_3 between levels A and F was about 18 %. The biggest energy advantage Δ_3 corresponded to positions of nickel atoms (*1,4*; Fig. 20.7) and coincided with Δ_2 criteria. This is due to the change of central symmetry of cluster in the case when the carbon atom is located in the central octahedral interstitial site on mirror symmetry, when the carbon atom is located on the mid-rib between the nickel atoms in configuration *1,4*.

It should be noted that the formation of an energetically favorable configuration of a pair of nickel atoms and a carbon atom on the surface of the fcc subnanocluster does not mean the creation of a new chemical compound that requires the formation of a new surface and probably cannot be energetically favorable. The described tendencies only mean that the presence of nickel atoms creates additional energetically favorable conditions for the drift of the carbon atom exactly in the direction of the surface on the middle edge of the fcc cluster where these nickel atoms are located.

20.4 Conclusion

The energy of the fcc subnanocluster of system Fe–Ni–C depends on the position of nickel atoms in the first and/or second surrounding of the carbon atom.

The energy barrier for the carbon atom in the fcc Ni–C subnanocluster is larger by about 50 % than for the Fe–C case. This is due to the difference in size of the octahedral internodes of both systems and indicates the greater stability of Ni–C fcc atomic group.

The most energetically favorable is the position of the nickel atoms that form the octahedral interstitial site. This configuration corresponds to the minimum energy consumption or even its reduction of $\Delta U < 0$ when interstitial impurity (a carbon) drifts toward the nickel atoms. Such conditions correspond to the changes of the symmetry of the atomic group from central-symmetric to the axial (one atom Ni) or mirror (two atoms Ni) symmetry that increases the entropy $\Delta S > 0$.

Thus, the energy state of the fcc atomic group of system Fe–Ni–C significantly depends on the behavior of the impurities atoms. By the influence of these atoms, a complex energy picture of changes in the lattice energy is formed: formation of energy states, their splitting into levels and sublevels, and further combination in new configurations. Reducing the symmetry in such a system is a condition for spontaneity of the process that requires the increase of entropy and creates conditions for the growth of the new phase.

Acknowledgments I am grateful to Prof. V. E. Olshanetsky and Ms. N. V. Bondarenko for their advice and assistance. I thank my son D. A. Nedolya for his invaluable assistance in the preparation of this chapter.

References

1. Cahn J (1960) Theory of crystal growth and interface motion in crystalline materials. Acta Metall 8:554–562. doi:10.1016/0001-6160(60)90110-3
2. Mullin JW (2001) Crystallization, 4th edn. Butterworth-Heinemann, Oxford
3. Mutaftschiev B (2001) The atomistic nature of crystal growth. Springer, Berlin
4. Gibbs JW (1961) The scientific papers of J. Willard Gibbs. In: Thermodynamics, vol 1. Dover, New York
5. Curie P (1970) Pierre Curie: on the formation of crystals and capillary constants of their different faces. J Chem Educ 47:636. doi:10.1021/ed047p636
6. Wulff G (1901) Zur frage der geschwindigkeit des wachstums und der auflösung der krystallflagen. Z Kryst Mineral 34(5/6):449–530
7. Mamonova MV, Prudnikov VV, Prudnikova IA (2014) Surface physics. Theoretical models and experimental methods. CRC Press, New York
8. Winegard WC (1964) An introduction to the solidification of metals. Institute of Metals, London
9. Kashchiev D (2000) Nucleation: theory and basic applications. Butterworth-Heinemann, Oxford
10. Ring TA (2001) Nano-size cluster nucleation. Adv Colloid Interface Sci 91:473–499. doi:10.1016/S0001-8686(00)00073-7
11. Hudke M, Sitarz M, Rokita M (2003) Nanolikwacja i nanokrystalizacja w szkłach krzemianowo-fosforanowych (Nanoliquation and nanocrystallisation in the phospho-silicate glasses). Archiwum Nauki o Materiałach 24(4):467–475

12. Finney EE, Finke RG (2008) Nanocluster nucleation and growth kinetic and mechanistic studies: a review emphasizing transition-metal nanoclusters. J Colloid Interface Sci 317 (2):351–374. doi:10.1016/j.jcis.2007.05.092
13. Alonso JA (2005) Structure and properties of atomic nanoclusters. World Scientific, Singapore. doi:10.1142/9781860947414_0006
14. Venables JA, Spiller GDT, Hunbucken M (1984) Nucleation and growth of thin. Rep Prog Phys 47:399–459. doi:10.1088/0034-4885/47/4/002
15. Habraken WJEM, Tao J, Brylka LJ, Friedrich H, Bertinetti L, Schenk AS, Verch A, Dmitrovic V, Bomans PHH, Frederik PM, Laven J, van der Schoot P, Aichmayer B, de With G, DeYoreo JJ, Sommerdijk NAJM (2013) Ion-association complexes unite classical and non-classical theories for the biomimetic nucleation of calcium phosphate. Nat Commun 4:1507. doi:10.1038/ncomms2490
16. Baumgartner J, Dey A, Bomans PHH, Coadou CL, Fratzl P, Sommerdijk NAJM, Faivre D (2013) Nucleation and growth of magnetite from solution. Nat Mater 12:310–314. doi:10.1038/nmat3558
17. Kumar R (1969) Clusters in liquid metals. Contemp Phys 10(1):49–58. doi:10.1080/00107516908204562
18. Styles GA (1967) Influence of short-range atomic order on nuclear magnetic resonance in liquid alloys. J Adv Phys 16(62):275–286. doi:10.1080/00018736700101385
19. Helmy HM, Ballhaus C, Fonseca ROC, Wirth R, Nagel T, Tredoux M (2013) Noble metal nanoclusters and nanoparticles precede mineral formation in magmatic sulphide melts. Nat Commun 4:2405. (www.nature.com/naturecommunications). doi:10.1038/ncomms3405
20. Berry RS, Smirnov BM (2014) Ions in liquid metal clusters. Theor Chem Acc 133:1543. doi:10.1007/s00214-014-1543-0
21. Woehl TJ, Evans JE, Arslan I, Ristenpart WD, Browning ND (2012) Direct in situ determination of the mechanisms controlling nanoparticle nucleation and growth. ACS Nano 6 (10):8599–8610. doi:10.1021/nn303371y
22. Lim B, Jiang M, Yu T, Camargo PHC, Xia Y (2010) Nucleation and growth mechanisms for Pd-Pt bimetallic nanodendrites and their electrocatalytic properties. Nano Res 3:69–80. doi:10.1007/s12274-010-1010-8
23. Sree Harsha KS (2006) Principles of physical vapor deposition of thin films. Elsevier, Oxford
24. Smirnov BM (2010) Cluster processes in gases and plasmas. Wiley-VCH Verlag GmbH & Co. KGaA, Weinheim. doi:10.1002/9783527628650.ch5
25. Padovani S, D'Acapio F, Cattaruzza E, De Lorenzi A, Gonella F, Mattei G, Maurizio C, Mazzoldi P, Montagna M, Ronchin S, Tosello C, Ferrari M (2002) Metal nanocluster formation in silica films prepared by rf-sputtering: an experimental study. Eur Phys J B 25:11–17. doi:10.1140/e10051-002-0002-1
26. Yamamuro S, Sumiyama K, Suzuki K (1999) Monodispersed Cr cluster formation by plasma-gas-condensation. J Appl Phys 85(1):483–489. doi:10.1063/1.369476
27. Ferrando R, Jellinek J, Johnston RL (2008) Nanoalloys: from theory to applications of alloys clusters and nanoparticles. Chem Rev 108(3):845–910. doi:10.1021/cr040090g
28. Rossi G, Ferrando R (2009) Searching for low-energy structures of nanoparticles: a comparison of different methods and algorithms. J Phys Condens Matter 21(8):084208. doi:10.1088/0953-8984/21/8/084208 (11pp)
29. Martin TP (1996) Shells of atoms. Phys Rep 273:199–241. doi:10.1016/0370-1573(95)00083-6
30. Auer S, Frenkel D (2001) Suppression of crystal nucleation in polydisperse colloids due to increase of the surface free energy. Nature 413:711–713. doi:10.1038/35099513
31. Yi X-H, Liu R-S, Tian Z-A, Hou Z-Y, Li X-Y, Zhou Q-Y (2008) Formation and evolution properties of clusters in liquid metal copper during rapid cooling processes. Trans Nonferrous Met Soc China 18:33–39. doi:10.1016/S1003-6326(08)60007-2

32. Li ZN, Young NP, Di Vece M, Palomba S, Palmer RE, Bleloch AL, Curley BC, Johnston RL, Jiang J, Yuan J (2008) Three-dimensional atomic-scale structure of size-selected gold nanocluster. Nature 451:46–49. doi:10.1038/nature06470
33. Cherian R, Gerard C, Mahadevan P, Cuong NT, Maezono R (2010) Size dependence of the bulk modulus of semiconductor nanocrystals from first-principles calculation. Phys Rev B 82:2553321. doi:10.1103/PhysRevB.82.235321
34. Lewars EG (2011) Computational chemistry: introduction to the theory and applications of molecular and quantum mechanics, 2nd edn. Springer, Berlin. doi:10.1007/978-90-481-3862-3
35. Ramachandran KI, Deepa G, Namboori K (2008) Computational chemistry and molecular modelling. Principles and applications. Springer, Heidelberg. doi:10.1007/978-3-540-77304-7
36. Lennard-Jones JE (1924) On the determination of molecular fields. Proc R Soc Lond A 106 (738):463–477. doi:10.1098/rspa.1924.0082
37. Doye JPK, Miller MA, Wales DJ (1999) Evolution of the potential energy surface with size for Lennard-Jones clusters. J Chem Phys 111:8417–8428. doi:10.1063/1.480217
38. Yang Q, To AC (2015) Multiresolution molecular mechanics: a unified and consistent framework for general finite element shape function. Comput Methods Appl Mech Eng 283:384–418. doi:10.1016/j.cma.2014.09.031
39. Verlet L (1967) Computer experiments on classical fluids. I. Thermodynamical properties of Lennard-Jones molecules. Phys Rev 159:98–103. doi:10.1103/PhysRev.159.98
40. Hairer E, Lubich C, Wanner G (2003) Geometric numerical integration illustrated by the Störmer-Verlet method. Acta Numer 12:399–450. doi:10.1017/S096249290200144
41. Stark JP (1976) Solid state diffusion. Wiley, New York

Chapter 21
Large-Scale Solution for Superhydrophobic Surfaces

O.V. Myronyuk, A.V. Prydatko, and V.A. Raks

Abbreviations

CAH	Water contact angle hysteresis
SBM	Poly(styrene-butyl methacrylate)
SEM	Scanning electron microscopy
WCA	Water contact angle
WSA	Water sliding angle

21.1 Background

The effect of superhydrophobicity of natural surfaces has been discovered recently. Since then, it has been established that high hydrophobic properties of a wide variety of natural objects, from lotus leaves to body elements of some insects and animals, are determined by two main factors: the complex structure of the surface and its relative hydrophobicity. However, the first factor plays the most important role in the appearance of the effect.

Promising areas of industrial application of this effect are the creation of de-icing, antifriction, self-cleaning, and water-repellent coatings.

O.V. Myronyuk • A.V. Prydatko
National Technical University of Ukraine "Kyiv Polytechnic Institute", 37, Prospekt Peremohy, Kyiv 03056, Ukraine

V.A. Raks (✉)
Department of Analytical Chemistry, Faculty of Chemistry, Taras Shevchenko National University of Kyiv, 64/13, Volodymyrska Street, Kyiv 01601, Ukraine
e-mail: victoriia2005@gmail.com

O. Fesenko, L. Yatsenko (eds.), *Nanophysics, Nanophotonics, Surface Studies, and Applications*, Springer Proceedings in Physics 183,
DOI 10.1007/978-3-319-30737-4_21

There are a number of works dealing with the optimal geometric configuration of superhydrophobic materials surface—from the first works of Cassie [1] and Wentzel [2] to the recent works [3–5]. The value of the water contact angle of superhydrophobic surface, the values of advancing and receding water contact angles, and the value of corresponding wetting hysteresis and the water sliding angle are the most commonly used parameters in the process of theory development and optimization of material properties. Complex parameters that characterize the stability of the superhydrophobic state such as the time that a drop deposited on the surface of the compound in a state of Cassie [6] and the boundary fall speed drops, in which the transition to the Wentzel is not observed [7], are also informative.

The development of theoretical models of superhydrophobicity is also accompanied by numerous experimental attempts to produce coatings with high water repellency. At the moment, there are a large number of works devoted to the modeling of three-dimensional textures on different surfaces. Common methods include plasma deposition of surface structure elements (in the case of carbon nanotubes), lithography [8], chemical etching [9], laser ablation [10], spin coating, and combinations thereof. Generally, proposed method allows obtaining samples with highly hydrophobic structure at a small scale. Thus, scaling of such technologies to industrial applications is quite difficult. This problem was solved by some authors developing one-stage processes for the production of superhydrophobic coating with dual micro-nanohierarchical structure based on structure fillers with complex geometry. Authors in papers [11, 12] synthesized raspberry-like particles followed by their immobilization on the substrate. The works [13–15] are devoted to the creation of statistical superhydrophobic structures based on polymer solutions and dispersions (isotactic polypropylene, polystyrene, and mixtures of polyphenylene sulfide and polytetrafluorethylene). It can be achieved through the processes control of supramolecular structure formation, and it can result in a suitable hierarchical structure. Disadvantages of this approach are the relatively low mechanical strength of obtained structures and their low adhesion to the substrate. Furthermore, the use of directional solidification processes hinders the practical use of the achievements on a massive scale.

This work was devoted to obtaining robust superhydrophobic coatings based on conventional materials for the paint industry. Statistical hierarchical structures were made by the use of a mixture of different filler particle size formulations. The solution of the problem makes it possible to scale the technology without significant cost of equipment improvement and will provide the unlimited surface area while high values of the WCA are up to 160°, the values of WSA are less than 4°, and the values of CAH are within the limits of 3°. Thus, such coatings have increased adhesion to a number of substrates (steel, glass, mineral construction materials) as well as they have increased wear resistance in comparison with conventional superhydrophobic. This achievement can be used as a basis for the creation of a number of nontransparent coatings to protect metal structures, facades of buildings against the rain, and a hard frost.

21.2 Methods

21.2.1 Materials, Equipment, and Coating Preparation

Compositions were produced using a film forming poly(styrene-butyl methacrylate) (SBM) (NeoCryl B-880, DSM NeoResins) in a medium of *o*-Xylene (Sigma-Aldrich). Grounded marble (Normcal-20, SOM DENIZ SANAYI ve TICARET AS, Turkey), talc (MITAL 15–90, GEOKOM, Russia), wollastonite (MIVOLL 30–97, GEOKOM, Russia), and diatomite (Celite 545, Celiton, Washington, USA) were used as microsized fillers; fumed silica modified with dimethyldichlorosilane (AEROSIL R 972, Resource Efficiency Evonik GmbH) was used as a nanosized filler. All coatings were applied by pouring onto a glass surface and subsequently drying at 50 °C to remove the solvent.

Stearic acid was purchased from Sigma-Aldrich. Sodium propyl siliconate was obtained from Evonik Resource Efficiency GmbH.

Geometrical and dimensional parameters of fillers were obtained by analyzing scanning electron microscopy (SEM) images, microscope (REM- 106 I (SELMI, Ukraine)).

Values of WCA, CAH, and WSA of 5 μL of distilled water drop were measured using a digital goniometer. For the analysis of the morphology of a drop of water on the surface, the camera Delta Optical HCDE-50 and related software ScopeTek View were used.

21.2.2 Filler Surface Treatment

Grounded marble (100 g) was treated with 114 mL of 0.6 wt% solution of stearic acid in *o*-Xylene. A mixture of stearic acid and grounded marble in *o*-Xylene was left for 2 h with further complete evaporation of solvent at 80 °C. Diatomite (100 g) was hydrophobically treated with 100 mL of 40 wt% aqueous solution of sodium propyl siliconate. The milling of diatomite was conducted in a bead mill for 10 min.

21.3 Results and Discussion

The main idea of the work was to evaluate the possibility of using statistical systems and dual systems of available nano- and microfillers to create coatings with robust water-repellent properties. Particle sizes of microfillers, which are common to the paint industry, are in the range from 1 to 25 μm. These dimensions are also typical for a number of micro-roughness structural elements, often used to create superhydrophobic effect [16, 17]. Various trademarks of hydrophobically treated silica with particle sizes in the range of 10–50 nm were used for controlling of

nanostructured coatings [18]. To create a complete composition based on micro- and nanoscale fillers, the film forming agent, SBM polymer, was used. It has the average value of hydrophobicity: the value of WCA is 85°. In accordance with the primary objective of the work, research was focused on the following tasks: determining the structure and particle size of microfillers, assessing hydrophobicity factors of microfiller-polymer systems, establishing the influence of the nanofiller's nature on hydrophobicity parameters of coating, determining optimal ratios in the film formers—nano- and microfiller systems—and, finally, assessing the possibility of obtaining stable superhydrophobic materials based on this system.

These approaches allows us to obtain compositions in which the structural elements are arranged statistically; this type of coating can be applied over large surface and cured under ambient operating conditions without the need for additional processing.

21.3.1 Microscale Structure Formation

Figure 21.1 shows SEM images of microsized fillers. Size distribution parameters of materials and geometry are given in Table 21.1.

An average primary particle size of the material is in the range of 4.5–100.0 μm. Cylindrical filler particles (wollastonite and diatomite) are significantly larger than those for marble and talc. Fillers are characterized different values of specific surface: grounded marble, 1.4 m^2/g; talc, 3.4 m^2/g; wollastonite,1.3 m^2/g; diatomite, 65 m^2/g. This fact might determine values of optimal ratios of filler-binder compositions.

It was determined that the correlation between WCA and filler concentration in systems for all materials has similar character (Fig. 21.2).

Surface roughness is monotonically increasing with filler content up to 70 wt%; at the same time projections are relatively smooth, and interparticle volumes are blocked with a polymer. Pores between particles start to fill the air due to lack of polymer in the structure at filler content above 80 wt%. A filler content of 87–95 wt % leads to the formation of wetting optimum in terms of Cassie state. Maximum values of WCAs reach up to 124°, 111°, and 115° for systems filled with wollastonite, talc, and grounded marble, respectively. At the same time, the value of the WSA for surfaces is about 90°.

Surfaces based on diatomite behave in a complicated manner due to complex two-level geometric configuration of micro- and nanoparticles. The maximum value of the WCA reaches up to 157°, when the content of the filler in a matrix is about 60 wt% (Fig. 21.3a). However, the value of CAH is also high and increases up to 70°. Nonuniform distribution of values of CAH in the range from 20 to 40 wt% might be related to the increase in filler content that also leads to dramatically increase the receding angle while the value of the ascending angle and WCA are kept constant. At the next stage, receding angle remains almost constant. The value of WCA increases, and this leads to increase of CAH. It was found that hysteresis

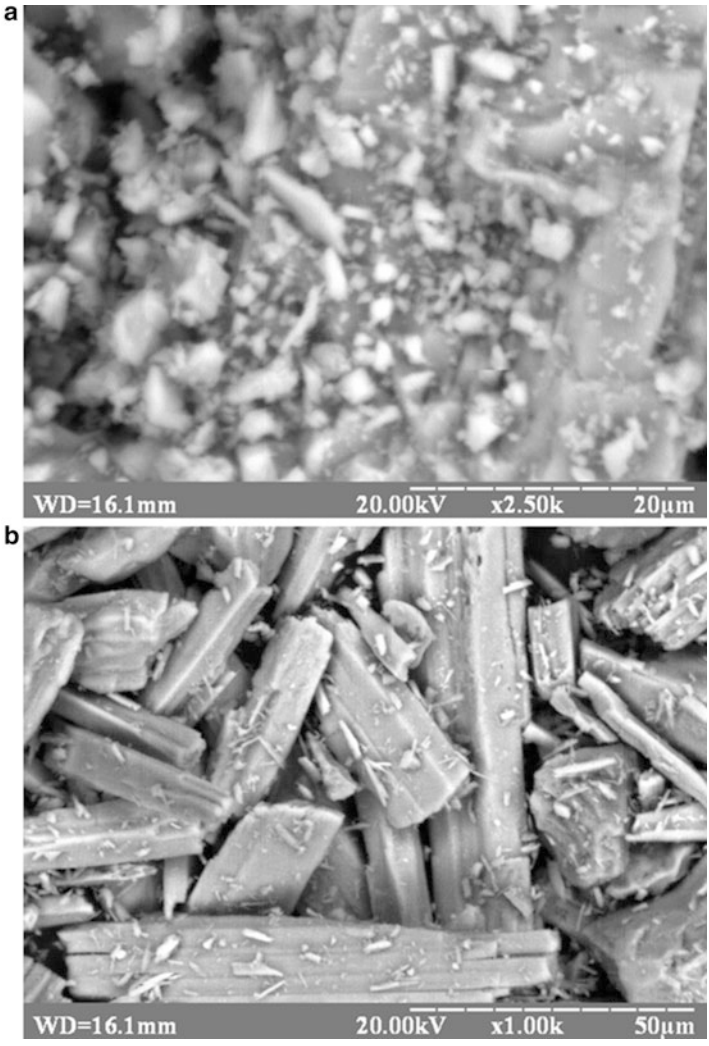

Fig. 21.1 SEM microphotographs of microscale fillers used in paint industry with different magnification: (**a**) grounded marble (×2500), (**b**) wollastonite (×1000), (**c**) talc (×2500), (**d**) diatomite (×1000)

can be significantly reduced by hydrophobic treatment of the diatomite surface. The maximum value of CAH reaches up to 95° at a diatomite content of 25 wt% and reduces up to 7° at a filler content of 60 wt% (Fig. 21.3b). Mechanical disruption of the particle structure of diatomite in a bead mill leads to formation of sharp pieces of primary cells, providing the value of CAH nearly 6° even at a filler concentration of 50 wt% (Fig. 21.3c). The value of WCA increases up to 164°.

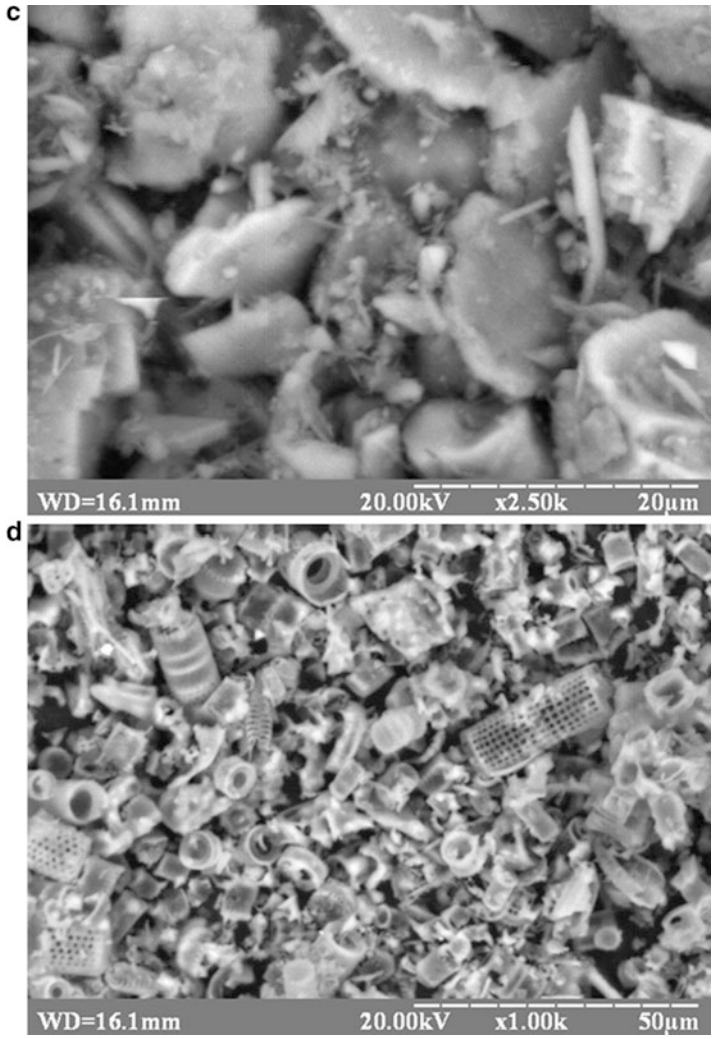

Fig. 21.1 (continued)

Using microfillers allows us to obtain a primary level of a hierarchical structure of composite coating. Surfaces of such coatings are ordered only in a statistical sense that allows us to achieve sufficiently high values of WCA (up to 164°).

It was observed that the correlation between the parameters of the filler particles and the wetting characteristics of resulting coatings can be described by such regularities: (a) The greater the degree of anisotropy and spatial inhomogeneities microfiller particles have, the higher values of WCA may be reached. For example, maximum values of WCAs of systems based on grounded marble and wollastonite reach up to 115° and 124°, correspondingly. Mechanical activation changes the

Table 21.1 Filler properties

Filler	Average primary particle size (μm)	*F* factor of integral size distribution curve	Geometry of particles	WCA (°)
Grounded marble	4.5	1.3	Cleaved polygon	29
Wollastonite	100.0	1.4	Needlelike	40
Talc	6.5	1.5	Lamellar	70
Diatomite	18.0	1.5	Hollow cylinders	47

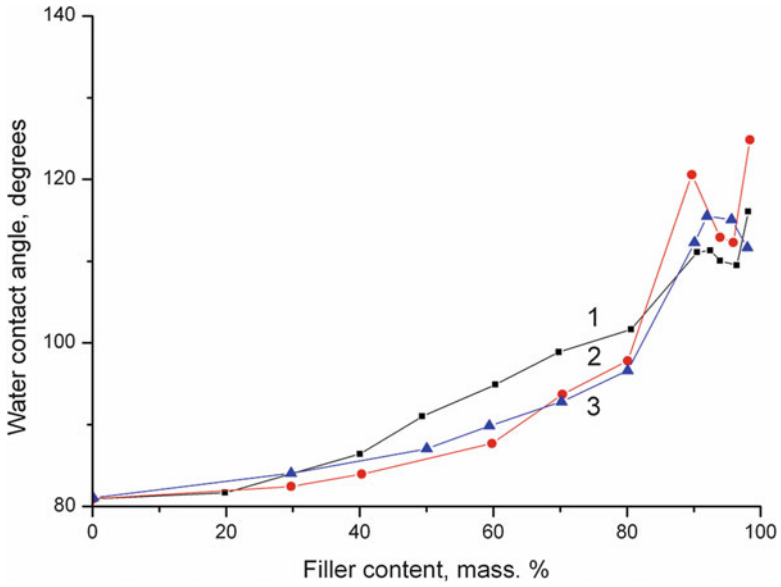

Fig. 21.2 Water contact angle of polymer-filler composites. The relation between the water contact angle and different filler content in their compositions with SBM polymer: (*1*) grounded marble, (*2*) wollastonite, (*3*) talc

geometry of the primary particles and induces the formation of "sharp" edges, which in accordance with a relation derived in [19] leads to the increase of WCA in the coating.(b) The WCA of the compositions can be substantially increased by the use of microparticles with a textured surface (as in the example of diatomite). The same fact was stated in [20] and [21], where texturing is performed after the formation of the microstructure; (c) CAH can be significantly reduced by hydrophobic treatment of filler particles. This can be attributed to the fact that in systems with a high degree of filler content, the film forming polymer does not completely cover surfaces of hydrophilic filler.

Despite the high values of contact angles, such systems, however, cannot be attributed to the robust superhydrophobic ones due to the high values of CAH and high values of WSAs. This problem can be solved by formation of the nanoscale structure of the second layer.

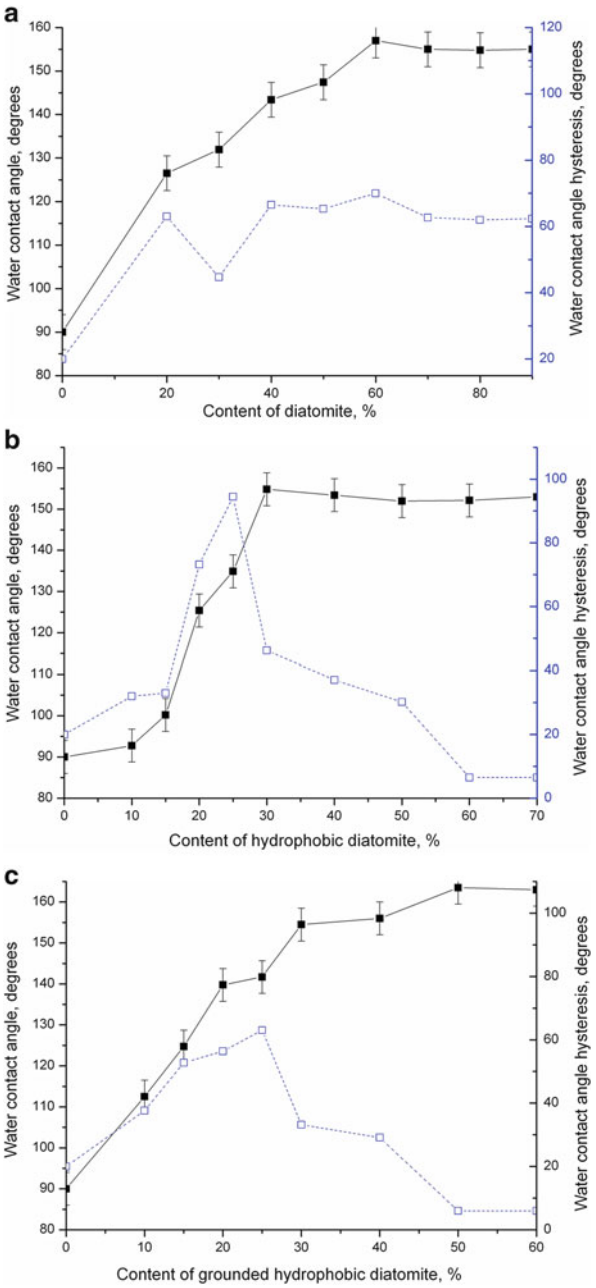

Fig. 21.3 Dependencies of content of diatomite in SBM coatings from WCA (*solid line*) and CAH (*dashed line*) in systems filled with: (**a**) untreated diatomite, (**b**) hydrophobized diatomite, (**c**) hydrophobized and grounded diatomite

21.3.2 Nanoscale Structure Formation

In this work, dimethyldichlorosilane-treated silica particles were used for the formation of nanoscale level of hierarchical structure. The specific surface of the material is 192 m^2/g, and a primary particle size is about 12 nm. For compositions of this filler with SBM, the maximum WCA can be observed at a filler concentration of 48 wt% (Fig. 21.4). Such low sufficient critical content can be explained by the high value of the specific surface of silica in comparison to other considered materials. The maximum value of WCA is 162°. The WSA is less than 5° at 50 wt% of the silica.

Composition filled with grounded marble was selected as the basic for the two-level structure formation. As it can be seen from Fig. 21.5a, the effect of the nanofiller introduction is evident at its content in the system of several percent. Obviously, this is due to the formation of a thin layer of the nanoscale particle layer on the already existing microstructure. The maximum value of the WCA reaches 164° at a content of 3 % of silica by weight of grounded marble, and CAH during the formation of continuous layer on microstructure surface drops to 3° at silica content 3.5 wt%. WSA for this system is 2°.

In systems with hydrophobically treated marble, CAH reduction is achieved at silica content at 3 wt% (Fig. 21.5b); the WSA also is 2°.

Obviously, during the transition from a microscale structure to a dual-level hierarchical structure, the surface turns into robust superhydrophobic state, as

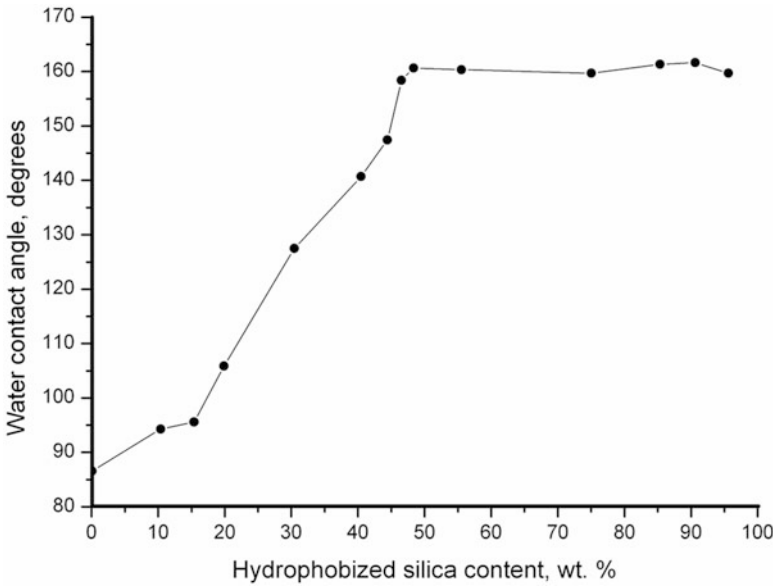

Fig. 21.4 Water contact angles hydrophobized silica-based SBM coatings. The relation between the filler content and WCA of system filled with hydrophobized silica

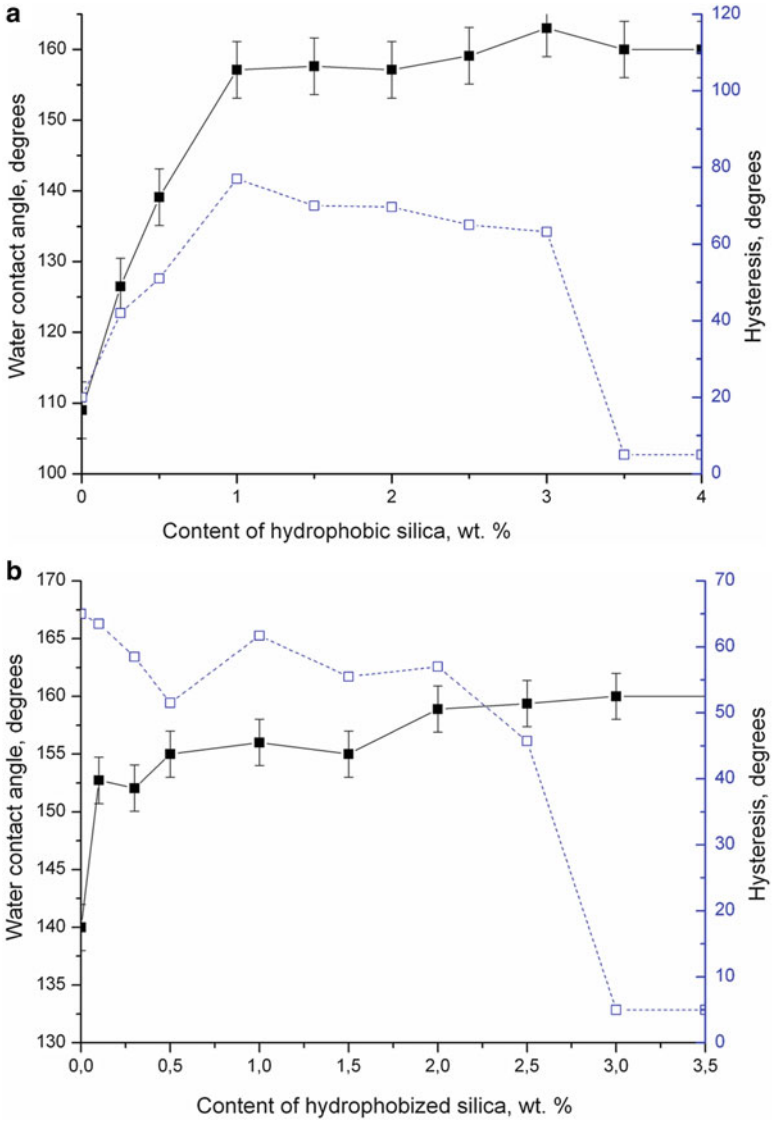

Fig. 21.5 Water contact angles and CAH of grounded marble silica-based SBM coatings. The relation between the nanoscale filler content, WCA (*solid line*), and CAH (*dashed line*) in systems, microscale filler of which is: (**a**) untreated grounded marble, (**b**) stearic acid treated grounded marble

evidenced by a significant decrease of CAH (3°) and WSA (2°). This transition takes place upon condition of completed nanoparticles layer of on the surface of the elements of the microstructure formation. An interesting fact is that the transition to a robust superhydrophobic state is relatively sharp at the concentrations of nanosized filler 3–3.5 wt%. This could be caused by the difference between

contributions of nanosized particles that are located in the bottom and on the top parts of the microstructure elements. In the first case, they do not affect the ability of a liquid droplet to be fixed on the surface, while in the second case, the effect is evident. The hypothesis about the main contribution of structure top elements in WCA and CAH values is indirectly confirmed by the fact that the hydrophobic pretreatment of microfillers can significantly reduce the CAH.

Proposed coatings with the hierarchical structure, formed by statistically distributed roughness elements, exhibit a high level WCA and low level of WSA and CAH, even compared with superhydrophobic surfaces obtained by conventional methods.

It should be noted, however, that such compositions have sufficiently high adhesion to the substrate, and they are not prone cracking, even in relatively thick layers—up to 150 μm. They have limited resistance to abrasion (as compared with conventional industrial coatings). However, in case of erasing the upper layer, the coating retains superhydrophobic behavior. These mechanical properties of dual-level structure coatings exceed only the properties of nanostructured surfaces.

21.4 Conclusions

In this work, we obtained the series of superhydrophobic coatings based on mixtures of fillers with primary particle sizes of micro- and nanoscale by the use of the conventional one-step technology and ambient curing. It was shown that such coatings, despite their surfaces are ordered only statistically, can exhibit WCA values of 160°, CAH of 3°, and WSA of 2°. Thus, microsized filler exhibits a reinforcing function in the coating, increasing the resistance to abrasion and cracking on the surface, and a nanoscale filler is responsible for the formation of high water repellency. The improvement of hydrophobic characteristics of such composites was observed using irregularly shaped microfillers (fragmented structures after mechanical activation, fibrous materials such as wollastonite), as well as when they were hydrophobically pretreated. Due to the microstructure formed, an effective content of the nanosized filler to achieve a robust superhydrophobic state is relatively low—up to 4 %. The advantage of the proposed method of obtaining the nontransparent superhydrophobic coatings is its scalability and ease of use in the industry for coating of large surfaces, one-stage application process, as well as the relative availability of the raw materials used. Coatings based on this basic approach could potentially be used to produce water-repellent surfaces in civil and industrial construction industry, top coating of metal systems, de-icing coatings.

21.5 Competing Interests

The authors declare that they have no competing interests.

21.6 Author's Contributions

VR and OM provides guidance regarding research; AP obtained series of superhydrophobic coatings based on mixtures of fillers and carried out research; OM, AP and VA have made substantial contributions to the analysis and interpretation of data and contributed to the draft of the manuscript. All authors read and approved the final manuscript.

Acknowledgments We are thankful to the organizing committee of the Conference of Nanotechnology and Nanomaterials (NANO-2015), which was held in the framework of the FP7 project Nanotwinning, for the opportunity to publish our paper.

References

1. Cassie ABD, Baxter S (1944) Wettability of porous surfaces. Trans Faraday Soc 40:546–551
2. Wenzel RN (1949) Surface roughness and contact angle. J Phys Chem 53(9):1466–1467
3. Nosonovsky M, Bhushan B (2008) Roughness-induced superhydrophobicity: a way to design non-adhesive surfaces. J Phys Condens Matter 20:225009
4. Synytska A, Ionov L, Dutschk V, Stamm M, Grundke K (2008) Wetting on regularly structured surfaces from "Core–Shell" particles: theoretical predictions and experimental findings. Langmuir 24:11895–11901
5. Tuteja A, Choi W, McKinley GH, Cohen RE, Rubner MF (2008) Design parameters for superhydrophobicity and superoleophobicity. MRS Bull 33:752–758
6. Papadopoulos P, Mammen L, Deng X, Vollmer D, Butt HJ (2013) How superhydrophobicity breaks down. Proc Natl Acad Sci 10(9):3254–3258
7. He B, Patankar NA, Lee J (2003) Multiple equilibrium droplet shapes and design criterion for rough hydrophobic surfaces. Langmuir 19:4999–5003
8. Lay Y, Lin C, Wang H, Huang J, Zhuang H (2008) Superhydrophilic-superhydrophobic micropattern on TiO_2 nanotube films by photocatalytic lithography. Electrochem Commun 10:387–391
9. Zhou Y, He B, Yang Y, Wang F, Liu W, Wang P, Zhang W, Bello I, Lee ST (2011) Construct hierarchical superhydrophobic silicon surfaces by chemical etching. J Nanosci Nanotechnol 11 (3):2292–2297
10. Chun DM, Davaasuren G, Ngo CV, Kim CS (2014) Fabrication of transparent superhydrophobic surface on thermoplastic polymer using laser beam machining and compression molding for mass production. Manuf Technol 63(1):525–528
11. D'Acunzi M, Mammen L, Singh M, Deng X, Roth M, Auernhammer GK, Butt HJ, Vollmer D (2010) Superhydrophobic surfaces by hybrid raspberry-like particles. Faraday Discuss 146:35–48
12. Wang R, Liu H, Wang F (2013) Facile preparation of raspberry-like superhydrophobic polystyrene particles via seeded dispersion polymerization. Langmuir 29(36):11440–11448
13. Erbil HY, Demirel AL, Avci Y, Mert O (2003) Transformation of a simple plastic into a superhydrophobic surface. Science 299:1377–1380
14. Tu CW, Tsai CH, Wang CF, Kuo SW, Chang FC (2007) Fabrication of superhydrophobic and superoleophilic polystyrene surfaces by a facile one-step method. Macromol Rapid Commun 28:2262–2266

15. Yang Q, Luo Z, Tan S, Luo Y, Wang Y, Zhang Z, Liu W (2014) Well-ordered polymer nanofibers with self-cleaning property by disturbing crystallization process. Nanoscale Res Lett 9 (1):352
16. Zhang Y, Sundararajan S (2008) Superhydrophobic engineering surfaces with tunable air-trapping ability. J Micromech Microeng 18(3):035024
17. Tsai PS, Yang YM, Lee YL (2007) Hierarchically structured superhydrophobic coatings fabricated by successive Langmuir-Blodgett deposition of micro-/nano-sized particles and surface silanization. Nanotechnology 18(46):465604
18. Hanemann T, Szabó DV (2010) Polymer-nanoparticle composites: from synthesis to modern applications. Materials 3:3468–3517
19. Teisala H, Tuominen M, Kuusipalo J (2011) Adhesion mechanism of water droplets on hierarchically rough superhydrophobic rose petal surface. J Nanomater 2011:818707
20. Zhang X, Di Q, Zhu F, Sun G, Zhang H (2013) Superhydrophobic micro/nano dual-scale structures. J Nanosci Nanotechnol 13(2):1539–1542
21. Yoon Y, Kim D, Lee JB (2014) Hierarchical micro/nano structures for super-hydrophobic surfaces and super-lyophobic surface against liquid metal. Micro Nano Syst Lett 2(1):1–18

Chapter 22
Comparison of Stability Properties of Nanozirconia Aqueous Suspension in the Presence of Selected Biopolymers

Małgorzata Wiśniewska and Katarzyna Szewczuk-Karpisz

22.1 Introduction

Nanotechnology has many areas of its applications and it is present in practically every field of human activity. The most important of them are medicine and pharmacy, nanobiotechnology, microelectronics, optical engineering, agriculture and bioengineering, nanofibres and nanocomposites, cosmetology as well as energetics and microelectronics [1–5].

Nanotechnology has a very extensive use in medicine. It gives new perspectives in the treatment of various diseases and provides innovative possibilities for diagnostics [6–9]. Prospects for the use of nanomaterials in medicine are surprising. They include construction of a nanorobot fighting against pathogenic microorganisms or removal of cholesterol deposits in blood vessels. Current experiments are focused on the construction of a nanorobot which will render cancer cells harmless. For this purpose, anti-tumour 'bomb'—a chemotherapeutic or substance that contains radioactive atoms (i.e. actinium)—is introduced to cancer cells. This formulation operates inside the tumour cells and destroys them.

Another possibility is the development of diagnostics by the use of microcameras equipped with recorders for transmitting an image from the internal organs (the endoscopy replacement).

Nanotechnology is also used in gene therapy. It is based on the addition to the cells of specific material which eventually replaces the gene of an incorrect sequence of amino acids.

M. Wiśniewska (✉) • K. Szewczuk-Karpisz
Department of Radiochemistry and Colloid Chemistry, Faculty of Chemistry, Maria Curie-Sklodowska University, Maria Curie-Sklodowska Sq. 3, 20-031 Lublin, Poland
e-mail: wisniewska@hektor.umcs.lublin.pl

O. Fesenko, L. Yatsenko (eds.), *Nanophysics, Nanophotonics, Surface Studies, and Applications*, Springer Proceedings in Physics 183,
DOI 10.1007/978-3-319-30737-4_22

Nanomaterials are used in various types of implants. It turned out that protein adsorption on the metal oxide surface plays an essential role in the implantation process [10–13]. The biopolymer adsorption occurs immediately after the implantation and it enables cell interactions with the implant surface. It decides about implant acceptance or rejection. Their favourable properties such as high mechanical strength, corrosion resistance, very low chemical activity and most of all the excellent biocompatibility with the human tissue contribute to wide application of metal nano-oxides in this field of medicine.

The aim of the present study is determination of adsorption and stability mechanism in the colloidal system in which mesoporous zirconia nanoparticles are dispersed in the aqueous biopolymer solution. The obtained results can be helpful in the development of modern implant coatings as scaffold for tissue regeneration [14, 15]. There were used the following natural polymers: bovine serum albumin (BSA), lysozyme (LSZ) and exopolysaccharide (EPS) synthesized by the bacteria *Sinorhizobium meliloti*. The applied zirconia was characterized by a nanoscale size of pores and solid grain (about 30 and 100 nm, respectively). The stability of the ZrO_2 suspension in the biopolymer presence was determined using the turbidimetry method on the basis of calculated Turbiscan Stability Index (TSI). Application of this technique in such systems is novel. Moreover, the mechanism of nanozirconia particles stabilization (or destabilization) in the biopolymer presence was proposed. This was made possible by the analysis of the data concerning adsorbed amounts of polymer, surface charge density and zeta potential values of solid particles covered with biopolymer layers.

22.2 Materials

Zirconium (IV) oxide (ZrO_2, zirconia) was used in the experiments as an adsorbent. This is a white, finely crystalline solid of the average particle size less than 100 nm. In the ZrO_2 structure, the mesopores of average size equal to 31 nm are present. The zirconia-specific surface area was 21.7 m^2/g. The average pore size and specific surface area of the adsorbent were determined by the BET method. The average particle size was measured using a Mastersizer (*Malvern Instruments*) [16].

The following biopolymers, BSA, LSZ and EPS, were used in the study as adsorbates. BSA and LSZ are proteins of different properties. BSA is a 'soft protein' characterized by a low internal stability. This means that its denaturation during the adsorption is highly probable. The BSA isoelectric point is in the range 4.7–4.9 [17], and its mass is about 66 kDa [18]. In turn, LSZ is a 'hard protein', i.e. it has a high internal stability. This is equivalent with low probability of conformational changes during adsorption on the solid surface. The LSZ isoelectric point is about 11 and its mass is equal to 14.3 kDa [19, 20].

EPS is a bacterial polysaccharide synthesized by the bacteria *Sinorhizobium meliloti*. It is mainly a succinoglycan composed of seven glucose molecules and one galactose molecule linked by β-1,3, β-1,4 and β-1,6-glycosidic bonds. Its skeleton is

modified by acetyl, pyruvyl and succinyl substituents [21]. The EPS high molecular weight (HMW) fraction is in the range 10^3–10^4 kDa [22]. It is worth mentioning that the EPS pK_a value, calculated based on the potentiometric titration results, is about 3.8. This means that at pH 3.8 the number of dissociated carboxylic groups (COO^-) in the EPS macromolecules is the same as that of undissociated ones (COOH). Using the appropriate formulae, the EPS dissociation degree (α) at various pH values was also determined. At pH 3, it was approximately 0.14 and at pH 6, 9–0.99 [23].

22.3 Experimental Methods

22.3.1 Potentiometric Titration

The potentiometric titration is a method which allows, inter alia, the determination of solid surface charge (σ_0) in the absence and presence of a macromolecular compound. This parameter is established by the computer program 'titr_v3' developed by W. Janusz using the following equation [24]:

$$\sigma_0 = \frac{\Delta V \cdot c \cdot F}{m \cdot S_w} \tag{22.1}$$

where ΔV is the difference in the base volume added to a suspension and a supporting electrolyte solution that leads to the specific pH value ($\Delta V = V_S - V_e$), c the base concentration, F the Faraday constant, m the metal oxide mass in a suspension, and S_w the metal oxide surface area.

The apparatus consisted of Teflon thermostated vessel, water thermostat RE 204 (*Lauda*), glass and calomel electrodes (*Beckman Instruments*), pH metre PHM 240 (*Radiometer*), automatic microburette Dosimat 765 (*Metrohm*), PC and printer.

At the beginning the supporting electrolyte (0.01 M NaCl) was titrated. Then the titration of the zirconia suspension in the absence and presence of biopolymer was performed. The ZrO_2 weight used for the suspension preparation was equal to 0.8 g. The biopolymer concentration was 50 ppm. All probes were titrated with 0.1 M NaOH. The measurements started at the pH value approximately 3.5.

22.3.2 Electrokinetic Potential Measurements

The electrokinetic potential (zeta potential, ζ) of the zirconia particles in the absence and presence of biopolymer was measured based on microelectrophoresis. In this method, solid particles move in the electric field in the electrophoretic cell, and zeta potential reading is made automatically when the particle movement is

compensated by the applied voltage. According to Hückel, the speed (u) of the particles moving in the electric field is connected with the zeta potential by the formula

$$u = \frac{2}{3}\frac{\zeta\varepsilon}{\eta} \tag{22.2}$$

where ε is the dielectric constant and η is the viscosity.

The zeta potential was measured using a Zetasizer Nano ZS (*Malvern Instruments*). The apparatus was connected with a titrator which changes the suspension pH value automatically.

The experiments began with the measurement of the zirconia zeta potential without the biopolymer. Then the systems with it were examined. The ZrO_2 weight taken for the sample preparation was 0.0075 g. The biopolymer concentration was 100 ppm. All probes were sonicated for 3 min. The examined pH range was 3–9. One result was the average of three measurements and the measurement error did not exceed 5 %.

22.3.3 Adsorption Measurements

The biopolymer concentration was determined by a spectrophotometric method (spectrophotometer UV–Vis *Cary 100*, *Agilent Technology*). The BSA concentration was measured at a wavelength of 279 nm and the LSZ concentration at 280 nm. In the EPS concentration measurement, the method developed by Dubois et al. [25] was used.

The biopolymer-adsorbed amount on the ZrO_2 surface was established based on the difference in its concentration before and after the adsorption process. At first, the suspension was prepared using 0.045 g (for BSA and LSZ) or 0.035 g (for EPS) of ZrO_2. The solid was added to 10 cm^3 of the solution containing the supporting electrolyte (0.01 M NaCl) and the proper biopolymer (10–500 ppm). Then the pH value of the probes was adjusted (3, 6 or 9). The adsorption process was carried out until the equilibrium was attained, i.e. 8 h for the systems with proteins and 20 h with EPS. The above time was determined based on the kinetic measurement results. After the adsorption completion, the samples were centrifuged and the polymer concentration was established. The single result was the average of three repetitions. The measurement error did not exceed 5 %.

22.3.4 Stability Measurements

The turbidimetric method (*Turbiscan TLab*^{Expert} with a cooling module *TLab Cooling*) was used in the experiments to determine the zirconia suspension stability in the absence and presence of biopolymer. Each sample was prepared by adding

0.015 g ZrO_2 to 20 cm^3 of the solution containing the supporting electrolyte (0.01 M NaCl). All samples were sonicated for 3 min. In the next step, the biopolymer was added (100 ppm) and the pH value was determined (3, 6 or 9). A single measurement of stability lasted 3 h for the probes containing proteins and 15 h for those with EPS.

The results were presented in the form of the curves of transmission and backscatter of light passing through the sample during the measurement. The low transmission level and high backscatter level confirmed high stability of the system. On the other hand, the lower the system stability, the higher the transmission and the lower the backscatter. Moreover, the specialized computer software connected with a turbidimeter allowed the calculation of TSI, which is very useful in the system stability estimation. TSI is a statistical quantity which takes into account all the processes occurring in the sample, i.e. thickness of the sediment and clean layer, rate of solid particles sedimentation. TSI is a parameter taking a value from 0 to 100. The higher the TSI value is, the smaller system stability is observed. The above parameter was calculated from the following equation:

$$\mathrm{TSI} = \sqrt{\frac{\sum_{i=1}^{n} (x_i - x_{\mathrm{BS}})^2}{n-1}} \tag{22.3}$$

where x_i is the average backscatter for each minute of measurement, x_{BS} is the average x_i value, and n is the scans number.

22.4 Results

The potentiometric titration showed that the point of zero charge (pH_{pzc}) of zirconia surface is about 6. The biopolymer adsorption moves this point and changes the density of solid surface charge. The results obtained for the examined systems at a biopolymer concentration equal to 50 ppm are shown below.

The electrokinetic potential measurements showed that the isoelectric point (pH_{iep}) of the solid is also 6. In the biopolymer presence, there was the pH_{iep} shift and change in the zeta potential values of the ZrO_2 particles. The obtained results are presented below.

On the basis of the adsorption measurement results, it was found that all polymers adsorb on the zirconia surface. The highest adsorption was observed for EPS at pH 3 and the lowest for LSZ at pH 3 (there was no adsorption under these conditions). The obtained results are shown in Fig. 22.3.

Stability measurements provided a significant information about the biopolymer influence on the zirconia suspension stability. The biopolymer impact varies considerably for the selected macromolecular compounds. In Figs. 22.4 and 22.5, the TSI values are summarized and in Fig. 22.6 the transmission and backscatter curves for EPS at pH 9 are shown.

22.5 Discussion

The potentiometric titration and zeta potential measurements provided information about electrokinetic properties of the zirconia/supporting electrolyte (biopolymer) systems. The point of zero charge (pH_{pzc}) of the zirconium (IV) oxide surface is about 6. This means that at pH 6 the concentrations of $ZrOH_2^+$ and ZrO^- groups on the solid surface are identical. The biopolymer addition moves this point to more acidic pH values. In the BSA presence, pH_{pzc} is 5.2, whereas in the LSZ and EPS presence, about 5.5. What is more, the biopolymer adsorption reduces the density of zirconia surface charge. This reduction is very slight as well as very similar for all biopolymers (Fig. 22.1).

The protein adsorption influence on the solid surface charge depends mainly on the type of amino acids which are closest to the adsorbent surface [26]. Moreover, the observed reduction of ZrO_2 surface charge in the protein presence can be associated with the following reaction:

$$-\mathrm{ZrOH} + \mathrm{NH_3^+} - \mathrm{R} \rightarrow -\mathrm{ZrO^-NH_3^+} - \mathrm{R} + \mathrm{H^+}$$

The NH_3^+ groups, i.e. protonated amino groups, are present in the protein macromolecules mainly at pH values below the protein isoelectric point. They can react with the surface groups $-ZrOH$, which causes the proton disconnection from them. As a consequence, the negative groups $-ZrO^-$ are formed on the adsorbent surface.

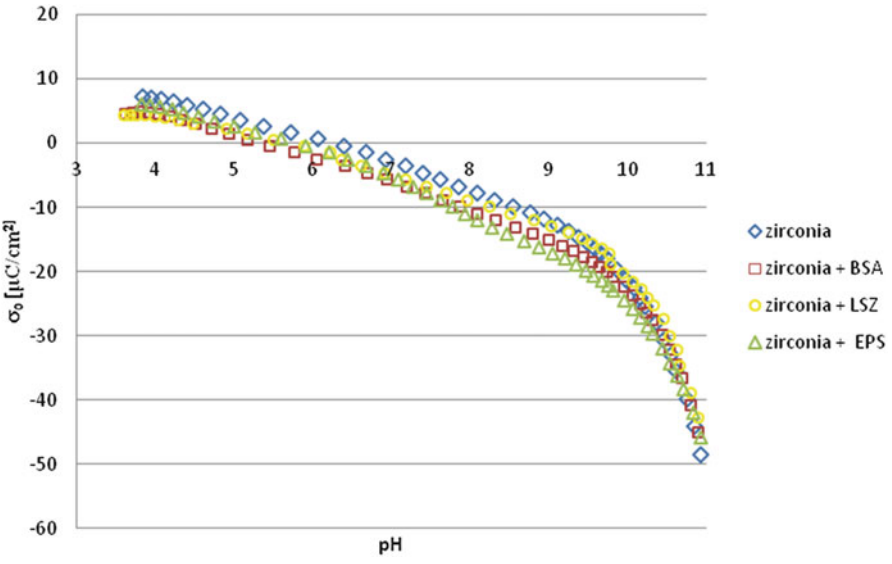

Fig. 22.1 Density of zirconia surface charge in the absence and presence of biopolymers ($C_{biopolymer} = 50$ ppm)

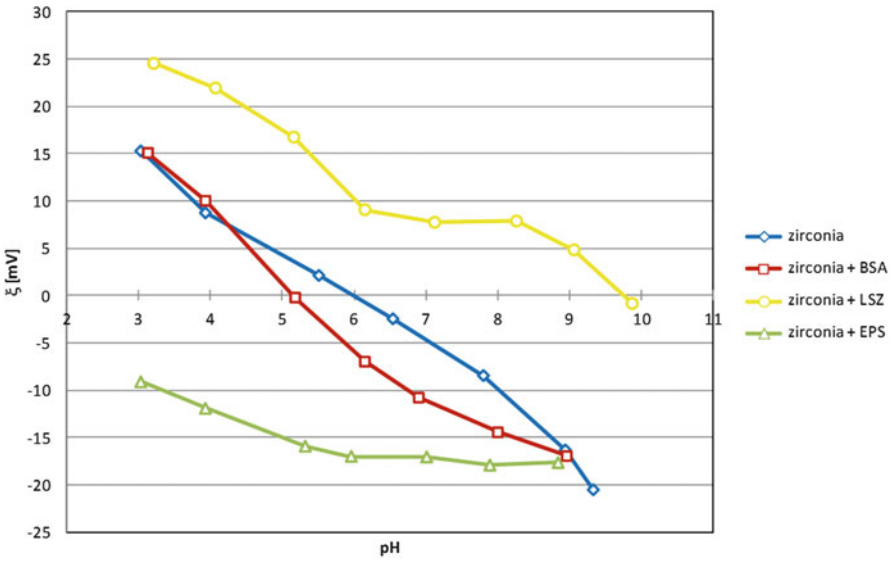

Fig. 22.2 Electrokinetic potential of zirconia in the absence and presence of biopolymers ($C_{biopolymer} = 100$ ppm)

The described phenomenon was also observed during the study on the systems containing synthetic polymers [27, 28].

EPS presence decreases the adsorbent surface charge insignificantly. The EPS macromolecules contain the carboxylic groups –COOH. The higher the pH value, the higher the amount of dissociated $-COO^-$ groups in the macromolecules. These COO^- groups occur in both solution layer indirectly adjoining to the solid surface and polymer segments not linked to the adsorbent (forming loop and tail structures). Probably, they are responsible for the metal oxide surface charge reduction.

The zeta potential measurements showed that the zirconia isoelectric point (pH_{iep}) is equal to 6 (Fig. 22.2). This means that at pH 6, in the ZrO_2 slipping plane, the number of positive groups is equal to that of negative groups. The protein adsorption changes the value of the ZrO_2 isoelectric point. In the BSA presence at the 100 ppm concentration, the pH_{iep} value is about 5, and in the LSZ presence at the same concentration, it is about 10. In this way, the isoelectric point of the solid (pH_{iep}) becomes extremely similar to the isoelectric point of the protein (pI). This proves that during the adsorption, the entire metal oxide surface is coated with the macromolecules of LSZ or albumin. Consequently, the adsorbent surface gains the properties similar to those of the protein. An analogous phenomenon has been observed by other scientists [29].

The EPS adsorption causes an evident decrease in the ZrO_2 electrokinetic potential values. In the EPS presence at the 100 ppm concentration, pH_{iep} does not occur, because the ζ potential values are negative in the whole pH range. This situation is primarily related to the slipping plane shift by loops and tails of the

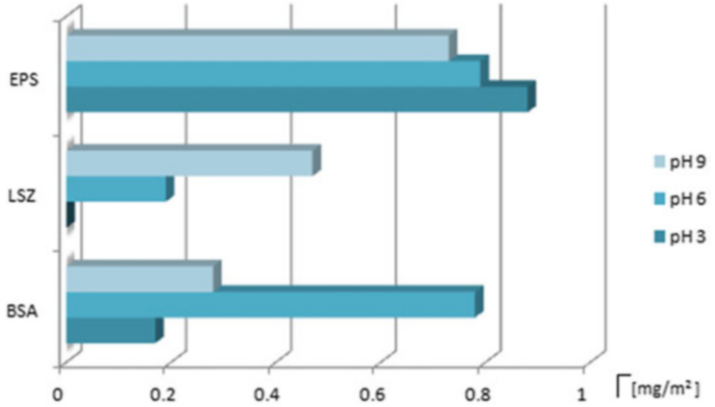

Fig. 22.3 Adsorbed amount of BSA, LSZ and EPS on the zirconia surface at various pH values ($C_{biopolymer} = 100$ ppm)

adsorbed polymer macromolecules. These structures are located close to the adsorbent surface and contain many dissociated carboxylic groups, which further affect the potential reduction.

The observed adsorbed amount on the zirconia surface differs significantly for the examined biopolymers (Fig. 22.3). BSA and LSZ are the proteins of different structural and adsorptive properties. BSA has a low internal stability (soft protein), which means that its macromolecules are strongly denaturing at the extreme pH values. Furthermore, the BSA denaturation on the solid surface is very likely during the adsorption. Khan [30] stated that in the pH range 4.3–8, the α-helices content in the BSA macromolecules is equal to 55 % (N conformation). In the pH range 3.5–4.3, the macromolecules contain 45 % of α-helices (F conformation). On the other hand, at pH > 8, they contain 48 % α-helices (B conformation). The macromolecules structure translates in the adsorption level on the ZrO_2 surface. The highest adsorption amount was observed at pH 6 because under these conditions, the macromolecules have the most packed conformation and, as a result, their maximum number is adsorbed on the zirconia surface. At pH 3 and 9, the adsorption levels are relatively lower which is connected with the protein denaturation. A single macromolecule takes up more space on the ZrO_2 surface and therefore adsorption level drops dramatically. At pH 3 the macromolecule sizes are larger than at pH 9, so fewer macromolecules adsorb in the first case. Additionally, at pH 3 and 9, there is a strong electrostatic repulsion between the adsorbent and the proteins, which makes their mutual contact difficult. Then hydrogen bonds are the most important force causing adsorption.

LSZ is a protein of high internal stability (hard protein). This means that it has a stable structure in the pH range 1–8 [31] and its denaturation on a solid surface is unlikely. As a consequence, the LSZ adsorption amount on the zirconia surface depends mainly on the electrostatic interactions occurring in the system. At pH 3 there is no LSZ adsorption on the ZrO_2 surface because of the electrostatic

repulsion between the positive solid and positively charged adsorbate. This interaction makes the adsorption impossible. On the other hand, at pH 6 and 9, the LSZ macromolecules adsorb on the zirconia particles. In the first case, the solid surface charge is equal to 0, so there are no electrostatic forces that hinder the substrate contact. At pH 9, the adsorption level is the largest due to electrostatic attraction between the positive macromolecules and negative surface.

The solution pH value also affects the EPS adsorption level. The higher the pH value is, the lower adsorption amount was observed. This is probably related to the EPS conformation and electrostatic adsorbent–adsorbate interactions. At pH 3 the EPS dissociation degree (α) is about 0.14, and therefore a relatively small number of dissociated carboxylic groups contribute to coiled macromolecule conformation. Such structure allows the adsorption of a maximum number of EPS macromolecules on a unit adsorbent area. What is more, under these conditions, electrostatic attractions between the biopolymer macromolecules and the metal oxide particles occur. Thus this contributes to a higher adsorption level. At pH 6 and 9, the EPS structure is very well developed because the dissociation degree is close to 1 (almost all carboxylic groups are dissociated). Then a single macromolecule occupies a large area on the ZrO_2 surface and, as a result, the adsorption level decreases significantly. At pH 9, both the adsorbate and adsorbent are negatively charged, so they repel each other. Additionally this phenomenon decreases the adsorption level.

The zirconia suspension is relatively stable at pH 3 and 9 which is due to the electrostatic stabilization phenomenon occurring in the system. Under these conditions, each solid particle is surrounded by the layer of ions coming from the supporting electrolyte (Cl^- at pH 3, Na^+ at pH 9). These structures prevent the particle collision and, as a result, the system is stable. At pH 6 the zirconia suspension has a low stability. It is associated with the point of zero charge (pH_{pzc}) as well as the isoelectric point (pH_{iep}) of the ZrO_2 surface. Then the particles do not repel each other, so the suspension is unstable.

LSZ, BSA and EPS change the ZrO_2 suspension stability differently (Figs. 22.4 and 22.5). The BSA adsorption causes a slight stability increase, which is probably connected with the electrosteric stabilization mechanism. It is based on both steric repulsion of the adsorption layers and the electrostatic repulsion between the adsorbed macromolecule charges.

The LSZ presence contributes to the decrease or increase in the zirconia suspension stability. At pH 3, there is no adsorption in the system, but the macromolecules, present in the solution, block the particle contact. Owing to this, the suspension stability becomes larger. At pH 6, LSZ also increases the system stability, but a different mechanism is responsible for this phenomenon. Under the above-mentioned conditions, the electrosteric stabilization contributes to the stability growth. At pH 9 a clear destabilization is observed in the system. Then the negative charge of the solid is neutralized by the positive LSZ macromolecules. As a consequence, the ZrO_2 particles stop repelling each other, and their mutual contact and the aggregation become possible.

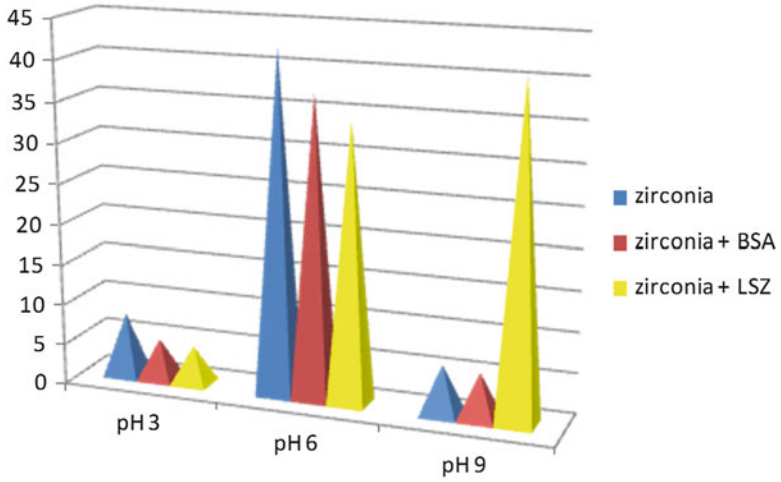

Fig. 22.4 TSI values for the zirconia suspension in the absence and presence of proteins ($C_{biopolymer} = 100$ ppm)

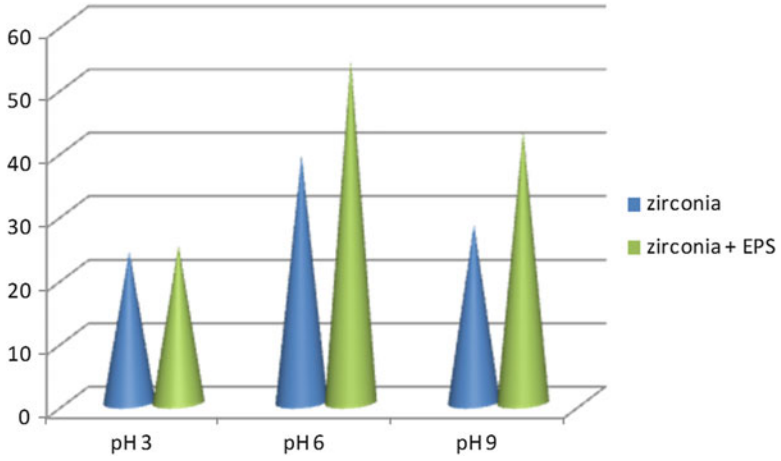

Fig. 22.5 TSI values for the zirconia suspension in the absence and presence of exopolysaccharide ($C_{biopolymer} = 100$ ppm)

Regardless of solution pH, EPS reduces the zirconia suspension stability (Fig. 22.6). At pH 3, destabilization is due to the ZrO_2-positive charge neutralization by the adsorbed polymer chains. The particles stop repelling and start forming aggregates. At pH 6 and 9, the stability drop is the result of polymeric bridges formation (bridging flocculation). Due to the EPS high molecular weight, its chains have a length sufficient for their simultaneous adsorption at least on two particles. This favours formation of large ZrO_2 flocs.

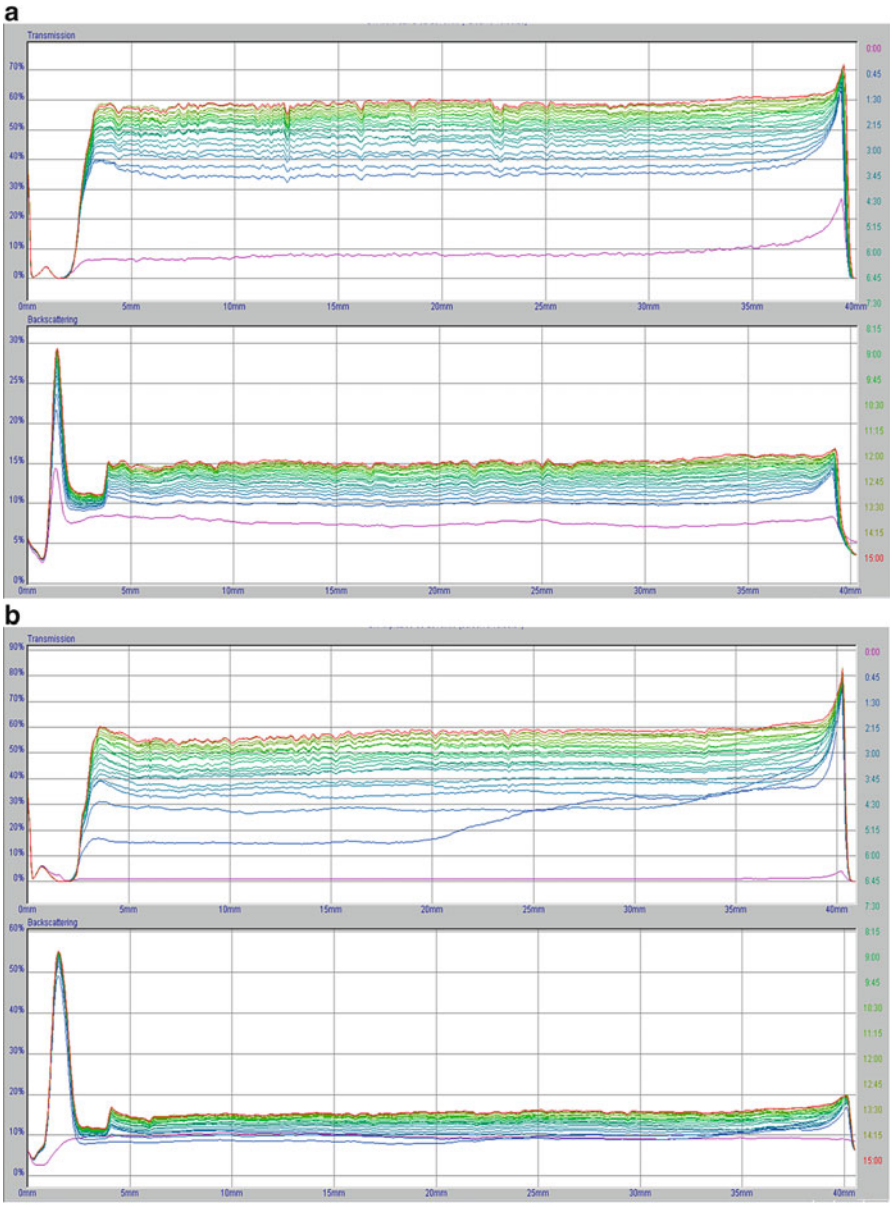

Fig. 22.6 Transmission and backscatter curves for the systems: (**a**) ZrO_2, (**b**) ZrO_2—EPS, pH 9 ($C_{biopolymer} = 100$ ppm)

References

1. Bhardwaj A, Bhardwaj A, Misuriya A, Maroli S, Manjula S, Singh AK (2014) Nanotechnology in dentistry: present and future. J Int Oral Health 6:121–126
2. Gupta J (2011) Nanotechnology applications in medicine and dentistry. J Invest Clin Dent 2:81–88
3. Mukhopadhyay SS (2014) Nanotechnology in agriculture: prospects and constraints. Nanotechnol Sci Appl 7:63–71
4. Najim TS, Salim AJ (2014) Polyaniline nanofibers and nanocomposites: preparation, characterization, and application for Cr(VI) and phosphate ions removal from aqueous solution. Arabian J Chem. doi:10.1016/j.arabjc.2014.02.008
5. Raj S, Jose S, Sumod US, Sabitha M (2012) Nanotechnology in cosmetics: opportunities and challenges. J Pharm Bioallied Sci 4:186–193
6. Egusquiaguirre SP, Igartua M, Hernández RM, Pedraz JL (2012) Nanoparticle delivery systems for cancer therapy: advances in clinical and preclinical research. Clin Transl Oncol 14:83–93
7. Lee PY, Wong KK (2011) Nanomedicine: a new frontier in cancer therapeutics. Curr Drug Deliv 8:245–253
8. Misra R, Acharya S, Sahoo SK (2010) Cancer nanotechnology: application of nanotechnology in cancer therapy. Drug Discov Today 15:842–850
9. Wang X, Wang Y, Chen ZG, Shin DM (2009) Advances of cancer therapy by nanotechnology. Cancer Res Treat 41:1–11
10. Quiquampoix H, Burns RG (2007) Interactions between proteins and soil mineral surfaces: environmental and health consequences. Elements 3:401–416
11. Salinas AJ, Vallet-Regi M (2007) Evolution of ceramics with medical applications. Z Anorg Allg Chem 633:1762–1773
12. Silva-Bermudez P, Rodil SE (2013) An overview of protein adsorption on metal oxide coatings for biomedical implants. Surf Coat Technol 233:147–158
13. Werner C, Maitz MF, Sperling C (2007) Current strategies towards hemocompatible coatings. J Mater Chem 17:3376–3384
14. Vallet-Regi M (2006) Ordered mesoporous materials in the context of drug delivery systems and tissue engineering. Chem Eur J 12:1–11
15. Vallet-Regi M, Arcos D (2006) Nanostructured hybrid material for bone tissue regeneration. Curr Nanosci 2:179–189
16. Szewczuk-Karpisz K, Wiśniewska M, Myśliwiec D (2015) Albumin adsorption influence on the stability of the mesoporous zirconia suspension. J Ind Eng Chem 32:113. doi:10.1016/j.jiec.2015.08.005
17. Dawson RMC (1986) Data for biochemical research, 3rd edn. Clarendon, Oxford
18. Reed RG, Putnam FW, Peters T (1980) Sequence of residues 400–403 of bovine serum albumin. Biochem J 191:867–868
19. Canfield RE (1963) The amino acid sequence of egg white lysozyme. J Biol Chem 238:2698–2707
20. Watter LR (1951) Immunological studies on egg white proteins: IV. Immunochemical and physical studies of lysozyme. J Biol Chem 192:237–242
21. Reinhold BB, Chan SY, Reuber TL, Marra A, Walker GC, Reinhold VN (1994) Detailed structural characterization of succinoglycan, the major exopolysaccharide II of *Rhizobium meliloti* Rm1021. J Bacteriol 176:1997–2002
22. Gharzouli R, Cerpene MA, Couderc F, Benguedouar A, Poinsot V (2013) Relevance of fucose-rich extracellular polysaccharides produced by *Rhizobium sullae* strains nodulating *Hedysarum coronarium L.* legumes. Appl Environ Microbiol 79:1765–1776
23. Szewczuk-Karpisz K, Wiśniewska M, Pac M, Choma A, Komaniecka I (2014) *Sinorhizobium meliloti* 1021 exopolysaccharide as a flocculant improving chromium(III) oxide removal from aqueous solutions. Water Air Soil Pollut 225:2052

24. Janusz W (1999) Electrical double layer at metal oxide-electrolyte interface in 'interfacial forces and fields theory and applications'. M. Dekker, New York
25. Dubois M, Gilles KA, Hamilton J et al (1956) Colorimetric method for determination of sugars and related substances. Anal Chem 28:350–356
26. Hartvig RA, Van de Weert M, Ostergaard J et al (2011) Protein adsorption at charged surfaces: the role of electrostatic interactions and interfacial charge regulation. Langmuir 27:2634–2643
27. Chibowski S, Patkowski J, Grządka E (2009) Adsorption of polyethyleneimine and polymethacrylic acid onto synthesized hematite. J Colloid Interf Sci 329:1–10
28. Ostolska I, Wiśniewska M (2015) Investigation of the colloidal Cr_2O_3 removal possibilities from aqueous solution using the ionic polyamino acid block copolymers. J Hazard Mater 290:69–77
29. Rezwan K, Meier LP, Rezwan M et al (2004) Bovine serum albumin adsorption onto colloidal Al_2O_3 particles: a new model based on zeta potential and UV–Vis measurements. Langmuir 20:10055–10061
30. Khan MY (1986) Direct evidence for the involvement of domain III in the N–F transition of bovine serum albumin. Biochem J 236:307–310
31. Ogasahara K, Hamagichi K (1966) Structure of lysozyme: XII. Effect of pH on the stability of lysozyme. J Biochem 61(2):199–210

Part IV
Nanochemistry and Biotechnology

Chapter 23
Hierarchical Structure of the Derma Affected by Chemical Treatment and Filling with Bentonite: Diagnostics with a Method of Standard Contact Porosimetry

Elena Mokrousova, Yuliya Dzyazko, Yurii Volfkovich, and Nadejda Nikolskaya

23.1 Multilevel Organization of the Derma. Investigation of Porous Structure of the Composites

Materials of hierarchical structure are widespread elsewhere: in animate and inanimate nature as well as in everyday life. Typical examples are soils, the multiple organizations of which are provided by clay and organics [1], walls of plant cells [2], paper [3], textile [4], and leather [5, 6]. The structure elements of each level perform certain functions providing a number of useful properties of the materials. From this point of view, collagen proteins, which are a base of convective tissues of human and animals, focus a special interest. The lowest organization level of collagen is triplets of polypeptide chains (helices, macromolecules) with a thickness of 1.5 nm [5, 6]. The second level is microfibrils (several nanometers); the third one is cross-linked fibrils (≈20–100 nm). Fibrils are combined into bundles of micron size; the fibril bundles form fibers (up to 50–100 μm).

Such collagen-based material as the derma is used for leather industry: the way from feedstock to end products involves various stages of chemical treatment, particularly tanning, retanning, and filling with inorganic constituents. This allows

E. Mokrousova
Kyiv National University of Technology and Design of the MES of Ukraine, Kyiv, Ukraine

Y. Dzyazko (✉)
V.I. Vernadskii Institute of General and Inorganic Chemistry of the NAS of Ukraine, Kyiv, Ukraine
e-mail: dzyazko@gmail.com

Y. Volfkovich • N. Nikolskaya
A.N. Frumkin Institute of Physical Chemistry and Electrochemistry of the RAS, Moscow, Russia

O. Fesenko, L. Yatsenko (eds.), *Nanophysics, Nanophotonics, Surface Studies, and Applications*, Springer Proceedings in Physics 183,
DOI 10.1007/978-3-319-30737-4_23

one to influence certain hierarchical level and form gradually functional properties of the material. The pre-tanning processes provide fluffing of fibers and removal of non-collagen inclusions [5]. Tanning procedure stabilizes porous structure of the derma; final porosity is formed during retanning and filling. Filling of the derma with inorganic substances (bentonite, kaolin) prevents adhesion of fibers during the processing after tanning and retanning. The filling also improves hygienic and operational properties of leather [7–10].

Since collagen is a labile polymer, a change of the structure at a particular hierarchical level can influence the next or previous level. However, these effects have not been considered earlier, though such information would be useful for the development of the techniques of derma treatment and purposeful formation of functional properties of leather. Moreover, there is no information about correlation between the total porosity of natural materials, which are characterized by hierarchical structure, and porosity caused by its elements. The aims of the work were to investigate evolution of hierarchical structure of collagen-based material during different stages of its treatment and to establish quantitative regularities of the evolution. Special interest is focused on the effect of filling with inorganic substance on the porous structure of the derma.

Simultaneous investigation of all "floors" of hierarchical structure is difficult due to restrictions of known methods. Small-angle X-ray scattering allows one to determine only the structure elements, a size of which is smaller than 200 nm [11]. Low-temperature nitrogen adsorption technique is applied to determine pores, a radius of which is not higher than 100 nm [12]. Methods of scanning and transmission electron microscopy (SEM and TEM, respectively) require analysis of many images to obtain the most complete information about the objects of investigations [13]. Mercury intrusion porosimetry allows one to determine pores in a wide interval: from micropores up to voids, a radius of which is several tens of microns [14]. However, high pressure is necessary to determine small pores, which can be destroyed under these conditions. As a result, the probability of error increases dramatically with a decrease of pore size [15]. Moreover, a wetting angle of mercury is unknown for many materials. Practical application of the method is also limited by toxicity of mercury.

The method of standard contact porosimetry (SCP), which provides the use of octane or decane (ideally wetting liquids) as working liquids, is free from these disadvantages [15–17]. The technique is recognized by the IUPAC [18]. SCP gives a possibility to determine pores in a wide diapason (1 nm–100 μm) including total volume of micropores (0.3–1 nm). The SCP technique can be applied to all the materials of different functionality, particularly to polymers and their composites [19–21]. Analysis of pore size distribution allows us to estimate the effect of inorganic constituent on porous structure of polymers [19, 20] and fibers [22]. Mathematical treatment of the porosimetry data gives information about fractal dimension of the particles [23], porous structure and particle size of each constituent of the composites [24]. Thus, the SCP method opens wide perspectives for investigations of natural collagen-based materials.

23.1.1 Chemical Treatment of the Derma and Its Modification with Bentonite: Characterization of the Composites

Natural raw material, namely, the saddlecloth (back) part of cattle skin, which had been preliminarily conserved in a saturated NaCl solution, was used. The procedures of obtaining of the samples for investigations were as follows:

- Sample I: maceration of the conserved raw material in a solution containing Na_2SiF_6 and Na_2CO_3 (degreasing, antiseptic treatment)
- Sample II (pelts): sequential processing of sample I with: (i) combining solution containing $Ca(OH)_2$ and Na_2S (to remove follicles from epidermis, i.e. upper part of the derma, and fluff collagen structure), (ii) $(NH_4)_2SO_4$ solution (to remove alkaline reagents), (iii) pancreatin solution (softening), and (iv) combining solution containing H_2SO_4, CH_3COOH, and NaCl (for further fluffing of the fibers)
- Sample III: tanning of sample II with a $Cr(OH)SO_4$ solution followed by treatment with a $NaHCO_3$ solution (neutralization)
- Sample IV: vegetable retanning (using tannins at pH 5) of sample IV
- Sample V: modification of sample IV with bentonite as described lower.

Cherkassy bentonite (Ca-form) was used for preparation of filling agent. The clay contained 26 % Si, 7 % Al, 5 % Fe, 1.8 % Ca, and 11 % H_2O. Its specific surface area and pore volume were 39 $m^2\ g^{-1}$ and 0.09 $cm^3\ g^{-1}$, respectively.

The filling agent was obtained by modification of bentonite dispersion (60 g dm^{-3}) with sodium polyphosphate (6 g dm^{-3}). The solution of sodium polyphosphate was gradually added into the dispersion under intensive agitation at 40–45 °C; the activated suspension has been agitated for 1.5–2.0 h.

The clay dispersion was employed for modification of sample IV; the duration of filling process was 60 min. Then a solution of aluminum potassium sulfate (20 g dm^{-3}) was added to provide maximal deposition of filling agent in the pores of the sample. The sample was washed with water, treated with acetone, and dried at room temperature. The amount of bentonite particles in the air-dry sample was found to be about 3 mass %.

The technique of the measurements within the framework of the SCP method is described in detail earlier [15–17]. The samples were preliminarily impregnated in octane under vacuum conditions at 353 K and fixed between two ceramic standards, a contact between them was provided at 0.1 MPa. The measurements were performed during evaporation of working liquid. Opened pores were determined by this manner. Both opened and closed pores were determined with a pycnometer method [25].

SEM images of cross-section of the samples were obtained by means of a *JEOL JSM 6700 F* scanning electron microscope (*Jeol*). Previously a thin layer of platinum was deposited onto the surface at 3 Pa using a *JEOL JFC-1600* auto-fine

coater (*Jeol*). TEM images were obtained with a *JEOL JEM 1230* transmission electron microscope (*Jeol*). The fibers were preliminary taken from the samples.

23.1.2 Main Characteristics of Porous Structure

Some characteristics of porous structure of the samples treated with different manners are given in Table 23.1. The highest bulk density has been found for the pristine derma (sample I). Chemical treatment was found to result in a decrease of bulk density (transition from sample I to sample IV); this means increase of porosity (ε_t). Similar effect is observed for the sample filled with bentonite: its porosity is lower in a comparison with sample IV. Closed pores have been found for samples I and II. Other samples demonstrate only opened porosity.

Typical integral pore size distributions are plotted in Fig. 23.1; here V is the pore volume and r is the pore radius. Intersection of the curves with the ordinate axes corresponds to microporosity. Chemical treatment causes a decrease of derma microporosity (transition from samples I to II; see Table 23.1); however, tanning provides an increment of the micropore volume (sample II → sample III). Further retanning as well as filling with bentonite leads to a decrease of micropore volume. Similar regularity has been found for specific surface. Micropores make the greatest contribution into the total surface (73–95 %).

Several half-waves are visible in the curves. A slope of buildup and plateau of the integral pore size distribution characterizes regularity of pores. A rapid growth of pore volume followed by almost horizontal plateau means regular pores without narrowing and widening. More visual information about multiple structures can be obtained from differential pore size distributions (Fig. 23.2). These curves are plotted as $\frac{dV}{d(\log r)}$ vs. $\log r$. Since $\frac{dV}{d(\log r)} = 2.3r\frac{dV}{dr}$, the peak area gives the pore volume caused by different types of structure elements: microfibrils, fibrils, fibril bundles, or fibers.

Since sizes of the elements of hierarchical structure and the voids between them are comparable, it is possible to recognize each structural level. Let us consider, for

Table 23.1 Characteristics of porous structure of the derma samples

Sample	Density, kg m^{-3}		ε_t		Micropores		Total specific surface, $m^2\ g^{-1}$
	ρ'	ρ	Opened and closed	Opened	Volume, $cm^3\ cm^{-3}$	Specific surface, $m^2\ g^{-1}$	
I	1400	772	0.45	0.42	0.039	102	140
II	1410	680	0.52	0.49	0.029	95	114
III	1420	660	0.53	0.53	0.066	202	216
IV	1410	620	0.55	0.55	0.059	187	197
V	1420	630	0.56	0.56	0.058	182	194

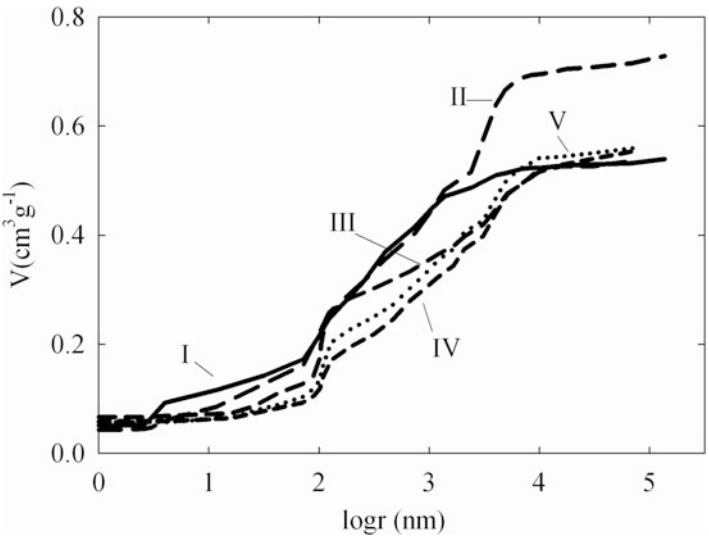

Fig. 23.1 Integral pore size distributions. The numbering of the curves corresponds to that of the samples

instance, sample I. Microporosity is evidently attributed to helices and non-collagen inclusions (elastogen, glycosaminoglycans, globulins, albumins, grease, etc.). The functions of inclusions are to support structure of the derma, provide its elasticity, concentrate nutrients, etc. The first half-waves of the integral pore size distribution (up to $r \approx 3$ nm) and corresponding sharp peak of the differential distribution are evidently due to rather regular pores between microfibrils (see Figs. 23.1 and 23.2). Regular structure of the pores between the microfibrils provides fast water transport. These nanosized structure elements can be recognized in TEM image as dark spots (Fig. 23.3a).

The microfibrils form disordered and ordered fibrils. The irregular pores are seen in Figs. 23.1 and 23.2 as a region at 4–65 nm. As follows from the TEM image, a radius of cross-section of the disordered fibrils is ≈10–20 nm (see Fig. 23.3a).

The next rapid buildup of the integral pore size distributions and sharp peak of the differential distributions at $r = 100$ nm are related to pores formed by regular fibrils. These structure elements, the thickness of which is ≈100–200 nm, are seen in SEM image (Fig. 23.3b). Characteristic thickenings are related to non-collagen inclusions. Thus, the regular fibrils form pores, which are responsible for fast water transport. At the same time, the smaller disordered fibrils control this transport. The final stage of water supply to the lowest structure elements is evidently the transport through pores formed by the regular microfibrils.

The pores, a radius of which is higher than 120–160 nm, can be also related to fibril bundles; the pores with $r > 1$ μm are attributed to fibers (see Figs. 23.1 and 23.2), which are seen in Fig. 23.3c. These pores are tortuous; moreover,

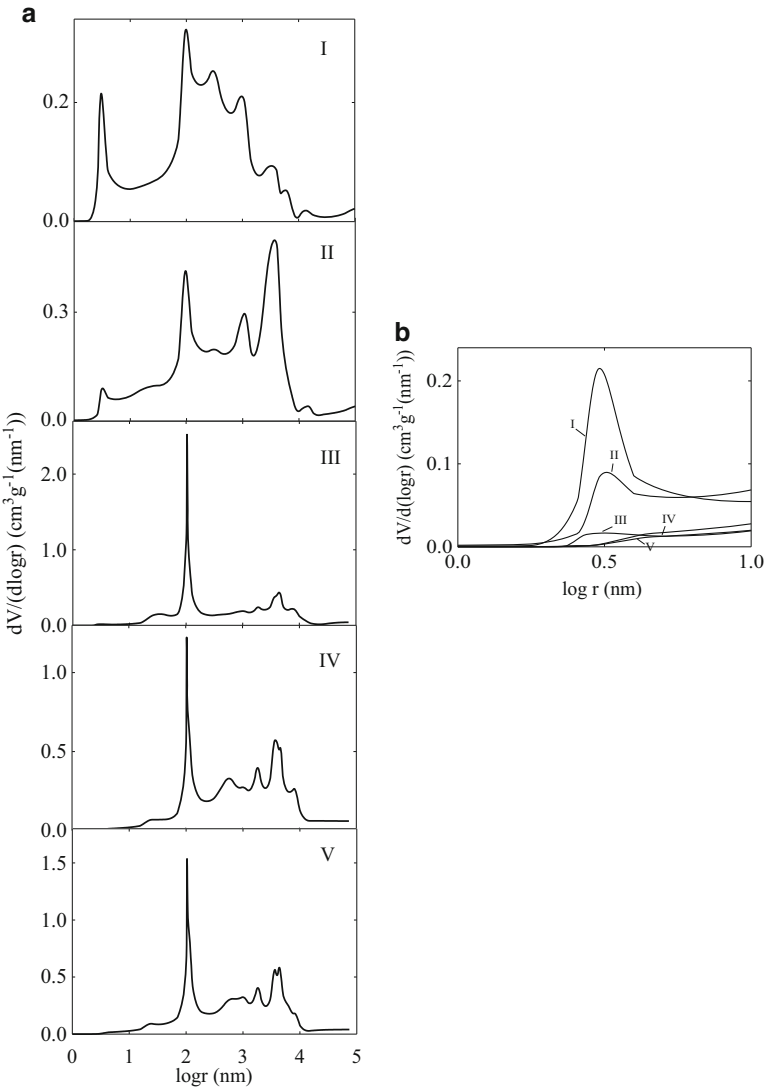

Fig. 23.2 Differential pore size distributions represented in a scale of $r = 1$ nm–10 μm (**a**) and 1–10 nm (**b**). The numbering of the plots (**a**) and curves (**b**) corresponds to that of the samples

they are an alternation of narrowings and widenings. As a result, the corresponding peaks of differential pore size distributions are rather diffuse. The pores formed by fibril bundles and fibers are evidently responsible for gas and heat exchange.

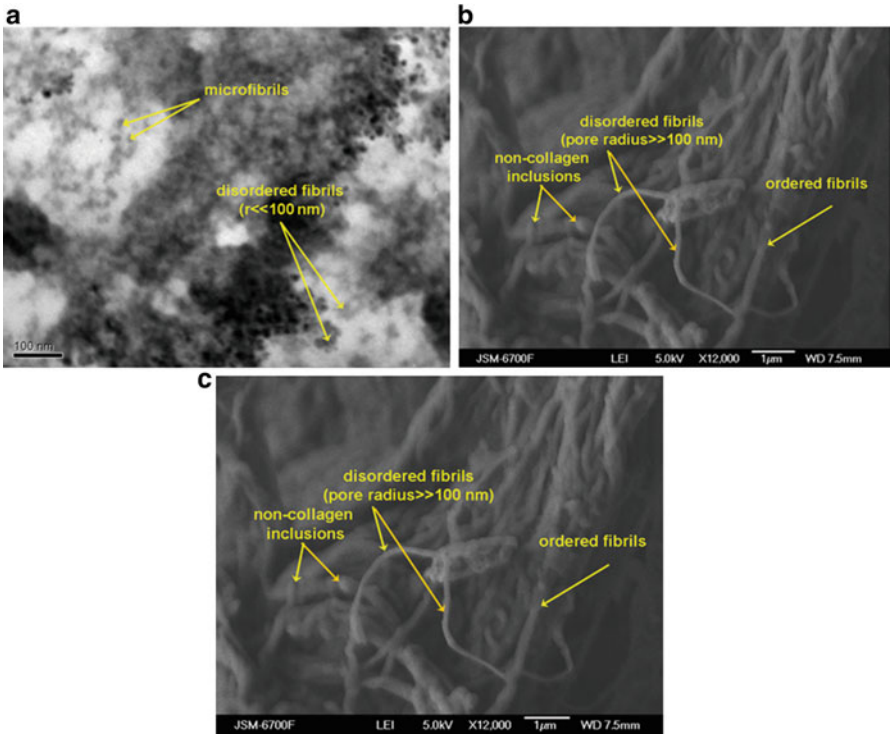

Fig. 23.3 TEM (**a**) and SEM (**b**, **c**) images of the pristine derma. Microfibrils as well as cross-sections of fibrils are seen in TEM image as dark spots (**a**). SEM images show fibrils (**b**), fiber bundles, and fibers (**c**)

23.1.3 Quantitative Analysis of Pore Size Distributions

In order to estimate a change of porous structure at different levels, we have taken several intervals of pore radius based on the data of Figs. 23.1, 23.2, and 23.3. The microporosity ($r < 1$ nm) is evidently caused by helices as well as non-collagen inclusions. The second diapason is related to pores formed by nanosized microfibrils (1.5 nm $< r <$ 4 nm); the third one is attributed to pores between both irregular and regular fibrils (4 nm $< r <$ 130 nm). The next interval is assumed to cover pores between the fibril bundles (130 nm $< r <$ 1.5 μm); the larger pores are related to the fibers. Porosity due to each element was determined from the integral pore size distributions for chosen intervals of pore radius. We assumed that microporosity is caused only by the lowest elements of the structure (helices). A volume unit of the samples (V_s, $V_s = 1$ cm^3 cm^{-3}) includes the volumes of helices (V_{hl}) and pores, which are formed by all the structure elements ($V^{/}$). The $V^{/}$ values correspond to porosity (ε, see Table 23.1). Thus:

$$V_{\mathrm{hl}} = V_{\mathrm{s}} - V^{/} \tag{23.1}$$

The volume of microfibrils (V_{mcf}), fibrils (V_{fb}), fibril bundles (V_{fbu}), and fibers (V_{fbr}) in the sample volume unit is as follows:

$$V_{\mathrm{mcf}} = V_{\mathrm{hl}} + V^{/}_{\mathrm{hl}}; \tag{23.2}$$

$$V_{\mathrm{fb}} = V_{\mathrm{mcf}} + V^{/}_{\mathrm{mcf}}; \tag{23.3}$$

$$V_{\mathrm{fbu}} = V_{\mathrm{fb}} + V^{/}_{\mathrm{fb}}; \tag{23.4}$$

$$V_{\mathrm{fbr}} = V_{\mathrm{fbu}} + V^{/}_{\mathrm{fbu}}. \tag{23.5}$$

It is possible to calculate the porosity (ε_{f}) caused by one or other element of the hierarchical structure assuming that the sample consists of only this nonporous fiber (Fig. 23.4). For instance, for helices $\varepsilon_{\mathrm{f}} = \frac{V^{/}_{\mathrm{hl}}}{V_{\mathrm{hl}}+V^{/}_{\mathrm{hl}}}$. An increase of the ε_{f} and $V^{/}$ parameters shows loosening of the structure; their decrease indicates compaction. Growth and reduction of the volume of a structure element reflect its shrinkage (or removal of non-collagen inclusions) and swelling, respectively.

23.1.4 Transformation of Porous Structure Before Tanning

The decrease of microporosity during chemical treatment of the derma before tanning (transition from sample I to sample II) is evidently due to the removal of non-collagen inclusions, which form secondary porous structure and partially closed pores. Indeed, the V_{hl} parameter decreases. As seen from Fig. 23.2, no shifts of the maxima of the $\frac{dV}{d(\log r)} - \log r$ curves are observed for sample II in a comparison with sample I. However, the peaks caused by fibrils, fibril bundles, and fibers become sharper and larger indicating ordering of structure elements and increase of porosity caused by them. A change of porosity is also reflected in Fig. 23.4. It means that the non-collagen inclusions partially block pores between fibrils, fibril bundles, and fibers. These "corks" besides supporting the structure, regulate water transport, gas and heat exchange.

Regarding the microfibrils, a decrease of the V_{hl} and $V^{/}_{\mathrm{hl}}$ parameters for sample II evidences about shrinkage of these structure elements (a reduction of the V_{mcf} magnitude). Sample II demonstrates also lower porosity caused by microfibrils in a comparison with sample I. At the same time, no change of pore size (maxima at $r = 3.2$ nm for these samples) has been found (see Fig. 23.2). This can be a result of non-collagen inclusions: their porous structure involves not only micropores but also pores, which are similar to those between microfibrils.

The fibrils show loosening due to shrinkage (decrease of the V_{mcf} and $V^{/}_{\mathrm{mcf}}$ parameters); no saving of packing compactness is provided (see Fig. 23.4).

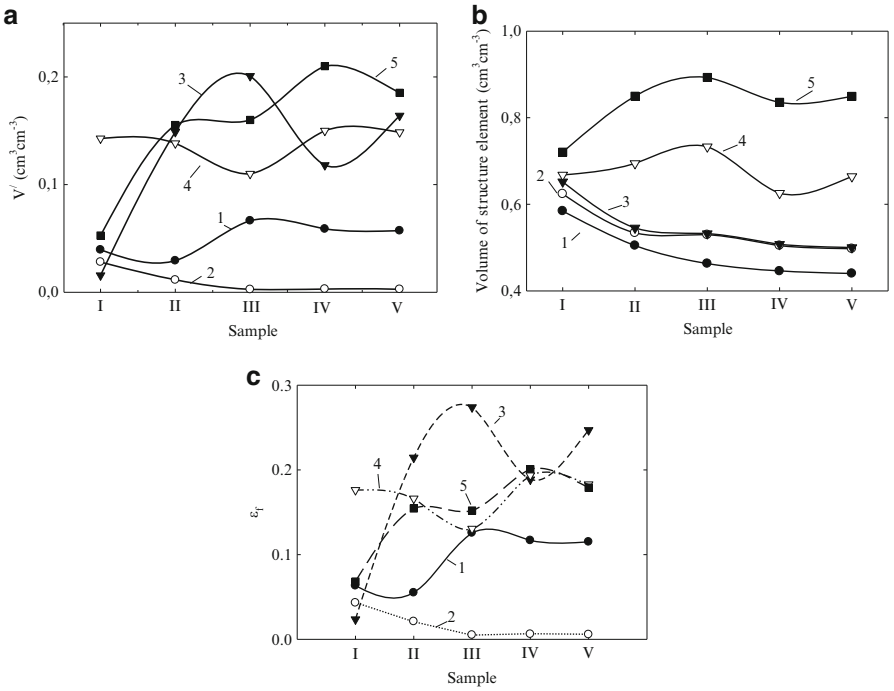

Fig. 23.4 Porosity due to each element of the hierarchical structure (**a**), volume of the elements (**b**), and porosity calculated based on assumption that the sample consists of only one nonporous element (**c**). The data are given for each sample (*X* axis). Levels: helices (1), microfibrils (2), fibrils (3), fibril bundles (4), fibers (5)

The packing evidently becomes more loose after pre-tanning treatment; thus, it is possible to say about fluffing of the fibrils. This is confirmed by TEM image of sample II (Fig. 23.5). Loosening was also found both for the fibril bundles and fibers. Swelling of the fibril bundles is due to more sufficient growth of porosity of the fibrils (0.13 $cm^3\ cm^{-3}$) in a comparison with a reduction of the V_{fb} parameter (0.09 $cm^3\ cm^{-3}$; see Fig. 23.4). The fibers also swell, but due to both swelling of the fibril bundles and increase of their porosity. Disordering of the fibril bundles and fibers is also observed: the corresponding peaks of the differential pore size distributions become wider (see Fig. 23.2). Moreover, the peak at $r = 6$ μm disappears due to widening of the maxima at $r = 3$ μm.

23.1.5 Tanning and Retanning

Tanning (transition of sample II to sample III) causes increase of microporosity as well as a shift of the peak attributed to microfibrils from $r = 3.2$ nm to $r = 2.8$ nm (see Fig. 23.2). This is probably due to shrinkage of helices (decrease of the

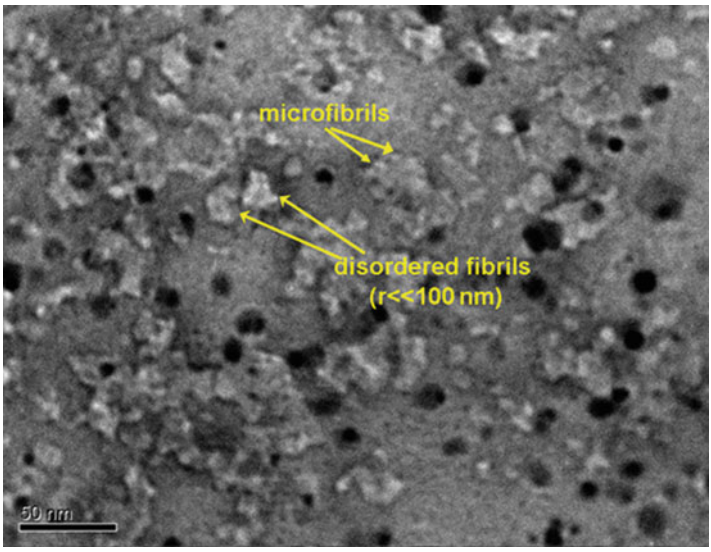

Fig. 23.5 TEM image of sample II. Microfibrils as well as cross-sections of fibrils are visible as light spots

V_{hl} parameter). During tanning, the adjacent polypeptide chains of collagen are bonded because of the formation of Cr(III) complexes with −COOH groups, which are located close to each other. The increase of microporosity is evidently caused by reduction of size of pores, which correspond to $r < 2.5$ nm for sample II. Another reason can be a deposition of tanning products. A reduction of the V_{hl} parameter is compensated with a growth of microporosity caused by helices (see Fig. 23.4). No sufficient change of the microfibril volume is observed: the V_{mcf} values for samples II and III are close to each other.

Retanning (sample III → sample IV), which provides cross-linkage of the lowest structure elements due to formation of tannin bridges between polypeptide chains, involves collagen amino groups. The processing evidently causes merger of some helices (decrease of microporosity) as well as disordering of the microfibrils and their shrinkage (a decrease of the V_{mcf} parameter, see Fig. 23.4). As a result, the corresponding peak is shifted from $r = 2.8$ nm to $r \approx 4$ nm and overlapped by the maxima for irregular fibrils (see Fig. 23.2). Both tanning and retanning lead to ordering of the irregular fibrils: the peak at $r = 10$–60 nm becomes more expressed. These fibrils as well as the microfibrils are seen in Fig. 23.6 as dark spots. The tanning results in additional ordering of the regular fibrils: the peak at $r = 100$ nm becomes sharper. Moreover, tanning results in loosening of all the fibrils (see Fig. 23.4) evidently due to their shrinkage, which is accompanied by looser packing. Retanning causes compaction of the fibrils evidently due to shrinkage of the microfibrils: the fibrils are hitched in this manner.

Both the fibril bundles and fibers become more disordered after tanning and retanning: the corresponding peaks are more diffuse (see Fig. 23.2). Swelling of the

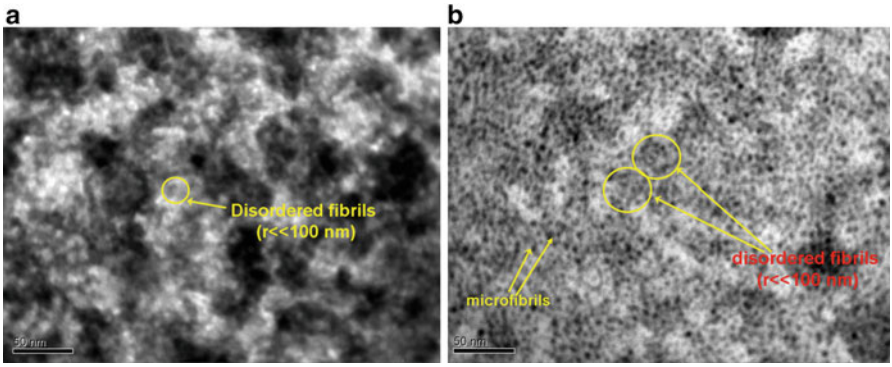

Fig. 23.6 TEM images of samples III (**a**) and IV (**b**). Microfibrils as well as cross-sections of fibrils are visible as dark spots

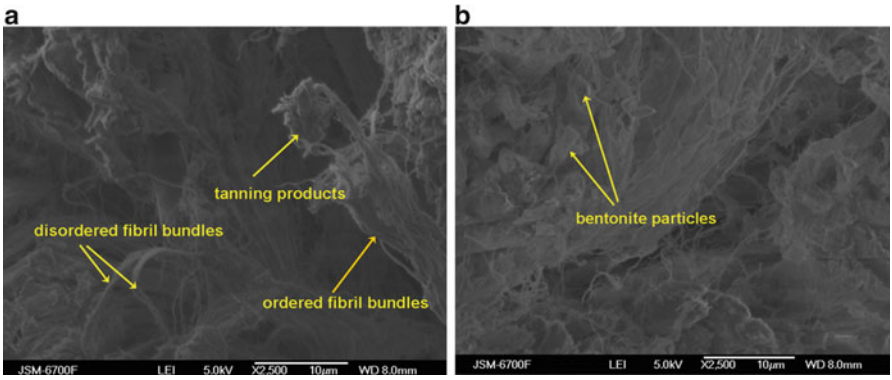

Fig. 23.7 SEM images of samples IV (without bentonite) and V (filled with bentonite)

fibril bundles after tanning is due to the increase of fibril porosity. More compact structure of these fibers was also found for sample III in a comparison with sample II (see Fig. 23.4). At the same time, no change of the V'_{fbr} parameter is observed: the porosity of this level is not affected by tanning. Retanning causes loosening both of the fibril bundles and fibers; simultaneously their shrinkage is observed. The reduction of the V_{fbu} parameter is due to fibril compaction; the decrease of the V_{fbr} value is caused by thinning of the primary fibers.

23.1.6 Filling with Betonite

The size of the clay plates is several microns. Thus, they can penetrate only into larger pores and cover large structure elements (Fig. 23.7). Filling with bentonite causes a change of positions of peaks at $r = 200$ nm–10 μm. The maxima, which are

located at $r > 200$ nm, are as follows: 0.58, 1.00, 1.84, 3.74, 4.59, and 8.07 μm (sample IV) and 0.65, 0.99, 1.82, 3.65, 4.36, and 7.94 μm (sample V). Thus, the peaks are shifted toward lower r value evidently due to compaction of fibers and fibril bundles under the influence of the inorganic filler. Moreover, it is possible to say about ordering of the structure elements, which form pores with a radius of 100 nm–10 μm. The size of the peak due to fibrils becomes sharper indicating ordering of these fibers.

23.1.7 Contributions of Structure Elements into Total Porosity

The $\varepsilon - \varepsilon_f$ plots for each level (ε values are determined for the structure elements from Fig. 23.1) are approximated by linear polynomial functions (Fig. 23.8):

$$\varepsilon = a + b\varepsilon_f, \tag{23.6}$$

where a and b are the empirical parameters. The a value together with the correlation coefficient characterizes a deviation of the model from linearity, since normally $\varepsilon = b\varepsilon_f$. This coefficient is about 2–5 % of experimental ε values for different structure elements. The b coefficient reflects the effect of treatment procedures on porosity of various levels. Neglecting the a coefficient, total porosity can be expressed through the b parameters:

$$\varepsilon_t = 0.45\varepsilon_{mcm} + 0.66\varepsilon_{mcf} + 0.71\varepsilon_{fb} + 0.66\varepsilon_{fbl} + 1.19\varepsilon_{fbr} \tag{23.7}$$

The ε_f values can be found from Fig. 23.4c. **The strongest effect of derma treatment** is expressed for fibers; the weakest one is for helices. This effect is practically the same for microfibrils, fibrils, and fibril bundles.

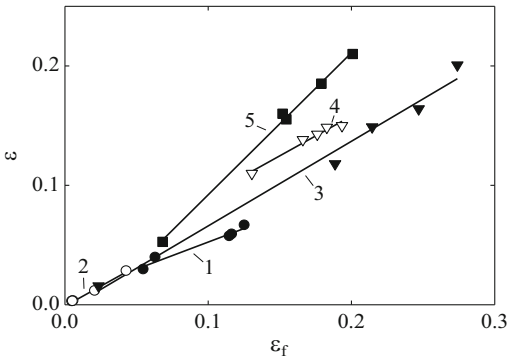

Fig. 23.8 Porosity due to each element of the hierarchical structure as a function of the ε_f parameter. Numbers of lines corresponds to one or other structure level (see capture of Fig. 23.4)

23.1.8 Conclusions

The SCP method as well as SEM and TEM has been applied for diagnostics of the hierarchical structure of the derma. Pores, which are formed by helices, microfibrils, fibrils, fibril bundles, and fibers, were determined. The model, which describes hierarchical structure and involves the porosimetry data, has been developed. The contribution of elements of each structure levels into the total porosity of the derma was determined by this manner. The parameters, which characterize porosity due to the elements and allow us to estimate loosing-compaction and shrinkage-swelling of the hierarchical structure, have been proposed. It was found that the dependence of total porosity on porosity of the structure elements can be described with a linear polynomial function.

Chemical treatment before tanning results in transformation of porous structure due to the removal of non-collagen inclusions, which evidently form own porous structure inside the derma. Removal of the inclusions results in fluffing of the derma structure on the levels of fibrils, fibril bundles, and fibers. Tanning and retanning also influence each level of the structure. Particularly, retanning leads to loosening of the fibril bundles and fibers. Filling of the derma with bentonite particles of micron size causes compaction of these elements. Additional prospects are associated probably with a modification with finer particles; this would give a possibility to act on lower levels of the hierarchical structure.

References

1. Lal R, Shukla MK (2004) Principles of soil physics. Marsel Dekker, New York
2. Evert RF (2006) Esau's plant anatomy. meristems, cells, and tissues of the plant body: their structure, function and development, 3rd edn. Wiley, Hoboken, NJ
3. Chinga-Carrasco G (2009) Exploring the multi-scale structure of printing paper—a review of modern technology. J Microsc 234:211–242
4. Lomov SV, Huysmans G, Verpoest I (2001) Hierarchy of textile structures and architecture of fabric geometric models. Text Res J 71:534–543
5. Covington AD (2009) Tanning chemistry: the science of leather. RSC Publishing, Cambridge
6. Fratzl P, Weinkamer R (2007) Nature's hierarchical materials. Prog Mater Sci 52:1263–1334
7. Kozar O, Mokrousova O, Woznyak B (2014) Deformation characteristics of leather for shoe upper, filled with natural minerals. J Chem Chem Eng 8:47–53
8. Lakshmiarayana Y, Jaisankar SN, Ramalingam S et al (2002) A novel water dispersable bentonite: acrylic graft copolymer as filler cum retanning agent. J Am Leather Chem Assoc 97:14–22
9. Mokrousova OR, Danilkovich AG (2006) Formation of collagen structure of derma by mineral dispersions. Sci Proc Riga Tech Univ, Ser 1 Materialzinat Lietiska Kim 14:83–91
10. Mokrousova O, Danylkovich A, Palamar V (2015) Resources-saving chromium tanning of leather with the use of modified montmorillonite. Rev Chim 66:353–357
11. Guinier A, Fournet G (1955) Small-angle scattering of x-rays. Chapman and Hall, London
12. Gregg SJ, Sing KSW (1991) Adsorption, surface area, and porosity, 2nd edn. Academic, London

13. Pyrz WD, Buttrey DJ (2008) Particle size determination using TEM: a discussion of image acquisition and analysis for the novice microscopist. Langmuir 24:11350–11360
14. Wittemore OJ, Halsey GD (1983) Pore structure characterization by mercury porosimetry. In: Rossington DR, Condrate RA, Snyder RL (eds) Advances in materials characterization, vol 15, Materials science research. Plenum Press, New York, pp 147–157
15. Volfkovich YM, Bagotsky VS (2014) Experimental methods for investigation of porous materials and powders. In: Volfkovich YM, Filippov AN, Bagotsky VS (eds) Porous materials and powders used in different fields of science and technology. Springer, London, pp 1–8
16. Volfkovich YM, Sosenkin VE (2012) Porous structure and wetting of fuel cell components as the factors determining their electrochemical characteristics. Russ Chem Rev 81:936–959
17. Volfkovich YM, Sosenkin VE, Bagotzky VS (2010) Structural and wetting properties of fuel cell components. J Power Sources 195:5429–5441
18. Rouquerol J, Baron G, Denoyel R et al (2012) Liquid intrusion and alternative methods for the characterization of macroporous materials (IUPAC Technical Report). Pure Appl Chem 84:107–136
19. Dzyazko Y, Rozhdestveskaya L, Zmievskii Y et al (2015) Heterogeneous membranes modified with nanoparticles of inorganic ion-exchangers for whey demineralization. Mater Today: Proc 2:3864–3873
20. Dzyazko YS, Ponomaryova LN, Volfkovich YM et al (2013) Polymer ion-exchangers modified with zirconium hydrophosphate for removal of Cd^{2+} ions from diluted solutions. Sep Sci Technol 48:2140–2149
21. Kononenko NA, Fomenko MA, Volfkovich YM (2015) Structure of perfluorinated membranes investigated by method of standard contact porosimetry. Adv Colloid Interface Sci 222:425–435
22. Yartsev DV, Lakhin AV, Vol'fkovich YM et al (2010) Study of the porous structure of a monolayer carbon-ceramic composite material of the C-SiC composition. Russ J Non-Ferrous Metals 51:364–368
23. Neimark AV, Robens E, Unger KK et al (1994) Self similarity in swelling systems: fractal properties of peat. Fractals 2:45–53
24. Dzyazko YS, Volfkovich YM, Sosenkin VE et al (2014) Composite inorganic membranes containing nanoparticles of hydrated zirconium dioxide for electrodialytic separation. Nanoscale Res Lett 9:271
25. Jones FE, Schoonover RM (2002) Handbook of mass measurements. CRC Press, London

Chapter 24
Structured Silicon Surface via Cavitation Processing for the Photovoltaic and Biomedical Application

R.K. Savkina and A.B. Smirnov

24.1 Introduction

Silicon is a key element in semiconductor high-technology devices. Its importance cannot be overestimated for micro- and nanoelectronic technology, integrated circuits, and optoelectronic technique [1]. Moreover, silicon has found energy-related applications in solar cells and mechanical applications in microelectromechanical systems. An increasing number of silicon-containing materials are being studied for application in biomedical materials and devices. It is not surprising that thousands of papers related to silicon theme are being published annually.

All of this became possible thanks to the development of such booster technologies as chemical vapor deposition and reactive ion etching, implantation and lithography, rapid thermal processing, ion and plasma processing, electron and laser irradiation, etc. [2]. Ultrasound for silicon technology is used extensively in mechanical engineering for bonding and manipulation in micromachines, for cleaning in electronic engineering, and for nondestructive control and measurement [3]. Extreme conditions of the ultrasonic cavitation such as local temperature and pressure are widely used to synthesize nano-materials, to enhance the electrochemical reactions and to modify the surface properties of electrodes, as well as to generate the novel materials in a liquid medium [4–7]. The ultrasonic irradiation is a powerful tool in promoting chemical reactivity in liquids near solid surfaces also.

With respect to semiconductors, the main application of the ultrasonic cavitation is a cleaning. The behavior of semiconductor surfaces under the acoustic cavitation remains little studied. Sonication of silicon is principally focused on surface

R.K. Savkina (✉) • A.B. Smirnov
V. Lashkaryov Institute of Semiconductor Physics, NAS of Ukraine, 41, Nauki av., Kyiv 03028, Ukraine
e-mail: r_savkina@lycos.com; alex_tenet@isp.kiev.ua

O. Fesenko, L. Yatsenko (eds.), *Nanophysics, Nanophotonics, Surface Studies, and Applications*, Springer Proceedings in Physics 183,
DOI 10.1007/978-3-319-30737-4_24

cleaning [8, 9] or development of porous luminescent structures [10, 11]. The effectiveness of gettering by backside damage introduced into a silicon wafer with a cavitating jet was also demonstrated [12].

In our previous work, the suitable cavitation conditions to cause modification of GaAs surface up to the microscale pattern formation as well as in a change in the chemical composition of semiconductor have been successfully established [13, 14]. The nitrogen atoms incorporated into the GaAs lattice and the formation of an ordered system of microscopic $(GaN)_m(GaAs)_n$ clusters ($m = n = 1$), which results in deformation of the matrix, were found. It was also revealed that the characteristic dimension of the peculiarities on the semiconductor surface depended on the exposure parameters and can be controlled (from micron- to nanoscale dimension) by the regulation of the acoustic frequency.

In this investigation, we focus on the cavitation process at silicon surface. We present a detailed characterization of the sonicated samples. Chemical and structural transformations on a silicon surface are demonstrated. Topological features induced by sonication on the semiconductor material can be useful for the photovoltaic (PV) and biomedical application.

24.2 Experiment

24.2.1 Materials

Materials used in this study were boron-doped (100)-oriented *p*-type silicon wafers with a diameter of about 76.2 mm grown by the liquid-encapsulated Czochralski method. Samples were cut into 5 mm ×5 mm squares and were cleaned for 10 min in ethanol and then in ddH_2O (water for analytical laboratory use, ISO 3696:1987). The initial surface was found to be totally flat, devoid of defects, with a measured roughness lower than 1 nm. The roughness was determined by atomic force microscopy (AFM) on a few randomly chosen areas of 40×40 μm^2. All samples were treated by the cavitation impact in cryogenic fluid such as liquid nitrogen (LN_2). XRD pattern studies for the initial samples denote the existence of a small amount of amorphous phase on the Si substrate surface investigated. We believe that this layer is removed during the sonication since the modified region is integrally below the original surface. After sonication some samples were annealed in the nitrogen vapor at 1100 °C for 2 h. Another group of samples were annealed in the atmospheric ambient at 980 °C for 1 h.

24.2.2 The Ultrasonic Processing

For cavitation activation, we used a high-frequency system (MHz) with focused energy resonator [13]. We initiate cavitation in liquid nitrogen. It is known that the cavitation phenomenon occurs when acoustic intensity exceeds a certain threshold value. Utilization of the focusing in our experiment has allowed increasing power of the high-frequency acoustic system as well as concentrating exposure on the exact position of the solid surface so as not to affect surrounding regions. It should also be noted that the operating temperature of LN_2 (78 K) is near the critical temperature of this fluid, and thermodynamic effect of cavitation can be easily reached.

The experimental setup consisted of a reactor vessel and US equipment. A pumped stainless steel tank with internal copper cell filled with technical nitrogen was used for the reactor vessel (see Fig. 24.1). A ceramic piezoelectric transducer (PZT-19) with a diameter of 12 mm and a resonant frequency of 3 MHz (or 6 MHz) acoustically drove the cell. The output voltage of US generator did not exceed 5 V, and the initial value of the acoustic intensity W_{US} did not exceed 1 W/cm^2.

A cylindrical copper concentrator (lens) was used for US intensity enhancement. Intensity gain of the acoustic system (PZT + copper lens) can be estimated as [15]:

$$k_I = \frac{4Ff_{US}}{c_1} \sin\gamma \tag{24.1}$$

where f_{US} is an ultrasonic frequency, γ is an opening angle of a wave front, c_1 is an acoustic impedance of the LN_2, and F is a focal distance:

$$F = R_{cu}\left(1 + \frac{n^2}{1-n^2}\cos\beta\left(1 + \sqrt{1 + \frac{1-n^2}{n^2}\cos\beta}\right)\right) \tag{24.2}$$

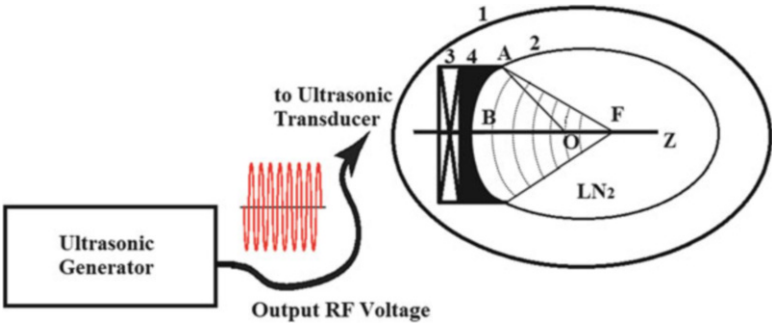

Fig. 24.1 A schematic image of the ultrasonic cell (*top view*): stainless steel tank (*1*) with internal copper cell (*2*) equipped with an acoustic system, a piezoelectric transducer (*3*), and copper lens (*4*); AO = R_{cu} is a curvature radius, AF = F is a focal distance, ∠AOB = β, ∠AFB = γ

$$n = \frac{c_1}{c_2} \tag{24.3}$$

Intensity gain of the acoustic system estimated according to (24.1) was about 58. The acoustic matching of the PZT to copper lens is sufficient for satisfying the condition of transparent boundary (~98 %). The acoustic impedance in liquid nitrogen ($c_1 \sim 0.7 \times 10^6$ kg m^{-2} s^{-1}) is small as compared to the impedance of the copper lens ($c_2 \sim 3 \times 10^7$ kg m^{-2}s^{-1}). As a consequence, the ratio of the emitted acoustic power to the dissipated power is ~55 %.

Semiconductor target was placed inside the acoustically driven copper cell in the focus region (see Fig. 24.1). The maximal value of pressure was about ~ 8 bar in the focus of the acoustic system.

24.2.3 Material Characterization

All processed surfaces were examined after fixed cavitation intervals using optical and atomic force microscopy (Digital Instruments NanoScope IIIa operating in the tapping mode). Scanning electron microscopy (SEM) characterization was realized using JSM-6490 microscope supplemented with energy dispersive X-ray analysis (EDXA). The optical characteristics of the typical annealed sample were studied by ellipsometry. The measurements were performed on a laser ($\lambda = 632.8$ nm) photoelectric compensation null ellipsometer (LEF 3G-1). The ellipsometric parameters Δ and ψ were determined from the results of multi-angle measurements in a range of incidence angle $\phi = 50$–75°.

The structural characterization of the silicon samples was carried out by X-ray diffraction (XRD) in the standard symmetric reflection geometry using CuK_α radiation. X-ray rocking curves and symmetric ω-2θ scan for samples investigated before and after sonication were obtained using a PANalytical X'Pert PRO triple-axis X-ray diffractometer. The $CuK_{\alpha 1}$ radiation was separated out using a four-bounce (440) Ge monochromator.

Micro-Raman spectra were measured in backscattering geometry at room temperature using triple Raman spectrometer T-64000 Horiba Jobin-Yvon, equipped with cooled charge-coupled device detector. The line 488 nm of Ar–Kr ion laser was used for excitation. Exciting radiation with power of 1–2 mW was focused on the sample surface to the spot of 1 μm in diameter.

24.3 Results and Discussions

24.3.1 Surface Morphology and Elemental Composition

It was found that the MHz sonication of the silicon samples in LN_2 has resulted in the essential change of the physical and structural properties of semiconductor

surface [16, 17]. The cavitation-induced changes depended both on the processing duration and on the power and frequency of ultrasound. In contrast to kHz processing mode [18], the megasonic treatment does not lead to semiconductor surface degradation, crack formation, and fracture. All samples exhibited negligible surface modification up to at least the first 5 min. Optical microscopy reveals small pits on the surface. After about 10–15 min of testing time, we observed the formation of the micron- and nanoscale complex structures (see AFM images in Fig. 24.2). Their characteristic dimension decreased at a frequency changing from 3 to 6 MHz that can be explained by the decrease of the mean cavitating bubble size at the frequency rise [19]. We have also shown that the overlapping of the metal grid on the surface of the semiconductor target leads to the formation of a two-dimensional array of the bumps (see a cross-sectional view of the structured surface in Fig. 24.3). It should be noted the results of AFM surface reconstruction showed that the structured surface occurs significantly below the initial surface level.

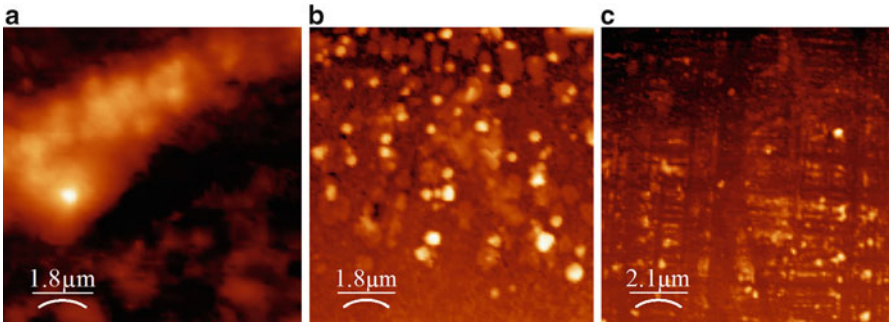

Fig. 24.2 Typical AFM images of ultrasonically structured regions of Si samples: (**a**) 3 MHz, (**b**) 6 MHz, (**c**) 6 MHz and at overlapping of the metal grid on the surface

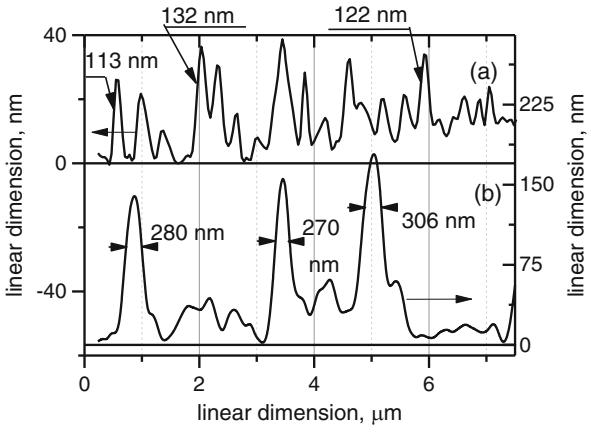

Fig. 24.3 A cross-sectional view of the structured surface: (**a**) sonication at 6 MHz and at overlapping of the metal grid on the surface, (**b**) sonication at 6 MHz without metal grid on the Si surface

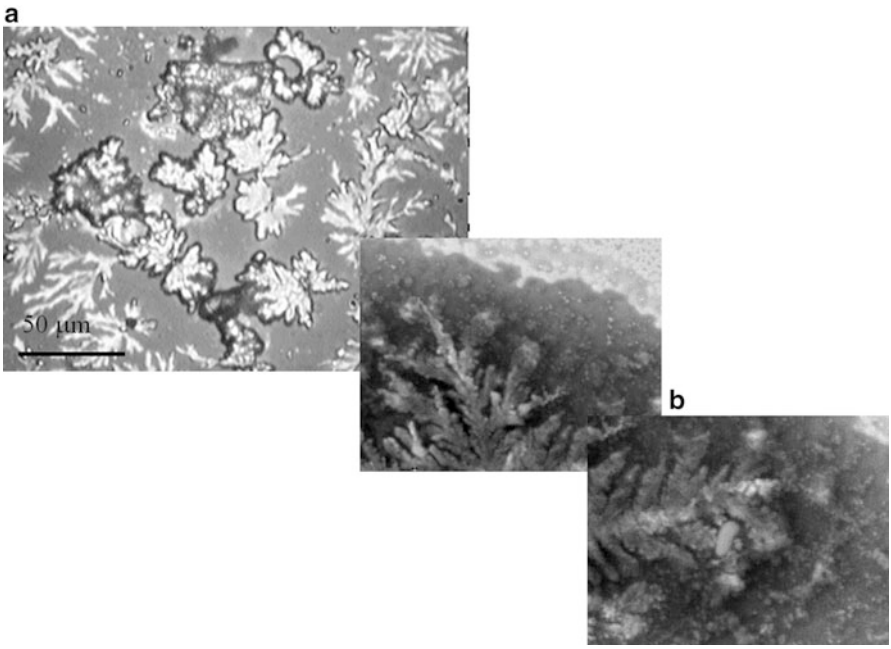

Fig. 24.4 Optical micrograph (**a**) and SEM (7 kV, 2000 ×) images (**b**) for a typical Si sample after 3 MHz sonication (15 W/cm^2, 30 min)

Thereupon, the character of surface modification becomes more complex. In particular, it was found that the prolonged cavitation treatment of silicon wafer resulted in the dendritic structure formation. Figure 24.4 presents the optical (a) and SEM (b) images of the silicon surface that show the creation of dendritic objects inside of the ultrasonically structured region and a content of different atoms incorporated into the structured silicon surface exposed to the acoustic cavitation. In the previous work [16], we found that the ultrasonically structured regions with the dendrite-like structures have a silicon nature; contain a number of alkali and alkaline earth metals such as Na, K, and Ca; and are surrounded with the oxidized surface. Weight percent of the elements determined by EDXA technique on numerous randomly chosen areas of 5×5 μm of silicon sample sonicated in LN_2 is 0.6–1.37 % for Na, 0.16–2.5 % for K, and 0.19–2.07 % for Ca. Weight percent of the oxygen in some areas reached 12 %. We found not only a surprising amount of impurities on the silicon surface but also compounds having a crystal structure such as $Na_2Ca_3(Si_3O_{10})$ and $CaSiO_3$ (see Ref. [20]).

Thus, we have demonstrated that the cavitation impact initiated by focusing a high-frequency acoustic wave into liquid nitrogen at a frequency ranging from 3 to 6 MHz resulted in Si surface modification up to the micro- and nanoscale pattern formation as well as in a change in the chemical composition of semiconductor. Then, the samples to study were divided into two groups. In the first groups silicon samples were annealed in the atmospheric ambient (see Part 24.2.1) after

sonication. The second group of samples was sonicated in LN_2 with an addition to the reactor vessel of a certain amount of calcium and was annealed in the nitrogen vapor (see Part 24.2.1). The properties of the structured and annealed Si samples were investigated using an ellipsometry, μ-Raman spectroscopy, and XRD techniques.

24.3.2 Ellipsometry

The study of the optical characteristics of the samples, carried out by ellipsometry, points to the formation of the complex optical system with two transition layers after sonication and annealing in the atmospheric ambient at 980 °C for 1 h [16]. The total thickness of the layers was about 1 μm. The top layer had optical parameters, which are closed to SiO_2 compound, whereas the layer on the substrate may be associated with the Si-rich SiN_x compound. At the same time, thermal annealing of the samples in the nitrogen vapor results in the formation of the layer with the thicknesses ~700 nm and optical parameters closed to SiO_2 compound (refractive index $n \sim 1.46$ and extinction coefficient $k \to 0$ at $\lambda = 632.8$ nm). But the accurate interpretation of the ellipsometric results became possible only after introducing an additional top layer with the thicknesses ~15 nm and the refractive index ~1.

24.3.3 XRD Investigation

XRD results in the coherent-scattering region point out to the compression of the structured layer. The initial XRD pattern reveals the Si (400) diffraction peak at $2\theta = 69.05°$ that indicates on (100) orientation of the silicon wafer. XRD patterns from the initial samples besides the Si (400) diffraction peak reveal higher-intensity background in the range of $2\theta = 20–30°$ that denotes the existence on the Si substrate surface of amorphous thin film, obviously from the amorphous native silicon oxides which are removed during the sonication.

After sonication an essential increase in the Si (400) diffraction peak intensity as well as splitting of this line was found (see Fig. 24.5). In the right side of the intense peak at $2\theta = 69.27°$ corresponding to the reflection from the (400) plane of the silicon, the intense peak at $2\theta = 69.74°$ and the peak with intensity $0.5I_{400}$ detected between the mentioned peaks were observed (see inset in Fig. 24.5). This splitting is probably related to the reflection from the surface layer formed during the sonication and silicon wafer without abrupt interface. Using the strong (400) peak at 69.27° in the XRD pattern, the lattice parameters of the processed silicon are calculated to be $a = 5.4248$ Å. These values are about 0.2 % lower than the results for initial sample ($a_o = 5.4344$ Å, $2\theta = 69.05°$).

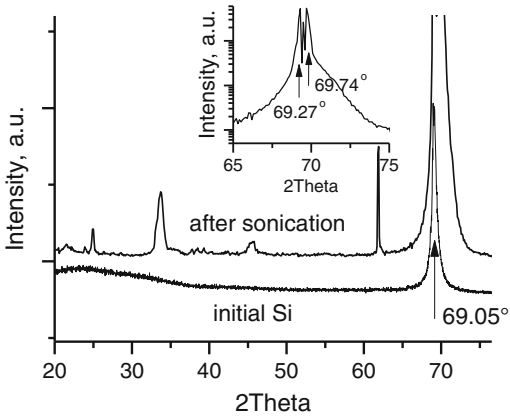

Fig. 24.5 XRD peaks for a typical Si sample after 6 MHz sonication (15 W/cm^2, 30 min). Inset: Si (400) diffraction peak for sample after cavitation treatment

It is well known that such change in XRD patterns as lines split as well as lines broaden and shift can be connected with lattice strain. In our case, the upward shift of the silicon (400) peak, in comparison to the initial position of the first, points to a compressive strain due to defect and chemical inhomogeneity in silicon after sonication. In particular, it can be related with the multilayer structure formation demonstrated by the ellipsometric data. The presence of coupled layer on the crystal surface with different structure parameters induces the lattice strains. Estimation gives a localized residual stress of ~ 1.55 GPa, which corresponds to a strain of about 1.19 % [17]. Rocking curve broadening out and shifting toward the larger angle after cavitation processing with respect to the rocking curve for initial state confirms the appearance of compressive strains in perpendicular direction to the silicon surface. After post-sonication annealing, the Si (400) peak splitting remained, but became smaller that can be connected with the partial interdiffusion of the additional element in the structured region and silicon wafer [16].

The phase composition of the subsurface layer of the sonicated and annealed Si samples was studied by X-ray diffraction in grazing geometry. The incidence angle of the X-ray beam was chosen as 5°. For the typical sample from the first group annealed in the atmospheric ambient, a series of peaks corresponding to SiO_2 lattice reflections of CuK_α photons were observed. In particular, such polymorphs of SiO_2 as quartz and cristobalite were found. In addition, small peaks at $2\theta = 29.9°$ and $2\theta = 45.2°$ corresponding to the $CaSiO_3$ phase were identified. For the typical sample from the second group, a series of peaks corresponding to SiO_2 as well as Ca and calcium compounds ($CaSiO_3$ and Ca_2SiO_4) were found.

24.3.4 μ-Raman Investigations

In addition to the interatomic distances, the strains ultrasonically generated at the Si surface may modify the lattice vibration frequencies of the crystalline structure.

The untreated crystalline silicon samples exhibit a cubic diamond structure (space group Fd-3 m) characterized by a one first-order Raman-active phonon located at the center Γ point of the Brillouin zone corresponding to a phonon wave vector ~520 cm^{-1} (phase conventionally labeled Si–I). After sonication, spectra measured around localized defects were found to present a broadened LTO(Γ) c-Si band, with a measured full width at half maximum up to Δ_{FWHM} ~8.34 cm^{-1} (see Fig. 24.6). The LTO peak broadening can be attributed to both an increase in the density of defects within the crystals and to a phonon confinement effect resulting from the nanocrystalline silicon formation (nc-Si) [21]. Its line shape becomes asymmetric with a little tail on the low-energy side extending to 470–480 cm^{-1} for all spectra which indicates a partial amorphous-like structure. Note that according to deconvolution and in agreement with the literature, broad peak between 100 and 200 cm^{-1} (at 160 cm^{-1}) and peaks at 300 cm^{-1} indicate the presence of an amorphous Si phase in sonicated samples (Fig. 24.7).

In contrast to untreated Si, one can see enhancement of the first-order scattering from transfer TA(L) acoustical phonons at 230 cm^{-1} and from optical phonon LO

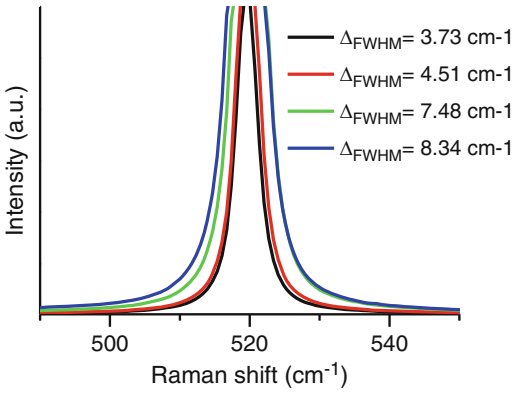

Fig. 24.6 μ-Raman spectra measured around localized defects after 3 MHz sonication (15 W/cm^2, 30 min). Spectrum of the untreated silicon is depicted as black

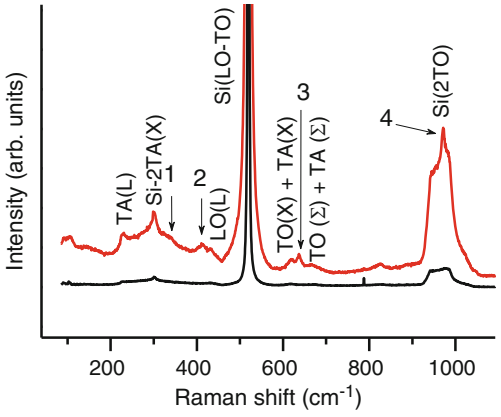

Fig. 24.7 μ-Raman spectra measured around localized defects after 3 MHz sonication (15 W/cm^2, 30 min). (*1*) 336 cm^{-1}, (*2*) 412 cm^{-1}, (*3*) 642 cm^{-1}, (*4*) 971 cm^{-1}. Spectrum of the untreated silicon is depicted as black

(L) at 430 cm^{-1} as well as the second-ordered scattering from transfer 2TA acoustical phonons at 300 cm^{-1} [22]. In addition, the peak at 620 cm^{-1} probably corresponds to the combination TO(X) + TA(X) modes and weaker peak at 670 cm^{-1} corresponds to TO (Σ) + TA (Σ) [21]. Note that the peak at ~430 cm^{-1} can be attributed to polymorphic metastable phase of crystalline Si-III (bc8, body-centered cubic structure, eight atoms per unit cell) in accord with the literature [23].

Discussed features characterize all samples after sonication and annealing. At the same time, a close inspection of the Raman spectra for the second group of samples (see Fig. 24.7) detects an appearance of Ca–O local vibrational mode at about 336 and 412 cm^{-1} and Raman features at 642 and 971 cm^{-1} corresponding to the stretching vibration of the monomer SiO_4 and the stretching vibration of the chain SiO_4 tetrahedron, respectively [24]. These modes, as it is known [24], characterize wollastonite form of $CaSiO_3$.

24.3.5 Multifunctional Application of Silicon Strained and Structured via Cavitation Effect

Thus, the experimental study demonstrates the structurization as well as change of the chemical composition on the silicon surface after the cavitation processing. Besides, the XRD and μ-Raman investigation pointed to the strain in the semiconductor lattice induced by the cavitation effect. So, what relevant changes of the silicon properties can we expect?

First of all, structuring of the surface is a known method to change the optical parameters and as a consequence to increase the efficiency of silicon solar cells. Flat silicon is fairly reflective even in the visible wavelength range. Thus, silicon surface structurization and, as a result, reduction of the reflection of visible light increase the visible absorptance, making silicon surface more photosensitive. On the other hand, advantageous strain engineering application modifies the band structure of silicon in a way that the carrier mobility is increased. In particular, strain removes the degeneracy in the four in-plane valleys (Δ_4) and the two out-of-plane valleys (Δ_2) of the conduction band minimum by splitting that can result in two effects in favor of higher mobility for in-plane transport: the Δ_2 valleys are preferentially occupied by electrons, and the other is the suppression of intervalley scattering between Δ_4 and Δ_2 due to energy splitting [25].

Thus, expecting improvement in the photoelectric properties of silicon samples exposed to the US cavitation processing in the LN_2, we have investigated their spectral distribution of the surface photovoltage (SPV). These measurements were performed using a lock-in scheme with modulation at 300 Hz at low level of homogeneous excitation by a monochromatic light in a wavelength range of $\lambda = 0.45$–2 μm.

Si samples in the initial state exhibit a very low level of the photosensitivity. After sonication, a significant rise (1000 times) in value of the photosensitivity and

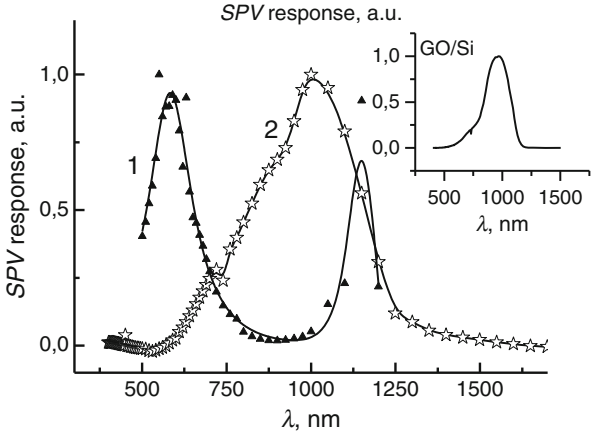

Fig. 24.8 SPV spectra of the typical silicon sample after MHz sonication and annealing: (*1*) in the atmospheric ambient at 980 °C and (*2*) in the nitrogen vapor at 1100 °C. The dots indicate the experimental data and the solid lines present the results of the fitting procedure. The lines show approximation by the Lorentzian model. Inset: the SPV spectrum of the graphene oxide film with addition of Ni deposited on Si substrate [28]

the expansion of the spectral range of photosensitivity toward the visible region are observed. Figure 24.8 illustrates SPV spectra of the typical silicon sample after post-sonication annealing. An abrupt increase of photoresponse at about 1100 nm corresponding to the silicon bandgap $E_g = 1.158$ eV (300 K) and the appearance of a wide-gap (500–700 nm) feature on the SPV spectrum of the typical sample from the first group (Fig. 24.8, curve 1) are seen. At the same time, SPV spectrum of the typical sample from the second group annealed in the nitrogen vapor (Fig. 24.8, curve 2) is a broadband of the photosensitivity between 600 and 1200 nm. It is similar to the SPV spectrum of the graphene oxide film with the addition of Ni deposited on Si substrate (see inset in Fig. 24.8)

Besides improvement in the photoelectric properties of silicon samples exposed to the sonication, a new chemical phase was synthesized at the silicon surface. We obtained silicates which are of great interest for certain areas of technical mineralogy and industrial inorganic chemistry. The system Na_2O–CaO–SiO_2, for example, is of fundamental importance for the production of commercial soda-lime glasses. Calcium inosilicate (wollastonite, $CaSiO_3$) is a biomaterial with excellent bioactivity and biocompatibility. It is commonly used as bone repair material (artificial bone) and dental root [26]. Currently many research works have been carried out to produce $CaSiO_3$ via chemical precipitation method. Mechanochemical process is an alternative process route to prepare $CaSiO_3$ powder. This process exhibits several advantages such as lower sintering temperature, homogeneous particle size with narrow particle size distribution, and formation of $CaSiO_3$ at ambient temperature by using oxide materials which are inert [27].

The method of the calcium silicate synthesis proposed in our work is not only much cheaper and environmentally friendly compared to the chemical precipitation or mechanochemical process. Using the ultrasonic cavitation to manipulate semiconductor surfaces on a small scale allowed us to obtain silicon with a unique combination of PV properties and biocompatibility. As a result, it becomes possible the integration of a key element of semiconductor electronics with biological systems. We believe that development of the biocompatible PV cell on the base of $Si/CaSiO_3$ structure can find an application in bioelectronics. Thus, our future efforts will be made just in this direction.

24.4 Conclusions

Thus, an attempt to drive the chemical and structural transformations on a semiconductor surface by the ultrasonic cavitation effect was made. We have demonstrated that the cavitation impact initiated by focusing a high-frequency acoustic wave into liquid nitrogen at a frequency ranging from 3 to 6 MHz resulted in Si surface structurization and deformation at the nanometer scale. This result is confirmed by the XRD and μ-Raman investigation. An ellipsometric measurement demonstrates that sonication with post-annealing processing leads to the formation of a complex optical system on Si surface. A surprising improvement in the photoelectric properties of silicon samples exposed to the megasonic processing was also found. The concept of biocompatible photovoltaic cell on the base of $Si/CaSiO_3$ structure for bioelectronics application was proposed.

Acknowledgment The authors gratefully acknowledge Dr. O. Lytvin, Dr. A. Nikolenko, and Dr. A. Gudymenko for their helpful cooperation in the surface characterizations.

References

1. Zimmermann H (2010) Integrated silicon optoelectronic, 2nd edn. Springer, Berlin
2. Yoshio N, Doering R (eds) (2007) Handbook of semiconductor manufacturing technology, 2nd edn. CRC Press, Boca Raton, FL
3. Savkina RK (2013) Recent progress in semiconductor properties engineering by ultrasonication. Rec Pat Electr Electron Eng 6:157–172
4. Bang JH, Suslick K (2010) Applications of ultrasound to the synthesis of nanostructured materials. Adv Mater 22:1039–1059
5. Xu H, Zeiger BW, Suslick KS (2013) Sonochemical synthesis of nanomaterials. Chem Soc Rev 42:2555–2567
6. Shchukin DG, Mohwald H (2006) Sonochemical nanosynthesis at engineered interface of cavitation microbubble. Phys Chem Chem Phys 8:3496–3506
7. Muthupandian A, Timothy JM (2007) Sonochemistry. In: Kirk-Othmer encyclopedia of chemical technology. Wiley, New York

8. Podolian A, Nadtochiy A, Kuryliuk V, Korotchenkov O, Schmid J, Drapalik M, Schlosser V (2011) The potential of sonicated water in the cleaning processes of silicon wafers. Sol Energy Mater Sol Cells 95(2):765–772
9. Nadtochiy A, Podolian A, Korotchenkov O, Schmid J, Kancsar E, Schlosser V (2011) Water-based sonochemical cleaning in the manufacturing of high-efficiency photovoltaic silicon wafers. Phys Status Solidi C 8(9):2927–2930
10. Chandler-Henderson RR, Coffer JL, Files-Sesler LA (1994) The impact of sonication on the structure and properties of stain-etch porous silicon. J Electrochem Soc 141(12):L166–L168
11. Skorb E, Andreeva DV, Mohwald H (2012) Ultrasonically induced pathways of silicon modification towards a porous luminescent structure. Angew Chem Int Ed 51:5138–5142
12. Kumano H, Sasaki T, Soyama H (2004) Evaluation of the effectiveness of back-side damage gettering in silicon introduced by a cavitating jet. Appl Phys Lett 85(17):3935–3937
13. Savkina RK, Smirnov AB (2010) Nitrogen incorporation into GaAs lattice as a result of the surface cavitation effect. J Phys D Appl Phys 43(42):425301–425307
14. Savkina RK, Smirnov AB (2015) Ultrasound-induced nitride formation on the surface of single-crystalline GaAs in cryogenic fluid. Tech Phys Lett 41(2):164–172
15. Rozenberg LD (1969) In: Sources of high-intensity ultrasound (Ultrasonic Technology), vol 1. Springer, Berlin, p 223–315
16. Savkina RK, Smirnov AB, Kryshtab T, Kryvko A (2015) Sonosynthesis of microstructures array for semiconductor photovoltaics. Mater Sci Semicond Process 37:179–184
17. Savkina RK, Smirnov AB (2015) The photoresponse of crystalline silicon strained via ultrasonic cavitation processing. Phys Status Solidi C 12(8):1090–1093
18. Virot M, Pflieger R, Skorb EV, Ravaux J, Zemb T, Mçhwald H (2012) Crystalline Silicon under acoustic cavitation: from mechanoluminescence to amorphization. J Phys Chem C 116:15493–15499
19. Brotchie A, Grieser F, Ashokkumar M (2009) Effect of power and frequency on bubble-size distribution in acoustic cavitation. Phys Rev Lett 102:084302
20. Kryshtab T, Savkina RK, Smirnov AB (2013) Nanoscale structuration of semiconductor surface induced by cavitation impact. MRS Proc 1534:A87–A92
21. Wang RP, Zhou GW, Liu YL, Pan SH, Zhang HZ, Yu DP, Zhang Z (2000) Raman spectral study of silicon nanowires: high-order scattering and phonon confinement effects. Phys Rev B 61(24):16827–16832
22. Zhao XS, Ge YR, Schroeder J, Persans PD (1994) Carrier-induced strain effect in Si and GaAs nanocrystals. Appl Phys Lett 65:2033–2035
23. Domnich V, Gogotsi Y (2002) Phase transformations in silicon under contact loading. Rev Adv Mater Sci 3:1–36
24. Serghiou GC, Hammack WS (1993) Pressure induced amorphization of wollastonite ($CaSiO_3$) at room temperature. J Chem Phys 98:9830
25. Takagi SI, Hoyt JL, Welser JJ, Gibbons JF (1996) Comparative study of phonon-limited mobility of two-dimensional electrons in strained and unstrained Si metal-oxide-semiconductor field-effect transistors. J Appl Phys 80:1567
26. Hazar ABY (2007) Preparation and in vitro bioactivity of $CaSiO_3$ powders. Ceram Int 33:687–692
27. Palaniandy S, Jamil NH (2009) Influence of milling conditions on the mechanochemical synthesis of $CaTiO_3$ nanoparticles. J Alloy Compd 476(1):894–902
28. Okhay O, Krishna R, Titus E, Andreeva K, Savkina R, Smirnov A (2015) Photovoltage study of graphene oxide with Ni nanoparticles. Mater Today: Proc 2:431–435

Chapter 25
Molecular Dynamics Simulations of *N*-Acetyl-*p*-aminophenol Molecules Embedded in High-Density Lipoprotein

Zygmunt Gburski and Violetta Raczyńska

25.1 Introduction

Paracetamol consists of a benzene ring, substituted by one hydroxyl group and one nitrogen atom of an amide group. In the human body, *N*-acetyl-*p*-aminophenol alleviates the symptoms of illness; it does not treat the cause of poor health. Acetaminophen is rapidly and completely metabolized; therefore, it can be easily eliminated from the human body [1–3].

In this work we embedded paracetamol molecules in high-density lipoprotein (HDL) aggregate. The role HDL plays in human blood arteries is to remove cholesterol from the artery walls, thereby preventing the development of cardiovascular diseases [4–8].

Three various amount of paracetamol molecules ($n = 50, 100, 150$) were placed inside the HDL aggregate. HDL aggregate can be treated as a potential nanocontainer for selected drugs, capable of transporting them to the different parts of the human body.

25.2 Simulation Details

Our research was performed using molecular dynamics simulations (MD method), the useful technique for the theoretical study of various physical systems [9–29]. NAMD 2.8 simulation code was adapted [30, 31] and the results were visualized in VMD [32].

Z. Gburski (✉) • V. Raczyńska
Institute of Physics, University of Silesia, Uniwersytecka 4, 40-007 Katowice, Poland
e-mail: zygmunt.gburski@us.edu.pl

O. Fesenko, L. Yatsenko (eds.), *Nanophysics, Nanophotonics, Surface Studies, and Applications*, Springer Proceedings in Physics 183,
DOI 10.1007/978-3-319-30737-4_25

HDL aggregate consists of 370 molecules of 1-palmitoyl-2-oleoyl-sn-glycero-3-phosphocholine (POPC) which were modeled using CHARMM 27 force field [33]. The paracetamol molecules embedded inside HDL were modeled using CHARMM 35 force field, taken from [34, 35]. All simulations were performed in water environment. Water was modeled with TIP3P, CHARMM-adapted model [36].

All simulations were fully atomistic. The four temperatures ($T = 290$, 300, 310, and 320 K) were taken into account. The time step was equal to 0.5 fs.

The initial configurations of the systems were obtained from the series of NPT simulations (1 ns), with the assumption of the atmospheric pressure (1 atm). The initial simulation box was set to $12 \times 12 \times 12$ nm and the size of it was adjusted during the first part of equilibration. Next, the systems were simulated in NVT ensemble up to 1 ns. After the equilibration process, we started "production" simulation runs, collecting the data up to 5 ns.

25.3 Results

Figure 25.1 shows the snapshots of the studied systems at the physiological temperature. In each system paracetamol molecules inside HDL keep together, forming a fusiform shape cluster. This behavior of paracetamol molecules in the clusters is the result of their polarity. Hydrophilic acetaminophen molecules are surrounded by the large number of hydrophobic phospholipid tails. In the smallest cluster (Fig. 25.1a), they have enough room to move, but they prefer to keep together—the molecules in cluster are close to each other and only few penetrate the shell of POPC molecules.

HDL aggregate shell tries to surround inner clusters tightly. It is the most difficult in the case of the smallest cluster where the change of standard HDL

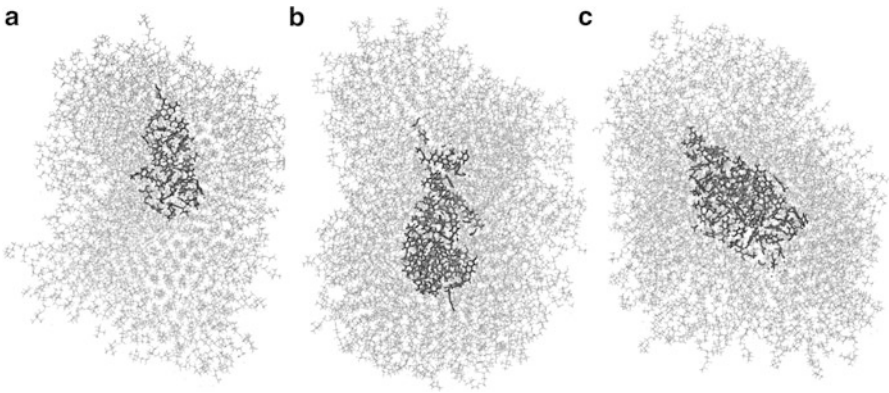

Fig. 25.1 The instantaneous configuration of the system composed of (**a**) $n = 50$, (**b**) $n = 100$, and (**c**) $n = 150$ paracetamol molecules placed inside HDL aggregate, at $T = 310$ K

shape must be the largest. The changes in HDL shape are not surprising, because in a blood, when HDL aggregates are not yet filled with cholesterol, their contour resembles a disc.

As seen in Fig. 25.1 for all paracetamol clusters, the molecules keep together, but there are some differences in their dynamics. To visualize and analyze these differences, the mean square displacement $\left\langle |\Delta \vec{r}(t)|^2 \right\rangle$ and translational diffusion coefficients D were calculated.

An example of the $\left\langle |\Delta \vec{r}(t)|^2 \right\rangle$ of the center of mass of paracetamol, where $\Delta \vec{r}(t) >=< \vec{r}(t) - \vec{r}(0) >$ and $\vec{r}$ is the position of the single-molecule mass center, is shown in Fig. 25.2. Values of D, obtained from the Einstein relation $\left\langle |\Delta \vec{r}(t)|^2 \right\rangle \approx 6Dt$, are shown in Fig. 25.3.

The largest mobility of the molecules is in the smallest cluster. The large molecular dynamics for the smallest cluster, compared to the others, can be also observed for other temperatures studied (see Fig. 25.3). As we pointed previously, POPC molecules do not surround $n = 50$ cluster as tightly, as other larger clusters. This leads to a slight increase in the separation distance between POPC and paracetamol molecules, thus creating additional volume for more vigorous motion of acetaminophen molecules.

There are no strong differences in the clusters consisting of $n = 100$ and $n = 150$ molecules. These clusters are more tightly surrounded by POPC molecules; the dynamics of paracetamol molecules is lower there.

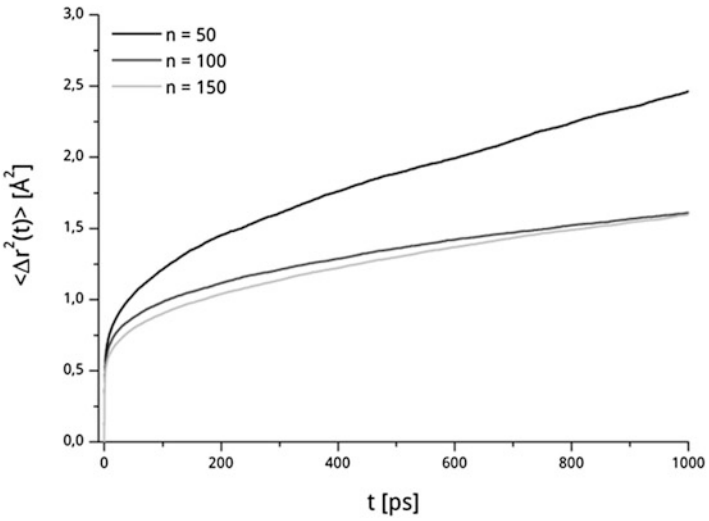

Fig. 25.2 The mean square displacement of the center of mass of paracetamol for the systems composed of (a) $n = 50$, (b) $n = 100$, and (c) $n = 150$ molecules placed inside HDL aggregate, at $T = 310$ K

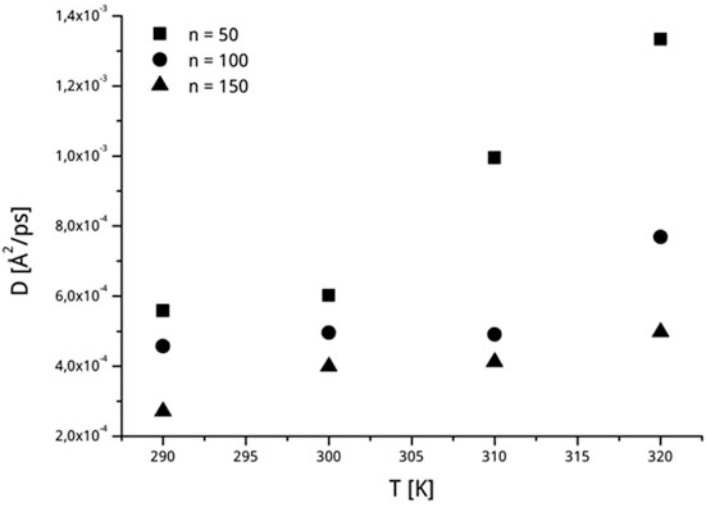

Fig. 25.3 The temperature dependence of the diffusion coefficient for all systems studied

In Fig. 25.2, a very small slope of $\left\langle |\Delta \vec{r}(t)|^2 \right\rangle$ can be observed. It indicates that the clusters are in a solid, amorphous phase.

We have also calculated Lindemann index δ_{L} [37], defined as:

$\delta_{\mathrm{L}} = \frac{2}{N(N-1)} \sum_{i<j}^{N} \frac{\left(\left\langle r_{ij}^2 \right\rangle - \left\langle r_{ij} \right\rangle^2 \right)^{\frac{1}{2}}}{\left\langle r_{ij} \right\rangle}$, where r_{ij} is the distance between the center of mass of ith and jth molecules.

Obtained results are shown in Fig. 25.4. The evolution of the Lindemann index does not show any pronounced differences between consecutive temperatures. This indicates the absence of the phase transitions in the studied temperature range, in all studied systems.

The radial distribution function $g(r)$ is shown in Fig. 25.5. The plots of $g(r)$ look similar; there are no significant differences which might indicate the various phases of clusters. The shape of $g(r)$ plots confirms that the clusters are in the solid, amorphous state. Three peaks are clearly visible in each plot. First, the most pronounced is related to the distance to the nearest neighbors. The two others, less visible and fuzzy, indicate the distance to the second and third nearest neighbors. These peaks are fuzzy because the neighboring paracetamol molecules are arranged in various ways, one with respect to the other.

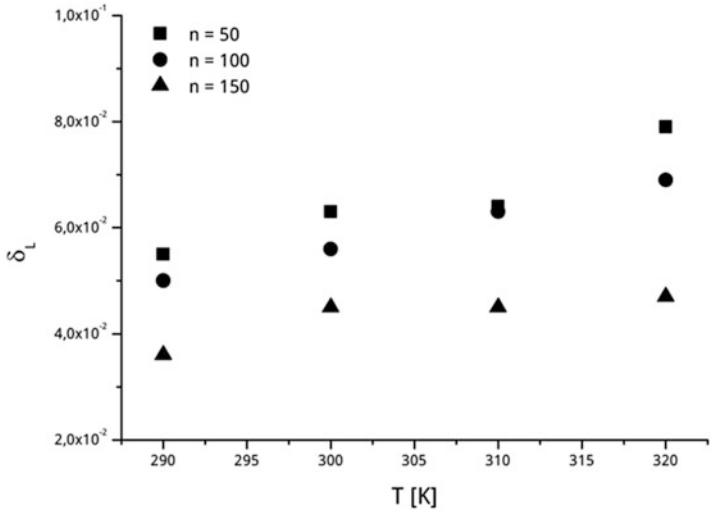

Fig. 25.4 The temperature dependence of the Lindemann index for all systems studied

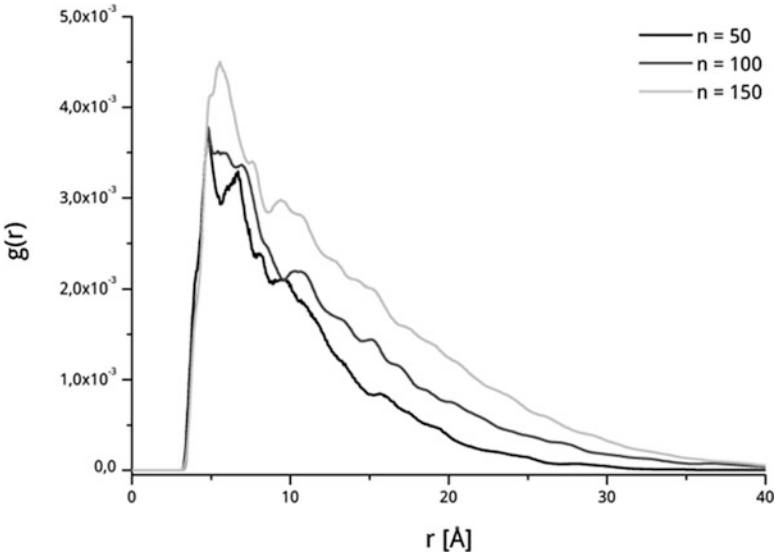

Fig. 25.5 The radial distribution function of the center of mass of paracetamol for the system composed of (a) $n = 50$, (b) $n = 100$, and (c) $n = 150$ molecules placed inside HDL aggregate, at $T = 310$ K

25.4 Conclusions

The clusters composed of $n = 50$, 100, and 150 paracetamol molecules were placed inside HDL aggregate, forming the internal cluster. These systems were simulated at four temperatures ($T = 290$, 300, 310, and 320 K) and in the water environment.

Our fully atomistic simulations show that HDL container is able to change its shape, adopting to the pattern of internal cluster. The shape adaptation of HDL shell was much less pronounced in the case of the smallest cluster inside.

Paracetamol molecules inside HDL form a solid, amorphous phase; the phase transitions do not occur in the studied temperature range.

Our simulations, where we studied the paracetamol molecules (common drug) in confined space, might contribute to the search for nanocontainers capable of selective drug delivery.

References

1. Dar AI, Saxena RC (2013) Novel herbs for liver disorders: paracetamol induced hepatotoxicity and its herbal remedy. LAP LAMBERT Academic, Saarbrücken
2. Pacifici GM, Allegaert K (2015) Clinical pharmacology of paracetamol in neonates: a review. Curr Ther Res Clin Exp 77:24–30. doi:10.1016/j.curtheres.2014.12.001
3. de Fays L, Van Malderen K, De Smet K, Sawchik J, Verlinden V, Hamdani J, Dogne J-M, Dan B (2015) Use of paracetamol during pregnancy and child neurological development. Dev Med Child Neurol 57:718–724. doi:10.1111/dmcn.12745
4. Kontush A, Chapman MJ (2012) High-density lipoproteins structure, metabolism, function, and therapeutics. Wiley, Hoboken
5. Fielding CJ (2007) High-density lipoproteins: from basic biology to clinical aspects. Wiley-VCH, Weinheim
6. Balder J-W, Staels B, Kuivenhoven JA (2013) Pharmacological interventions in human HDL metabolism. Curr Opin Lipidol 24:500–509. doi:10.1097/MOL.0000000000000018
7. Holzer M, Trieb M, Konya V, Wadsack C, Heinemann A, Marsche G (2013) Aging affects high-density lipoprotein composition and function. Biochim Biophys Acta 1831:1442–1448. doi:10.1016/j.bbalip.2013.06.004
8. Phillips MC (2013) Thematic review series: high density lipoprotein structure, function, and metabolism new insights into the determination of HDL structure by apolipoproteins. J Lipid Res 54:2034–2048. doi:10.1194/jlr.R034025
9. Allen MP, Tildesley DJ (1989) Computer simulation of liquids. Oxford University Press, Oxford
10. Rapaport DC (2004) The art of molecular dynamics simulation. Cambridge University Press, Cambridge
11. Frenkel D, Smit B (2001) Understanding molecular simulation: from algorithms to applications, 2nd edn. Academic, New York
12. Dawid A, Gburski Z (1999) Interaction-induced light scattering in xenon clusters: molecular dynamics study. J Mol Struct 482:271–276. doi:10.1016/S0022-2860(98)00668-1
13. Gorny K, Raczynski P, Dendzik Z, Gburski Z (2015) Odd-even effects in the dynamics of liquid crystalline thin films on the surface of single walled carbon and silicon carbide nanotubes: computer simulation study. J Phys Chem C 119:19266–19271. doi:10.1021/acs.jpcc.5b05961

14. Xu X-T, Tang F-L, Xue H-T, Yu W-Y, Zhu L, Rui Z-Y (2015) Molecular dynamics simulations of void shrinkage in gamma-TiAl single crystal. Comput Mater Sci 107:58–65. doi:10.1016/j.commatsci.2015.05.007
15. Dawid A, Gburski Z (2003) Rayleigh light scattering in fullerene covered by a spherical argon film—a molecular dynamics study. J Phys Condens Matter 15:2399–2405. doi:10.1088/0953-8984/15/14/315
16. Volz SG, Chen G (1999) Molecular dynamics simulation of thermal conductivity of silicon nanowires. Appl Phys Lett 75:2056–2058. doi:10.1063/1.124914
17. Dendzik Z, Kosmider M, Sokól M (2008) Dielectric relaxation of water clusters encapsulated in carbon nanotubes—computer simulation study. J Non-Cryst Solids 354:4300–4303. doi:10.1016/j.jnoncrysol.2008.06.042
18. Yamakov V, Wolf D, Phillpot SR, Gleiter H (2002) Grain-boundary diffusion creep in nanocrystalline palladium by molecular-dynamics simulation. Acta Mater 50:61–73. doi:10.1016/S1359-6454(01)00329-9
19. Gburski Z, Zerda T (1980) Vibrational dephasing and intermolecular interactions in liquids. Acta Phys Pol A 57:447–454
20. Berneche S, Roux B (2000) Molecular dynamics of the KcsA K+ channel in a bilayer membrane. Biophys J 78:2900–2917
21. Raczynski P, Dawid A, Gburski Z (2006) The dynamics of cholesterol in cholesterol-phospholipid assembly localized near carbon nanotube surface: MD study. J Mol Struct 792:212–215. doi:10.1016/j.molstruc.2006.01.063
22. Greiner M, Elts E, Schneider J, Reuter K, Briesen H (2014) Dissolution study of active pharmaceutical ingredients using molecular dynamics simulations with classical force fields. J Cryst Growth 405:122–130. doi:10.1016/j.jcrysgro.2014.07.046
23. Raczyński P, Górny K, Dawid A, Gburski Z (2014) Delivery of nitric oxide to the interior of mammalian cell by carbon nanotube: MD simulation. Arch Biochem Biophys 554:6–10. doi:10.1016/j.abb.2014.04.014
24. Dendzik Z, Górny K, Gburski Z (2009) Cooperative dipolar relaxation of a glycerol molecular cluster in nanoscale confinement—a computer simulation study. J Phys Condens Matter 21:425101
25. Skoulidas AI, Sholl DS (2005) Self-diffusion and transport diffusion of light gases in metal-organic framework materials assessed using molecular dynamics simulations. J Phys Chem B 109:15760–15768. doi:10.1021/jp051771y
26. Kosmider M, Dendzik Z, Palucha S, Gburski Z (2004) Computer simulation of argon cluster inside a single-walled carbon nanotube. J Mol Struct 704:197–201. doi:10.1016/j.molstruc.2004.02.050
27. Freddolino PL, Arkhipov AS, Larson SB, McPherson A, Schulten K (2006) Molecular dynamics simulations of the complete satellite tobacco mosaic virus. Structure 14:437–449. doi:10.1016/j.str.2005.11.014
28. Raczyński P, Górny K, Samios J, Gburski Z (2014) Interaction between silicon–carbide nanotube and cholesterol domain. A molecular dynamics simulation study. J Phys Chem C 118:30115–30119. doi:10.1021/jp505532f
29. Stassen H, Gburski Z (1994) Instantaneous normal-mode analysis of binary-liquid Ar–Kr mixtures. Chem Phys Lett 217:325–332. doi:10.1016/0009-2614(93)E1390-3
30. Kale L, Skeel R, Bhandarkar M, Brunner R, Gursoy A, Krawetz N, Phillips J, Shinozaki A, Varadarajan K, Schulten K (1999) NAMD2: greater scalability for parallel molecular dynamics. J Comput Phys 151:283–312. doi:10.1006/jcph.1999.6201
31. Phillips JC, Braun R, Wang W, Gumbart J, Tajkhorshid E, Villa E, Chipot C, Skeel RD, Kalé L, Schulten K (2005) Scalable molecular dynamics with NAMD. J Comput Chem 26:1781–1802. doi:10.1002/jcc.20289
32. Humphrey W, Dalke A, Schulten K (1996) VMD—visual molecular dynamics. J Mol Graph 14:33–38

33. MacKerell BD, Bellott D, Evanseck JD, Field MJ, Fischer S, Gao J, Guo H, Ha S, Joseph-McCarthy D, Kuchnir L, Kuczera K, Lau FTK, Mattos C, Michnick S, Ngo T, Nguyen DT, Prodhom B, Reiher WE, Roux B, Schlenkrich M, Smith JC, Stote R, Straub J, Watanabe M, Wiórkiewicz-Kuczera J, Yin D, Karplus M (1998) All-atom empirical potential for molecular modeling and dynamics studies of proteins. J Phys Chem B 102:3586–3616. doi:10.1021/jp973084f
34. Vanommeslaeghe K, Hatcher E, Acharya C, Kundu S, Zhong S, Shim J, Darian E, Guvench O, Lopes P, Vorobyov I, Mackerell AD Jr (2010) CHARMM general force field: a force field for drug-like molecules compatible with the CHARMM all-atom additive biological force fields. J Comput Chem 31:671–690. doi:10.1002/jcc.21367
35. Yu W, He X, Vanommeslaeghe K, MacKerell AD (2012) Extension of the CHARMM general force field to sulfonyl-containing compounds and its utility in biomolecular simulations. J Comput Chem 33:2451–2468. doi:10.1002/jcc.23067
36. Jorgensen WL, Chandrasekhar J, Madura JD, Impey RW, Klein ML (1983) Comparison of simple potential functions for simulating liquid water. J Chem Phys 79:926. doi:10.1063/1.445869
37. Jena P, Rao BK, Khanna SN (2013) Physics and chemistry of small clusters. Springer, Berlin

Chapter 26
Computer Simulations of Homocysteine Molecules Embedded in High-Density Lipoprotein

Zygmunt Gburski and Przemysław Raczyński

26.1 Introduction

Lipoproteins are the particles composed of proteins and lipids. They circulate in blood, collecting lipids such as cholesterol or fatty acids. One of the major representative of lipoproteins is the high-density lipoprotein (HDL), also regarded as a good cholesterol [1–4] due to its ability to remove cholesterol from the walls of blood arteries and protect against atherosclerosis [5–7].

Homocysteine, given by formula $C_4H_9NO_2S$, is a homologue of the cysteine amino acid [8–10]. A high level of homocysteine seems to be one of the risk factors for cardiovascular diseases [11–14]. Elevated level of homocysteine may also lead to many other illness and maladies [15–19].

Here, we report the dynamics of homocysteine molecules embedded in HDL aggregate, and we compare the results with the free sample, where the homocysteine molecules are not surrounded by water. To perform our studies, we used the well-known, computer simulation technique, namely, molecular dynamics (MD) simulations [13, 20–43]. MD is a very useful technique when one wants to get detailed insight on dynamics of complex biosystems.

26.2 Simulation Details

Molecular dynamics simulations were performed with NAMD 2.8 simulation code [44] and visualized with VMD [45, 46].

Z. Gburski (✉) • P. Raczyński
Institute of Physics, University of Silesia, Uniwersytecka 4, 40-007 Katowice, Poland
e-mail: zygmunt.gburski@us.edu.pl

O. Fesenko, L. Yatsenko (eds.), *Nanophysics, Nanophotonics, Surface Studies, and Applications*, Springer Proceedings in Physics 183,
DOI 10.1007/978-3-319-30737-4_26

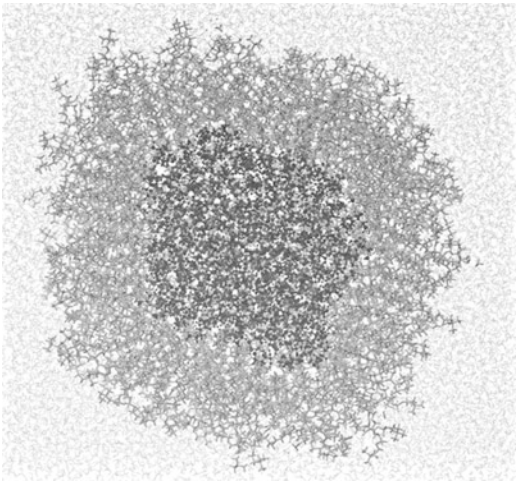

Fig. 26.1 The snapshot of HDL with homocysteine molecules inside, surrounded by water. The water molecules are coloured in silver, POPC molecules in grey and the cholesterols in black

The HDL aggregate consisted of 370 molecules of 1-palmitoyl-2-oleoyl-sn-glycero-3-phosphocholine (POPC) which were modelled using CHARMM27 force field [47]. Six hundred and seventy homocysteine molecules were placed in HDL aggregate. The homocysteine molecules were modelled with CHARMM27 force field for nucleic acids [48]. The charge distribution in it was calculated using ab initio method with 6-31G** basis set. Water was described with TIP3, CHARMM adapted model [49].

All fully atomistic simulations were performed at the physiological temperature $T = 310$ K with the time step equal to 0.5 fs. In the case of the system with water, the initial simulation box was set to $12 \times 12 \times 12$ nm. The snapshot of the system with water is shown in Fig. 26.1.

The initial configurations of the systems were obtained from the series of NPT (2×10^6 time steps) and, next, NVT (2×10^6 time steps) simulations in the case of system with water and from the series of NVT (2×10^6 time steps) simulations in the case of systems without water. Equilibrating NPT simulations were performed with the assumption of atmospheric pressure ($p = 1013 \times 10^5$ Pa). After equilibration process, the data were collected for the next 1×10^7 NVT simulation steps.

26.3 Results

Figure 26.1 shows the snapshot of instantaneous configuration of the system composed of homocysteine embedded in HDL aggregate. HDL container is surrounded by water. The homocysteine molecule is much smaller than cholesterol molecules so it is possible that these small molecules can migrate from HDL interior outside of it. This migration could lead to the destruction of HDL structure. Figure 26.1 shows that after the equilibration and main simulations (i.e. after simulation time equal to 7 ns), the homocysteine molecules are still kept together;

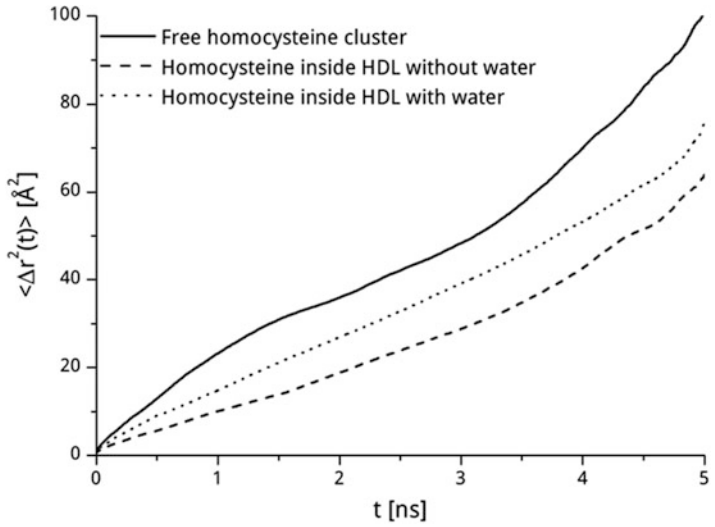

Fig. 26.2 The mean square displacement of the centre of mass of homocysteine molecule

homocysteine molecules do not penetrate POPC shell and do not leave the container.

Figure 26.2 shows the mean square displacement $\left\langle |\Delta\vec{r}(t)|^2 \right\rangle$ of the centre of mass of homocysteine, where $< \Delta\vec{r}(t) > = < \vec{r}(t) - \vec{r}(0) >$ and $\vec{r}$ is the position of a single molecule mass centre. The homocysteine molecules located inside HDL aggregate exhibit lower dynamics that their counterparts in a free cluster because they are surrounded by POPC tails; that means smaller free volume to move. In the cluster without POPC, the distinction between the molecules forming the core of the cluster and these outside of it should be taken into account. Homocysteine molecules inside the core of the cluster are tightly surrounded by these located on the outer layer of the cluster.

The differences between dynamics of the system composed of POPC and homocysteines, with and without water, can be also observed. The dynamics of homocysteine molecules is faster, when POPC molecules are surrounded by water. When POPC molecules turn their hydrophilic heads towards the water, it means they are a little "pulled" by water, and the interior of HDL aggregate is slightly larger. This effect is very weak, but causes the slight increase of homocysteine dynamics for the system with water.

This observation can be confirmed by the values of the translational diffusion coefficient D of the POPC molecules, which equal to 3.53×10^{-4} Å^2/ps for the system with water and $D = 2.97 \times 10^{-4}$ Å^2/ps for the system without it. Water increase the dynamics of POPC molecules and it has also impact on the homocysteine molecules in HDL.

The values of D were calculated also for the homocysteine molecules. They are equal to: 4.87×10^{-3} Å^2/ps for the homocysteine molecules in pure cluster (without

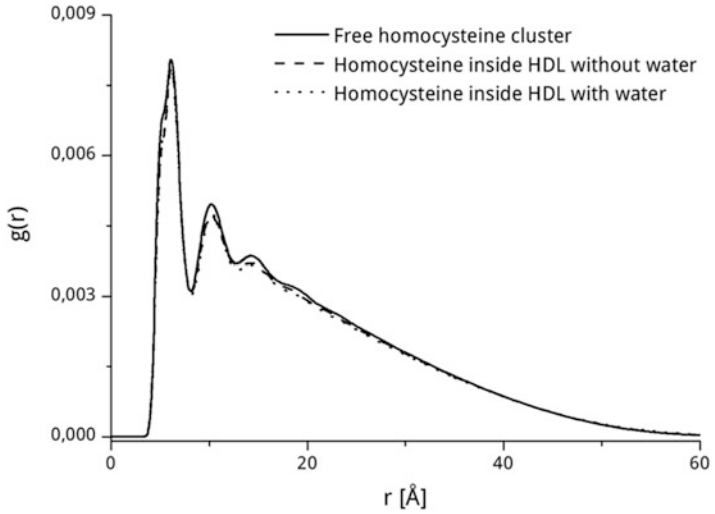

Fig. 26.3 The radial distribution function of the centre of mass of homocysteine molecules

POPC), 2.2×10^{-3} Å^2/ps for the homocysteine surrounded by POPC molecules (without water) and 3.26×10^{-3} Å^2/ps for the homocysteine molecules in system with water. The values of D conform the previous conclusions on homocysteine dynamics.

The values of D were calculated from the Einstein relation: $\left\langle |\Delta \vec{r}(t)|^2 \right\rangle \approx 6Dt$ [49]. This relation links the mean square displacement with diffusion coefficient.

The radial distribution function $g(r)$ of the centre of mass of cholesterol is shown in Fig. 26.3. There are no strong differences between all studied systems. The first significant peak is clearly visible. The maximum of these peaks is located at 6.15 Å, and it is the distance between the nearest neighbours. The second and weak third peaks, indicating the distance to next degree neighbours, can be also observed. The height of all visible peaks is similar, which indicates that the number of first, second and third neighbours is similar for all systems. The $g(r)$ functions reach zero approximately at 60 Å in the case of all systems. This distance indicates the diameter of the group of homocysteine molecules in cluster or placed inside HDL, and, moreover, it is equal to the inner diameter of the HDL aggregate.

We have estimated the values of the second-rank order parameter S_2 defined as the highest eigenvalue of ordering matrix [20]:

$$Q_{\alpha\beta} = \frac{1}{N} \sum_{j=1}^{N} \left(\frac{3}{2} \hat{e}_{j\alpha} \hat{e}_{j\beta} - \frac{1}{2} \delta_{\alpha\beta} \right), \quad \alpha, \beta = x, y, z,$$

where Q is a second-rank tensor, $\hat{e}_j$ is a unit vector along the molecular long axis and $\delta_{\alpha\beta}$ is the Kronecker delta. Diagonalization of this matrix gives three

eigenvalues and $\hat{n}$ is the eigenvector associated with the largest eigenvalue. The $\hat{n}$ vector is usually called the director of the sample. Value of S_2 is usually calculated as:

$$S_2 = \langle P_2(\hat{e} \cdot \hat{n})\rangle = \langle P_2(\cos\theta)\rangle = \left\langle \frac{3}{2}\cos^2\theta - \frac{1}{2} \right\rangle,$$

where P_2 is the second order Legendre polynomial, θ is the angle between the molecular axes and the director n and $<>$ denote average over ensemble and time.

The obtained values of S_2 are: 4.6×10^{-2} for the homocysteine cluster not surrounded by POPC, 3.83×10^{-2} for the homocysteine cluster surrounded by POPC (without water) and 2.5×10^{-2} for the homocysteine in the system with water.

We have also calculated the Lindemann index δ_L [50] defined as:

$$\delta_L = \frac{2}{N(N-1)} \sum_{i<j}^{N} \frac{\left(\left\langle r_{ij}^2 \right\rangle - \left\langle r_{ij} \right\rangle^2 \right)^{\frac{1}{2}}}{\left\langle r_{ij} \right\rangle},$$

where r_{ij} is the distance between the centre of mass of ith and jth molecules.

The values of δ_L of homocysteine are equal to: 9.1×10^{-2} for the free cluster, 6.82×10^{-2} for the system with POPC and without water and 9.0×10^{-2} for the system with POPC and water.

The low values of S_2 combined with low values of δ_L suggest that the homocysteine forms an amorphous solid at the studied temperature.

26.4 Conclusions

The dynamics of homocysteine molecules embedded inside the HDL lipoprotein exhibit lower dynamics comparing to the homocysteine in free cluster. Water moderates the dynamics of both: POPC molecules and homocysteine molecules placed inside the HDL aggregate. The homocysteine molecules in all systems studied do not form any spatially ordered structure. The calculated values of second-rank order parameter and Lindemann index suggest that homocysteine forms the amorphous condensed phase.

Acknowledgment Calculations were performed at ICM University of Warsaw, Grant no. G53-6.

References

1. Kontush A, Chapman MJ (2012) High-density lipoproteins structure, metabolism, function, and therapeutics. Wiley, Hoboken, NJ

2. Fielding CJ (2007) High-density lipoproteins: from basic biology to clinical aspects. Wiley-VCH, Weinheim
3. Andersen CJ, Fernandez ML (2013) Dietary approaches to improving atheroprotective HDL functions. Food Funct 4:1304–1313. doi:10.1039/c3fo60207a
4. Phillips MC (2013) Thematic review series: high density lipoprotein structure, function, and metabolism new insights into the determination of HDL structure by apolipoproteins. J Lipid Res 54:2034–2048. doi:10.1194/jlr.R034025
5. Lewis GF, Rader DJ (2005) New insights into the regulation of HDL metabolism and reverse cholesterol transport. Circ Res 96:1221–1232. doi:10.1161/01.RES.0000170946.56981.5c
6. Fielding C, Fielding P (1995) Molecular physiology of reverse cholesterol transport. J Lipid Res 36:211–228
7. Nofer JR, Kehrel B, Fobker M, Levkau B, Assmann G, von Eckardstein A (2002) HDL and arteriosclerosis: beyond reverse cholesterol transport. Atherosclerosis 161:1–16. doi:10.1016/S0021-9150(01)00651-7
8. McCully KS (1999) The homocysteine revolution: medicine for the new millennium. Keats, Los Angeles
9. Carmel R, Jacobsen DW (2011) Homocysteine in health and disease. Cambridge University Press, New York
10. Graham I, Refsum H, Rosenberg IH, Ueland PM, Shuman JM (1997) Homocysteine metabolism: from basic science to clinical medicine. Springer, Boston, MA
11. Robinson K (2000) Homocysteine and vascular disease. Springer, Dordrecht
12. Fakhrzadeh H, Ghotbi S, Larijani B (2007) The role of homocysteine in health and disease. Iran J Diabetes Lipid Disord 7:135–149
13. Huang C, Zhang L, Wang Z, Pan H, Zhu J (2011) Endothelial progenitor cells are associated with plasma homocysteine in coronary artery disease. Acta Cardiol 66:773–777. doi:10.2143/AC.66.6.2136962
14. Houcher Z, Houcher B, Touabti A, Begag S, Egin Y, Akar N (2012) Nutritional factors, homocysteine and C677T polymorphism of the methylenetetrahydrofolate reductase gene in algerian subjects with cardiovascular disease. Pteridines 23:14–21
15. Nagele P, Tallchief D, Blood J, Sharma A, Kharasch ED (2011) Nitrous oxide anesthesia and plasma homocysteine in adolescents. Anesth Analg 113:843–848. doi:10.1213/ANE.0b013e31822402f5
16. Enneman AW, van der Velde N, de Jonge R, Heil SG, Stolk L, Hofman A, Rivadeneira F, Zillikens MC, Uitterlinden AG, van Meurs JBJ (2012) The association between plasma homocysteine levels, methylation capacity and incident osteoporotic fractures. Bone 50:1401–1405. doi:10.1016/j.bone.2012.03.013
17. Reyna-Villasmil E, Mejia-Montilla J, Torres-Cepeda D, Santos-Bolívar J, Aragon-Charrys J, Reyna-Villasmil N, Bravo-Henríquez A (2012) Efecto de las hormonas sexuales sobre las concentraciones de homocisteína en preeclámpticas y embarazadas normales. Prog Obstet Ginecol 55:226–231
18. Brozek W, Hassler N, Varga F, Klaushofer K, Paschalis EP (2012) Effect of bisphosphonates on gene expression of fibroblasts cultured in the presence of homocysteine. Bone 51:S8. doi:10.1016/j.bone.2012.08.021
19. Bergen NE, Jaddoe VWV, Timmermans S, Hofman A, Lindemans J, Russcher H, Raat H, Steegers-Theunissen RPM, Steegers EAP (2012) Understanding health behaviours in a cohort of pregnant women at risk of gestational diabetes mellitus: an observational study. Int J Obstet Gynaecol 119:739–751. doi:10.1111/j.1471-0528.2012.03321.x
20. Frenkel D, Smit B (2001) Understanding molecular simulation, second edition: from algorithms to applications, 2nd edn. Academic, London
21. Allen MP, Tildesley DJ (1989) Computer simulation of liquids. Oxford University Press, Oxford
22. Rapaport DC (2004) The art of molecular dynamics simulation. Cambridge University Press, Cambridge

23. Raczynski P, Dawid A, Sakol M, Gburski Z (2007) The influence of the carbon nanotube on the structural and dynamical properties of cholesterol cluster. Biomol Eng 24:572–576. doi:10.1016/j.bioeng.2007.08.010
24. Kolev V, Freger V (2015) Molecular dynamics investigation of ion sorption and permeation in desalination membranes. J Phys Chem B 119:14168–14179
25. Raczynski P, Dawid A, Dendzik Z, Gburski Z (2005) Dielectric relaxation in water–cholesterol mixture cluster: molecular dynamics simulation. J Mol Struct 750:18–21. doi:10.1016/j.molstruc.2005.03.036
26. Rahman A, Stilling FH (1971) Molecular dynamics study of liquid water. J Chem Phys 55:3336–3359. doi:10.1063/1.1676585
27. Kosmider M, Dendzik Z, Palucha S, Gburski Z (2004) Computer simulation of argon cluster inside a single-walled carbon nanotube. J Mol Struct 704:197–201. doi:10.1016/j.molstruc.2004.02.050
28. Hunt TA (2016) Periodic boundary conditions for the simulation of uniaxial extensional flow of arbitrary duration. Mol Simul 42:347–352. doi:10.1080/08927022.2015.1051043
29. Toukan K, Rahman A (1985) Molecular-dynamics study of atomic motions in water. Phys Rev B 31:2643–2648. doi:10.1103/PhysRevB.31.2643
30. Raczynski P, Dawid A, Gburski Z (2005) Depolarized light scattering in small fullerene clusters—computer simulation. J Mol Struct 744:525–528. doi:10.1016/j.molstruc.2004.12.064
31. Chaban VV, Prezhdo OV (2015) Synergistic amination of graphene: molecular dynamics and thermodynamics. J Phys Chem Lett 6:4397–4403
32. Gorny K, Dendzik Z, Raczynski P, Gburski Z (2012) Dynamic properties of propylene glycol confined in ZSM-5 zeolite matrix—a computer simulation study. Solid State Commun 152:8–12. doi:10.1016/j.ssc.2011.10.020
33. Dawid A, Gburski Z (1997) Dynamical properties of the argon–krypton clusters: molecular dynamics calculations. J Mol Struct 410–411:507–511. doi:10.1016/S0022-2860(96)09512-9
34. Pabis A, Geronimo I, York DM, Paneth P (2014) Molecular dynamics simulation of nitrobenzene dioxygenase using AMBER force field. J Chem Theory Comput 10:2246–2254. doi:10.1021/ct500205z
35. Smith L, Zimmerman JA, Hale LM, Farkas D (2014) Molecular dynamics study of deformation and fracture in a tantalum nano-crystalline thin film. Model Simul Mater Sci Eng 22:045010. doi:10.1088/0965-0393/22/4/045010
36. Raczynski P, Gburski Z (2010) Molecular dynamics and dielectric relaxation of homocysteine layer between graphite walls—computer simulation. Rev Adv Mater Sci 23:175–179
37. Duke JR, Ananth N (2015) Simulating excited state dynamics in systems with multiple avoided crossings using mapping variable ring polymer molecular dynamics. J Phys Chem Lett 6:4219–4223
38. Gburski Z, Raczynski P (2010) Influence of carbon nanotube on cholesterol lodgment: molecular dynamics simulation. Rev Adv Mater Sci 23:64–69
39. Grest G, Kremer K (1986) Molecular-dynamics simulation for polymers in the presence of a heat bath. Phys Rev A 33:3628–3631. doi:10.1103/PhysRevA.33.3628
40. Gburski Z (1985) Convergence of memory functions for the vibrational dephasing process in liquids. Chem Phys Lett 115:236–240. doi:10.1016/0009-2614(85)80687-4
41. Gao Y, Liu J, Shen J, Wu Y, Zhang L (2014) Influence of various nanoparticle shapes on the interfacial chain mobility: a molecular dynamics simulation. Phys Chem Chem Phys 16:21372–21382. doi:10.1039/c4cp03019b
42. Robertson JC, Cheatham TE (2015) DNA backbone BI/BII distribution and dynamics in E2 protein-bound environment determined by molecular dynamics simulations. J Phys Chem B 119:14111–14119
43. Gburski Z, Zerda T (1980) Vibrational dephasing and intermolecular interactions in liquids. Acta Phys Pol A 57:447–454

44. Phillips JC, Braun R, Wang W, Gumbart J, Tajkhorshid E, Villa E, Chipot C, Skeel RD, Kalé L, Schulten K (2005) Scalable molecular dynamics with NAMD. J Comput Chem 26:1781–1802. doi:10.1002/jcc.20289
45. Humphrey W, Dalke A, Schulten K (1996) VMD—visual molecular dynamics. J Mol Graph 14:33–38
46. Price S (2011) Importing medicines: the VMD's special import and special treatment schemes. Vet Rec 168:445–446. doi:10.1136/vr.d2617
47. MacKerell BD, Bellott D, Evanseck JD, Field MJ, Fischer S, Gao J, Guo H, Ha S, Joseph-McCarthy D, Kuchnir L, Kuczera K, Lau FTK, Mattos C, Michnick S, Ngo T, Nguyen DT, Prodhom B, Reiher WE, Roux B, Schlenkrich M, Smith JC, Stote R, Straub J, Watanabe M, Wiórkiewicz-Kuczera J, Yin D, Karplus M (1998) All-atom empirical potential for molecular modeling and dynamics studies of proteins. J Phys Chem B 102:3586–3616. doi:10.1021/jp973084f
48. MacKerell ADJ, Banavali N, Foloppe N (2000) Development and current status of the CHARMM force field for nucleic acids. Biopolymers 56(4):257–265. doi:10.1002/1097-0282(2000)56:4<257::AID-BIP10029>3.0.CO;2-W
49. Jorgensen WL, Chandrasekhar J, Madura JD, Impey RW, Klein ML (1983) Comparison of simple potential functions for simulating liquid water. J Chem Phys 79:926. doi:10.1063/1.445869
50. Jena P, Rao BK, Khanna SN (2013) Physics and chemistry of small clusters. Springer, Berlin

Chapter 27
Comparative Study of Ferromagnetic and Superparamagnetic Iron Oxide Nanoparticles Loaded with Antitumor Drug Doxorubicin

V. Orel, A. Shevchenko, M. Zabolotny, A. Romanov, O. Rykhalskyi, E. Kruchkov, A. Burlaka, S. Lukin, and Yu. Prylutskyy

27.1 Introduction

In the last years, thorough studies have been made in the field of nanosized magnetic particles, because of their potential for biomedical applications such as improving the quality of magnetic resonance imaging, drug delivery, and magnetic particle by induction hyperthermia treatment for tumor. Magnetic nanoparticle hyperthermia (MNH) appears well suited as an effective tumor therapy: (1) the concentration of nanoparticles in the tumor is both sufficiently high and significantly higher than in surrounding, normal tissue; (2) the use of nanoparticles, which can combine both therapeutic and diagnostic capabilities in one dose, has the potential to lead toward personalized oncology and better outcomes for patients; and (3) the particles possess a high enough specific absorption rate. However, after intense study and clinical trials of MNH, most forms of human cancer are still not curable. The primary limiting factor is the lack of understanding of the mechanisms of therapeutic intervention. While some success has been achieved in treating certain types of neoplasms, there are a number of limitations of MNH such as:

V. Orel • A. Romanov • O. Rykhalskyi • E. Kruchkov
National Cancer Institute, Kyiv, Ukraine

A. Shevchenko (✉)
G.V. Kurdyumov Institute for Metal Physics of the National Academy of Sciences of Ukraine, Kyiv, Ukraine
e-mail: admit@imp.kiev.ua

M. Zabolotny • Y. Prylutskyy
Taras Shevchenko National University of Kyiv, Kyiv, Ukraine

A. Burlaka • S. Lukin
R.E. Kavetsky Institute of Experimental Pathology, Oncology and Radiobiology of the National Academy of Sciences of Ukraine, Kyiv, Ukraine

O. Fesenko, L. Yatsenko (eds.), *Nanophysics, Nanophotonics, Surface Studies, and Applications*, Springer Proceedings in Physics 183,
DOI 10.1007/978-3-319-30737-4_27

(1) therapy by nanoparticles (NP) within the temperature range 43–70 °C can be accompanied by the formation of drug resistance due to the induction of heat shock proteins, (2) the temperature above 45 °C may shut down tumor tissue perfusion, and (3) a targeted therapy with magnetic NP is often not suitable for disseminated and abdominal tumors [1–4].

To overcome the mentioned problems, we have developed a new cancer magnetic nanotherapeutic technology based on the ability of external electromagnetic field to induce the changes in electron transitions in complex composed of semiconductor materials such as ferromagnetic iron oxide Fe_3O_4 nanoparticles (FMION) and antitumor drug [5]. The technology is based on known semiconductor materials' ability, in FMION, to generate oxygen radicals and oxidative stress in biological media. The occurrence of these effects depends on similarities in the energetic states of the nanomaterials and ambient redox-active aqueous substances. It is observed that Fe_3O_4 has conduction band positions which are lower than biological redox potential. Although the theory based on the overlap of conduction band energy with the cellular redox potential correlates reasonably with in vitro and in vivo toxicity results, this does not necessarily mean the NP toxicity potential was only determined by the "overlap." This could include the Fermi levels of metal oxide NP as well as the energy levels of the antitumor drug and biomolecules [6–8]. Based on the advanced studies of electromagnetic irradiation (EI) on the oxidative stress reactions, the potential effect of EI on living organisms is that exposure to magnetic field can increase the activity, concentration, and lifetime of paramagnetic free radicals, which might cause oxidative stress, genetic mutation, and/or apoptosis [9, 10]. In proposed technology, the heating temperature of FMION does not exceed 40 °C. We have also shown that electromagnetic field initiated the concentration increase of the free radicals in tumor. This differs essentially from conventional MNH.

It is well known that in the superparamagnetic iron oxide Fe_3O_4 nanoparticles (SPION), thermal fluctuations are strong enough to demagnetize spontaneously a previously saturated assembly; therefore, these particles have zero coercivity and have no hysteresis [11]. SPION are known as more suitable heating elements for magnetic hyperthermia than FMION. This is because the amount of heat generated by SPION is readily controllable by tuning magnetizing force and frequency of electromagnetic radiation outside the body [12]. FMION is difficult to control because it is more dependent upon particle size and is markedly decreased at >16 nm. However, superparamagnetism is expressed only at a particle size <10 nm, so SPION "leak" from the pores of fenestrated capillaries in normal tissues: the pores are a few dozen nanometers and are smaller than the pores of the vascular walls in tumors. Hence, SPION do not accumulate in tumors. However, the clustering of SPION can be a way out of this dilemma. SPION clustering increases the particle size up to the optimum size making use of the enhanced permeability while maintaining their superparamagnetic properties [1, 13].

The above properties motivated us to use the SPION for cancer magnetic nanotherapy. In our early pilot studies on animals with Lewis carcinoma, it has been shown that SPION with a doxorubicin (DOXO) in the magnetic nanocomplex (MNC) have greater antitumor and antimetastatic effect than MNC of FMION and

DOXO [14]. Therefore, in this paper in order to enhance understanding of antitumor effect for magnetic nanotherapy, we have compared physical properties of FMION and SPION loaded with antitumor drug DOXO.

27.2 Experimental Studies

27.2.1 Magneto-Mechanochemical Synthesis

MNC consisted of iron oxide (II, III) NP (Sigma-Aldrich) with diameters of 50 and 5 nm and antitumor drug DOXO (Pfizer, Italy). The MNCs were divided into two magnetic groups: MNC1 comprised of FMION (50 nm) and DOXO; MNC2 comprised of SPION (5 nm) and DOXO. The synthesis of MNC was performed in a magneto-mechanical reactor (National Cancer Institute, Ukraine). Mechanical processing was performed in the chamber at a frequency of vertical vibrations 36 Hz and an amplitude of 9 mm for 5 min with 20 W/g mechanical energy supply. Simultaneously, EI was applied for 5 min at 42 MHz by an induction coil with 40 W initial power and permanent magnets with constant magnetic field (CMF) intensity 11 mT (in the center) [15]. We have investigated conventional DOXO in the concentration of 1.8 mg/mL and magneto-mechanochemical synthesized MNC comprising of DOXO (1.8 mg/mL) and Fe_3O_4 NP (0.31 mg/mL) in 0.2 mL 0.9 % sodium chloride solution (9 mg/mL).

27.2.2 Magnetic Studies

The magnetic properties were studied by magnetometry using a "Vibrating Magnetometer 7404 VSM" (Lake Shore Cryotronics, Inc., USA) with magnetic fields up to 13 kOe. The magnetometer's sensitivity is 10^{-7} emu, and that allowed measuring the magnetic moment of samples weighing milligrams. The mass was determined by an electronic microbalance AB135-S/FACT with auto-identification (Mettler Toledo, Switzerland), which has a sensitivity of 10^{-5} g.

27.2.3 Electron Spin Resonance Spectroscopy

In order to measure the *g*-factor and the concentration of paramagnetic centers in the samples, electron spin resonance (ESR) spectra were recorded with the spectrometer RE1307 at liquid nitrogen temperatures (77 K) in a cylinder resonator with the mode H_{011} and frequency 9.15 GHz. The power microwave radiation was 40 mW and the magnetic field modulation frequency was 100 kHz. The samples were placed in a quartz Dewar with an inner diameter of 4.5 mm. *g*-factor was calculated according to the formula of the resonance condition

$$h\nu = g\beta B, \tag{27.1}$$

where $h\nu = 9.15$ GHz is microwave frequency, $\beta = 1.39968$ GHz/kG is Bohr magneton, and B is magnetic induction.

27.2.4 Absorption Spectroscopy

Interaction of Fe_3O_4 NP with molecules of DOXO after magneto-mechanochemical synthesis in saline (0.9 % NaCl) was characterized by measuring the absorption spectra of supernatant from MNC, which were performed on a double-beam spectrophotometer UNICO SpectroQuest 4802 (USA), running in the spectral range (190–1100) nm with a spectral resolution of 0.1 nm. Measurement of absorption spectra was performed at 20 °C.

27.2.5 The Interaction Between Magnetic Field and Magnetic Nanoparticles

As it is shown in papers [13, 16], SPION and FMION assemblies have different magnetic properties. In order to evaluate the interaction between magnetic fields and NP, we have measured the changes in AMF intensity inside the inductive applicator for SPION or FMION at different values of CMF. The changes of AMF intensity was measured in geometrical center of inductive applicator (diameter 7 cm). We have compared the SPION and FMION (0.31 mg/mL) in 1 mL of 0.9 % sodium chloride solution at 20 °C. The prototype of apparatus "Magnetotherm" (Radmir, Ukraine) for medical treatment was used to generate alternating electromagnetic field and to produce eddy currents in solution with NP [17]. The frequency of EI was 42 MHz with an initial power of 75 W (Fig. 27.1). We have used the neodymium ($Nd_2Fe_{14}B$) permanent magnets: adhesive force 40 kg, diameter 4.4 cm, and height 1.5 cm. CMF measurements were performed in geometrical center at the bottom of the glass cuvette by magnetic sensor based on the Hall effect [18]. The magnetic induction in the center of permanent magnet at a distance of 1 cm from the surface was $B = 0.38$ T.

27.3 Results and Discussion

27.3.1 Magnetic Studies

The analysis of hysteresis loops and ESR spectra (Figs. 27.2 and 27.3 and Table 27.1) shows that investigated samples of FMION, MNC1, and MNC2 are soft ferromagnetic materials unlike superparamagnetic SPION. DOXO possesses

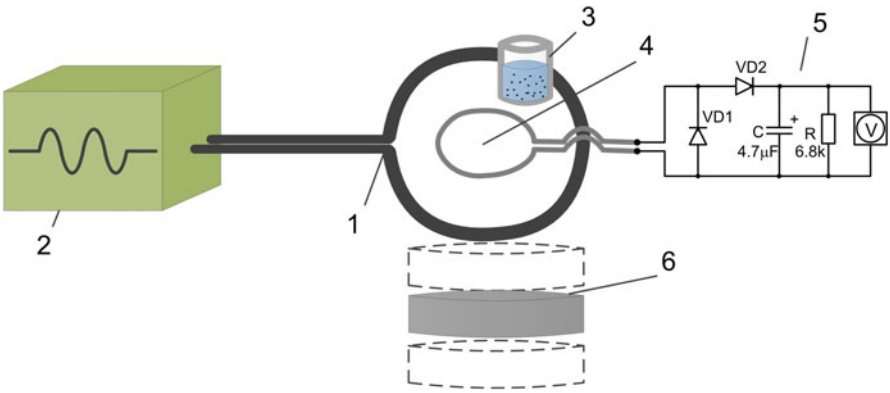

Fig. 27.1 The scheme for measuring the interaction between magnetic field and NP: inductive applicator (*1*), generator (*2*), NP solution (*3*), sensor for measuring of AMF (*4*), registration unit of AMF (*5*), permanent magnet (*6*)

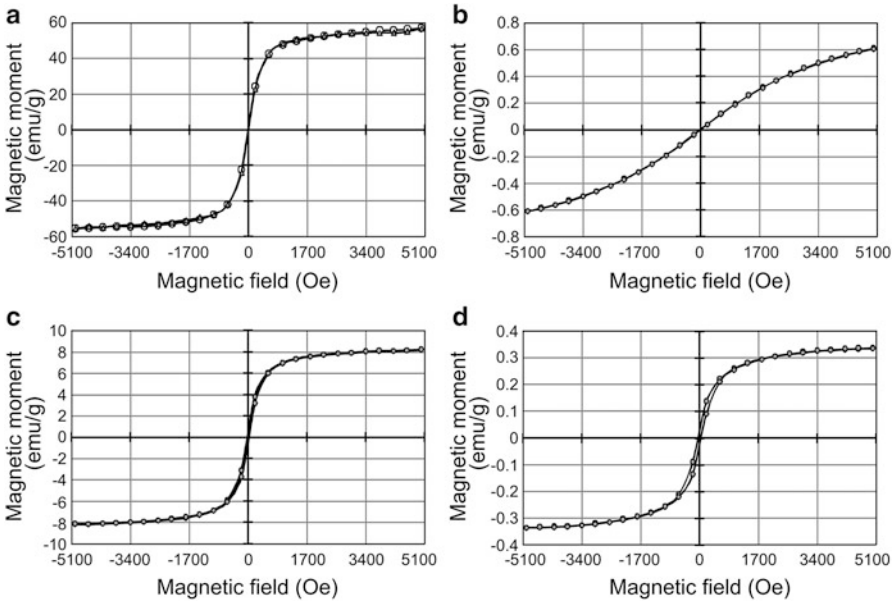

Fig. 27.2 Hysteresis loops at 300 K: (**a**) FMION, (**b**) SPION, (**c**) MNC1, (**d**) MNC2

diamagnetic properties. Magneto-mechanochemically synthesized complex MNC1 comprising of FMION has significantly greater saturation magnetic moment and magnetic hysteresis loop area as compared to MNC2 comprising of SPION. However, MNC2 are characterized by greater coercive force. Magnetic hysteresis is a nonequilibrium process. This means that after shutting off the external magnetic field, the macroscopic remanent magnetization will tend to vanish with a typical relaxation time.

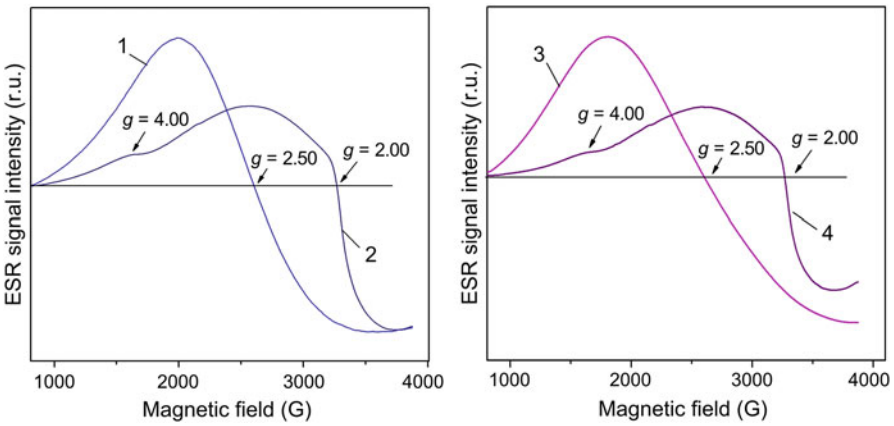

Fig. 27.3 Electron spin resonance spectrum: FMION (*1*), SPION (*2*), MNC1 (*3*), MNC2 (*4*)

Table 27.1 Magnetic properties of the samples

Parameter	Samples			
	FMION	SPION	MNC1	MNC2
	The loop of magnetic hysteresis[a]			
Saturation magnetic moment m_s, emu/g	56.31	–[b]	8.17	0.34
Coercive field H_c, Oe	6.48	–	19.14	40.11
Area of the hysteresis loop, erg/g	350.95	–	610.12	49.77
	Electron spin resonance spectrum[c]			
g-factor	2.50	4.00	2.50	4.00
		2.30		2.30
		2.00		2.00
ESR signal intensity, relative units	1	1	1.8	1

[a]DOXO is diamagnetic, magnetic moment $m = -1.18$ emu/g at 3 kOe
[b]SPION is superparamagnetic, saturation magnetic moment $m = 0.61$ emu/g at 5 kOe
[c]DOXO ESR signal intensity 10^{-4} r.u.; *g*-factor 1.97, 2.003, and 2.005 [25]

27.3.2 ESR Spectroscopy Study

The ESR data have revealed significant difference in MNC *g*-factors depending on magnetic properties of iron oxide NP. MNC1 comprising of FMION and DOXO had the *g*-factor of 2.50. MNC2 comprising of SPION and DOXO had different values of *g*-factor equal to 2.00, 2.30, and 4.00. The integrated intensity of ESR signal was higher for MNC1 (80 %). This difference was conditioned by the fact that FMION is larger and it has greater number of paramagnetic centers as compared to single-domain SPION. However, free radical reactions affecting the intensity of oxidative stress are initiated mainly by surface paramagnetic centers.

27.3.3 Absorption Spectroscopy Study

The results of absorption spectra measurements of supernatant from MNC are presented at Fig. 27.4. The analysis of absorption spectra (using their decomposition by Gaussian distribution) shows that the position of the point of maximum absorption and extrapolation dispersion depends on the size distribution of NP. In a pure solution of DOXO, the absorption maximum is in the neighborhood of (485–492) nm [19]. SPION with DOXO in MNC2 complex have absorption maximum shifts in the region of (465–480) nm. The presence of FMION with DOXO leads to the existence of the absorption maximum in the range of (390–430) nm in MNC1. In order to interpret the obtained results, it should be taken into account the aggregation of FMION due to remanent magnetization and accumulating of DOXO by dendrites on the NP surface. Such behavior of the absorption spectrum directly indicates the presence of interaction between the molecules of DOXO and NP in complex [20, 21]. The shift of absorption spectrum maximum to shorter wavelengths indicates a possible deformation of DOXO molecule under the influence of NP resulting in the decrease in the region of localization of the optical electron. It is important due to the fact that with increase of NP size, the strength of its interaction with the disposition of a number of DOXO molecules also increases. These results indicated that the DOXO molecules located in saline solution can form a complex with iron oxide NP after magneto-mechanochemical synthesis of MNC.

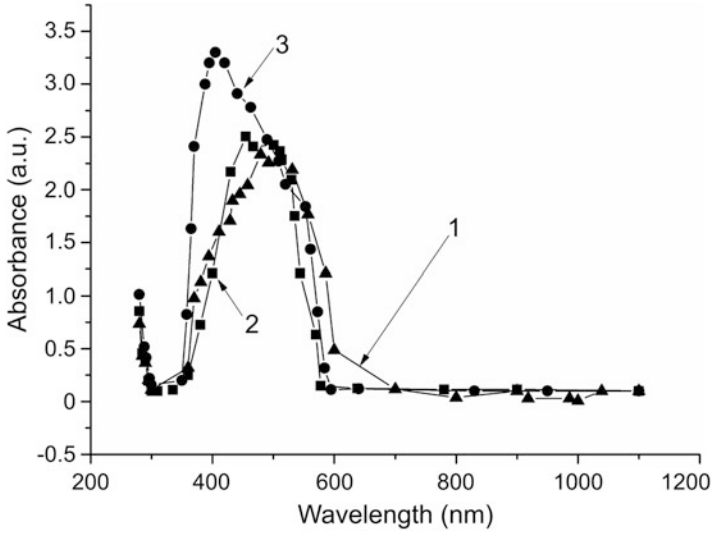

Fig. 27.4 Absorption spectra of solutions: DOXO (*1*), MNC2 (*2*), and MNC1 (*3*)

27.3.4 The Interaction Between Magnetic Field and Magnetic Nanoparticles

We have analyzed the changes of electromagnetic waves from SPION and FMION under the influence of CMF. The experimental results are shown in Fig. 27.5. Analysis of the results indicates that conventional sodium chloride solution significantly changes the AMF intensity at different values of CMF. The influence of permanent magnet is only significantly and oppositely smaller. There is clearly visible difference between the influence of SPION and FMION. AMF intensity at different values of CMF for SPION is 11 % higher on average as compared to FMION. The changes of the external magnetic field can be more pronounced for single-domain SPION in contrast to multi-domain FMION due to the properties of their heterogeneous structure in MNC [22].

What is the interrelation between physical properties and antitumor molecular effects? It is possible to assume that increase in antitumor and antimetastatic effect of MNC comprising of SPION and DOXO as compared to MNC composed of FMION and DOXO is related to the phenomenon of spin-dependent electron transport between iron oxide and aromatic rings of DOXO and hexose rings of lactose, which included in anthracycline antibiotic as ingredient, during EI [23]. Since the reactivity of the magnetic particles depends on their spin state, it is possible to control the kinetics of free radical reactions by external magnetic fields [24].

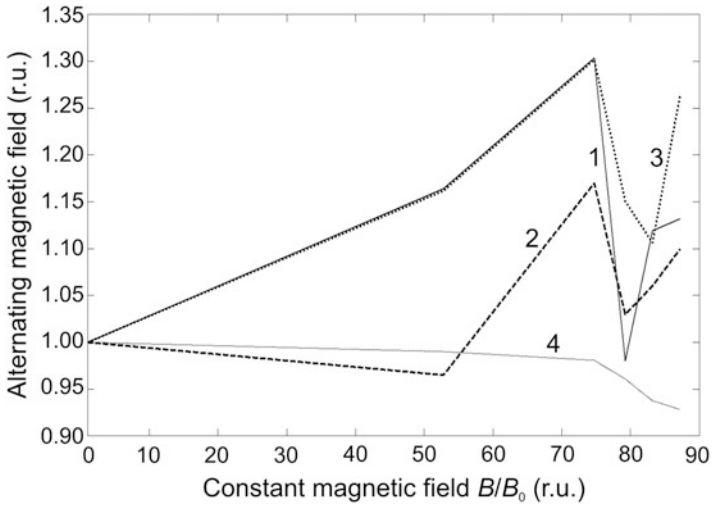

Fig. 27.5 An influence of magnetic NP on the intensity of very high-frequency electromagnetic field: 0.9 % sodium chloride solution (*1*), FMION (*2*), SPION (*3*), permanent magnet (*4*). *B* is induction of CMF during the measurement; B_0 is induction of CMF at a maximum distance of 10 cm

27.4 Conclusion and Future Perspectives

Our study clearly demonstrates that SPION in MNC loaded with antitumor drug DOXO have significantly different magnetic properties as compared to FMION. With the increase in the geometric dimensions of Fe_3O_4 NP, the maximum of absorption spectrum for supernatant from MNC solution is shifted to shorter wavelengths, indicating the deformation of DOXO molecule under the influence of iron oxide NP due to the decrease in the region of localization of the optical electron. In our previous studies, we reported that magnetic nanotherapy of animals with Lewis lung carcinoma induced greater antitumor and antimetastatic effects [5]. It opens up promising prospect for future studies of cancer magnetic nanotherapy using MNC of SPION and DOXO based on the principles of semiconductor spintronics for clinical implementation of remotely controlled by electromagnetic field drug delivery and a local toxicity in tumor.

References

1. Hayashi K, Nakamura M, Sakamoto W et al (2013) Superparamagnetic nanoparticle clusters for cancer theranostics combining magnetic resonance imaging and hyperthermia treatment. Theranostics 3(6):366–376
2. Ortega D, Pankhurst QA (2013) Magnetic hyperthermia. In: O'Brien P (ed) Nanoscience, vol 1, Nanostructures through chemistry. Royal Society of Chemistry, Cambridge, pp 60–88. doi:10.1039/9781849734844-00060
3. Giustini AJ, Petryk AA, Cassim SM et al (2010) Magnetic nanoparticle hyperthermia in cancer treatment. Nano Life 1(01n02):17–32. doi:10.1142/S1793984410000067
4. Dutz S, Hergt R (2013) Magnetic nanoparticle heating and heat transfer on a microscale: basic principles, realities and physical limitations of hyperthermia for tumour therapy. Int J Hyperthermia 29(8):790–800
5. Orel V, Shevchenko A, Romanov A et al (2015) Magnetic properties and antitumor effect of nanocomplexes of iron oxide and doxorubicin. Nanomed Nanotech Biol Med 11(1):47–55
6. Zhang H, Ji Z, Xia T et al (2012) Use of metal oxide nanoparticle band gap to develop a predictive paradigm for oxidative stress and acute pulmonary inflammation. ACS Nano 6 (5):4349–4368. doi:10.1021/nn3010087
7. Burello E, Worth AP (2011) A theoretical framework for predicting the oxidative stress potential of oxide nanoparticles. Nanotoxicology 5(2):228–235. doi:10.3109/17435390.2010.502980
8. Xu Y, Schoonen MAA (2000) The absolute energy positions of conduction and valence bands of selected semiconducting minerals. Am Mineral 85(4):543–556
9. Ghodbane S, Lahbib A, Ammari M et al (2015) Does static magnetic field-exposure induced oxidative stress and apoptosis in rat kidney and muscle? Effect of vitamin E and selenium supplementations. Gen Physiol Biophys 34:217–219
10. Okano H (2008) Effects of static magnetic fields in biology: role of free radicals. Front Biosci 13:6106–6125
11. Chomoucka J, Drbohlavova J, Huska D (2010) Magnetic nanoparticles and targeted drug delivering. Pharmacol Res 62(2):144–149. doi:10.1016/j.phrs.2010.01.014
12. Hayashi K, Moriya M, Sakamoto W et al (2009) Chemoselective synthesis of folic acid-functionalized magnetite nanoparticles via click chemistry for magnetic hyperthermia. Chem Mater 21:1318–1325

13. Bedanta S, Kleemann W (2009) Supermagnetism. J Phys D Appl Phys 42(1):013001. doi:10.1088/0022-3727/42/1/013001
14. Orel V, Romanov A, Rykhalskyi A (2016) Antitumor effect of superparamagnetic iron oxide nanoparticles conjugated with doxorubicin during magnetic nanotherapy of Lewis lung carcinoma. Materialwiss Werkstofftech 47:165–171
15. Orel VE, Shevchenko AD, Rykhalskyi OY (2015) Investigation of nonlinear magnetic properties magneto-mechano-chemical synthesized nanocomplex from magnetite and antitumor antibiotic doxorubicin. In: Fesenko O, Yatsenko L (eds) Nanocomposites, nanophotonics, nanobiotechnology and applications. Springer Proceedings in Physics, vol 156. pp 103–110. doi:10.1007/978-3-319-06611-0_8
16. Laurent S, Mahmoudi M (2011) Superparamagnetic iron oxide nanoparticles and cancer. Int J Mol Epidemiol Genet 2(4):367–390
17. Nikolov N, Orel V, Smolanka I et al (2008) Apparatus for short-wave inductothermy "Magnetotherm". In: Katushev A, Dekhtyar Y, Spigulis J (eds) Proceedings of NBC. Springer, Berlin, pp 294–298
18. Orel VE, Dzyatkovskaya NN, Kruchkov EI et al (2014) The effect of the inhomogeneous magnetic fields on the antitumor activity of magnetic nanotherapy. In: 2014 I.E. 34th International Conference on Electronics and Nanotechnology (ELNANO), pp 329–333. doi:10.1109/ELNANO.2014.6873909
19. Panchuk RR, Prylutska SV, Chumak VV et al (2015) Application of C_{60} fullerene-doxorubicin complex for tumor cell treatment in vitro and in vivo. J Biomed Nanotechnol 11(7):1139–1152
20. Prylutskyy YI, Evstigneev MP, Pashkova IS et al (2014) Characterization of C_{60} fullerene complexation with antibiotic doxorubicin. Phys Chem Chem Phys 16(42):23164–23172
21. Prylutskyy YI, Evstigneev MP, Cherepanov VV et al (2015) Structural organization of C_{60} fullerene, doxorubicin and their complex in physiological solution as promising antitumor agents. J Nanopart Res 17(1):45–49
22. Ustinov VV, Rinkevich AB, Perov DV et al (2013) Giant antiresonance in electromagnetic wave reflection from a 3D structure with ferrite spinel nanoparticles. Tech Phys 58(4):568–577
23. Orel VE, Romanov AV (2014) Cancer magnetic nanotherapy. LAP Lambert Academic, Saarbrücken
24. Liu H, Li XZ, Leng YJ, Wang C (2007) Kinetic modeling of electro-Fenton reaction in aqueous solution. Water Res 41:161–167
25. Orel VE, Kudryavets YI, Bezdenezhnih NA et al (2005) Mechanochemically activated doxorubicin nanoparticles in combination with 40MHz frequency irradiation on A-549 lung carcinoma cells. Drug Deliv 12(3):171–178

Chapter 28
The Effect of the Synthesis Conditions on Morphology of Tin (IV) Oxide Obtained by Vapor Transport Method

Svitlana Nagirnyak, Victoriya Lutz, Tetiana Dontsova, and Ihor Astrelin

28.1 General

28.1.1 Introduction

Tin (IV) oxide belongs to the class of materials which combine high electrical conductivity (n-type semiconductor oxide with a wide energy gap of 3.6 eV at 300 K [1]) with a number of functional properties—low electrical resistance, high optical transparency in the visible spectrum, chemical stability at high temperatures, excellent optical and electrical properties [2].

SnO_2 has only one stable phase and crystallizes in tetragonal rutile structure with lattice constants $a = b = 4.7373$ Å, $c = 3.1864$ Å [3]. In the rutile structure, tin atoms are located in the center and surrounded by six oxygen atoms placed in the corners of almost regular octahedron. The atoms of oxygen are surrounded by three tin atoms that form an equilateral triangle (Fig. 28.1).

Tin (IV) oxide is widely used for transparent electrodes [4, 5], displays and photoelectron parts of heterostructure solar cells [6, 7], and rechargeable Li-batteries, as a catalyst for oxidation of organic compounds, and as gas sensor [2].

S. Nagirnyak (✉) • V. Lutz • T. Dontsova • I. Astrelin
Department of Chemistry, National Technical University of Ukraine "KPI",
Prospect Peremogy, 37, Kyiv 03056, Ukraine
e-mail: nagirnyak_sv@ukr.net; vika_lyts@mail.ru; dontsova@ua.fm; i.m.astrelin@xtf.kpi.ua

O. Fesenko, L. Yatsenko (eds.), *Nanophysics, Nanophotonics, Surface Studies, and Applications*, Springer Proceedings in Physics 183,
DOI 10.1007/978-3-319-30737-4_28

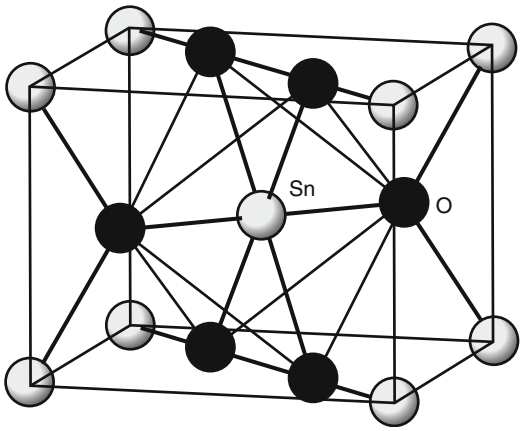

Fig. 28.1 SnO_2 structure [3]

28.1.2 Methods of Obtaining Tin (IV) Oxide

On the potential application, physical and chemical properties of materials have a significant influence, which in turn depend on the method of synthesis. In particular, in the case of the gas sensor, preference is given to nanoscale materials that have a high surface to volume ratio and high adsorption capacity and, as a result, are characterized by the highest values of the sensor signal. The increase of surface to volume ratio leads to significant changes in sensor sensitivity, and from this point of view, 1D nanostructures deserve a special attention.

Thus, the synthesis of tin (IV) oxide nanostructures with desired structure and morphology is one of the main directions in the field of nanoscience and nanotechnology. And the development of ways for controlling structure, dimensions, and properties of obtained powders has a great scientific and technical value.

Many methods for fabrication of 1D tin (IV) oxide nanostructures have been developed. The most common of them are hydrothermal synthesis, sol–gel method, template synthesis, and vapor transport method (called method CVD).

Hydrothermal synthesis involves use of water as a solvent at elevated temperatures (usually to 300 °C) and pressures in a closed system. It is carried out in autoclaves, often lined with Teflon. Processing time ranges from 10 min to 24 h. In the process of heating is an increase in vapor pressure above the solution to values above 0.1 MPa (1 atm).

To obtain tin (IV) oxide nanostructures by hydrothermal synthesis, tin (IV) chloride is commonly used as precursor [8–10]. This method allows to obtain SnO_2 nanowires and nanoneedles with a diameter of 50–150 nm and a length of 10–100 mm [8] and nanorods with a diameter of 20–40 nm and a length of 100–300 nm [2, 9–11]. However, it should be noted that hydrothermal synthesis is difficult in maintenance and energy-consuming enough.

Sol–gel method implemented by hydrolysis and subsequent polycondensation of SnO_2 precursors in water and aqueous-alcoholic environments [12]. In this method

to obtain 1D SnO_2 nanostructures as precursor uses tin (IV) chloride [13–17]. A significant advantage of the sol–gel technology method is the ability to achieve high homogeneity of materials due to mixing all starting materials at the molecular level. Thus, we can provide high purity and highly developed surface of materials.

Using the method of sol–gel, nanofibers of tin (IV) oxide with an average diameter in the range of 100–300 nm and a length of 10 m are obtained [14].

Template synthesis is the technique for the controlled synthesis of nanostructured materials under the influence of various factors spatial constraints due to a kind of pattern—template. In the case of 1D nanostructures, template provides channels for guiding the growth or deposition of materials in 1D form. Template method also can be combined with electrodeposition methods, sol–gel technology, and chemical vapor deposition [18, 19]. Method of template synthesis allows to obtain SnO_2 nanofibers with a diameter of 50–200 nm, from 5 to 50 mm in length and with a wall thickness of 13 nm [20] and nanowires with a diameter of 8 nm [21]. The disadvantage of template method is quite a lengthy synthesis process.

Vapor transport method (method CVD) is a simple process in which condensed or powder source material is vaporized in inert atmosphere at an elevated temperature (1300 °C), and the resultant vapor phase condenses under certain conditions (temperature, pressure, atmosphere, substrate, etc.) to form the desired product [22–30]. Metallic tin [23, 25–27, 29], tin (II) oxide [22], and a mixture of powdered carbon and tin (IV) oxide are used as precursors [24].

This method makes it possible to obtain nanowires and nanoribbons of tin (IV) oxide with a diameter of 40–200 nm and a length from a few dozen to several hundred micrometers [23, 24, 26]. This method deserves special attention because it secures superior performance in conjunction with relative simplicity and availability. In addition, this method allows to obtain single crystals of SnO_2 controlled and varied morphology with a high degree of crystallinity [24, 31, 32].

In the case of CVD method, there are several processing parameters, such as evaporation temperature, synthesis duration, and precursors, which have a significant influence on the morphology of obtained powders. The influence of these parameters on characteristics of the products was investigated.

28.2 Experimental

28.2.1 Obtaining of Tin (IV) Oxide Samples

SnO_2 samples were synthesized from SnC_2O_4. Tin (II) oxalate was obtained by direct deposition from different precursors: in the first case, tin chloride (II) and oxalic acid and, in the second case, tin chloride (II) and ammonium oxalate as shown in [33].

For SnO_2 tin (II) oxalate was decomposed in a horizontal-type furnace in an inert atmosphere at different processing temperature. The inert atmosphere was

Table 28.1 Conditions for the synthesis of SnO_2 samples

Sample	Precursor for SnC_2O_4	Treatment temperature, K	Treatment duration, hours
Sample 1	$H_2C_2O_4$	723	1
Sample 2	$H_2C_2O_4$	873	1
Sample 3	$H_2C_2O_4$	973	1
Sample 4	$H_2C_2O_4$	1073	1
Sample 5	$H_2C_2O_4$	1123	1
Sample 6	$H_2C_2O_4$	1073	1 + 24
Sample 7	$(NH_4)_2C_2O_4$	1123	1
Sample 8	$(NH_4)_2C_2O_4$	1223	1
Sample 9	$(NH_4)_2C_2O_4$	1323	1

Table 28.2 Composition and structural parameters of obtained SnO_2 samples

Sample	Composition[a]	Crystallite size, nm	Lattice constant, nm	
			a	*c*
Sample 1	SnO_2—64.7 %	33.0	4.74	3.19
	SnO—28.0 %	77.9	3.80	4.84
	Sn—4.6 %	58.3	5.83	3.18
Sample 2	SnO_2—64.7 %	78.8	4.74	3.19
	Sn—35.3 %	74.9	5.83	3.18
Sample 3	SnO_2—64.7 %	68.8	4.74	3.19
	Sn—35.3 %	–	5.83	3.18
Sample 4	SnO_2—57.0 %	58.6	4.74	3.19
	Sn—43.0 %	–	5.83	3.18
Sample 5	SnO_2—100 %	57.9	4.74	3.19
Sample 6	SnO_2—100 %	60.6	4.74	3.19
Sample 7	SnO_2—100 %	57.8	4.74	3.19

[a]X-ray diffraction data

implemented by nitrogen with 0.005 % oxygen impurity. Gas flow was 100 cm^3 per minute. Thus, the 9 samples of tin (IV) oxide were obtained (see Table 28.1).

28.2.2 X-Ray Analysis

XRD (X-ray diffraction) measurements of SnO_2 samples were conducted using X-ray diffractometer Ultima IV Rigaku with CuKa radiation. The data from a study of the obtained samples by X-ray analysis is presented in Table 28.2.

On the XRD spectra shown in Fig. 28.2 can be observed a change in composition of the product depending on the temperature. Thus, Sample 1, produced at a temperature 723 K, contains in its composition three compounds: cassiterite SnO_2 (64.7 %), romarchite SnO (28.8 %), and metallic tin Sn (4.6 %). With temperature

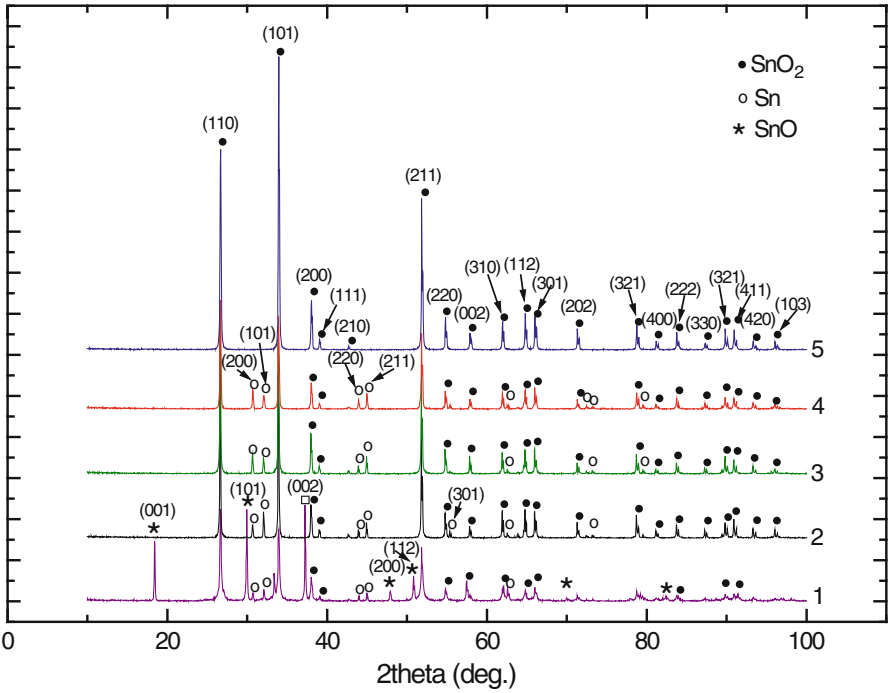

Fig. 28.2 The XRD patterns of SnO_2: *1*, Sample 1; *2*, Sample 2; *3*, Sample 3; *4*, Sample 4; *5*, Sample 5

increasing, since the processing temperature of 873 K, the reaction product composition contains only two compounds: SnO_2 and Sn.

The phase transformation $SnO \rightarrow SnO_2$ occurs above the temperature of 723 K due to reaction disproportionation:

$$2SnO = SnO_2 + Sn. \quad (28.1)$$

Accordingly, with temperature increasing rises the percentage of a desired product and at the processing temperature of 1073 K a pure SnO_2 formed.

As the atmosphere of the synthesis contains oxygen, oxidation reaction of metallic tin takes place at a temperature of 1073 K:

$$Sn + O_2 = SnO_2. \quad (28.2)$$

The most distinct peaks at XRD spectra observed at values of $2\theta = 26.6$, 33.9, and 51.8° and according to a standard database USER (COD) (cards №1000062, 9007533, 9007433) are indexed as the (110), (101), and (211) crystal faces that fit to the tetragonal structure of the obtained sample. The average crystallite size of the obtained sample of SnO_2 ranges from 33 to 79 nm.

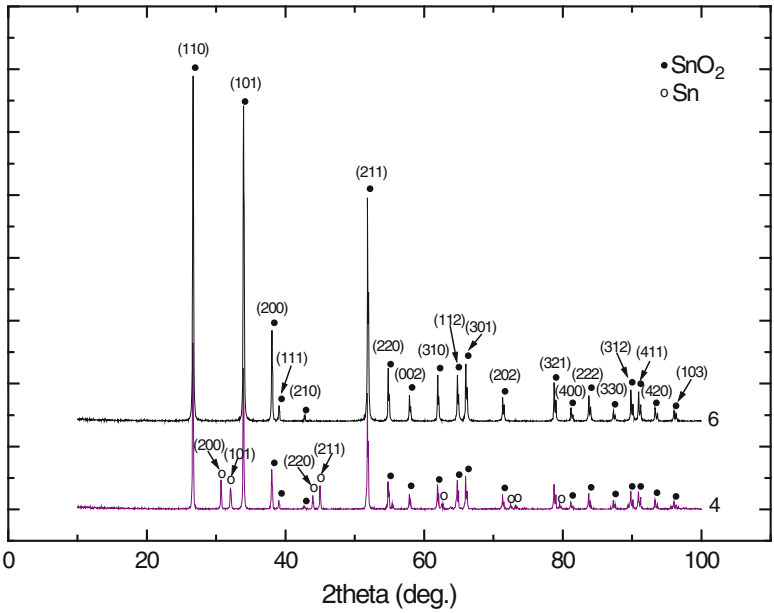

Fig. 28.3 The XRD patterns of SnO_2 powders: *4*, Sample 4; *6*, Sample 6

Duration of treatment also has an important impact on the formation of final product. Figure 28.3 shows the X-ray diffraction patterns of samples obtained at the same temperature (1073 K), but the processing time of Sample 4 was 1 h and Sample 6 was left in off furnace for 24 h after the end of synthesis. XRD spectra show that for Sample 6 the formation of pure tin (IV) oxide was observed, while the percentage of SnO_2 in Sample 4 is 57 %.

If the temperature and duration of treatment mainly affect the product yield, purity, and degree of crystallinity of the product, the precursor may alter the morphology of obtained powder. In this case, even reagents that are used to obtain precursor have an influence on the product characteristics. The effects of precursor SnC_2O_4 obtained from different reagents (oxalic acid for Sample 5 and ammonium oxalate for Sample 7) on the characteristics of tin (IV) oxide obtained by CVD were investigated [33].

XRD spectra of the samples presented in Figures 28.4 and 28.5 show that for Sample 5 the most distinct peak is (110), while for Sample 7, which was obtained from ammonium oxalate, the peak is (101), which indicates the beginning of growth of 1D nanostructures [34].

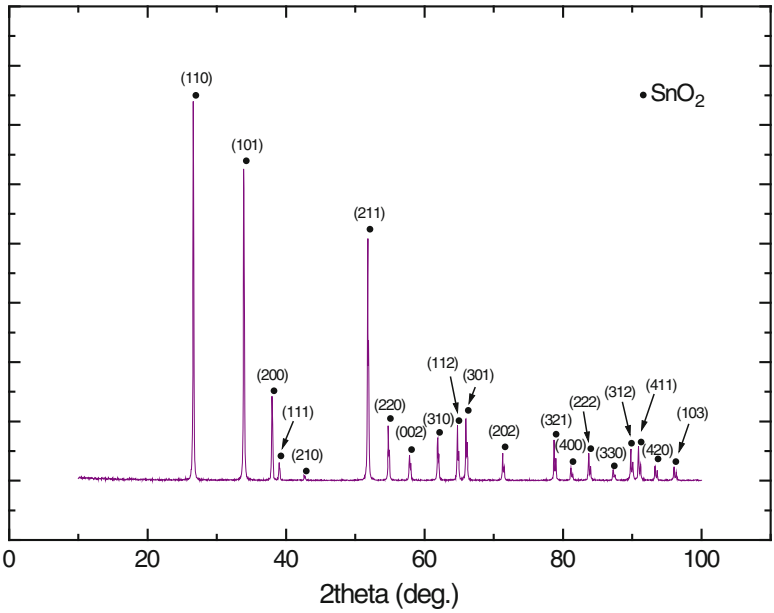

Fig. 28.4 The XRD patterns of Sample 5 [33]

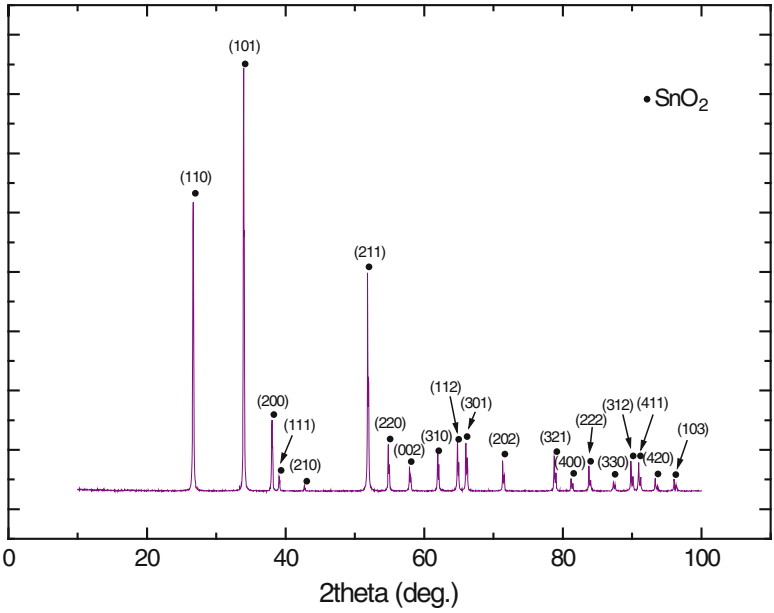

Fig. 28.5 The XRD patterns of Sample 7 [33]

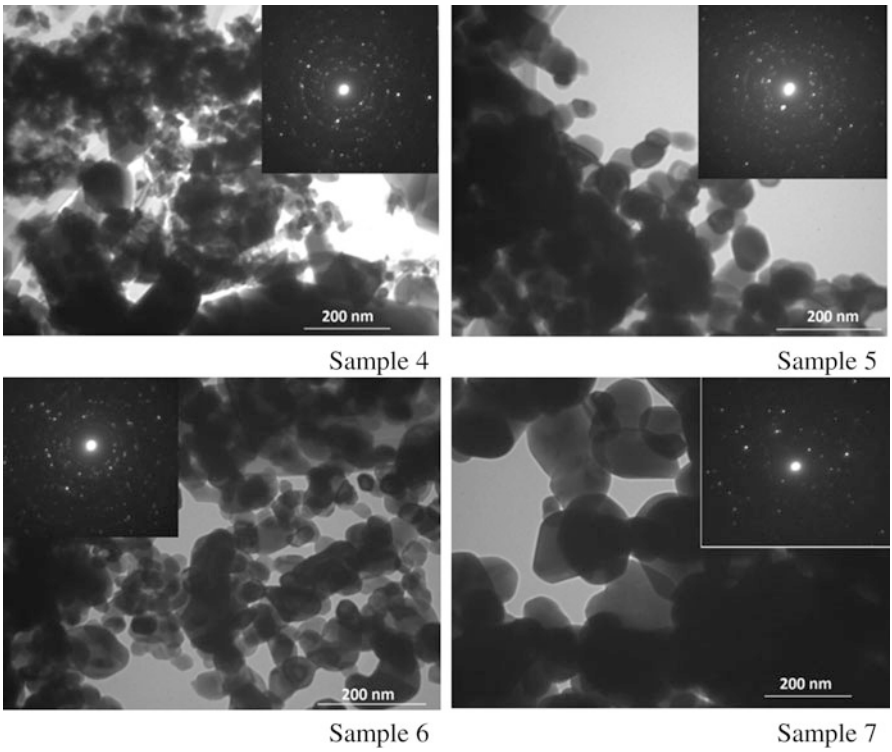

Fig. 28.6 TEM-images of synthesized samples of tin (IV) oxide: Samples 4–7

28.2.3 Microscopy

Samples 4–7 were studied by electron microscopy using a transmission electron microscope TEM 100-01.

TEM-image of Sample 4 shows globules associated in bigger agglomerates of amorphous tin (IV) oxide. Particles of Sample 5 and Sample 6 have uncertain form and the average size is 60–80 nm. Particle formation of the most definite form is observed for Sample 7. The powder of Sample 7 represented as individual particle that has a pronounced hexagonal shape and size near 200 nm. Presented SAED patterns of the samples demonstrate single-crystalline spots [33] (Fig. 28.6).

Because the use of ammonium oxalate as a precursor of tin (II) oxalate allows to obtain better crystals of tin (IV) oxide, additional research concerning the effect of temperature increase on the morphology of the tin (IV) oxide powders, prepared from the appropriate tin oxalate, was performed. Tin (IV) oxide powders were obtained by decomposition of tin (II) oxalate at 1223 K and 1323 K [35].

Obtained SnO_2 samples were analyzed with a scanning electron microscope SEM-106. The corresponding SEM images are presented in Fig. 28.7 and show that the rise of 1D nanostructures at the 1223 K is just beginning, while SEM image

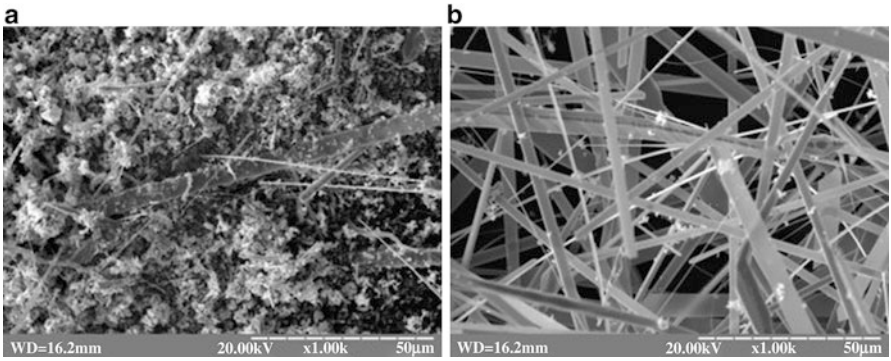

Fig. 28.7 SEM image of SnO_2 obtained by CVD method at 1223 K (**a**) and 1323 K (**b**)

SnO_2 obtained at 1323 K shows nanobelts with an average diameter of 300–500 nm and length of a few ten micrometers to hundred micrometers.

28.3 Conclusions

SnO_2 nanostructures with special morphologies attracted great interest due to their unique properties, and synthesis method of such structures is the main task nowadays. One of the most perspective synthetic procedure is the vapor transport method, which allows to obtain single crystals of SnO_2 with a high degree of crystallinity. But, besides the choice of synthesis method, an also important step is the choice of process conditions. In the case of CVD method, the most significant parameters are the process temperature, treatment duration, and type of precursor.

This study considered the influence of these parameters on composition and morphology of obtained tin (IV) oxide powders. It was shown that the pure SnO_2 is formed at the processing temperature of 1123 K and treatment duration of 1 h. But the morphology of obtained powder depends on the precursor used. Tin (IV) oxide samples produced from two different precursors (with using oxalate acid and ammonium oxalate) were considered. It was established that 1D nanostructures are formed using ammonium oxalate as precursor. The growth of 1D SnO_2 nanostructures is just begins at 1123 K and the sufficient temperature for obtaining of 1D nanostructures is 1323 K.

Acknowledgments The authors thank the Faculty of Physical Engineering of National Technical University of Ukraine "KPI" for their support in conducting this research.

References

1. Munnix S, Schmeits M (1982) Surface electronic structure of tin (IV) oxide. Solid State Commun 43:867
2. Tan L, Wang L, Wang Y (2011) Hydrothermal synthesis of SnO_2 nanostructures with different morphologies and their optical properties. J Nanomater 2011:1–10
3. Zaynullina VM (2008) Kvantovo-himicheskoe modelirovanie elektronnoy structury i magnitnyh svoystv $Sn_{1-x-y}M_xSb_yO_2$, M = Cr, Mn, Co, Ni (x = 0.25; y = 0, 0.25) (Quantum-chemical modeling of electronic structure and magnetic properties $Sn_{1-x-y}M_xSb_yO_2$, M = Cr, Mn, Co, Ni (x = 0.25; y = 0, 0.25)). Physika tverdogo tela 50(7):1200–1205
4. Batzill M, Diebold U (2005) The surface and material science of tin oxide. Prog Surf Sci 79:7–154
5. Panov EV, Malevannyi SM, Kolomuvcev DV et al (2010) Electrodnye materialy na osnove nanokristallicheskyh oksidov olova, margantsa i kobalta (Electrode materials based on nano-crystalline tin oxides, manganese and cobalt). Visnyk Kharkivskogo natsionalnogo universitety 41:224–230
6. Comini E (2006) Metal oxide nano-crystals for gas sensing. Anal Chim Acta 568(1–2):28–40
7. Obvintseva LA (2008) Polyprovodnikovye metaloksidnye sensory dlya opredeleniya khimicheski aktivnyh gasovyh primesey v vozdushnoy srede (Semiconducting metal oxide sensors for the determination of reactive trace gases in air). J Ros Khim Ob-va im D.I. Mendeleeva LII(2):113–121
8. Lupan O, Chow L, Chai G et al (2009) A rapid hydrothermal synthesis of rutile SnO_2 nanowires. Mater Sci Eng B 157:101–104
9. Xuan HV, Duc VD, Duc CN (2011) Synthesis of tin dioxide nanoparticles and nanorods by hydrothermal method and gas sensing characteristics. e-J Surf Sci Nanotechnol 27(9):503–507
10. Kiran J, Abhilasha S, Rashmi R (2006) Synthesis and controlling the morphology of SnO_2 nanocrystals via hydrothermal treatment. ECS Trans 1(21):1–7
11. Wang H, Wang M, Li B (2014) Hydrothermal synthesis and electrochemical properties of tin titanate nanowires coupled with SnO_2 nanoparticles for Li-ion batteries. CrystEngComm 16:7529–7535
12. Dontsova T, Ivanenko I, Astrelin I et al (2014) Stabilization of nanoscale tin (IV) oxide on the surface of carbon nanotubes. J Electr Eng 2(1):34–38
13. Gajendiran J, Rajendran V (2011) Size controlled and optical properties of Zn-doped SnO_2 nanoparticles via sol-gel process. Optoelectron Adv Mater 5(1):44–48
14. Cao H, Qui X, Lianq Y et al (2006) Sol-gel template synthesis and photoluminescence of n- and p-type semiconductor oxide nanowires. Chemphyschem 7(2):497–501
15. Zhang G, Liu M (1999) Preparation of nanostructured tin oxide using a sol-gel process based on tin tetrachloride and ethylene glycol. J Mater Sci 34(13):3213–3219
16. Hassanzadeh A, Moazzez B, Haghgooie H et al (2008) Synthesis of SnO_2 nanopowders by a sol-gel process using propanol-isopropanol mixture. Cent Eur J Chem 6(4):651–656
17. Köse H, Aydin AO, Aydin H (2012) Sol-gel synthesis of nanostructured SnO_2 thin film anodes for Li-ion batteries. Acta Physica Polonica A 121(1):227–229
18. Meyyappan M, Mahendra K (2010) Inorganic nanowires: applications, properties, and characterization. Taylor & Francis, Boca Raton
19. Cao G, Wang Y (2011) Nanostructures and nanomaterials: synthesis, properties and applications. World Scientific, Singapore, p 581
20. Park S, An S, Park S et al (2013) Synthesis of Au-functionalized SnO_2 nanotubes using TeO_2 nanowires as templates and their enhanced gas sensing properties. Appl Phys A 110 (2):471–477
21. Zhang H, Tan Z, Xu P et al (2011) Preparation of SnO_2 nanowires by solvent-free method using mesoporous silica template and their gas sensitive properties. J Nanosci Nanotechnol 11 (2):11114–11118

22. Ryabtsev SV, Hadiya NM, Domashevskaya EP (2010) Morphologiya nanokristallov oksida olova, polychennyh metodom gasotransportnogo synteza (The morphology of tin oxide crystals obtained by gas transport synthesis). Pisma v ZTPh 36(12):7
23. Shaposhnik A, Ryabtsev S, Shao F et al (2012) Comparison of hydrogen sulfide sensing characteristics of individual SnO_2 nanowire and SnO_2 sol-gel nanocomposite. Procedia Eng 47:1398–1401
24. Duy KL, Thanh BN, Thanh BLT et al (2008) SnO_2 nanostructures synthesized by using a thermal evaporation method. J Korean Phys Soc 52(5):1689–1692
25. Xiangming H, Bing Z, Shaokang G et al (2008) Gas sensing properties of SnO_2 nanobelts synthesized by thermal evaporation of Sn foil. J Alloys Compd 461(1–2):L26–L28
26. Choi Y, Hwang I, Park J et al (2008) Novel fabrication of an SnO_2 nanowire gas sensor with high sensitivity. Nanotechnology 19(9):095508
27. Woo KH, Woo LJ, Hyun SS et al (2007) Controlled growth of SnO_2 nanorods by thermal evaporation of Sn powders. J Korean Phys Soc 51(1):198–203
28. Hashim A (2011) Nanowires—implementations and Applications. In Tech, Manhattan, p 538
29. Park S, Hong C, Kang J et al (2009) Growth of SnO_2 nanowires by thermal evaporation on Au-coated Si substrates. Curr Appl Phys 9(3):S230–S233
30. Nabiyouni G, Boroojerdian P, Parvan Z (2011) Synthesis and characterization of tin oxide nanowires using vapor-liquid-solid technique. J Mater Sci Eng 5:71–75
31. Dai ZR, Pan ZW, Wang ZL (2003) Novel nanosturctures of functional oxides synthesized by thermal evaporation. Adv Funct Mater 13:9–24
32. Castillo DN, Becerril TD, Andres ER et al. (2012) VLS synthesis and characterization of SnO_2 nanowires method. Mater Res Soc. 33–38.
33. Nagirnyak SV, Lutz VA, Dontsova TA et al. (2015) Synthesis and properties of tin (IV) oxide obtained by chemical vapor deposition method. NanoScale Res Lett. (accepted for publication)
34. Choi Y, Hwang I, Park J et al (2008) Novel fabrication of an SnO_2 nanowire gas sensor with high sensitivity. Nanotechnology 19:4
35. Nagirnyak SV, Lutz VA, Dontsova TA (2015) The temperature influence on the morphology of SnO_2 nanostructures obtained by vapor transport method. Paper presented at the international research and practice conference Nanotechnology and nanomaterials (NANO 2015), Lviv, 26–29 Aug 2015

Chapter 29
Effect of Aluminum-Based Colloid Solutions on Purification of Products of Sugar Production

Kira Liapina, Andrii Marynin, Peter Dulnev, Valentyn Olishevskyy, Natalia Pushanko, Anatoliy I. Ukrainets, and Anatoliy I. Ustinov

29.1 Introduction

The sugar production includes several technological processes which are very closely connected between themselves. The efficiency of each next process directly depends on the efficiency of the previous stage. It is evident that to achieve the necessary quality of the ready products, i.e., granulated sugar, the high efficiency of all the technological stages of its production of both main and also auxiliary ones is required. In addition, it is necessary to take also into account the fact that assurance of high-quality characteristics of production should not lead to the increase of consumption of auxiliary materials (feed water, lime, saturation gas, and other reagents) and also wastes of production. It should be added that under advanced conditions of production intensification, the relation between the economic and ecological factors is changed, in principle, toward the formation of ecologically clean productions on the basis of wasteless technological structures.

The formation of the quality characteristics of the white sugar occurs already at the very first stages of its production, starting from the raw material, as very often the beet with the low technological quality is supplied for the treatment. As a result, the diffusion juice, produced in a beet-processing shop section, has a high content

K. Liapina (✉) • A.I. Ustinov
E.O. Paton Electric Welding Institute, Kyiv, Ukraine
e-mail: kirulya@mail.ru

A. Marynin • V. Olishevskyy • N. Pushanko • A.I. Ukrainets
National University of Food Technologies, Kyiv, Ukraine

P. Dulnev
Institute of Bioorganic Chemistry and Petrochemistry, Kyiv, Ukraine

O. Fesenko, L. Yatsenko (eds.), *Nanophysics, Nanophotonics, Surface Studies, and Applications*, Springer Proceedings in Physics 183,
DOI 10.1007/978-3-319-30737-4_29

of different compounds (so-called nonsugars) which reduce significantly its purity. The degree of perfection of the process of producing the diffusion juice depends on the quality characteristics of the feed water. The feed water is the water, prepared in a special way for the realization of the process of the sucrose extraction from the beet slices. Depending on the technological conditions of operation the water from the external source, condensate, produced by device for evaporation, or water, produced after extraction of the desugarized slices (pulp), or the pulp-press water can be used as the feed water. These types of waters are differed by their chemical composition and require different technologies of preparation. It is most profitable to apply the water from the external source or condensate, as this water does not require complicated schemes of preparation. However, in the present conditions of a rational water application in the beet-sugar production, the technological scheme of producing the diffusion juice envisages a partial replacement of "fresh" water by the pulp-press water and condensate. This affects greatly on the quantitative and qualitative parameters of the extractor and main technical-economic values of the factory. Moreover, much more attention is paid to the repeated use of the pulp-press water, as it contains the sucrose [1].

If the pulp-press water is not used in the process of extraction, then this will cause the increase in losses of the sucrose at the extractor. On the other hand, the return of the pulp-press water in extraction of the sucrose is connected with introduction of an additional amount of nonsugars into the juice (especially protein and pectin) that can lead to the additional expenses for purification of the produced diffusion juice and reduction almost to minimum of the effect of the pulp-press water return.

The efficiency of the process of application of the pulp-press water depends greatly on its quality characteristics: weighed and dissolved elements, degree of microbiological contamination, content of the sucrose, and so on. The amount of water in application of the continuous advanced extractors is approximately 35–60 % against the mass of beet depending on technological characteristics of the press for the pulp extraction. Discharge of such amount of water with a large content of organic substances and sucrose is inadmissible from the ecological point of view. In order to use this water repeatedly, a special preparation is required, which includes, as a rule, the deposition (coagulation) of the protein and pectin materials.

At the domestic beet-sugar factories, the return of the pulp-press water is rather an exception as compared with the foreign ones, where this element allows obtaining the low losses of the sucrose in the pulp. The main difference of pressing the desugarized slices (pulp) at the foreign sugar factories consists in that it is carried out up to the higher content of solids in the pulp due to the application of the more powerful pulp presses [2].

The applying of additional reagents in the technology of producing and purification of the sugar-containing solutions is a rather actual problem for the sugar complex of Ukraine, as this is a simple and economic way for improving the quality

characteristics of the ready products. This problem was studied in many works, in particular in [2–8]. However, in these works the reagents were used either at the stage of sucrose extraction from the beet slices or at the stage of purification of the produced diffusion juice. Taking into account the problem of implementation of the cycling application of water at the beet-sugar factories, the investigation of possibility of water preparation by using additional reagents represents an interest.

However, the variety of processes and factors, affecting on them, occurring under the conditions of the feed water preparation, does not give opportunity to evaluate sufficiently precisely the mechanism of interaction of the introduced additional chemical reagents with the feed water impurities. It concerns, first of all, the process of coagulation of colloids (albumen and protein). On the other hand, the introduction of additional reagents at the stage of production and purification of the diffusion juice should meet a number of conditions, in particular, a minimum dose of the reagent while retaining high efficiency, absence of interaction with the sucrose, full removal in its production process, and a minimum content not exceeding the norms of LAC (limiting admissible concentration) [9].

Recently, the more attention is paid to the scientific direction, connected with using the materials of a nanosized scale with ultra-dispersed characteristics in engineering and technologies, in particular in food ones [10, 11]. Due to a specific structure of the nanoparticles and their unique physical, chemical, and biological properties, the progress of investigations in this direction makes it possible to develop the economically profitable, ecologically safe technologies [12].

The application of properties of the nanomaterials allows producing new coagulants based on metals (dioxide of titanium, iron, and oxide of aluminum), which have high coagulation properties. These coagulants provide producing of the coagulant particles of the larger sizes, than the application of traditional coagulating agents. And also, the produced complexes have the more dense structure [13–15]. It is shown in the work of [16] that the residual amount of aluminum when used in nanoform in the purified solutions is 30 % lower than that in the application of the traditional aluminum-containing coagulant.

The application of nanoparticles for the additional purification of semi-products of the sugar production is given in the works [17, 18]. However, in spite of a large amount of data, which confirm the high efficiency of proceeding of processes of water preparation by using the nanoreagents, the mechanism of their purifying action and conditions of proceeding the processes in different systems is a little studied.

29.2 Method of Producing the Encapsulated Al Nanopowder and High-Viscosity Suspension Preparation, Using Encapsulated Al Nanopowder as Precursors

To produce the aluminum nanoparticles, the method was used, based on evaporation of metal and salt (halogenides of alkali metals) in a closed volume with subsequent combined condensation of their vapor flows, during which the encapsulation of metallic particles into chemically inert matrix occurs [19] (Fig. 29.1).

The statistic processing of results of measurement using the computer program Image-Pro Plus is given in Table 29.1 that allowed plotting the diagram of distribution of nanoparticles by sizes, presented in Fig. 29.3. It is seen from the diagram that the sizes of these particles amount to 6–7 nm.

This composite structure can store for long time encapsulated nanoparticles in conventional atmosphere and then to use them for producing the colloid solution by dissolving the salt coats [20].

To provide the long-time stabilization of nanopowders in the form of the colloid solution, the method of dispersion of these powders in composition of polyethylene glycols—PEGs (PEG 1500–8000 in the volume of 4–7 parts and PEG 400–600 in the volume of 3–6 parts)—was developed. The initial powder, placed into fluid, was subjected to dispersion during 60 min, accompanying with heating up to 60–80 °C. However, this system, as any colloid, will tend to agglomerate under the effect of external factors or time. Therefore, to prevent this phenomenon, a rapid cooling of the colloid solution is used at the final stage of producing. This approach can store

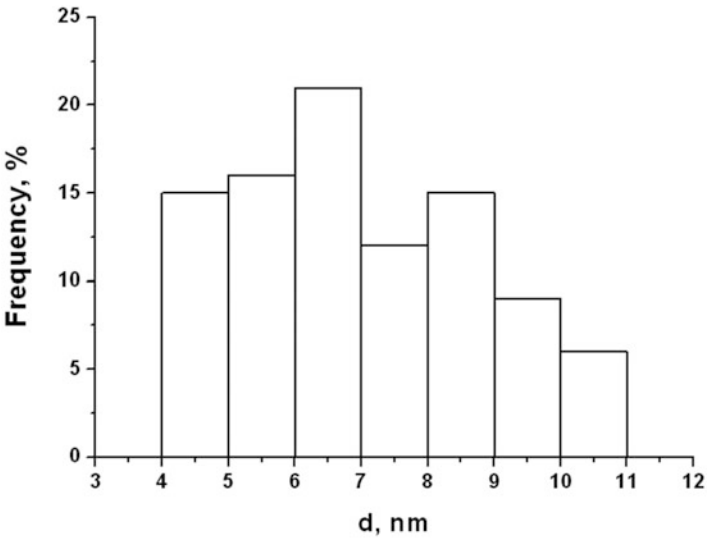

Fig. 29.1 Distribution of Al particles by size

Table 29.1 Statistic processing of results of measurements of nanoparticles by using the computer program Image-Pro Plus

Diameter of particles, nm	Frequency, %	Number of particles being investigated
4	15	298
5	16	325
6	21	421
7	12	236
8	15	292
9	9	185
10	6	124
11	6	128

Fig. 29.2 Appearance of high-viscosity colloid solution on the base of Al nanoparticles

the produced gel for a long time in a compact form. The appearance of the high-viscosity colloid solution (gel) is shown in Fig. 29.2.

Investigations on the possibility of applying aluminum in nanoform for the preparation of the feed water in the process of producing the diffusion juice were carried out using two modifications of the reagents: ДАl4(No.807) and ДАl5 (No.805). Characteristic of these agents is presented in Table 29.2. To increase the viscosity of this gel is possible by adding the water into the suspension. The properties of thus produced suspension were investigated by means of the device Malvern Zetasizer Ver. 6.20. It is seen from the Fig. 29.4, at which the distribution

Table 29.2 Characteristic of high-viscosity colloid solutions (gels)

№ agent	Characteristic of agent		
	Volume fraction of nanoparticles in precursor (%)	Concentration of nanoparticles of Al in high-viscosity colloid solution	$D_{aver.}$ Nm
ДАl4 (No.807)	25	52 mg/10 g	1.2–1.5
ДАl5 (No.805)	30	51 mg/10 g	1.2–1.5

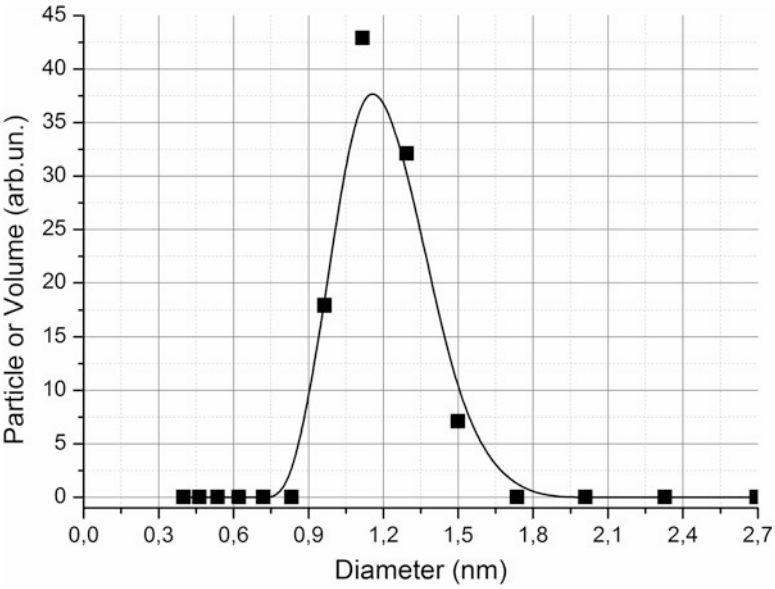

Fig. 29.3 Distribution of aluminum particles by sizes in colloid solution

of particles by sizes is presented, that this decrease of viscosity does not cause the aggregate process. The particle size remains in the nanorange [21] (Fig. 29.3).

It can be concluded by comparing Figs. 29.3 and 29.4 that the average size of particles is smaller than that in the precursor. It can be assumed that the particles in the precursor are more agglomerated, and in the solution production process, in particular, with the effect of the ultrasound, the separation of the agglomerated particles occurred.

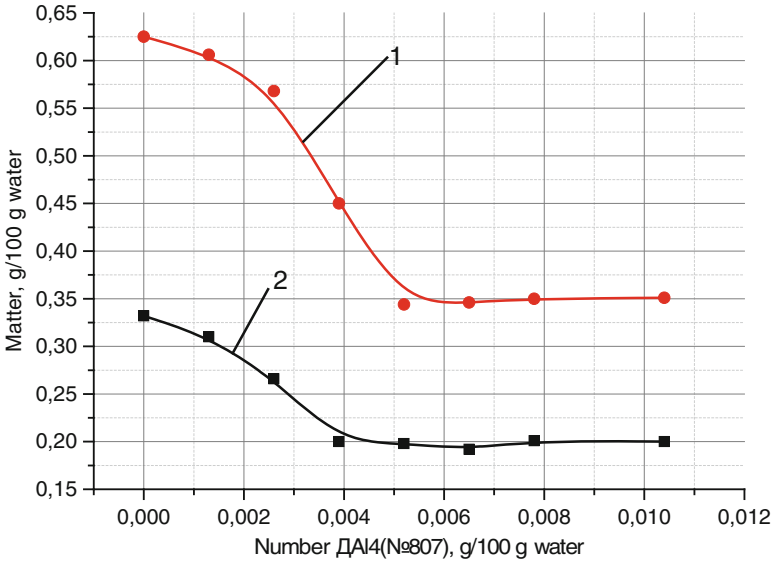

Fig. 29.4 Content of protein (*1*) and pectin (*2*) in the feed water after treatment by the nanoaluminum gel

29.3 Application of High-Viscosity Colloid Solutions on the Aluminum Base for Additional Treatment of Semi-Products in the Beet-Sugar Production

To investigate the efficiency of the coagulation effect of gel of the nanoaluminum, a feed water (pulp-press water), produced in the laboratory conditions after extraction of the desugarized slices (pulp), was used. The evaluation of the technological efficiency included the study of main parameters: amount of the reagent, time, and temperature of treatment.

For the preliminary evaluation of nanoaluminum agent in the purification of the pulp-press water, the comparative investigation was made, in which the traditional reagents (sulfate and aluminum chloride) and gels of nanoaluminum with content of 5.2 mgAl/g ДАl4(No.807) and 5.1 mgAl/g ДАl5(No.805) were used. For convenient dosing and possibility of comparison, the solution of similar concentration was prepared from all the investigated samples.

In the process of experiment, the change in quality characteristics of the pulp-press water during purification was investigated. In the investigated samples, the purity, pH, and content of protein and pectin were determined in accordance with procedures, described in [21]. The initial characteristics of the pulp-press water were as follows: purity,70.08 %; content of protein, 1.22 % by MW.; and content of pectin, 0.826 % by MW. Temperature of process conductance was ±50 °C, and time of contact with reagent was 10 min.

During investigations the following procedure was applied: four samples of water were heated up to temperature 50 °C, and then the solutions of coagulants in the amount of 2 % by MW were added. In addition, in the first 2 min, the samples were intensively stirred and the next time was slow. This condition of stirring at the first stage gives the feasibility of uniform distribution of the coagulant in the sample volume, and at the second stage, it creates the conditions for the formation of the sediment structure. The adding of coagulant solution into the purified solution should proceed so that at the first stage of coagulation, as much as possible fine aggregates were formed at the surface of which the particles of aluminum hydroxide would be adsorbed having the high adsorption activity with respect to colloid components of the solution being purified. But the stirring should be intensive to avoid the fracture of the formed particles.

The last (fifth sample) was purified without application of coagulants but by the scheme accepted as standard at the sugar factory: preheating up to 90 °C, soaking for 5 min at this temperature, and sedimentation.

All the samples after completion of the experiment were filtered, and the purity and content of protein and pectin elements were determined in filtrates. Results are given in Table 29.3.

It is seen from the obtained data that the samples of reagents ДАl4(No.807) and ДАl5(No.805) showed the highest efficiency: water purity was increased due to removal of the protein elements by 42 %, and pectin elements in this case were removed by more than 80 %. It can be concluded from the table data that the degree of removal of pectin elements is rather higher than protein ones; it is, probably, connected with the fact that aluminum hydroxide formed as a result of hydrolysis in the solution has a positive charge which gives possibility to remove the negatively charged molecules of pectin elements and some part of protein molecules with the negative charge ДАl5(No.805). However, for the sample ДАl5(No.805), the results of purification occurred to be somewhat lower; therefore, for the next experiments on investigation of efficiency of the feeder water treatment by the nanoreagents, the sample of agent ДАl4(No.807) was selected.

The rational amount of the selected coagulant ДАl4(No.807) was determined as follows. Eight samples of the feeder water of 100 cm^3 volume were preheated up to temperature 50 °C. Then, at a constant stirring the preliminary calculated amount of reagent in the range of 0.25–3.0 g (with content of nanoparticles in the ranges of 0.0013–0.0104 g) was added. The process of stirring and time of contact was

Table 29.3 Comparative investigations of efficiency of purification of the feed water at applying of different coagulants

	Purity, %	Content of protein, %	pH	Content of pectin, %
Feed water (reference)	70.98	1.123	7.05	0.726
Feed water + $AlCl_3$	71.97	0.759	6.7	0.22
Feed water + $Al_2(SO_4)_2$	71.52	0.788	6.81	0.19
Feed water + ДАl4(No.807)	73.04	0.608	6.73	0.110
Feed water + ДАl5(No.805)	72.96	0.640	6.71	0.117

similar to the previous experiment. In the obtained samples, the following was determined: change in content of protein and pectin elements. Results of investigations are given in Fig. 29.4.

As is seen from the data given in the figures, the consumption of the nanoaluminum gel, which provides the maximum degree of removal of protein and pectin elements from the treated feed water, is the value in the ranges of 2–2.5 g of agent per 100 g of water that corresponds to the content of aluminum nanoparticles in the ranges of 0.005–0.0065 g.

It is also seen from the figures that increase in reagent consumption does not lead to the noticeable changes in quality characteristics of the treated water. Therefore, for further investigations it is possible to accept the reagent consumption for the feed water purification from protein and pectin elements in the range of 2–2.5 g per 100 g of water.

As is known, the coagulants containing aluminum have their own temperature optimum, at which coagulating action is maximally effective. Therefore, the aim of the next experiment was to determine the rational temperature of the purification process conductance. For this purpose, the samples of water were treated at different temperatures in the range from 50 up to 80 °C by the similar amount of nanoaluminum gel solution (2.5 g per 100 g of water) during 10 min. The obtained samples were filtered and the purity of the produced water was determined in the filtrates. Results of investigations are presented in Fig. 29.5.

Analysis of the Figure data shows that the maximum effect of treatment of the feed water is observed in the ranges of temperatures 55–60 °C. The increase of temperature above 60 °C leads to the decrease in efficiency of the coagulation

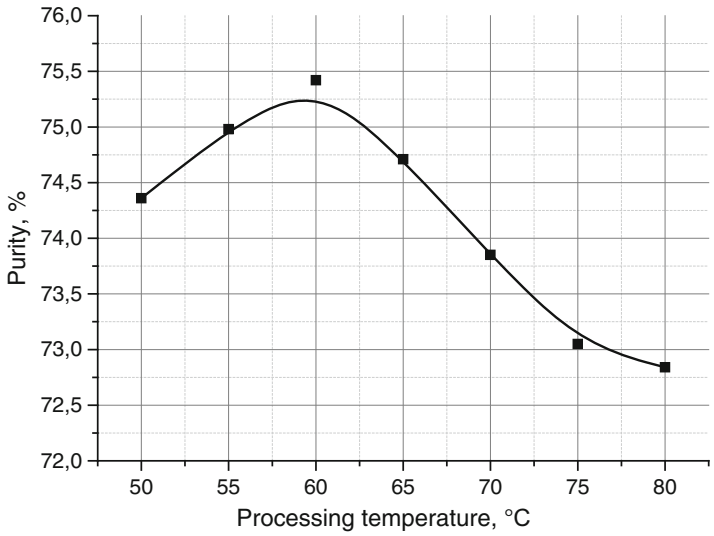

Fig. 29.5 Change in quality characteristics of purified water depending on the process temperature

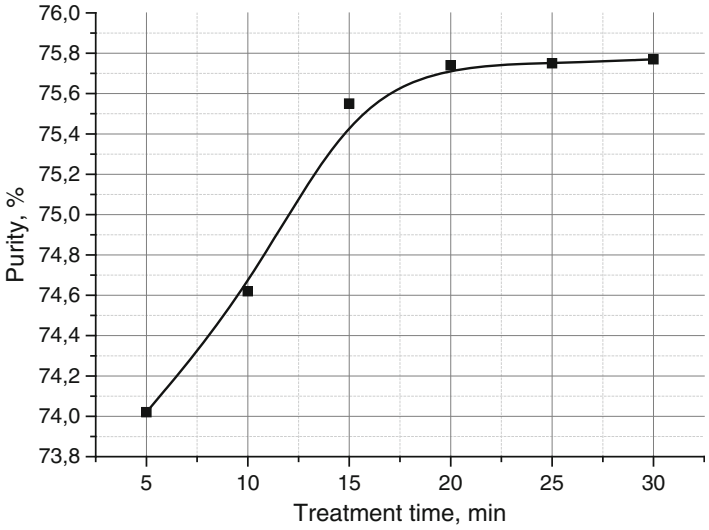

Fig. 29.6 Change in quality characteristics of water depending on time of contact with reagent

process, which is, probably, connected either with decrease in the coagulant activity or with the temperature hydrolysis of pectin and protein elements, and these products are not capable to coagulate. To clarify this fact, further investigations are necessary.

One more parameter, which is necessary to find for the more complete evaluation of the efficiency of the nanoaluminum gel coagulant, is the time of reagent contact with the purified water for the formation of the optimum coagulation structure of the sediment. Coming from the earlier obtained results (Fig. 29.4), the parameters of these investigations were as follows: the amount of added nanoaluminum gel was 2.5 g per 100 g of water, and the process temperature was 55 °C. The time was changed from 5 to 30 min at 5 min interval. Then, these obtained samples were filtered and their quality characteristics were determined. Results of experiment are presented in Fig. 29.6.

Results, given in Fig. 29.6, show that 15 min is sufficient to reach the maximum effect of purification; here the content of protein elements in the feed water is decreased almost by 50 % and pectin ones to 70 %. This also confirms the general tendency that the pectin elements are removed more completely than the protein ones. In addition, the increase in time of treatment increases the effect of purification; however, this increment is not essential. Also, from the technological point of view, it is not rational to increase the time of treatment of the feed water as it can influence the efficiency of the whole scheme of the water preparation. Such increase in time can lead to the increase of activity of microorganisms, because the water being treated is a good feeding medium for their breeding. Therefore, for next experiments the duration of process of the feed water treatment by the nanoaluminum gel of 15 min was accepted.

29.4 Conclusions

The feed water produced by pressing of the desugarized slices after the process of extraction contains a considerable amount of colloid impurities (protein and pectin elements which makes it impossible to use it repeatedly without additional preparation). The existing schemes of such water preparation at the sugar factories have some drawbacks and do not always provide the high effect of purification. Taking into account the advanced tendencies of applying the nanomaterials in the preparation and purification of drinking and sewage waters, it can be stated that the use of these materials in preparation of the pulp-press water will have a positive effect. The results of investigations showed that treatment of the pulp-press water by a reagent with a content of nanoaluminum decreases the content of protein and pectin elements. The parameters of the process conductance were established: temperature is 55–60 °C, which allows the exclusion of the additional heating or cooling of water, time of contact between reagent and water is 10–15 min, and amount of added reagent is 2–2.5 g per 100 g of water. When applying the reagent, the effect of water purification is increased by 10 from 13 % up to 23 % that confirms the feasibility of the repeated use of such water.

Thus, during experiments the efficiency of reagents containing aluminum in nanoform on the degree of removal of colloid dispersion elements in the purification process of the pulp-press water in the beat-sugar production is shown. In the future, these investigations will be continued to determine the rational condition of stirring and effect of pH medium at which the maximum degree of coagulation of pectin and protein elements will be observed.

References

1. Asadi M (2006) Beet-sugar handbook. Wiley, Hoboken
2. Shtangeev VO, Kober VT, Belostotskiy LG, Lagoda VA, Shestakovskij VA (2003) Modern technologies and equipment of beet sugar production, Cukor, Ukraine, P.1, 352p
3. Reva LP, Pushanko NN, Zamura SA (2008) Application of activated silicic acid for additional treatment of diffusion juice. Cukor Ukrainy, No.3, pp 11–16
4. Reva LP, Pushanko NN, Zamura SA (2011) Method of diffusion juice purification. Patent of Ukraine #93206
5. Reva LP, Pushanko NN, Alekseeva LV (2008) Improvement of efficiency of diffusion juice purification by its treatment with filter-pearlite. Cukor Ukrainy, № 2, pp 24–27
6. Olyanska SP, Tsyrulnikova VV (2015) Intensification of process of extraction using the chemical reagents. Cukor Ukrainy, № 4(112), pp 14–18
7. Lipets AA, Gusyatinskaya NA (2015) Modern methods of intensification of process of sucrose extraction from bee slices. Cukor Ukrainy, № 1(109), pp 44–50
8. Gusyatinskaya NA, Lipets AA (2005) Application of coagulants for improving the diffusion juice quality, Sugar, № 5, pp 37–40
9. (2007) Rules of conductance of technological process of sugar production from sugar beets (Rules of established practice 15.83-37-106:2007). Naukova Dumka, Kyiv, 419p

10. Duran N, Marcato PD (2013) Nanobiotechnology perspectives. Role of nanotechnology in the food industry: a review. Int J Food Sci Technol 48(6):1127–1134
11. Amin MT, Alazba AA, Manzoor U (2014) A review of removal of pollutants from water/wastewater using different types of nanomaterials. Adv Mater Sci Eng 2014(3):10–38
12. Zimon AD (2010) Colloid chemistry of nanoparticles. Peculiarity and properties of nanoparticles. Manual for students of technological specialties of all forms of education. MGutu, 370p
13. Wang D, Wang S, Huang C, Chow CW (2011) Hydrolyzed Al(III) clusters. Speciation stability of nano-Al13. J Environ Sci (China) 23(5):705–710
14. Wang Y, Gao B, Xu X, Xu W (2010) The effect of total hardness and ionic strength on the coagulation performance and kinetics of aluminum salts to remove humic acid. Chem Eng J 160(1):150–156
15. Xu H, Wang D, Ye C (2014) Survey of treatment process in water treatment plant and the characteristics of flocs formed by two new coagulants. Colloids Surf 456:211–221
16. Xu W, Gao B, Du B, Xu Z, Zhang Y, Wei D (2014) Influence of shear force on floc properties and residual aluminum in humic acid treatment by nano-Al13. J Hazard Mater 271:1–8
17. Lopatko KG, Tkachenko SV, Olishevskij VV, Verchenko LM, Marynin AI, Arodinskij OV (2012) Nanotechnologies in sugar industry. Naukovyi visnyk NUBiPU. Series "Technika ta energetika APK", Issue 170, P.1, pp 361–366
18. Marynin AI, Olishevskij VV, Pushanko NN, Dulnev PG (2015) The influence of colloidal solutions on the basis of aluminium on clearing of sugar manufacture products. Third International research and practice conference "Nanotechnology and nanomaterials". Lviv, Ukraine
19. Ustinov AI, Melnichenko TV, Liapina KV, Chaplyuk VI (2008) Method to produce encapsulated nanopowders and unit for its implementation. Patent of Ukraine #82448
20. Ustinov Al, Melnichenko TV, Liapina KV, Chaplyuk VI (2013) Method of producing encapsulated nanopowders and installation for its implement US 8491972B2
21. Dulnev PG, Liapina KV, Davidova OE, Ustinov AI (2014) The method of dispersion and stabilization of copper nanoparticles in aqueous solutions. Patent Ukraini #91374

Chapter 30
Non-covalent Functionalization of Carbon Nanotubes for Efficient Gene Delivery

Olga Burlaka, Alla Yemets, Yaroslav Pirko, and Yaroslav Blume

30.1 Introduction

Extensive generation of research data together with development of advanced technologies in many fields gives a rise to revolutionary solutions merging achievements of nanotechnology, biology, and medicine that are viewed to boost the present state of art in these areas on a new level. One of the most remarkable issues nowadays is the development of methods for efficient and safe delivery of exogenous genetic material into living cells [1, 2]. In biology many fundamental researches and insights into basic mechanisms of living cells are based on the studies involving manipulations with genetic material, in particular genetic transformation [3]. In biotechnology delivery of exogenous genes allows obtaining genetically modified organisms with improved existing and introduced new desired properties for sustainable farming, industry, food, drugs, raw material production, etc. [4–6]. In medicine it poses the background for the gene therapy of numerous diseases, such as genetic deficiencies, cancer, viral infections, autoimmunity, diabetes, cardiovascular pathology, neurodegenerative conditions, hemophilia, AIDS, asthma, etc., thus enabling alleviation of worldwide health impairment burden [7, 8]. Nanostructures as novel materials with unique properties when used for the development of gene delivery approaches are viewed to provide outstanding precision, efficiency, as well as a number of novel advantages meeting the growing demands in biological and biomedical fields. Among other nanostructures, carbon nanotubes (CNTs) earn great interest now as potential vehicles for gene delivery into living cells; therefore, factors influencing and governing their applicability and

O. Burlaka • A. Yemets • Y. Pirko • Y. Blume (✉)
Institute of Food Biotechnology and Genomics, National Academy of Sciences of Ukraine, Osipovskogo Str., 2a, Kyiv 04123, Ukraine
e-mail: burlaka29@gmail.com; yemets.alla@gmail.com; yarvp1@gmail.com; cellbio@cellbio.freenet.viaduk.net

O. Fesenko, L. Yatsenko (eds.), *Nanophysics, Nanophotonics, Surface Studies, and Applications*, Springer Proceedings in Physics 183,
DOI 10.1007/978-3-319-30737-4_30

high output are widely investigated and discussed. In this review we consider the potential and possible advantages of non-covalent surface modification of CNTs to make them biocompatible for the creation of gene delivery systems.

30.2 CNTs for Delivery of Genes: Key Points

The development of nanotechnology-based gene delivery systems is viewed to be advantageous in accuracy, efficiency, wide taxonomic applicability, safety, and reproducibility in comparison with existing methods of genetic transformation [9]. Moreover, these methods present the outstanding possibility to conduct gene delivery and to govern genes functioning in highly precise and controllable manner in target cells avoiding gene silencing and other undesirable effects [10]. Being significant and valuable, the advantages brought by the use of nanocarriers for gene delivery vary depending on the field of application. Thus, in gene therapy existing viral vectors present a significant risk to patients, while non-viral nano-based carriers are expected to be safer and less immunogenic, with simple preparation and a possible versatile surface modification [7]. Genetic transformation of plants often has reduced efficiency due to the presence of thick outer barrier that hinders efficient gene transfer—cellulose cell wall [11–13]. Exploiting natural *Agrobacterium*- or viral particle-based plant transformation techniques is associated with taxonomic limitations and safety concerns, while other widely used methods are often technically complex or demonstrate low efficiency [14]. Nanostructure-based strategies for gene delivery into plant cells are of great interest nowadays, as they are viewed to overcome existing limitations due to the ability to easily penetrate many biological barriers.

In this regard, among the nanoparticles that are considered suitable for the development of methods for delivering genes into cells are polymer-based nanoparticles, calcium phosphate, magnesium phosphate, manganese, silicon, gold, magnetite, carbon nanomaterials, etc. [7]. CNTs being almost one-dimensional needlelike nanostructures with high length-to-diameter ratio and extremely large surface area suitable for binding of different molecular cargoes, on the one hand, and demonstrating the acceptable levels of biocompatibility, on the other hand, are of remarkable interest in terms of their possible use for directed delivery of molecules of interest, including the exogenous genetic material, into cells [14–18]. CNTs have already been applied successfully to deliver plasmid DNA, small interfering RNA, proteins, and therapeutic agents into mammalian cells [19–29]. By using CNTs, genetic transformation of bacterial and mammalian cells was conducted [25, 28, 30–34].

Several studies have demonstrated the ability of CNTs to deliver molecules of interest into plant protoplasts [17, 35] and walled plant cells [36–39]. Success of CNT application in this field is strongly determined by the parameters of used CNTs such as structure, morphology, length, and the type of surface

functionalization [38–41]. Therefore, proper functionalization is viewed to be the key parameter for successful CNT exploitation for molecular cargo delivery into cells.

Being highly hydrophobic, pristine CNTs undergo surface functionalization for their further use in living organisms [42, 43]. Numerous existing methods of covalent functionalization of CNTs are mainly based on the use of critical and energy-consuming reaction conditions as well as hazardous toxic reagents and may generate a product with low biological compatibility [44–46]. Therefore, the development and implementation of environmentally safe and biocompatible CNT functionalization methods, based on van der Waals and π–π-stacking interactions between the molecules of aromatic substances, surfactants, polymers of different natures, and the surface of CNTs, is of great interest now [47–49]. Promising for this aim substances are biocompatible polymers, in particular molecules of biological origin having polymeric structure and possessing both hydrophobic and hydrophilic properties [50–53].

Since being discovered in 1991 [54], CNTs have already found a great number of applications in electronics, composite material production, hydrogen storage, etc. During the last 15 years, their significant potential in biological and biomedical approaches was revealed [55, 56]. Structurally CNTs are rolled into seamless tube graphene layers in which carbon atoms form a hexagonal lattice. Depending on the number of layers, CNTs are generally classified as multi-walled CNTs (MWCNTs) and single-walled carbon nanotubes (SWCNTs) [57]. MWCNTs have lower chemical reactivity and are more likely to possess structural defects resulting in a less stable structure than SWCNTs [58]. Modifications of synthesis methods allow production of CNTs of different shapes for various applications: straight, wavy, aligned, extra-long, toroidal, ringed, with "beads," branching, curved, cup stacked, etc. [59]. For gene delivery approaches, it is preferable to use shortened CNTs, which demonstrate better cell penetration frequency than longer CNTs [60, 61]. Moreover, studies show that CNTs shortened to lengths of 100 nm and less enter subcellular organelles such as plastids, nucleus, etc. This, in turn, inspires the development of CNT-based approaches for modification of plastids and mitochondria genome [17, 18]. Extremely shortened CNT-derived structures (10–20 nm lengths) possessing empty inner space are viewed to be suitable for encapsulation of target molecules [9].

Generally, the structure of CNT is distinguished into two functionally distinct areas: tube with hexagonal carbon atom placement and end zones (caps), built of alternating five- and six-membered cycles, similar to a hemisphere of the fullerene molecule [62]. During the functionalization reactions, binding of functional groups to the surface of CNTs primarily occurs in the end zones and in the sidewall defects (pentagon–heptagon couples, sp^3-hybridized carbon atoms, vacancies in the lattice of the nanotubes, "open" ends, etc.), having higher reactivity compared to an ideal polyaromatic surface of nanotube [63]. Normal reactivity of CNTs is associated with incompliance of π-orbitals of adjacent carbon atoms due to deformation caused by the spatial deformation [64]. Abovementioned properties determine the

behavior of CNTs during the functionalization process, in particular their ability to bind substances via non-covalent hydrophobic interactions.

30.3 Functionalization of CNTs

For various applications the surface of CNTs is usually modified through covalent and non-covalent functionalization techniques. Covalent functionalization causes the appearance of numerous breaks in continuous π-network and significant change or loss of specific mechanical, optical, and electronic properties of CNTs [65]. One of the most common approaches of covalent functionalization is treatment with harsh chemicals (acids, esters, aldehydes, chromates, etc.), often—in combination with applying microwaves, ultrasound, pulsed discharge, cryogenic destruction, γ-irradiation [44, 45, 63]. The reactions that take place in case of covalent modification include oxidation, cycloaddition, cyclopropanation, grafting of polymers, fluorination, hydrogenation, ozonolysis, electrophilic addition, etc. [66–68]. Thus, the introduction of novel covalent bonds disrupts the sp^2 network of pristine CNTs altering the basic properties of CNTs.

Covalent modification of CNTs is of considerable practical importance for many fields where a strong bond is required between the nanotubes and the molecules of interest [69]. In drug delivery and other biological and medical approaches, in particular for imaging techniques, the most commonly used type of covalent functionalization of CNTs is amination or carboxylation [9]. Introduced groups on the surface of CNTs are then activated and subsequently exploited to covalently attach various biological molecular functionalities [22, 70–72]. However, non-desirable outcome of covalent functionalization process may include a significant loss of material and a partial loss of optical properties and electronic structure of the CNTs [73]. Nevertheless, for many fields the preservation of intrinsic properties of CNTs after functionalization is necessary [74]. This as well as reversibility, good applicability, low or absent material loss, and other specific advantages may be achieved through the use of non-covalent functionalization approaches that are of growing interest now [75]. In comparison with covalent functionalization, non-covalent approaches are also thought to be energy- and cost-saving and ecologically more compatible. Also there exist substantial differences between behavior of covalently and non-covalently functionalized CNTs in living organisms, namely, their traffic, accumulation, distribution, interaction with host compounds, degradation, etc. [76–78]. In addition, it should be noted that non-covalent functionalization approaches are in good correspondence with current actual trend of turning technologies to follow the “green” chemistry principles which underline the importance of environmental and energy optimization by preferential use of renewable resources, moderate reaction conditions, and safe compounds where possible [79].

30.3.1 Non-covalent Functionalization of CNTs

Methods of non-covalent functionalization of CNTs involve hydrophobic interactions between amphiphilic molecules of surfactants and polymers that contain different nonpolar and polyaromatic regions [47, 48, 80, 81]. In this case used molecules alter the surface properties of CNTs by either adsorbing onto or wrapping the CNTs [82]. Among commonly used chemicals for non-covalent functionalization for water dispersing of CNTs in different fields are sodium dodecyl sulfate, cetyltrimethylammonium bromide [83], sodium cholate, cetyltrimethylammonium p-toluenesulfonate, sodium dodecane-1-sulfonate, sodium 4-dodecylbenzenesulfonate [84, 85], pyrene-containing polymers [86], Triton [87], poly[p-{2,5-bis(3-propoxysulfonic acid sodium salt)}phenylene] ethynylene [88], poly(vinyl pyrrolidone), polystyreneblock-poly(acrylic acid) [89], poly(styrene sulfonate) [90], Pluronic, etc. [82, 91]. Widely used approach is the adsorption of surfactants onto the nanotubes due to their cheapness, ready commercial disposability, and simplicity of use [91]. Hydrophobic tail of the surfactant molecule adsorbs onto the hydrophobic nanotube wall, and a hydrophilic head promotes affinity of formed conjugates to the aqueous environment. Appearing repulsive forces, in turn, prevent CNT aggregation. It is indicated that ionic surfactants stabilize CNT dispersion by electrostatic repulsion, while nonionic surfactants form solvation shell around the nanotube [82]. It is important to note that many of named compounds are able to form stable coating on the nanotube surface only in media that contain excess of used functionalizing agent—which in turn is not acceptable for use in living organisms due to toxic effects [52].

Polyaromatic derivatives interact with CNT surface through the π–π-stacking interactions with the graphitic surfaces of nanotubes [85]. Studies show that for many polymers wrapping CNTs in aqueous media is thermodynamically favorable [92]. For biological applications polyamidoamine dendrimers and polyethylenimine are widely used [9]. Poly(ethylene glycol) is often used to eliminate the nonspecific binding of the proteins on the surface of CNTs [93]. There are many examples of polymers that favor CNT dispersion in water [75, 91]; however, for exploiting in living organisms, their range is limited to biocompatible polymers.

Due to the presence of numerous aromatic regions together with both hydrophobic and hydrophilic properties, natural biologic molecules are shown to be able to mediate the efficient dispersion of CNTs in water environments [91]. In this context, one promising field is the investigation of whether and how bio-derived molecules can be used for the functionalization of CNTs to create efficient gene delivery vectors. Additional benefits can be taken from using biologically derived functionalization coating in design of specific recipient organism response to internalized CNTs with different types of "masking" molecules on its surface. Thus, such factors as the type of functionalization, spatial placement of functional groups, and morphological and structural changes of CNTs after modification strongly affect their behavior in biological systems and determine the scenario of their interaction with the object [9, 40, 94]. The most common outcome of proper

functionalization technique is the reduction of the damaging effect of CNTs on living systems [17, 18, 39, 41]. It should be noted also that non-covalent functionalization, unlike covalent, does not change the specific properties of CNTs [49]. However, non-covalent functionalization, as covalent, can be a basic step for further binding of target molecules to the surface of dispersed in aqueous medium CNTs [95]. Generally, for biology ideal non-covalent functionalization coating is suggested to possess following features: (a) the coating substance must be biocompatible and nontoxic; (b) stability of the coating should be high enough to avoid detachment from the CNT surface in biological environments; (c) functional groups of the coating molecules should be available for bioconjugation; otherwise there should exist a free surface of nanotubes available for binding molecular cargoes [96].

The strength of the π-stacking and other non-covalent interactions depends on the CNT structural parameters, as the diameter and chirality [97]. Being more weak than covalent, these interactions can be effective due to their large numbers [75]. In particular, non-covalently functionalized with pyrene, CNTs were used to anchor biomolecules [98]. In work [99] non-covalent layer-by-layer functionalization of CNTs is described using Triton and biotin conjugated to the poly(ethylene glycol) chains with the subsequent possibility to bind streptavidin which demonstrates high affinity to biotin. Non-covalently functionalized with 1-pyrene butanoic acid succinimidyl ester, CNTs were able to bind proteins efficiently [100]. CNTs functionalized with poly(ethylene glycol) adsorbed cyclic arginine–glycine–aspartic acid onto their surface, and accumulation of formed conjugates in tumor cells was shown [101]. Generally, non-covalent interactions may be strong enough due to changes in combined electronic structure of formed conjugates [102]. - Non-covalent bonds also allow the development of controlled reversible functionalization approaches [91, 103]. Reversibility, in turn, may be reached through the use of molecules capable of responding to different external stimuli [104].

30.3.2 Biological Compounds for Non-covalent Dispersion of CNTs

Generally, studies on dispersion of CNTs in an aqueous media are conducted using non-covalent functionalization with natural and synthetic nucleic acids, proteins, polypeptides, polysaccharides, compounds of lipid nature, etc. [50, 105–112]. In water environment strong van der Waals forces reaching 500 eV per μm of CNT's length between the individual CNTs lead to their aggregation into bundles and ropes [45, 91, 113]. In the case of non-covalent functionalization using biomolecules, hydrophobic interactions between the domains of amphiphilic molecules and the surface of the CNTs cause supramolecular adsorption or wrapping various functional molecules around nanotubes [14, 32, 49]. In turn, the distal orientation of hydrophilic domains adsorbed to the surface of CNT molecules mediates

dispersion of formed conjugates in water. To initiate separation of CNTs as well as for partial unfolding of biomolecules with partial disclosure of their hydrophobic sites, commonly mechanical treatment is necessary.

The most efficient and widely used for this aim is mild- or high-power sonication, but sometimes mixing is also exploited instead of ultrasound treatment [114, 115]. Thus, the mechanism of action of ultrasound is to overcome van der Waals interactions between hydrophobic surfaces of CNTs and disaggregate the latter in the aqueous environment, as well as to change the conformation of functionalizing molecules [91]. This process is physically caused by ultrasound-induced cavitation of the liquid phase, which presents a formation, growth, and collapse of small cavities in the medium [114]. In non-biological approaches, sonication is often carried out in N,N-dimethylformamide and results in dispersion of CNTs which remain stable during time periods up to a few hours [116, 117]. For biological use this approach is non-applicable due to both dispersion short stability time and toxicity of solvent. Sonication of CNTs with different biological molecules results in good stability of CNT aqueous dispersions with no need of adding excess of functionalizing agent due to strong hydrophobic interactions and subsequent absorption or wrapping of biomolecules onto the rolled graphitic surface [82].

Ultrasound treatment if necessary may be tuned to result in slight changes of CNT structure such as their shortening, appearance of point sidewall defects with high reactivity, as well as formation of "open" ends [45]. Commonly mild and short-time ultrasound treatment is sufficient for inducing surface non-covalent functionalization via biomolecule binding. In addition, it is known that ultrasonication may be a useful approach for eliminating metallic impurities from CNTs which are toxic to living systems and thus increase biocompatibility of CNTs [118, 119].

Nucleic acids. Upon the formation of complexes of nucleic acids and their compounds, nitrogenous bases come into π–π-stacking interaction with the surface of CNTs, while hydrophilic sugar-phosphate groups turn toward the water environment [120]. DNA chains surrounding CNTs in aqueous media provide electrostatic repulsion. Therefore, obtained colloidal systems demonstrate high stability as well as capacity to disperse CNTs at high concentrations [82]. Aromatic regions of double-stranded DNA molecules commonly exist in thermodynamically most favorable condition in which stacking occurs between adjacent base pairs. Ultrasound treatment or heating induces the appearance of non-equilibrium conditions resulting in the attachment of aromatic regions of DNA to CNT surface. This can be exploited both for the DNA-mediated water dispersing of CNTs and, with mild treatment, for the reversible attachment of cargo nucleic acid with its further release from the gene delivery scaffold inside the cell [96]. There are reports indicating that the CNTs dispersed in water, even after generation on their surface carboxyl groups, mostly do not interact with supercoiled plasmid DNAs [121]. While obtained by restriction of the plasmid DNA, linear DNA molecules adhere non-covalently to the surface of CNTs. This effect is explained by spatial constraints associated with high compaction of supercoiled DNA and spatial inaccessibility of nitrogenous bases in its composition. At the same time, it is thought that

resulting from the restriction of plasmid DNAs, linear double-stranded DNA molecules in terms of absent sonication interact with the surface of the CNTs mainly in the single-chain regions—"sticky ends." However, it is also shown that spontaneous binding of linear double-stranded DNAs with "blind" ends also takes place. In this case possible mechanism is thought to be the appearance of partially unwind regions in DNA molecules in the presence of CNTs. In particular, it has been shown previously that SWCNTs induced destabilization of the double helix of DNA [122].

Good ability of nucleic acids to wrap and disperse CNTs in aqueous environments was reported in many studies [24, 123–128]. It should be noted that covalent binding of DNAs, RNAs, etc. is conducted in fields of the design of nano-based sensors as well as for gene therapy [129]. In this case, preliminary modification make CNTs suitable for subsequent covalent attachment of nucleic acid. At the same time as it was mentioned above, nucleic acids and their compounds may act as functionalizing agents themselves. In non-biological approaches, a different affinity of dNTPs to CNT surface depending on a type of nanotube (zigzag, armchair, and chiral) is used to separate them [130, 131]. For this aim, artificially synthesized nucleic acid sequences, single-stranded DNA, and individual dNTPs are exploited [132–134]. On the one hand, the described phenomenon is referred to as the background for developing methods of extracting linear single-stranded or denatured DNAs from mixtures. On the other hand, in biological approaches, nucleic acids and their compounds are suitable substances for non-covalent functionalization and dispersing of CNTs in water for a wide spectrum of applications including design of gene delivery approaches [135–137].

Proteins. Interaction of CNTs with water-soluble proteins and subsequent formation of water-dispersed conjugates is associated with conformational changes that are realized as unfolding and refolding of protein molecules under the influence of ultrasonic treatment [138]. Hydrophobicity of proteins is largely determined by their amino acid composition and sequence [139]. Therefore, various studies have shown different results for protein-mediated non-covalent CNT functionalization for water dispersing: some proteins were suitable for this purpose (amylase, lysozyme, bovine serum albumin, hydrophobins, hemoglobin, trypsin, glucose oxidase, histones, streptavidin, synthetic oligopeptides, etc.), while others were not (pepsin) [45, 46, 109, 110, 139, 140]. There is evidence that the presence of amino acids such as histidine and tryptophan in the protein molecule favors the ability of proteins to come into π–π-stacking interactions with CNT surface [141]. Generally, aromatic amino acids strongly determine the ability of proteins to disperse CNTs [138]. On the one hand, the design of specific peptides that can wrap CNTs may be used to introduce desired properties to nanotubes for biological applications. On the other hand, it may be a useful tool for size separation of CNTs.

Other biological substances. Apart from the abovementioned, non-covalent functionalization of CNTs is also reported with the use of carboxymethylcellulose, chitosan and its derivatives, alginic acid, cellulose derivatives, and flavin mononucleotide [74, 142–146]. The applicability of the aqueous extract of the vitreous humor (inner part of an eye of livestock animals, used in pharmacy) for

non-covalent CNT functionalization and dispersion in water is also shown [147]. The main components of the water extract of the vitreous humor that are thought to be involved in the process are collagen, proteoglycans, and hyaluronic acid. Controlled reversible non-covalent binding to CNTs is reported for poly-L-lysine [148], folic acid [149], and selected polysaccharides [150]. CNTs non-covalently wrapped with amylose, sodium alginate, and chitosan demonstrated good biocompatibility [151–154]. Flavin mononucleotide showed better capacity to bind non-covalently to CNTs than widely used in non-biological approaches sodium dodecyl sulfate, while sodium cholate that is a surfactant of biological origin demonstrated particular efficiency in dispersing CNTs with the absence of any sonication [155, 156]. Non-covalently functionalized with anionic and cationic lipids, CNTs demonstrated good water dispersion stability, high efficiency and biocompatibility, as well as possibility to bind desired functional groups to nanotubes without additional chemical surface modifications [157].

30.4 Conclusions

Non-covalent surface functionalization of CNTs together with covalent functionalization methods gives a wide range of solutions for existing challenges in biological and biomedical fields that are to be solved through the use of nanotechnology. Covalent approaches being necessary where strong binding of molecules and radicals is obligatory in gene delivery approaches may be substituted by the non-covalent functionalization with subsequent reversible nucleic acid binding. Being weaker than covalent bonds, non-covalent interactions are viewed to be effective due to their large number in a wide range of applications. Thus, it is possible to introduce few generations of different functionalities onto the CNT surface through the non-covalent attachment. In addition, the main characteristic features of non-covalent functionalization approaches that could bring advantages to certain applications are their reversibility, simplicity, wide range of suitable substances, good applicability, minimal loss of material, possibility to create biocompatible product, as well as the preservation of basic properties of CNTs.

References

1. Silva AT, Nguyen A, Ye C et al (2010) Conjugated polymer nanoparticles for effective siRNA delivery to tobacco BY-2 protoplasts. BMC Plant Biol 10:291
2. Sokolova V, Epple M (2008) Inorganic nanoparticles as a carrier for nucleic acid into cells. Angew Chem Int Ed 47:1382–1395
3. Liu W, Yuan JS, Stewart CN Jr (2013) Advanced genetic tools for plant biotechnology. Nat Rev Genet 14:781–793
4. Alvarez MA (ed) (2011) Genetic transformation. InTech, Rijeka

5. Clive J (2014) Global status of commercialized biotech/GM crops: 2014. ISAAA Brief No. 49. ISAAA, Ithaca.
6. Hernández AC, Guillén JC (2012) How to get exogenous DNA to cross the cell membrane of plants: comment on "Physical methods for genetic transformation in plants" by Rivera et al. Phys Life Rev 9(3):348–349
7. Dizaj SM, Jafari S, Khosroushahi AY (2014) A sight on the current nanoparticle-based gene delivery vectors. Nanoscale Res Lett 9:252–260
8. Rai M, Deshmukh S, Gade A, Abd-Elsalam KA (2012) Strategic nanoparticle-mediated gene transfer in plants and animals—a novel approach. Curr Nanosci 8:170–179
9. Karimi M, Solati N, Ghasemi A et al (2015) Carbon nanotubes part II: a remarkable carrier for drug and gene delivery. Expert Opin Drug Deliv 12(7):1089–1105
10. Chen ZY, Liang K, Qiu RX, Luo LP (2011) Ultrasound- and liposome microbubble-mediated targeted gene transfer to cardiomyocytes in vivo accompanied by polyethylenimine. Ultrasound Med 30:1247–1258
11. Cha TS, Chen CF, Yee W et al (2011) Cinnamic acid, coumarin and vanillin: alternative phenolic compounds for efficient *Agrobacterium*-mediated transformation of the unicellular green alga, *Nannochloropsis sp*. J Microbiol Methods 84:430–434
12. Darbani B, Farajnia S, Toorchi M et al (2008) DNA-delivery methods to produce transgenic plants. Biotechnol 7(3):385–402
13. Taylor NJ, Fauquet CM (2002) Microparticle bombardment as a tool in plant science and agricultural biotechnology. DNA Cell Biol 21(12):963–977
14. Rafsanjani MSO, Alvari A, Samim M et al (2012) Application of novel nanotechnology strategies in plant biotransformation: a contemporary overview. Recent Pat Biotechnol 6:69–79
15. Al-Jamal KT, Gherardini L, Bardi G et al (2011) Functional motor recovery from brain ischemic insult by carbon nanotube-mediated siRNA silencing. Proc Natl Acad Sci U S A 108 (27):10952–10957
16. Klumpp C, Kostarelos K, Prato M et al (2006) Functionalized carbon nanotubes as emerging nanovectors for the delivery of therapeutics. Biochim Biophys Acta 1758(3):404–412
17. Serag MF, Kaji N, Gaillard C et al (2011) Trafficking and subcellular localization of multiwalled carbon nanotubes in plant cells. ACS Nano 5(1):493–499
18. Serag MF, Kaji N, Venturelli E et al (2011) Functional platform for controlled subcellular distribution of carbon nanotubes. ACS Nano 5(11):9264–9270
19. Ali-Boucetta H, Al-Jamal KT, McCarthy D et al (2008) Multiwalled carbon nanotube-doxorubicin supramolecular complexes for cancer therapeutics. Chem Commun 4:459–461
20. Bhirde A, Patel V, Gavard J et al (2009) Targeted killing of cancer cells in vivo and in vitro with EGF-directed carbon nanotube-based drug delivery. ACS Nano 3:307–316
21. Dong H, Ding L, Yan F et al (2011) The use of polyethylenimine-grafted graphene nanoribbon for cellular delivery of locked nucleic acid modified molecular beacon for recognition of microRNA. Biomaterials 32(15):3875–3882
22. Hao Y, Xu P, He C et al (2011) Impact of carbodiimide crosslinker used for magnetic carbon nanotube mediated GFP plasmid delivery. Nanotechnology 22(28):285103
23. Herrero MA, Toma FM, Al-Jamal KT et al (2009) Synthesis and characterization of a carbon nanotube–dendron series for efficient siRNA delivery. J Am Chem Soc 131:9843–9848
24. Kam NWS, O'Connell M, Wisdom JA, Dai H (2005) Carbon nanotubes as multifunctional biological transporters and near-infrared agents for selective cancer cell destruction. Proc Natl Acad Sci U S A 102:11600–11605
25. Liu Y, Wu DC, Zhang WD et al (2005) Polyethylenimine-grafted multiwalled carbon nanotubes for secure non-covalent immobilization and efficient delivery of DNA. Angew Chem Int Edn 44(30):4782–4785
26. Podesta JE, Al-Jamal KT, Herrero MA et al (2009) Antitumor activity and prolonged survival by carbon-nanotube-mediated therapeutic siRNA silencing in a human lung xenograft model. Small 5:1176–1185

27. Qin W, Yang K, Tang H et al (2011) Improved GFP gene transfection mediated by polyamidoamine dendrimerfunctionalized multi-walled carbon nanotubes with high biocompatibility. Colloids Surf B Biointerfaces 84(1):206–213
28. Singh R, Pantarotto D, McCarthy D et al (2005) Binding and condensation of plasmid DNA onto functionalized carbon nanotubes: toward the construction of nanotube-based gene delivery vectors. J Am Chem Soc 127:4388–4396
29. Wang T, Upponi JR, Torchilin VP (2012) Design of multifunctional non-viral gene vectors to overcome physiological barriers: dilemmas and strategies. Int J Pharm 427(1):3–20
30. Mattos IB, Alves DA, Hollanda LM et al (2011) Effects of multi-walled carbon nanotubes (MWCNT) under *Neisseria meningitides* transformation process. J Nanobiotechnology 9:53
31. Nunes A, Amsharov N, Guo C et al (2010) Hybrid polymer-grafted multiwalled carbon nanotubes for in vitro gene delivery. Small 6(20):2281–2291
32. Pantarotto D, Singh R, McCarthy D et al (2004) Functionalized carbon nanotubes for plasmid DNA gene delivery. Angew Chem Int Ed 43:5242–5246
33. Raffa V, Vittorio O, Costa M et al (2012) Multiwalled carbon nanotube antennas induce effective plasmid dna transfection of bacterial cells. J Nanoneurosci 2(1):56–62
34. Rojas-Chapana J, Troszczynska J, Firkowska I et al (2005) Multi-walled carbon nanotubes for plasmid delivery into *E. coli* cells. Lab Chip 5:536–539
35. Yuan H, Hu S, Huang P et al (2011) Single walled carbon nanotubes exhibit dual-phase regulation to exposed Arabidopsis mesophyll cells. Nanoscale Res Lett 6:44
36. Burlaka OM, Pirko YV, Yemets AI, Blume YB (2015) Plant genetic transformation using carbon nanotubes for DNA delivery. Cytol Genet 49(6):349–357
37. Liu Q, Chen B, Wang Q et al (2009) Carbon nanotubes as molecular transporters for walled plant cells. Nano Lett 9(3):1007–1010
38. Serag MF, Kaji N, Tokeshi M et al (2012) The plant cell uses carbon nanotubes to build tracheary elements. Integr Biol 4:127–131
39. Serag MF, Kaji N, Tokeshiac M, Baba Y (2012) Introducing carbon nanotubes into living walled plant cells through cellulase-induced nanoholes. RSC Advances 2:398–400
40. Dahl JA, Maddux BLS, Hutchison JE (2007) Toward greener nanosynthesis. Chem Rev 107:2228–2269
41. Wu Y, Phillips JA, Liu H et al (2008) Carbon nanotubes protect DNA strands during cellular delivery. ACS Nano 2(10):2023–2028
42. Mohanpuria P, Rana N, Yadav S (2008) Biosynthesis of nanoparticles: technological concepts and future applications. J Nanopart Res 10:507–517
43. Yang W, Thordarson P, Gooding JJ et al (2007) Carbon nanotubes for biological and biomedical applications. Nanotechnology 18:412001
44. Chen J, Chen Q, Ma Q (2012) Influence of surface functionalization via chemical oxidation on the properties of carbon nanotubes. J Colloid Interface Sci 370(1):32–38
45. Karousis N, Tagmatarchis N, Tasis D (2010) Current progress on the chemical modification of carbon nanotubes. Chem Rev 110(9):5366–5397
46. Kharisov BI, Kharissova OV, Gutierre HL, Mendez UO (2009) Recent advances on the soluble carbon nanotubes. Ind Eng Chem Res 48:572–590
47. Clark MD, Subramanian S, Krishnamoorti R (2011) Understanding surfactant aided aqueous dispersion of multi-walled carbon nanotubes. J Colloid Interface Sci 354(1):144–151
48. Ramos-Perez V, Cifuentes A, Coronas N et al (2013) Modification of carbon nanotubes for gene delivery vectors. In: Bergese P, Hamad-Schifferli K (eds) Nanomaterial interfaces in biology: methods and protocols. Methods in molecular biology, vol 1025. Springer, New York, pp 261–269
49. Sanchez-Pomales G, Pagan-Miranda C, Santiago-Rodriguez L, Cabrera CR (2010) DNA-wrapped carbon nanotubes: from synthesis to applications. In: Marulanda JM (ed) Carbon nanotubes. InTech, Vukovar, pp 721–748

50. Goodwin AP, Tabakman SM, Welsher K et al (2009) Phospholipid-dextran with a single coupling point: a useful amphiphile for functionalization of nanomaterials. J Am Chem Soc 131:289–296
51. Tasis D, Papagelis K, Douroumis D et al (2008) Diameter-selective solubilization of carbon nanotubes by lipid micelles. J Nanosci Nanotechnol 8:420–423
52. Zhang J, Wang Q, Wang L, Wang A (2007) Manipulated dispersion of carbon nanotubes with derivatives of chitosan. Carbon 45:1917–1920
53. Zhang LW, Zeng L, Barron AR et al (2007) Biological interactions of functionalized single-wall carbon nanotubes in human epidermal keratinocytes. Int J Toxicol 26(2):103–113
54. Iijima S (1991) Helical microtubules of graphitic carbon. Nature 354:56
55. Lacerda L, Raffa S, Prato M et al (2007) Cell-penetrating CNTs for delivery of therapeutics. Nano Today 2:38–43
56. Prato M, Kostarelos K, Bianco A (2008) Functionalized carbon nanotubes in drug design and discovery. Acc Chem Res 41:60–68
57. Dresselhaus MS, Dresselhaus G, Avouris P (2001) Carbon nanotubes: synthesis, structure, properties and applications. Springer, Berlin
58. Foldvari M, Bagonluri M (2008) Carbon nanotubes as functional excipients for nanomedicines: I. Pharmaceutical properties. Nanomedicine 4(3):173–182
59. Zhang M, Li J (2009) Carbon nanotube in different shapes. Materials today 12(6):12–18
60. Kam NWS, Liu ZA, Dai HJ (2006) Carbon nanotubes as intracellular transporters for proteins and DNA: an investigation of the uptake mechanism and pathway. Angew Chem Int Ed 45:577–581
61. Raffa V, Ciofani G, Nitodas S et al (2008) Can the properties of carbon nanotubes influence their internalization by living cells? Carbon 46:1600–1610
62. Bekyarova E, Ni Y, Malarkey EB et al (2005) Applications of carbon nanotubes in biotechnology. J Biomed Nanotechnol 1(1):3–17
63. Tasis D, Tagmatarchis N, Bianco A, Prato M (2006) Chemistry of carbon nanotubes. Chem Rev 106:1105–1136
64. Niyogi S, Hamon MA, Hu H et al (2002) Chemistry of single-walled carbon nanotubes. Acc Chem Res 35:1105–1113
65. Chen J, Hamon MA, Hu H et al (1998) Solution properties of single-walled carbon nanotubes. Science 282:95–98
66. Flavin K, Kopf I, Del Canto E et al (2011) Controlled carboxylic acid introduction: a route to highly purified oxidised single-walled carbon nanotubes. J Mater Chem 21:17881–17887
67. Guryanov I, Toma FM, Montellano López A et al (2009) Microwave-assisted functionalization of carbon nanostructures in ionic liquids. Chem Eur J 15:12837–12845
68. Strano MS, Dyke CA, Usrey ML et al (2003) Electronic structure control of single-waited carbon nanotube functionalization. Science 301:1519–1522
69. Tan JM, Arulselvan P, Fakurazi S et al (2014) A review on characterizations and biocompatibility of functionalized carbon nanotubes in drug delivery design. J Nanomater 2014, 917024, 20 pageshttp://dx.doi.org/10.1155/2014/917024
70. Darabi HR, Roozkhosh A, Tehrani MJ et al (2014) Characterization of ester- or thioamide-functionalized single-walled carbon nanotube-azithromycin conjugates. Appl Surf Sci 288:122–129
71. Ghini G, Trono C, Giannetti A et al (2013) Carbon nanotubes modified with fluorescein derivatives for pH nanosensing. Sens Actuat B 179:163–169
72. Qi H, Ling C, Huang R et al (2012) Functionalization of single-walled carbon nanotubes with protein by click chemistry as sensing platform for sensitized electrochemical immunoassay. Electrochim Acta 63:76–82
73. Peretz S, Regev O (2012) Carbon nanotubes as nanocarriers in medicine. Curr Opin Coll Interface Sci 17(6):360–368
74. Takahashi T, Tsunoda K, Yajima H, Ishii T (2004) Dispersion and purification of single-wall carbon nanotubes using carboxymethylcellulose. Jpn J Appl Phys 43(6A):3636–3639

75. Bilalis P, Katsigianopoulos D, Avgeropoulos A, Sakellariou G (2014) Non-covalent functionalization of carbon nanotubes with polymers. RSC Adv 4:2911–2934
76. Bianco A (2004) Carbon nanotubes for the delivery of therapeutic molecules. Expert Opin Drug Deliv 1(1):57–65
77. Kam NWS, Dai H (2005) Carbon nanotubes as intracellular protein transporters: generality and biological functionality. J Am Chem Soc 127:6021–6026
78. Mu Q, Broughton DL, Yan B (2009) Endosomal leakage and nuclear translocation of multiwalled carbon nanotubes: developing a model for cell uptake. Nano Lett 9 (12):4370–4375
79. Virkutyte J, Varma RS (2011) Green synthesis of metal nanoparticles: Biodegradable polymers and enzymes in stabilization and surface functionalization. Chem Sci 2:837–846
80. Park C, Lee S, Lee JH et al (2007) Controlled assembly of carbon nanotubes encapsulated with amphiphilic block copolymer. Carbon 45(10):2072–2078
81. Tu W, Lei J, Ju H (2009) Functionalization of carbon nanotubes with water-insoluble porphyrin in ionic liquid: Direct electrochemistry and highly sensitive amperometric biosensing for trichloroacetic acid. Chem Eur J 15:779–784
82. Kim SW, Kim T, Kim YS et al (2012) Surface modifications for the effective dispersion of carbon nanotubes in solvents and polymers. Carbon 50(1):3–33
83. Moore VC, Strano MS, Haroz EH et al (2003) Individually suspended single-walled carbon nanotubes in various surfactants. Nano Lett 3(10):1379–1382
84. Attal S, Thiruvengadathan R, Regev O (2006) Determination of the concentration of single-walled carbon nanotubes in aqueous dispersions using UV-visible absorption spectroscopy. Anal Chem 78:8098–8104
85. Islam MF, Rojas E, Bergey DM et al (2003) High weight fraction surfactant solubilization of single-wall carbon nanotubes in water. Nano Lett 3(2):269–273
86. Yan Y, Cui J, Potschke P, Voit B (2012) Dispersion of pristine singlewalled carbon nanotubes using pyrene-capped polystyrene and its application for preparation of polystyrene matrix composites. Carbon 48(9):2603–2612
87. Ding K, Hu B, Xie Y et al (2009) A simple route to coat mesoporous SiO_2 layer on carbon nanotubes. J Mater Chem 19(22):3725–3731
88. Kang YK, Lee O-S, Deria P et al (2009) Helical wrapping of single-walled carbon nanotubes by water soluble poly(p-phenyleneethynylene). Nano Lett 9(4):1414–1418
89. Kang Y, Taton TA (2003) Micelle-encapsulated carbon nanotubes: a route to nanotube composites. J Am Chem Soc 125(19):5650–5651
90. Zhao W, Liu YT, Feng QP et al (2008) Dispersion and noncovalent modification of multiwalled carbon nanotubes by various polystyrene-based polymers. J Appl Polym Sci 109(6):3525–3532
91. Crescenzo A, Ettorre V, Fontana A (2014) Non-covalent and reversible functionalization of carbon nanotubes. Beilstein J Nanotechnol 5:1675–1690
92. O'Connell MJ, Boul P, Ericson LM et al (2001) Reversible water-solubilization of single-walled carbon nanotubes by polymer wrapping. Chem Phys Lett 342(3–4):265–271
93. Harris JM, Zalipsky S (1997) Poly(ethylene glycol): chemistry and biological application. In: Szycher M (ed) Biocompatible polymers, metals and composites (1983). Am Chem Soc, Technomic, Washington, DC
94. Lacerda L, Russier J, Pastorin G et al (2012) Translocation mechanisms of chemically functionalised carbon nanotubes across plasma membranes. Biomaterials 33(11):3334–3343
95. Holder PG, Francis MB (2007) Integration of a self-assembling protein scaffold with water-soluble single-walled carbon nanotubes. Angew Chem Int Ed 46:4370–4373
96. Dolatabadi JEN, Omidi Y, Losic D (2011) Carbon nanotubes as an advanced drug and gene delivery nanosystem. Curr Nanosci 7:297–314
97. Orellana W, Correa JD (2014) Noncovalent functionalization of carbon nanotubes and graphene with tetraphenylporphyrins: Stability and optical properties from ab-initio calculations. J Mater Sci 50:898–905, arXiv:1506.00282

98. Chen RJ, Zhang Y, Wang D, Dai H (2001) Noncovalent sidewall functionalization of single-walled carbon nanotubes for protein immobilization. J Am Chem Soc 123(16):3838–3839
99. Shim M, Kam NWS, Chen RJ et al (2002) Functionalization of carbon nanotubes for biocompatibility and biomolecular recognition. Nano Lett 2:285–288
100. Teker K, Sirdeshmukh R, Sivakumar K et al (2005) Applications of carbon nanotubes for cancer research. NanoBiotechnol 1:171–182
101. Liu Z, Sun X, Nakayama-Ratchford N, Dai H (2007) Supramolecular chemistry on water-soluble carbon nanotubes for drug loading and delivery. ACS Nano 1(1):50–56
102. Fernando KAS, Lin Y, Wang W et al (2004) Diminished band-gap transitions of single-walled carbon nanotubes in complexation with aromatic molecules. J Am Chem Soc 126 (33):10234–10235
103. Heister E, Neves V, Tilmaciu C et al (2009) Triple functionalization of single-walled carbon nanotubes with doxorubicin, a monoclonal antibody, and a fluorescent marker for targeted cancer therapy. Carbon 47(9):2152–2160
104. Lemasson F, Tittmann J, Hennrich F et al (2011) Debundling, selection and release of SWNTs using fluorene-based photocleavable polymers. Chem Commun 47:7428–7430
105. Alpatova AL, Shan W, Babica P et al (2010) Single-walled carbon nanotubes dispersed in aqueous media via non-covalent functionalization: effect of dispersant on the stability, cytotoxicity, and epigenetic toxicity of nanotube suspensions. Water Res 44(2):505–520
106. Chen Y, Liu H, Ye T et al (2007) DNA-directed assembly of single-wall carbon nanotubes. J Am Chem Soc 129:8696–8697
107. Filip J, Sefcovicova J, Tomcik P et al (2011) A hyaluronic acid dispersed carbon nanotube electrode used for a mediatorless NADH sensing and biosensing. Talanta 84(2):355–361
108. Gandra N, Chiu PL, Li W et al (2009) Photosensitized singlet oxygen production upon two-photon excitation of single-walled carbon nanotubes and their functionalized analogs. J Phys Chem 113:5182–5185
109. Karajanagi SS, Yang H, Asuri P et al (2006) Protein-assisted solubilization of single-walled carbon nanotubes. Langmuir 22(4):1392–1395
110. Kurppa K, Jiang H, Szilvay GR et al (2007) Controlled hybrid nanostructures via protein mediated noncovalent functionalization of carbon nanotubes. Angew Chem Int Ed 46:6446–6449
111. Witus LS, Rocha JD, Yuwono VM et al (2007) Peptides that non-covalently functionalize single-walled carbon nanotubes to give controlled solubility characteristics. J Mater Chem 17:1909–1915
112. Yang Q, Shuai L, Pan X (2008) Synthesis of fluorescent chitosan and its application in noncovalent functionalization of carbon nanotubes. Biomacromolecules 9:3422–9326
113. Girifalco LA, Hodak M, Lee RS (2000) Carbon nanotubes, buckyballs, ropes, and a universal graphitic potential. Phys Rev B 62:13104–13110
114. Cheng Q, Debnath S, Gregan E, Byrne HJ (2010) Ultrasound-assisted SWNTs dispersion: effects of sonication parameters and solvent. J Phys Chem C 114:8821–8827
115. Nakashima N, Okuzono S, Murakami H et al (2003) DNA dissolves single-walled carbon nanotubes in water. Chem Lett 32(5):456–457
116. Ausman KD, Piner R, Lourie O et al (2000) Organic solvent dispersions of single-walled carbon nanotubes: toward solutions of pristine nanotubes. J Phys Chem B 104:8911–8915
117. Bergin SD, Nicolosi V, Streich PV et al (2008) Towards solutions of single-walled carbon nanotubes in common solvents. Adv Mater 20:1876–1881
118. Sharifi S, Behzadi S, Laurent S et al (2012) Toxicity of nanomaterials. Chem Soc Rev 41 (6):2323–2343
119. Toh RJ, Ambrosi A, Pumera M (2012) Bioavailability of metallic impurities in carbon nanotubes is greatly enhanced by ultrasonication. Chemistry 18(37):11593–11596
120. Battigelli A, Ménard-Moyon C, Da Ros T et al (2013) Endowing carbon nanotubes with biological and biomedical properties by chemical modifications. Adv Drug Delivery Rev 65:1899–1920

121. Shakhmaeva II, Bulatov ER, Bondar OV et al (2011) Binding and purification of plasmid DNA using multi-layered carbon nanotubes. J Biotechnol 152:102–107
122. Li X, Peng Y, Qu X (2006) Carbon nanotubes selective destabilization of duplex and triplex DNA and inducing B-A transition in solution. Nucleic Acids Res 34(13):3670–3676
123. Barisci JN, Tahhan M, Wallace GG et al (2004) Properties of carbon nanotube fibers spun from DNA-stabilized dispersions. Adv Funct Mater 14(2):133–138
124. Dwyer C, Guthold M, Falvo M et al (2002) DNA-functionalized single-walled carbon nanotubes. Nanotechnology 13:601–604
125. Kim JH, Kataoka M, Shimamoto D et al (2009) Defect-enhanced dispersion of carbon nanotubes in DNA solutions. Chem Phys Chem 10(14):2414–2417
126. Li Z, Wu Z, Li K (2009) The high dispersion of DNA-multiwalled carbon nanotubes and their properties. Anal Biochem 387(2):267–270
127. Simon S, Biris AR, Lupu DM et al (2009) Dispersion of carbon nanotubes by single-stranded DNA wrapping for advanced biomedical applications. J Phys Conf Ser 182(1):012079
128. Wang R, Sun J, Gao L, Zhang J (2010) Dispersion of single-walled carbon nanotubes by DNA for preparing transparent conductive films. J Mater Chem 20(33):6903–6909
129. Rai M, Bansod S, Bawaskar M et al (2015) Nanoparticles-based delivery systems in plant genetic transformation. In: Rai M, Ribeiro C, Mattoso L, Duran N (eds) Nanotechnologies in food and agriculture. Springer, Switzerland, pp 209–239
130. Arnold MS, Stupp SI, Hersam MC (2005) Enrichment of single-walled carbon nanotubes by diameter in density gradients. Nano Lett 5:713–718
131. Maji B, Samanta SK, Bhattacharya S (2014) Role of pH controlled DNA secondary structures in the reversible dispersion/precipitation and separation of metallic and semiconducting single-walled carbon nanotubes. Nanoscale 6:3721–3730
132. Albertorio F, Hughes ME, Golovchenko JA, Branton D (2009) Base dependent DNA-carbon nanotube interactions: activation enthalpies and assembly-disassembly control. Nanotechnology 20(39):395101
133. Johnson RR, Johnson ATC, Klein ML (2010) The nature of DNA-base-carbon-nanotube interactions. Small 6(1):31–34
134. Tu X, Zheng MA (2008) DNA-based approach to the carbon nanotube sorting problem. Nano Res 1:185–194
135. Furusawa Y, Fujiwara Y, Campbell P et al (2012) DNA double-strand breaks induced by cavitational mechanical effects of ultrasound in cancer cell lines. PLoS One 7(1):e29012
136. Xu Y, Pehrsson PE, Chen L et al (2007) Double-stranded DNA single-walled carbon nanotube hybrids for optical hydrogen peroxide and glucose sensing. J Phys Chem C 111:8638–8643
137. Zheng M, Jagota A, Semke ED et al (2003) DNA assisted dispersion and separation of carbon nanotubes. Nat Mater 2:338–342
138. Zorbas V, Smith AL, Xie H et al (2005) Importance of aromatic content for peptide/single-walled carbon nanotube interactions. J Am Chem Soc 127:12323–12328
139. Nepal D, Geckeler KE (2007) Proteins and carbon nanotubes: close encounter in water. Small 3:1259–1265
140. Matsuura K, Saito T, Okazaki T et al (2006) Selectivity of water-soluble proteins in single-walled carbon nanotube dispersions. Chem Phys Lett 429:497–502
141. Wang S, Humphreys ES, Chung S-Y et al (2003) Peptides with selective affinity for carbon nanotubes. Nat Mater 2(3):196–200
142. Liu Y, Liang P, Zhang HY, Guo DS (2006) Cation-controlled aqueous dispersions of alginic-acid-wrapped multi-walled carbon nanotubes. Small 2(7):874–878
143. Long D, Wu G, Zhu G (2008) Noncovalently modified carbon nanotubes with carboxymethylated chitosan: a controllable donor-acceptor nanohybrid. Int J Mol Sci 9:120–130
144. Shieh YT, Wu HM, Twu YK, Chung YC (2010) An investigation on dispersion of carbon nanotubes in chitosan aqueous solutions. Colloid Polym Sci 288(4):377–385

145. Takahashi T, Luculescu CR, Uchida K et al (2005) Dispersion behavior and spectroscopic properties of singlewalled carbon nanotubes in chitosan acidic aqueous solutions. Chem Lett 34(11):1516–1517
146. Zheng W, Li Q, Su L et al (2006) Direct electrochemsitry of multi copper oxidases at carbon nanotubes noncovalently functionalized with cellulose derivatives. Electroanalysis 6:587–594
147. Burlaka OM, Pirko YV, Kolomys OF et al (2015) Functionalization of carbon nanotubes using different biomolecules for stable dispersion in water. Biotechnologia Acta 8(4):71–81
148. Wang D, Chen L (2007) Temperature and pH-responsive single-walled carbon nanotube dispersions. Nano Lett 7:1480
149. Ikeda A, TotsukaY NK, Kikuchi J (2009) Reversible solubilisation and precipitation of carbon nanotubes by temperature and pH control in water. J Mater Chem 19:5785–5789
150. Shiraki T, Dawn A, Le TNL et al (2011) Heat and light dual switching of a single-walled carbon nanotube/thermo-responsive helical polysaccharide complex: a new responsive system applicable to photodynamic therapy. Chem Commun 47:7065–7067
151. Fu CL, Meng LJ, Lu QH et al (2007) Large-scale homogeneous helical amylose/SWNTs complexes for biological applications. Macromol Rapid Commun 28:2180–2184
152. Kim OK, Je J, Baldwin JW et al (2003) Solubilization of single-wall carbon nanotubes by supramolecular encapsulation of helical amylose. J Am Chem Soc 125:4426–4427
153. Star A, Steuerman DW, Heath JR, Stoddart JF (2002) Starched carbon nanotubes. Angew Chem Int Ed 41:2508–2512
154. Zhang X, Meng L, Lu Q (2009) Cell behaviors on polysaccharide-wrapped single-wall carbon nanotubes: a quantitative study of the surface properties of biomimetic nanofibrous scaffolds. ACS Nano 3:3200–3206
155. Cambré S, Wenseleers W (2011) Separation and diameter-sorting of empty (end-capped) and water-filled (open) carbon nanotubes by density gradient ultracentrifugation. Angew Chem Int Ed 50:2764–2768
156. Oh H, Sim J, Ju S-Y (2013) Binding affinities and thermodynamics of noncovalent functionalization of carbon nanotubes with surfactants. Langmuir 29:11154–11162
157. Ciofani G, Obata Y, Sato I et al (2009) Realization, characterization and functionalization of lipidic wrapped carbon nanotubes. J Nanopart Res 11:477–484

Chapter 31
Photocatalytic Properties of Semiconductor Dye–Polymer Films

O. Nadtoka, O. Linnik, N. Chorna, and N. Smirnova

31.1 Introduction

The significance of the wastewater treatment, management, and its disposal gradually increases in the modern times, and it becomes a major concern for public health scientific interest. All existing protocols for treatment of wastewater are categorized as physical, chemical, and biological processes. The low-cost and nontoxic semiconductor composites based on titania are perspective materials for solar energy utilization in the processes of soil and water purification as well as photovoltaic materials.

Titanium dioxide is a demanded photocatalyst at the degradation process of many pollutants. The interaction of the semiconductor particles with quanta of light leads to the appearance of the active radicals that are capable of the simultaneous oxidation and reduction reactions. In our previous works, we have showed the high catalytic activity of synthesized mesoporous titania thin films in various redox processes [1]. The semiconducting nanomaterials such as thin films with high surface area are of great significance for the strong dye adsorption which leads to the higher solar energy absorption efficiency and photocurrent density. Titania possesses optical properties at UV light trapping which is corresponded to its bandgap energy. Moreover, it is cheap and nontoxic substance, which enjoys a large application for photocatalysis, gas sensors, photovoltaic materials, and dye–dye-sensitized solar cells. A significant improvement of photocatalytic efficiency is

O. Nadtoka (✉)
National Taras Shevchenko University of Kyiv, 60, Volodymyrska Str., Kyiv 01601, Ukraine
e-mail: oksananadtoka@ukr.net

O. Linnik • N. Chorna • N. Smirnova
Chuiko Institute of Surface Chemistry NASU, 17 General Naumov Str., Kyiv 03680, Ukraine

O. Fesenko, L. Yatsenko (eds.), *Nanophysics, Nanophotonics, Surface Studies, and Applications*, Springer Proceedings in Physics 183,
DOI 10.1007/978-3-319-30737-4_31

achieved by the synthesis of TiO_2/SiO_2 nanocomposites where silica matrix provides the transport of reagents to TiO_2 nanoparticles via porous structure, generation of the new active sites, and improved mechanical strength, thermal stability, and surface area of titania [2].

In the field of up-to-date materials, the creation of light-controlled high-sensitivity polymeric systems is the most topical question to date. Amorphous polymer materials with side-chain azochromophore groups are attractive due to some of their properties. Different derivatives of azobenzene show the best advantage as photoactive fragments [3]. Illumination of these materials with exciting light stimulates reversible or irreversible trans–cis isomerization of azochromophores. The role of the various excited states of azobenzene in photoisomerization reaction has attached close attention. Excitation of the n–π^* bands of *cis*- and *trans*-azobenzene resulted in isomerization with quantum yields of 0.70 and 0.20, respectively. However, π–π^* excitation is also accompanied by isomerization, and this state could be also involved. In the latter case, quantum yields of 0.44 and 0.10 are observed for the cis- and trans-isomers, respectively [4]. To create photocatalytic semiconductor dye–polymer films, the methacrylic azobenzene-containing polymers were used. Azopolymers having polymethacrylate main chain are able to form qualitative thin films and, as is known, to transmit light in range from 300 nm that is suitable for spectrometric investigations.

Among the conducting polymers, polycarbazole (PCz) is attributed with good electroactivity, thermal, electrical, and photophysical properties [5]. However, π–π electron system along its backbone imparts rigidity to the polymer and, therefore, makes it infusible and poorly processable. The increasing interest in PCz is determined by its role as a hole-transport material and an efficient photoluminescence unit. Derivatives of carbazole are easily prepared by the substitution at nitrogen atom, and thus, the solubility and functionality of the resulting polymers could be improved. More importantly, the substituted groups influence on the effective conjugation length which is promising for making materials used in emitting light devices.

31.2 Experimental

31.2.1 Samples

Tetraethoxysilane $Si(OC_2H_5)_4$, aqueous solution of hydrochloric acid, deionized water, and Pluronic P123 (BASF) were used to prepare silica sols. To control hydrolysis–condensation reaction rates and to prevent oxide precipitation, acetylacetone was used as the complexing agent. Silica–titania films (10 and 30 wt% TiO_2) were obtained via addition of TiO_2 in anatase crystalline form (6–7 nm) [6] to SiO_2 sol. Dip-coating procedure was used for film forming

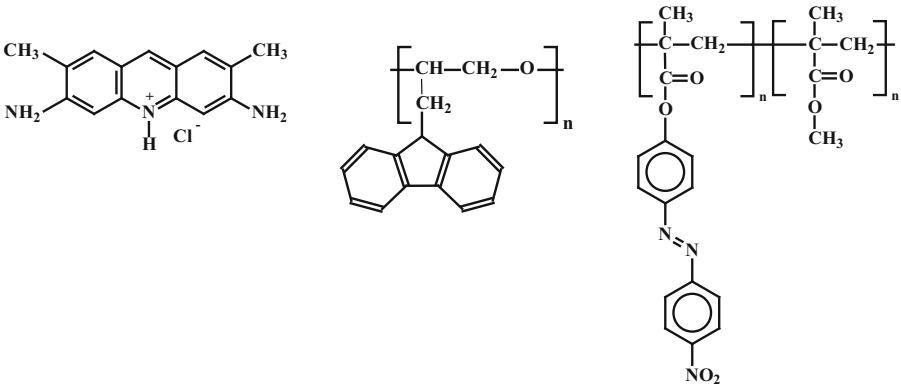

Acridine Yellow (AY) | Polyepoxypropyl-carbazole (PEPC) | Azopolymer (AzoP)

Fig. 31.1 Structural formulas of dye (AY), semiconductor polymer (PEPC), and azopolymer (AzoP)

(withdrawal rate was 1.5 mm/s). The clean and dried glass substrates were used for this target. Thermal treatment of films was performed at 350 °C.

Acridine yellow (AY) (1×10^{-6} mol/L) was applied onto the films for 24 h for adsorption. After film drying on the air, the polyepoxypropylcarbazole (PEPC) (5 % PEPC in benzene) was twice covered onto adsorbed AY. The composites were left for 48 h at the room temperature. The obtained composites are signed as x%TiO_2/SiO_2//AY//PEPC. They consist of 10 or 30 wt% of titania in silica mesoporous thin films, AY dye, and PEPC layers.

Methacrylic azopolymer (AzoP) having azobenzene moieties with strong π–π electron system in side chain was used as photosensitive material too [3]. It was dissolved in dichloroethane up to the final concentration of 1.5 w/w %. Obtained solution was used for dip coating onto freshly synthesized films. The systems were dried on the air for 48 h. The synthesized composites are signed as x%TiO_2/SiO_2// AzoP where x means the amount of titania in the silica matrix (10 or 30 %).

The chemical structure of used substances is presented in Fig. 31.1.

The composite film was immersed in 40 mL of an aqueous solution of potassium dichromate (the initial concentration of dichromate ions was 2×10^{-4} M). The reducing agent (disodium salt of ethylenediaminetetraacetic acid (Na_2EDTA)) in the molar ratio 1:1 was adjusted to pH $\geq$ 2 by perchloric acid.

31.2.2 Observation and Measurements

The XRD spectrum of TiO_2 sol was recorded with DRON-4-07 diffractometer (CuK_α radiation). Calculation of apparent crystallite size for titania has been performed by Debye–Scherrer formula $\beta\ (2\theta) = 0.94\,\lambda/(D\cos\theta)$, using (1 0 1) reflections employing the FWHM procedure.

Optical spectra of the composites were recorded with a double beam spectrophotometer (Lambda 35, PerkinElmer) within the wavelength range of 190–1200 nm.

The Cr(VI) ion concentration change was monitored by a Lambda 35 UV–Vis spectrophotometer (Lambda 35, PerkinElmer) every 20 min at $\lambda = 350$ nm.

The Brunauer–Emmett–Teller (BET) surface area and pore size distribution of the thin films were measured from hexane adsorption–desorption isotherms. Hydrophilic properties of films were estimated by measurements of water contact angle using the sessile drop method with a MIR-1 microscope (LOMO, St. Petersburg, Russia). Measurements were carried out at room temperature (20 ± 2 °C).

31.3 Results and Discussion

The shape of hexane adsorption–desorption isotherm of the TiO2/SiO2 films (Fig. 31.2) indicates its IV type. The presence of two hysteresis loops on the isotherm shows the formation of the mesoporous structure.

The irreversible structural deformation and formation of the so-called ink bottle type of porosity was observed [7, 8]. The specific surface area and effective pore radii values obtained from BET analysis of the isotherm are 1300 m^2/g and 4–10 nm, respectively. XRD investigation pointed out the anatase formation in titania sol used for the film synthesis with the average crystallite size of the particles 6–7 nm. Particle size was calculated from the most intense diffraction peak (101) using the Scherrer equation through fitting the peak by a Lorentzian function (not shown here). We have shown [2] that the mixing of titania and silica sols with

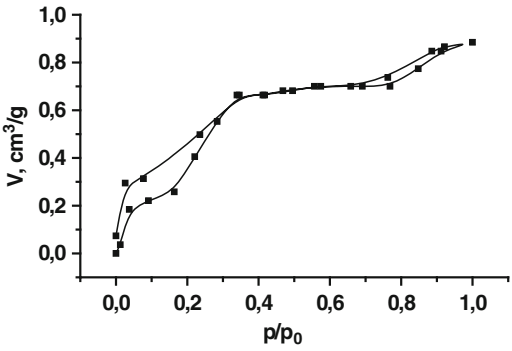

Fig. 31.2 Hexane adsorption isotherm and the distribution function of pore size—*insets* of SiO_2/TiO_2—10 % film sintered at 350 °C

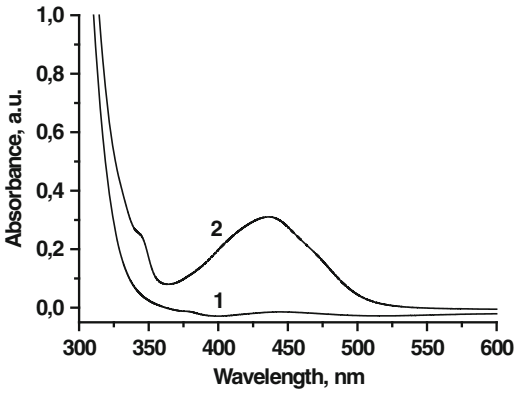

Fig. 31.3 Absorption spectra of 10 % TiO_2/SiO_2// PEPC (*1*) and 10 % TiO_2/ SiO_2//AY//PEPC (*2*) composites

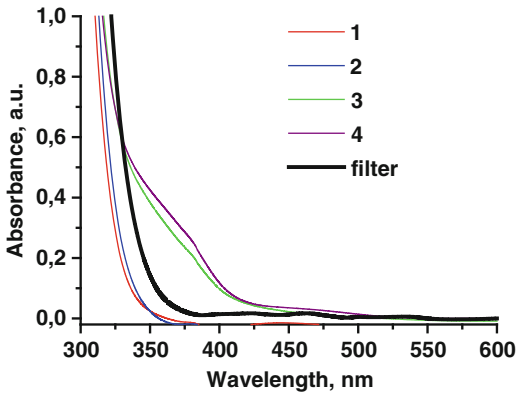

Fig. 31.4 Absorption spectra of cutoff filter (*bold curve*), 10 % TiO_2/SiO_2 (*1*), 30 % TiO_2/SiO_2 (*2*), 10 % TiO_2/SiO_2//AzoP (*3*), and 30 % TiO_2/SiO_2//AzoP (*4*) films

further Ti–O–Si bond formation is a key factor affecting surface properties such as level of surface hydroxylation and surface acidity as well as the catalytic function of the films. Freshly prepared TiO_2/SiO_2 films show the high hydrophilic properties with the water contact angles being ca. 12 before and 5° after UV irradiation. In addition, the enhanced adsorption of AY on SiO2/TiO2 film (1.5–2 times higher) in comparison with that on the parent oxide (on SiO_2 or TiO_2 film surfaces) coincides with high acidity, surface area, and hydrophilicity of synthesized films. Thus, strong adsorption of AY on specific surface sites of SiO_2/TiO_2 films is responsible for its high efficiency of light absorption and its stability. The appeared maximum at 435 nm is signed to the adsorbed AY molecules onto TiO_2/SiO_2 surface (Fig. 31.3). Desorption of AY and consequently the decrease in the intensity of the absorption band at 443 nm were observed when the mixture of ethanol and water in the ratio 1:1 and pure ethanol was applied (not shown here). No stable systems were also obtained when the adsorbed AY amount was doubled and the TiO2/SiO2//AY was covered by a single layer of PEPC.

AzoP covered onto TiO_2/SiO_2 films influences on the red shift in the absorption region of the composites (Fig. 31.4) where two-layered films exhibit an optimum

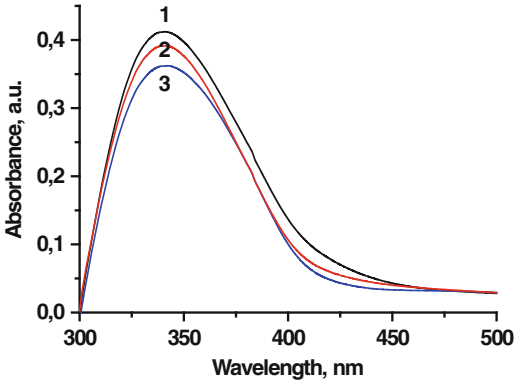

Fig. 31.5 The differences between the absorption spectra of 10 % TiO_2/SiO_2 and 10 % TiO_2/SiO_2//AzoP: before the contact with 25 % EtOH (*1*), after 60 min (*2*) and 24 h (*3*)

absorption shift (all reported results are related to two-layered systems only). At the same time as shown on Fig. 31.4, no significant change in the absorption spectra is observed for the systems contained 10 and 30 % of titania.

Such nanocomposites were quite stable not only in aqueous media but also in aqueous ethanol for a long time (Fig. 31.5).

Photocatalytic activity was increased slightly for 10 % TiO_2/SiO_2//AY//PEPC and doubled for 30 % TiO_2/SiO_2//AY//PEPC in comparison with the AY-free composites in dichromate reduction process under visible light (Fig. 31.6a). It should be noted that the AY-free composites were completely inert under the visible light. Upon the visible light, the exciting of AY molecule takes place with the following charge carrier transfer from the excited (AY*) molecules to the CB of TiO_2 known as dye-sensitization process. The reduction of the oxidized species ($AY^{\bullet+}$) by electron donor (EDTA) or processes involving electrons from the CB with the following dichromate reduction can be considered. When light with energy higher than 3.2 eV interacts with titania particles, an electron transition from the valence band (VB) of semiconductor to the conduction band (CB) occurs. The photocatalytic activity of AY-free TiO_2/SiO_2//PEPC enhances compared with the blank experiment and depends on TiO_2 amount. This fact indicates that the photogenerated electrons became to be trapped and/or directly move through PEPC layer to the redox couple. Almost no influence on the photocatalytic performance under UV light was observed for TiO_2/SiO_2//AY//PEPC.

The TiO_2/SiO_2//AzoP composites possessed much lower photocatalytic activity than TiO_2/SiO_2 systems. It can be caused by insufficient electron transferring from the semiconductor through the polymer layer to the liquid phase when UV or visible light is applied (Fig. 31.6b).

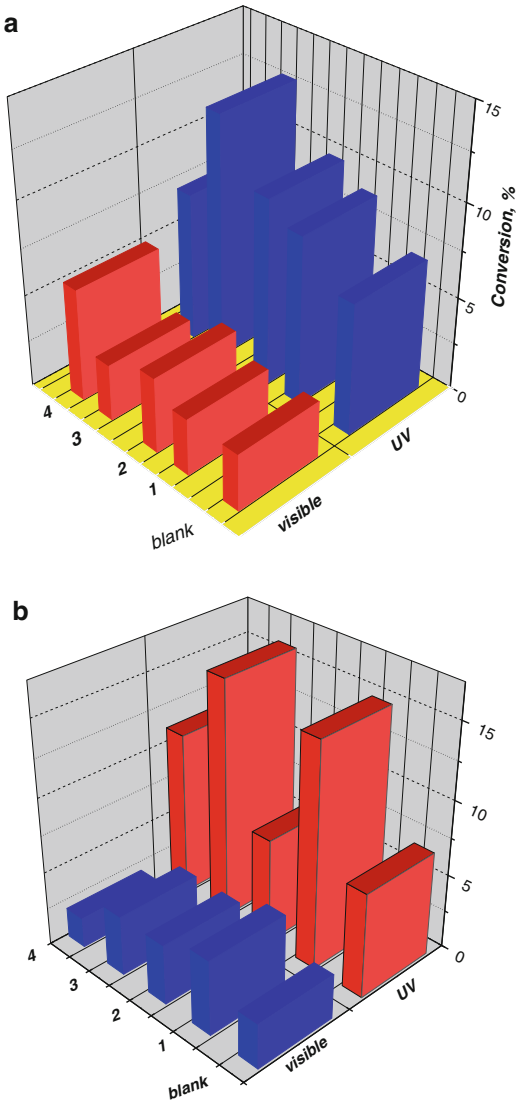

Fig. 31.6 Photocatalytic activity of the composites tested in the reduction of dichromate ions: (**a**) 10 % TiO_2/SiO_2//PEPC (*1*), 10 % TiO_2/SiO_2//AY//PEPC (*2*), 30 % TiO_2/SiO_2//PEPC (*3*), 30 % TiO_2/SiO_2//AY//PEPC (*4*); (**b**) 10 % TiO_2/SiO_2 (*1*), 10 % TiO_2/SiO_2//AzoP (*2*), 30 % TiO_2/SiO_2 (*3*), 30 % TiO_2/SiO_2//AzoP (*4*)

31.4 Conclusions

Hence, the complex composites based on the mesoporous TiO_2/SiO_2 thin films with adsorbed AY dye and PEPC as well as azopolymer are designed. The double PEPC covering prevents the penetration of AY molecules to the liquid phase when aqueous solution is applied.

The presence of acidic sites on surface of TiO_2/SiO_2 thin films, the amount of adsorbed AY, and the number of PEPC layers have influenced on the stability of the

composites. The TiO_2/SiO_2//AY//PEPC films can be used as the new type of photocatalytic systems in ecological photocatalysis as the significant increase in the photoactivity under visible light for reduction process is reported.

It was shown that TiO_2/SiO_2//AzoP composites possess much lower photocatalytic activity compared with TiO_2/SiO_2//AY//PEPC. However, further investigation has to be done to find out the appropriate synthesis conditions to improve their photocatalytic activity and stability to the more aggressive media as well as to find out the new opportunities for the photochromic materials with azobenzene moieties.

References

1. Linnik O, Zhukovskiy M, Starukh G et al (2015) Photocatalytic destruction of tetracycline hydrochloride on the surface of titanium dioxide films modified by gold nanoparticles. J Appl Spectrosc 81(6):990–995
2. Kumar D, Xavier J, Shyla J et al (2013) Synthesis and structural, optical and electrical properties of TiO_2/SiO_2 nanocomposites. J Mater Sci 48(10):3700–3707
3. Yaroshchuk O, Bidna T, Nadtoka O et al (2005) The initial and photoinduced 3d orientational order in polymethacrylates with azobenzene side groups. Mol Cryst Liq Cryst 437:1377–1390
4. Taudi H, Bernede J, Valle D et al (2001) Influence of the electrochemical conditions on the properties of polymerized carbazole. J Mater Sci 36(3):631–634
5. Pavlova-Verevkina O, Politova E, Nazarov V (1999) Preparation and structure of stable dispersions of uniform TiO_2 nanoparticles. Colloid J 61:359–362
6. Gregg SJ, Sing KSW (1982) Adsorption, surface area and porosity. Academic, London, p 303
7. Kruk M, Jaroniec M, Sayari A (1997) Application of large pore MCM-41 molecular sieves to improve pore size analysis using nitrogen adsorption measurements. Langmuir 13 (23):6267–6273
8. Andrulevicˇius M, Tamulevicˇius S, Gnatyuk Y et al (2008) Ag/Au nanodalelėmis modifikuotų TiO2/ZrO2/SiO2 dangų RFS tyrimas. Mater Sci (Medzˇiagotyra) 14(1):8–14

Chapter 32
Branched Copolymers Dextran-Graft-Polyacrylamide as Nanocarriers for Delivery of Gold Nanoparticles and Photosensitizers to Tumor Cells

V.A. Chumachenko, I.O. Shton, E.D. Shishko, N.V. Kutsevol, A.I. Marinin, and N.F. Gamaleia

Photodynamic therapy (PDT) is a modern promising method of cancer therapy [1, 2]. It is characterized by lower systemic toxicity and fewer side effects as compared with radiation therapy and chemotherapy. The method works when three factors—light, a light-responsive substance (photosensitizer), and molecular oxygen—interact. Each of these individual components is harmless. However, upon irradiation with light of an appropriate wavelength, the photosensitizer becomes excited and transfers its energy to the surrounding molecular oxygen to generate cytotoxic singlet oxygen. The singlet oxygen can oxidize cellular macromolecules, inducing cell permeability alterations with the consequence of tumor cell death through apoptosis or necrosis [3].

However, the photosensitizer's clinical use is limited because of poor water solubility and inefficient delivery to target tumor tissues. One of the strategies applied for overcoming these limitations is to enhance photosensitizer specificity for the tumor by using nano-sized drug carriers. It has been reported that some photosensitizer-encapsulated nano-sized carriers could enhance the tumor target specificity and therapeutic efficacy in cancer treatment, compared to free

V.A. Chumachenko (✉) • N.V. Kutsevol
Department of Chemistry, Taras Shevchenko National University of Kyiv,
60 Volodymyrska Str., Kyiv 01601, Ukraine
e-mail: chumachenko_va@ukr.net

I.O. Shton • E.D. Shishko • N.F. Gamaleia
Laboratory of Quantum Nanobiology, R.E. Kavetsky Institute for Experimental Pathology, Oncology and Radiobiology,
Vasilkivska, 45, Kiev 03022, Ukraine
e-mail: gamaleia@onconet.kiev.ua

A.I. Marinin
Problem Research Laboratory, National University of Food Technology, Volodymyrska str. 68, Kyiv 01601, Ukraine

O. Fesenko, L. Yatsenko (eds.), *Nanophysics, Nanophotonics, Surface Studies, and Applications*, Springer Proceedings in Physics 183,
DOI 10.1007/978-3-319-30737-4_32

photosensitizer [4]. In particular, attempts were made to control the photosensitizer's activity using gold nanoparticles (AuNPs) which can enhance the PDT efficiency in targeted tumor tissues [5].

It is of special interest to utilize for this purpose the water-soluble, polymer-based, nano-sized carriers containing both a photosensitizer and AuNPs. In [6] it was shown that branched polymers used for nanocarrier preparation have more compact molecular structure with higher local concentration of functional groups in comparison with their linear analogue polyacrylamide. Also, it was reported [7] that such structure peculiarities give the advantages for application of branched polymer systems in nanotechnologies.

Therefore, proceeding from the data, we now set the task to study these earlier characterized polymers as carrier/stabilization systems in experiments on antitumor photodynamic therapy in vitro and in vivo with chlorin e6 as a photosensitizing agent.

32.1 Materials

Tetrachloroauric acid ($HAuCl_4$) and sodium borohydride ($NaBH_4$) were purchased from Aldrich and used without further purification. Specific singlet oxygen ($^1O_2$) sensor Singlet Oxygen Sensor Green (SOSG) was purchased from Invitrogen (USA).

Copolymers dextran-graft-polyacrylamide (D-g-PAA) in noncharged and anionic form were used for fabrication of nanocarriers containing both AuNPs and photosensitizer. Synthesis, molecular parameters, and peculiarities of macromolecular structure of starlike copolymer D-g-PAA were discussed in details in [6, 8]. The molecular parameters of the polymer used as a nanocarrier were $M_w = 1.57 \times 10^6$ g/mol, Rg = 67 nm, and $M_w/M_n = 1.81$. Anionic form of the copolymer (referred throughout as D-g-PAA(PE)) was obtained via alkaline hydrolysis of initial copolymer during 30 min using NaOH. The fraction of mers which bore carboxylate groups was evaluated by potentiometric titration and was equal to approximately 37 %.

32.1.1 AuNPs Preparation

The AuNPs were synthesized by the chemical reduction of Au precursor ($HAuCl_4$). In the process, the polymer played a role of a matrix capable to act as a nucleating, capping, and stabilizing agent simultaneously. 0.012 mL of 0.1 M $HAuCl_4$ aqueous solution was added to 0.5 mL of aqueous polymer solution ($c = 1.10^{-3}$ g cm^{-3}) and stirred for 20 min. Then, 0.047 mL of 0.1 M aqueous solution of $NaBH_4$ was added. The final solution was stirred for 30 min. It turned ruby-red in color; thus, the

formation of AuNPs was indicated. The reduction process was performed at $T = 5$ °C.

32.1.2 Photosensitizing Nanocomposite Creation

Chlorin e6 was dissolved in 1 volume of dimethyl sulfoxide and mixed with 5 volumes of Hanks' balanced salt solution without phenol red. To determine the optimal ratio of chlorin e6 and AuNPs, a series of nanocomposite solutions were prepared with different mass correlation of the photosensitizer and gold (1:1, 1:10, and 1:100). To estimate the concentration of the unbound chlorin e6, nanocomposites were precipitated by centrifugation for 10 min (12,000 r/min), and absorption spectra of supernatants were recorded.

32.2 Methods

32.2.1 UV-Visible Spectroscopy

UV-visible absorption spectra of gold sols from 200 to 800 nm were recorded by Varian Cary 50 scan UV-Vis spectrophotometer (Palo Alto, CA, USA).

32.2.2 Transmission Electron Microscopy

For the sample preparation, 400 mesh Cu grids with plain carbon film were rendered hydrophilic by a glow discharge treatment (Elmo, Cordouan Technologies, Bordeaux, France). A 5 μL drop was deposited and allowed to be adsorbed for 1 min, and then the excess of solution was removed with a piece of filter paper. The observation of the AuNPs was carried out with two transmission electron microscopies (TEMs), Tecnai G2 and CM12 (FEI, Eindhoven, the Netherlands), and the images were acquired with a ssCCD Eagle camera in the Tecnai and a Megaview SIS camera in the CM12.

32.2.3 Quasi-Elastic Light Scattering

Quasi-elastic light scattering (QELS) measurements were carried out using Zetasizer Nano ZS90 (Malvern Instruments Ltd., UK). The apparatus includes a

4 mW He-Ne laser with a wavelength of 632.8 nm, and the scattered light is detected at an angle of 60°.

32.2.4 Singlet Oxygen Registration

Singlet oxygen formation was monitored using specific sensor SOSG. The 5 mM stock solution of fluorescent SOSG reagent in methanol was prepared, stored at −20 °C, and used following the manufacturer's instructions. The singlet oxygen generation was determined in solutions of chlorin e6 and its nanocomposite after the addition of 2 μM SOSG. The probes were irradiated by semiconductor laser ($\lambda = 658$ nm, "Fotonika Plus," Ukraine) fractionally, up to a dose of 2 J/cm^2, and SOSG fluorescence at 530 nm was registered using fluorospectrometer NanoDrop 3300 (NanoDrop, USA).

32.2.5 Experiments on Malignant Cells In Vitro

The MT-4 cells (human T-cell leukemia line) were obtained from the culture bank of R.E. Kavetsky Institute of Experimental Pathology, Oncology and Radiobiology, National Academy of Sciences of Ukraine. Cells were maintained in RPMI-1640 medium containing 10 % of fetal bovine serum, at 37 °C in 95 % air and 5 % carbon dioxide.

For PDT experiments, cell suspensions (0.5×10^6 per mL) in Hank's balanced salt solution were prepared from a culture of the leukemic cells in log phase of growth. After 1.5 h incubation (37 °C) in Hank's solution with free chlorin e6 or with its nanocomposite, the cells were washed twice with tenfold volume of fresh Hank's solution and then exposed to the red laser light (658 nm, power density 1.1 mW/cm^2, dose 1 J/cm^2). After irradiation, cells were transferred to the growth medium and incubated at 37 °C for 18 h for completion of photodynamic-induced apoptosis process. Cell viability was determined by trypan blue dye exclusion test.

32.2.6 Experiments In Vivo

Antitumor photodynamic activity of nanocomposites was studied in C57Bl/6 mice (bred at the animal facility of R.E. Kavetsky Institute for Experimental Pathology, Oncology and Radiobiology, NAS of Ukraine) with Lewis lung carcinoma transplanted into mouse footpads. The photodynamic therapy was carried out when tumor diameter reached 3.5–5.0 mm. The animals were divided into three groups: (1) control (untreated) animals; (2) animals, in tale vein of which free photosensitizer chlorin e6 was introduced in a dose of 1.5 mg/kg; and (3) animals

introduced with the same dose of chlorin e6 but in a form of the nanocomposite. In 1 h after the photosensitizer injection, tumors were subjected to laser irradiation ($\lambda = 658$ nm, power density of 50 mW/cm^2, dose of 45 J/cm^2).

32.3 Results and Discussion

It was shown that the copolymers D-g-PAA are starlike polymers, consisting of a compact dextran core and long polyacrylamide arms. As it was previously reported [6, 9], the average conformation of grafted PAA chains is partially controlled by the grafting ratio. PAA grafts in starlike copolymers D-g-PAA even in uncharged form have local wormlike conformation. Starlike copolymers and linear PAA were transformed into polyelectrolytes by alkaline hydrolysis. The process of D-g-PAA hydrolysis was not attended by irrelevant processes (breaking or cross-linking of the macromolecules). It is evident that saponified polymers contain two types of functional groups: carbamide and carboxylate ones. The pH value of the solutions was equal to 7.33 after dissolving PAA(PE) in bi-distilled water. Thus, carboxylate groups of the polymer were partially hydrolyzed in such conditions. Obviously, the nucleation process occurring just after reductant addition differs for gold ions interacting with carbamide or carboxylate moiety. That could lead to difference in size distribution for AuNPs obtained in uncharged and charged matrices. Moreover, it was shown [10] that there is a difference in the internal molecular structure of uncharged and charged D-g-PAA, namely, that D-g-PAA(PE) has extremely extended grafts and its structure is much more rigid in comparison with uncharged molecules. This factor can affect the Au sol stability.

In situ synthesis of AuNPs into (dilute) aqueous solutions of polymers resulted in rather stable colloids. However, the difference in the color of Au sols obtained testifies to the impact of polymer matrix chemical nature on the AuNP formation process.

The storage stability and the changes in size distribution of AuNPs in time are very important characteristics of the nanosystems especially if they are used for biomedical applications, e.g., for the nanocarrier preparation.

Nanoparticle size distribution in Au sols prepared with D-g-PAA and D-g-PAA (PE) was analyzed for 2 months. Dependence of nanoparticle number on their diameter for the D-g-PAA-containing nanosystem is shown in Fig. 32.2(a). The size distribution dependence reveals the existence of AuNPs of mainly 20 nm in size in fresh sol synthesized in uncharged polymer matrix. In 1 week, in addition to the well-expressed maximum characterizing the particles with diameter of 20 nm, the second maximum corresponding to the particles of 60–90 nm appears. It is evident that these particles are not numerous and correspond to the aggregates or nonspherical particles. In 2 months the presence of small nanoparticles of 4–7 nm in size and particles of 10–15 nm was registered in addition to the particles of 20 nm which were detected at once after synthesis.

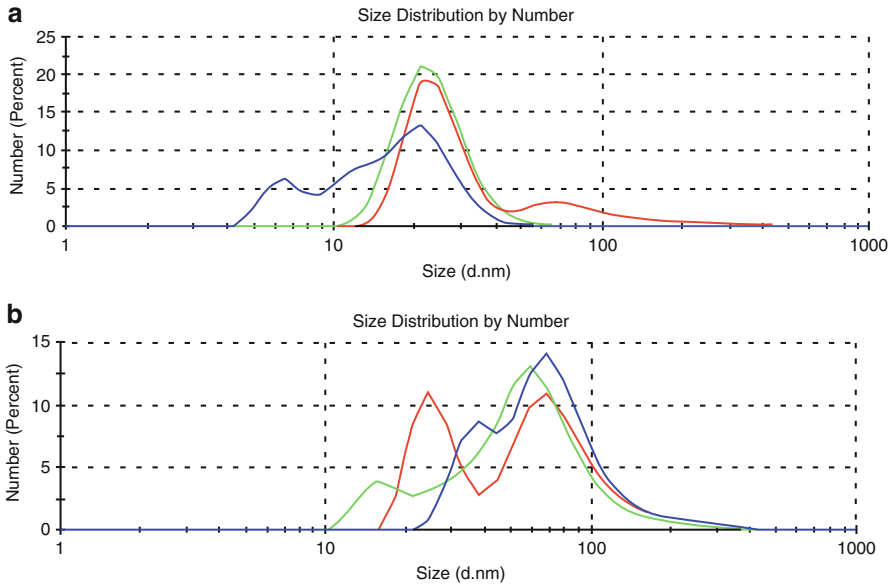

Fig. 32.1 Evolution in time of nanoparticle size in Au sols synthesized in D-g-PAA (**a**) and D-g-PAA(PE) (**b**) matrices. *Green line,* 1st day; *red line,* 8th day; *blue line,* 60th day

The size distribution for Au sols obtained in solutions of D-g-PAA(PE) matrix drastically differs from sols synthesized in the uncharged polymer (Fig. 32.1b). Just after synthesis, two well-expressed maxima corresponding to the nanoparticles of 12–18 nm and 60 nm are present. The second maximum can pertain to the aggregates. In 1 week, the nanosystem substantially changes. The significant increase in the size of small AuNPs (from 12–18 to 18–25 nm) was observed, and also the second maximum slightly shifted (from 60 to 70 nm).

In 2 months, the particles of 12–18 nm grew to 30–40 nm. The maximum, corresponding to particles or aggregates with a size of 30–40 nm, almost did not changed its position, but the amount of these particles increased (Fig. 32.1b, red curve).

TEM study confirmed the QELS data (Fig. 32.2). For nanosystems, synthesized in D-g-PAA matrix, the spherical nanoparticles and the presence of some aggregates were observed. Also, it is evident that sols contain mainly the AuNPs measuring 10–20 nm.

Gauss fitting results of size distribution function in time is shown in Table 32.1.

Nanocomposite photosensitizer used in the study was obtained by mixing chlorin e6 solution with Au sols. Examination of supernatant absorption spectra for the precipitated samples of chlorin e6/gold mixtures with a weight ratio 1:1 revealed the presence of unbound chlorin e6 (Fig. 32.3a). On the other hand, free chlorin e6 was not found in supernatants of the nanocomposite with weight ratio 1:10 (Fig. 32.3b), indicating complete chlorin e6 binding to nanoparticles.

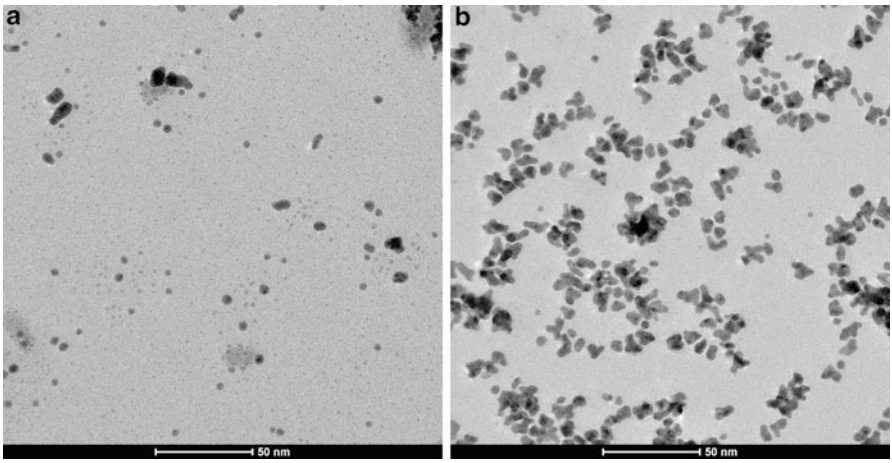

Fig. 32.2 TEM images of AuNPs in D-g-PAA (**a**) and D-g-PAA(PE) (**b**) matrices (2 months after synthesis)

It was established that such nanocomposite at light exposure ($\lambda = 658$ nm) produces singlet oxygen at a level, comparable to free chlorin e6 (Fig. 32.4).

Experiments in vitro on transformed human lymphocyte cell culture MT-4 showed that Au sol, prepared in charged polymer matrix, in contrast to prepared in D-g-PAA polymer, was toxic to cells down to the concentration 2.5 mkg/mL (Fig. 32.5).

Chlorin e6 nanocomposites with sols, containing 2.5 mkg/mL Au, exhibited no dark cytotoxicity. After laser irradiation, mortality of lymphocytes which were preincubated with the nanocomposite, based on charged polymer matrix, was almost twice higher than mortality of cells, incubated with free chlorin e6 in the same photosensitizer concentration, while composite obtained in uncharged polymer matrix showed photocytotoxicity, equal to that of the free chlorin e6 (Fig. 32.6). Thus, chlorin e6 complexation with gold nanoparticles in D-g-PAA (PE) matrix doubled the in vitro photodynamic activity of the photosensitizers—2.5 mkg/mL.

Enhanced photodynamic antitumor activity of the nanocomposite, based on charged polymer matrix, was confirmed in in vivo experiments on mice with transplanted Lewis lung carcinoma. On the 10th day after light exposure, the average tumor volume in animals which were treated with the nanocomposite was 1.5 times less than in the group of mice treated with free photosensitizer (Fig. 32.7).

For the last decades, various polymeric substances were more and more widely applied in biological research and medical practice. In particular, polymers are often utilized to stabilize metal (gold, silver) nanoparticles. In PDT, polymers are used to impart water solubility to hydrophobic photosensitizers, to make nanoparticles more biocompatible masking them from the immune system effectors and protecting them from elimination by the reticuloendothelial system.

Table 32.1 Size analysis of nano Au sols in time

Sample	Time (days)	D (nm)							
		Pick position at max. (nm)	FWHM	Pick position at max. (nm)	FWHM	Pick position at max. (nm)	FWHM	Pick position at max. (nm)	FWHM
D-g-PAA	1	–	–	–	–	24	11	72	52
	8	–	–	–	–	23	14	–	–
	60	7	5	13	8	22	20	–	–
D-g-PAA (PE)	1	–	–	–	–	25	12	71	45
	8	–	–	–	–	17	10	62	50
	60	–	–	–	–	35	10	71	50

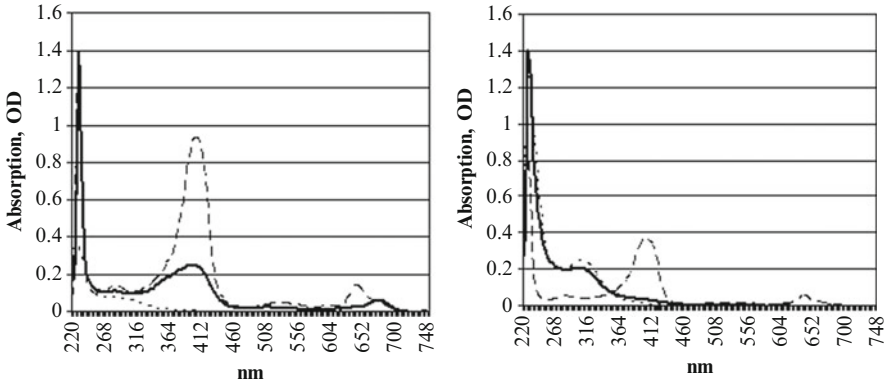

Fig. 32.3 Absorption spectra of chlorin e6 + Au sol supernatants and (Au sol prepared in charged polymer matrix). (**a**) Chlorin e6/Au mass ratio 1:1 (150:150 mkg/mL); (**b**) chlorin e6/Au mass ratio 1:10 (50:500 mkg/mL). *Solid line,* nanocomposite; *dashed line,* chlorin e6; *dotted line,* gold nanoparticles

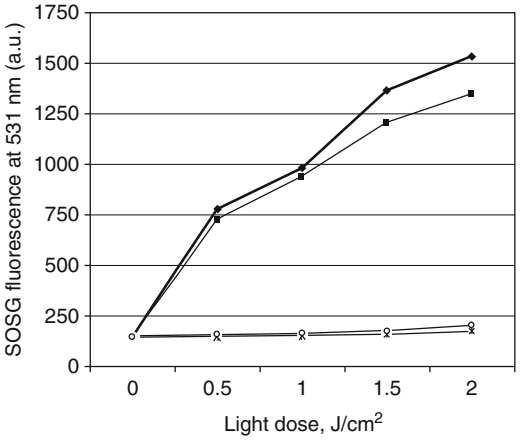

Fig. 32.4 Singlet oxygen generation by chlorin e6 and its nanocomposite after laser irradiation, $\lambda = 660$ nm (Au sol prepared in charged polymer matrix). (*filled diamond*), chlorin e6; (*filled square*), nanocomposite; (*asterisk*), gold nanoparticles; (*white circle*), copolymer

Among the most frequently employed polymeric agents is polyethylene glycol. Thus, Cheng Y. et al. created a highly efficient vector for rapid delivery to the tumor of composite phthalocyanine-based photosensitizer comprising gold nanoparticles and stabilized with polyethylene glycol [11]. An example of successful project in this vein is the antitumor drug CYT-6091, Cytimmune Sciences, Inc. (USA). It consists of gold nanoparticles functionalized with tumor necrosis factor and stabilized by thiolated polyethylene glycol [12]. The drug selectively accumulates in the tumor tissue. Currently it is undergoing clinical trials for the treatment of solid tumors.

In our previous work, to increase photosensitizer delivery to tumor cells, we devised and tested composites which were based on nanoscaled gold, stabilized by polyvinylpirrolidone. In one of the nanocomposites, hematoporphyrin was used as a

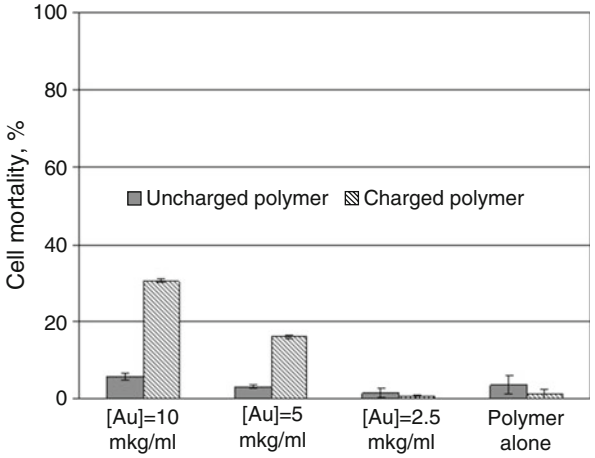

Fig. 32.5 Cytotoxicity of Au sols, prepared in uncharged and charged polymer matrices

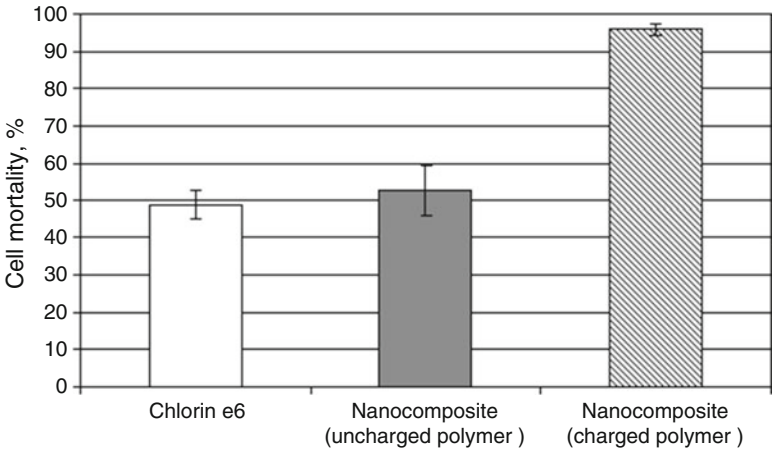

Fig. 32.6 Photocytotoxicity of chlorin e6 nanocomposites with Au sols, prepared in D-g-PAA (uncharged) and D-g-PAA(PE) (charged) polymer matrices. Chlorin e6 concentration in all probes, 0.25 mkg/mL; Au concentration in nanocomposites, 2.5 mkg/mL

photosensitizer [13] and in another—chlorin e6 [14]. Experiments on malignant cells in vitro and on mice bearing carcinomas showed higher photodynamic activity of the nanocomposites compared to free photosensitizers.

The composite photosensitizer presented in this work is of significant interest and deserves further thorough studies. On light exposure, it generates singlet oxygen (Fig. 32.4) which is considered to be the main tumor-damaging factor in PDT. Figure 32.6 shows that singlet oxygen production by the nanocomposite is slightly lower than with free chlorin e6. However, in experiments in vitro and in vivo nanocomposites, antitumor photodynamic activity proved to be much higher than activity of the free chlorin e6. A likely explanation lies in that the

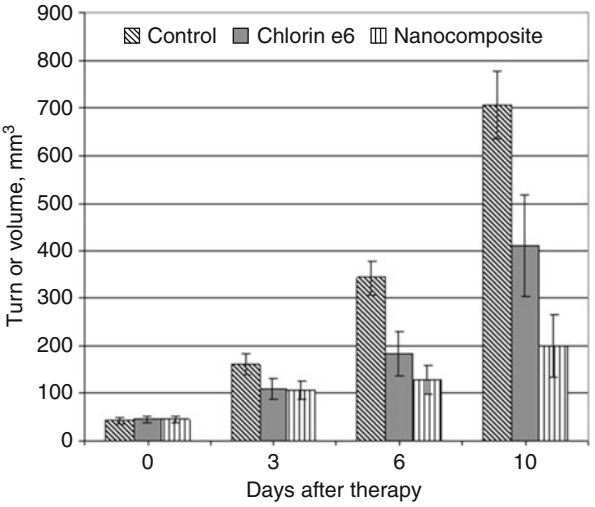

Fig. 32.7 Photodynamic therapy of Lewis lung carcinoma using chlorin e6 or its nanocomposite, based on D-g-PAA(PE) polymer matrix

nanocomposite delivers to tumor cells considerably more photosensitizer molecules than it takes place when the free chlorin e6 is administered.

In conclusion, we have created a composite photosensitizer consisting of gold nanoparticles in copolymer dextran-graft-polyacrylamide matrix and chlorin e6. In in vitro experiments on malignant cell line MT-4, the nanocomposite photosensitizer demonstrated twofold increase of photodynamic efficacy compared to the free photosensitizer. Significant antitumor photodynamic activity of the nanocomposite photosensitizer was confirmed in experiments on photodynamic therapy of Lewis lung carcinoma, transplanted into laboratory mice, that warrants the photosensitizer prospective preclinical studies.

Acknowledgments The work of N.F. Gamaleia and I.E. Shton was supported in part by the NATO SPS Programme Multi-Year Project No. 984702.

References

1. Huang Z (2005) A review of progress in clinical photodynamic therapy. Techno Cancer Res Treat 4:283–293. doi:10.1177/153303460500400308
2. Allison RR (2014) Photodynamic therapy: oncologic horizons. Future On col 10:123–124. doi:10.2217/fon.13.176
3. Agostinis P, Berg K, Cengel KA et al (2011) Photodynamic therapy of cancer: an update. CA Cancer J Clin 61:250–281. doi:10.3322/caac.20114
4. Chatterjee DK, Fong LS, Zhang Y (2008) Nanoparticles in photodynamic therapy: an emerging paradigm. Adv Drug Deliv Rev 60:1627–1637. doi:10.1016/j.addr.2008.08.003
5. Gamaleia NF, Shton IO (2015) Gold mining for PDT: great expectations from tiny nanoparticles. Photodiagnosis Photodyn Ther 12:221–231. doi:10.1016/j.pdpdt.2015.03.002

6. Kutsevol N, Bezugla T, Bezuglyi M, Rawiso M (2012) Branched Dextran-graft-polyacrylamide copolymers as perspective materials for nanotechnology. Macromol Symp 317–318 (1):82–90
7. Chumachenko V, Kutsevol N, Rawiso M et al (2014) In situ formation of silver nanoparticles in linear and branched polyelectrolyte matrices using various reducing agents. Nanoscale Res Lett 9:164. doi:10.1186/1556-276X-9-164
8. Kutsevol N, Bezuglyi M, Bezugla T, Rawiso M (2014) Star-like Dextran-graft-(polyacrylamide-co-polyacrylic acid) copolymers. Macromol Symp 335:12–16. doi:10.1002/masy.201200115
9. Kutsevol N, Guenet J-M, Melnik N et al (2006) Solution properties of dextran–polyacrylamide graft copolymers. Polymer (Guildf) 47:2061–2068. doi:10.1016/j.polymer.2006.01.024
10. Kutsevol NV, Chumachenko VA, Rawiso M et al (2015) Dextran-G-polyacrylamide star polymers: prospects of application in nanotechnology. J Struct Chem 56:1016–1023
11. Cheng Y, Samia AC, Meyers JD et al (2008) Highly efficient drug delivery with gold nanoparticle vectors for in vivo photodynamic therapy of cancer. J Am Chem Soc 130:10643–10647. doi:10.1021/ja801631c
12. Powell AC, Paciotti GF, Libutti SK (2010) Colloidal gold: a novel nanoparticle for targeted cancer therapeutics. Methods Mol Biol 624:375–384. doi:10.1007/978-1-60761-609-2_25
13. Gamaleia NF, Shishko ED, Dolinsky GA et al (2010) Photodynamic activity of hematoporphyrin conjugates with gold nanoparticles: experiments in vitro. Exp On col 32:44–47
14. Gamaleia NF, Shishko ED, Shton IA et al (2012) Photodynamic activity of second-generation sensitizers Fotolon (chlorin e6) and its gold nanocomposite: in vitro and in vivo studies. Photobiol Photomed 9:99–103 [In Ukrainian]

Chapter 33
Supercritical Water as Nanomedium for Gasification of Lignite–Water Suspension

Raisa Korzh and Valerii Bortyshevskyi

33.1 Introduction

The traditional processes of steam gasification of raw coal response by a general scheme:

$$C_xH_yS_nN_mO_z + H_2O \rightarrow H_2 + CO + CO_2 + \ldots \quad (33.1)$$

The gasification of the aqueous suspensions of coal feedstock under the supercritical water conditions is dramatically different from the steam gasification (Table 33.1). Thus, the temperature of the supercritical conversion is twice lower than the corresponding figures for the steam process, and the pressure is higher in order. Nothing differs more from the superheated steam as a reaction medium than supercritical fluid, although represented by the same agent—water.

When water is heated above 170 °C, the net of hydrogen bonds of 150–200 molecules is destroyed and formed "flickering" system of water clusters with from one to five molecules of water [1, 2]. It was shown by the method of molecular dynamics that in the subcritical temperature region, three molecule clusters dominate over the unbound molecules (Fig. 33.1). The last ones are dominated in the supercritical region of water state (up to 75 %). In turn, this transformation of the reactive medium provides changing of the distribution of formed products. The synthesis gas dominated product of steam gasification. We have shown that the products of the supercritical gasification of lignite have no carbon monoxide within detection up to a temperature of 500 °C (see Table 33.1).

R. Korzh (✉) • V. Bortyshevskyi
Institute of Bioorganic Chemistry and Petrochemistry of National Academy of Sciences of Ukraine, 1, Murmanska str., Kyiv 02094, Ukraine
e-mail: korzh.rw@gmail.com

O. Fesenko, L. Yatsenko (eds.), *Nanophysics, Nanophotonics, Surface Studies, and Applications*, Springer Proceedings in Physics 183,
DOI 10.1007/978-3-319-30737-4_33

Table 33.1 The comparison of the supercritical and steam gasification of coal

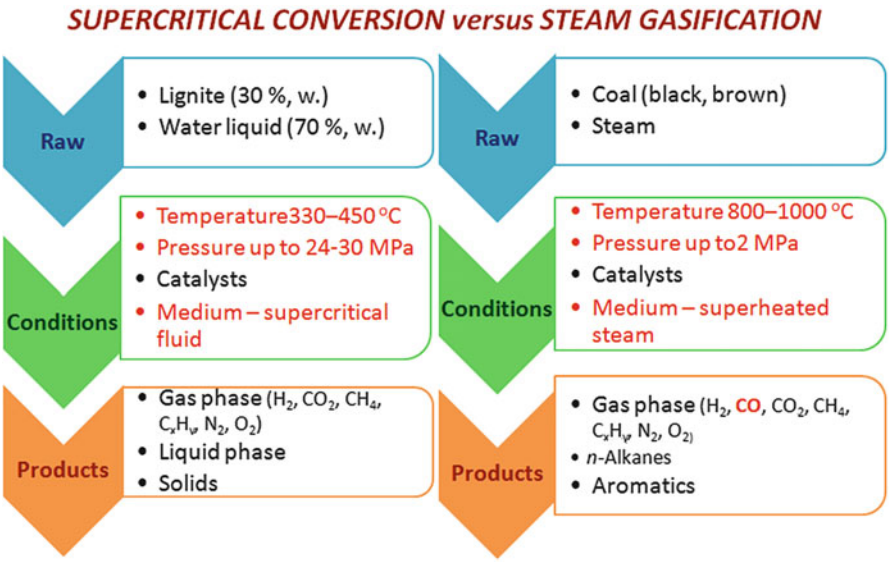

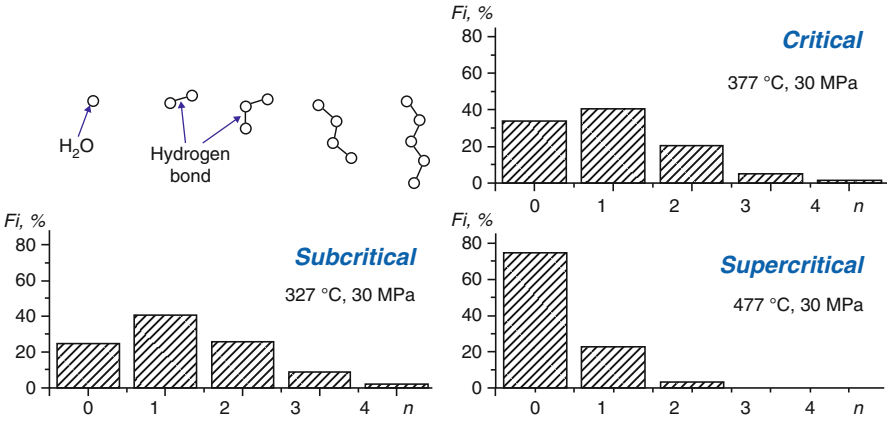

Fig. 33.1 The distribution of hydrogen bonds for the supercritical water (by [2])

These changes of conditions, medium, and products of the supercritical gasification are caused by the changes of the mechanism of coal converting. The aim of the work was to clear the general scheme of the mechanism gasification of coal–water slurry under the supercritical conditions by water. The primary problem was faced while assessing the impact of supercritical water properties on the transformation of organic matter of lignite.

33.2 Materials and Methods

The catalytic gasification of coal–water slurry was studied under the supercritical water conditions at the facility presented in schematic diagram in Table 33.2. The technological conditions of the research are summarized. More details are in [3, 4]. The main evaluated parameter was the initial rate of the formation of three major gaseous products such as hydrogen, carbon dioxide, and methane.

33.3 Results and Discussion

33.3.1 Supercritical Gasification

The dry lignite of Alexandria deposit (Ukraine) has the general formula $C_{3.785}H_{2.175}S_{0.112}N_{0.051}O_{1.151}$. When it is the part of the aqueous suspension, it starts to gasify under the pressure of 24 MPa without the addition of catalysts at 260 °C (Table 33.3). The process of the gasification of the aqueous suspension of lignite involves its interaction with water under the simplified scheme:

$$C_{3.785}H_{2.175}S_{0.112}N_{0.051}O_{1.151} + H_2O \rightarrow H_2 + CH_4 + CO_2 + \ldots \quad (33.2)$$

Table 33.2 The conditions of the supercritical gasification of lignite aqueous suspension

Parameter		Supercritical gasification [3, 4]	Facility scheme
Raw		Lignite (30 %, mass.)	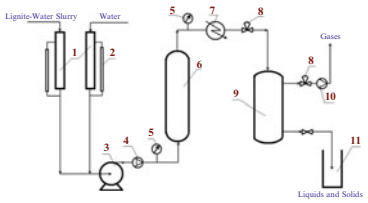
		Water (70 %, mass.)	
Conditions	Temperature, °C	330–450	
	Pressure, MPa	24–30	
	Catalysts	NaOH, $Ca(OH)_2$, $NiO\text{-}MoO_3\text{-}Al_2O_3$ (ANM)	
	Media	Supercritical fluid	
Products	Gaseous phase	H_2, CO_2,CH_4, C_xH_y, N_2, O_2	1—feedstock reservoirs; 2—level meter; 3—high pressure pump; 4—back valve; 5—manometers; 6—reactor; 7—condenser; 8—pressure regulator; 9—separator; 10—gas meter; 11—reservoir for liquid and solids
	Other products	Liquids: organics + water soluble compounds (oxygenates and inorganics)	
		solids	

Table 33.3 The experimental results of the gasification of lignite aqueous suspension under the supercritical conditions

Catalyst	T, °C	Initial rate of gas formation, mg/h		
		CO_2	CH_4	H_2
Without catalyst	270	37.34	0.338	0.0376
	290	35.73	0.575	0.044
	330	76.47	2.7	0.214
	450	66.1	9.89	4.3
NiO–MoO_3–Al_2O_3 (AMN 10 % to coal)	330	78.06	2.856	0.38
	390	30.57	6.695	1.6
	450	15.416	18.843	3.1
NaOH (5 % to coal)	330	16.19	0.828	0.172
	390	56.44	3.017	2.17
	450	68.07	26.663	4.905
$Ca(OH)_2$ (10 % to coal)	330	41.986	2.742	1.006
	390	66.873	8.975	2.153
	450	201.56	95.727	20.442

The resulting product is divided into three phases: gas, liquid, and sludge [3]. The main gaseous products are hydrogen (volume fraction of 30–50 %), methane (15–20), carbon dioxide (40–60), nitrogen (up to 5), and light hydrocarbons (up to 5). The gasification is accelerated in the temperature range of 300–350 °C, which is considered as subcritical according to [1]. Notable rate of formation of carbon dioxide, methane, and hydrogen can be achieved under supercritical temperatures above 400 °C. The addition to the reaction mixture of mineral acid catalysts and alkaline nature increases the rate of formation of hydrogen, methane, and carbon dioxide with maximum values for calcium hydroxide (Table 33.3).

33.3.2 Origin of Elements

Analysis of the gas distribution and at the same time the carbon conversion at the initial rate registration and the assumption of proportional transformation of raw coal allow determining the origin of oxygen and hydrogen in the products of the supercritical process (Fig. 33.2). Oxygen balance calculation indicates that for the subcritical temperatures below 370 °C, about 83 % oxygen passes in the gas phase from water or mineral part and only 17 % from coal. For the supercritical temperature, oxygen of inorganic origin is reduced to 63 %, but oxygen of coal origin is increased to 37 %.

According to the calculations, the own hydrogen of coal is enough for the formation of all the hydrogen gas phase at the subcritical temperature from the organic mass of coal. When operating the process at the supercritical temperature,

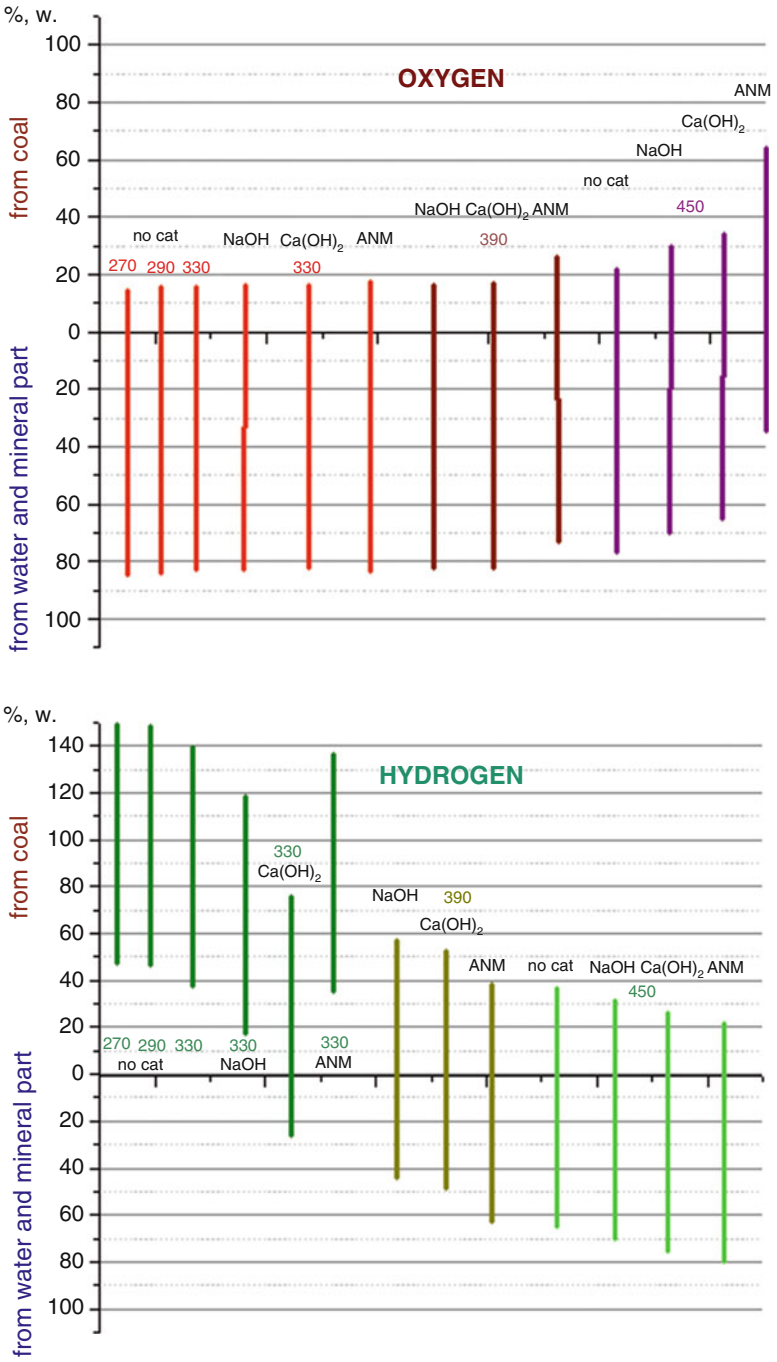

Fig. 33.2 The origination of oxygen and hydrogen in gaseous products of the supercritical gasification of lignite aqueous suspension

the own hydrogen of converted coal is not enough to form hydrogen of gas phase. So 70 % of the gaseous hydrogen is produced from water and mineral parts.

Combining the two graphs from Fig. 33.2 shows the trend of the system of "brown coal–water–mineral substance" to the inversion. In the first approximation, the carbon of lignite at the subcritical temperature behaves like an acid, and water is like a basis; under the supercritical temperature, they switch their roles.

33.3.3 The Influence of Reactive Medium

Special attention attracts the influence of the supercritical water medium and the mineral part of lignite to the coal conversion. The indicative result was no transformation in the conversion by the supercritical water pure carbon materials like graphite at temperatures ranging from 300 to 500 °C. Only when the organic, mineral, and water components are combined at the supercritical pressure, the carbon is gasified. It allows us to predict the effect of mutual stimulation (or inter amplification) of reagents in the supercritical conversion.

It was above mentioned that the structure of the supercritical water fluid is a dynamic net of clusters from one to five molecules. Our rough calculation estimates that the size of water clusters varies in the range of 1–3 nm (Fig. 33.3a). So the sub- and supercritical fluid could be considered as nanoscale medium for carbon conversion. Actually, it is nanoscale water what initiates coal gasification. The nanoscale clusters of the supercritical water interact with both the organic and mineral substances of lignite. Particularly, water reacts with organic matter by the formation of dipole-inductive and dipole-dispersive associates. Water and mineral matter produce ion-inductive interactions with the formation of nanoscale ion associates (Fig. 33.3b; e.g., calcium ion pair from [5]). In our view, the formed nanoscale associates are responsible for the further transformation of organic and mineral parts of lignite in the supercritical medium.

Macroscopic display of the formation of ion pairs is falling of the conductivity of electrolyte solutions. We experimentally showed that with the transition from 300 to 450 °C under the supercritical pressure, the intensity of current through

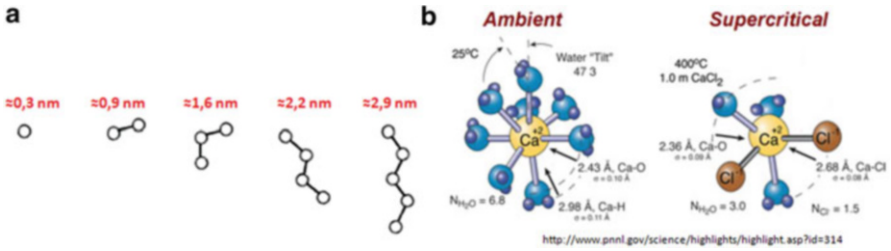

Fig. 33.3 (a) Nanosizes of the supercritical water clusters. (**b**) The contact-ion pair of $CaCl_2$ by XAFS. Adopted from [5]

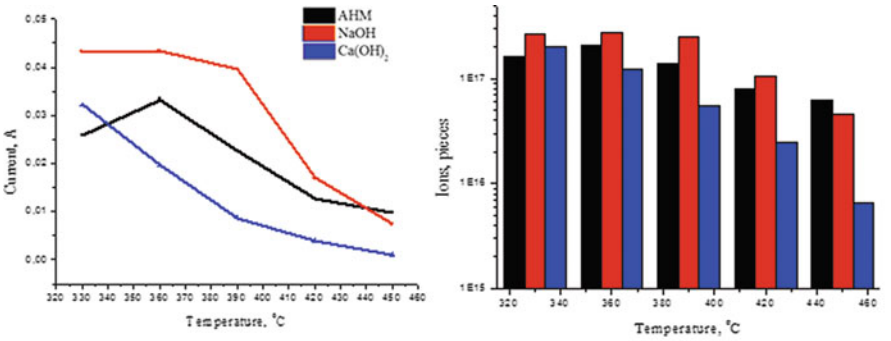

Catalyst	ANM	NaOH	$Ca(OH)_2$
Decreasing of charges amount, from 330 to 450 C degrees, times	2,6	6	30
Increasing of amount of ionic pairs , from 330 to 450 C degrees , on %	61,84	83,11	96,75

Fig. 33.4 Electric conductivity of lignite aqueous suspension under the supercritical pressure while gasification processing and the calculations of number of ion pairs formed

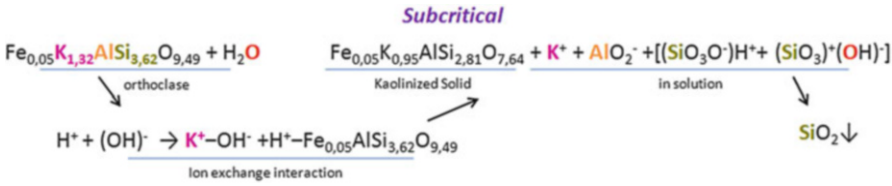

Scheme 33.1 The reaction of orthoclase with the subcritical water

lignite–water suspension decreased from 0.045 to 0.003 A (Fig. 33.4). Current strength could be scaled to the quantity of charges. It was demonstrated that the number of charges was reduced 2.5 times for the lignite gasification in the presence of $NiO–MoO_3–Al_2O_3$ (AMN), 6 times for NaOH, and 30 times for $Ca(OH)_2$. It may indirectly indicate that at 450 °C from 60 to 96 % of carriers are transformed to the state of ion associates.

The process of the transformation of mineral substances in the supercritical water was separately investigated by the example of orthoclase feldspar. It was shown that orthoclase reacts with the nanoscale supercritical water with the precipitation of solid kaolinized phase and the saturation of the solution by-products of dissociation. In particular, at subcritical temperature, the potassium cations and aluminate anions with unstable silicon hydroxides pass from orthoclase solid into solution (Scheme 33.1). They form nanoscale ion associates which could accelerate the coal gasification. At the supercritical temperature, iron cations are also included to the ion exchange following the redox transition and formation of flaky sediment (Scheme 33.2).

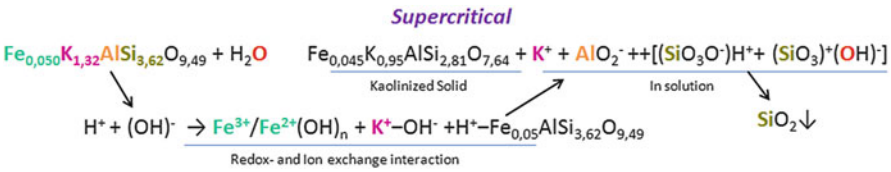

Scheme 33.2 The reaction of orthoclase with the supercritical water

Table 33.4 The scheme of the subcritical lignite–water slurry gasification

SUBCRITICAL CONVERSION

HYDROGEN	1) 100 % from coal	OXYGEN	2) 17 % from coal
			3) 83 % from water + mineral

I	1+2	$C_{3,29}H_{1,89}O \rightarrow H_2\uparrow + CO_2\uparrow$	17 %
II	1+3	$C_{3,29}H_{1,89}O + H_2O$ [mineralized] $\rightarrow H_2\uparrow + CO_2\uparrow + CH_4\uparrow$	83 %
III		$Fe_{0,05}K_{1,32}AlSi_{3,62}O_{9,49} + H_2O \rightarrow Fe_{0,05}K_{0,95}AlSi_{2,81}O_{7,64} + K^+ + AlO_2^- + Si(OH)_4$	

Solid Solute

$SiO_2\downarrow$

33.3.4 *General Scheme of Lignite Gasification in Supercritical Water*

Compiled data from 3.2 and 3.3 allows proposing the general scheme of the mechanism of the conversion of lignite–water slurry under the supercritical pressure. Thus, there are two types of interactions at the subcritical temperatures (Table 33.4): (**I**) a reaction in which hydrogen comes from coal and oxygen comes from coal (1 + 2) and (**II**) the reaction of the involvement of hydrogen from carbon and oxygen from nanoscale mineralized water (1 + 3). The probability of their occurrence is estimated at 17/83. In the first place (or at the same time), compounds of alkali and alkaline earth metals of coal mineral part are dissolved for the formation of nanoscale ion associates by Scheme 33.2.

Operating at the supercritical temperature mode extends the matrix of the sources of hydrogen by nanoscale mineralized water (Table 33.5). Thus, the first and second types of interactions described above are stored. The scheme of gasification (Table 33.4) is added by an interaction (**III**) hydrogen from nanoscale mineralized water and oxygen from coal (2 + 3) and (**IV**) both hydrogen and oxygen from nanoscale mineralized water (2 + 4). Interaction **III** leads to the formation of water, and so we take it in parentheses. Probability of **I**, **II**, and **IV** reactions is

Table 33.5 The scheme of the supercritical lignite–water slurry gasification

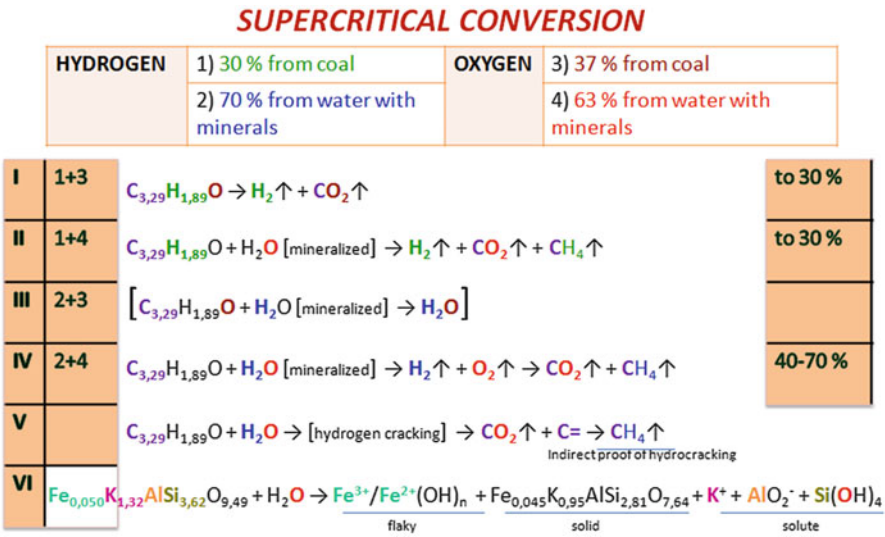

Highlights

- Supercritical water is a nanoscale medium of the gasification of lignite–water suspension for hydrogen and methane production
- Supercritical water with ion associates of lignite minerals is a source of hydrogen and oxygen
- Alkaline catalysts enhance the yield of hydrogen from water
- Acid catalysts accelerate the yield of oxygen from coal

estimated at 30, 30, and 40 %. The scheme also involved the reaction of coal hydrocracking **V**. The indirect evidence of hydrocracking is the catalytic function of the aluminosilicate-based mineral substance and formed methane as a product. Ion-exchange interaction of mineral water **VI** is extended by dissolving and reducing transition metal compounds.

33.4 Conclusions

Comprehensive experimental investigation of the gasification of lignite–water slurry under the supercritical pressure shows the mutually stimulating interaction of the components of the system "brown coal–water–mineral matter" due to the influence of nanoscale water medium on the formation of dipole-inductive, dispersive, and ionic associates. Oxygen source for the gaseous products of the lignite supercritical conversion in the temperature range 300–450 °C is mainly ion-associative nanoclustered water. The source of hydrogen for the subcritical temperature is an organic part of lignite and for the supercritical temperature is the

nanoscale medium with ion associates. Addition of acid–base catalyst accelerates the formation of hydrogen and methane. The acid catalysts under supercritical temperature twice more attracted to convert oxygen of organic part of lignite. The alkaline catalysts enhance the transition to the gas phase of hydrogen from nanoclustered supercritical water and mineral part of lignite.

Acknowledgments This work has been funded by Target Complex Program of Scientific Research of NAS of Ukraine "Biomass as a fuel" ("Biofuels"), project 24, 2009–2012.

References

1. Kruse A, Dinjus E (2007) Hot compressed water as reaction medium and reactant. Properties and synthesis reactions. J Supercrit Fluids 39:362–380
2. Gurina DL, Abakumova NA, Antipova ML, Petrenko VE (2010) Hydrogen bonds in sub- and supercritical water near the saturation curve: topological aspect. Vestnik TGTU 16(4):848–857
3. Korzh RV, Bortyshevskyi VA (2014) Conversion of carbonic raw material under the supercritical conditions. Perspectives for fuel and fine chemicals production, VIIth Intern. scientific-technical conf. "Advance in petroleum and gas industry and petrochemistry" (APGIP-7), Ukraine, Lvi'v, 2014, 19–24 May, pp 32–35.
4. Korzh RV, Bortyshevskyi VA, Burdeynyi VG (2012) Catalytic gasification of coal-water suspension under the supercritical conditions. Catalysis and Petrochemistry (Kataliz i neftechimia) 21:63–69
5. Fulton JL, Chen Y, Heald SM, Balasubramanian M (2004) High-pressure, high-temperature x-ray absorption fine structure transmission cell for the study of aqueous ions with low absorption-edge energies. Rev Sci Instrum 75(12):5228–5231. doi:10.1063/1.1813131

Chapter 34
Coding of Amino Acids by Nucleotides: Consideration of the Problem from the Viewpoint of Physics of Proteins

L.V. Shmeleva and A.D. Suprun

34.1 Introduction

Since the times of G. Gamow and F. Watson [1, 2], the problem of amino acid sequence coding of proteins[1] is traditionally considered from the viewpoint of nucleic acids. According to this consideration all the amino acids are considered as equal. It means that the primary structure of proteins is taken into account in the problem of nucleoprotein accordance only. It could be mentioned that above the primary level, there are three additional levels of protein structure: secondary, tertiary, and quaternary. The last two of these are of functional nature, and the first two provide the proper functioning of proteins by means of the amino acid sequence. The main idea of traditional consideration is that the amino acids are coded in RNA by a three-positional codon, every position of which can be occupied by one of four nucleotides: adenine (A), guanine (G), cytosine (C), and uracil (U).[2] The results of such a traditional consideration were eventually summarized [3–5] in the so-called canonical[3] table of the codes and amino acid correspondence (Table 34.1). This table has been formed based predominantly on experimental studies with *Escherichia coli*.

As for the higher organisms, a number of questions still remain unclear [6]. It was observed, for example, that the UGA codon could be meaningful for the higher organisms. It is still unclear why during the RNA formation within the transcription

[1] Actually the sequence of 19 amino acids and 1 imino acid proline.

[2] DNA contains thymine (T) instead of uracil (U).

[3] Such a code compliance is sometimes also called the standard.

L.V. Shmeleva (✉) • A.D. Suprun
Departments of Theoretical Physics, Faculty of Physics, Taras Shevchenko National University of Kyiv, Volodymyrska Street, 64/13, Kyiv 01601, Ukraine
e-mail: LShmel@univ.kiev.ua

O. Fesenko, L. Yatsenko (eds.), *Nanophysics, Nanophotonics, Surface Studies, and Applications*, Springer Proceedings in Physics 183,
DOI 10.1007/978-3-319-30737-4_34

Table 34.1 Genetic RNA code for amino acids and proline

"First" letter	"Second" letter								"Third" letter
	U		C		A		G		
U	UUU	Phe	UCU	Ser	UAU	Tyr	UGU	Cys	U
	UUC	Phe	UCC	Ser	UAC	Tyr	UGC	Cys	C
	UUA	Leu	UCA	Ser	UAA	Stop synthesis	UGA	Stop synthesis	A
	UUG[a]	Leu	UCG	Ser	UAG		UGG	Trp	G
C	CUU	Leu	CCU	Pro	CAU	His	CGU	Arg	U
	CUC	Leu	CCC	Pro	CAC	His	CGC	Arg	C
	CUA	Leu	CCA	Pro	CAA	Gln	CGA	Arg	A
	CUG	Leu	CCG	Pro	CAG	Gln	CGG	Arg	G
A	AUU	Ile	ACU	Thr	AAU	Asn	AGU	Ser	U
	AUC	Ile	ACC	Thr	AAC	Asn	AGC	Ser	C
	AUA	Ile	ACA	Thr	AAA	Lys	AGA	Arg	A
	AUG[a]	Met	ACG	Thr	AAG	Lys	AGG	Arg	G
G	GUU	Val	GCU	Ala	GAU	Aspartic acid	GGU	Gly	U
	GUC	Val	GCC	Ala	GAC		GGC	Gly	C
	GUA	Val	GCA	Ala	GAA	Glutimic acid	GGA	Gly	A
	GUG[a]	Val		Ala			GGG	Gly	G

[a]Indicates codons that determine the start of protein (polypeptide) chain synthesis

process thymine (T) is replaced by uracil (U). If based on the equality of amino acids, then what explains the expressed unevenness of coding, when some amino acids have only one codon (according to Table 34.1 this is methionine and tryptophan), but other amino acids have six codons (leucine and serine)? The traditional view of the coding cannot explain this discrepancy.

But, oddly enough, in the main, that is not quite clear: it is the role of DNA in the coding of genetic information. Indeed, if for storage of protein information in RNA molecules it is enough to have a simple one-dimensional nucleotide chain, then what is the sense of having two parallel nucleotide chains in DNA molecules, one of which is complementary to another standard canonical one? Mention can be found in recent studies [7, 8] of the critical importance of having just the first two nucleotides in the nucleotide sequence of a three-positional codon for the identification of organic acids of a protein. The third nucleotide is less important, and in many cases it can be of any sort; that is, in fact, it is not specific. In Table 34.1 this property of accordance, code, the amino acid is easily visible.

These questions and a number of other issues could remain without answer within the framework of a conventional approach to the coding problem,[4] if the proteins are not included as an active component that improves understanding of the issue.

[4] Only from the viewpoint of nucleic acids considering all the amino acids and the imino acid proline as equal.

34.2 Materials, Methods, Results and Discussions

In this chapter we attempt to consider the problem of coding in terms of physical and structural properties of amino acids. For this purpose, some of these properties should be kept in mind [9, 10].

Radicals of all 19 amino acids could be divided into three groups:

1. Electrically neutral (seven in total): glycine, alanine, valine, leucine, isoleucine, phenylalanine, and methionine. Further, they will sometimes be marked with the prefix "(0)" after their name.
2. Polar (six in total, have stationary dipole moment): cysteine, serine, threonine, asparagine, glutamine, and tryptophan. This group will be marked with the prefix "(→)."
3. Charge neutral[5] (six in total): among which three amino acids could be negatively charged (acid) aspartic acid, glutamic acid, and tyrosine and three positively charged (alkaline) arginine, lysine, and histidine. They will be marked with the prefix "(−)" or "(+)," respectively.

Protein molecules instead of amino acids might contain the imino acid proline, which could be referred to the first group (electrically neutral).

A feature of all 20 acids in the protein is that at the level of the primary structure, to which the traditional approach appeals, they do look similar. However, beginning from the secondary structure, the situation is significantly different; it becomes clear that organic acids differ from each other not only by the physical properties of the radical groups mentioned above but also by their influence on proper formation at all higher structural levels of the protein molecule: secondary, tertiary, and quaternary. Furthermore, thorough analyses of the higher structural levels demonstrate that there are acids, the positions of which in the primary structure must be strictly fixed; any sort of mistake can lead to altering of the function (most often to the loss or impairment of functional status). And there are acids, the mutual replacement of which will pass practically unnoticed. It reflects a different significance (or different status) of organic acids for the protein molecule.

In Table 34.2 all 19 amino acids and 1 imino acid are presented in the decreasing order of their conditional significance. The accepted priorities are the following: organic acids that influence the proper dislocation and the length of the secondary structure regions (α-spirals, β-forms, unstructured sites) are considered as the most significant. These are the first of five organic acids: proline(0), glycine(0), aspartic acid(−), arginine(+), and serine(→). They are referred to as the most significant inasmuch as the mistake of their dislocation at the primary structural level[6] could be fatal for the protein molecule viability (i.e., functioning).

The following priority belongs to the only amino acid, cysteine (→). It fixes a certain mutual dislocation within the space of the secondary structural regions.

[5] Can be either neutral or charged. Sometimes they are referred to as a polar group.

[6] Appearance in the "wrong" place or even its absence.

Table 34.2 Structural-functional properties of amino acids and proline

No	Amino acid	Structural-functional property
1	*Proline*(0) [−0.57 e]	Disrupts secondary structures
2	*Glycine*(0)	Together with aspartic acid or arginine or serine disrupts secondary structures
3	*Aspartic acid*(−)	Together with glycine disrupts secondary structures
		Fixes quaternary structures with salt bridges
4	*Argenine*(+)	Together with glycine disrupts secondary structures
		Fixes quaternary structures with salt bridges
5	*Serine*(→)	Together with glycine disrupts secondary structures
6	*Cysteine*(→) [+1e]	Fixes tertiary structure with disulfide bridges
		Regulates average-oxygenic electronic structure
7	*Methionine* (0) [+0.75e]	Regulates average-oxygenic electronic structure
8	*Phenylalanine* (0) [−0.91e]	Regulates average-oxygenic electronic structure
9	*Tryptophan*(→) [−1e]	Regulates average-oxygenic electronic structure
10	*Tyrosine*(−) [−0.83e]	Fixes quaternary structures with salt bridges
		Regulates average-oxygenic electronic structure
11	*Histidine*(+) [−0.7e]	Fixes quaternary structures with salt bridges
		Regulates average-oxygenic electronic structure
12	*Glutamic acid*(−)	Fixes quaternary structures with salt bridges
13	*Lysine*(+)	Fixes quaternary structures with salt bridges
14	Alanine(0)	–
15	Valine(0)	–
16	Leucine(0)	–
17	Isoleucine(0)	–
18	Threonine(→)	–
19	Glutamine(→)	–
20	Asparagine(→)	–

The first 13 organic acids are significant, and the remaining 7 are statisticians

Strictly speaking, mistakes of its dislocation at the primary structural level are almost as fatal as those of the first five amino acids mentioned above. But in the case of cysteine's mistake (meaning only its occurrence in the wrong place), the probability of preserved functionality is a bit higher.

The next ones are methionine(0), phenylalanine(0), and tryptophan(→), which are noted in Table 34.2 as the regulators of the average oxygen electronic structure of the protein molecule. It needs some explanation, but in advance it should be noted that cysteine (→), tyrosine(−), and histidine(+) also have the same regulatory properties (in total six amino acids). This regulating function is related to the fact that all the amino acid residues, except the six mentioned above, have nearly oxygenic configuration (on average, eight electrons per heavy atom) with a slight deviation to decreasing (i.e., charge deficiency). And only those six have abnormally significant

deviations, with two amino acids—cysteine (→) and methionine(0)—which not only have significant but positive deviations (i.e., charge excess).[7] Regulatory effects of these six amino acids are provided, according to some evidence, by their occurrence at certain primary structure places or sites resulting in supporting an average electronic configuration of the whole protein molecule or, probably, its moieties, at a level close or even equal to the average oxygenic level. Some role of ribosome might be supposed in this regulating process.

The following amino acids in the adopted priority are tyrosine(−) and histidine (+); they fix the quaternary structure of the protein molecules. However, first, not all the protein molecules have a quaternary structure, and second, possible mistakes are ensured here by aspartic acid(−) and arginine(+) from the first five amino acid group and also by glutamic acid(−) and lysine(+) (Table 34.2).

Further there are glutamic acid(−) and lysine(+). They provide fixing quaternary structures; on the other hand, there is no necessity to mark them as significant as they seem to play some static role for aspartic acid(−), tyrosine(−), arginine(+), and histidine(+). Regarding this they should be considered as statisticians.

The last seven amino acids—alanine(0), valine(0), leucine(0), isoleucine(0), threonine(→), asparagine(→), and glutamine(→)—are typical statisticians. To date there is no evidence concerning their structural-functional significance. Their only function (common to all organic acids) is to be a building material for the protein molecule. It is obvious that all the statisticians play their role only in relation to each other and to the significant amino acids with similar physical properties (neutral in relation to neutral one etc.).

Thus, there are eleven structurally significant organic acids and nine statisticians.

The question arises as to whether this differentiation of amino acids is reflected in the genetic code.

Genetic information for the protein structure is considered to be coded in DNA molecules in the form of the long sequence of pairs of nucleotides. In the DNA molecule are used four types of nucleotides: adenine (A), thymine (T), guanine (G), and cytosine (C). Transcribing the information from DNA results in synthesis of the molecules of informational-matrix RNA in which, first, thymine (T) is replaced with uracil (U), and second, these molecules consist of the simple sequences of nucleotides, not of nucleotide pairs as in DNA. According to Gamov, as mentioned above, in RNA a three-positional codon is used, every position of which might have four meanings (A, G, C, U). Such a type of codon is capable of coding 64 amino acids. It is not too difficult to calculate that on average there must be three codons for every amino acid (with four reserved codons).

Table 34.1, built in conformity with the presented view, reflects deviation from the mean values of three codons for one acid without any explanation. Considering Table 34.1 from the point of structural significance analyses for the different amino acids, presented in Table 34.2, it could be noticed that, for instance, imino acid

[7] Proline(0) has a special place here. Its deficit charge is large enough, but the order of its magnitude is almost identical to the average deficit for all 17 "negative" amino acids.

proline(0) is supplied with four different codons. It exceeded mean value "three codons per one organic acid" and in fact indicates the "increased attention" to this acid from the side of genetic code. The same concerns amino acids glycine(0) and arginine(+): they are also supplied with four codons. As to serine (→) and aspartic acid(−)—two other acids that follow glycine(0)—there is a certain abnormality, aspartic acid(−) that is only supplied with two codons, and serine(→)—with six codons. Although in terms of structural significance of these two amino acids for the proteins it should be the opposite. It should be noted also that six codons (twofold as much as mean value) for aspartic acid(−) is too much as well. Such abnormality for serine might mean either an experimental mistake or another significance of serine(→) for proteins in addition to that discussed above. The abnormality for aspartic acid (−) decreases significant amino acid to the rank of statisticians. Thorough comparing of analyses in Tables 34.1 and 34.2 provides other similar abnormalities.[8]

When the DNA molecule is considered as an ordinary polymer of one-dimensional crystal type with the complex elementary cell comprising two nucleotides (two molecules in terms of solid-state physics), this pair of nucleotides during DNA synthesis is known to be located at the cross-direction of the polymerizing process. That's why DNA molecules look like two nucleotide chains, linked complementarily, that is, so that in the pair that forms the separate elementary cell, adenine (A) is always linked with thymine (T) or guanine (G) is linked with cytosine (C).[9] Consequently, from the point of considering the DNA molecule as a one-dimensional molecular crystal, all the unit cells consist only of two randomly located linked pairs of nucleotides: AT or GC.

This leads to the idea that pairs of AT and GC could be considered with two possible meanings—1 and 0—of some informational variable that could be called the major one. For the certainty of further consideration let's assume that pair GC corresponds to the meaning 0, and the pair of AT to the meaning 1. As the three-positional codon currently is commonly accepted, then while determining the codon in the DNA molecule, we also use the definition of a three-positional structure, but not for the individual nucleotides as in RNA, but for their pairs: AT or GC.

This raises the problem: each of three positions of such a codon can have just two but not four meanings (GC ≡ 0 or AT ≡ 1). It is not difficult to calculate that in such a case there could only be eight different situations, which is not enough for the identification of 20 amino acids. On the other hand, it could be quite enough for the identification not of the isolated acids but their groups[10] or structurally the most significant acids.[11]

[8] For instance, the typical statistician leucine for some reason also has six codes.

[9] Such selectivity might suggest that the formation of these pairs could be the primary polarizing process on the whole.

[10] The maximum number of groups—4: polar, electrically neutral and two charge-neutral.

[11] The minimal number of significant acids is also four: proline(0), glycine(0), cysteine(→) and any of the three amino acids accompanying glycine(0). They are: aspartic acid (−), arginine (+), or serine (→).

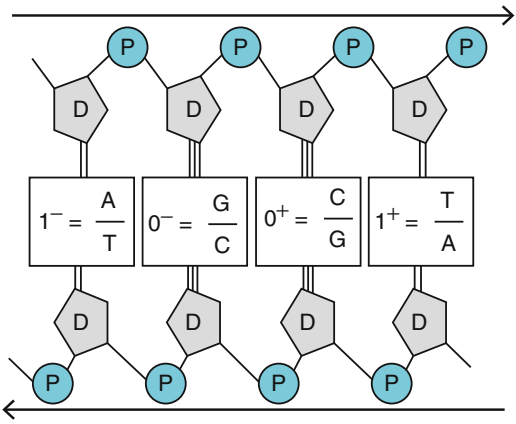

Fig. 34.1 Illustration of the markings $1^{\pm}$, $0^{\pm}$ on the schematic structure of DNA. *P* phosphoric acid residue, *D* deoxyribose

Increasing the number of coding combinations in the case of DNA could be linked with the fact that both pairs in the DNA molecule might be in two different "polarizations": pair GC might have "polarizing" CG, and pair AT, "polarizing" TA. Therefore each of the two meanings of the major informational variable also forms an informational variable. It could be called a polarizing variable and its meanings differentiated with the signs "+" and "−". It means that every position (informational cell) of the considered herein three-positional DNA codon might not have just two meanings, 0 and 1, but as in RNA molecules four: 0^-, 0^+, 1^-, 1^+. It is understood that the number of different codes will be equal to those of RNA: 64.

By accepting such a way of reading the coding letter in DNA we should logically come to the question of what the meaning is of Table 34.1, namely in terms of such manner of coding in DNA. For this purpose, first of all, all the codes of this table should be written with the replacement of uracil (U) by thymine (T). For instance, one of the codes, UCA, which relates to serine, with this replacement is transformed into TCA. After that, in conformity with the complementary principle, there should be formed the triplet of nucleotide pairs. In the considered example this would look like: $\frac{\mathbf{A}}{\mathbf{T}}\frac{\mathbf{G}}{\mathbf{C}}\frac{\mathbf{T}}{\mathbf{A}}$. The bold type in this triplet is used to mark the nucleotide sequence taken from Table 34.1. If one agrees with those presented in Fig. 34.1: then the serine in DNA would respond to the mark 1^- 0^- 1^+, and Table 34.1 could transform into Table 34.3.

Even a quick look at this table would be enough to notice the presence of some regularities.

Thus, the polar group totally occupies the third pair of rows. There are only two abnormalities, related to glutamine (presented in the second pair of rows) and to asparagine (presented in the fourth pair of rows). The first pair of rows is totally occupied with amino acids of the electrically neutral group, however, here also there is abnormality related to arginine (it responds to the charge-neutral group). Such symmetry of the Table 34.3 structure inevitably leads to the thought that an

Table 34.3 Genetic code for amino acids and proline

	− − +	− − +	− + −	− + +	+ − −	+ − +	+ + −	+ + +
000	Pro(0)	Pro(0)	*Arg*(+)	*Arg*(+)	Ala(0)	Ala(0)	Gly(0)	Gly(0)
	(CCC)	(CCG)	(*CGC*)	(*CGG*)	(GCC)	(GCG)	(GGC)	(GGG)
001	Pro(0)	Pro(0)	*Arg*(+)	*Arg*(+)	Ala(0)	Ala(0)	Gly(0)	Gly(0)
	(CCU)	(CCA)	(*CGU*)	(*CGA*)	(GCU)	(GCA)	(GGU)	(GGA)
010	Leu(0)	Leu(0)	*His*(+)	**Gln**(→)	Val(0)	Val(0)	*Asp*(−)	*Glu*(−)
	(CUC)	(CUG)	(*CAC*)	(**CAG**)	(GUC)	(GUG)	(*GAC*)	(*GAG*)
011	Leu(0)	Leu(0)	*His*(+)	**Gln**(→)	Val(0)	Val(0)	*Asp*(−)	*Glu*(−)
	(CUU)	(CUA)	(*CAU*)	(**CAA**)	(GUU)	(GUA)	(*GAU*)	(*GAA*)
100	**Ser**(→)	**Ser**(→)	**Cys**(→)	**Try**(→)	**Thre**(→)	**Thre**(→)	**Ser**(→)	*Arg*(+)
	(**UCC**)	(**UCG**)	(**UGC**)	(**UGG**)	(**ACC**)	(**ACG**)	(**AGC**)	(*AGG*)
101	**Ser**(→)	**Ser**(→)	**Cys**(→)	The End	**Thre**(→)	**Thre**(→)	**Ser**(→)	*Arg*(+)
	(**UCU**)	(***UCA***)	(**UGU**)	(UGA)	(**ACU**)	(**ACA**)	(**AGU**)	(*AGA*)
110	Phen(0)	Leu(0)	*Thyr*(−)	The End	Ileu(0)	Met(0)	**Asn**(→)	*Lys*(+)
	(UUC)	(UUG)	(*UAC*)	(UAG)	(AUC)	(AUG)	(**AAC**)	(*AAG*)
111	Phen(0)	Leu(0)	*Thyr*(−)	The End	Ileu(0)	Ileu(0)	**Asn**(→)	*Lys*(+)
	(UUU)	(UUA)	(*UAU*)	(UAA)	(AUU)	(AUA)	(**AAU**)	(*AAA*)

Polar group amino acids are marked with bold type, amino acids of charge-neutral group are in italics. For easier understanding of this table, reading amino acid Serine, which is used as an example, is underlined. The canonical code from Table 34.1 is presented under the name of every amino acid

accepted reading of the coding letter in the DNA molecules expresses in direct (or nearly direct) correspondence of the acid physical property with a certain pair of rows in Table 34.3. Some authors note the presence of similar symmetries already at the standard canonical table level (see, e.g., [8]).

Further it can be seen that amino acids and proline are located in compact groups, mostly by two or by four. In addition, if the acid has four cells, every such quartet, at first, is located so that it occupies two neighboring rows and two neighboring columns, and, for the second, completely "indifferent" towards the third letter. Of special note is that amino acids, represented with two codes, are located within two neighboring rows and almost never within two neighboring columns.[12] It has to be noted also that for every quartet, related to separate acids (8 out of possible 20 are presented in Table 34.3), as mentioned above, only the first two letters are significant for identification. The third one could be of any kind. This observation has disturbed researchers for a long time [7, 8], as it is well observed also in Table 34.1. The only thing that does not abandon the three-position codon without a pass in favor of a two-positional codon with a pass is the perception of all amino acids and proline as equal.

[12] Isoleucine is an exception, which could be considered as some misunderstanding rather than the rule exception. A similar misunderstanding seems to take place also for one code for tryptophan and a "spare" code UGA for the end of the synthesis of arginine.

But it is well shown in Table 34.2 that separate code is needed only for 11 significant acids (proline and 10 amino acids right after proline), and to identify the remaining 9 amino acids it is enough not more than four codes (but not less than three). It means that with taking into consideration physical and structural properties of amino acids and proline $14 \div 15$ codes would be enough, that is, a two-positional codon. Thus there are still 1 or 2 two-position codes for the servicing of an interruption of the synthesis process. Significant acids with such a way of coding always correspond to one code, and the statisticians may correspond to one code for 2 or even 3 acids. As a matter of fact, proline always corresponds to one code. With two-positional codons redundancy of the genetic code and genetic code degeneracy becomes reciprocal: one code corresponds to not less than one amino acid.[13]

To resolve the discrepancy between the three-positional and two-positional codons would be enough to agree that the third letter in the standard canonical code is not merely a letter but just an interval between the words with some possible punctuation meaning. The fact that it is most likely a skip between words is confirmed by a full or partial arbitrariness of the third letter[14] (see Tables 34.1 and 34.3).

It is interesting to analyze the transformation of Table 34.3 in terms of genetic DNA code if only to link it to the first two nucleotides of the coding word. In the technical aspect such a transformation is provided by the simple combining of each of the 16 quartets of Table 34.3, related to the similar first two nucleotide letters and simultaneously to the various third letters, into one cell. This transformation of Table 34.3 resulted in a new data setting as displayed in Table 34.4.

Every cell of this table has such structure. In the simplest case it comprises shortened names of the acid, and below in brackets, two of its code: RNA-code and DNA code. To date it was considered, as mentioned above, that there are eight of this type of case (the simplest): proline(0^-0^-), arginine(0^-0^+), alanine(0^+0^-), glycine(0^+0^+), leucine(0^-1^-), valine(0^+1^-), serine(1^-0^-), and threonine(1^+0^-). However, currently only four acids could be included in such a type: proline(0^-0^-), alanine(0^+0^-), glycine(0^+0^+), and serine(1^-0^-). It could be suggested that the codes have been estimated with no mistakes only for these acids. For the remaining four acids: arginine(0^-0^+), leucine(0^-1^-), valine(0^+1^-), and threonine(1^+0^-) as shown in Table 34.4, recently in experiments with mitochondria of higher organisms, other amino acids and signals of synthesis start have been tested under the same code. Such extra situations are included in the respective cells below both of the codes. In addition to the described situation, some other similar ones have been observed (see below).

[13] According to the standard canonical genetic code superfluity (degeneracy) this is the opposite: not less than 1 code corresponds to the one amino acid.

[14] Two-positional codon with skipping (instead of a three-positional one without skipping) has been confirmed with the latest experimental evidence that reflect significant violation of currently accepted principle of three-positional code degeneracy.

Table 34.4 Genetic code for amino acids and proline in two-positional codon expression

	− −	− +	+ −	+ +
00	Pro(0)	*Arg*(+)	Ala(0)	Gly(0)
	(**C C**) $\left(\frac{G}{C}\frac{G}{C}\right)$	(**C G**) $\left(\frac{G}{C}\frac{C}{G}\right)$ Try (CGG)	(**G C**) $\left(\frac{C}{G}\frac{G}{C}\right)$	(**G G**) $\left(\frac{C}{G}\frac{C}{G}\right)$
01	Leu(0)	*His*(+)/**Gln** (→)	Val(0)	*Asp*(−)/*Glu*(−)
	(**C U**) $\left(\frac{G}{C}\frac{A}{T}\right)$	(**C A**) $\left(\frac{G}{C}\frac{T}{A}\right)$	(**G U**) $\left(\frac{C}{G}\frac{A}{T}\right)$	(**G A**) $\left(\frac{C}{G}\frac{T}{A}\right)$
	Thre, **Ser** (**CUG**)		Start of synthesis (**GUG**)	
	Start of synthesis (**CUG**)			
10	**Ser** (→)	**Cys** (→)//	**Thre** (→)	Ser (→)/*Arg* (+)
	(**U C**) $\left(\frac{A}{T}\frac{G}{C}\right)$	//**Try** (→) (**UGG**)/End of synthesis (**UGA**)	(**A C**) $\left(\frac{T}{A}\frac{G}{C}\right)$	(**A G**) $\left(\frac{T}{A}\frac{C}{G}\right)$
		(**U G**) $\left(\frac{A}{T}\frac{C}{G}\right)$	Start of synthesis (**ACG**)	End of synthesis Ser (**AGA**)
		Selenocysteine (**UGA**)		
11	Phen(0)/Leu(0)	*Tyr*(−)/End of synthesis	Ileu(0)/Met (0) (**AUG**)	**Asn** (→)/*Lys*(+)
	(**U U**) $\left(\frac{A}{T}\frac{A}{T}\right)$	(**U A**) $\left(\frac{A}{T}\frac{T}{A}\right)$	(**A U**) $\left(\frac{T}{A}\frac{A}{T}\right)$	(**A A**) $\left(\frac{T}{A}\frac{T}{A}\right)$
	Start of synthesis (**UUG**)	**Gln** (→) (**UAA**)	Start of synthesis	**Asn** (→)(**AAA**)

Further there are more complicated cases, codes for which are considered to be estimated with no mistake. At the same time, in these cases one cell corresponds to two amino acids at the level of standard canonical code if read as two letters with a skip. In Table 34.4 the names of such amino acids are given with slashes (in order of their occurrence in the respective quartet of Table 34.3). The names of both codes are also given below. There are six types of such cases: histidine/glutamine(0^-1^+), aspartic acid/glutamic acid(0^+1^+), serine/arginine(1^+0^+), phenylalanine/leucine(1^-1^-), tyrosine/the end of synthesis(1^-1^+), and asparagine/lysine(1^+1^+). However, in this case for the last four mentioned pairs of acids other amino acids and terminating signals have been tested as well under the same code.

The remaining two cases, despite the fact that they are considered as standard-canonical—a cysteine/tryptophan/end of the synthesis(1^-0^+) and isoleucine/methionine(1^+1^-)—are patently identified with an error. The first of them is significantly overloaded with amino acids and terminating synthesis signal, and all of them are of the approximately equal level of significance. The second one comprises three isoleucine acids which are typical statisticians and one methionine acid which belongs to significant acids. Furthermore, in both cases additional options have been tested: in the first one, selenocysteine, and in the second one, a terminating signal.

If Table 34.4 is considered in terms of the first two coding letters (nucleotides) and strictly corresponds with the standard canonical Table 34.1 (or to its modified option, Table 34.3), and is only updated by currently available additional data of experimental studies, the following becomes evident.

1. Consequent consideration of the physical and structurally functional properties of amino acids and proline allows setting the question about a two-positional codon with a skip instead of a three-positional codon without a skip in the aspect of conducting additional experimental studies in this field.
2. Table 34.4 well demonstrates some violations of the three-positional principle for genetic code redundancy (degeneracy) when one code corresponds only with one acid. For instance, in the cell $0^{-}0^{+}$ for three-positional code CGG not only arginine has been tested but also tryptophan; in the cell $0^{-}1^{-}$ along with leucine also threonine, serine, and a terminating signal have been tested. All of them could be considered as weak but available experimental evidence for a two-positional codon with a skip.
3. Table 34.4 has one important advantage in comparison to the standard-canonical Table 34.1: it displays the possible manner of two-positional amino acids coding in DNA. For example, it is obvious that the first row of this table is completely devoted to the electrically neutral amino acids group; on the other hand, two-positional codes for DNA namely consist only of two GC pairs. The exception is represented by arginine which belongs to the charge-neutral group but has evidently been tested ambiguously suggesting the possible mistake in its nucleotide decoding. Given that a similar situation has also been observed with leucine, which belongs to the electrically neutral group, there is the question about additionally testing their possible recoding so that both amino acids could "take their places," that is, just exchange their places. In such a case the entire first row of Table 34.4 would consist exclusively of electrically neutral amino acids and comprise DNA codes consisting strictly of two GC pairs. With such a place-switching it is expected that the whole second row of Table 34.4 would be completely devoted to the charge-neutral group as well, with the exception of valine which belongs to the electrically neutral group and is expected to be located in the first row, and for glutamine whose place is in the third row. It turned out to be that there are no significant obstacles for such a recoding given valine and alanine are not only statisticians from the same group but also are rather close by their atomic-molecular organization so that one code would be enough for both of them, for instance, an alanine code $0^{+}0^{-}$. It suggests that the cell $0^{+}1^{-}$ gets free for the "inner task solving" of the second charge-neutral row. As for glutamine, it has easily recoded toward threonine($1^{+}0^{-}$) because both of them are typical statisticians (currently) and one code for them is enough. Immediately it will be noticed that the same applies to asparagine in the cell ($1^{+}1^{+}$). It is also easily re-encoded to threonine, because it is a statistician, as a glutamine and threonine (see Table 34.2).
4. It could be possible to offer some hypothetic modification of Table 34.4 (see Table 34.5) in the framework of the code ordering process mentioned above taking into consideration: (a) maximum compliance of the table row and amino acid physical property (more correctly, its radical); (b) significance of amino acids and proline; (c) keeping the principle of minimum code changing with respect to the standard-canonical codes (meaning the first two code letters).

Table 34.5 predominantly demonstrates the possibility of "painless" transition from a three-positional codon without a skip toward a two-positional codon with a

Table 34.5 Hypothetic modification of Table 34.4

	−−	−+	+ −	+ +
00	Pro(0)	Leu(0)	Ala(0)	Gly(0)
	(**C C**) $\left(\frac{\mathbf{G}}{\mathbf{C}}\frac{\mathbf{G}}{\mathbf{C}}\right)$	Ileu(0)	Val(0)	(**G G**) $\left(\frac{\mathbf{C}}{\mathbf{G}}\frac{\mathbf{C}}{\mathbf{G}}\right)$
		(**C G**) $\left(\frac{\mathbf{G}}{\mathbf{C}}\frac{\mathbf{C}}{\mathbf{G}}\right)$	(**G C**) $\left(\frac{\mathbf{C}}{\mathbf{G}}\frac{\mathbf{G}}{\mathbf{C}}\right)$	
01	*Arg*(+)	*His*(+)	*Glu*(−)	*Asp*(−)
	(**C U**) $\left(\frac{\mathbf{G}}{\mathbf{C}}\frac{\mathbf{A}}{\mathbf{T}}\right)$	*Lys*(+)	(**G U**) $\left(\frac{\mathbf{C}}{\mathbf{G}}\frac{\mathbf{A}}{\mathbf{T}}\right)$	(**G A**) $\left(\frac{\mathbf{C}}{\mathbf{G}}\frac{\mathbf{T}}{\mathbf{A}}\right)$
		(**C A**) $\left(\frac{\mathbf{G}}{\mathbf{C}}\frac{\mathbf{T}}{\mathbf{A}}\right)$		
10	**Ser** (→)	**Cys** (→)	**Thre** (→)	**Try** (→)
	(**U C**) $\left(\frac{\mathbf{A}}{\mathbf{T}}\frac{\mathbf{G}}{\mathbf{C}}\right)$	(**U G**) $\left(\frac{\mathbf{A}}{\mathbf{T}}\frac{\mathbf{C}}{\mathbf{G}}\right)$	**Gln** (→)	(**A G**) $\left(\frac{\mathbf{T}}{\mathbf{A}}\frac{\mathbf{C}}{\mathbf{G}}\right)$
		Selenocysteine	**Asn** (→)	
			(**A C**) $\left(\frac{\mathbf{T}}{\mathbf{A}}\frac{\mathbf{G}}{\mathbf{C}}\right)$	
11	Phen(0)	End of synthesis	Meth(0)	*Thyr*(−)
	(**U U**) $\left(\frac{\mathbf{A}}{\mathbf{T}}\frac{\mathbf{A}}{\mathbf{T}}\right)$	(U A) $\left(\frac{\mathbf{A}}{\mathbf{T}}\frac{\mathbf{T}}{\mathbf{A}}\right)$	(**A U**) $\left(\frac{\mathbf{T}}{\mathbf{A}}\frac{\mathbf{A}}{\mathbf{T}}\right)$	(**A A**) $\left(\frac{\mathbf{T}}{\mathbf{A}}\frac{\mathbf{T}}{\mathbf{A}}\right)$

skip by considering the different significance of amino acids and proline as well as their physical properties. This table version allows us to state that all the electrically neutral acids, with the exception of phenylalanine and methionine, at the level of the DNA molecule have a two-positional code, consisting only of GC pairs. Similar symmetries could be observed for other amino acid groups as well.

In fact, Table 34.5 has its drawbacks from the viewpoint of standard-canonical code (regarding the first two code letters). The most significant shortcoming seems to be the necessity of certain recoding of some amino acids.

The strongest recoding concerns the statisticians, isoleucine $\left(\left(\frac{\mathrm{TA}}{\mathbf{AT}}\right) \Rightarrow \left(\frac{\mathrm{GC}}{\mathbf{CG}}\right)\right)$ and leucine $\left(\left(\frac{\mathrm{AA}}{\mathbf{TT}}\right), \left(\frac{\mathrm{GA}}{\mathbf{CT}}\right) \Rightarrow \left(\frac{\mathrm{GC}}{\mathbf{CG}}\right)\right)$. Less significant recoding relates to valine $\left(\left(\frac{\mathrm{CA}}{\mathbf{GT}}\right) \Rightarrow \left(\frac{\mathrm{CG}}{\mathbf{GC}}\right)\right)$, arginine $\left(\left(\frac{\mathrm{GC}}{\mathbf{CG}}\right) \Rightarrow \left(\frac{\mathrm{GA}}{\mathbf{CT}}\right)\right)$, lysine $\left(\left(\frac{\mathrm{TT}}{\mathbf{AA}}\right) \Rightarrow \left(\frac{\mathrm{GT}}{\mathbf{CA}}\right)\right)$ and asparagine $\left(\left(\frac{\mathrm{TT}}{\mathbf{AA}}\right) \Rightarrow \left(\frac{\mathrm{TG}}{\mathbf{AC}}\right)\right)$, of which only arginine does not belong to the statisticians. And finally, the weakest recoding relates to such amino acids as glutamic acid $\left(\left(\frac{\mathrm{CT}}{\mathbf{GA}}\right) \Rightarrow \left(\frac{\mathrm{CA}}{\mathbf{GT}}\right)\right)$, glutamine $\left(\left(\frac{\mathrm{GT}}{\mathbf{CA}}\right) \Rightarrow \left(\frac{\mathrm{TG}}{\mathbf{AC}}\right)\right)$, tryptophan $\left(\left(\frac{\mathrm{AC}}{\mathbf{TG}}\right) \Rightarrow \left(\frac{\mathrm{TC}}{\mathbf{AG}}\right)\right)$ and tyrosine $\left(\left(\frac{\mathrm{AT}}{\mathbf{TA}}\right) \Rightarrow \left(\frac{\mathrm{TT}}{\mathbf{AA}}\right)\right)$, of which only glutamine belongs to the statisticians.

34.3 Conclusions

The last table, as well as everything discussed in the chapter, primarily shows a possible trend of searches aimed at improving our understanding of the "protein–nucleic acid" accordance, in particular, to answer the questions listed at the beginning of this chapter, and especially the question of how the information about amino acids is encoded in the DNA.

References

1. Crick FHC (1993) On genetic code. Science 139:461–464
2. Nirenberg MW (1963) The genetic code: II. Sci Am 208:80–94
3. Soyfer VN (1969) The molecular mechanisms of mutagenesis. Nauka, Moscow, p 511
4. Dubinin NP (1970) General genetics. Nauka, Moscow, p 590
5. Aznakayev EG (2005) Biophysics. Book Publisher of National Aviation University, Kiev, p 308
6. Crick FHC, Barnett L, Brenner S, Watts-Tobin RJ (1961) General nature of the genetic code for proteins. Nature 192(4809):1227–1232. doi:10.1038/1921227a0
7. Inge-Vechtomov SG (1996) Translation as a way of living systems existence, or what is the sense of the "senseless" codons. Soros Educ J 12:2–10
8. Ratner VA (2000) Genetic code as a system. Soros Educ J 6(3):17–22
9. Davydov AS (1979) Biology and quantum mechanics. Naukova dumka, Kiev, p 296
10. Petrov EG (1984) Charge transition physics in biosystems. Naukova dumka, Kiev, p 368

Chapter 35
Amine-Functionalized Nanospheres, Synthesized Using 1.2-Bis(triethoxysilyl) ethane

N.V. Stolyarchuk, M. Barczak, I.V. Melnyk, and Yu. L. Zub

35.1 Introduction

Hybrid organic–inorganic materials are very interesting due to its unique properties, resulting from the combined influence of the organic and inorganic components on the structure and characteristics of the final product. The bridged polysilsesquioxanes (BPS) are particularly interesting as they can be obtained by hydrolytic polycondensation of polyfunctional "molecular building blocks" [1]. Recently the synthesis of spherical particles based on BPS is very popular and commonly used for its practical applications. A number of works devoted to obtaining spherical ethylene [2] and benzene [3] bridging particles of about 2 μm in size have been published. However, obtaining mesoporous structures using special templates significantly increases the cost and complicates the synthesis process. Shea et al. published their results on obtaining nano-micrometer size particles by non-emulsion method [4, 5]. However, the reception preparation of nonporous spherical particles with functional groups on their surface is still topical, and it will significantly expand the area of their applications. In this paper, amino-containing spherical particles were synthesized based on the 1.2-bis (triethoxysilyl)ethane and 3-aminopropyltriethoxysilane using the modified Stöber method. The influence of various factors (ratio of reacting components, the order of their introduction and the stirring time, the amount of solvent and catalyst) on the morphology and particle size was studied.

N.V. Stolyarchuk (✉) • I.V. Melnyk • Y.L. Zub
Chuiko Institute of Surface Chemistry, NAS of Ukraine, 17, General Naumov Str., Kyiv 03164, Ukraine
e-mail: stonata@ukr.net

M. Barczak
Maria Curie Skłodowska University, Lublin 20-031, Poland

O. Fesenko, L. Yatsenko (eds.), *Nanophysics, Nanophotonics, Surface Studies, and Applications*, Springer Proceedings in Physics 183,
DOI 10.1007/978-3-319-30737-4_35

35.2 Experimental

35.2.1 Materials

Initially the following compounds were used: 1.2-bis(triethoxysilyl)ethane, $(C_2H_5O)_3Si(CH_2)_2Si(OC_2H_5)$ (BTESE, ABCR, 97 %);3-aminopropyltriethoxysilane, $(C_2H_5O)_3Si(CH_2)_3NH_2$ (APTES, Aldrich, 98 %); NH_4F (Reahim, Ukraine, analytical grade); ethanol (96 %); NH_4OH (Macrochem, Ukraine, 25 %); 0.1 N HCl, 0.1 N NaOH - fixanal concentrates (Reahim, Ukraine); methyl orange (analytical grade, Reahim, Ukraine); $Cu(NO_3)_2 \cdot 3H_2O$ (Macrochem, Ukraine); $NaNO_3$ (chemically pure, Macrochem, Ukraine).

35.2.2 Synthesis of Particles

The sample **1**. 0.9 cm^3 of BTESE, 0.6 cm^3 of APTES and 1.8 cm^3 of ammonia solution were added to 25 cm^3 of ethanol solution while stirring at room temperature. After stirring for 3 h, a white precipitate was centrifuged (5000 rpm/10 min). The operation was repeated three times, each time washing the precipitate with ethanol. The sample was dried in oven at 80 °C during 24 h. Sample **2** was obtained in a similar way as **1**, but the amount of ethanol was 2 cm^3 and time of stirring 6 h. Samples **3** and **4** were obtained in a similar way as **1** with the following modifications: for **3** 1.8 cm^3 of ammonia solution was added after 1 h, and the suspension was stirred at room temperature for 6 h; for **4;** 0.6 cm^3 of APTES and 1.8 cm^3 of ammonia solution were added after an hour, and the suspension was stirred at room temperature for 6 h.

In the case of sample **5,** the amount of the initial materials was increased fourfold. Samples **6**, **7**, **8**, **9**, **10**, **11**, and **12** were synthesized in similar way as sample **4** with the prior hydrolysis of BTESE in the presence of NH_4F (Si:F = 200:1 for samples **6**, **7**, **8** and Si:F = 100:1 for samples **9**, **10**, **11**, **12**). For sample **7,** the volume of ethanol was 100 cm^3. For **8,** the hydrolysis of BTESE lasted 3 h. For sample **10,** the amount of reagents increased fourfold, the hydrolysis of BTESE lasted 3 h, and jelly-like solution was stirred for 1 h. For samples **11** and **12,** the ratios of BTESE/APTES were 2:1 and 4:1, respectively; the solution was stirred for 1 h.

35.2.3 Methods

The contents of the amino groups in the obtained samples were determined by acid–base titration [6]. The morphology of the samples was investigated by means of the scanning electron microscope (SEM) JSM 6060 LA (Jeol, Japan). SEM images

were obtained using secondary electrons at the acceleration voltage of 30 kV. To prevent accumulation of positive charges and to obtain contrasting images, the surface of the samples was covered with a thin continuous layer of gold or platinum by cathodic sputtering in vacuum. The transmission electron microscopy (TEM) analysis was performed by means of the high-resolution transmission electron microscope Titan G2 60-300 (FEI) equipped with the energy-dispersive X-ray spectroscopy (EDS) module with a Si(Li) detector for elemental analysis and mapping. The CHN elemental analysis was carried out using the Perkin Elmer CHN 2400 analyzer. FTIR spectra were recorded on a Thermo Nicolet Nexus FTIR spectrometer using the diffuse reflection mode "SMART Collector" in the 400–4000 cm^{-1} range, with a resolution of 8 cm^{-1}. The samples were ground with KBr at the mass ratios of sample/KBr = 1/30. The low-temperature nitrogen adsorption–desorption isotherms were recorded with a Kelvin-1042 instrument at −196 °C. The samples were predegassed at 120 °C for 2 h. The specific surface area of nanoparticles was calculated by the BET method [7], and the pore size distribution was determined by the approach described in [8]. Copper (II) ions sorption was studied in static conditions. The sorbent batch of 0.05 g was placed in 50 cm^3 weighing bottle, and poured with 20 cm^3 of metal solution for 20 h. Metal concentration in aqueous medium was determined by atom-absorption method using resonance signal 324.7 nm on spectrophotometer C-115-M1 in depleted flame (acetylene/air mixture). The source of resonance radiation was spectral lamp LS-2. The X-band EPR spectra of the samples were recorded at room temperature using radio spectrometer PE-1306 equipped with frequency meter ChZ-54 and frequency converter YaZCh-87. The magnetic field was calibrated using 2,2-diphenil-1-pycrilhydrazyl (DPPH) ($g = 2.0036$) and ions of Mn^{2+} in MgO matrix ($g = 2.0015$).

35.3 Results and Discussion

The monodispersed spherical particles in the ammonium solution were obtained by the Stöber technique [9]. However, there is not enough information about the synthesis of functionalized spherical particles using one-step procedure. In this paper, the attempt is made to apply the known Stöber method for obtaining amino-containing nanoparticles from bridging bis(trialkoxysilanes), in particular using 1.2-bis(triethoxysilyl)ethane as the structure agent. Analysis of the literature suggests different stirring time necessary to achieve particles' final size, from a few tens of minutes [9] to several days [10]. So, initially it was important to investigate the stirring time of the reaction mixture. In addition, our experience with BPS shows the necessity for prior hydrolysis of BTESE [11]. Samples **1**, **2**, **3,** and **4** (BTESE:APTES ratio 1:1), which differ in the order of input components of the reaction mixture, were synthesized, and **2** was obtained with less amount of ethanol. Samples **1** and **2** were obtained by immediate mixing of the components, but with different amounts of solvent. SEM showed that the presence of a small amount of

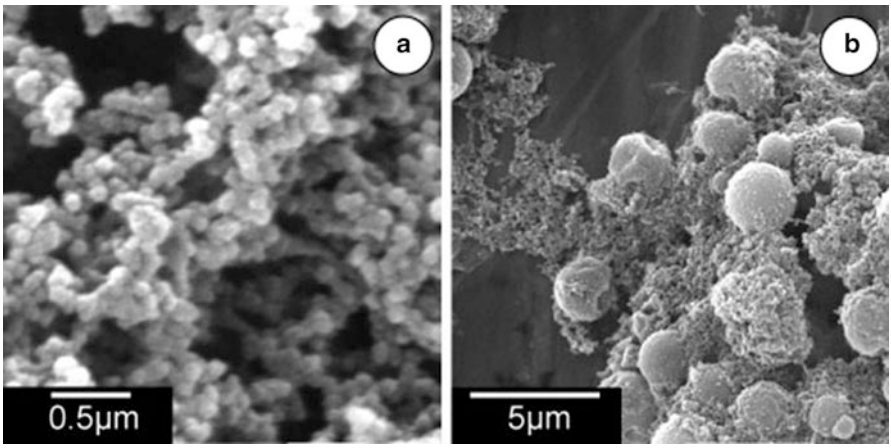

Fig. 35.1 SEM images of samples **1** (a) and **2** (**b**)

ethanol produced radically different particle size from 100 nm to 2.5 μm (Fig. 35.1b) under the same conditions, but the diluted reaction medium formed 80 nm size particles (Fig. 35.1a). The yield was negligible, less than 5 %.

During synthesis of sample **3,** ammonia solution was added to the ethanol solution of BTESE and APTES only after 1 h. So, after 1 h spherical particles about 500 nm were formed surrounded by 60 nm ones and oligomeric net-like structure. The particle size was about 140 nm after 2 h. The particles of different sizes, including the net-like structures, appeared after 6 h. The particle size was in the range 100–150 nm. Apparently, the time of the reaction of the hydrolytic polycondensation increased to 6 h strongly affects the homogeneity of spherical particles. During synthesis of sample **4,** APTES and ammonia solutions were added to the BTESE alcohol solution only after 1 h.

Increasing the time of hydrolytic polycondensation reaction leads to a decrease in particle size. The particle size reached 260 nm after 1 h stirring; 220–300 nm after 2 h; 60 and 180–200 nm after 3 and 6 h, respectively. Thus, it should be noted that for both samples **3** and **4,** the optimal reaction time was 2–3 h. However, the yield was very low for all syntheses; it does not exceed 5 %. No improvement was observed in the case of fourfold increase of the amount of precursor (sample **5**). The SEM images are shown in Fig. 35.2a; the particle size is 70 nm. The previous experiments with BPS [11, 12] show the efficiency of ammonium fluoride as a catalyst for increasing the degree of condensation of reacting polysilsesquioxane precursors. Therefore, further synthesis was carried out with the prior hydrolysis of BTESE. The SEM analysis shows that the samples synthesized at the ratio Si: F = 200:1, regardless of the amount of ethanol (**6**, **7**: 25 ml and 100 ml, respectively), were formed by small particles that are connected to the solid material (Fig. 35.2b, c). However, the yield increased only slightly, and even changing time of silane hydrolysis (sample **8**) did not improve this, although 60–80 nm particles are visible on the SEM image (Fig. 35.2d). The amount of catalyst increased

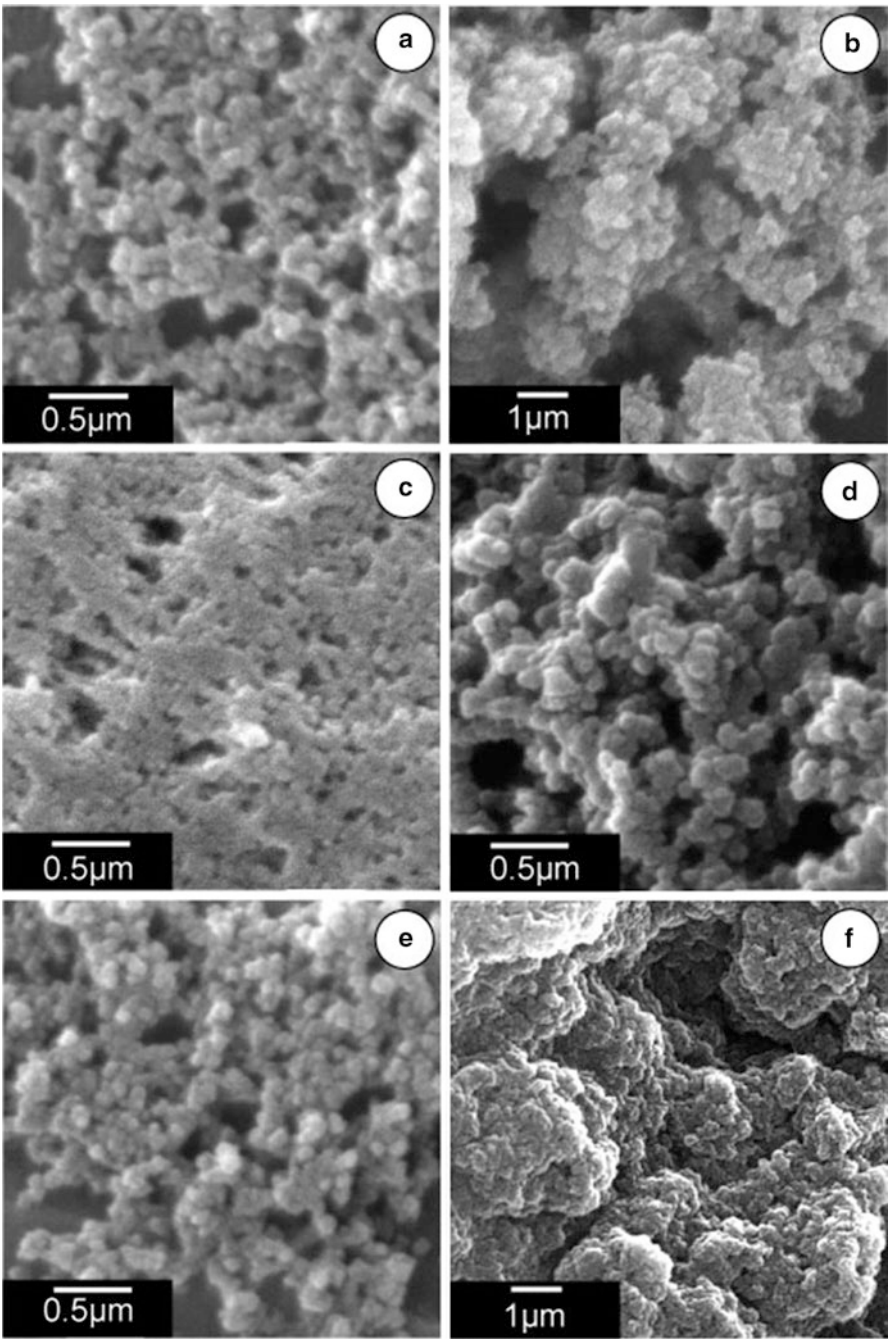

Fig. 35.2 SEM images of samples **5** (**a**), **6** (**b**), **7** (**c**), **8** (**d**), **9** (**e**), **10** (**f**), **11** (**g**), and **12** (**h**)

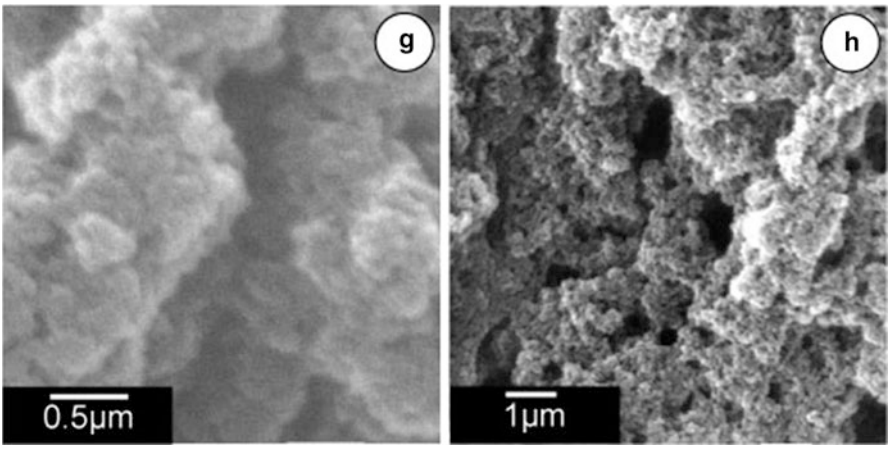

Fig. 35.2 (continued)

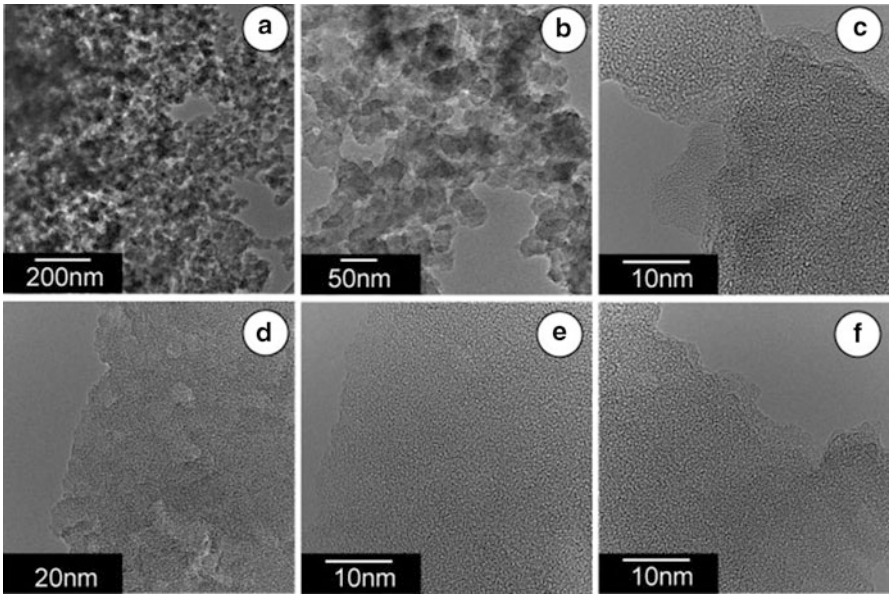

Fig. 35.3 TEM for samples **5** (**a–c**), **9** (**d, e**), and **10** (**f**)

twofold for the next syntheses (Si:F = 100:1) while BTESE pre-hydrolysis time for sample **9** was 1 h and the stirring time 3 h. It turned out that the yield of this synthesis was ~ 90 %. According to SEM, the size of the nanospheres was about 70 nm (Fig. 35.2e).

In the case of sample **10,** BTESE pre-hydrolysis time was reduced, while the stirring was increased. When the amount of BTESE in the reaction solution

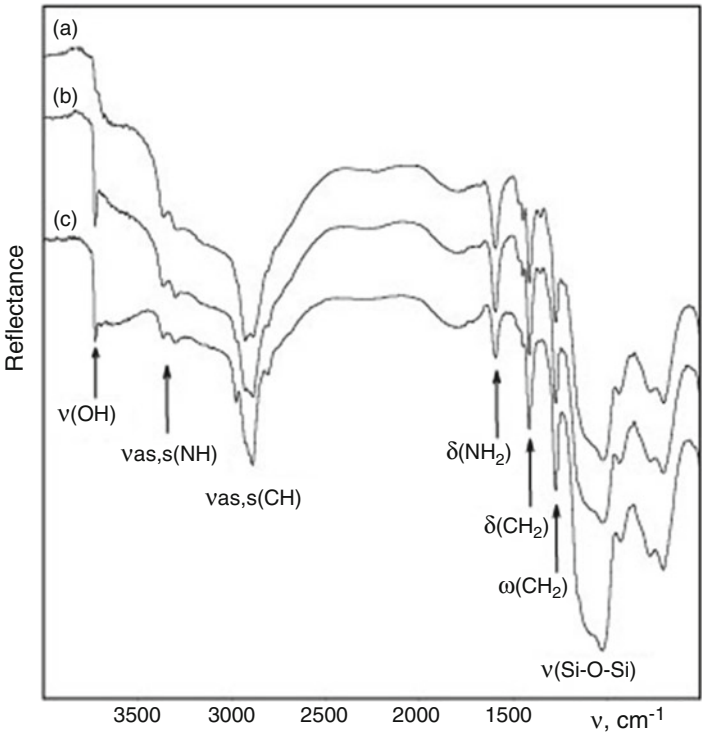

Fig. 35.4 IR spectra of samples **10** (**a**), **11** (**b**), and **12** (**c**)

(samples **11** and **12**) was increased, the stirring time of the suspension was reduced from 3 to 1 h, as gel formation was observed (BTESE hydrolysis time was 1 h). In this case, the obtained nanoparticles had a smaller size, but were tightly connected to each other forming solid material.

Samples **5**, **9,** and **10** consist of interconnected particles of approximately 50–70 nm (Fig. 35.3a–f) according to the TEM data. The aggregated primary particles and nonideal spherical particles, combined into globules, could be identified. The size of these globules was estimated by detailed analysis of TEM photos, and it was about 5–7 nm. The TEM revealed the absence of ordered structures and disordered location of polysilsesquioxane chains that is characteristic feature for the materials obtained from BTESE [13].

The synthesized materials were investigated using IR spectroscopy. The presence of $-CH_2-$ units in the ethylene spacer of BTESE and propyl chain of APTES is manifested by absorption bands in the region 2893–2977 cm^{-1}, corresponding to the symmetrical and asymmetrical valence vibrations of C—H. Two sharp absorption bands at ~1270 cm^{-1} and ~1416 cm^{-1} can be attributed to $\omega(CH_2)$ and $\delta(CH_2)$ of $\equiv Si-CH_2-CH_2-Si \equiv$ bridges (Fig. 35.4).

The IR spectra of the obtained samples recorded during heating up to 150 °C (to remove water) show the presence of amino groups. In the region, at

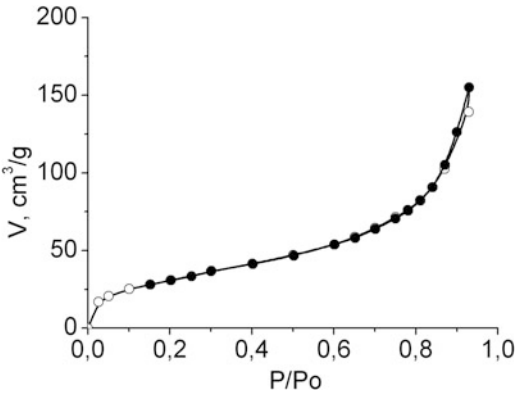

Fig. 35.5 Nitrogen adsorption–desorption isotherm for sample **5**

Table 35.1 The content of functional groups and structure-adsorption parameters for obtained samples

Sample	Initial ratio of BTESE/APTES	Content of functional groups, mmol/g	Particles size, nm	Structure-adsorption characteristics		
				S_{BET}, m^2/g	V_p, cm^3/g	d, nm
5	1:1	–	70	117	0.24	5.3
9	1:1	2.4	70	40	–	–
10	1:1	3.8	60	20	–	–
11	2:1	2.5	50	480	1.23	6.7
12	4:1	1.0	40	440	1.52	8.9

3300–3366 cm^{-1}, two low-intensity absorption bands are observed, corresponding to the stretching vibrations $\nu_{s,as}(NH)$ of amino groups. In addition, at 1590 cm^{-1}, a low-intensity absorption band is identified, which can be attributed to $\delta(NH_2)$. Thus, it can be concluded from the IR spectroscopy spectra that the obtained materials contain both organic bridges and aminopropyl functional groups, introduced during synthesis.

The structure-adsorption characteristics of the obtained samples were also investigated. Figure 35.5 shows the nitrogen adsorption–desorption isotherm of sample **5** (samples **9**, **11** ,and **12** have similar type of isotherms). The structure-adsorption parameters of the obtained samples were calculated and are presented in Table 35.1. The type of isotherms indicates the specific surface area due to the surface of the nanoparticles. The values of structure-adsorption parameters for samples **11** and **12** are close to the corresponding xerogels [11]. High values of specific surface area can be explained by a smaller particle size.

As commonly known, the introduction of amine functional groups can strongly enhance the sorption properties of materials with regard to metal ions [14]. However, the question arises about the topography of functional groups on the surface. In the case of amino-functionalized xerogels synthesized using bis-silanes as structure agents, we have proposed to solve this problem, using the probe method [14, 15].

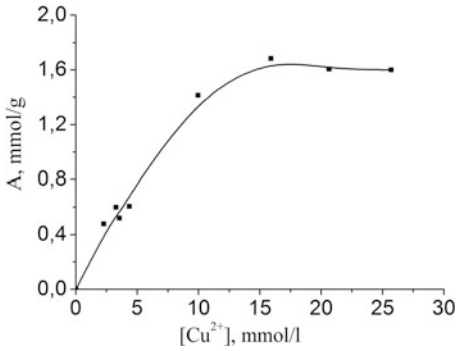

Fig. 35.6 Sorption isotherms of Cu^{2+} for sorbent **10** (—C_2H_4—/—NH_2, 1:1) ($V = 20$ cm^3; $m = 0.05$ g; $\tau = 20$ h)

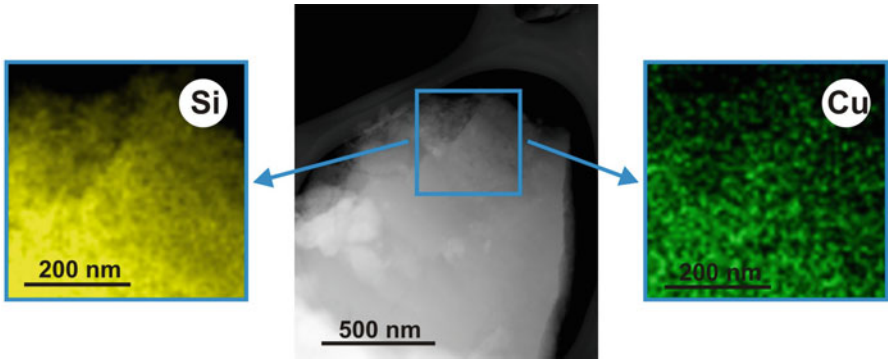

Fig. 35.7 HAADF-STEM-EDS elemental mapping of sample **10** after sorption of copper(II) ions: Si (on the left) and Cu (on the right)

The copper(II) ions were chosen as it can form strong amino complexes. For these systems, there are evident correlations between composition, structure and data of EPR spectroscopy. Studying the EPR spectra of copper(II) adsorbed on the surface of amino-containing material, assumptions about the location of functional groups can be made. Therefore, sorption of copper(II) ions from aqueous solutions was studied under static conditions for sample **10** (3.8 mmol/g). The sorption isotherm of Cu(II) for sample **10** is presented in Fig. 35.6. As it can be seen, the saturation of the surface layer is achieved when the ratio of metal/ligand is equal to 1:2. The EPR spectra of complexes of amine and Cu(II), formed on the surface of samples, were obtained. The values of g_{II} for copper (II) on the surface change in the range 2.21–2.27 by varying the copper content. These values are typical of copper complex structure $Cu[N_2O_2]$ [16].

Only two atoms of nitrogen of the amino-containing functional groups in the coordination sphere of copper (II) may indicate their proximity. The data of EDS analysis (Fig. 35.7) indicate homogeneous mixing during synthesis and uniform location of groups on the surface.

35.4 Conclusions

Amino-containing polysilsesquioxane nanoparticles were synthesized by means of the Stöber technique using ethylene bridge silanes. According to the SEM images, they have an average particle size of 50–80 nm. It was shown that pre-hydrolysis of bis-silane should be conducted in the presence of a catalyst. It was found that increasing the content of bissilane and stirring time leads to a reduction of the final particle size. The addition of a catalyst can increase yield of the final product. As follows from IR spectroscopy, the obtained materials contain organic bridges and aminopropyl functional groups introduced during synthesis. The prepared amino-containing particles are characterized by low values of specific surface area. The EPR and EDS results indicate formation of complexes 2:1 (L:M) on the surface of the obtained materials and uniform location of functional groups.

Acknowledgments MB thanks funding from the People Programme (Marie Curie Actions) of the European Union's Seventh Framework Programme FP7/2007–2013/under REA grant agreement n° PIRSES-GA-2013-612484.

References

1. Loy DA, Shea KJ (1995) Bridged polysilsesquioxanes: highly porous hybrid organic-inorganic materials. Chem Rev 95:1431–1442
2. Xia Y, Yang Z, Mokaya R (2006) Simultaneous control of morphology and porosity in nanoporous carbon: graphitic mesoporous carbon nanorods and nanotubules with tunable pore size. Chem Mater 18:1141
3. Kapoor MP, Inagaki S (2004) Synthesis of phenylene bridged mesoporous silsesquioxanes with spherical morphology in ammonia solution. Chem Lett 33:88
4. Hu LC, Khiterer M, Huang SJ, Chun JC, Davey J, Shea KJ (2010) Uniform, spherical bridged polysilsesquioxane nano- and microparticles. Chem Mater 22:244–250
5. Khiterer M, Shea KJ (2007) Spherical, monodisperse, functional bridged polysilsequioxane nanoparticles. Nano Lett 7:2684–2687
6. El-Nahhal IM, Parish V, Organomet J (1993) Insoluble ligands and their applications: III. Polysiloxane diaminoethane derivatives. J Organomet Chem 452:19–22
7. Rouquerol F, Rouquerol J, Sing K (1998) Adsorbtion by powders and porous solids. Principles, methodology and application. Academic Press, San Diego, p 467
8. Barrett EP, Joyner LG, Halenda PP, Am J (1951) The determination of pore volume and area distributions in porous substances. I. Computations from nitrogen isotherms. J Am Chem Soc 73:373–380
9. Stöber W, Fink A, Bohn E (1968) Controlled growth of monodisperse silica spheres in the micron size range. J Colloid Interface Sci 26:62–69
10. Melnyk IV, Tomina VV, Zub Yu.L (2013) Synthesis submicro- and nanoscale spherical silica particles with 3-aminopropyl groups in the surface layer. Paper presented at the 3rd international conference nanomaterials: application and properties, 16–21 Sept, 2013: Proceedings, Alushta (the Crimea, Ukraine), V.2, N2, P. 02PCN40-1 -02PCN40-3
11. Dabrowski A, Barczak M, Stolyarchuk NV, Melnyk IV, Zub YL (2005) Bridged polysilsesquioxane xerogels functionalizated by amine- and thiol-groups: synthesis, structure, adsorption properties. Adsorption 11:497–513

12. Zub YL, Stolyarchuk NV, Melnyk IV, Chuiko AA, Dabrowski A, Barczak M (2005) Novel adsorbents on the basis of bridged polysilsesquioxanes containing 3-mercaptopropyl functional groups. Mendeleev Commun 15:168–170
13. Stolyarchuk NV, Melnyk IV, Zub YL (2014) The structure of xerogels containing 3-aminopropyl groups in the surface layer. Proceedings of the Universities. Physics 57(7/2):161–166
14. Stolyarchuk NV, Melnyk IV, Kozak NV, Zub YL (2006) Adsorption of copper (II) from acetonitrile solutions by aminocontaining bridged polysilsesquioxane xerogels. Bull Donetsk Univ Ser A Nat Sci 1:283–288
15. Stechenko OV, Yakubovich TN, Teslenko VV, Zub YL, Chuiko AA (1997) Study of copper (II) absorption by polyaminosiloxane from acetonitrile solutions. Chem Phys Technol Surf 2:62–67
16. Solozhenkin PM, Semikopny AI, Sharf VZ, Lisichkin GV (1988) EPR surface complexes of copper (II) on the modified silica. J Phys Chem 62:477–481

Chapter 36
The Influence of Cu и Co Nanoparticles on Growth Characteristics and Biochemical Structure of *Mentha Longifolia* In Vitro

T.E. Talankova-Sereda, K.V. Liapina, E.A. Shkopinskij, A.I. Ustinov, A.V. Kovalyova, P.G. Dulnev, and N.I. Kucenko

36.1 Introduction

Despite the big achievements in biotechnology of plants, there are certain difficulties in definition of necessary components and concentration of macroelements, microelements, and growth regulators in nutrient medium for various kinds and grades of plants, purposely to receive the greater quantities of plants regenerants.

It is known that microelements activate definite enzymatic systems by direct participation in structure of enzymes molecules or by their activation. Enzymes, which contain copper, influence carbohydrate and nitric metabolism. Thanks to the influence on phenolic nature growth inhibitors, copper raises plant stability to lodging and to other stress factors. Cobalt in plants can be found in the ionic form and as a part of vitamin B_{12}. It activates glycolysis enzyme phosphoglucomutase and enzyme arginase, which hydrolyzes arginine, participates in

T.E. Talankova-Sereda (✉)
Medical college of Zaporozhian state medical university, Zaporozhye, Ukraine
e-mail: tt77-07@mail.ru

K.V. Liapina • A.I. Ustinov
E.O. Paton Electric Welding Institute, Kyiv, Ukraine

E.A. Shkopinskij
Zaporozhian National University, Zaporozhye, Ukraine

A.V. Kovalyova
Zaporozhian National Technical University, Zaporozhye, Ukraine

P.G. Dulnev
Institute of Bioorganic Chemistry and Petrochemistry, Kyiv, Ukraine

N.I. Kucenko
Research Station of Medicinal Plants of Agroecology and Nature Management Institute, NAAS, Berezotocha, Lubenskiy, Poltavskiy, Ukraine

O. Fesenko, L. Yatsenko (eds.), *Nanophysics, Nanophotonics, Surface Studies, and Applications*, Springer Proceedings in Physics 183,
DOI 10.1007/978-3-319-30737-4_36

biosynthesis of leghemoglobin and also in oxidizing processes, and activates enolase and kinase enzymes in the process of pyruvic acid transformation.

It is known from references that metal nanoparticles influence seed sprouting and plant development in an open ground [1, 2], and also on tylosis tissues [3, 4], but we did not find any accessible information about nanometal influence on growth and biochemical indices at medicinal essential oil plant microreproduction.

That is why the investigation of copper and cobalt nanoparticles influences *Mentha longifolia* explant growth characteristics depending on nanoparticles concentration at clonal reproduction (cultivation) in vitro, and changes of basic biochemical indices of essential oils are actual.

36.2 Method to Produce the Object of Research

As the object of research, *Mentha longifolia* plants from the collection of research station of medicinal plants of Agroecology and Nature Management Institute have been used. One hundred explants with Cu and 100 explants with Co were used for investigation, and all experiments were repeated three times.

Explant sterilization and all further work were spent in aseptic conditions according to standard techniques [5, 6].

Copper and cobalt nanoparticles were received by joint sedimentation from a steam phase of metal and alkaline metal halogenide (NaCl) [7, 8]. Stable colloidal solutions of high viscosity (gels) simultaneously with two and more amides were received further on the basis of nanoparticles data [9, 10]. The properties of received colloidal solutions were investigated by means of device Malvern Zetasizer Nano S (Malvern Instruments Ltd., the Great Britain) Ver. 6.20 in which particle size is defined by their movement with the use of Einstein-Stokes relation.

Distribution of particles on sizes in colloidal solutions is shown in Fig. 36.1 (a for copper, b for cobalt). Distribution is monomodal with a mode which lays in the range of sizes from 0.5 to 2 nm.

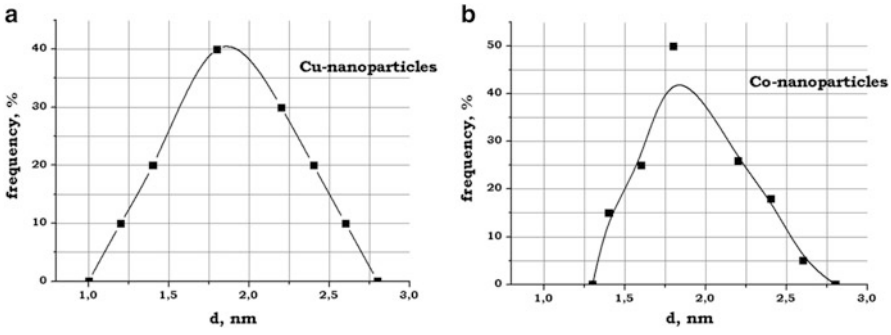

Fig. 36.1 Distribution of copper (**a**) and cobalt (**b**) particles on sizes in colloidal solutions on the basis of amines

Given the colloidal solutions, concentrations to be added into the nutrient medium are 0.4, 0.8, and 1.2 mg/L and 0.5, 1.0, and 1.5 mg/L.

Sterile explants were placed on modified Murashige and Skoog (MS) nutrient medium [11] (pH 5.6–5.8) which contains 0.75 mg/L of 6-benzylaminopurine, 0.1 mg/L of adenine, and 0.5 mg/L of gibberellic acid and separates copper and cobalt nanoparticles in the concentration specified above. The control variant of explants was placed on MS nutrient medium with the same structure, except nanometals.

Explants were cultivated in a cultural room at temperatures 23–25 °C, air-relative humidity 70 % and illumination 2500–3000 luxes with the photoperiod of 16 h.

The growth index analysis was spent on the 28th day. Shoot height, growth index, internode quantity, shoot quantity, and reproduction coefficient were measured and estimated for this purpose.

In 28–30 days, plant regenerants were grafted and placed on MS nutrient medium for rooting: half concentration of macro- and microsalts, 2 % sucrose, indole-3-acetic acid, and indole-3-butyric acid in concentration of 0.5 mg/L.

In 30 days, *Mentha longifolia* plants with well-developed root system were taken out from flasks, washed from agar rests, and bedded out in sterile substratum: peat-sand-vermiculite with a ratio of 2:1:1. In 40–45 days, strike root plants were bedded out in open ground conditions and covered with an agricultural fiber for 10–12 days.

Dry raw materials were used for essential oil receipt: they were prepared in mass flowering period and distilled by Ginsberg's method (distillation with water steam) without cohobation [12–15].

Biochemical screens were spent by chromatography mass spectrometry method on chromatograph Agilent Technology 6890 N with mass spectrometer detector 5973 N at National Institute of Grapes and Wine "Magarach" of the Ukrainian academy of agricultural sciences according to standard technique [16–19].

The library base of NIST05 and *Wiley* 2007 mass spectrometers with a total quantity of spectrums more than 470000 by means of the program for identification AMDIS and NIST was used for component identification [14, 20, 21].

Mathematical analysis of research results was spent with the use of mathematical statistics methods by means of the program Microsoft Office Excel 2007.

36.3 Results and their discussion

Growth processes initiation in the form of first pair of leaves unfolding was observed in the 4th–5th day. In the process of research, it has been defined that explant development on the 28th day was more intensive on nutrient medium with copper concentration of 0.5 mg/L and on nutrient medium with cobalt concentration of 0.8 mg/L. This was confirmed by growth indices, which are illustrated in Table 36.1.

According to results in Table 36.1, it is possible to draw a conclusion that copper and cobalt nanoparticles positively influence growth indices. So *Mentha longifolia* shoot height on the 28th day in control samples was 4.6 ± 0.48 sm and on nutrient medium with copper 6.83 ± 0.74 sm, and it has increased to 48.4 %, and shoot

Table 36.1 Growth indices of *Mentha longifolia* on the 28th day

Shoot height (sm)	Growth index	Shoot quantity (pcs.)	Internode quantity (pcs.)	Reproduction coefficient
Control				
4.6 ± 0.48	11.5	5.48 ± 1.28	10.26 ± 1.47	1:10
MS with Cu (0.5 mg/L)				
6.83 ± 0.74***	17.1	8.53 ± 1.12***	13.74 ± 1.86***	1:14
48.5 %		55.6 %	33.9 %	
MS with Co (0.8 mg/L)				
6.67 ± 0.50***	16.7	9.11 ± 1.76***	13.28 ± 1.68***	1:13
45 %		66.2 %	29.4 %	

Note: *** (at $p \leq 0.001$)—significant difference between the group and control group

Fig. 36.2 Mentha longifolia *on the 18th day of cultivation with cobalt* (0.8 mg/L)

height on nutrient medium with cobalt was 6.67 ± 0.50 sm and was 45 % bigger than in control samples. Shoots average quantity from one explant on the 28th day in control samples was 5.48 ± 1.28 pcs. while—8.53 ± 1.12 pcs. and has increased on 55.6 %, and shoot height on nutrient medium with cobalt was 9.11 ± 1.76 pcs. and that was on 66.2 % bigger than in control samples (Fig. 36.2). The internode average quantity at control explants was 10.26 ± 1.47 pcs.; on nutrient medium with copper nanoparticles 13.74 pcs. (33.9 % bigger than in control); and on nutrient medium with cobalt 13.28 pcs. (29.4 % bigger than in control). Also such indices as growth index (which at control plants was 11.5 and at experimental plants on nutrient medium with copper nanoparticles 17.1 and on nutrient medium with

Fig. 36.3 Plant regenerant is ready to be planted in substratum

Table 36.2 Characteristics of essential oil

Investigated samples	Essential oil output (%)	Linalool content in essential oil (%)	Linalyl acetate content in essential oil (%)	Linalool and linalyl acetate total content, g/100 g of raw material
control	1.164	85.97	6.057	1.071
MS c Cu	2.226	91.33	4.689	2.137
MS c Co	2.190	93.00	0.169	2.04

cobalt nanoparticles 16.7) and reproduction coefficient (which was 1:10 on the 28th day at control plants, 1:14 at experimental plants on nutrient medium with copper nanoparticles, and 1:13 on nutrient medium with cobalt nanoparticles) have accordingly increased.

On the 28th–30th day, plant regenerants were grafted on MS nutrient medium with half concentration of macro- and microsalts for rooting.

The first signs of root formation appeared on the 8th–10th days, and in 30 days, microplants with well-developed root system were bedded in substratum (Fig. 36.3). Strike root regenerants to substratum, which consisted of peat-sand-vermiculite in ratio 2:1:1, was 96 %.

In July 2015, at the same time, the raw materials have been gathered, from which the essential oil was isolated (Table 36.2).

Essential oil was analyzed on chromatograph Agilent Technology 6890 N with the mass spectrometer detector 5973 N. Results of the research are shown in Tables. 36.3, 36.4, and 36.5.

Table 36.3 Component composition of *Mentha longifolia* essential oil (control plants)

№	Substance output time (min)	Substance content (%)	Substance
1	6.626	0.060	β-Myrcene
2	6.829	0.033	Isobutyl isovalerate
3	7.555	0.356	1,8-Cineole
4	7.609	0.043	Limonene
5	7.875	0.102	*Trans*-ocimene
6	8.191	0.079	*Cis*-ocimene
7	8.755	0.376	*Trans*-linalool oxide
8	9.206	0.151	*Cis*-linalool oxide
9	9.323	0.020	α-Terpinolene
10	9.535	0.206	2,2,6-Trimethyl-3-keto-6-vinyltetrahydropyran
11	9.905	85.970	Linalool
12	10.049	0.137	Oct-1-en-3-ol acetate
13	10.460	0.466	3-Octylacetate
14	11.019	0.109	Menthone
15	11.163	0.022	Iso-menthone
16	11.392	0.027	Menthofuran
17	12.187	0.041	Menthol
18	12.377	0.912	P-menth-1-en-8-ol
19	13.842	0.013	Pulegone
20	13.960	0.043	Hexyl isobutyrate
21	14.036	0.093	Piperitone
22	14.623	6.057	Linalyl acetate
23	15.728	0.078	Dihydroedulan
24	17.951	0.257	Neryl acetate
25	18.560	0.378	Geranyl acetate
26	18.795	0.060	β-Bourbonen
27	19.598	0.076	α-Gurjunene
28	19.796	0.744	*Trans*-caryophyllene
29	20.608	0.264	α-Cubebene
30	20.793	0.037	Gumelen
31	21.059	0.443	β-Farnesene
32	21.591	0.911	Germacrene D
33	22.047	0.071	Bicyclogermacrene
34	22.281	0.054	Germacrene A
35	22.561	0.036	γ-Cadinene
36	22.660	0.080	*Cis*-calamenene
37	22.863	0.054	δ-Cadinene
38	23.273	0.055	α-Muurolene
39	24.243	0.196	Caryophyllene oxide
40	24.654	0.142	Ledol
41	25.317	0.355	α-Cubenol
42	25.980	0.104	τ-Cadinol
43	26.273	0.288	α-Cadinol

Table 36.4 Component composition of *Mentha longifolia* essential oil (on MS with Cu 0.5 mg/L)

№	Substance output time (min)	Substance content (%)	Substance
1	6.626	0.266	β-myrcene
2	6.901	0.016	Isobutyl isovalerate
3	7.564	0.221	1,8-Cineole
4	7.618	0.058	Limonene
5	7.880	0.218	*Trans*-ocimene
6	8.196	0.078	C*is*-ocimene
7	8.457	0.015	γ-Terpinene
8	8.647	0.037	*Trans*-sabinene hydrate
9	8.764	0.180	Trans-linalool oxide
10	9.337	0.031	α-Terpinolene
11	9.896	91.335	Linalool
12	10.464	0.274	3-Octylacetate
13	11.019	0.314	Menthone
14	11.299	0.067	Iso-menthone
15	11.461	0.031	Menthofuran
16	11.975	0.030	Terpinene-4-ol
17	12.169	0.062	Menthol
18	12.377	0.781	P-menth-1-en-8-ol
19	13.215	0.051	Nolil acetate
20	13.960	0.036	Hexyl isobutyrate
21	14.627	4.689	Linalyl acetate
22	15.042	0.211	Geranial
23	15.737	0.074	Menthyl acetate
24	17.956	0.221	Neryl acetate
25	18.542	0.419	Geranyl acetate
26	19.805	0.088	*Trans*-caryophyllene
27	21.077	0.049	β-Farnesene
28	21.604	0.084	Germacrene D
29	22.060	0.042	Bicyclogermacrene
30	24.252	0.021	Caryophyllene oxide

According to the received data, there are 43 individual components in control plant essential oil: 22 of them are presented having more than 0.1 % content and 21 having less than 0.1 % content. Linalool (85.97 %) and linalyl acetate (6.057 %) have the greatest content at control plant essential oil.

At the same time, in *Mentha longifolia* essential oil on MS with Cu 0.5 mg/L, there are 30 individual components: 12 of them are presented having more than 0.1 % content and 18 having less than 0.1 % content. Linalool (91.335 %) and linalyl acetate (4.689 %) have the greatest content at control plant essential oil.

Also in *Mentha longifolia* essential oil on MS with Co 0.8 mg/L, there are 39 individual components: 18 of them are presented having more than 0.1 % content and 21having less than 0.1 % content. Linalool (93.003 %) and linalyl acetate (1.568 %) have the greatest content at control plants essential oil.

Table 36.5 Component composition of *Mentha longifolia* essential oil (on MS with Co 0.8 mg/L)

№	Substance output time, min	Substance content, %	Substance
1	1.430	0.155	Ethanol
2	6.134	0.046	Sabinene
3	6.216	0.022	β-Pinene
4	6.626	1.040	β-Myrcene
5	6.897	0.100	Octane-3-ol
6	7.551	1.568	1,8-Cineole
7	7.605	0.116	Limonene
8	7.875	0.107	*Trans*-ocimene
9	8.187	0.023	*Cis*-ocimene
10	8.444	0.026	γ-Terpinene
11	8.624	0.850	*Trans*-sabinene hydrate
12	8.759	0.217	*Trans*-linalool oxide
13	9.201	0.254	*Cis*-linalool oxide
14	9.332	0.034	α-Terpinolene
15	9.909	93.003	Linalool
16	10.469	0.043	3-Octylacetate
17	11.023	0.041	Menthone
18	11.163	0.031	Iso-menthone
19	11.569	0.057	Terpin hydrate
20	11.966	0.139	Terpinene-4-ol
21	12.386	0.262	P-menth-1-en-8-ol
22	13.838	0.124	Neral
23	13.955	0.080	Hexenyl isovalerate
24	14.618	0.169	Linalyl acetate
25	14.862	0.169	Geranial
26	15.209	0.059	Citronellol
27	15.732	0.041	Dihydroedulan
28	16.043	0.065	Geranyl formate
29	17.965	0.054	Neryl acetate
30	18.572	0.086	Geranyl acetate
31	19.796	0.370	*Trans*-caryophyllene
32	20.621	0.021	α-Cubebene
33	20.793	0.033	Gumelen
34	21.059	0.058	β-Farnesene
35	21.586	0.292	Germacrene D
36	22.042	0.092	Bicyclogermacrene
37	22.281	0.020	Germacrene A
38	22.858	0.016	δ-Cadinene
39	24.257	0.118	α-Cubenol

On the basis of the aforesaid findings, it is possible to draw a conclusion that copper and cobalt nanoparticles positively influence *Mentha longifolia*'s development in vitro; however, the results depend on copper and cobalt nanoparticle concentration. Copper and cobalt nanoparticles used in nutrient mediums at clonal reproduction increase plant height and growth index to 45–48.5 %, internode quantity 29.4–33.9 %, shoot quantity 55.6–66.2 %, and reproduction coefficient 30–40 %.

At the chromatographic research of the essential oil, received from blossoming plants, distinction in number of the basic components (linalool and linalyl acetate) between control plants and the samples, which has grown up on nutrient mediums with the addition of copper and cobalt nanoparticles, is observed. It is possible to draw a conclusion that changes in metabolism, occurring under copper and cobalt nanoparticle action, remain for a considerable period of growth and in some months continue to influence the formation of essential oil components.

References

1. Polishchuk SD, Nazarova AA, Kutskir MV (2013) Productivities and biochemical structure of sunflower at processing of seeds by copper nanoparticles. Bulletin RGATU 2(18):104–106
2. Polishchuk SD, Nazarova AA, Stepanova IA, Kutskir MV, Churilov DG (2014) Biologically active preparations on a basis of metals nanodimensional particles in an agricultural production. Nanotechnology 1(37):72–81
3. Bugara IA, Maltseva OA (2011) *Mentha piperita L.* tylosis culture receiving and their cytological characteristic at growing on nutrient mediums with different selenium concentration. Scientific Notes of Taurida V.I. Vernadsky National University. Biology, chemistry, vol 24(63), No 4, pp 17–23
4. Kopach OV, Kuzovkova AA, Azizbekyan SG (2013) Microelements nanoparticles use in biothechnology of medicinal plants: the copper nanoparticles influence on *Silybum marianum* L. cell structures. Proceedings of Byelorussian State University. Physiological, biochemical and molecular principles of biosystems functioning, vol 8, P.2, pp 20–23
5. Kushnir GP, Sarnatskaya VV (2005) Plants microclonal reproduction. Scientific book, Kiev
6. Bugara IA (2006) Induced morphogenesis and clonal microreproduction of perspective mint grades: the thesis for the candidate of biological sciences degree in specialty 03.00.20. NBS-NNTS, Yalta, 20p
7. Ustinov Al, Melnichenko TV, Liapina KV, Chaplyuk VI (2008) Method to produce encapsulated nanopowders and unit for its implementation. Patent of Ukraine #82448
8. Ustinov Al, Melnichenko TV, Liapina KV, Chaplyuk VI (2013) Method of producing encapsulated nanopowders and installation for its implement. US Patent #8491972B2
9. Dulnev PG, Liapina KV, Davidova OE, Ustinov AL (2014) Sposob dispergirovaniya I stabilizacii nanochastic medi v vodnih sredah. Patent of Ukraine #91374
10. Murashige TA (1962) Revised medium for rapid growth and bioassays with tobacco tissue culture. Physiol Plant 15(13):473–497
11. Sheludko LO (2004) *Mentha piperita* (selection and seed farming). Poltava, 204p
12. Rudnik AM (2013) Gemma carboxylic acids of balsamic poplars. Pharm J 4:34–36
13. Sychov CS, Ilyin MM, Davankov VA, Sochilina KO (2004) Elucidation of retention mechanism sonhypercrosslinked polystyrene use dascolumn packing material for highperformance liquid chromatography. J Chromatogr A 1:17–24
14. Vlasyuk PA (1969) Biological elements in plants vital activity. Publishing house "Scientific thought", Kiev, p 526

15. Kutckir MV (2014) Definition of nanomaterials ecological safety on the basis of morphophysiologycal and biochemical indices of agricultural crops: dissertation for the candidate of biological sciences degree in specialty 03.02.08. Ryazan, 133p
16. Churilov GI (2009) Iron, copper, cobalt nanopowders influence in the system ground-plant. Herald of OSU. 12(106):148–151
17. Ampleeva LE, Stepanova IA, Nazarov AA (2009) Nanocrystalline metals influence on accumulation of biologically active compounds in plants, Herald of RGATU of P. A. Kostycheva. 2:34–36
18. Nazarova AA, Kutckir MV (2012) Peculiarities of nanodimensional copper particles action on physiological processes in vegetative organism. Collected theses of XXIV conference "Modern chemical physics", Tuapse, pp 93–94
19. Nazarova AA, Polischuk SD (2011) Prospects of metals nanopowders use in plant growing, Works of the All-Russia council of young scientists and experts of agrarian educational and scientific institutions "Actual problems of development of agrarian and industrial complex in scientific researches of young scientists", Moscow, pp 52–57
20. Fedorenko VF (2008) Nanotechnology and nanomaterials in agriculture. Scientific publishing house, Moscow, "Rosinformagrotech", 148p
21. Churilov GI Nazarova AA, Ampleeva LE, Polischuk SD, Tcherkasov OV (2010) Biological action of nanodimensional metals on various groups of plants, monography. Ryazan, 153p

Part V
Nanocomposites and Nanomaterials

Chapter 37
Gel Nanocomposites with Immobilized Bioelements for Plant Nutrition

K.V. Kalinichenko, G.N. Nikovskaya, Yu. M. Samchenko, and Z.R. Ulberg

37.1 Introduction

A growing population, limited food resources, and anthropogenic wastes raise the problem of an increase of plant productivity and quality. This problem faces many communities. At present many scientific works on nanomaterial (AgNPs, CuNPs, etc.) usage only for phytopathogen inhibition and providing a crop of high quality have been published [1–3]. We suggest that for the above-mentioned problem, solution nanocomposite soil substrates based on pH-sensitive acrylic hydrogels and sludge biogels (sludge solids of wastewater treatment plant) with immobilized plant essential nutrients can be used. One may consider that sludge biogel and acrylic hydrogel are, respectively, natural and synthetic nanocomposites. We have studied the colloid and chemical regularities of heavy metal (bioelement) immobilization in the gel templates [4–6]. It is well known that the most harmonious plant growth occurs in the presence of bioelements in water-insoluble forms, such as water-stable soil aggregates, granules, pellets, and so on [7]. Thus, biogel and hydrogel water-insoluble matrices containing plant nutrients can be suitable forms of soil fertilizers or soil substrates. From these objects a plant can release the necessary heavy metals (micro- and macroelements) due to the complex metabolites mixed with chelating properties to metals and in chelated forms assimilate them [8].

In addition, there is a possibility of the rational solution of the challenge of disposal of huge amounts of sludge (Table 37.1) produced annually all over the world and occupying vast suburban fields. Sludge solids contain essential plant nutrients [14, 15], including nitrogen, phosphorus, potassium, vitamins, amino

K.V. Kalinichenko (✉) • G.N. Nikovskaya • Y.M. Samchenko • Z.R. Ulberg
Colloidal Technologies of the Natural Systems Department, F.D. Ovcharenko Institute of Biocolloidal Chemistry, National Academy of Sciences of Ukraine, 42, Ac. Vernadsky Blvd, Kiev 03680, Ukraine
e-mail: KirKa_@bigmir.net

O. Fesenko, L. Yatsenko (eds.), *Nanophysics, Nanophotonics, Surface Studies, and Applications*, Springer Proceedings in Physics 183,
DOI 10.1007/978-3-319-30737-4_37

Table 37.1 Sludge solids produced after biological wastewater treatment

Country	Amount of sediment (million tons/year)	Source of information	Country	Amount of sediment (million tons/year)	Source of information
Austria	0.266–0.320	[9–11]	Latvia	0.030	[11]
Belgium	0.075–0.125	[9–11]	Lithuania	0.080	[11]
Bulgaria	0.029–0.047	[9–11]	Luxembourg	0.007–0.015	[10–12]
Cyprus	0.011	[11]	Netherlands	0.280–0.550	[10–12]
Czech Republic	0.220	[11]	Poland	0.523	[11]
Denmark	0.140–0.150	[11, 12]	Portugal	0.200–0.408	[10–12]
Estonia	0.026	[11]	Romania	0.134–0.165	[11, 15]
Finland	0.147	[11]	Russia	77.678	[16]
France	0.524–1.021	[11–13]	Slovakia	0.054	[11]
Great Britain	1.640	[9, 11, 12]	Slovenia	0.025	[11]
Germany	2.059–2.750	[10–12]	South Korea	1.902	[17]
Greece	0.125–0.200	[11, 12]	Spain	0.300–1.280	[10, 11]
Hungary	0.125	[11]	Sweden	0.180–0.210	[9, 11, 18]
Ireland	0.024–0.042	[10–12]	Switzerland	0.215	[10]
Italy	0.800–1.070	[10, 11]	Ukraine	1.802	[19]
Japan	2.300	[14]	United States	>7.000	[9, 20, 21]

acids, organic matter, and clusters of heavy metal compounds, such as slightly soluble or insoluble forms of phosphates, sulfates, carbonates, hydroxides, sulfides, and so on. These all constitute the value of biogel for soil quality enhancement, however, there is an obstacle for its application as a fertilizer: the high concentration of heavy metals. Depending on the population density and industrial activity of the region, the amounts of heavy metals (microelements) in sewage sludge can vary quite considerably and substantially exceed the maximum permissible concentrations (Table 37.2). In this connection a "green technology" for remediation of municipal sludge solids contaminated by heavy metals is proposed by us [33]. It is based on promotion of the vital ability of heterotrophic sludge biota by adding easily metabolized nutrients and complementary stabilization (rendering harmless) of sludge sediment in an alkaline medium followed by partial neutralization and drying.

Acrylic hydrogels are long polymeric chains cross-linked by covalent bonds in a three-dimensional grid. The hydrogels are a new generation of sorbents ("smart hydrogels"), which have a unique property of fast and repeated volume changes in cycles, "swelling-compression/collapse," even with small changes in the parameters of the environment, in particular pH. Bioelement incorporation into the hydrogel matrix from an external solution takes place synchronically with swelling and their release, at compression (collapse). The optimal pH value for swelling is 8.5–9.0 [36, 37]. They can absorb up to 70% water along with substances of

Table 37.2 Heavy metal content of sewage sludge after biological treatment of municipal wastewater

Country	Concentration mg/kg of dry matter					Source of Information
	Cr	Cu	Ni	Pb	Zn	
Canada	2650–2800	1700–8300	420–900	920–1100	4200–5700	[22, 23]
China	53–2243	492–648	55–202	49–86	1108–4692	[24]
Great Britain	50–5190	200–5050	75–2020	300–1000	200–6000	[25–27]
Netherlands	75	75	30	100	300	[26]
New Zealand	2600	1775–9300	920–1090	920	5700–9700	[28]
Poland	50–666	70–143	34–235	N/A	1077–3249	[29]
Russia	434–1000	900–2740	310–600	900–2023	2740–4649	[30]
Singapore	1901	7746	2053	584	18,062	[31]
South Korea	1152	2340	829	222	4529	[32]
Spain	N/A	100–175	300–400	750–1200	2500–4500	[26]
Sweden	100	600	50	100	800	[26]
Ukraine	620	1800	110	71	2600	[33]
United States	3000–99,000	4300–17,000	420–5300	840–26,000	7500–49,000	[26, 34]
EU limits	1000	1000	300	750	2500	[35]

different natures and prolonged-release them under the changes in the environment. In addition, the hydrogels have nanosizing pores ($d = 10–30$ nm) providing the penetration of molecules with corresponding diameter [36]. These circumstances allow several interaction mechanisms of polymer gels with different substances. We have studied heavy metal salt absorption by hydrogels of acrylic series: polyacrylamide, copolymers of acrylamide–acrylic acid, and acrylamide–acrylonitrile [4]. The maximum absorptive capacity was demonstrated by copolymers of acrylamide and acrylic acid.

The aim of our investigation is formation of nanocomposites on the base of sludge biosolids and pH-sensitive acrylic hydrogel with immobilized bioelements and estimation of their efficacy for plant growth.

37.2 Experiment

The objects of this study were bio- and hydrogels. The biogels are sludge solids from municipal wastewater treatment that were stabilized (secured from pathogens) in aerobic and anaerobic conditions. Sludge samples were collected from the special sludge fields (located in the region of Kyiv, Ukraine). The sludge solids have the characteristics: pH—6.8–7.2; organic matter content—52% of dry matter; enterobacteria—220 PFU $\cdot$ g^{-1}; and heavy metal concentration (μg g^{-1}): Zn—3092, Cu—735, Mn—2535, Co—48, Pb—291, Ni—567, and Cr—510.

In our investigation we used biocompatible and biosafe pH-sensitive acrylic hydrogels, copolymers of acrylamide and acrylic acid. The hydrogel was synthesized at a monomer ratio of 5:3 and a concentration of cross-linked agent (N, N′-methylenebisacrylamide), 0.654%. The gel formation was provided at room temperature in a water medium and was initiated by a redox initiator system of potassium persulfate, sodium metabisulfite. The hydrogel grains with particle size near 1 mm were washed by deionized water from residual monomers and dried at vacuum.

Partial removal of heavy metals from biogels was provided by the bioleaching methods described in detail in References [38, 39].

The concentration of metals (Cu, Zn, Mn, Co, Pb, Ni, Cr) in the supernatant was determined by atomic absorption and X-ray fluorescence methods, described in Reference [5]. The total metal content in sludge solids was analyzed similarly after burning in a muffle furnace at 600 °C and dissolution in a mixture of concentrated hydrochloric and nitric acids (in the ratio 1:3) at heating.

The ratio of the mineral and organic components in sludge solids (initial and after bioleaching) was determined by the weight loss after the samples were burned at 600 °C.

Enterobacterial content as a direct indicator of pathogen level was calculated after seeding on agarized Endo medium.

The quality of the bio- and hydrogel nanocomposites was demonstrated in vegetation experiments. Sweet basil (*Ocimum basilicum*) and cucumber

Table 37.3 Composition of Hoagland solution

Component	Stock solution	mL Stock solution/1 L
Macronutrients		
2 M KNO_3	202 g/L	2.5
1 M $Ca(NO_3)_2 \cdot 4H_2O$	236 g/0.5 L	2.5
Fe-EDTA	15 g/L	1.5
2 M $MgSO_4 \cdot 7H_2O$	493 g/L	1.0
1 M NH_4NO_3	80 g/L	1.0
Micronutrients		
H_3BO_3	2.86 g/L	1.0
$MnCl_2 \cdot 4H_2O$	1.81 g/L	1.0
$ZnSO_4 \cdot 7H_2O$	0.22 g/L	1.0
$CuSO_4 \cdot 5H_2O$	0.051 g/L	1.0
$Na_2MoO_4 \cdot 2H_2O$	0.12 g/L	1.0
Phosphate		
1 M KH_2PO_4 (pH to 6.0)	136 g/L	0.5

(*Cucumis sativus*) were selected to study the influence of the nanocomposites on plant growth in the pots. During the experimental period, the temperature varied between 20 and 25 °C. The pots with plants were watered daily as required. Low-nutrient soil was placed in every pot. No fertilizer was added to the control sample. In the experimental ones, the nanocomposites under study were added at an application rate of 4% (weight of dry matter/weight of soil). Its effect on the growth and yield of the plants over a period of 3–5 weeks was analyzed by weighting raw herbs after the release from soil and washing.

The hydrogel matrix was saturated by a Hoagland nutrient solution [40]. Its composition is shown in Table 37.3. The procedure of the solution preparation includes these stages: (1) compose stock solutions and store in separate bottles with appropriate label; (2) add each component to 800 mL deionized water and then fill to 1 L; and (3) calcium nitrate solution must be added at the end.

37.3 Results and Discussion

37.3.1 Hydrogel Nanocomposite

We have proposed the scheme of obtaining a gel nanocomposite for artificial soil formation by sequential treatment of a hydrogel template by a Hoagland nutrient solution with intermediate settling and separation of hydrogel granules enriched by bioelements (Fig. 37.1).

For processing hydrogels the individual solutions of bioelements by Hoagland were used in the following sequence as mentioned above. This sequence of processing the hydrogel matrix provides chemical binding of bioelements by

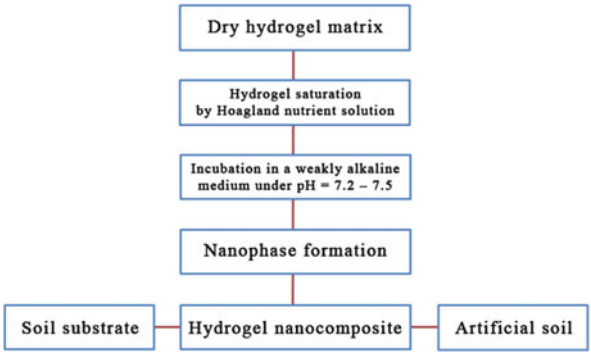

Fig. 37.1 Scheme of obtaining the nanocomposite on the base of acrylic hydrogels for plant nutrition

hydrogel active groups, along with their filling the inner space by the physical sorption mechanism. The hydrogel matrix was saturated in a Hoagland solution, slightly acid (pH ~ 6.5) at swelling. Then the hydrogel, saturated by bioelements, was transferred in a solution of pH 6.8–7.2. Under these conditions, OH ion entry into the interior of the hydrogel templates occurred. This resulted in the formation of sparingly soluble hydroxides (particularly, with ions of copper and zinc) and carbonates by a reaction with air carbon dioxide at the air drying of the hydrogel beads. There was a complex microfertilizer formation in the pores of the hydrogel. It consisted of slightly soluble nanoparticles capable, along with bioelements in the form of cations and anions, to diffuse through hydrogel nanopores in the outer solution under the action of organic acids of plant origin.

In a special experiment we observed that mixing the bioelement solutions after Hoagland with slight alkalization gave rise to turbidity, which was retained after seven days of exposition (Fig. 37.2). It may be considered as a proof of the nanophase rise from simple salts of heavy metals under their copresence and interaction in limited volume. In essence, a hydrogel matrix with immobilized bioelements, organized in nanophase, is a nanoreactor. First, the acrylic hydrogel at swelling sorbs bioelements from the slightly acid nutrient solution; then following swelling in the solution with pH 6.8–7.2 and alkalization of inner hydrogel medium, a complex nanophase of slightly soluble and insoluble nanoparticles of hydroxycarbonate metal salts forms. Under the action of plant root exudates, containing organic acids and complex polysaccharides capable to chelate heavy metals, a weakening of bonds between the nanophase particles and outlet of bioelements from the hydrogel template to the surrounding space (rhizosphere, plant roots) as metal chelates takes place.

37.3.2 Biogel Nanocomposite

The results of our earlier investigations on heavy metal bioleaching from the sludge biogel [39, 40] can serve as a base for working out the process of the conversion into

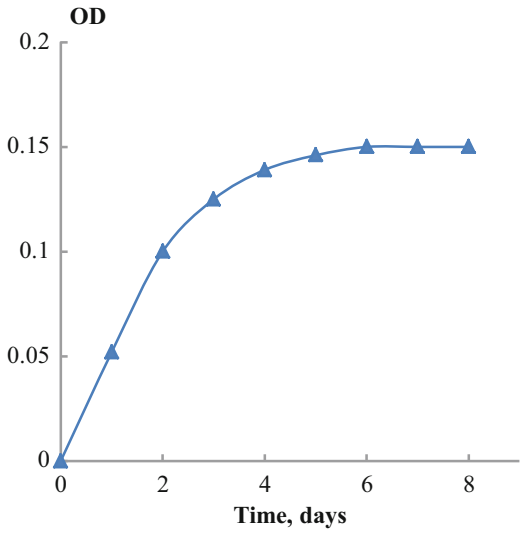

Fig. 37.2 The dynamics of the optical density of Hoagland solution saturating the hydrogel matrix

a fertilizer nanocomposite (Fig. 37.3). The entity of the process is an initiation of microbiological activity in sludge solids by adding easily metabolized nutrients such as sodium acetate to provide an alkaligeneous metabolism vector. Heterotrophic sludge biocenosis oxidizes this substance up to carbon dioxide. This metabolite is capable of transferring heavy metals from the solid phase of sludge suspension to the liquid phase as slightly soluble hydroxycarbonate nanosized complexes that are ecofriendly [41]. The efficacy of heavy metal removal reaches up to 80% (Zn) and follows the raw:

$$\text{Zn} > \text{Mn} > \text{Cu} > \text{Ni} > \text{Co} > \text{Pb} > \text{Cr}.$$

The biocolloidal process includes the stages: (1) heterophase cultivation of heterotrophic sludge biocenosis; (2) microbial biosynthesis of metabolites with the properties of flocculants and heavy metal extractants; (3) bioleaching of heavy metals, bioflocks flocculation, and sedimentation; and (4) separation of sludge suspension into liquid and solid phases. The composition of the solid phase (biogel) meets heavy metals' and pathogens' EU requirements [35] and is an effective nanocomposite fertilizer (Table 37.4). The liquid phase (bioextract) also contains essential plant nutrients in a form of ecofriendly slightly soluble hydroxycarbonate nanosized complexes of heavy metals. Thus, the bioextract can serve as the source of bioelements for hydrogel saturation and nanocomposite formation.

The biocolloid process can be realized in two days at static conditions (at mixing) or two months at composting. Such methods of waste sludge processing are technologically similar to tanks and heap-leaching metals from ores in the mining industry, respectively [42].

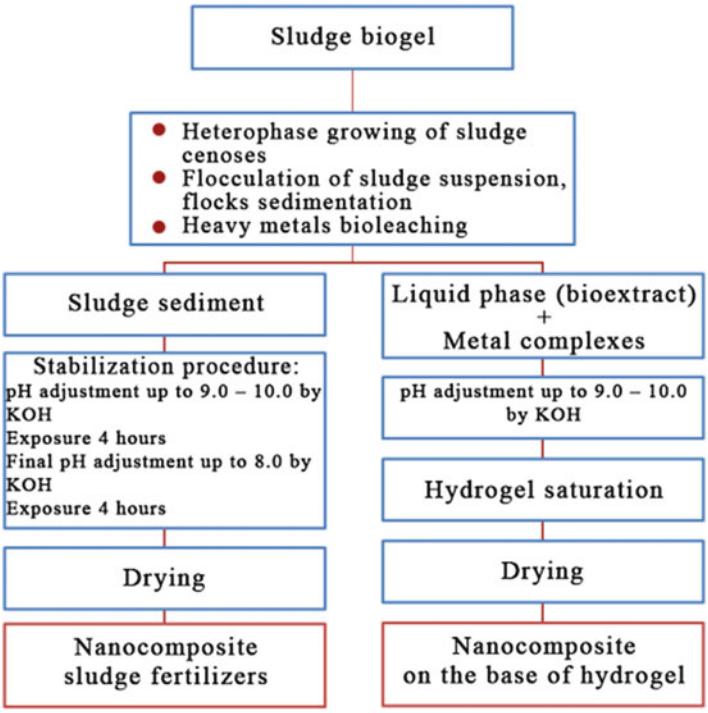

Fig. 37.3 Scheme of obtaining the nanocomposite on the base of sludge biogels for plant nutrition

Table 37.4 Characteristics of sludge nanocomposite fertilizer

Parameter	Content	
	Sludge solids	EU limits [36]
Cu (μg g^{-1})	257	1000
Zn (μg g^{-1})	618	2500
Mn (μg g^{-1})	887	2000
Co (μg g^{-1})	25	100
Pb (μg g^{-1})	224	750
Ni (μg g^{-1})	228	300
Cr (μg g^{-1})	433	1000
Enterobacteria (PFU g^{-1})	90	<100
Organic matter, %	65.0	>40
pH	8.0	5.5–8.5

A distinctive feature of our development is complex nonwaste "green technology" of complete utilization of sludge from wastewater treatment plants as an effective soil substrate for land application.

37.3.3 Study on Prolonged Desorption of Bioelements from Gel Nanocomposites

The interaction in the soil–plant system has a complex nature: soil provides bioelements for the plant and through its roots the plant excretes the products of complete (CO_2) and incomplete (amino acids, carbonic acids, etc.) elements obtained in photosynthesis. Soil nutrients enter the intercellular space of the plant as a result of diffusion (nonmetabolic pathway) and ion exchange between the soil and root systems (metabolic pathway). In the latter case, a plant selection of the necessary bioelements in appropriate concentrations occurs [8].

It is known [8] that plant root exudates have a complex composition. There have been at least 24 amino acids, 20 hydroxy carboxylic acids, 11 carbohydrates, 6 vitamins and enzymes, and 5 nucleotides identified. The dominant component of root exudates is citric acid. Its concentration can reach 10 μM per 1 g of dry weight of roots and depends on the type of plant and soil. In addition, the pH value in the rhizosphere can reach 5.5.

In the modeling process of bioelement desorption from bio- and hydrogel nanocomposites with immobilized nanoparticles of heavy metal compounds, the dynamic of their desorption with an example of copper was studied under the action of natural extractants. A solution of citric acid (~pH 5.5) and plant root exudates of meadow grass (pH 5.8) were used as eluent. The latter was obtained by 4 daily exposure 700 g of the roots in 500 mL of distilled water, and the extractant solution was separated by centrifugation. The grass was previously washed from the soil by deionized water.

We analyzed the step desorption efficiency of bioelements from the nanocomposites under study. The biogel nanocomposite was subjected to preliminary swelling in deionized water for 3 days to loosen the structure and weaken the coagulation contacts between metal-containing nanoparticles, microbial cells, and metabolites (heteropolysaccharides) in aggregates. The desorption procedure included four cycles and consisted of these stages: (1) biogel and hydrogel samples were incubated in desorbing solutions with stirring for 1 day or 1 h, respectively; (2) the solid phase was separated by centrifugation; and (3) the solid phase samples were poured a new portion of the desorbing solution. The amount of bioelement (copper) desorbed was analyzed in the supernatant.

The results obtained (Fig. 37.4) demonstrate a prolonged desorption of bioelements from the gel nanocomposites under the action of exudates excreted by growing plants.

37.3.4 Vegetation Experiments

The obtained nanocomposites of prolonged action with immobilized bioelements were assayed in vegetation tests. The results of plant growth are shown in Fig. 37.5.

Soil enrichment with nanocomposite gel fertilizers resulted in a faster growth of plants and substantial harvest increase (5–10 times) as compared with control

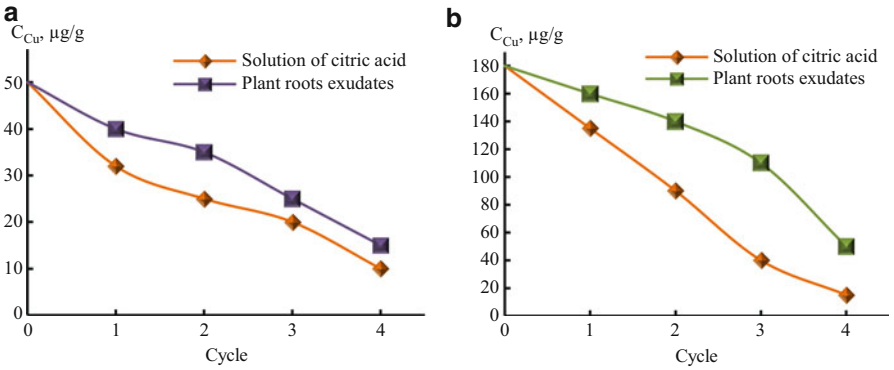

Fig. 37.4 The step desorption efficacy of bioelements from the hydrogel (**a**) and biogel (**b**) nanocomposites

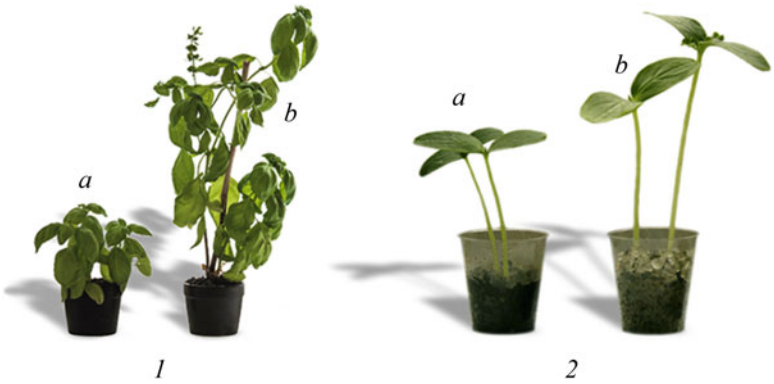

Fig. 37.5 Effect of the biogel (*1*) and hydrogel (*2*) nanocomposite application on plant growth: (**a**) control, unfertilized, soil; (**b**) soil sample with added nanocomposite at an application rate of 4% (weight of dry matter/weight of soil)

(unfertilized) soil. In addition, there were no phytophthora (blight) symptoms in plants grown both in control and fertilized soil samples.

37.4 Conclusions

We proposed the technologies of obtaining nanocomposites with immobilized heavy metal compounds (micro- and macroelements) on the base of pH-sensitive acrylic hydrogel and sludge biogel as soil substrates for land application. They include bioelement incorporation into a hydrogel template or biogel conditioning from heavy metals accessed by bioleaching due to sludge biota activation. These are nanocomposite prolonged-action fertilizers. Soil enrichment with the gel

nanocomposites has resulted in faster growth of plants and a substantial harvest increase as compared with the control (unfertilized) soil.

References

1. Jo Y-K, Kim B, Jung G (2009) Antifungal activity of silver ions and nanoparticles on phytopathogenic fungi. Plant Dis 93(10):1037–1043
2. Krishnaraj C, Ramachandran R, Mohan K et al (2012) Optimization for rapid synthesis of silver nanoparticles and its effect on phytopathogenic fungi. Spectrochim Acta A Mol Biomol Spectrosc 93:95–99
3. Kasprowicz MJ, Koziol M, Gorczyca A (2010) The effect of silver nanoparticles on phytopathogenic spores of Fusarium culmorum. Can J Microbiol 56(3):247–253
4. Nikovskaya GN, Godinchuk NV, Samchenko YM (2011) Removal of heavy metals from aqueous solutions by hydrogels. J Water Chem Technol 33(6):363–368
5. Nikovskaya GN, Kalinichenko KV, Legenchuk AV et al (2011) Heavy metals in sludge sediment after biochemical purification of municipal wastewaters. J Water Chem Technol 33 (5):333–338
6. Kalinichenko KV, Nikovskaya GN, Ulberg ZR (2013) Changes in the surface properties and stability of biocolloids of a sludge system upon extraction of heavy metals. Colloid J 75 (3):274–278
7. Trenkel ME (2010) Slow- and controlled-release and stabilized fertilizers: an option for enhancing nutrient efficiency in agricultural. IFA, Paris
8. Dakora FD, Phillips DA (2002) Root exudates as mediators of mineral acquisition in low-nutrient environments. Plant and Soil 245(1):35–47
9. Berbecea A, Radulov I, Sala F (2008) Agricultural use of sewage sludge pros and cons. Res J Agric 40(2):15–20
10. Chang AC, Pan G, Page AL et al. (2001) Developing human health-related chemical guidelines for reclaimed waster and sewage sludge applications in agriculture. Prepared for World Health Organization
11. Gendebien A (2009) Environmental, economic and social impacts of the use of sewage sludge on land. Draft Summary Report 1, Assessment of Existing Knowledge. Milieu Ltd and WRc for the European Commission
12. Vesilind PA, Spinosa L (2001) Sludge production and characterization. Production and regulations. In: Spinosa L, Vesilind PA (eds) Sludge into biosolids. Processing, disposal and utilization. IWA Publishing, London, pp 3–18
13. Maisonnave V, Montrejaud-Vignoles M, Bonni C (2002) Impact on crops, plants and soils of metal trace elements transfer and flux, after spreading of fertilizers and biosolids. Water Sci Technol 46(10):217–224
14. Wang J-Y, Stabnikova O, Tay STL et al (2004) Biotechnology of intensive aerobic conversion of sewage sludge and food waste into fertilizer. Water Sci Technol 49(10):147–154
15. Constantinescu L (2008) Fertilizing agricultural fields with the sludge resulted from sewage water treatment stations. Res J Agric 40(2):41–44
16. Kalyuzhnyiy SV (2008) Energeticheskiy potentsial anaerobnogo sbrazhivaniya othodov s polucheniem biogaza i ispolzovaniem mikrobnyih toplivnyih elementov v usloviyah Rossii. Biotehnologiya 3:3–12
17. Ahn Y-H, Choi H-C (2004) Municipal sludge management and disposal in South Korea: Status and a new sustainable approach. Water Sci Technol 50(9):245–253
18. Plaza E, Levlin E, Hultman B (1999) Trends in Swedish sludge handling. Sustainable municipal sludge and solid waste handling (5)

19. Nezdoyminov VI, Chernyisheva OA (2010) Migratsiya ionov tyazhelyih metallov pri ispolzovanii osadkov gorodskih stochnyih vod v kachestve udobreniya. VIsnik Donbaskoyi NatsIonalnoyi Akademiyi budIvnitstva I arhItekturi 82(2):150–157
20. McClellana KR, Haldena U (2010) Pharmaceuticals and personal care products in archived US biosolids from the 2001 EPA National Sewage Sludge Survey. Water Res 44(2):658–668
21. O'Connor GA, Chinault SL (2006) Environmental impacts of land applying biosolids. Fla Water Resour J 59(5):50–54
22. Shooner F, Tyagi RD (1996) Thermophilic microbial leaching of heavy metals from municipal sludge using indigenous sulphur-oxidizing microbiota. Appl Microbiol Biotechnol 45 (3):440–446
23. A review of the current Canadian legislative framework for wastewater biosolids (2010) Canadian Council of Ministers of the Environment
24. Wong JWC, Li K, Fang M et al (2001) Toxicity evaluation of sewage sludges in Hong Kong. Environ Int 27(5):373–380
25. Sterritt RM, Lester JN (1981) Concentrations of heavy metals in forty sewage sludges in England. Water Air Soil Pollut 1:125–131
26. Matthews P (2001) Options for biosolids utilization and sludge disposal. Agricultural and other land uses. In: Spinosa L, Vesilind PA (eds) Sludge into biosolids. Processing, disposal and utilization. IWA Publishing, London, pp 41–73
27. Defra report (2007) Long term effects of sewage sludge applications on soil fertility. Setting the results of SP0130 in a policy context. Ministerium für Umwelt, Ernährung und ländliche Angelegenheiten: London
28. Ogilvie D (1998) National study of the composition of sewage sludge. Published by the Drainage Managers Group, A Subgroup of the New Zealand Water and Wastes Association, New Zealand
29. Jakubus M, Czekala J (2001) Heavy metal speciation in sewage sludge. Pol J Environ Stud 10 (4):245–250
30. Zyikova IV (2001) Utilizatsiya izbyitochnyih aktivnyih ilov. Ekologiya i promyishlennost Rossii 12:20–25
31. Wang JY, Zhang DS, Stabnikova O (2004) Processing dewatered sewage sludge using electrokinetic technology. Water Sci Technol 50(9):205–211
32. Ryu HW, Moon HS, Lee EY (2003) Leaching characteristics of heavy metals from sewage sludge by acidithiobacillus thiooxidans MET. J Environ Qual 32(3):745–750
33. Kalinichenko KV, Nikovskaya GN, Ulberg ZR (2014) Biotransformatsiya ilov biologicheskoy ochistki munitsipalnyih stochnyih vod v udobreniya. Biotehnologiya 5:59–65
34. Mortvedt JJ (1996) Heavy metal contaminants in inorganic and organic fertilizers. Fertil Res 43:55–61
35. Council of the European Communities (1986) Council directive 86/278/EEC on the protection of the environment, and in particular of the soil, when sewage sludge is used in agriculture. Official Journal L. 18: 6–12
36. Yu S, Ulberg Z, Korotych O (2011) Multipurpose smart hydrogel systems. Adv Colloid Interface Sci 168:247–262
37. Okay O (2009) General properties of hydrogels. In: Gerlach G, Arndt K-F (eds) Hydrogel sensors and actuators. Springer, Berlin, pp 1–14
38. Kalinichenko KV, Nikovskaya GN, Ulberg ZR (2012) Bioextraction of heavy metals from colloidal sludge systems. Colloid J 74(5):553–557
39. Nikovskaya GN, Kalinichenko KV (2013) Bioleaching of heavy metals from sludge after biological treatment of municipal effluent. J Water Chem Technol 35(2):80–85
40. Sonneveld C, Voogt W (2009) Plant nutrition of greenhouse crops. Springer, London
41. Diels L, De Smet M, Hooyberghs L, Corbisier P (1999) Heavy metals bioremediation of soil. Mol Biotechnol 12(2):149–158
42. Bosecker K (1997) Bioleaching: metal solubilization by microorganisms. FEMS Microbiol Rev 20:591–604

Chapter 38
Nanocomposites Based on Multicomponent Polymer Matrices and Nanofiller Densil for Biomedical Application

L.V. Karabanova, Yu. P. Gomza, S.D. Nesin, O.M. Bondaruk, E.P. Voronin, and L.V. Nosach

38.1 Introduction

For the nanocomposites preparation, the individual polymers have been used most often as polymer matrices [1–5]. Meantime, an essential interest for this purpose could represent the multicomponent polymer matrices obtained by method of interpenetrating polymer networks (IPNs) [6–8]. The existence of several levels of chemical and structural heterogeneities in such matrices could provide the additional opportunities for regulation of nanocomposites' properties. It is known that structure and properties of the IPNs are controlled in particular by kinetics of polymer networks formation and by the thermodynamics of polymer components mixing [9, 10]. Introduction of fillers into such systems could lead to increasing the compatibility of polymer components [11–14]. According to the concepts of equilibrium and nonequilibrium compatibilization of the constituents of IPNs by presence of the fillers [13, 15], the first one occurs due to decreasing of the free energy of mixing of two networks in the presence of fillers, and the second one is associated with the adsorption of polymers on the surface of fillers that inhibits the process of phase separation. So, when creating the nanocomposites based on interpenetrating polymer networks, the problem of the relationship between the conditions of phase separation of the components and peculiarities of their interaction with the filler arises. Depending on the nature of the surface, the filler

L.V. Karabanova (✉) • Yu. P. Gomza • S.D. Nesin • O.M. Bondaruk
Institute of Macromolecular Chemistry of National Academy of Sciences of Ukraine, Kharkov Road 48, Kiev 02660, Ukraine
e-mail: lyudmyla_karaban@ukr.net

E.P. Voronin • L.V. Nosach
Chuiko Institute of Surface Chemistry of National Academy of Sciences of Ukraine, Kiev 03164, Ukraine

O. Fesenko, L. Yatsenko (eds.), *Nanophysics, Nanophotonics, Surface Studies, and Applications*, Springer Proceedings in Physics 183,
DOI 10.1007/978-3-319-30737-4_38

influenced the concentration of components in the volume and near the surface, and the filler influenced also the mobility of macromolecules on the boundaries with the surface. These alter the speed of microphase separation during the formation of interpenetrating polymer networks and leads to the formation of materials which significantly modified the complex of properties [6, 8, 16]. The investigation of interfacial interactions in such systems is one of the most important objectives since the formation of polymer–filler interactions in the filled systems is crucial, and it generally determines the structure and the properties of the created nanocomposites [16]. Therefore, evaluation of thermodynamic affinity between fillers and polymer components in the filled polymer systems has the practical interest.

We have previously synthesized and investigated the semi-IPNs based on polyurethane (PU), and poly(2-hydroxyethyl methacrylate) (PHEMA) [17–21], and the 3D diamond- [22, 23] and oxide-containing [8, 24] nanocomposites based thereon, as the materials for biomedical applications and damping materials. The dynamic mechanical behavior, segmental motions, mechanical properties, and structural peculiarities have been studied in such systems using atomic force microscopy (AFM), dynamic mechanical analysis (DMA), laser-interferometric creep rate spectroscopy (CRS), differential scanning calorimetry (DSC), and small-angle X-ray scattering (SAXS) techniques [8, 17–26]. It was shown that these systems have basically two-phase, nanoheterogeneous structure with incomplete phase separation, and the pronounced dynamic heterogeneity within the extraordinarily broadened PHEMA and PU glass transitions.

The goal of this study is the investigation of the thermodynamic of polymer–filler interactions within formation of the nanocomposites, consisting of a three-dimensional polyurethane, poly(2-hydroxyethyl methacrylate) and nanofiller densil, the evaluation of structural features, and physical and dynamic mechanical properties of the created nanocomposites.

38.2 Materials and Testing Methods

38.2.1 Materials

Neat PU and PHEMA, semi-IPNs based on PU and PHEMA, and nanofiller densil containing nanocomposites based thereon were prepared as described previously [23, 27]. First, the PU network was obtained from the adduct of trimethylol propane, toluene diisocyanate, and poly(oxypropylene)glycol (PPG) with $M_w = 2$ g mol^{-1}. The semi-IPNs with 17 and 37 wt% of PHEMA were obtained by swelling of PU network with 2-hydroxyethyl methacrylate (HEMA) and its subsequent photopolymerization (the wavelength of UV light 340 nm).

For preparing the nanocomposites with PU, PHEMA, and semi-IPN matrices, the nanofiller densil was used. Densil is the product of nanosilica A-300 (~8 nm in diameter and ~50 g/dm^3 in density) modification by mechano-sorptive method

[28]. The result of such modification is the changes in asperity of surface and porosity of nanofiller (densil, 325–330 g/dm^3 in density) [28].

Densil was introduced with the amounts of 1–15 wt% into a polymer system at the stage of PU synthesis or into HEMA in the case of preparing the nanocomposite based on neat PHEMA. The prepared films with 1 mm thickness were post-cured for 2 h at 100 °C and then were held for 36 h at 80 °C in vacuum 10^{-5} Pa.

38.2.2 Testing Methods

Vapor Sorption and Thermodynamic Calculations

The dichloromethane vapor sorption by semi-IPN samples and by nanocomposites samples was studied using a vacuum installation and a McBain balance [15]. The changes in partial free energy of dichloromethane by sorption (dissolution) were determined from the experimental data using (38.1)

$$\Delta\mu_1 = (1/M)RT\ln(P/P_0), \tag{38.1}$$

where M is the molecular mass of dichloromethane and P/P_0 is the relative vapor pressure. The value $\Delta\mu_1$ changes with solution concentration from 0 to $-\infty$.

To calculate the free energy of mixing of the polymer components with the solvent, the changes in partial free energy of the polymers (native polymers, semi-IPNs, nanocomposites) need to be determined. This requires the calculation of the difference between the polymer chemical potential in the solution of a given concentration and in pure polymer under the same conditions ($\Delta\mu_2$). $\Delta\mu_2$ for the polymer components were calculated using the Gibbs–Duhem equation:

$$\omega_1 d(\Delta\mu_1)/d\omega_1 + \omega_2 d(\Delta\mu_2)/d\omega_1 = 0, \tag{38.2}$$

where ω_1 and ω_2 are the weight fractions of a solvent and of a polymer. This can be rearranged to give (38.3)

$$\int d(\Delta\mu_2) = -\int (\omega_1/\omega_2) d(\Delta\mu_1) \tag{38.3}$$

Equation 38.3 allows the determination of $\Delta\mu_2$ for each polymer from the experimental data by integration over definite limits. The average free energy of mixing of solvent with the individual components, semi-IPNs of various compositions for the solutions of different concentration, was then estimated using (38.4) and using computational analysis:

$$\Delta g^m = \omega_1\Delta\mu_1 + \omega_2\Delta\mu_2 \tag{38.4}$$

Small-Angle X-ray Scattering

The peculiarities of the microheterogeneous structure of the unfilled semi-IPNs and nanocomposites based on semi-IPNs matrices have been investigated by small-angle X-ray scattering. Small-angle X-ray scattering (SAXS) studies have been carried out with a vacuum Kratky camera. X-ray source was a CuK_{α} line monochromated with total internal reflection and nickel filters [29]. Data collection has been carried out in a regime of multiple step scanning of a scintillation detector in the range of scattering angles of 0.03–4.0°, which corresponded to the values of wave vectors q of 0.022–2.86 nm^{-1} ($q = 4\pi \cdot \sin \theta/\lambda$, where θ is a half of the diffraction angle 2θ and λ is the wavelength of X-ray radiation emitted by the copper anode $\lambda = 0.154$ nm). SAXS method is sensitive to local variations of the density due to the presence of domains of higher-than-average density or voids with smaller-than-average density and distribution of such heterogeneity with characteristic dimensions (determined as $2\pi/q$) in the range of 2–280 nm. The initial treatment of the data has been performed with the FFSAXS program [30], including the procedures of background noise subtraction, normalizing of the diffraction curves to the absolute values of scattering, and application of collimation corrections. The treated diffraction curves were then used for calculations of the mean square fluctuations of the electron density and three-dimensional correlation functions in accordance to the procedures described in [31].

Dynamic Mechanical Analysis

The dynamic mechanical analysis (DMA) measurements were carried out using a Dynamic Mechanical Thermal Analyzer Type DMA Q800 from TA Instruments over the temperature range from −100 to +220 °C and at fixed frequency 10 Hz with a heating rate of 3 °C/min. The experiments were performed in the tension mode on rectangular specimens (35 mm × 5 mm × 1 mm). As poly(2-hydroxyethyl methacrylate) is a hydroscopic polymer, all samples were dried at 80 °C for 48 h under vacuum before measurements. The samples were subsequently subjected to the following thermal cycle during DMA measurements: a first run from 20 °C up to100 °C and then second run from −100 °C up to +220 °C. The second run was used for analysis of the results.

Mechanical Testing

Mechanical properties of the neat PU and PHEMA, their semi-IPNs, and nanofiller densil containing nanocomposites were measured using a Series IX Automated Instron Materials Testing System. The samples were cut into micro dumbbell shapes with gauge length of 20 mm, widths between 4 and 5 mm, and sample thickness between 0.7 and 0.9 mm. Samples were processed at a continuous strain rate of 25 mm/min.

38.3 Results and Discussion

38.3.1 Thermodynamic of Polymer–Filler Interactions in the Nanocomposites

Figure 38.1 shows the isotherms of dichloromethane vapor sorption at 20 °C by samples of the semi-IPN with 17 % PHEMA (curve 1), of the nanocomposites with polymer matrix that is the semi-IPN with 17 % PHEMA and nanofiller densil (curves 2–4), and of native nanofiller (curve 5). As could be seen (Fig. 38.1), the unfilled semi-IPN with 17 % PHEMA has a maximum sorption capacity (curve 1), and the introduction of nanofiller lead to decrease of the nanocomposite's sorption capacity (curves 2–4). This indicates about the formation of tightly packed boundary layers of polymers on the surface of densil in the nanocomposites. The curves for the nanocomposites containing 10 and 15 % of densil are almost identical (Fig. 38.1). This may be the result of densil's particles aggregation in the nanocomposite with its content of 15 %. The last leads to a relative reduction of the effective surface of the filler's particles, on which the boundary layers of the polymers are formed.

Figure 38.2 shows the isotherms of dichloromethane vapor sorption at 20 °C by samples of the semi-IPN with 37 % PHEMA (curve 1), of the nanocomposites with polymer matrix that is the semi-IPN with 37 % PHEMA and nanofiller densil (curves 2–4), by sample of native nanofiller (curve 5). For the nanocomposite with the highest amount of densil (15 %), the decrease of sorption capacity is observed (Fig. 38.2, curve 4) in comparison with the matrix (Fig. 38.2, curve 1). For nanocomposite with 3 % of densil, the increased vapor sorption of dichloromethane (Fig. 38.2, curve 2) in comparison with the matrix (Fig. 38.2, curve 1) could be seen. For example, containing 10 % of densil (Fig. 38.2, curve 3), the vapor sorption isotherm is almost the same as for polymer matrix (Fig. 38.2,

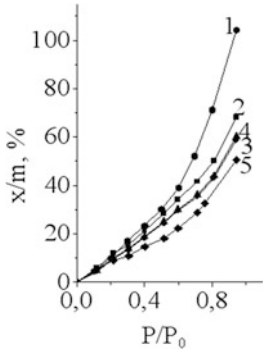

Fig. 38.1 Isotherms of dichloromethane vapor sorption at 20 °C by samples: *1*, semi-IPN with 17 % PHEMA; *2*, nanocomposite with matrix semi-IPN with 17 % PHEMA and 3 % of densil; *3*, nanocomposite with matrix semi-IPN with 17 % PHEMA and 10 % of densil; *4*, nanocomposite with matrix semi-IPN with 17 % PHEMA and 15 % of densil; *5*, nanofiller densil

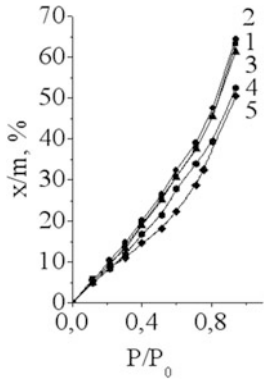

Fig. 38.2 Isotherms of dichloromethane vapor sorption at 20 °C by samples *1*, semi-IPN with 37 % PHEMA; *2*, nanocomposite with matrix semi-IPN with 37 % PHEMA and 3 % of densil; *3*, nanocomposite with matrix semi-IPN with 37 % PHEMA and 10 % of densil; *4*, nanocomposite with matrix semi-IPN with 37 % PHEMA and 15 % of densil; *5*, nanofiller densil

curve 1). The differences in the sorption capacity of the nanocomposites based on two matrices (containing 17 % of PHEMA and 37 % of PHEMA) may be connected with the changes in conditions of phase separation of polymer components and with peculiarities of their interaction with a filler with an increased amount of PHEMA in the semi-IPN from 17 to 37 %. It was shown [32] that the semi-IPNs of intermediate compositions have a significant part of interfacial layers which is characterized by the excessive free volume. The nanocomposite's sorption capacity is the result of these two processes competition: the formation of dense surface layers on the surface of the nanofiller and the formation of interfacial layers with the excessive free volume.

The use of the thermodynamic methods and calculations based on experimental data of vapor sorption of dichloromethane by nanocomposites samples allowed us to estimate a number of characteristics of the systems, namely, the free energy of interaction of polymers with solid surfaces. In [33] the thermodynamic parameters of the polymer–polymer interactions estimation are described. For this the approach based on the fundamental assumptions of independence of thermodynamics enthalpy and free energy of the system from the way of the process was used [33]. In [34, 35] this approach for the polymer–filler systems was applied. Under this approach, we can calculate the parameters of interaction of polymer with a filler when parameters of the interaction of each of them and their mixtures with fluid are known. Based on isotherms of sorption, the change of the partial free energy of dichloromethane $\Delta\mu_1$ was calculated using (38.1). The change in the partial free energy of individual polymer components, semi-IPNs, and filled systems under sorption process $\Delta\mu_2$ was determined in accordance with the Gibbs–Duhem equation (38.2). Free energy of mixing of individual polymers and semi-IPNs with solvent Δg^{m} was determined in accordance with the (38.4).

In Fig. 38.3 the calculated values of Δg^{m} for the semi-IPN, nanocomposites, and nanofiller densil are presented. It is evident that all the systems under investigation,

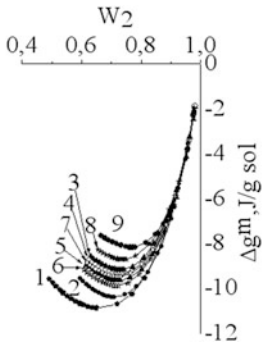

Fig. 38.3 Free energies of mixing of polymers and nanofiller with solvent dichloromethane Δg^{m}: *1*, semi-IPN with 17 % PHEMA; *2*, nanocomposite with matrix semi-IPN with 17 % PHEMA and 3 % of densil; *3*, nanocomposite with matrix semi-IPN with 17 % PHEMA and 10 % of densil; *4*, nanocomposite with matrix semi-IPN with 17 % PHEMA and 15 % of densil; *5*, semi-IPN with 37 % PHEMA; *6*, nanocomposite with matrix semi-IPN with 37 % PHEMA and 3 % of densil; *7*, nanocomposite with matrix semi-IPN with 37 % PHEMA and 10 % of densil; *8*, nanocomposite with matrix semi-IPN with 37 % PHEMA and 15 % of densil; *9*, nanofiller densil

semi-IPN (dichloromethane), nanocomposites (dichloromethane), nanofillers (dichloromethane), are thermodynamically stable ($d^2\Delta g^{m}/dW_2{}^2 > 0$), although the affinity of dichloromethane to semi-IPN with 17 % PHEMA (Fig. 38.3, curve 1) is the highest.

With the introduction of densil into the polymer matrix, the affinity of dichloromethane to the nanocomposites decreases (Fig. 38.3, curves 2–4). The affinity of dichloromethane is lower in the case of the semi-IPN with 37 % PHEMA (Fig. 38.3, curve 5) in comparison with the semi-IPN with 17 % PHEMA (Fig. 38.3, curve 1). The affinity of dichloromethane to the nanocomposites based on polymer matrix semi-IPN with 37 % PHEMA decreases with the content of nanofiller (Fig. 38.3, curves 6, 7, 8). But there is the nonmonotonic dependence of affinity of dichloromethane with the amount of nanofiller.

Based on the concentration dependence of the average free energy of mixing of the solvent with individual polymers PU, PHEMA, and nanocomposites, the values ΔG_1 and ΔG_{111} were obtained. ΔG_1 and ΔG_{111} are the free energies of interaction of polymer and nanocomposite with lots of solvent. For ΔG^{*}_{p-f} calculation (free energy of polymer–filler interaction), the (38.5) was used:

$$\Delta G^{*}_{p-f} = \Delta G_1 + n\Delta G_{11} - \Delta G_{111}, \tag{38.5}$$

where ΔG_{11} is the free energy of interaction of the filler with lots of solvent.

The calculation of $\Delta\mu_{2(fil)}$ for filler have been conducted according to the Gibbs–Duhem equation, as it was done above for polymers. Then the (38.6) was used for calculation of free energy of interaction of dichloromethane with densil:

$$\Delta g^{m} = W_1\Delta\mu_1 + W_2\Delta\mu_{2\,(fil)}, \tag{38.6}$$

Table 38.1 The free energy of interaction of the semi-IPNs with nanofiller densil ΔG^*_{p-f} in the nanocomposites

Sample	Free energy of polymer–filler interaction ΔG^*_{p-f}, J/g polymer
Semi-IPN with 17 % PHEMA + 3 % densil	−3.16
Semi-IPN with 17 % PHEMA + 10 % densil	−5.11
Semi-IPN with 17 % PHEMA + 15 % densil	−4.92
Semi-IPN with 37 % PHEMA + 3 % densil	+0.55
Semi-IPN with 37 % PHEMA + 10 % densil	+0.02
Semi-IPN with 37 % PHEMA + 15 % densil	−1.54

The dependence of $\Delta g^m = f(W_2)$ for filler (Fig. 38.3, curve 9), as well as for three-dimensional polymers, has the form of curves with a minimum and cut off at the critical amount of solvent.

Using the obtained values of the free energy of filler interaction with solvent (ΔG_{11}), according to the (38.5), the values of the free energy of interaction of semi-IPNs with nanofiller were calculated. The results of such calculations are shown in Table 38.1.

As could be seen, the values of free energy of interaction of densil with polymer matrix (Table 38.1), which is the semi-IPN with 17 % PHEMA, are negative for all concentrations of nanofiller. It is evidence about the thermodynamic stability and the strength of the filled samples of semi-IPN and about the high adhesion of polymer components to the nanofiller densil.

With increasing the PHEMA amount in the polymer matrix from 17 to 37 %, the values of the free energy of polymer–filler interaction became positive for filler content of 3 and 10 % (Table 38.1). Only with increasing filler content up to 15 %, it again becomes negative. This is, for our opinion, the result of competition between two processes: the formation of the dense layers of polymers on the surface of the filler and the formation of interfacial layers with the excessive free volume in the nanocomposites based on polymer matrix, which is semi-IPN with 37 % of PHEMA.

38.3.2 Structure Peculiarities of the Nanocomposites by SAXS

In Fig. 38.4 the small-angle scattering curves for the two semi-IPNs based on polyurethane and poly (2-hydroxyethyl methacrylate), containing 17 and 37 wt% of PHEMA, and for nanofiller densil are presented. The structure of semi-IPNs was investigated and described in detail in previous work [36]. It was shown that such materials are two-phase systems with incomplete microphase separation and with the presence of two hierarchical levels of heterogeneity. The first level is the concentration fluctuations with sizes of 30–40 Å which are fixed in the early stage of spinodal decomposition, the second level of heterogeneity corresponds to

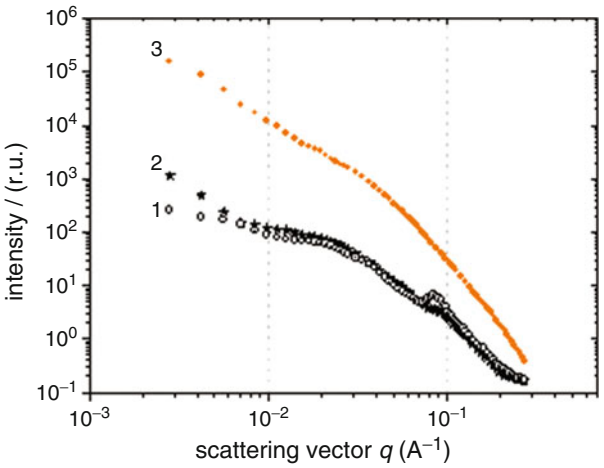

Fig. 38.4 SAXS intensity $I(q)$ versus scattering vector q, for semi-IPN with 17 % PHEMA (*1*), semi-IPN with 37 % PHEMA (*2*), and nanofiller densil (*3*)

later stages of microphase separation, and it is characterized by the release of almost pure polyurethane microinclusions and PHEMA domains that include polyurethane chains [36].

The main difference between the curves for the two semi-IPNs presented in Fig. 38.4 is the different degree of expression of polyurethane diffraction peak, located at $q^* = 0.8$. It is well defined for semi-IPN containing 17 % PHEMA and virtually traced for semi-IPN with a higher content of PHEMA.

Curve scattering by densil (Fig. 38.4, curve 3) is characterized by two linear sections of intensity plot: the first one is in the range of q from 0.027 to 0.200 nm^{-1}, with a slope of −4.0, and the second one is in the range of q from 0.5 to 2.7 nm^{-1}, with a slope of −2.1. The value of the slope of the first section −4.0 reflects the presence of nearly smooth surface of nanofiller. The slope of the second section displays the mass–fractal nature of the aggregation of the primary particles of nanofiller [37, 38].

The plot kink between them (ranging q from 0.2 to 0.5 nm^{-1}) corresponds to the Guinier contribution, which allows to calculate the radius of gyration of the nanofiller's particle R_g assuming their spherical shape [39]. The calculations, carried out in accordance to the algorithm Guinier, gave values of $R_g = 5.0$ nm. For spherical particles, this corresponds to a diameter $d_{sf} = R_g\ 2.58 = 12.9$ nm.

In Fig. 38.5a, the small-angle scattering curves for native polyurethane, for the nanofiller densil, and for a series of nanocomposites containing densil from 1 to 15 % by weight are presented. As could be seen from Fig. 38.5a, the curve for the native polyurethane is characterized by a diffraction peak with a maximum at wave vector value $q^* = 0.8$ nm^{-1}. This corresponds to a periodicity of $2\pi/q^*$ equal to 7.9 nm, which fits to the spatial periodicity of microinclusions location enriched by rigid component [29].

From Fig. 38.5a, it is evident that introduction of already a minimum amount of nanofiller densil into the polymer matrix, which is in this case the polyurethane,

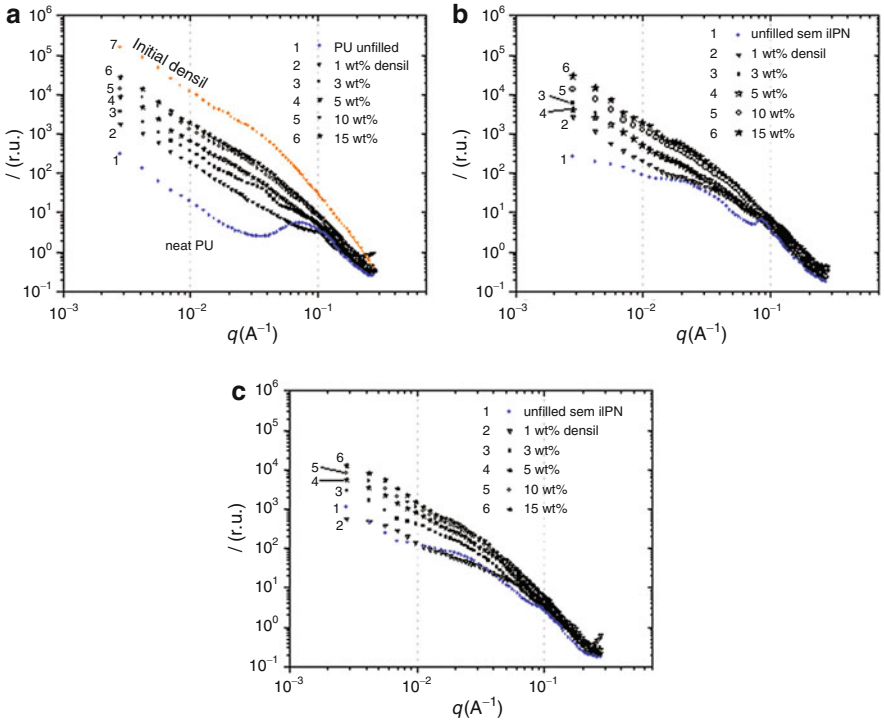

Fig. 38.5 SAXS intensity $I(q)$ versus scattering vector q, for the nanocomposites containing nanofiller densil based on PU matrix (**a**), based on matrix semi-IPNs with 17 wt% PHEMA (**b**), and based on matrix semi-IPNs with 37 wt% PHEMA (**c**)

results in essential changes in small-angle scattering. The scattering intensity in the range of wave vector value q^* from 0.027 to 0.6 is substantially higher for the nanocomposite, as compared with the scattering intensity for the native polyurethane. Additionally, the polyurethane's dispersion maximum, observed on the curve of native polyurethane, almost completely disappears in the nanocomposite. With further increasing of the nanofiller content in the nanocomposites (3–15 %), the systematic evolution of nanocomposite's curve dispersion to the curve characteristic for the nanofiller is observed.

That is, after introduction of nanofiller in quantities exceeding 3 %, we are able to detect on the scattering curves of the nanocomposites only this component, whereas the contribution of the polyurethane matrix becomes neglectly small. This reflects the fact that the level of scattering by the nanofiller is about three orders of magnitude higher than the scattering intensity by the polyurethane matrix.

For better understanding the nature of structural changes in the polyurethane matrix with the introduction of a minimum amount of nanofiller, we should take into account the fact that the average size of nanofiller particles is approximately two times higher than the value of spatial periodicity of the microregion's location

Table 38.2 Values of the slopes of the linear sections of small-angle X-ray scattering (SAXS) curves

Samples	Filler content (wt%)	$S_{1\ (slope)}$	$S_{2\ (slope)}$
PU neat	0	−2.7	−1.8
PU + 3 % densil	3	−3.0	−2.1
PU + 5 % densil	5	−3.5	−2.1
PU + 10 % densil	10	−3.3	−2.0
PU + 15 % densil	15	−3.3	−2.1
semi-IPN17 neat	0	−3.3	−1.8
semi-IPN17 + 3 % densil	3	−3.5	−1.9
semi-IPN17 + 5 % densil	5	−3.6	−2.0
semi-IPN17 + 10 % densil	10	−3.7	−2.0
semi-IPN17 + 15 % densil	15	−3.7	−2.1
semi-IPN37 neat	0	−3.0	−1.3
semi-IPN37 + 3 % densil	3	−3.0	−1.5
semi-IPN37 + 5 % densil	5	−3.5	−1.7
semi-IPN37 + 10 % densil	10	−3.7	−1.7
semi-IPN37 + 15 % densil	15	−3.7	−1.8
Densil	100	−4.0	−2.1

enriched by rigid component. It should also be noted that the introduction of the nanofiller occurs into the monomer mixture before polymer synthesis. This means that polyurethane formation occurs in the presence of nanofiller distributed in the reaction mass. The surface of nanofiller affects the formation of the polymer matrix. So, the fact of complete disappearance of polyurethane maximum on the curve of nanocomposite with 1 % of nanofiller could be consider as indirect evidence of approximate uniform distribution of nanofiller in the bulk of the nanocomposite.

When the content of nanofiller in the polyurethane matrix increases from 3 to 15 %, the manifestations of polyurethane diffraction peak on the corresponding scattering curves disappear completely. The scattering curves of nanocomposites, like the original scattering curve of nanofiller densil (Fig. 38.4, curve 3), are characterized by the presence of two linear sections. Table 38.2 shows the values of slopes of the linear sections. As could be seen from Fig. 38.5a and Table 38.2, the value of slope S_2 is −1.8 for the nanocomposite with filler content 1 % and comes close to −2.1 by increasing the nanofiller content from 3 to 15 % which is the value for native densil. At the same time, there is a gradual transition of the scattering curves of the nanocomposites in Fig. 38.5a to the curve characteristic of pure nanofiller. This fact can be interpreted in favor of the assumption of a process of loosening of nanofiller's aggregates at 1 % filler content and the almost complete preservation of the character of its aggregation at concentrations of nanofiller ranging from 3 to 15 % in the nanocomposites.

From the above presented analysis, we could suggest homogeneous distribution of nanofiller in the nanocomposite at its minimum content (1 %) and its aggregation with content of nanofiller exceeding this value (3–15 %) in the nanocomposites based on polyurethane matrix.

Table 38.2 shows the values of the slopes of the two linear sections of the scattering curves observed in Fig. 38.5b. Comparison with the corresponding values of the slopes for the nanocomposites based on the polyurethane matrix leads to the conclusion about the expansion of the limit of homogeneous nanofiller distribution from 1 % (in the case of polyurethane matrix) to 3 % (in the case of semi-IPN17 as a matrix).

The results for the nanocomposites based on the semi-IPN containing 37 % of linear PHEMA as matrix are presented in Fig. 38.5c. As could be seen, for the native polymer matrix, unlike the previous matrices, only traces of the polyurethane diffraction peak (in the range of wave vector value about 1.0 nm^{-1}), so that it makes no sense to attribute them to any spatial periodicity. At the introduction of 1 % of nanofiller into this polymer matrix, the traces of polyurethane diffraction peak disappear completely, similar to the case of the semi-IPN17 matrix. The main difference in the results of the investigation of this system and the nanocomposite based on the semi-IPN17 is the following. For the nanocomposite based on semi-IPN17 containing 1 % of nanofiller, a significant excess of scattering was observed, as compared with the unfilled system (Fig. 38.5b). For the nanocomposite based on semi-IPN37, on the contrary, changes are hardly observed: the scattering curve for the nanocomposite containing 1 % nanofiller is very close to the scattering curve for the native polymer matrix (Fig. 38.5c). This result could be the indirect evidence that in the matrix of semi-IPN37 the nanofiller is distributed not only in the flexible part of the polyurethane component (as in the case of nanocomposites based on polyurethane matrix) but also in the domains containing linear PHEMA. Analysis of the changes of the slope of the second linear section of the scattering curves with concentration (Table 38.2) is in favor of the assumption of further homogenization of nanofiller distribution in the nanocomposites based on semi-IPN37 in the region up to 5 % nanofiller content. The values of the mass–fractal dimension of nanofiller aggregates are much lower for the nanocomposites based on semi-IPN37 than those observed for semi-IPN17.

Thus, the investigation of the structural features of the binary nanocomposites polyurethane–densil allows the following conclusions about the behavior of nanofiller particles in the system. Nanofiller at minimum content (1 %) is almost uniformly distributed in the polyurethane matrix, while by increasing its content in the matrix, aggregation occurs in the form of mass–fractal structures, typical for the native nanofiller. When we use the multicomponent polymer matrix (semi-IPNs), the second polymer component in the matrix promotes the homogenization of nanofiller distribution in case of PHEMA 17 from 1 to 3 % and in the case of PHEMA 37 from 1 to 5 %. Raising the threshold of homogenization of nanofiller distribution is the result of reorganization of filled polyurethane during the process of formation of nanocomposites based on the multicomponent polymer matrix. When the swelling of filled polyurethane with the monomer HEMA occurs during the formation of nanocomposites, destruction of loose aggregates of nanofiller and improvement of its uniform distribution could take place. The uniform distribution is further supported by photopolymerization of the monomer HEMA. On the basis of these results, we could assume optimum physical and mechanical properties of

the systems where the concentration of nanofiller is near its respective threshold for aggregation (i.e., 1 % for the nanocomposites with polyurethane matrix, 3 % for those with semi-IPN 17 matrix, and 5 % for those with semi-IPN 37 matrix).

38.3.3 *Dynamic Mechanical Properties of the Nanocomposites*

Figure 38.6 shows the temperature dependences of mechanical loss tangent δ for neat polyurethane (curve 1), for poly(2-hydroxyethyl methacrylate) (curve 2), and for two semi-IPNs, which contain 17 % (curve 3) and 37 % (curve 4) of PHEMA (semi-IPN17PHEMA and semi-IPN37PHEMA, respectively). As could be seen for the unfilled polyurethane, the abnormally wide glass transition with a maximum at −25 °C (Fig. 38.6, Table 38.3) is observed. The neat PHEMA shows the intense maximum of mechanical loss tangent δ at + 140 °C. For semi-IPN with a low amount of PHEMA (17 %), two peaks of mechanical loss tangent δ, according to the presence of two polymers, are observed. The amplitude of polyurethane maximum in semi-IPN17PHEMA somewhat decreases, due to the restriction effect of PHEMA on the segmental motion in polyurethane, but its temperature position is practically unchanged. The maximum of PHEMA in semi-IPN17 significantly decreases and shifts toward low temperatures (Fig. 38.6, curve 3) in comparison with neat PHEMA, which is the result of incomplete phase separation in the system [15, 17].

For semi-IPN which contain 37 % of PHEMA (Fig. 38.6, curve 4), the significant differences in comparison with the curve for semi-IPN17could be seen: the polyurethane maximum shifts to low temperatures, the maximum of PHEMA is much higher, and it is located in the temperature range of the neat polymer. The plateau between the two maxima located considerably below for semi-IPN37 in

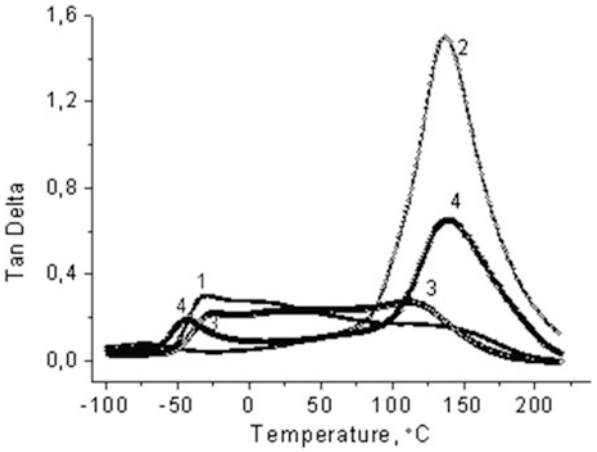

Fig. 38.6 Dynamic mechanical measurements of tan δ versus temperature at a frequency of 10 Hz for samples *1*, PU; *2*, PHEMA; *3*, semi-IPN with 17 % PHEMA; *4*, i-IPN with 37 % PHEMA

Table 38.3 The glass transition temperatures of polymer components and storage modulus of the nanocomposites depend on the ratio of components in the semi-IPNs and the filler content

Sample	Temperature of glass transition (tangent δ maximum), °C		Storage modulus at +25 °C, MPa	Storage modulus at −25 °C, MPa
	PU	PHEMA		
PU	−25	–	59	689
PHEMA	–	+140	3140	4448
IPN 17 PHEMA	−25	+112.5	150	1380
IPN 17 PHEMA + 3 % densil	−32.5	+125	254	1077
IPN 17 PHEMA + 5 % densil	−28.7	+125	440	1689
IPN 17 PHEMA + 10 % densil	−28.7	+115	248	1254
IPN 17 PHEMA + 15 % densil	−25	+107.5	356	1714
IPN 37 PHEMA	−42.5	+140	580	1333
IPN 37 PHEMA + 3 % densil	−33.7	+125	349	1222
IPN 37 PHEMA + 5 % densil	−35	+125	480	1527
IPN 37 PHEMA + 10 % densil	−37.5	+132.5	595	1642
IPN 37 PHEMA + 15 % densil	−33.7	+127.5	723	2191

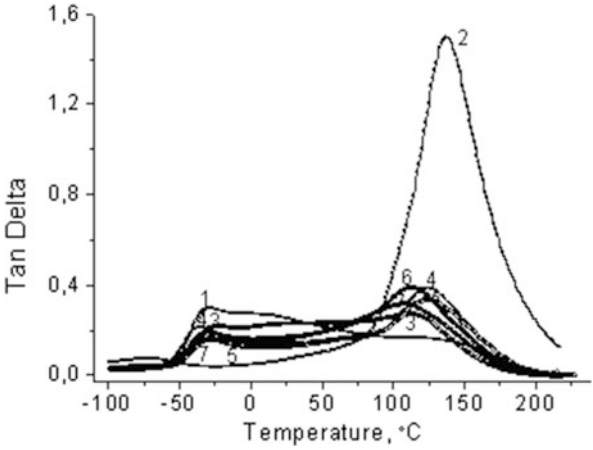

Fig. 38.7 Dynamic mechanical measurements of tan δ versus temperature at a frequency of 10 Hz for samples PU (*1*), PHEMA (*2*), semi-IPN with 17 % PHEMA (*3*), nanocomposites based on semi-IPN with 17 % PHEMA contained 3 % of densil (*4*), contained 5 % of densil (*5*), contained 10 % of densil (*6*), contained 15 % of densil (*7*)

comparison with semi-IPN17 that could indicate about significantly deeper microphase separation in the semi-IPN37.

Figure 38.7 presents the temperature dependence of mechanical loss tangent δ for polyurethane (curve 1); for neat poly(2-hydroxyethyl methacrylate) (curve 2); for semi-IPN, which contain 17 % of PHEMA (curve 3); and for the nanocomposites filled with nanofiller densil (curves 4–7). As could be seen, the maximum of mechanical loss tangent δ, associated with segmental motion in PHEMA, in the nanocomposites, as well as in the semi-IPN17, shifts to lower temperatures and reduced by amplitude. The maximum of mechanical loss tangent δ which associated with segmental motion in polyurethane, in the nanocomposites,

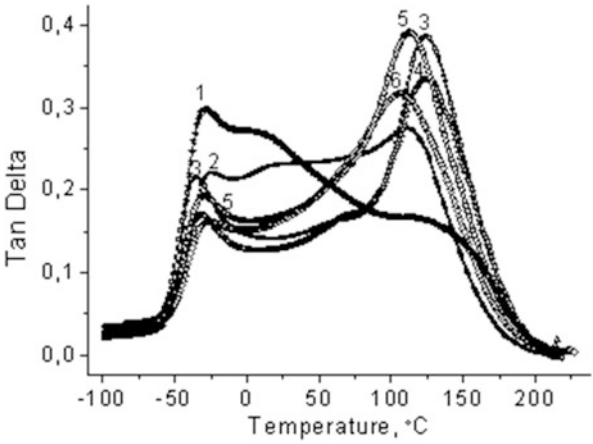

Fig. 38.8 Dynamic mechanical measurements of tan δ versus temperature at a frequency of 10 Hz for samples PU (*1*), semi-IPN with 17 % PHEMA (*2*), nanocomposites based on semi-IPN with 17 % PHEMA contained 3 % of densil (*3*), contained 5 % densil (*4*), contained 10 % of densil (*5*), contained 15 % of densil (*6*)

also decreases compared to the neat polymer. These processes are shown in Fig. 38.8 in details. From Fig. 38.8, it is clear that, in general, the maxima of mechanical loss tangent δ of polyurethane in the nanocomposites decrease by amplitude in comparison with polyurethane in semi-IPN. It is evidence about the restriction of the segmental motion in polyurethane by nanofiller densil in the filled systems. For the maxima of mechanical loss tangent δ of PHEMA in the nanocomposites (Fig. 38.8, curves 3–6), the opposite effect is observed: after introduction of densil in the semi-IPN, they increase by the amplitude and shift on the temperature scale. The growth of PHEMA maxima in the nanocomposites means a more free segmental motion of PHEMA in the nanocomposite's samples. The last could indicate that nanofiller densil mainly concentrated in the nanodomains of polyurethane that leads to the restriction of its segmental motion. On the other hand, the introduction of nanofiller in the semi-IPN17 also leads to the deepening of microphase separation between the polymer components. As result, we observe the increase of the maxima of PHEMA in the nanocomposites and the deepening of the minimum between two maxima (PU and PHEMA) in comparison with the unfilled semi-IPN (Fig. 38.8, curve 2).

Figure 38.9 shows the storage modulus of polyurethane (curve 1), PHEMA (curve 2), semi-IPN with 17 % PHEMA (curve 3), and the nanocomposites with different amount of densil (curves 4–7). As could be seen, the PHEMA demonstrates the highest storage modulus in all temperature range, and polyurethane demonstrates the minimal storage modulus. The storage modulus of the semi-IPN and of the nanocomposites increases in comparison with the polyurethane, particularly in the temperature range from −50 to +50 °C. Table 38.3 shows the values of the storage modulus of the samples at 25 °C and at −25 °C. As could be seen, the storage modulus of nanocomposites at −25 °C is significantly higher than the storage modulus of polymer matrices (Table 38.3). At −25 °C the nonmonotonic change of storage modulus of nanocomposites with content of nanofiller is observed.

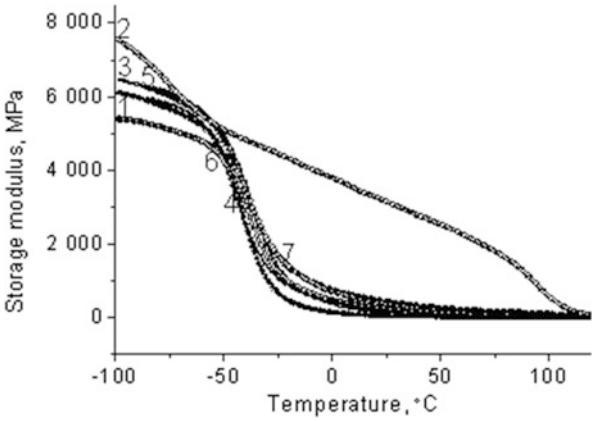

Fig. 38.9 The temperature dependence of the storage modulus at a frequency of 10 Hz for samples PU (*1*), PHEMA (*2*), semi-IPN with 17 % PHEMA (*3*), nanocomposites based on semi-IPN with 17 % PHEMA contained 3 % of densil (*4*), contained 5 % of densil (*5*), contained 10 % of densil (*6*), contained 15 % of densil (*7*)

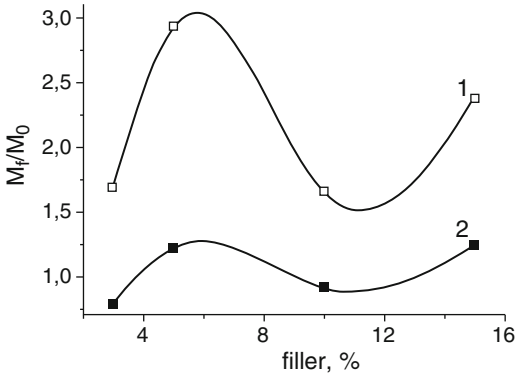

Fig. 38.10 The concentration dependence of the ratio of storage modulus of the nanocomposites to the storage modulus of the unfilled matrix semi-IPN PU/PHEMA 83/17 at different temperatures: *1*, at +25 °C; *2*, at −25 °C

In Fig. 38.10 the ratio of the storage modulus of nanocomposites to the storage modulus of matrix M_n/M_o with nanofiller content is presented. As could be seen, the value of M_n/M_o nonmonotonously varies with filler content. With introduction of 3–5 % of densil, the modulus of nanocomposites increases by 1.5–3 times. With further growing of filler content up to 10 %, the relative decreasing of storage modulus of nanocomposite is observed. With the introduction of 15 % densil, the storage modulus of nanocomposite begins to grow again. This nonmonotonic dependence of the storage modulus with the filler content, for our opinion, associated with the formation of aggregates and clusters of nanofiller at concentrations exceeded 5 % by weight. As a result, the specific surface area of the nanofiller, which affects the properties of the matrix, decreases. The similar dependence from filler content is also found for the mechanical properties of the nanocomposites [40], where the maximum of stress at break was observed for nanocomposites, which contained 5 % densil by weight.

In Fig. 38.11 the temperature dependence of mechanical loss tangent δ for neat polyurethane (curve 1), for semi-IPN, contained 37 % PHEMA (curve 2) and, for the nanocomposites, filled with nanofiller densil (curves 3–6) is presented.

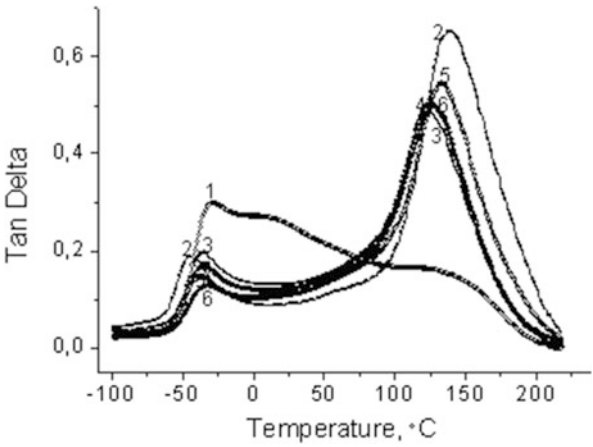

Fig. 38.11 Dynamic mechanical measurements of tan δ versus temperature at a frequency of 10 Hz for samples PU (*1*), semi-IPN with 37 % PHEMA (*2*), nanocomposites based on semi-IPN with 37 % PHEMA contained 3 % of densil (*3*), contained 5 % of densil (*4*), contained 10 % of densil (*5*), contained 15 % of densil (*6*)

The maximum of polyurethane in the semi-IPN37 is significantly lower by amplitude in comparison with neat polymer, and it is shifted toward low temperatures. This is due to restriction of the segmental motion of PU by the presence of PHEMA which at the temperatures in the beginning of the segmental motion in PU is in the glassy state. The shift of the PU's temperature of glass transition toward low temperatures may be connected with the loss of the cooperativity of segmental motion of polyurethane in the presence of PHEMA. For the nanocomposites, the restriction of the segmental motion in polyurethane is also observed, but the temperature of glass transition is in the same temperature range as in the neat polyurethane (Fig. 38.11, curves 3–6). The maxima of PHEMA in the nanocomposites (Fig. 38.11, curves 3–6) are also decreased by amplitude in comparison with the maximum in the semi-IPN37 (Fig. 38.11, curve 2) and shifted toward low temperatures. This could mean that in the nanocomposites based on semi-IPN37 matrix, the surface layers are formed on the surface of the nanofiller densil which consist of both polyurethane and PHEMA. As a result, for PHEMA in the nanocomposites, the restriction of the segmental motion (reducing of amplitude) is also observed, and the loss of the cooperativity of the segmental motion in PHEMA occurs, resulting in the shift of the temperature of glass transition to low temperatures.

In Fig. 38.12 the temperature dependence of storage modulus for polyurethane (curve 1) for PHEMA (curve 2), for semi-IPN with 37 % of PHEMA (curve 3), and for the nanocomposites with different amounts of densil (curves 4–7) are presented. As could be seen, the PHEMA demonstrates the highest storage modulus in all temperature range under investigation, and polyurethane is characterized by minimal storage modulus. For semi-IPN37 and for the nanocomposites, similar to the nanocomposites based on semi-IPN17, storage modulus increases in comparison with the polyurethane, and it is especially noticeable in the temperature range from −50 to +50 °C. Table 38.3 presents the values of storage modules of the samples at 25 °C and at −25 °C. We could observe that at 25 °C, storage modulus of nanocomposites, unlike to the nanocomposites based on semi-IPN17 matrix, is

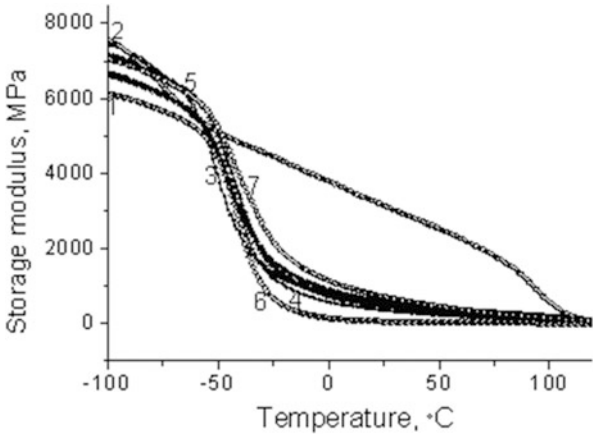

Fig. 38.12 The temperature dependence of the storage modulus at a frequency of 10 Hz for samples PU (*1*), PHEMA (*2*), semi-IPN with 37 % PHEMA (*3*), nanocomposites based on semi-IPN with 37 % PHEMA contained 3 % of densil (*4*), nanocomposites based on semi-IPN with 37 % PHEMA contained 5 % of densil (*5*), nanocomposites based on semi-IPN with 37 % PHEMA contained 10 % of densil (*6*), nanocomposites based on semi-IPN with 37 % PHEMA contained 15 % of densil (*7*)

reduced relative to the storage modulus of the neat matrix semi-IPN37 at content of densil 3–5 % by weight. With increasing the filler content up to 10–15 % by weight, an increase in the storage modulus of the nanocomposites in comparison with the matrix semi-IPN37 occurs (Table 38.3). At −25 °C, there is a relative drop of the storage modulus only for nanocomposite with densil amount of 3 %, and with increasing filler content, there is the growth of the storage modulus of the nanocomposites compared with the matrix semi-IPN37. Such nonmonotonic dependence of the storage modulus of the nanocomposites based on the matrix semi-IPN37 with filler content, for our point of view, is the result of competition of two processes: the formation of the surface layers of polymers on the surface of nanofiller and the microphase separation between the components of the polymer matrix. The first process leads to the higher storage modulus [41]; the second could be the reason of decreasing of this parameter [6].

As shown in previous investigations [18, 19], semi-IPNs based on PU and PHEMA is a two-phase system with incomplete phase separation. The degree of polymer components segregation α in such systems is a measure of the phase separation. If $\alpha = 1$, the phase separation in polymer system is complete. If $\alpha = 0$, the polymer components are compatible at the molecular level [42]. We calculated the degree of polymer components segregation α for the unfilled semi-IPN, and for the nanocomposites, contained nanofiller densil, by method proposed in [42]. The results of such calculations are presented in Table 38.4.

As could be seen from Table 38.4, the degree of polymer component segregation α for unfilled semi-IPNs increases with the amount of PHEMA. For semi-IPN with

Table 38.4 The degree of polymer components segregation in the semi-IPNs based on PU and PHEMA and in the nanocomposites contained nanofiller densil

	Maximum tan δ for the components of phase 1 and phase 2		The shift of the corresponding maxima along the temperature scale		The parameter which takes into account shift of the maxima	The degree of polymer components segregation
Sample	$h1$	$h2$	$l1$	$l2$	λ_m	α
PU-PHEMA ($L = 175$)	0.282	1.440				
IPN 17 PHEMA	0.010	0.065	0	27.5	0.0102	0.038
IPN 17 PHEMA + 3 %densil	0.080	0.247	7.5	15	0.0469	0.163
IPN 17 PHEMA + 5 %densil	0.045	0.210	3.8	15	0.0189	0.137
IPN 17 PHEMA + 10 % densil	0.035	0.235	3.8	25	0.0343	0.137
IPN 17 PHEMA + 15 % densil	0.015	0.170	0	32.5	0.0315	0.089
IPN 37 PHEMA	0.110	0.570	17.5	0	0.0110	0.388
IPN 37 PHEMA + 3 % densil	0.075	0.362	8.7	15	0.0348	0.234
IPN 37 PHEMA + 5 % densil	0.057	0.392	10.0	15	0.0369	0.240
IPN 37 PHEMA + 10 % densil	0.050	0.450	12.5	7.5	0.0228	0.277
IPN 37 PHEMA + 15 % densil	0.027	0.400	8.7	12.5	0.0299	0.231

17 % PHEMA, it is equal to 0.038, and for semi-IPN with 37 % of PHEMA, it is equal to 0.388. This means that the phase separation in a semi-IPN with 17 % PHEMA is stopped at the initial stage and in the semi-IPN with 37 % PHEMA the phase separation is more significant.

With introduction of nanofiller densil into the matrix with 17 % PHEMA, the degree of polymer components segregation increases. This means that the introduction of nanofiller densil leads to deepening of the microphase separation between the polymer matrix components.

With introduction of nanofiller densil into the polymer matrix with 37 % of PHEMA, which is characterized by high degree of polymer components segregation equal to 0.388, the opposite phenomenon is observed—the decrease of the degree of polymer components segregation (Table 38.4). From our point of view, this could be due to formation of the surface layers of polymers on the surface of nanofiller, which consists of polyurethane and PHEMA, that leads to a change in the ratio of components in a volume of matrix and, as a result, leads to decreased level of polymer matrix components segregation in the matrix with 37 % of PHEMA.

38.3.4 Mechanical Properties of the Nanocomposites

Figure 38.13 shows the stress–strain curves for three-dimensional polyurethane, for linear PHEMA, for semi-IPN with 17 % of PHEMA, and for the nanocomposites based on semi-IPN with 17 % PHEMA containing different amount of nanofiller densil. As could be seen, the introduction of nanofiller densil into the polymer matrix leads to significant increase of the physical and mechanical parameters of the nanocomposite in the range of all concentration of nanofiller compared with the neat matrix. With introduction of 3 % of densil into polymer matrix (Fig. 38.13, curve 2), there is growing stress at break and strain at break of nanocomposite compared to the matrix (Fig. 38.13, curve 1). With further increasing of nanofiller content up to 5 % (Fig. 38.13 curve 3), sample of nanocomposite demonstrates a sharp increase in stress at break, but strain at break somewhat decreases in comparison with the matrix. The sample containing 5 % of densil demonstrates the maximum value of Young's modulus among the nanocomposites which is obtained based on this matrix. With further increasing the filler content up to 10 and 15 %, the relative decreasing of the stress at break occurs compared with the sample of 5 % densil. We could observe also decreasing of strain at break for these nanocomposites (Fig. 38.13, curves 4, 5). The latter could indicate the uniform distribution of nanofiller densil in the nanocomposites containing 3 and 5 % of nanofiller but the formation of aggregates of nanofiller in the nanocomposites with its contents 10 and 15 %. This result is in agreement with the data of nanocomposite's structure investigation by small-angle X-ray scattering described above (Chap. 3.2).

Figure 38.14 presents the results of physical and mechanical properties testing of semi-IPN which contain 37 % of PHEMA and of the nanocomposites based thereon, which is filled with nanofiller densil. It is evident that for the nanocomposites based on polymer matrix semi-IPN with 37 % PHEMA (Fig. 38.14), there is another behavior compared with the nanocomposites based on the semi-IPN with 17 % PHEMA (Fig. 38.13). Introduction of densil

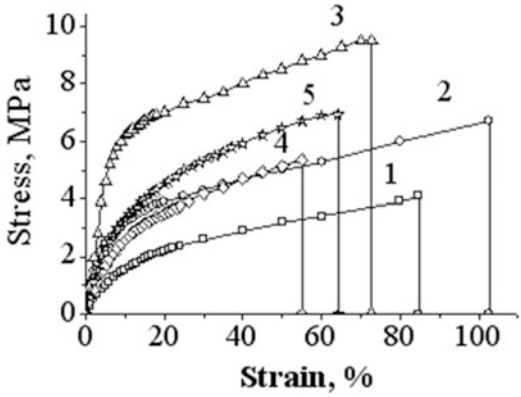

Fig. 38.13 The stress–strain curves for semi-IPN with 17 % PHEMA (*1*), nanocomposites based on semi-IPN with 17 % PHEMA contained 3 % of densil (*2*), contained 5 % of densil (*3*), contained 10 % of densil (*4*), contained 15 % of densil (*5*)

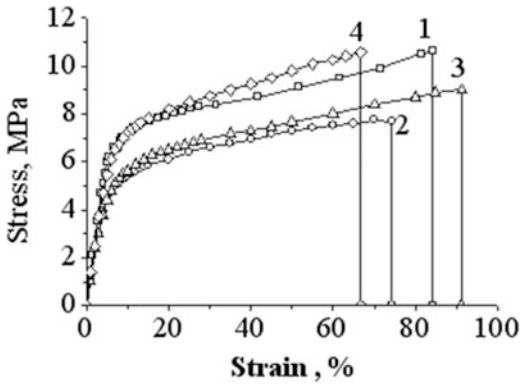

Fig. 38.14 The stress–strain curves for semi-IPN with 37 % PHEMA (*1*), nanocomposites based on semi-IPN with 37 % PHEMA contained 3 % of densil (*2*), contained 5 % of densil (*3*), contained 15 % of densil (*4*)

with the amount of 3 and 5 % into the semi-IPN, which contain 37 % of PHEMA, lead to the decrease of physical and mechanical parameters of the nanocomposites in comparison with the matrix (Fig. 38.14, curves 2, 3). Only with increasing amount of densil up to 15 %, the nanocomposites have shown some growth in stress at break (Fig. 38.14, curve 4). At the same time, Young's modulus for the unfilled semi-IPN with 37 % PHEMA is the highest in comparison with the nanocomposites. The reason of such behavior could be the changes in the process of microphase separation in the multicomponent polymer matrix with introduction of nanofiller. With increasing the PHEMA amount in the semi-IPN, the filler is distributed not only in the flexible PU domains but also in the hard PHEMA domains. In this case, the fragile surface layers of PHEMA are formed on the surface of nanofiller. This could lead to the decrease of the physical and mechanical parameters of the nanocomposites based on polymer matrix, which contain 37 % of PHEMA.

The results of physical and mechanical property investigations of the nanocomposites based on polymer matrix, which contain 37 % of PHEMA, are in agreement with the results of the thermodynamics of polymer matrix—filler interactions study in these nanocomposites (Table 38.1). The samples of nanocomposites which demonstrate the positive values of free energy of polymer–filler interaction, characterized by a decrease in the parameters of the physical and mechanical properties.

38.4 Conclusion

Nanocomposites based on multicomponent polymer matrix consists of polyurethane and poly(2-hydroxyethyl methacrylate), and nanofiller densil were prepared and investigated in the perspective of biomedical applications.

The structure peculiarities, thermodynamic miscibility, and dynamic mechanical and physical–mechanical properties of nanocomposites have been investigated.

The investigation of the structural features of the polyurethane–densil nanocomposites has shown that at minimum nanofiller content (1 %), it is almost

uniformly distributed in the polyurethane matrix. With increasing nanofiller content in the matrix, aggregation occurs in the form of mass–fractal structures, typical for the native nanofiller. When the multicomponent polymer matrix (semi-IPN) was used, the second polymer component in the matrix promotes the homogenization of nanofiller distribution in case of semi-IPN with PHEMA17 from 1 to 3 % and in the case of semi-IPN with PHEMA37 from 1 to 5 %. Raising the threshold of homogenization of nanofiller distribution is the result of reorganization of filled polyurethane during the process of formation of nanocomposites in case of multicomponent polymer matrix.

Based on experimental data of vapor sorption by filled composites and by nanofiller, the thermodynamic affinity of polymer components to the filler was estimated. The free energy of interaction between the polymer components and nanofiller was negative in case of matrix semi-IPN with 17 % of PHEMA, and it was positive in case of matrix semi-IPN with 37 % of PHEMA. This is the result of competition of two processes: the formation of the dense layers of polymers on the surface of nanofiller and the formation of interfacial layers with the excessive free volume in the nanocomposites based on polymer matrix, which is semi-IPN with 37 % of PHEMA.

The investigation of dynamic mechanical and physical–mechanical properties of composites has shown that optimum physical and mechanical properties demonstrate the systems with concentration of nanofiller which is near its respective threshold for aggregation (i.e., 1 % for the nanocomposites with polyurethane matrix, 3 % for those with semi-IPN 17 matrix, and 5 % for those with semi-IPN 37 matrix).

The results of investigations suggest that for creation of the nanocomposites based on multicomponent polymer matrix and nanofiller densil, it is expedient to use the matrix with smaller content of PHEMA (17 %). Nanocomposites are based on such matrix characterized by negative free energy of interaction between the polymer components and nanofiller that means by thermodynamic stability of the nanocomposites. The polymer matrix with smaller content of PHEMA (17 %) is characterized by initial stage of microphase separation and allows to get the nanocomposites with high physical and mechanical properties because the homogenization of nanofiller distribution in the volume of matrix occurs.

Acknowledgment The project N 6.22.7.21 of the STSTP of Ukraine “Nanotechnology and Nanomaterials” is greatly acknowledged.

References

1. Ray SS, Okamoto M (2003) Polymer-layered silicate nanocomposites: a review from preparation to processing. Polym Sci 28:1539–1641. doi:10.1016/j.progpolymsci.2003.08.002
2. Alexandre M, Dubois P (2000) Polymer-layered silicate nanocomposites: preparation, properties and uses of a new class of materials. Mater Sci Eng 28:1–16. doi:10.1016/S0927-796X(00)00012-7

3. Moniruzzaman M, Winey KI (2006) Polymer nanocomposites containing carbon nanotubes. Macromolecules 39:5194–5205. doi:10.1021/ma060733p
4. Hu Y, Shenderova OA, Hu Z, Padgett CW, Brenner DW (2006) Carbon nanostructures for advanced composites. Rep Prog Phys 69(6):1847–1897
5. Shaffer MSP, Sandler JKW, Advani S (2006) Processing and properties of nanocomposites. World Scientific, Singapore
6. Karabanova LV, Bershtein VA, Sukhanova TE et al (2008) 3D diamond-containing nanocomposites based on hybrid polyurethane–poly(2-hydroxyethyl methacrylate) semi-IPNs: composition-nanostructure-segmental dynamics-elastic properties relationships. J Polym Sci B 46(16):1696–1712. doi:10.1002/polb.21506
7. Zhang H, Wang B, Li H et al (2003) Synthesis and characterization of nanocomposites of silicon dioxide and polyurethane and epoxy resin interpenetrating network. Polym Int 52 (9):1493–1497. doi:10.1002/pi.1247
8. Bershtein VA, Gun'ko VM, Karabanova LV, Sukhanova TE, Yakushev PN, Egorova LM, Turova AA, Zarko VI, Pakhlov EM, Vylegzhanina ME, Mikhalovsky SV (2013) Polyurethane-poly(2-hydroxyethyl methacrylate) semi-IPN-nanooxide composites. RSC Adv 3:14560–14570. doi:10.1039/C3RA40295A
9. Lipatov YS et al (1995) Polymer reinforcement. ChemTech, Toronto. ISBN-10: 1895198089, ISBN-13: 978-1895198089
10. Lipatov YS, Karabanova LV (1994) Gradient interpenetrating polymer networks. In: Advances in interpenetrating polymer networks, vol 4. Technomic, Lancaster, PA, pp 191–212. ISBN-10: 0877627088, ISBN-13: 978-0877627081
11. Karabanova LV, Sergeeva LM, Boiteux G (2001) Filler effect on formation and properties of reinforced interpenetrating polymer networks. Compos Interfaces 8:207–219. doi:10.1163/15685540152594677
12. Lipatov YS, Karabanova LV, Sergeeva LM (1994) Thermodynamic state of reinforced interpenetrating polymer networks. Polym Int 34:7–13. doi:10.1002/pi.1994.210340102
13. Lipatov YS, Sergeeva LM, Karabanova LV (1988) Interpenetrating polymer networks on the basis of polyurethanes and polyurethane ionomers. Polymery (Warsaw) 33:169–174. doi:10.14314/polimery, ISSN 0032-2725
14. Sergeeva LM, Skiba SI, Karabanova LV (1996) Filler effect on formation and properties of interpenetrating polymer networks based on polyurethane and polyesteracrylate. Polym Int 39:317–325. doi:10.1002/(SICI)1097-0126(199604)39: 4<317::AID-PI499>3.0.CO;2-O
15. Karabanova LV, Boiteux G, Gain O et al (2004) Miscibility and thermal and dynamic mechanical behaviour of semi-interpenetrating polymer networks based on polyurethane and poly(hydroxyethyl methacrylate). Polym Int 53(12):2051–2058. doi:10.1002/pi.1627
16. Lipatov YS (1980) Interfacial phenomena on polymers. Naukova dumka, Kiev
17. Karabanova LV, Sergeeva LM, Svyatyna AV et al (2007) Heterogeneity of glass transition dynamics in polyurethane-poly(2-hydroxyethyl methacrylate) semi-interpenetrating polymer networks. J Polym Sci B 45(8):963–975. doi:10.1002/polb.21108
18. Karabanova LV, Boiteux G, Seytre G, Stevenson I, Lloyd A, Mikhalovsky S, Helias M, Sergeeva LM, Lutsyk ED, Svyatyna AV (2008) Phase separation in the polyurethane/poly (2-hydroxyethyl methacrylate) semi-interpenetrating polymer networks synthesized by different ways. Polym Eng Sci 48:588–597. doi:10.1002/pen.20965
19. Karabanova LV, Lloyd AW, Mikhalovsky SV, Helias M, Philips GP, Rose S, Mikhalovska L, Boiteux G, Sergeeva LM, Lutsyk ED (2006) Polyurethane/poly(hydroxyethyl methacrylate) semi-interpenetrating polymer networks for biomedical applications. J Mater Sci Mater Med 17:1283–1296. doi:10.1007/s10856-006-0603-y
20. Karabanova LV, Boiteux G, Seytre G, Stevenson I, Gain O, Shady C, Lutsyk ED, Svyatyna A (2009) Semi-interpenetrating polymer networks based on polyurethane and poly (2-hydroxyethyl methacrylate): dielectric study of relaxation behavior. J Non-Cryst Solids 355:1453–1460. doi:10.1016/j.jnoncrysol.2009.05.002

21. Karabanova L, Pissis P, Kanapitsas A, Lutsyk E (1998) Thermodynamic state, temperature transitions, and broadband dielectric relaxation behavior in gradient interpenetrating polymer networks. J Appl Polym Sci 68:61–171. doi:10.1002/(SICI)1097-4628(19980404)68:1<161::AID-APP18>3.0.CO;2-3
22. Karabanova LV, Lloyd AW, Mikhalovsky SV (2015) 3-D artificial nanodiamonds containing nanocomposites based on hybrid polyurethane-poly(2-hydroxyethyl methacrylate) polymer matrix. In: Springer Proceedings in "Physics: Nanoplasmonics, Nano-Optics, Nanocomposites, and Surface Studies" selected proceedings of the second FP7 conference and the Third International Summer School Nanotechnology: From Fundamental Research to Innovations, pp 149–164
23. Bershtein VA, Karabanova LV, Sukhanova TE et al (2008) Peculiar dynamics and elastic properties of hybrid semi-interpenetrating polymer network–3-D diamond nanocomposites. Polymer 49:836–842. doi:10.1016/j.polymer.2008.01.002
24. Bershtein VA, Gun'ko VM, Karabanova LV, Sukhanova TE, Yakushev PN, Egorova LM, Glievyy OB, Lutsyk ED, Pakhlov EM, Turova AA, Zarko VI, Vylegzhanina ME (2010) Hybrid polyurethane-poly(2-hydroxyethyl methacrylate) semi-IPN–silica nanocomposites: interfacial interactions and glass transition dynamics. J Macromol Sci Part B: Phys 49:18–32. doi:10.1080/00222340903343830
25. Kanapitsas A, Pissis P, Karabanova L, Sergeeva L, Apekis L (1998) Broadband dielectric relaxation spectroscopy in interpenetrating polymer networks of polyurethane-copolymer of butyl methacrylate and dimethacrylate triethylene glycol. Polym Gels Networks 6:83–102. doi:10.1016/S0966-7822(97)00018-X
26. Bershtein VA, Yakushev PN, Karabanova LV, Sergeeva LM, Pissis P (1999) Heterogeneity of segmental dynamics around T_g and nanoscale compositional inhomogeneity in polyurethane/methacrylate interpenetrating networks as estimated by creep rate spectroscopy. J Polym Sci Part B: Polym Phys 37:429–441. doi:10.1002/(SICI)1099-0488(19990301)37:5<429::AID-POLB3>3.0.CO;2-E
27. Klonos P, Chatzidogiannaki V, Roumpos K, Spyratou E, Georgiopoulos P, Kontou E, Pissis P, Gomza Yu, Nesin S, Bondaruk O, Karabanova L (2015) Structure–properties investigations in hydrophilic nanocomposites based on polyurethane/poly(2–hydroxyethyl methacrylate) semi-IPNs and nanofiller densil for biomedical application. J Appl Polym Sci. doi:10.1002/app.43122
28. Gun'ko VM, Voronin EF, Nosach LV, Pakhlov EM, Guzenko NV, Leboda R, Skubiszewska–Zięba J (2006) Adsorption and migration of poly(vinyl pyrrolidone) at a fumed silica surface. Adsorpt Sci Technol 24:143–157. doi:10.1260/026361706778529173
29. Lipatov YS, Shilov VV, Gomza YP, Kruglyac NE (1982) The X-rays graphic methods of studying polymer systems. Naukova Dumka, Kiev
30. Vonk CG (1975) A general computer program for the processing of small-angle X-ray scattering data. J Appl Crystallogr 8:340–341. doi:10.1107/S0021889875010618
31. Hosemann R, Bagchi SN (1962) Direct analysis of diffraction by matter. North Holland, Amsterdam
32. Karabanova LV, Lutsyk ED, Skiba SI, Sergeeva LM (1989) In: Collection of composite polymer materials, vol 40. Naukova dumka, Kiev, pp 49–53
33. Tager AA (1972) Thermodynamic stability of polymer–solvent and polymer–polymer systems. Visokomolecular Soed Serie A 14(12):2690–2698
34. Bessonov YS, Tager AA, Yushkova SM et al (1978) Thermodynamic investigations of interactions in filled polyvinylchloride. Visokomolecular Soed Serie A 20(1):99–105
35. Kwei T (1965) Polymer–filler interaction thermodynamic calculations and a proposed model. J Polym Sci A 3(9):3229–3237. doi:10.1002/pol.1965.100030917
36. Shilov VV, Karabanova LV, David L et al (2005) The structure peculiarities of the polyurethane/poly(hydroxyethyl methacrylate) semi-interpenetrating polymer networks. Polym J 27:255–263

37. Beaucage G (1995) Approximations leading to a unified exponential/power-law approach to small-angle scattering. J Appl Crystallogr 28:717–720. doi:10.1107/S0021889895005292
38. Beaucage G (1996) Small-angle scattering from polymeric mass fractals of arbitrary mass-fractal dimension. J Appl Crystallogr 29:134–136. doi:10.1107/S0021889895011605
39. Gin'e A (1961) X-ray-analysis of crystals. Theory and practice. Physicomathematical publishers, Moscow
40. Karabanova LV, Gomza YuP, Nesin SD, Bondaruk ON, Gerashcenko II, Voronin EF, Nosach LV, Zarko VI, Pahlov EM (2014) In: Nanosized systems and nanomaterials: current status and prospects of development of research in Ukraine. Academperiodica, Kiev, pp 724–730
41. Nilsen L (1978) Mechanical properties of polymers and polymer compositions. Chemistry, Moscow
42. Lipatov YS, Rosovitckyi VF (1986) Physics and chemistry of the multicomponent polymer systems. Naukova Dumka, Kiev

Chapter 39
Effects of Dispersion and Ultraviolet/ Ozonolysis Functionalization of Graphite Nanoplatelets on the Electrical Properties of Epoxy Nanocomposites

Olena Yakovenko, Ludmila Matzui, Yulia Perets, Iryna Ovsiienko, Oleksii Brusylovets, Ludmila Vovchenko, and Paweł Szroeder

39.1 Introduction

Recently, significant efforts have been made to improve physical properties of carbon/polymer NCs which are applied in different fields. In particular, graphite nanoplatelets (GNPs), a nanosized conductive material with a layered graphene structure, which is produced at low price, has attracted significant attention as the alternative to metal- and conventional carbon-based reinforcement used in conducting polymer composites fabrication [1]. The initial material for GNPs preparation represents graphite flakes intercalated with strong acids (H_2SO_4, HCl, HNO_3, $HClO_4$ etc.) which can be expanded as much as a few 100 times of their initial volume by heat treatment followed by mechanical or ultrasonic exfoliation into individual nanoparticles of 5–50 nm thickness. Because of their large surface area and sufficiently large aspect ratios, GNPs used as a filler can provide the NCs with good electrical, thermal, and mechanical properties at low filler contents and, which is important, at a very low cost [2, 3]. However, despite the fact that GNPs have a wide range of potential applications, their usage often remains problematic because of the problem which afflicts many carbon nanofillers, in particular agglomerations caused by strong interparticle van der Waals forces [4], which results in stress concentration, thus reducing the strength of the NCs. Various surface treatment methods, such as plasma treatment [5], liquid-phase coating,

O. Yakovenko (✉) • L. Matzui • Y. Perets • I. Ovsiienko
O. Brusylovets • L. Vovchenko
Departments of Physics and Chemistry, Taras Shevchenko National University of Kyiv, Volodymyrska 64/13, 01601 Kyiv, Ukraine
e-mail: alenka-ya@ukr.net

P. Szroeder
Institute of Physics, Faculty of Physics, Astronomy and Informatics, Nicolaus Copernicus University, Grudziadzka 5, 87-100 Torun, Poland

O. Fesenko, L. Yatsenko (eds.), *Nanophysics, Nanophotonics, Surface Studies, and Applications*, Springer Proceedings in Physics 183,
DOI 10.1007/978-3-319-30737-4_39

gas-phase oxidation [6], gamma irradiation [7], etc., have been proposed to overcome poor interfacial interaction and improve surface reactivity of carbon nanotubes [8, 9] or carbon fibers [10] with polymer matrix, and most of these methods, in principle, can be applied to GNPs/epoxy NCs [11].

The most effective method of improving the interfacial adhesion between composite components is a tailored chemical functionalization of filler, which could provide functional groups on the surface of carbon. The functional groups modify carbon surface state, create conditions for homogeneous distribution of nanocarbon filler in the polymer matrix, and provide a strong bond between filler particles and the matrix. Oxidation is the first step in many functionalization strategies. One of the most widely used methods of nanoparticle surface oxidation is the treatment by strong acids such as HNO_3 [12], H_2SO_4 [13], etc. Using acids as liquid-processing agents is expected to result in a high degree of nanocarbon dispersion due to formation of strong covalent bonds between functional groups and carbon atoms. In this case, however, the delocalized π-electronic system of graphite layer is destructed, and σ-bonds are partially broken, while free bonds that are formed provide the attachment of various functional groups to the nanocarbon surface. At the same time, chemical functionalization by strong acids results in the formation of a large quantity of defects on the nanocarbon surface [14]. On the one hand, the binding of nanocarbon filler to polymer matrix is improved, and mechanical properties of the NC become better. On the other hand, a significant quantity of defects in the nanocarbon filler leads to deterioration of its properties related to charge transfer [15, 16]. This causes the deterioration of NC electro-transport properties in general. Due to non-covalent functionalization by organic compounds, the bonds between functional groups and carbon atoms are formed by hydrophobic interactions or hydrogen bonds [17]. The significant benefit of non-covalent functionalization is explained by the fact that sp^2-graphene structure is not destructed, i.e., the nanocarbon filler preserves its unique properties. However, the weak bonds between carbon atoms and functional groups do not provide a strong interfacial interaction between the filler and polymer matrix.

The alternative to the wet oxidation by acids is dry oxidation by UV/ozone treatment of nanocarbon particles [18]. Ozone is easily generated by exciting molecular oxygen with UV [19], and, as shown in [20], UV/ozone treatment is able to improve both the electrical conductivity and mechanical properties of NCs by improving GNPs/epoxy interfacial adhesion.

The aim of this paper is to reveal how liquid dispersive mediums affect the degree of GNP surface modification and electric properties of GNPs/epoxy NCs depending on ultrasonic dispersion and UV/ozone treatment time. To achieve this goal, the initial GNPs were prepared in such dispersive mediums as water, isopropyl alcohol, and acetone. To prepare functionalized GNPs, the initial GNPs were subjected to UV/ozone treatment for different times. For our purposes, two kinds of GNPs/epoxy NCs were fabricated: with initial and UV-/ozone-treated GNPs.

39.2 Experimental

39.2.1 Preparation of GNPs

TEG, a highly porous carbon powder, was prepared by acid intercalation of graphite. Upon a rapid heating, the intercalated graphite was expanded explosively several 100 times along the thickness direction due to evaporation of intercalant. TEG was used as the initial material for GNPs preparation by ultrasonication in different dispersive liquid mediums, such as acetone, isopropyl alcohol, and water. Ultrasonic dispersion was carried out to exfoliate TEG particles into individual GNPs or GNPs bundles. The procedure of GNPs fabrication was the following: 20 mL of appropriate dispersive liquid was added to 400 mg of TEG and, after careful stirring, exposed to ultrasound of 50 W and 40 kHz for 3 h in acetone, 1.5 h in isopropyl alcohol, and 20 h in water medium. Ultrasonication was performed until complete breakage of TEG into individual GNPs, thus the time of ultrasonication was different for different mediums. After that the dispersed GNPs were dried until they reached the TEG starting weight. The resulting GNPs were labeled as follows: GNPs1, prepared in water; GNPs2, in isopropyl alcohol; and GNPs3, in acetone dispersive medium.

Then the GNP powders were divided in two parts. One part was subjected to UV/ozone treatment, while the other was left intact. UV/ozone treatment was performed by DRT-1000 equipped with electric-discharge arc lamp of high pressure inflated with mercury and argon compound that could release ultraviolet radiation of 50 W at 240–320 nm wavelength. The distance between the UV lamp and the sample stage was fixed at 11 cm. The initial GNP powders were subjected to UV/ozone treatment for 5, 10, 20, and 30 min.

39.2.2 Preparation of GNPs/Epoxy Composites

In order to prepare GNPs/epoxy NCs, the GNPs were incorporated into epoxy resin Larit 285 (viscosity of 600–900 mPa s) with H 285 (viscosity of 50–100 mPa s) as a hardening agent. The mass fraction of GNPs in polymer matrix was fixed at 5 wt% for all the samples. To improve the distribution of filler in the polymer matrix, the epoxy was diluted with a small amount of acetone prior to incorporation of GNPs. The microscale GNPs agglomerates which are formed in the result of interactions between carbon particles in GNPs/epoxy composite mixtures were broken by ultrasound of 50 W and 40 kHz applied for 15 min. Then the curing agent H 285 was added, and, when the solvent evaporated and the mixtures jellied as the polymerization started, the composite mixture was poured into molds and cured at room temperature. To complete the polymerization, the molds with composite mixtures were exposed to the temperature that gradually increased from 40 to 80 °C for 5 h.

39.2.3 Characterization Methods

The lateral dimensions of the prepared GNPs and morphology of GNPs/epoxy NCs were investigated by using optical microscope MIKMED-1 with the attached digital camera ETREK DCM-510 and probe NanoLaboratory INTEGRA. To estimate the average thickness and diameter of the GNPs, their optical and AFM images were converted into 3D images by program Nova, which created the histograms of GNPs density distribution.

The morphology of TEG and GNPs prepared in different dispersive mediums was examined by scanning electron microscope (SEM, Mira3 Tescan) at accelerating voltage of 10.0 kV.

To verify possible chemical functionalization in the result of UV/ozone treatment, the changes in qualitative composition of GNPs, the surface functional groups were analyzed by their IR-spectrums before and after UV/ozone treatment. The spectra were obtained by Perkin Elmer Spectrum BX FT-IR infrared spectrometer in the frequency range (4000–400) cm^{-1} in transmission mode. The specimens in the form of pellets with diameter of 10 mm were prepared from the powder mixture of fabricated GNPs and KBr. Also the IR spectrum of TEG sample was recorded.

Raman scattering spectra were obtained at room temperature in backscattering geometry by Perkin Elmer Raman Micro Raman microscope in conjunction with a confocal microscope (objective 25 ×) using a 785 nm laser line for Raman excitation.

The bulk electrical DC resistivity of GNPs/epoxy NCs samples with dimensions $6 \times 3 \times 3\ mm^3$ was measured at room temperature based on the two and four probe standard methods. The highest limit of the electrical resistance measurement system was set $10^{10}\ \Omega$. The error of measurement for resistance range 0.01–2.5 Ω did not exceed 0.5 %, for 2.5–10^7—1 %, for 10^8—5 %, and for 10^9—10 %.

39.3 Results and Discussion

39.3.1 Effects of Dispersive Methods and UV/Ozone Treatment on Morphology of GNPs

The influence of dispersive medium type used during TEG exfoliation on the GNPs morphology was investigated by optical, AFM, SEM, and Raman spectroscopy methods.

TEG represents a loosely bonded, porous, and wormlike rod, consisting of numerous preferentially oriented graphite layers, as shown in Fig. 39.1a, b.

In the result of ultrasonication, the TEG particles were exfoliated into individual particles and/or bundles of disk-shaped particles. Their thickness and diameter are strongly dependent of the dispersive medium and ultrasonication time. The results of microscopy investigations of the GNPs obtained under ultrasonication in acetone, isopropyl alcohol, and water dispersive mediums are presented in Figs. 39.2 and 39.3.

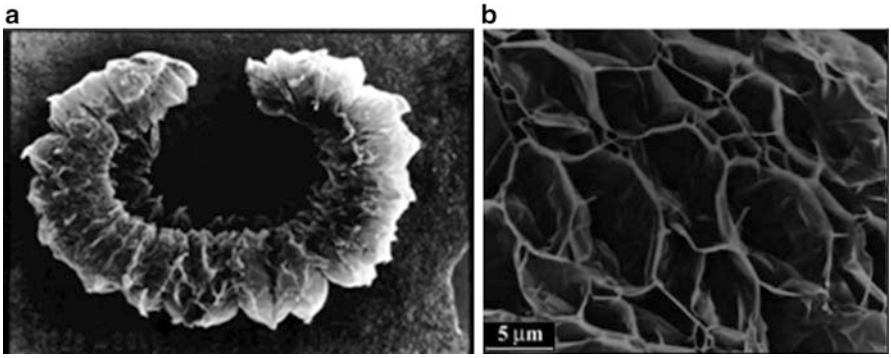

Fig. 39.1 SEM images of bundle-shaped thermally expanded graphite: (**a**) 100 × magnification, (**b**) 3000 × magnification

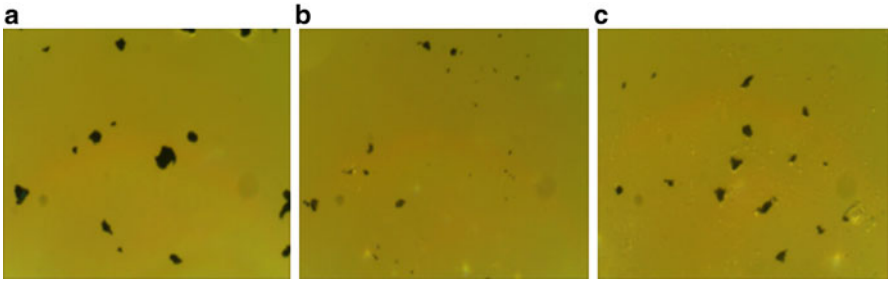

Fig. 39.2 Optical (740 × 740 μm) images of GNPs obtained in different dispersive mediums: (**a**) in water, (**b**) in isopropyl alcohol, (**c**) in acetone

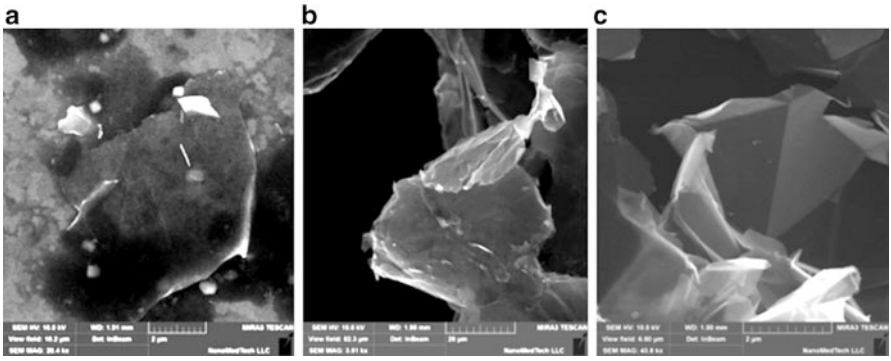

Fig. 39.3 SEM images of GNPs obtained in different dispersive mediums: (**a**) in water, (**b**) in isopropyl alcohol, (**c**) in acetone

The peculiarity of TEG ultrasonication process in the water medium is that the TEG particles do not sink but float on the surface. For this reason, TEG exfoliation into GNPs is complicated, and the time on GNPs formation increases compared to the time required for GNPs formation in acetone and isopropyl alcohol mediums. After 20 h of TEG ultrasonication in the water medium, the majority of the GNPs are of 100–1500 μm in diameter; however, small particles of 1–3 μm in diameter occur as well.

When isopropyl alcohol was used as dispersive medium for TEG ultrasonication, we observed the decreased quantity of porous TEG particles floating on the surface, while the quantity of the broken GNPs in the suspended matter rapidly increased with time. The optimum time of TEG ultrasonication to obtain GNPs in isopropyl alcohol is 1.5 h since within this time the majority of GNPs become as small as 20–50 μm in diameter.

In case of acetone used as the TEG dispersive medium, as shown in [21], the optimum time of TEG ultrasonication is 3 h. The analysis of optical images has shown that the average diameter of GNPs is 1–3 μm, but a small quantity of particles with diameter 5–10 μm occur as well.

On the basis of 3D-converted AFM images of GNPs obtained in different dispersive mediums, we carried out a comparative analysis of GNP thicknesses. The histograms of thickness distribution are presented in Fig. 39.4. Based on AFM results, the variation of thickness distribution for GNPs3 (obtained in acetone medium) was estimated to be 15–45 nm with the maximum of distribution at 30 nm. The variation of thickness distribution for GNPs2 (obtained in isopropyl alcohol medium) was 22–36 nm with the maximum of distribution at 32 nm. The variation of thickness distribution for GNPs1 (obtained in water medium) was 25–100 nm with the maximum of distribution at 50 nm. The estimation of lateral dimensions allowed the calculation of average aspect ratio of GNPs which is of ~10^2 for GNPs3, ~10^3 for GNPs2, and ~10^3–10^4 for GNPs1. Therefore, a conclusion can be made that the GNPs obtained in water dispersive medium possess the widest distribution of thicknesses and lateral dimensions, which results in a wide aspect ratio distribution whose value is the largest for these GNPs. This is certainly favorable for higher electrical conductivity of the composite with the filler of this kind.

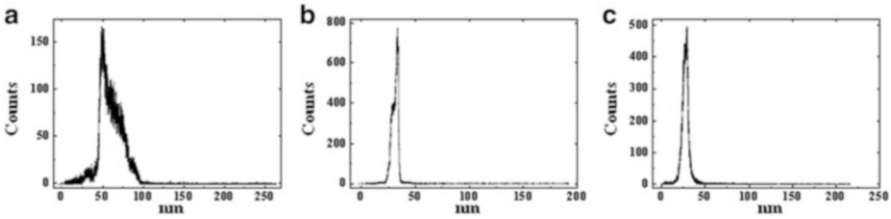

Fig. 39.4 Histograms of thickness distribution of GNPs obtained in different dispersive mediums: (**a**) in water, (**b**) in isopropyl alcohol, (**c**) in acetone

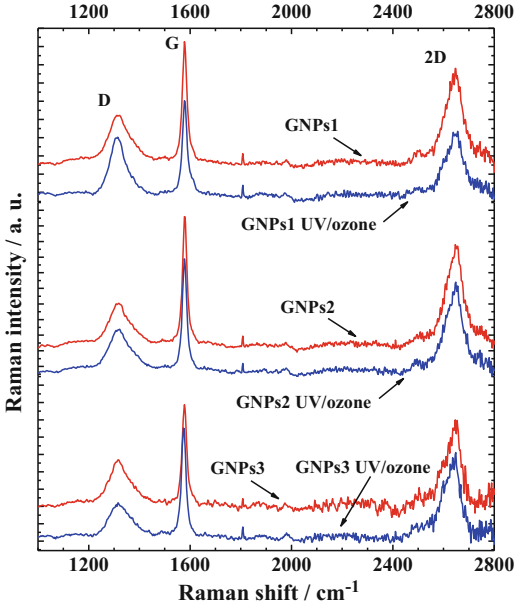

Fig. 39.5 Raman scattering spectra of GNPs obtained in different dispersive mediums: water (GNPs1), isopropyl alcohol (GNPs2), acetone (GNPs3) before and after 20 min of UV/ozone treatment

Thus, the most effective TEG exfoliation by time parameter occurs in isopropyl alcohol dispersive medium. The quantity of TEG dispersed into individual GNPs with respect to the total quantity of TEG is the highest in comparison to the quantity of GNPs in the other dispersive mediums within the same time interval. Although TEG exfoliation process takes the longest time in water dispersive medium, it produces the GNPs with the maximum aspect ratio (~10^4), which is the key factor in the formation of conductive chain.

The Raman spectra of initial GNPs and GNPs subjected to 20 min to UV/ozone treatment are shown in Fig. 39.5. The Raman spectra displays three main peaks: the G line, a primary in-plane vibrational mode (~1580 cm^{-1}), 2D (~2640 cm^{-1}), a second-order overtone of a different in-plane vibration, and the disorder-induced D mode (~1320 cm^{-1}). Due to weaker interactions between AB-stacked graphene layers in nanographite, G mode is slightly shifted (Table 39.1) to the red region in comparison with its position in the bulk graphite (1581 cm^{-1} in highly ordered pyrolytic graphite (HOPG)) [22]. It should be noted that the shift depends not on the type of dispersive medium but on the parameters of intercalated graphite thermoexfoliation. A weaker interaction between layers is also manifested in a higher ratio between integral peak intensities, A_{2D}/A_G [23]. The ratio varies from 2.45 to 3.9, but it is always much higher in comparison with HOPG (1.8). No effect of the UV/ozone treatment on the interlayer interactions in the GNPs has been found.

For all the samples, a vivid D peak is observed. The density of defects was estimated using the model curve obtained for graphene with point defects [24–26]. Using the semi-empiric formula [27],

Table 39.1 Parameters of the main Raman peaks and defects concentration value for GNPs obtained in different dispersive mediums: water (GNPs1), isopropyl alcohol (GNPs2), acetone (GNPs3) without and with 20 min of UV/ozone treatment

	$\widetilde{\nu}_D$ (cm^{-1})	$\widetilde{\nu}_G$	$\widetilde{\nu}_{2D}$	I_D/I_G	A_{2D}/A_G	n_D (cm^{-2})
GNPs1	1320 ± 3	1578.8 ± 0.4	2641 ± 1	0.392 ± 0.027	3.59 ± 0.16	1.86×10^{10}
GNPs1-UV/ozone	1315.2 ± 1	1579.3 ± 0.3	2643 ± 1	0.645 ± 0.060	2.70 ± 0.07	3.06×10^{10}
GNPs2	1320 ± 2	1579.1 ± 0.2	2644 ± 1	0.324 ± 0.027	3.11 ± 0.08	1.54×10^{10}
GNPs2-UV/ozone	1323 ± 3	1578.3 ± 0.4	2641 ± 1	0.352 ± 0.049	3.91 ± 0.19	1.67×10^{10}
GNPs3	1320 ± 2	1577.8 ± 0.4	2638 ± 1	0.548 ± 0.071	2.45 ± 0.11	2.60×10^{10}
GNPs3-UV/ozone	1320 ± 2	1575.0 ± 0.2	2633 ± 1	0.358 ± 0.037	2.65 ± 0.08	1.70×10^{10}

$$n_D\left(cm^{-2}\right) = \frac{(1.8 \pm 0.5) \times 10^{22}}{\lambda_L^4}\left(\frac{I_D}{I_G}\right)$$

where λ_L is the excitation laser wavelength (in nm), we estimated the defect concentration n_D (in cm^{-2}). The analysis of Raman spectra has shown that after UV/ozone treatment, the defect concentration increases (3×10^{10} cm^{-2}) in the sample of GNPs1 (prepared in water medium). And for the sample GNPs3, defect concentration decreases after UV/ozone action. The lowest concentration of defects was found in GNPs2 sample (1.5×10^{10} cm^{-2}), and after the treatment with UV/ozone, it slightly increased.

39.3.2 Effects of the Dispersive Medium and UV/Ozone Treatment on Surface Chemistry of GNPs

The IR absorption spectrums of TEG and GNPs obtained in different dispersive mediums are presented in Fig. 39.6a. As seen from the figure, TEG dispersion in acetone, isopropyl alcohol, or water medium is accompanied by the formation of various functional groups on GNP surfaces, and this process can be considered as the process of non-covalent functionalization when the bonds between functional groups and carbon atoms are formed by hydrophobic interactions or hydrogen bonds. Due to partial ionization, oxygen-containing groups create a small negative charge on the nanocarbon surface, and this makes nanocarbon particles repel from each other to stabilize their dispersion. The significant benefit of non-covalent functionalization is that sp^2-graphene structure is not destructed, i.e., the unique properties of the nanocarbon filler are preserved. However, the weak bonds between carbon atoms and functional groups prevent strong interfacial interaction between the filler and polymer matrix. It is obvious that IR spectrum of GNPs1 is similar to that of GNPs2, and the main changes are observed in the range ($3100 \div 3400$) cm^{-1}

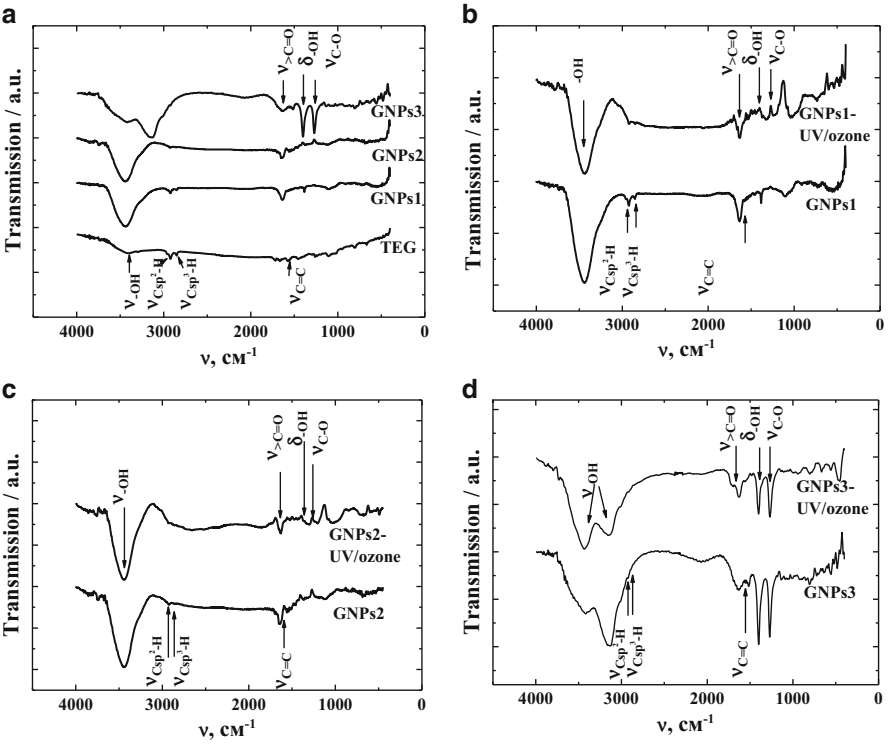

Fig. 39.6 IR absorption spectrums for (**a**) initial TEG and GNPs obtained in different dispersive mediums, (**b**) GNPs1 before and after 30 min of UV/ozone treatment, (**c**) GNPs2 before and after 30 min of UV/ozone treatment, (**d**) GNPs3 before and after 30 min of UV/ozone treatment

where the broad shoulder peaks assigned to the OH- vibrations appear after dispersion. The IR-spectrums of all the specimens contain three low-intensity bands which are caused by the hydrogen atoms bonded with sp^2- and sp^3-hybridized carbon atoms in the graphite skeleton: $C_{sp}{}^2$-H band near 2926 cm^{-1}, $C_{sp}{}^3$-H band near 2852 cm^{-1}, and the absorption band at 1564 cm^{-1} which is equal to the valence vibrations of multiple C = C bond. The band of valence vibrations of >C = O bond in carbonyl group is observed in the range (1700 ÷ 1650) cm^{-1} for TEG and all the GNPs obtained in different dispersive mediums. Two bands at 1277 and 1092 cm^{-1} are generated by C–O group vibrations in ethers (1092 cm^{-1}) and alcohols (1277 cm^{-1}).

The IR spectrum of GNPs obtained in acetone medium (GNPs3 sample) is characterized by the presence of two bands which correspond to OH- group vibrations: at 3445 cm^{-1} (free hydroxyl group or water) and at 3152 cm^{-1} (bound OH- group in alcohols or carboxylic acid) and by the presence of two groups of higher intensity which correspond to deformation vibrations of OH- group at (1400 ÷ 1390) cm^{-1} and C–O vibrations at 1277 cm^{-1}.

The IR absorption spectrums of GNPs1 (obtained in water), GNPs2 (in isopropyl alcohol), and GNPs3 (in acetone) before and after 30 min UV/ozone treatment are presented in Fig. 39.6b, c, d correspondingly. No significant qualitative changes in IR spectrum have been detected. However, in comparison with the IR-spectrums, there is a redistribution of intensities of absorption peaks of functional groups on the UV/ozone-treated GNP surfaces.

It should be noted that since the values of intensity on IR-spectrums are presented in arbitrary units, it is impossible to compare the values of peak intensities which correspond to different functional groups in different GNP specimens under investigation. Therefore, a certain criterion should be formulated to compare the peak intensities and determine what kind of functional groups is dominant in each of the different GNP specimens. For this purpose, the peak intensity corresponding to the vibration of aliphatic $C_{sp}{}^2$-H bond was selected. The aliphatic bond was found to occur on the crystallite boundaries of carbon material. Supposing that the size of crystallites does not change essentially during UV/ozone treatment, one can assume the amount of aliphatic $C_{sp}{}^2$-H bonds to remain constant as well. This is also confirmed by the data on Raman spectroscopy (as seen from Table 39.1, the value of I_D/I_G does not change essentially). Table 39.2 contains the normalized values of peak intensities which correspond to different functional groups on the GNPs surfaces according to the data on IR spectrometry for initial GNPs and GNPs after UV/ozone treatment. The intensity of $C_{sp}{}^2$-H peak was set equal to 100 %.

It has been found that UV/ozone treatment increases the relative contents of oxygen-containing functional groups on the GNPs surfaces, such as hydroxyl and ether, carboxyl, and carbonyl groups, as proven by the data presented in Table 39.2. More pronounced changes are observed for GNPs3 sample where the correspondence to stretching vibrations of C = O bond in COOH group appeared quiet distinctly in the absorption band at 1725 cm^{-1}. It should be noted that UV/ozone treatment

Table 39.2 Relative concentrations (related to the $C_{sp}{}^2$-H intensity) of functional groups on GNPs surface for different dispersive mediums before and after 30 min UV/ozone treatment

	GNPs1		GNPs2		GNPs3		
TEG	Initial	After 30 min UV/ozone treatment	Initial	After 30 min UV/ozone	Initial	After 30 min UV/ozone	Functional groups and their wave length (in cm^{-1})
141.6	3.4	89.5	3.8	85.7	48.7	79.7	~3438 (−OH)
100	100	100	100	100	100	100	~2926 ($C_{sp}{}^2$-H)
126.1	108.9	100	101.3	99.4	120.9	102.5	~2852 ($C_{sp}{}^3$-H)
85.7	81.0	97.2	70.9	97.4	83.4	98.2	~1650 (> C = O)
86.6	105.7	100.2	97.9	100.4	93.45	104.5	~1564 (C = C)
108.2	105.0	103.3	114.3	101.5	4.6	92.0	~1403 δ_{-OH}
116.4	123.1	103.5	122.3	101.3	15.5	91.1	~1277 (C–O) in alcohols
118.8	112.8	109.1	108.9	104.6	98.4	107.4	~1092 (C–O) in ethers

considerably decreased the intensities of $C_{sp}{}^2$-H band at 2926 cm^{-1} and $C_{sp}{}^3$-H band at 2852 cm^{-1}. In addition, for GNPs1 sample, the inversion of C = C band was observed.

It is quite possible that the decrease in $C_{sp}{}^2$-H band intensities at 2926 cm^{-1} and $C_{sp}{}^3$-H band intensities at 2852 cm^{-1} indicates that loosely bonded materials and organic contaminants on the GNPs surface have been removed during the etching process stimulated by ozone. As shown in [20], the UV/ozone-treated GNPs also exhibit a rougher surface along with clearer boundaries between the individual basal planes than the untreated graphite does.

39.3.3 Morphology of the GNPs/Epoxy Composites

To evaluate the dispersion of GNPs within the epoxy matrix, the optical images of thin slices of GNPs/epoxy NCs were made. Figure 39.7 presents the images of 5 wt % GNPs/epoxy NCs with the GNPs produced from TEG by ultrasonication in (a) acetone medium (GNPs3), (b) water medium (GNPs1), (c) isopropyl alcohol medium (GNPs2) without UV/ozone treatment, and (d) isopropyl alcohol medium (GNPs2) after 20-min UV/ozone treatment.

The analysis of optical images has revealed that GNPs3 and GNPs1 are distributed uniformly in the epoxy matrix and form a continuous cluster (Fig. 39.7a, b). GNPs2, however, assembles in rather large-scale clusters which are distributed irregularly and interact weakly with the polymer matrix (Fig. 39.7c). The distribution is slightly improved if GNPs2 filler undergoes 20-min UV/ozone treatment (Fig. 39.7d). It is obvious that UV/ozone treatment provides stronger binding of GNPs to the epoxy matrix and their more uniform distribution, which, in turn, helps to form conductive GNPs chains.

39.3.4 Electrical Properties of the GNPs/Epoxy Nanocomposites

Three types of 5 wt% GNPs/epoxy composites with GNP which were obtained in different dispersive mediums were prepared, and they demonstrated quiet different electrical conductivity (see additions in Fig. 39.8).

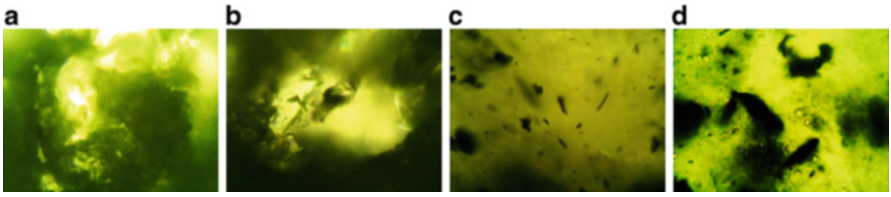

Fig. 39.7 Optical images of 5 wt% GNPs/epoxy NCs with the GNPs obtained from TEG by ultrasonication in (**a**) acetone medium, (**b**) water medium, (**c**) isopropyl alcohol medium without UV/ozone treatment, and (**d**) isopropyl alcohol medium after 20 min UV/ozone treatment of the GNPs filler. Magnification of 40 ×

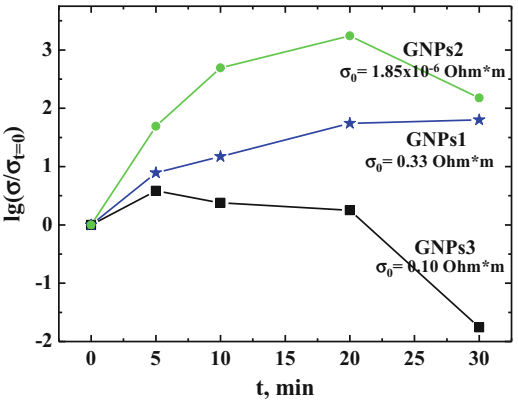

Fig. 39.8 The normalized electrical conductivity (relative to the appropriate conductivity of GNPs/epoxy NC without UV/ozone treatment of the filler) of 5 wt% GNPs/epoxy composites as a function of UV/ozone treatment time

It is known that several factors determine the value of conductivity of polymer composites with nanocarbon fillers: conducting filler content, proper conductivities of filler particles, filler aspect ratio, interfacial bonding between the filler and the matrix, and character of dispersion of filler within the matrix. As Raman investigation has shown, the crystal structure (crystalline size) of GNP did not essentially differ. So, in our case, it is the competition between the filler aspect ratio, interfacial bonding between the filler and the matrix, as well as the character of filler distribution within the matrix that determines the value of conductivity in GNPs/epoxy NCs. Among the NCs with GNPs which were obtained under different conditions, the highest value of conductivity was observed for 5 wt% GNPs1/epoxy NC, the filler aspect ratio of which is 10^4. Although the aspect ratio in GNPs3 is 10^2, it is characterized with a higher content of functional groups (distinctive peaks (C = O, O–H, C–O) in IR spectrum) on GNP surfaces which leads to efficient enhancement of interfacial adhesion in 5 wt% GNPs3/epoxy NC. In addition, the functional groups on GNP surfaces prevent the agglomeration of GNPs, which increases the probability of conductive network formation in the polymer matrix. As a result, the conductivity of 5 wt% GNPs3/epoxy NC is comparable (only three times lower) to the conductivity of 5 wt% GNPs1/epoxy NC despite much lower filler aspect ratio in comparison with GNPs1. A low ($\sim 10^{-6}$ Sm/m) value of conductivity for 5 wt% GNPs2/epoxy NC is caused by a high degree of GNPs agglomeration in the epoxy matrix and that they are disconnected in conductive network even despite rather high filler content.

The normalized electrical conductivity σ/σ_0 (σ_0 is the conductivity of GNPs/epoxy NC without UV/ozone treatment of the filler) of 5 wt% GNPs/epoxy composites is plotted as a function of UV/ozone treatment time in Fig. 39.8. The electrical conductivity increased with increasing treatment time for all types of composites and approached maximum after 20-min treatment. For all types of GNPs, the electrical conductivity increases with the increase of UV/ozone treatment time and approaches the maximum value after 20 min of UV/ozone treatment.

UV/ozone treatment caused the greatest relative changes of conductivity in 5 wt% GNPs2/epoxy NC (with obtained in isopropyl alcohol GNPs), which initially possessed the lowest conductivity.

Keeping in mind that changes of IR spectrum for this type of composite as well as for 5 wt% GNPs1/epoxy NC is not so crucial, we suppose that the removal of surface (organic) contaminants and weak materials from the graphite surface through the UV/ozone treatment promotes the formation of stronger conductive network. The organic contaminant and loosely bonded weak material not only decrease the adhesion between GNPs and epoxy but also may possess an electrically insulating character that creates large contact resistance between GNPs. It is known that among other things, the conductivity of is strongly dependent on contact resistance between nanocarbon particles in the conductive chains [28, 29]. For GNPs2/epoxy NC, in which the size of GNPs is rather small, the general conductivity of NC is very sensitive to the value of contact resistance between individual particles because of numerous links in one conductive chain. For GNPs1/epoxy NC, where the lateral size of GNPs reached 100–1500 μm, the number of individual particles in conductive network is sufficiently lower than in GNPs3/epoxy and GNPs2/epoxy NCs, and the effect of decrease in contact resistance after UV/ozone treatment is lower. In particular, this mechanism along with electrostatic repulsion of the functional groups which facilitate the dispersion of the GNPs and consequently contribute to conductive network formation is the reason of conductivity growth in the NCs with a UV-/ozone-treated filler.

39.4 Conclusions

In order to produce GNPs/epoxy NCs with desired electrical properties, several problems have to be overcome: GNPs agglomeration in epoxy matrix, lack of functional groups on initially inert graphite surface and, hence, poor interfacial adhesion, as well as the excess of weak bonds and contaminants which attach insulating properties to GNPs bonds in epoxy matrix.

The studies of morphology, surface state, and electrical conductivity of GNPs/epoxy NCs as a result of different conditions used for GNPs fabrication have shown that ultrasonication of TEG in the liquid dispersive medium strongly affects the time of dispersion process completion and dimensions of produced GNPs. The ultrasonication of TEG in alcohol medium has been found to be the most effective by the time parameter which allows producing GNPs with sufficiently high value of aspect ratio (10^2) and low level of defects. The ultrasonication of TEG in water medium requires a long time (up to 20 h), but the resulting GNPs have large lateral size and, therefore, are characterized by a large value of aspect ratio. Ultrasonication of TEG in acetone medium results not only in the effective dispersion of TEG in small (with diameter of 1–3 μm) particles but also is accompanied by formation of functional groups on the graphite surface.

The electrical conductivity investigations have shown that UV/ozone treatment enlarges the content of functional groups created on the GNPs surface and removes the organic contaminants and loosely bonded weak material, thereby improving the dispersion and distribution of GNPs in the epoxy matrix and, hence, electrical conductivity of GNPs NCs. The contact resistance between individual GNPs in conductive network decreases, thus enhancing the electrical conductivity of the composites.

Acknowledgments Publication is based on the research provided by the grant support of the State Fund For Fundamental Research (project NF61/88-2015).

References

1. Hahn HT, Choi O (2011) Graphite nanoplatelet composites and their applications. In: Composite materials. Springer, London, pp 169–186
2. Shen M-Y, Chang T-Y, Hsieh T-H, Li Y-L, Chiang C-L, Yang H, Yip M-C (2013) Mechanical properties and tensile fatigue of graphene nanoplatelets reinforced polymer nanocomposites. J Nanomater 2013:565401–565409
3. Wang Y, Yu J, Dai W, Song Y, Wang D, Zeng L, Jiang N (2014) Enhanced thermal and electrical properties of epoxy composites reinforced with graphene nanoplatelets. Polym Compos 36(3):556–565
4. Li D, Muller MB, Gilje S, Kaner RB, Wallace GG (2008) Processable aqueous dispersions of graphene nanosheets. Nat Nanotechnol 3(2):101–105
5. Paredes JI, Alonso AM, Tascon JMD (2000) Atomic force microscopy investigation of the surface modification of highly oriented pyrolytic graphite by oxygen plasma. J Mater Chem 10:1585–1591
6. Yang Y, He F, Wang M, Zhang B (1998) A new surface treatment method of carbon fibre—liquid-phase–gas-phase double effectiveness method (LGDE). J Mater Sci 33(14):3651–3654
7. Wan YZ, Wang YL, Huang Y, Luo HL, Chen GC, Yuan CD (2005) Effect of surface treatment of CFs with gamma-ray radiation on mechanical performance of their composites. J Mater Sci 40:3355–3359
8. Jang J, Baea J, Yoonb S-H (2003) A study on the effect of surface treatment of carbon nanotubes for liquid crystalline epoxide–carbon nanotube composites. J Mater Chem 13:676–681
9. Park O-K, Kim NH, Yoo G-H, Rhee KY, Lee JH (2010) Effects of the surface treatment on the properties of polyaniline coated carbon nanotubes/epoxy composites. Compos: Part B 41:2–7
10. Tiwaria S, Bijweb J (2014) Surface treatment of carbon fibers. Procedia Technol 14:505–512
11. Tang L-G, Kardos JL (1997) A review of methods for improving the interfacial adhesion between carbon fiber and polymer matrix. Polym Compos 18(1):100–113
12. Rios R, Alves D, Dalmázio I, Bento S, Donnici C, Lago R (2003) Tailoring activated carbon by surface chemical modification with O, S, and N containing molecules. Mater Res 6(2):129–135
13. Bikiaris D, Vassiliou A, Chrissafis K, Paraskevopoulos KM, Jannakoudakis A, Docoslis A (2008) Effect of acid treated multi-walled carbon nanotubes on the mechanical, permeability, thermal properties and thermo-oxidative stability of isotactic polypropylene. Polym Degrad Stab 93:952–967
14. Datsyuk V, Kalyva M, Papagelis K, Parthenios J, Tasis D, Siokou A, Kallitsis I, Galiotis C (2008) Chemical oxidation of multiwalled carbon nanotubes. Carbon 46:833–840
15. Zhang J, Zou H, Qing Q, Yang Y, Li Q, Liu Z, Guo X, Du Z (2003) Effect of chemical oxidation on the structure of single-walled carbon nanotubes. J Phys Chem B 107:3712–3718

16. Tchoul MN, Ford WT, Lolli G, Resasco DE, Arepalli S (2007) Effect of mild nitric acid oxidation on dispersability, size, and structure of single-walled carbon nanotubes. Chem Mater 19:5765–5772
17. Zhao Y-L, Stoddart JF (2009) Noncovalent functionalization of single-walled carbon nanotubes. Acc Chem Res 42(8):1161–1171
18. Kim J-H, Min BG (2010) Functionalization of multi-walled carbon nanotube by treatment with dry ozone gas for the enhanced dispersion and adhesion in polymeric composites. Carbon Lett 11(4):298–303
19. Simmons JM, Nichols BM, Baker SE, Marcus MS, Castellini OM, Lee C-S, Hamers RJ, Eriksson MA (2006) The effect of ozone oxidation on single-walled carbon nanotubes. J Phys Chem B 110(14):7113–7118
20. Li J, Kim J-K, Sham ML (2005) Conductive graphite nanoplatelet/epoxy nanocomposites: effects of exfoliation and UV/ozone treatment of graphite. Scr Mater 53:235–240
21. Perets YS, Matzui LY, Vovchenko LL (2013) Issledovaniya charactera granulometricheskogo sostava graphitovih nanoplastinok. Perspektivnie Materiali 5:68–73
22. Gupta A, Chen G, Joshi P, Tadigadapa S, Eklund PC (2006) Nano Lett 6:2667–2673
23. Ferrari AC, Meyer JC, Scardaci V, Casiraghi C, Lazzeri M, Mauri F, Piscanec S, Jiang D, Novoselov KS, Roth S, Geim AK (2006) Raman spectrum of graphene and graphene layers. Phys Rev Lett 97:187401
24. Lucchese M, Stavale F, Martins Ferreira E, Vilani C, Moutinho M, Capaz R, Achete C, Jorio A (2010) Quantifying ion-induced defects and Raman relaxation length in graphene. Carbon 48 (5):1592–1597
25. Martins Ferreira EH, Moutinho MVO, Stavale F, Lucchese MM, Capaz RB, Achete CA, Jorio A (2010) Evolution of the Raman spectra from single-, few-, and manylayer graphene with increasing disorder. Phys Rev B 82(12):125429
26. Szroeder P, Górska A, Tsierkezos N, Ritter U, Strupinski W (2013) The role of bandstructure in electron transfer kinetics. Mater Sci Eng Technol 44(23):226–230
27. Cançado LG, Jorio A, Ferreira EHM, Stavale F, Achete CA, Capaz RB, Moutinho MVO, Lombardo A, Kulmala TS, Ferrari AC (2011) Quantifying defects in graphene via Raman spectroscopy at different excitation energies. Nano Lett 11(8):3190–3196
28. Matzui LY, Vovchenko LL, Perets YS, Lazarenko OA (2013) Electrical conductivity of epoxy resin filled with graphite nanoplatelets and boron nitride. Mater Sci Eng Technol 44 (2–3):254–258
29. Vovchenko L, Lazarenko O, Matzui L, Perets Y, Zhuravkov A, Fedorets V, Normand FLE (2014) Mechanical and electrical properties of the epoxy composites with graphite nanoplatelets and carbon nanotubes. Phys Status Solidi A 211(2):336–341

Chapter 40
Polymer Nanocomposites for the Active Layers of Organic Photovoltaics

I.A. Savchenko and Ya. Vertsimakha

40.1 Introduction

Organic solar cells have been the low-cost alternatives of inorganic solar cells. The organic, polymer-based photovoltaic elements have introduced at least the potential of obtaining cheap and easy methods to produce energy from light [1]. The possibility of chemically manipulating the material properties of polymers combined with a variety of easy and cheap processing techniques has made polymer-based materials present in almost every aspect of modern society [2].

We choose subjects of inquiry, which, recently, were used for the development of polymer composites of polymethine dyes with high photosensitivity in a wide spectral range [3] including the near-infrared region [4].

In the last two decades, the preparation technology of polymer composite films, which are promising for the creation of cheap plastic solar cells (PSC) [5, 6], is actively developed. Due to the production technology improvement, the efficiency of plastic solar cells increases [7, 8], but it is not sufficient for their practical use. One of the important reasons for the poor PSC efficiency is their low photosensitivity in the region of intense solar radiation. They absorb sunlight and create charge carriers only in the region 1.8–3.1 eV.

At the same time, the most effective inorganic solar cells based on Si and $CuInSe_2$ efficiently absorb sunlight and create charge carriers in the region from 1 to 3.1 eV. Therefore, the technology of development of polymer composites,

I.A. Savchenko
National Taras Shevchenko University of Kyiv, 60, Volodymyrska str., 01601 Kyiv, Ukraine

Y. Vertsimakha (✉)
Institute of Physics, NASU, Prosp. Nauky 46, 03680 Kyiv, Ukraine
e-mail: yavertisi@iop.kiev.ua; yavertsi@gmail.com

O. Fesenko, L. Yatsenko (eds.), *Nanophysics, Nanophotonics, Surface Studies, and Applications*, Springer Proceedings in Physics 183,
DOI 10.1007/978-3-319-30737-4_40

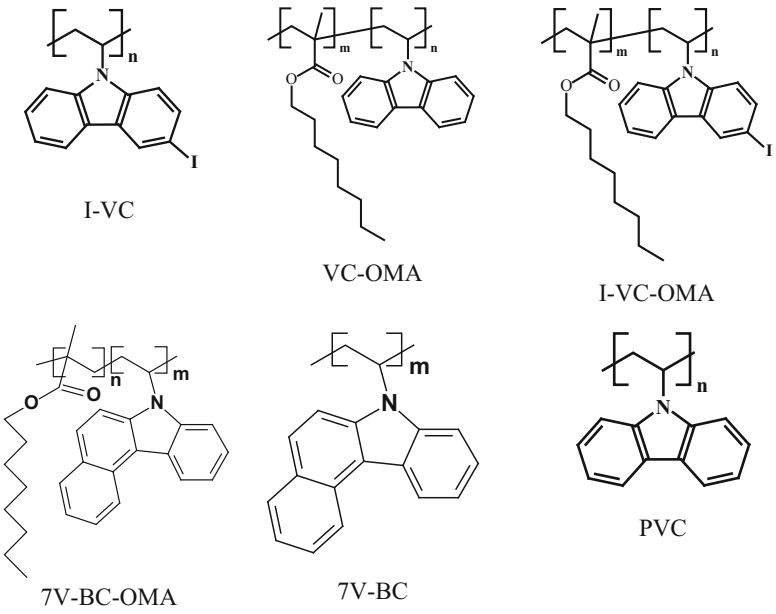

Fig. 40.1 Structures of polymers and copolymers

which has great potential for the creation of PSC photosensitive in a wide spectral region, was proposed [9] and experimentally confirmed.

By now, we have elaborated the physical and technological basis for the creation of composites photosensitive in the region 1.3–2.2 eV, which contains polymethine dyes and polyvinyl carbazole (PVC) derivatives [9].

Therefore, the aim of this work was a more detailed analysis of our data on the photovoltaic properties of composites, which consist of various matrices (Fig. 40.1) and polymethine [10–13] and phthalocyanine [14, 15] dyes, as well as the additional study of the influence of the molecular structures of components on the properties of photosensitive composites. This would allow us to substantiate the basic regularities of a further improvement of the photosensitivity of PSC and to extend its spectral region.

40.2 Experimental

40.2.1 Manufacturing Techniques of Photosensitive Film Polymer Composites

Composite films of dyes and polymers were prepared from their solutions. For the preparation of films, two types of substrates were used: glass substrates for

measuring the absorption of samples and a substrate coated with the magnetron sputtering by indium tin oxide layers (ITO), which served as an electrode in the measurements of the photovoltage of composites. The exemption from solvent residues was carried in air under the pumping in a fume hood in vacuum or without heating the substrate during the annealing at 60–120 °C. The annealing can significantly change the properties of the films. For example, the annealing at a temperature less than the glass transition temperature (softening) polymer leads typically to a partial ordering of the film structure, reducing the dispersion and increasing the thickness uniformity of films [16]. However, the annealing of polymer films at a temperature higher than the softening temperature of the polymer by 1.5–2.5 times leads, on the contrary, to a deterioration of the crystal structure of the films and even a partial destruction of polymer chains and/or oxidation.

The absorption spectra were measured with a spectrophotometer "Unicam Ultraviolet light (UV)-300."

40.3 Results and Discussion

40.3.1 The Selection Rules of Polymers for Creation of Polymeric Sensibilized Composites

For the formation of organic photovoltaic cells, conductive polymers and heterocyclic aromatic poly(*p*-phenylene-vinylene) (PPV), polyaniline, PVC, and polythiophenes are widely used [1, 3, 17, 18]. These organic photoconductive materials provide a sufficient photosensitivity and a dark current to create cheap photosensitive polymer composites that potentially could be used for the development of solar cells, radiation sensors, elements for recording information, etc., necessary to the fulfillment of certain requirements to these polymers.

You must select polymers such that:

- They are readily soluble in nontoxic volatile organic solvents (boiling point less than or equal to about 100 °C).
- Their solutions are stable under normal conditions (at least several days).
- Their films are plastic stable in the air for a long time.
- There are no dielectrics that allow the transfer of photoinduced carriers between molecules or their aggregates in the composite and electrodes.
- They have no significant ionic conductivity, which could lead to the transfer of ions (mass), to the instability and the adsorption of ions on the surface of photosensitive aggregates that would reduce the photogeneration of charge carriers due to changes in the potential barriers on the surface of photosensitive

aggregates, and to the formation of components with photovoltages of opposite signs.
– They should absorb light in the 400–550 nm region, where the majority of organic dyes and polyacenes are poorly absorbed and have low photosensitivity.

In the recent years, the interest in PVC copolymers with octyl methacrylate (OMA) significantly increases due to the need to obtain stable homogeneous films of polymers and their composites with photosensitive dyes.

To get thin PVC films is problematic because of the dissolubility of PVC in volatile organic solvents and the insufficient plasticity. Using vinylcarbazole (VC) copolymers with octyl methacrylate (OMA) greatly simplifies this task, since the presence of substituents in OMA in these copolymers (flexible chain of methylene groups 8) increases their solubility in some volatile organic solvents by almost an order of magnitude and increases the plasticity of films.

A comprehensive study of the optical properties (absorption, photoluminescence, and excitation of photoluminescence spectra) was performed for solutions and films of poly-*N*-vinylcarbazole (VC) polymers and copolymers — with octyl methacrylate (OMA) *N*-vinylcarbazole (Fig. 40.2a), *N*-vinyl-3-iodine carbazole (I-VC-OMA) (Fig. 40.2a), and *N*-vinyl-7H-benzo[b] carbazole (V7-BC–

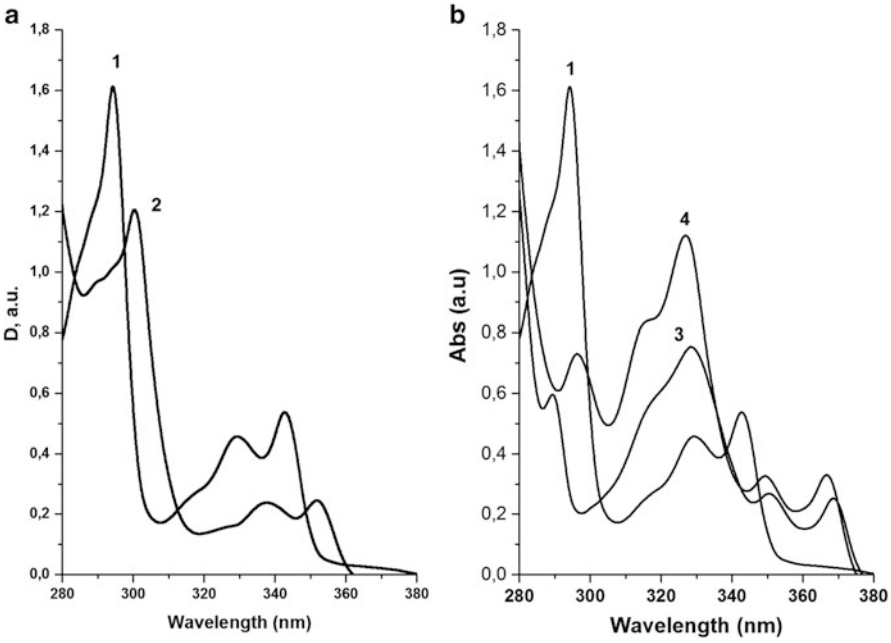

Fig. 40.2 Absorption spectra of solution in chloroform (a) *1*—VC-OMA, *2*—I-VC-OMA, (**b**) *3*—V7-BC, *4*—V7-BC-OMA

OMA) (Fig. 40.2b). For studies, the derivative copolymers were selected and used for the development of polymer composites with polymethine dyes with high photosensitivity in a broad spectral range [3], including the near-infrared region [19].

The analysis of the absorption spectra of solutions in chloroform and films obtained by the application of these solutions on quartz substrates showed that the transition from solution to film induces a slight shift of the maxima of absorption bands toward lower energies and a slight decrease in the half-widths of absorption bands, especially for polymers with OMA, and does not change the ratio of the intensities of absorption bands compared to the absorption bands of solutions.

The introduction of flexible OMA chains in the *N*-vinylcarbazole copolymer compared to homopolymers significantly increased solubility, flexibility, and orderliness of obtained PVC films. This is confirmed by measurements of the excimer fluorescence (Figs. 40.3). The introduction of OMA in the copolymer weakly influences the energy peaks and the structure of the $\pi-\pi^*$ conversions of absorption bands: a slight shift to 8–10 meV is observed, with virtually no change in the ratio of the intensities of absorption bands.

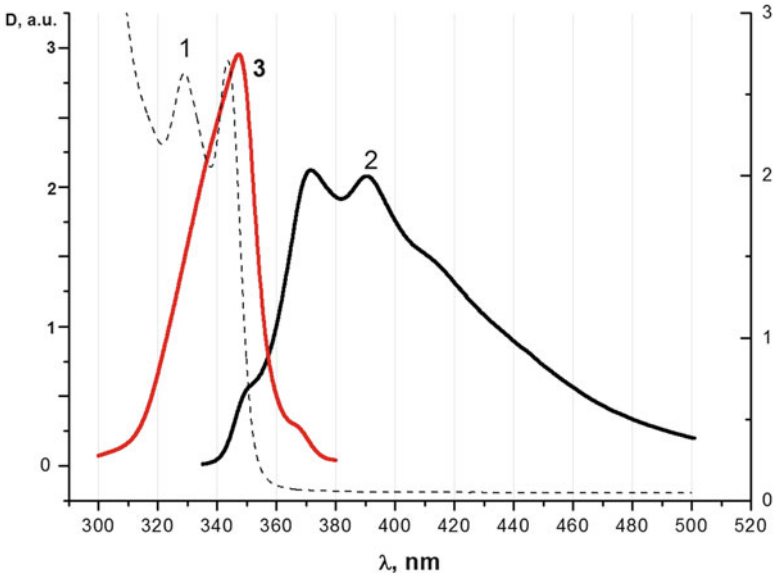

Fig. 40.3 Absorption spectra (*1*), photoluminescence (*2*), and excitation of luminescence (*3*) of films VC-OMA obtained by precipitation from solution in chloroform

The presence of flexible OMA chains in copolymers affects the energy bands and the ratio of the intensity peaks of the excimer fluorescence bands. For all the studied films, three absorption maxima of the excimer fluorescence are more clearly observed for films PVC with OMA in the fluorescence spectra (Fig. 40.3).

The last fact confirms the increasing degree of structure ordering of films I-VC-OMA and V7-BC-OMA compared to films I-VC and V7-BC, respectively, and the restructuring of polymer aggregates (complexes) in films.

Changes in spectra with the introduction of substituents in the molecule VC are strongly dependent on the size (volume) of substituents. For example, the introduction of iodine leads mainly to a significant (0.132 eV) shift of the $^1A \rightarrow {}^1L_a$ transition peak (Fig. 40.2a), which is polarized along the long axis of the polymer molecule and toward less energies without significant changes in the intensities of the bands. The introduction of more volumetric substituents such as a benzene ring leads to a significant increase in intensities of the shortwave bands of the $^1A \rightarrow {}^1L_b$ transition that is polarized along the short axis of a molecule VC and to an increase of the shift of long-wave $^1A \rightarrow {}^1L_a$ bands up to 0.388 eV.

These data allow one to constructively design the techniques aimed at a further increase of the photosensitivity of polymer composites in a wide spectrum region.

40.3.2 The Selection Rules of Molecular Structure of Polymethine Dyes

To create PSC, most works use the composites of electroconductive polymers with C_{60} derivatives, which form the charge-transfer complexes. To further increase the efficiency of such PSC, it is necessary to synthesize new C_{60} derivatives with greater solubility, greater lifetime of photogenerated carriers, and wider area of sunlight absorption. The first of these problems is almost solved, but the serious difficulties were met while solving two other problems.

Therefore, in this article we will focus on the analysis of other strategies to solve this problem. First, it is proposed to develop polymer materials, which will ensure the efficient light absorption in the region 1.4–1.8 eV, where the solar radiation intensity is large. Then we should find the ways to improve their photosensitivity in the region of shorter wavelengths (2.3–3 eV) and the near-infrared region.

To develop photosensitive organic composites promising to create plastic solar cells, composite dye should absorb light throughout the visible region of the next generation of photo carriers (as CdTe or Si). However, the dye molecule absorbs in the spectral range of 0.1 eV.

Therefore, in order to create photosensitive polymer composites the dyes must be selected take into consideration followed parameters:

1. The dye absorption maximum is in the spectral region of intense sun radiation (1.4–1.8 eV).
2. Dyes are derivatives of PVC or PPV and well dissolved in easily volatile organic solvents (evaporation less than 100 °C) which allow to obtain a homogeneous solution with polymers for deposition it to the desired substrate.
3. Dyes form photosensitive aggregates effectively.

Analysis of the properties of dyes shows that the greatest extent of these conditions can be achieved for polymethine dyes with maximum absorption at 1.5 eV, small photoluminescence efficiency, and aggregation in their solutions (Fig. 40.4).

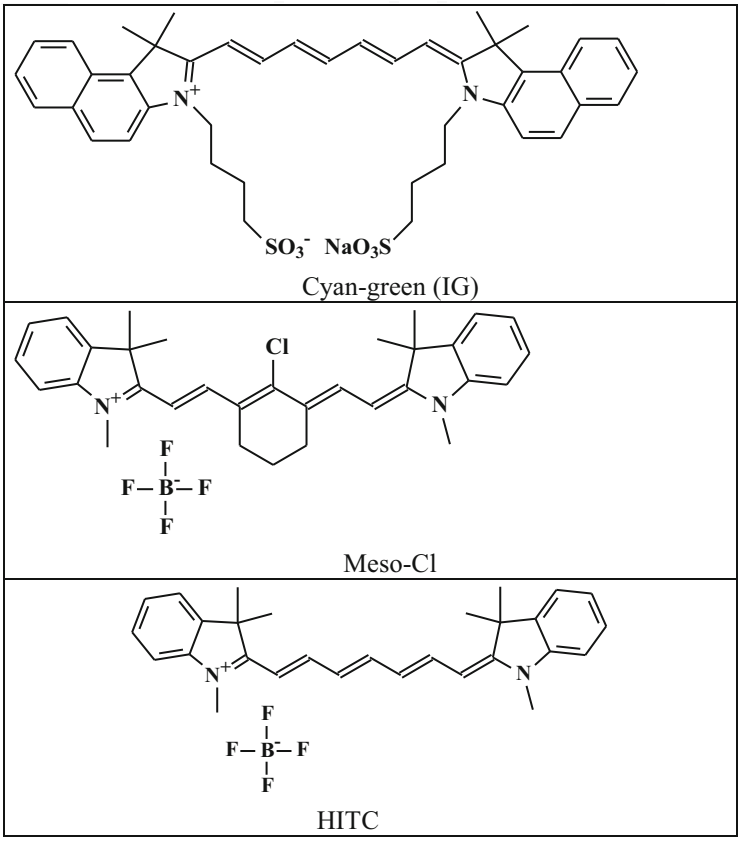

The maximum absorption bands of the first electronic transition of polymer composites (PC) in solutions of organic solvents are observed in the region $E_s = 1.58–1.64$ eV and, being injected into the polymer matrix, are shifted toward lower energies due the interaction between dye molecules and macromolecules.

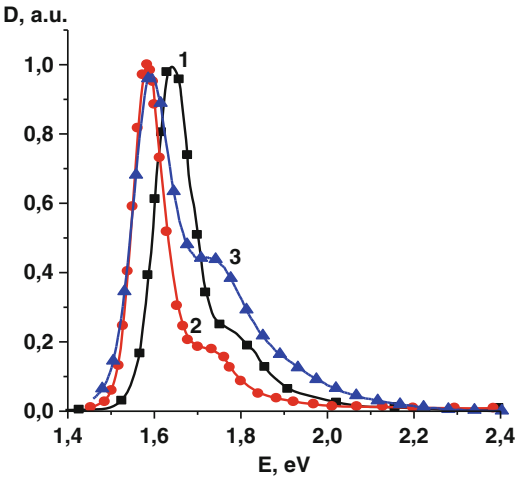

Fig. 40.4 Absorption spectra of dyes solution: HITC (*1*), meso-Cl (*2*), and ICG (*3*)

Table 40.1 Parameters of absorption bands of solution and films of photosensitive polymethine dyes at 300 K

	mCl	HITC	IG
Maximum of absorption in solution	1.584	1.640 eV	1.593
σ_-	0.021	0.026	0.033
σ_+	0.022	0.037	0.025
σ_+/σ_-	1.048	1.42	0.758
Maximum of absorption of polymer composites	820 nm (1.512)	770 nm (1.610)	807 nm (0.888)
			1.536 eV
ΔE, meV	72	30	57
σ_-	0.103	0.127	0.105
σ_+	0.637	0.539	0.511
σ_+/σ_-	6.184	4.244	4.867

A shift of the maximum power E_s into the region of less energies at 0.04–0.06 eV and a significant asymmetric expansion of absorption bands are observed for films of polymer composites (Table 40.1).

The shift E_s to the region of less energies is due to the weak interaction between the dye molecules and polymer molecules in the composite.

The strong asymmetry of expansion absorption bands, which increases several times with the energy of photons in the 1.5–2.2 eV region, shows that the additional absorption appears in films of polymer composites, which is not present in dye solutions, due to the formation of H-aggregates of different structures in composite films, which is typical of polymethine dyes [5].

The widening of absorption bands in the energy region $h\nu < E_s$ is due to the statistical disordering of dye molecules in the composite films.

The interaction of dye molecules and the polymer increases in the row HITC > ICG > mCl, and the asymmetry of the absorption band (due to the formation of H-aggregates) follows the row HITS > ICG > mCl.

40.3.3 Photovoltaic Properties of Composite Films in the Visible Spectrum Region

The properties of the composite films of IG-PVA and IG-V_2O_5 with the same optical density were investigated to identify the properties of the matrix, which is very important for the creation of photosensitive composites.

Figure 40.5 shows the spectral dependences of V_s for the PVA and V_2O_5 composite films with ICG at the same optical density. In the films based on PVA, V_s is higher than in xerogel films at the energies of formation of H-aggregates (1.9–2.2 eV) (curve 3, Fig. 40.5) and complexes with charge transfer (1.45–1.55 eV). These complexes are a result of the interaction between the polymer and dye molecules, and their energy must be lower than the excitation energy of quasineutral dye molecules. The probability of the generation of a complex with charge transfer is less than that of the formation of H-aggregates, and thus, the former is invisible in the V_s-spectra of some polymer composite films. The V_s-spectra of the composite films based on V_2O_5 testify to its practical absence. Therefore, the band corresponding to the charge-transfer complex in PVA films is formed due to a higher polymer plasticity, whereas the electrical conductivity of V_2O_5 films is much greater than that of PVA films.

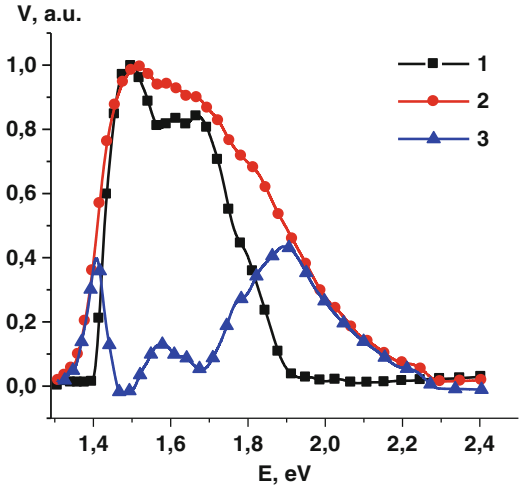

Fig. 40.5 Photovoltage spectra of composites of PVA + ICG (*1*), V_2O_5 + ICG (*2*), and their ratio (*3*)

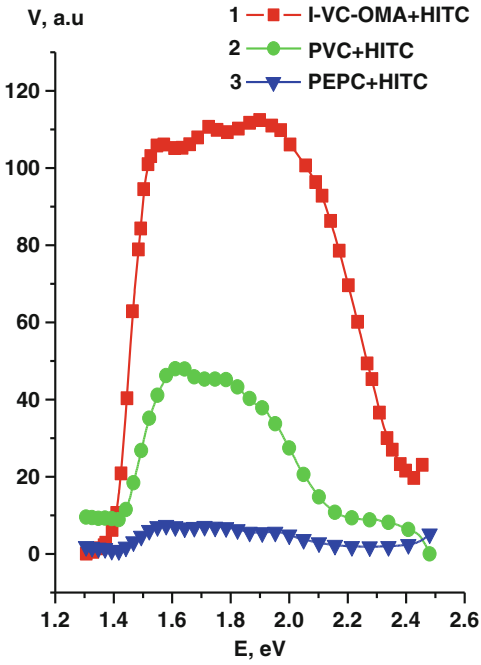

Fig. 40.6 Photovoltage spectra of polymer composites of I-VC-OMA (*1*), PVC (*2*), and PEPC (*3*) with HITC

Therefore, for the manufacture of composite materials, which are photosensitive in the visible spectrum, only polymer composites with polymethine dyes, whose maximum absorption in a solution under the intense solar radiation was observed at 1.6 eV, were selected.

All investigated composite films are photosensitive in the region 1.4–2.4 eV. In this case, the integrated photovoltage V_s and the value of V_s at the maximum of absorption bands depend mainly on the matrix material, as is shown in Fig. 40.6. It is seen that V_s increases much more in composites of HITC dye and polymers in a row poly-N-epoxypropylcarbazole (PEPC) > PVC > I-VC-OMA. In this case, V_s increases more in the region 1.7–2.3 eV, i.e., in the region of absorption of H-aggregates. In composite films HITC + I-VC-OMA (curve 1, Fig. 40.6), the values of V_s corresponding to about 1.7 and 1.9 eV are larger than those in the region of excitation of quasi-isolated molecules of HITC (1.6 eV). This fact suggests that the efficiency of the charge carrier photogeneration by these units is larger than that by the quasi-isolated molecules of HITC.

An increase of the asymmetry of V_s-bands is caused by the fact that the efficiency of the photogeneration of charge carriers in excited aggregates is larger than in excited isolated dye molecules. Especially, it is clearly demonstrated in the spectra of the ratio V_s/D (Fig. 40.7) normalized to the absorption spectra of V_s.

The energy state corresponding to the absorption maximum of dyes influences weakly the energy position of the maxima of H-aggregates (Fig. 40.8) in the strong-absorption region of the dyes.

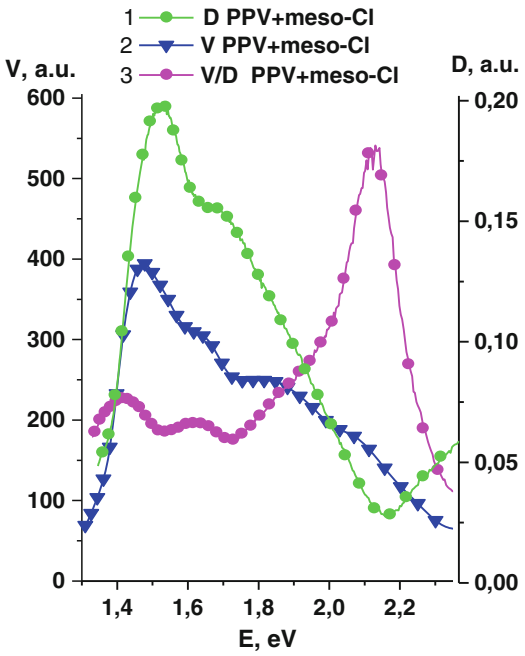

Fig. 40.7 Absorption (*1*), photovoltage spectra (*2*), and their ratio *V*/*D* (*3*) of composite films of PPV + meso-Cl

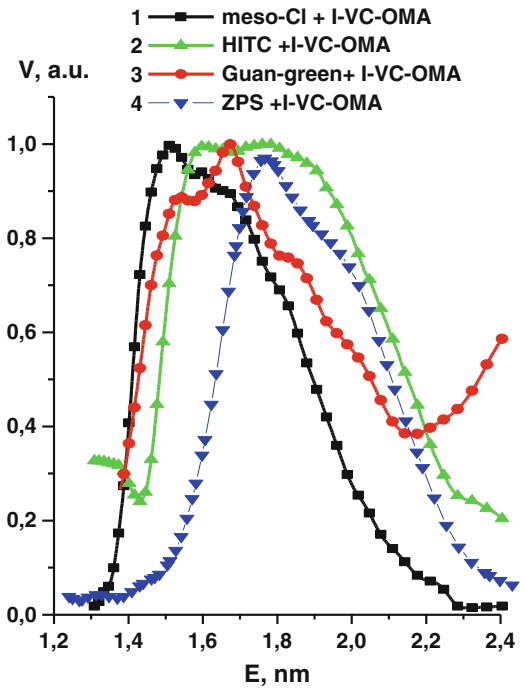

Fig. 40.8 Photovoltage spectra of polymer composites of meso-Cl (*1*), HITC (*2*), cyan-green (*3*), and ZnPc(Sulfonamide) (ZPS) (*4*) with I-VC-OMA

40.3.4 Ways to Improve the Sensitivity of Polymer Composites in the Shortwave Spectral Region

One disadvantage of photosensitive composites of polymethine dyes with carbazole-based polymers is their low photosensitivity in the spectral interval 2.1–2.7 eV (Fig. 40.9).

The photosensitivity in this region increases in the row PVC > PVE (polyvinyl ethylal) > I-VC > PEPC > I-VC-OMA, but does not exceed 10–20 % of their maximum value at 2.4 eV.

The analysis of the spectral dependence of the ratio *V*/*D* indicates that this weak photosensitivity is mainly due to a low probability of the formation of photosensitive aggregates in carbazole-based polymers with an energy greater than 2.1 eV (weak absorption of the dye aggregates and a polymer matrix in this region of the spectrum).

To test this assertion, the properties of composites HITC with PPV were investigated. Their films are photosensitive in the UV region and have else a significant photoluminescence, which should lead to a higher photosensitivity due to the absorption by aggregates with the energy 1.7–2.1 eV. The comparison of the spectra of composites HITC/PPV and HITC/I-VC-OMA (Fig. 40.10) shows that the composites with PPV have good photosensitivity in the visible and UV regions of the spectrum.

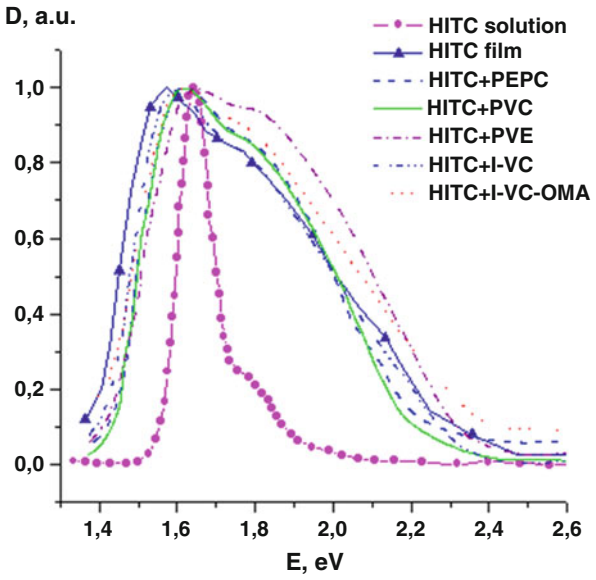

Fig. 40.9 Absorption spectra of HITC in polymer composites (2–5) and solution of HITC (*1*)

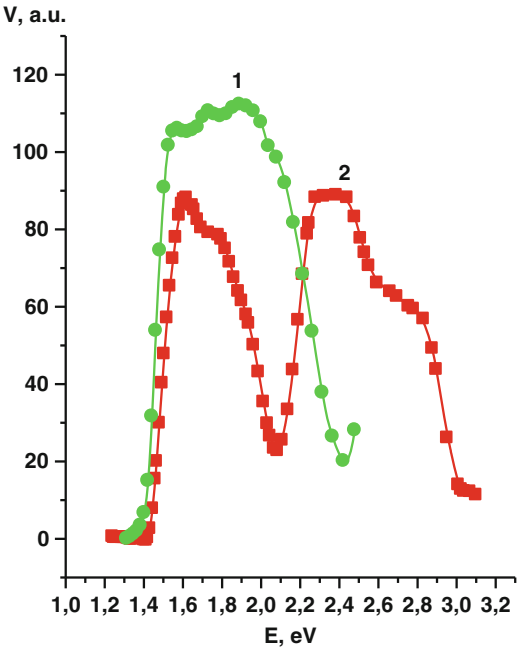

Fig. 40.10 Photovoltage spectra of polymer composites of PPV + HITC (*1*), I-VC-OMA + HITC (*2*)

The overall increase in the whole area is small due to the formation of non-photosensitive H-aggregates with the energy 2.1 eV in the composites HITC/PPV (Fig. 40.10).

40.3.5 Prospects for Expansion of Polymer Composites Photosensitivity in Long-Wavelength Region

Polymer composites, which are described in Sect. 3.4, on Si-based structures show high ability of absorption and conversion of sunlight in the region 1.1–3 eV. The analysis of the obtained data on the polymeric composites of polymethine dyes indicates that, for the expansion of the spectral region of absorption of these composites to the long-wave side up to 1.25 eV, it is necessary to utilize the polymethine dyes with a maximum of absorption in a solution, E_m, to be about 1.2 eV and with a considerable probability of the formation of dimer-like aggregates. For this purpose, it is necessary that their molecular structure has no bulky substituents in the meso-position of molecules and the luminescence efficiency be small.

Unfortunately, there are no criteria for the selection of such photosensitive composites at the present time, and hence, the presence of the efficient photogeneration of charge carriers in such composites should be tested experimentally. Therefore, we selected two dyes that possess the necessary properties. Their molecular structure is shown in Fig. 40.11. PVE polymer was used to make the composite films.

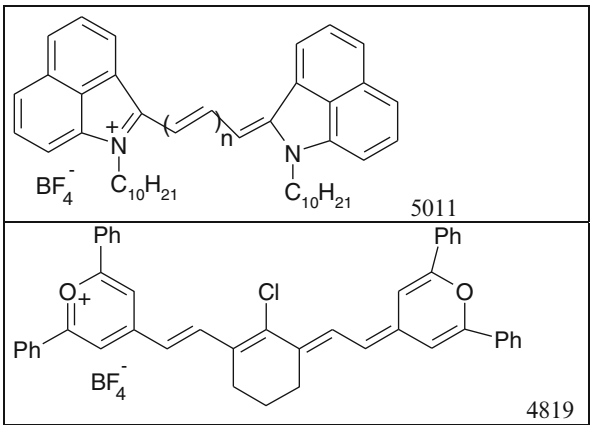

Fig. 40.11 Structures of dyes

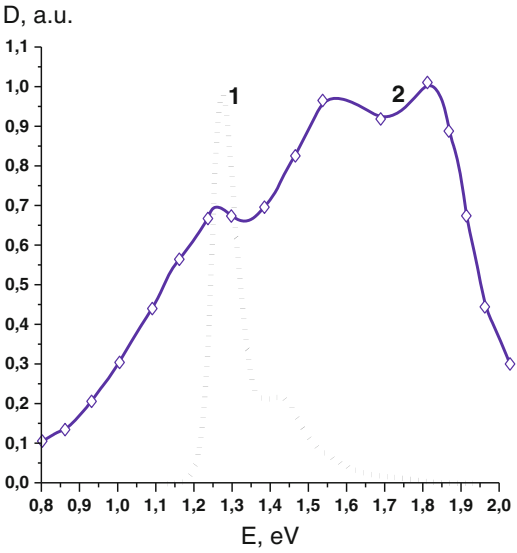

Fig. 40.12 Absorption spectra composite of 4819 and the dyes in solution of dichloroethane

The absorption spectra of the studied films of the composites in PVE with a dye concentration of 30 % are shown in Fig. 40.12. For the comparison, this figure also shows the absorption spectra of solutions of these dyes in ethylene dichloride.

The comparison of the spectra of these films and solutions indicates the following:

1. A small (20–40 meV) shift of the lowest electronic transition of a molecule ($E_m = 1.2$ eV) to the side of smaller energies is observed at the transition from a solution to a film of the composite. This is characteristic of the films of organic semiconductors and testifies to the presence of a weak (2–3 % E_m) intermolecular interaction of molecules of the dye and the polymer.

2. In the region of 1.5–2.0 eV in the absorption spectra of composite films of 4819 dye, there are two absorption bands with maxima near 1.58 and 1.181 eV, which have no analogs in the absorption spectra of these dyes in solutions and can be caused by the formation of two types of aggregates which are probably H-aggregates of the dimer-like type. The intensity of the absorption of these bands is higher than that of the absorption of quasi-isolated molecules in an aggregate at 1.2 eV. This testifies that the probability of the formation of dimer-like aggregates is great enough and more than that for aggregates on the basis of hexaindoletricarbocyanine (HITC) tetrafluoroborate and meso-Cl polymethine dyes. Only the peak at 1.52 eV is displayed clearly in the films of aggregates of 5011 t dye in this region. The intensity of this peak is greater than that for the peak at 1.2 eV, i.e., one type of aggregates with an energy of 1.52 eV is mainly formed in this composite. The presence of a weakly expressed shoulder in the absorption spectrum of this composite near 1.7 eV can be explained by the formation of an aggregate with low efficiency and other aggregates with low absorption.
3. In the low-energy region ($h\nu < E_m$), the spectra of the composites of both dyes reveal the additional absorption which is not present in the spectra of solutions of these dyes and is characterized by shoulders in the region of 1.0–1.1 eV. These shoulders can be related to the formation of complexes between molecules of the dye and the polymer. The absorption intensity in this region with respect to E_m is much more than that in the composites of HITC dye, i.e., the probability of the formation of complexes in the composites of 4819 dye is greater.

To check the efficiency of photogeneration of charge carriers under the excitation of the abovementioned aggregates and complexes, the measurements of the photovoltage V analogous to those previously described were carried out for films of these composites. The spectral dependences of V are shown in Fig. 40.13. From the comparison of curves in Figs. 40.12 and 40.13, it is seen that all aggregates and complexes, which were exhibited in the spectra of the films of 4819 dye-based composites, are photosensitive and generate charge carriers under illumination.

The greatest efficiency of the photogeneration of charge carriers is observed for the 1.58-eV aggregate (Fig. 40.13, curve 1), and it is greater than that under the excitation of quasi-isolated molecules of 4819 dye.

The situation is more complicated and atypical in the case of the films of aggregates of 5011 t dye. First, the aggregates of 5011 t dye with an energy of 1.52 eV are practically not photosensitive, which results in the appearance of a minimum on the spectral dependence of V in this spectral region. At the same time, the peak with a maximum near 1.72 eV is clearly displayed in the V-spectra. Second, the V-peak is clearly observed at 1.1 eV. This peak is caused by the formation of a complex between molecules of the dye and the polymer, and its intensity is greater than that in the region of E_m.

Thus, the efficiency of the photogeneration of charge carriers by this complex is greater than that of a quasi-isolated molecule.

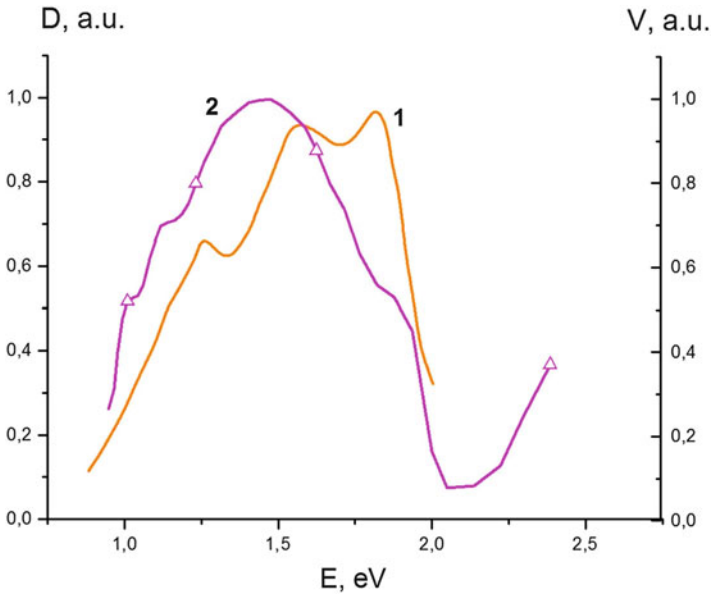

Fig. 40.13 Absorbance (D) and photovoltage (V) spectra of 5011 t and 4819 PVE composites

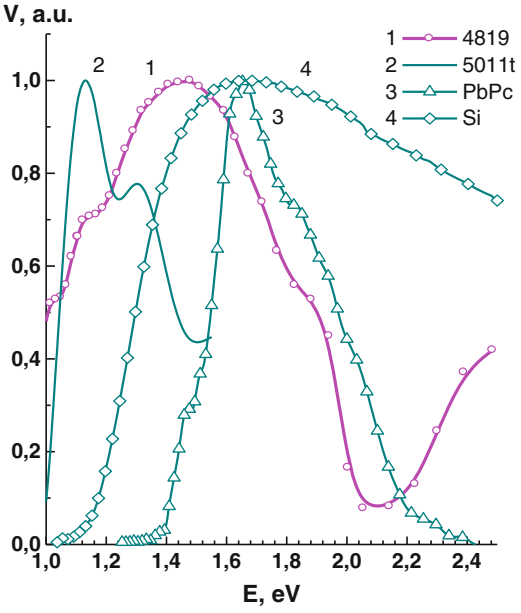

Fig. 40.14 Spectra of photovoltage of 4819 (*1*) and 5011 t (*2*) new polymethine dyes in polymer matrix, for comparison—lead phthalocyanine (PbPc) (*3*), and Si—photocell (*4*)

Since the shares of light absorbed by the different aggregates and complexes are different, we have plotted the spectral dependences of the photovoltage to the absorbance ratio ($V = D$ curves three and four, Fig. 40.14) in order to take this fact into account and to more correctly estimate the photosensitivity of different centers.

It is seen that the efficiency of the photogeneration of charge carriers in the films of 4819 dye for the 1.58-eV aggregate and complexes is higher than that for isolated molecules, and the absorption peak near 1.8 eV is caused by the formation of two aggregates with energies 1.71 and 1.96 eV with a small efficiency of the photogeneration. The peak of V at 1.72 eV in films 5011 t is caused by two aggregates with energies 1.72 and 1.98 eV with a small efficiency of the photogeneration as well.

Unfortunately, the efficiency of the photogeneration of charge carriers in these composites is not greater than that of isolated molecules of these dyes. According to the data from Sect. 3.2, the efficiency of the photogeneration of charge carriers can be essentially increased by the selection of a polymeric matrix.

In other words, the previous search for new polymethine dyes with a maximum near 1.2 eV has confirmed that they form the photosensitive composites in the region 0.8–2.4 eV depending on the molecular structure of a dye.

Thus, the opportunity of the preparation of cheap photosensitive composites for the development of plastic photoconverters photosensitive in a wider spectral range as compared with plastic photoconverters based on PbPc and Si has been confirmed.

40.4 Conclusions

1. Maximum sensitivity in films of polymer composites with polymethine dyes is observed in the spectral region of intense radiation from the sun. This is due to the formation of films of these composites with several H-aggregates of dyes with different energies. The efficiency of the photogeneration of charge carriers by some H-aggregates is higher than the efficiency of the photogeneration of charge carriers by quasi-isolated dye molecules. This leads to a substantial broadening of the spectral absorption region (as compared with the region of strong absorption by molecules in a solution) to shorter wavelengths from 1.6 to 2.2 eV. The energy positions of the maxima of H-aggregates depend weakly on the matrix molecular structure, and the photosensitivity at the H-aggregate maximum (1.4–2.2 eV) essentially depends on the molecular structure of the dye. The probability of formation of such phthalocyanine aggregates is much less.
2. In the shortwave spectral region (2.2–2.7 eV), the photosensitivity of nanocomposites is significantly less than that in the region of the absorption of H-aggregates and primarily depends on the photosensitivity of the matrix material. Maximum sensitivity is observed in the PPV composites in this region.
3. In composites with polymethine dyes, the dye molecules interact more effectively with the macromolecules, and the photosensitive charge-transfer complexes of a polymer and dye molecules are formed. This leads to the appearance of photosensitivity at energies, which are less than the excitation energy of the quasi-isolated dye molecule, which can be used for further development of structures which are photosensitive in the visible and near IR-regions (HITC + I-VC-OMA).

4. The spectral region of the sensitivity of composites, especially HITC/MDMO-PPV (poly[2-methoxy-5-(3′,7′-dimethyloctyloxy)-1,4-phenylene vinylene] and HITC/I-VC-OMA, is broader than that of the developed plastic solar cells based on conducting polymers with C_{60} derivatives. Therefore, the developed nanocomposite films based on HITC/MDMO-PPV are perspective for the development of photovoltaic devices photosensitive in IR and even UV, and the films based on HITC + I-VC-OMA are sensitive in the visible and near-infrared spectral regions.

References

1. Dou L, You J, Hong Z, Xu Z, Li G, Street R, Yang Y (2013) A decade of organic/polymeric photovoltaic research. Adv Mater 25:6642–6671
2. Xue J (2010) Perspectives on organic photovoltaics. Polym Rev 50:411–419
3. Vertsimakha Y, Verbitsky A (2008) New method of preparation of composites promising for the development of plastic solar cell. In: Carson J (ed) Solar cell research progress. Nova, Hauppauge, NY, pp 297–317 (Chapter 8)
4. Ya V, Verbitsky A, Ishchenko A, Syromyatnikov V, Pomaz I (2011) Effect of polymer molecular structure on photosensitivity of composites films based on infrared polymethine dye. Mol Cryst Liq Cryst 536:99
5. Akimov I, Meshkov A, Denisyuk I (1998) Nanostructured composite organic semiconductors. Funct Mater 5:363–369
6. Brabec C, Sariciftci Serdar N, Hummelen J (2001) Plastic solar cells. Adv Funct Mater 11:5–26
7. Winder C, Sariciftci Serdar N (2004) Low bandgap polymers for photon harvesting in bulk heterojunction solar cells. J Mater Chem 14:1077–1086
8. Brabec C, Dyakonov V, Scherf U (2008) Organic photovoltaics: materials, device physics, and manufacturing technologies. Wiley-VCH, Weinheim
9. Vertsimakha Ya, Verbitsky A, Ishchenko A, Derevyanko N (2002) Photovoltaic properties of photosensitive in wide spectral region heterostructures. In: Graja A, Bulka BR and Kajzar F (eds) Molecular low dimensional and nanostructured materials for advanced applications. NATO science series, II. Mathematics, physics and chemistry, vol 59. Kluwer Academic, Dordrecht, pp 311–314
10. Studzinsky S, Syromyatnikov V, Ishchenko A, Derevyanko N, Vertsimakha Ya, Verbitsky A (2003) Effect of polymer matrix on photosensitivity of polymethine dye-based composites. In: Book of Abstracts, NATO Advanced Research Workshop "Smart and Functional Organic Materials", p 96
11. Fenenko L, Ishchenko A, Verbitsky A, Ya V (2005) Photovoltaic effects in composites of V_2O_5 xerogel with polymethine dye. Mol Cryst Liq Cryst 426:157–169
12. Studzinsky S, Syromyatnikov V, Ishchenko A, Derevyanko N, Ya V, Verbitsky A (2005) Effect of polymer matrix on photosensitivity of polymethine dye based composites. Nonlinear Opt Quantum Opt 33(1–2):151–159
13. Beresina N, Syromyatnikov V, Ishchenko A, Verbitsky A, Ya V (2006) Effect of polymer matrix on photosensitivity of meso-Cl polymethine dye based composites. Funct Mater 13 (4):676–680
14. Syromyatnikov V, Pomaz I, Verbitsky A, Ya V, Nespurek S, Pochekaylov S (2009) Photosensitive in wide spectral region composites based on polyphenylenevinylene. J Semicond Phys Quantum Electron Optoelectron 12(1):01–07
15. Ya V, Mamykin S, Lutsyk P (2012) Substitution of phthalocyanines affecting the properties of their films and heterostructures. Chem Phys 404:16–21

16. Miller S, Fanchini G, Yu L, Li C, Chen C, Sub W, Chhowalla M (2008) Investigation of nanoscale morphological changes in organic photovoltaics during solvent vapor annealing. J Mater Chem 18:306–312
17. Abdulrazzaq O, Saini V, Bourdo S, Dervishi E, Biris A (2013) Organic solar cells: a review of materials, limitations, and possibilities for improvement. Part Sci Technol 31:427–442
18. Shaheen S, Ginley D (2009) Photovoltaics: organic-based solar cells. In: Dekker Encyclopedia of Nanoscience and Nanotechnology. Taylor & Francis Inc, Bosa Roca, United States
19. Yashchuk V (2004) Polymer photonics. Kyiv University, Kyiv, p 112

Chapter 41
Effect of Mechanochemical Treatment of Cellulose on Characteristics of Nanocellulose Films

V.A. Barbash, O.V. Yaschenko, S.V. Alushkin, A.S. Kondratyuk, O. Yu. Posudievsky, and V.G. Koshechko

41.1 Background

Creation of nanomaterials with advanced functional characteristics not available to their bulk analogues has been rapidly developing [1–5]. Nanocellulose is among the nanomaterials which attract great attention. Nanocellulose is a group of materials consisting of nanosized cellulose particles distinguished by plant raw materials and methods of preparation [6, 7]. The demand in nanocellulose is determined by its specific properties and ability to replace materials which are poor degradable at ambient conditions. It is widely used in research aimed at creation of new specific nanocomposites, adsorbents, functional materials for electrodes in chemical sources of power, optoelectronic devices [8–19] that determines high perspectives of these nanomaterials in electronics, medicine, food, pharmaceutical, and other industries.

Cellulose is one of the most abundant and renewed biopolymers on our planet with annual production up to 10^{11} tons [6]. During the process of photosynthesis, cellulose macromolecules form nano- and microfibril structures stabilized by hydrogen bonds [7]. Nanocrystalline cellulose, which consists of rod-shaped crystals with 2–20 nm cross-section diameter of and length from 100 nm to several micrometers [17], is prepared by removing amorphous regions from cellulose. Nanocrystalline cellulose could form stable aqueous suspensions with chiral

V.A. Barbash (✉) • O.V. Yaschenko • S.V. Alushkin
National Technical University of Ukraine "Kyiv Polytechnic Institute",
Prospekt Peremogy 37, Kyiv 03056, Ukraine
e-mail: v.barbash@kpi.ua

A.S. Kondratyuk • O. Yu. Posudievsky • V.G. Koshechko
L.V. Pisarzhevsky Institute of Physical Chemistry of the National Academy of Sciences of Ukraine, Prospekt Nauki 31, Kyiv 03028, Ukraine
e-mail: posol@inphyschem-nas.kiev.ua

O. Fesenko, L. Yatsenko (eds.), *Nanophysics, Nanophotonics, Surface Studies, and Applications*, Springer Proceedings in Physics 183,
DOI 10.1007/978-3-319-30737-4_41

nematic properties and, as cholesteric liquid crystals, possesses optical characteristics remaining in films even after solvent evaporation [18]. Nanocrystalline cellulose is characterized by strength five times higher than that of steel and coefficient of thermal expansion less than that of quartz [19]. Nanocrystalline cellulose-based films possess optical transparency due to their specific structure.

Physical, chemical, and enzymatic methods are known for preparation of nanocellulose. The essence of physical methods is an application of different forces to reduce the size of the natural cellulose fibers to nanoscale. This approach includes multiple passages of cellulose fibers through a high-pressure homogenizer requiring large energy consumption (above 25 kW/kg) [6]. Chemical methods are based on the cleavage of 1–4 glycosidic bonds of the cellulose chains and decrease of the molecule size [20]. Enzymatic methods consist in biosynthesis from monosaccharides or decreasing the size of cellulose fibers by fermentation. These enzymatic methods are more long term, and reagents for these processes are more expensive. However, preliminary treatment of cellulose by enzymes before mechanical grinding could assist in decreasing energy consumption necessary for preparation of nanocellulose [21].

The aim of the present work was to determine an opportunity of nanostructuring the bleached softwood sulfate pulp by mechanochemical treatment and study of optical characteristics (transparency in the visible spectrum range) and physical–mechanical properties (Young modulus, tensile strength) of the obtained films. The choice of the pulp is explained by its high overall production by the paper industry, while the choice of the studied characteristics is determined by further objective of the work consisting in creation of flexible transparent coatings (substrates) for optoelectronics, chemical sources of power, and so on.

41.2 Methods

Mechanical treatment of the bleached softwood sulfate pulp (Arkhangelsk CPF, Russia) was performed using laboratory milling complex LRK-1 (UkrSRIP, Ukraine) with the setting of diamond garniture from 0.1 to 0.4 mm for reaching 93 Schopper–Riegler degree freeness. Measurements of the beating rate were carried out by SR-2 device (CSRIP, Russia).

Hydrolysis of mechanochemically treated cellulose was carried out by sulfuric acid solutions with different concentration (from 18 to 64 %) at the solid-to-liquid ratio of 44:1 during 5–60 min. The calculated amount of sulfuric acid with the corresponding concentration was slowly added into the flask with the cellulose suspension, and the required volume of the acid with concentration above 50 % was added dropwise. The temperature of the reaction was maintained in the range of 60 ± 5 °C. Upon expiration of the processing time, the hydrolysis reaction was stopped by adding distilled water and cooling the suspension to room temperature.

The hydrolyzed cellulose was washed by multiple centrifugations until reaching neutral pH. Then it was diluted by distilled water to the concentration of ~1 % and

sonicated using ultrasound disintegrator UZDN-A (SELMI, Ukraine). The duration of the ultrasound treatment was 30–120 min. Eventually the suspension acquired the form of a homogenous gel-like dispersion.

The prepared dispersions were poured into Petri dishes and dried at room temperature on air to obtain cellulose films. The thickness of the films was in the range of 30 ± 5 μm. Their density was determined accordingly to the ISO 534:1988.

The determination of particle size distribution for cellulose dispersions was performed by dynamic light scattering (DLS) using analyzer Zetasizer Nano (Malvern Instruments). Transmission electron microscopy (TEM) images were obtained using electron microscope TEM125K (SELMI, Ukraine) operating at potential of 100 kV. Electron absorption spectra of the nanocellulose films in UV, visible, and near-infrared regions were registered on two-beam spectrophotometer 4802 (UNICO) with resolution of 1 nm. FTIR spectra were measured using spectrophotometer IFS66 (Bruker) with resolution of 2 cm^{-1}. X-ray diffraction patterns of the different cellulose samples were obtained by Ultima IV diffractometer (Rigaku). To determine the crystallinity degree (CD) of the samples, there was used the method proposed in [22], in terms of which $CD = (I_{200} - I_{am})/I_{200}$, where I_{200} is an intensity of (200) reflex about 23°, and I_{am}—an intensity of amorphous scattering at 18.5°.

Calculation of tensile strength (T) of the nanocellulose films was performed after measurement of breaking strength of the films (F) on RBM-10-2M device (UkrSRIP, Ukraine) using the formula: [23]: $T = \frac{F}{h \cdot b}$, where b and h—thickness and length of the samples. Young's modulus (E) was determined accordingly to [23]: $E = \frac{T \cdot l}{\Delta l}$, where l—distance between clamps, and Δl—extension.

41.3 Results and Discussions

The researches of spectral characteristics of the prepared cellulose materials showed that the films derived from non-hydrolyzed cellulose are nontransparent in visible spectral range. Carrying out of the acid hydrolysis as well as the ultrasound disintegration of the cellulose suspensions prepared by the mechanochemical treatment of the initial cellulose led to, from one side, increasing stability of the resultant aqueous dispersions and, from the other, formation of transparent cellulose films. Figure 41.1 presents electron absorption spectra of the samples prepared from different dispersions after acid hydrolysis of the mechanochemically treated cellulose with and without subsequent sonication. It is seen from the presented data that the hydrolysis of cellulose allows obtaining of the films with transparency more than 50 % in the visible spectral range. Also, Fig. 41.1 shows that the successive ultrasound treatment of the cellulose dispersions could lead to significant increase of the transparency. The transparency of the film prepared from the cellulose sample hydrolyzed by 43 % sulfuric acid achieves 78 % at the wavelength of 600 nm. The value of transparency of the obtained films is superior to thoroughly polished nanocellulose films prepared earlier in [19].

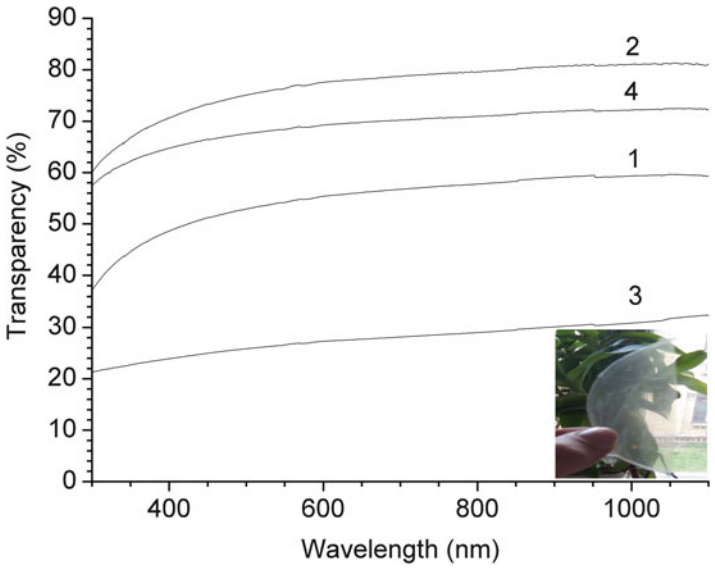

Fig. 41.1 Electron absorption spectra of the cellulose films prepared on the basis of cellulose hydrolyzed by 43 and 30 % sulfuric acid untreated (*1*, *3*) and treated (*2*, *4*) with ultrasound (photography of transparent nanocellulose film sample is in the right corner)

It should be noted that the films prepared on the basis of the cellulose hydrolyzed at high concentrations of sulfuric acid lost their transparency and acquired the brownish color due to destruction of the cellulose macromolecules confirmed by the FTIR data shown in Fig. 41.2. Indeed, the band about 1730 cm^{-1} appeared in the spectrum of the hydrolyzed sample indicating the appearance of the carbonyl groups in the macromolecules.

The data about the transparency of the films allowed us to assume that the sonication procedure applied after the mechanochemical treatment facilitated a decrease of the hydrolyzed cellulose particle size by destruction of its crystalline regions. To justify such hypothesis, the prepared cellulose samples were analyzed by DLS and TEM.

The results of the DLS analysis are presented in Fig. 41.3. It follows from the figure that the studied dispersions are characterized by the polydisperse particle size distributions, which should facilitate formation of more dense and more transparent cellulose films. It could be concluded also that the hydrolysis by sulfuric acid of higher concentration leads to formation of the smaller nanoparticles.

The morphology of the prepared nanocellulose samples was examined using TEM. As it follows from Fig. 41.4a, after the mechanical treatment in the laboratory milling complex, the cellulose consisted of nanofibers with diameter of 50–100 nm. The diameter of these nanofibers is clearly nonuniform that could be due to their formation as a result of agglomeration of separate nanoparticles possessing the size of several dozen nanometers or attachment of such nanoparticles to thin nanofibers

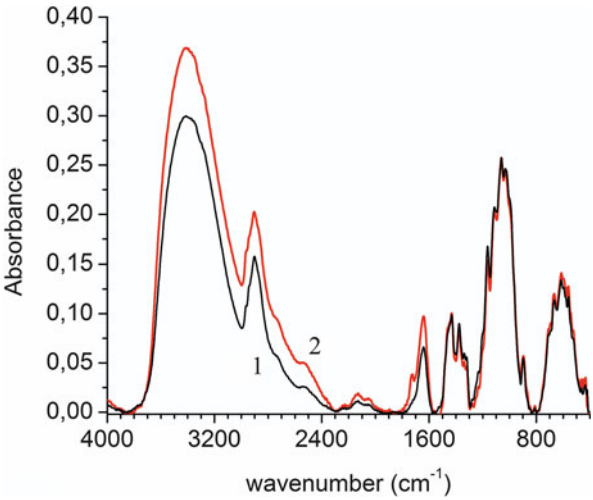

Fig. 41.2 FTIR spectra of the initial cellulose (*1*) and cellulose hydrolyzed by sulfuric acid (*2*)

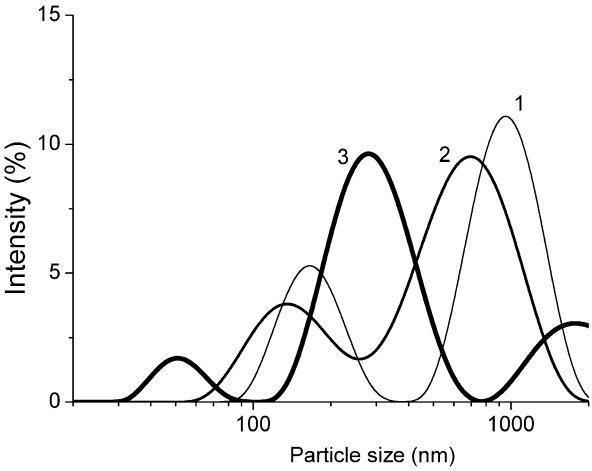

Fig. 41.3 Nanoparticles size distribution for dispersions prepared by ultrasound disintegration of the cellulose samples hydrolyzed by sulfuric acid of different concentrations: 30 % (*1*), 43 % (*2*), and 50 % (*3*)

with the diameter of ~10 nm. After hydrolysis, the morphology of nanocellulose significantly changed. Figure 41.4b shows that the hydrolyzed cellulose formed microsized agglomerates after evaporation of solvent. These agglomerates had dense-layered structure, and the nanoparticles, which form them, are hardly distinguished due to dense packing, which is caused, probably, by strong interaction between the particles induced by chemical modification of the cellulose macromolecules during hydrolysis (Fig. 41.2).

Studies of the physical–mechanical properties of the prepared nanocellulose films are summarized in Table 41.1. According to the presented data, an increase of the acid concentration during hydrolysis from 18 to 43 % led to an increase of the physical–mechanical characteristics of the nanocellulose films, so that they exceed

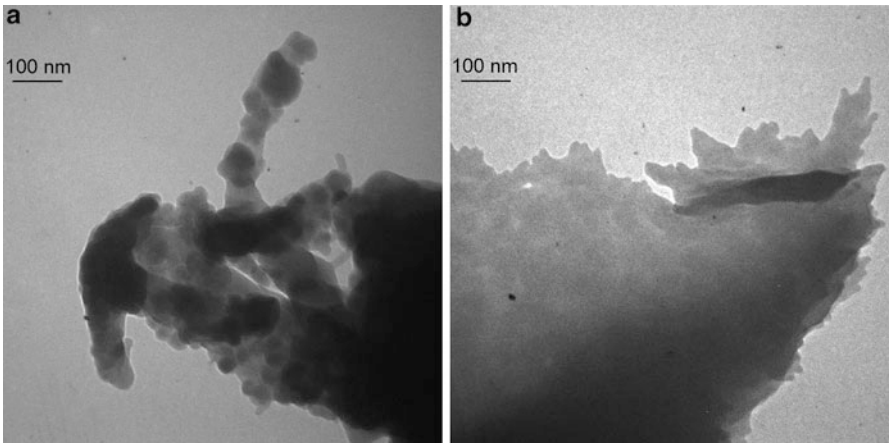

Fig. 41.4 TEM images of the cellulose after mechanical milling (**a**) and after further hydrolysis with 43 % sulfuric acid (**b**)

Table 41.1 Effect of sulfuric acid concentration on the density and strength of the nanocellulose films

H_2SO_4 concentration, %	Density, g/cm^3	Tensile strength, MPa	Young modulus, GPa
18	0.92	26,1	1.8
30	0.97	69,0	5.5
43	1.6	88	8.8
50	0.81	64,5	5,2
64	0.75	51,3	4,6

the values achieved by the authors of [24] for the softwood cellulose (Young modulus and tensile strength of 6.0 GPa and 80 MPa, respectively). And after a further increase of the acid concentration, a sharp decrease of all strength properties was observed. The obtained data showed that at mild conditions (low concentration of sulfuric acid), the hydrolysis of predominantly amorphous regions of the cellulose, relatively to crystalline ones, takes place leading to the increase of the physical–mechanical properties of the films, while the more severe conditions of hydrolysis (usage of sulfuric acid concentration above 50 %) leads to the destruction of both amorphous and crystalline regions of the cellulose that is consistent by the brownish color of the films mentioned above.

To confirm the abovementioned assumption, the cellulose samples were examined by X-ray diffraction. The measured X-ray diffraction patterns are presented in Fig. 41.5. It follows from the figure that milling and hydrolysis as well as further ultrasound treatment effect on the cellulose crystallinity. The crystallinity degree of the initial cellulose, the hydrolyzed cellulose, and the sonicated cellulose was calculated on the basis of the data shown in Fig. 41.5. It was established that the corresponding CD values are equal to 75, 78.3, and 79.8 %. The obtained data indicates that these treatments increase package ordering of the macromolecules.

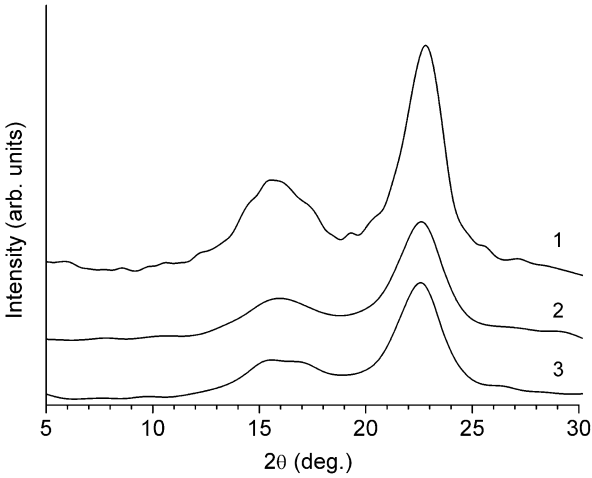

Fig. 41.5 X-ray diffraction patterns of the cellulose samples: initial cellulose (*1*), cellulose after milling and 43 % sulfuric acid hydrolysis (*2*) and cellulose after additional sonication (*3*)

To prove the X-ray diffraction data, we used FTIR spectra of the cellulose samples. According to the criterion proposed in [25], CD of cellulose changes symbatically to ratio between intensity of the bands at 1430 and 900 cm^{-1}. The calculations of the mentioned ratio showed that for the initial cellulose, the hydrolyzed cellulose, and the sonicated cellulose, its value is equal to 1.74, 1.82, and 1.86, respectively, that correlates well with the data obtained using X-ray diffraction.

41.4 Conclusions

Thus, in the present work, the effect of mechanical treatment, hydrolysis and sonication of the bleached softwood sulfate pulp on optical and physical–mechanical characteristics of the transparent nanocellulose films was studied. It was established that the films prepared on the basis of milled, hydrolyzed by 43 % sulfuric acid, and sonicated cellulose are characterized by high transparency in the visible spectral range (78 % at 600 nm) and high values of Young modulus and tensile strength (8.8 GPa and 88 MPa) due to the increased package ordering of the modified cellulose macromolecules.

41.5 Competing Interests

The authors declare that they have no competing interests.

41.6 Authors' Contributions

V. B. has conceived the study, interpreted the experimental data, and drafted the manuscript. O. Y. has performed the mechanical treatment and hydrolysis of the bleached softwood sulfate pulp, prepared the nanocellulose films, and analyzed its physical–mechanical characteristics. S. A. has determined the transparency of nanocellulose films and carried out ultrasound studies. A. K. has investigated the TEM images and FTIR spectra. O. P. has conceived the study, interpreted the experimental data, and drafted the manuscript. V. K. has made substantial contributions to the conception of the study and analysis of data. All authors read and approved the final manuscript.

References

1. Gleiter H (2000) Nanostructured materials: basic concepts and microstructure. Acta Mater 48:1–29
2. Zhang H (2015) Ultrathin two-dimensional nanomaterials. ACS Nano 9:9451–9469
3. Yao S, Zhu Y (2015) Nanomaterial-enabled stretchable conductors: strategies, materials and devices. Adv Mater 27:1480–1511
4. Yang C, Wei H, Guan L, Guo J, Wang Y, Yan X, Zhang X, Wei S, Guo Z (2015) Polymer nanocomposites for energy storage, energy saving, and anticorrosion. J Mater Chem A 3:14929–14941
5. Myung S-T, Amine K, Sun Y-K (2015) Nanostructured cathode materials for rechargeable lithium batteries. J Power Sources 283:219–236
6. Klemm D, Kramer F, Moritz S, Lindström T, Ankerfors M, Gray D, Dorris A (2011) Nanocellulose: a new family of nature-based materials. Angew Chem Int Ed 50:5438–5466
7. Habibi Y, Lucia LA, Rojas OJ (2010) Cellulose nanocrystals: chemistry, self assembly, and applications. Chem Rev 110:3479–3500
8. Liu S, Liu Y-J, Deng F, Ma M-G, Bian J (2015) Comparison of the effects of microcrystalline cellulose and cellulose nanocrystals on Fe_3O_4/C nanocomposites. RSC Adv 5:74198–74205
9. Aleshin AN, Berestennikov AS, Krylov PS, Shcherbakov IP, Petrov VN, Trapeznikova IN, Mamalimov RI, Khripunov AK, Tkachenko AA (2015) Electrical and optical properties of bacterial cellulose films modified with conductive polymer PEDOT/PSS. Synth Metals 199:147–151
10. Huang H-D, Liu C-Y, Li D, Chen Y-H, Zhong G-J, Li Z-M (2014) Ultra-low gas permeability and efficient reinforcement of cellulose nanocomposite films by well-aligned graphene oxide nanosheets. J Mater Chem A 2:15853–15863
11. Jiang F, Yin L, Yu Q, Zhong C, Zhang J (2015) Bacterial cellulose nanofibrous membrane as thermal stable separator for lithium-ion batteries. J Power Sources 279:21–27
12. Gao K, Shao Z, Li J, Wang X, Peng X, Wang W, Wang F (2013) Cellulose nanofiber–graphene all solid-state flexible supercapacitors. J Mater Chem A 1:63–67
13. Thiemann S, Sachnov SJ, Pettersson F, Bollström R, Österbacka R, Wasserscheid P, Zaumseil J (2014) Cellulose-based ionogels for paper electronics. Adv Func Mater 24:625–634
14. Lukach A, Thérien-Aubin H, Querejeta-Fernández A, Pitch N, Chauve G, Méthot M, Bouchard J, Kumacheva E (2015) Coassembly of gold nanoparticles and cellulose nanocrystals in composite films. Langmuir 31:5033–5041

15. Jung YH, Chang T-H, Zhang H, Yao C, Zheng Q, Yang VW, Mi H, Kim M, Cho SJ, Park D-W, Jiang H, Lee J, Qiu Y, Zhou W, Cai Z, Gong S, Ma Z (2015) High-performance green flexible electronics based on biodegradable cellulose nanofibril paper. Nat Commun 6:7170
16. Gadim TDO, Figueiredo AGPR, Rosero-Navarro NC, Vilela C, Gamelas JAF, Barros-Timmons A, Neto CP, Silvestre AJD, Freire CSR, Figueiredo FML (2014) Nanostructured bacterial cellulose−poly(4-styrene sulfonic acid) composite membranes with high storage modulus and protonic conductivity. ACS Appl Mater Interfaces 6:7864–7875
17. Holt BL, Stoyanov SD, Pelan E, Paunov VN (2010) Novel anisotropic materials from functionalised colloidal cellulose and cellulose derivatives. J Mater Chem 20:10058–10070
18. Majoinen J, Kontturi E, Ikkala O, Gray DG (2012) SEM imaging of chiral nematic films cast from cellulose nanocrystal suspensions. Cellulose 19:1599–1605
19. Nogi M, Iwamoto S, Nakagaito AN, Yono H (2009) Optically transparent nanofiber paper. Adv Mater 20:1–4
20. Zhu H, Parvinian S, Preston C, Vaaland O, Ruan Z, HuL (2013) Transparent nanopaper with tailored optical properties. Nanoscale 5:3787–3792
21. Pääkkö M, Ankerfors M, Kosonen H, Nykänen A, Ahola S, Österberg M, Ruokolainen J, Laine J, Larsson PT, Ikkala O, Lindström T (2007) Enzymatic hydrolysis combined with mechanical shearing and high-pressure homogenization for nanoscale cellulose fibrils and strong gels. Biomacromolecules 8:1934–1941
22. Ali NA, Noori FTM (2014) Crystallinity, mechanical, and antimicrobial properties of polylactic acid/microcrystalline cellulose/silver nanocomposites. Int J Appl Innov Eng Manag 3:77–81
23. Costa LA, Fonseca AF, Pereira FV, Druzian JI (2015) Extraction and characterization of cellulose nanocrystals from corn stover. Cellul Chem Technol 49:127–133
24. Zimmermann T, Pohler E, Geiger T (2004) Cellulose fibrils for polymer reinforcement. Adv Eng Mater 6:754–761
25. O'Connor RT, Du Pre E, Mitcham D (1958) Application of infrared absorption spectroscopy to investigations of cotton and modified cottons. Part I. Physical and crystalline modification and oxidation. Text Res J 28:382–392

Chapter 42
Electrical and Thermoelectric Properties of the Composite Polytetrafluoroethylene, Multi-Walled Carbon Nanotubes

M.M. Nishchenko, I. Ye. Galstian, G. Yu. Mykhailova, Yu. F. Bozbey, and V. Yu. Koda

It was shown by the measurement of electrical conductivity and Seebeck coefficient that the inclusion of metallic multilayer nanotubes to polymer structure opens up the possibility to develop new materials. Their electric and thermoelectric properties will differ from such properties of individual nanotubes as well as pure polymers.

It's means that only fluorine from all components of polytetrafluoroethylene can be joined to the carbon skeleton and the fact of most strongest carbon–fluorine bond, it can be said that the polymer has excellent combination of physical and chemical properties, which cannot be found in other materials.

The polytetrafluoroethylene molecules look like a zigzag helix chains. The polymer contains up to 80–85 % crystalline phase. The amorphous part has a glass transition temperature of −120 °C. But even at lower temperatures, the polymer do not loses elasticity due to the flexibility of the macromolecules and weak intermolecular bonds.

Slight growth of dependences of electrical conductivity on compression degree of the composite and no peak in the resistivity curve of CNT concentration indicate that CNTs in a polymer matrix of polytetrafluoroethylene (PTFE) do not deform (because deformation usually leads to a decrease of electrical conductivity of CNTs).

It can be assumed that the interaction of the surface of the CNT with the polymer molecules has a van der Waals nature. Also in the case of mechanical loading of composite, the nanotubes will suffer hydrostatic compression and be able to move almost free in the volume of the polymer—it allows to considerably increase their

M.M. Nishchenko • I. Ye. Galstian (✉) • G. Yu. Mykhailova • Yu. F. Bozbey • V. Yu. Koda
G.V. Kurdyumov Institute for Metal Physics NASU, Kiev, Ukraine
e-mail: nish@imp.kiev.ua; stenforti@ukr.net; mihaylova88@yandex.ua; posit@imp.kiev.ua; pioneer@ukr.net

O. Fesenko, L. Yatsenko (eds.), *Nanophysics, Nanophotonics, Surface Studies, and Applications*, Springer Proceedings in Physics 183,
DOI 10.1007/978-3-319-30737-4_42

conductivity. Experimentally the mechanical loading/unloading was realized by up–down moving of stroke in dielectric cylinder.

During the chemical interaction of nanotubes with polymer molecules, the interfacing processes of surfaces, increasing of strength, and inhomogeneous deformation of CNTs can be expected. It should be noted that for multilayer CNTs (with weak van der Waals interactions between adjacent layers of nanotubes), real interaction with the polymer occurs only due to the outer layer.

During the return stroke of the piston, the initial section of $\sigma(\rho)$ curve for a sample with 4 wt% CNT (Fig. 42.1) is almost matched with the curve which was obtained by the direct stroke of the piston. It indicates the elastic relaxation of the material.

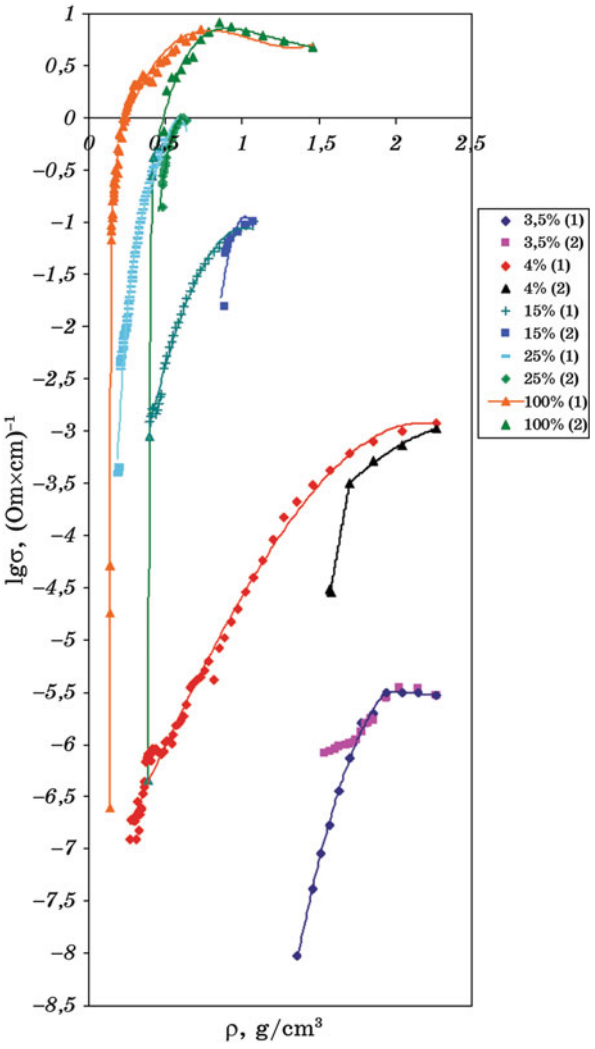

Fig. 42.1 Dependence of the logarithm of the electrical conductivity of the composite PTFE–CNT with density of the sample at various concentrations of CNTs

However, after density of 1.7 g/cm^3, the conductivity curve deviates from the curve of the stroke that moves down, and then at 1.6 g/cm^3 falls sharply. The latter is due to the reach of ultimate relaxation of pre-compressed powder material and the appearance of the gap in the electrical circuit between the electrodes of conductive cluster.

Thus, the long length of the nanotube and its small diameter lead to the fact that even with addition of 4–5 wt% CNTs into the matrix of PTFE, the CNTs are forming a single conductive network that changeover the composite from the dielectric state to the conducting state (percolation). Changing of nanotube concentration from 2 to 25 wt% causes the increase of the electrical conductivity of the composite by ten orders of magnitude (Figs. 42.2 and 42.3).

It was also shown that at low concentrations of CNT Seebeck coefficient is strongly dependent on the degree of compression of the nanocomposite under the piston: it ranges from 37 to 47 mV/K. The value of the Seebeck coefficient for PTFE 25 % of CNTs is in the range from 37.5 to 45.3 mV/K; for PTFE 5 % CNT, from 42.3 to 43.5 mV/K; and PTFE for 3 % CNT, from 43.8 to 46.8 mV/K.

For samples of the nanocomposite PTFE–CNT with a lower concentration of carbon nanotubes, a value of the Seebeck coefficient is higher, and their quality factor is higher (Figs. 42.4 and 42.5).

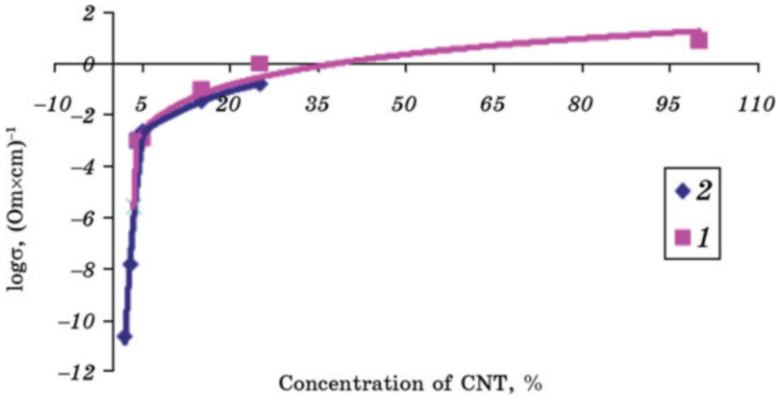

Fig. 42.2 Dependence of the logarithm of the electrical conductivity of the composite PTFE–CNT with concentration of CNTs for conductivity of powder samples (*1*) and compacted samples (*2*)

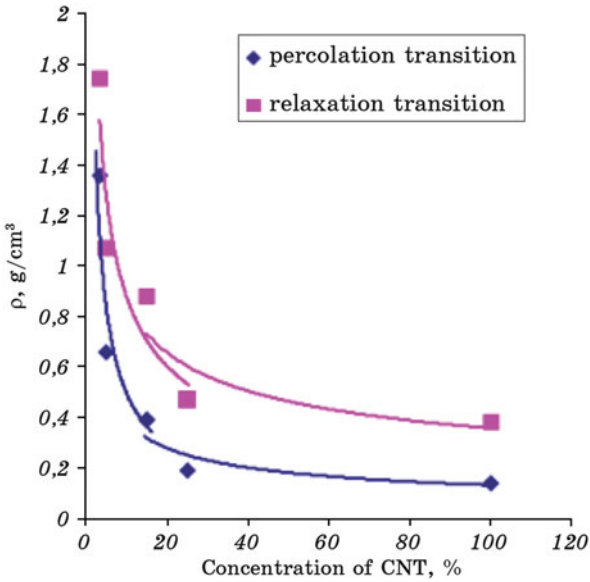

Fig. 42.3 The concentration dependence of percolation transition and relaxation transition with density of the composite PTFE–CNT

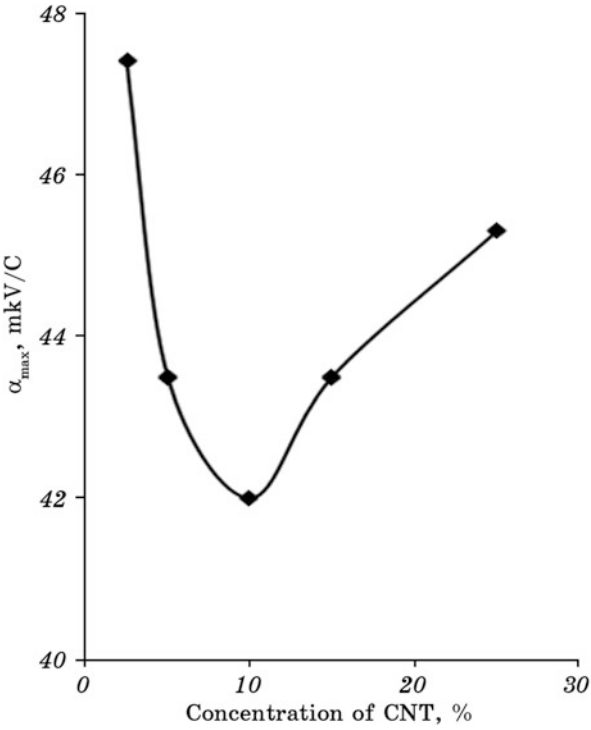

Fig. 42.4 The dependence of the maximums of Seebeck coefficient with the concentration of CNTs in PTFE

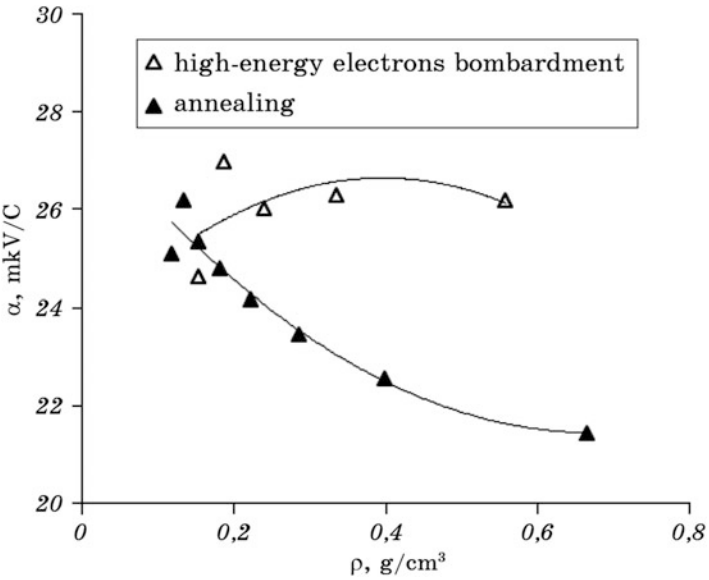

Fig. 42.5 Effect of annealing and high-energy electrons bombardment on conductivity and Seebeck coefficient (density dependence)

Chapter 43
Iron Oxides and Their Silica Nanocomposites as Biocompatible Systems for Biomedical Applications

Karolina Gdula, Ewa Skwarek, and Andrzej Dąbrowski

43.1 Iron Compounds

Iron is one of very common elements. It constitutes about 41 % of the earth mass and its content in the continental part of the earth crust is estimated to be 4.65 %. It occurs in some basalts in the native form. In other minerals iron occurs in the second or third degree of oxidation, depending on the environment. Its oxides and hydroxides are of great economic importance [1]. Iron creates many different organic and inorganic compounds, among which the most popular are those with magnetic properties.

Magnetic nanoparticles used in therapy and medical diagnosis should meet some requirements: (1) at room temperature they should be superparamagnetic, so that their magnetic moments with a lack of field are equal to zero; (2) in the outer magnetic field, their magnetic moments should be as large as possible, because then the applied fields can be small; (3) should not form agglomerates (i.e., strongly interact); and (4) must be biocompatible, not toxic, and well tolerated by living organisms. Therefore, the Fe_2O_3 nanoparticles are most frequently applied in two sizes. Small, about 10 nm nanoparticles have the advantage of easy and quick diffusion through cell membranes and possibility of obtaining their homogeneous distribution in the chosen tissue. However, their disadvantage is the very small resultant magnetic moment which makes it necessary to apply strong magnetic

K. Gdula (✉) • A. Dąbrowski
Department of Theoretical Chemistry, Maria Curie-Sklodowska University,
Maria Curie-Sklodowska Sq. 3, Lublin 20-031, Poland
e-mail: karolina.gdula@poczta.umcs.lublin.pl; carolina.gdula@gmail.com

E. Skwarek
Department of Radiochemistry and Colloid Chemistry, Maria Curie-Sklodowska University,
Maria Curie-Sklodowska Sq. 3, Lublin 20-031, Poland

O. Fesenko, L. Yatsenko (eds.), *Nanophysics, Nanophotonics, Surface Studies, and Applications*, Springer Proceedings in Physics 183,
DOI 10.1007/978-3-319-30737-4_43

fields. Large nanoparticles (even up to 100 nm) need much weaker fields, but cannot easily penetrate into the tissues, and often remaining in the circulation system, they can cause blood clots [2].

Iron oxide nanostructures are used in local therapy for drugs transport to the specific sites in the organism in treatment of tumors and immunomagnetic separation. Besides the therapy of nanostructures, they are used in medical diagnosis, e.g., as contrast agents in nuclear magnetic resonance. The essence of the local magnetic therapy is based on the fact that molecules of a drug are added to a specific site of human organism by application of the magnetic field gradient or through the blood vascular system or in the form of magnetic liquid injected directly into chosen areas. Particles are retained in the diseased tissues by means of the magnetic field till the end of the therapy (it means that all drug molecules are released into desired tissue and after all removed from the organism by changing the field gradient).

Immunomagnetic separation consists of binding harmful biomolecules (present in organism, e.g., as a result of poisoning), by other organic molecules which are bound with magnetic nanoparticles. The particles surrounded by organic ligands are introduced into the area, where the toxic molecules are, by using the external magnetic field. Such harmful substances are bound by ligands with magnetic particles, and then the as-formed bimetallic complexes are removed by applying a suitable magnetic field gradient.

Magnetic hyperthermia uses great sensitivity of tumorous cells to increase the temperature, much higher than that of healthy cells. This method consists of introducing magnetic particles into a tumor (through the blood vascular system and magnetic directing or simply one or multi-needle injection) then applying a variable magnetic field of such amplitude and frequency, to cause heating of molecules. The rise of temperature depends on properties of molecules, amplitude, and frequency of magnetic field [2].

Nuclear magnetic resonance is used in medical diagnosis for displaying tissues (MRI), whereby contrast magnification can be obtained by introducing magnetic admixtures. Intensity of MRI signal depends on kind and density of tissue, number of protons in a given area, as well as on time of their magnetic relaxation. Introducing magnetic admixtures, e.g., superparamagnetic particles to the examined tissue, increases relaxation rate of protons in these areas which, in turn, leads to better contrast between individual areas and gives possibility of distinguishing a pathological area from a healthy one [2].

43.1.1 Preparation of γ-Fe_2O_3

Polymorphic character of Fe_2O_3 has been known for many years. Its alpha and gamma forms are called hematite and maghemite, respectively. Both of them are very common compounds and occur as the natural minerals. Lately, the other forms like beta, epsilon, and all of them in nanometer size have been successfully

synthesized. Due to their properties, nanoparticles of iron oxides (especially maghemite) are widely used in medicine.

The most common method of γ-Fe_2O_3 preparation is thermal dehydration of lepidocrocite (γ-FeO(OH) and cautious oxidation of magnetite (Fe_3O_4). There were also successful other syntheses: thermal decomposition of iron(II) malate goethite (FeO(OH) or ferrihydrite ($Fe_5HO_8 \cdot 4H_2O$) heating in air at 450 °C in the presence of an organic substance, e.g., sucrose or thermal vacuum decomposition of $FeOOCH_3$ at 290 °C [3].

The superparamagnetic nanoparticles γ-Fe_2O_3 are most frequently synthesized during thermal transformation of iron(III) oxalate. Another method which can be used is heating of ferrate-carboxyl complexes. Thermolysis of organometallic precursors, e.g., iron pentacarbonyl in the presence of stabilizing polymer, gives 10–20 nm nanoparticles. It consists of precipitation of iron nanoparticles in a nonpolar liquid and their oxidation to iron oxide nanoparticles. In this case temperature plays a significant role.

Besides the above methods from the solid state, there are also those in solutions, e.g., slow oxidation of the Fe^{2+}/Fe^{3+} mixture in the inert environment, oxidation of the Fe^{2+} salt in the air, hexamethylenetetramine or sodium iodide or sodium nitrate, oxidation of iron salt in the air, in the presence of pyridine or sodium thiosulfate, as well as electrolysis of iron(III) nitrate [3].

The hydrothermal methods are also applied. In such kind of approaches, mixture of iron oxides and hydroxides with the addition of suitable metal is subjected to the reaction in water under critical conditions (like temperature above 200 °C and pressure higher than 14 MPa). Size and morphology of the product are controlled by temperature and time of the reaction. Two main processes lead to formation of nanoparticles under such conditions. These are (1) hydrolysis and oxidation of Fe (II) and (2) neutralization of hydroxide mixture. This method is considered to be low effective in terms of the possibility of obtaining specific properties of the product and also required using very complicated equipment [4, 5].

Horak et al. [4] report that one of the most common methods is coprecipitation of nanoparticles with a base. The ammonia solution is added to the aqueous solution of two and three valences of iron salts. The ratio of iron(II) and (III) salts is usually 2:1 (depending on oxide which is intended to obtain, the appropriate salt is used in excess). This process depends largely on the type and concentration of salts (chlorides are the most common) and bases. Moreover, the addition of chelating substances, reaction temperature, and rate of base addition affect the final product significantly. The pH increase in the range 8.5–10 is the most desirable. On the one hand, the slow addition of the base can lead to precipitation of nonmagnetic hydroxides. On the other hand, too rapid increase of pH may lead to precipitation of magnetite (Fe_3O_4). Also strong base (such as NaOH, KOH, and LiOH) can precipitate nonmagnetic products. However, it does not make much difference whether the base is added to the solution of iron salt or vice versa. Temperature also effects on precipitation and "growth" of sediment. In order to obtain nanoparticles of the size up to 10 nm, the temperature should be in the range 25–80 °C. The precipitate is set a left for some time, in order to obtain a suitable

size of nanoparticles. Then, the sediment is washed by repeated cycles of decantation on the magnet and redispersion in distilled water, leading to colloid formation. In most cases, nanoparticle colloids based on aqueous solutions are prepared without the addition of surfactants. The colloid stabilization is achieved by electric charge on nanoparticles, e.g., comes from perchlorate ions, citrate, nitrate, or tetramethylammonium providing an alkaline or acidic medium. Dispersion is stable, thanks to mutual repulsion of molecules possessing the same charge. However, it should be mentioned that such stabilization of colloid is limited only to solutions of very high or low pH values. Colloidal nanoparticles form aggregates of the sizes 5–100 nm, depending on the charge onto their surfaces.

The nanoparticles in the sediment can be stabilized in water or nonpolar liquid by the addition of surfactant, e.g., higher fatty acids or saccharides. Application of various surfactants leads to formation of various nano-γ-Fe_2O_3 of different sizes and magnetic properties. Iron nanoliquids can be stabilized by the addition of various polymers, such as polysaccharides (dextran), polyacrylamide, and others. Stabilizers are added during precipitation of sediment, as well as to the already precipitated sediment. However, the presence of polymer during sediment formation stimulates precipitation and nucleation and provides better stability of colloidal nanoparticles. Polymers improve biocompatibility of nanoparticles.

γ-Fe_2O_3 is a thermally unstable oxide. At higher temperatures this oxide transforms into hematite (α-Fe_2O_3). Temperature of transformation depends on crystal sizes, e.g., for well-formed crystals, the transformation temperature is about 400 °C. In the case of nano-γ-Fe_2O_3, temperature of such transformation is always higher and the transformation itself proceeds with appearance of the transition product ε-Fe_2O_3. According to Tronc et al., this reaction is connected with the degree of nanoparticle aggregation [6].

Magnetic character of the γ-Fe_2O_3 particles leads to the evaluation of new methods of synthesis from molecule aggregates of different morphology. Spherical and ellipsoidal γ-Fe_2O_3 molecules in nanometric sizes can be obtained from the reduction-oxidation reaction of α-Fe_2O_3 molecules, previously obtained by homogeneous hydrolysis. However, the spherical γ-Fe_2O_3 molecules can be obtained by pyrolysis of iron salts dissolved in aerosol [7].

43.1.2 Preparation of Fe_3O_4

Magnetite is a mixture of two oxides ($Fe_2O_3 \cdot FeO$). In this oxide, iron exists in II and III degree of oxidation. Due to the presence of iron at II degree of oxidation, it can easily undergo oxidation. Thus, this iron oxide is less stable, when compared with maghemite.

Up to now, there are several techniques allowing to obtain magnetite particles. These are (1) coprecipitation of iron salts [8, 9], (2) microemulsion approach [10], (3) hydrothermal synthesis [11], (4) sol–gel synthesis [12], (5) electrochemical [13] or (6) sonochemical deposition [14], (7) thermal decomposition [15], and many

others. Among them, coprecipitation of iron salts, microemulsion, and thermal decomposition are definitely the most popular techniques.

Coprecipitation technique can be carried out by two different ways: (1) partial oxidation of ferrous hydroxide suspension, by using oxidation agent, such as nitrate [9], or (2) addition of base to an aqueous solution of iron(II) and (III) mixture salts under oxygen-free environment, with the molar ratio between ferric (Fe^{3+}) and ferrous (Fe^{2+}) ions 2:1 [8]. Sugimoto and Matijevic [9] obtained particles which were characterized by wide size distribution (30–200 nm), while the method proposed by Massart [8] allowed to obtain particles with small sizes (up to 20 nm). Those results clearly show that the size of final particles, synthesized by coprecipitation method, strongly depends on the pH and ionic strength of the precipitating solution. Moreover, those parameters also influence on the electrostatic potential on the surface of these particles, which affects on their stability.

Smaller and more uniform nanoparticles can be obtained by microemulsion technique. In this method iron ferrous and ferric chlorides are precipitated to form an iron oxide in aqueous core, formed by micelles created by the addition of surfactant [10]. Due to controlled growth of micelles, the desired size range of magnetic nanoparticles can be also obtained.

Such advantages also provide another technique—thermal decomposition. Sun and Zeng [15] described the synthesis of highly monodisperse magnetite nanoparticles (in the range of diameter 3–20 nm) by using thermal degradation of iron(III) acetylacetonate in phenyl ether in the presence of alcohol, oleic acid, and oleylamine at 265 °C. They also proved that as-prepared magnetite nanoparticles can be easily transferred into maghemite (γ-Fe_2O_3) or hematite (α-Fe_2O_3) [75].

Besides the above-mentioned synthetic routes for the preparation of Fe_3O_4 particles, several examples of naturally produced magnetite particles by living organisms can be found. In 1962 Lowenstam [16] first discovered precipitation of magnetite on the "tongue" of sea molluscs. Those animals use it for hardening their teeth, which is very helpful in extracting food from rocks. In 1975 Blakemore [17] discovered bacteria possessing magnetic properties, i.e., being able to synthesize fine (50–100 nm) magnetic molecules, most frequently Fe_3O_4 or Fe_3S_4 which cover intramolecular membrane of vacuoles, forming structures called magnetosomes. Behavior of many organisms is also affected by the earth magnetic field which interacts with magnetic nanoparticles in the organism of, e.g., bees, pigeons, and salmons which are used for orientation in different sites, self-recovery, as well as searching for food. Table 43.1 presents the exemplary organisms synthesizing magnetic nanoparticles.

43.2 Silica Materials with Magnetic Properties

In order to improve properties of those two iron oxides, there is a need to modify their surface. This can be made by using broad range of outer shells, covering those magnetic nanoparticles (MNPs) by using, for example, silica [18–20], polymers

Table 43.1 The exemplary organisms synthesizing magnetic nanoparticles

Type of organism	Main name	Localization of magnetic nanoparticles	Type of nanoparticles
Microorganisms	Magnetically active bacteria	Magnetosome	Fe_3O_4
Protozoa	Algae	Magnetosome cells	Fe_3S_4
			Fe_3O_4
Insects	Bees	Abdomen	Fe_3O_4
	Magnetic ants	Abdomen	Fe_3O_4
Fishes	Salmon	Skull	Fe_3O_4
	Rainbow trout	Sense apparatus	Fe_3O_4
Birds	Domestic pigeon	Beak	Fe_3O_4
Mammals	Dolphin	Brain, heart	Fe_3O_4
	Man		Fe_3O_4

[21–24], carbon [25], and so on. Therefore, the magnetic nanoparticles are usually used in the form of biocompatible magnetic carriers. Two kinds of structures for magnetic carriers are widely used: (1) core/shell structures which consist of magnetic core covered by outer shell [26], such as silica, oleic acid, polystyrene, etc., and (2) composite materials, in which magnetic nanoparticles are dispersed into other matrixes [27, 28], e.g., mesoporous silica, carbon, and polyethylene glycol. The surface modification of magnetic nanoparticles is crucial not only for improving their biocompatibility and biodegradability but also for controlling their physicochemical properties and colloidal stability, which are very important in their further applications. What is more, covering those nanoparticles by outer layers provides them with a steric barrier against agglomeration and prevents aggregation. Such treatments allow to obtain compatible materials, especially when they are used in biomedical fields. Furthermore, incorporation of magnetic nanoparticles into the many various matrixes, based on silica or carbon, can lead to obtain new generation of materials with very interesting properties.

In the following part, magnetic structures based on both magnetite and maghemite covered by silica will be described, as well as their most popular applications in many fields of science, medicine, and industry. It is due to good properties of silica, such as biocompatibility, biodegradability, chemical and physical inertness, high thermal resistance, and good stability in a broad pH range.

43.2.1 Silica Materials with Magnetic Properties: Applications

In fact, silica materials in nanometer scale have gained much attention over the last two decades, for their application in adsorption, catalysis, separation, and (bio) sensors. It is due to the very interesting properties of silica nanomaterials.

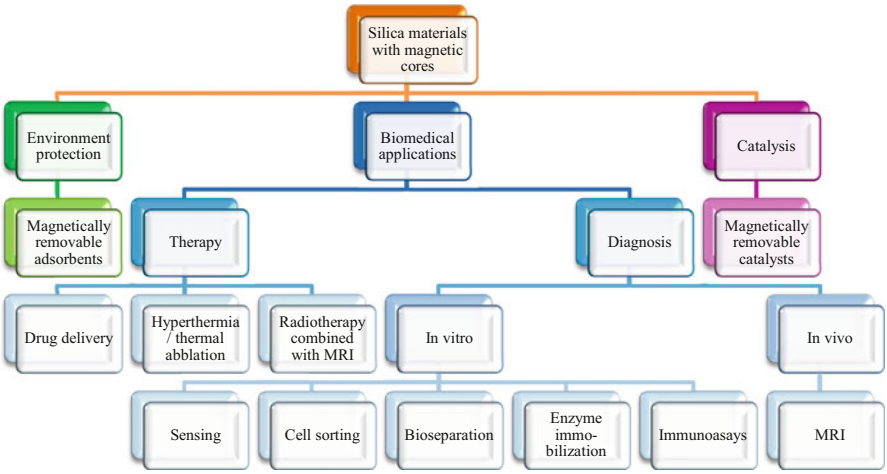

Fig. 43.1 The most popular applications of silica nanomaterials with magnetic cores

Especially, silica materials with magnetic properties have been in a great interest among many research groups and have found applications in various fields of science and industry. In Fig. 43.1, the most popular applications of magnetic nanoparticles with silica coatings are presented.

Such huge commercial applications of silica nanomaterials with magnetic cores are due to the fact that in the one hand, pure magnetic nanoparticles (MNPs) have been found to possess numerous interesting physical and chemical properties—especially, it has been proven that the magnetic anisotropy of magnetic nanoparticles can be much greater than those of their bulk counterparts, whereas differences in the Neel or Curie temperatures can reach hundreds of Celsius degrees [29]. On the other hand, the use of outer silica layer allows to obtain better biologically compatible [30] and more stable materials. It is due to the fact that isoelectric point of silica is reached at pH = 2–3 [31], which means that silica-coated MNPs are negatively charged at the pH of blood. In consequently, it causes electrostatic repulsion which helps to avoid the formation of aggregates. What is more, the interest in using silica materials with magnetic properties in many fields of medicine, science, and industry is increasing, because of many other reasons:

1. Amorphous silica is a nontoxic material [32].
2. The outer silica layer tunes of the potential interaction between magnetic particles prevent their aggregation.
3. Magnetic nanoparticles can be effectively entrapped inside silica particles; thus such encapsulation provides a protective layer around magnetic nanoparticles, reducing oxygen molecule penetration, both in the air and aqueous media.
4. Silica is resistant to swelling; therefore the size of silica particles remains unchanged in a wide range of solvents.

5. Many facile synthesis routes are available to cover magnetic nanoparticles by silica layer, e.g., the Fe_3O_4 or γ-Fe_2O_3 particles can be encapsulated in a sol–gel method [33, 34, 76] or modified Stober synthesis [35, 36, 77].
6. Silica surface can be easily modified by broad range of functional groups (such as amine, thiol, etc.), which is mainly related to the presence of hydroxyl surface groups, which provide intrinsic hydrophilicity and allow surface attachment by covalent binding of many biomolecules.
7. Silica is relatively inexpensive. Such property combination of both magnetic nanoparticles and silica expands using such hybrid systems.

Herein, a short review devoted to silica nanomaterials with magnetic properties will be presented, with the special emphasis to the Fe_3O_4 and γ-Fe_2O_3 as magnetic cores and their use in biomedical fields, such as hyperthermia, magnetic resonance imaging, and targeted drug delivery systems (TDDS).

Hyperthermia and MRI

The above-mentioned magnetic properties of such materials are particularly used in hyperthermia treatment and magnetic resonance imaging (MRI). There are several magnetic nanomaterials that have been widely used in hyperthermia treatment, in which the most popular are, described in the first chapter, iron oxides: Fe_3O_4 (magnetite) and γ-Fe_2O_3 (maghemite).

Hyperthermia technique is a promising tool for cancer treatment, because it allows to easily get to the diseased tissues and, when compared with chemo- or radiotherapy, has almost no side effects [37]. Magnetic hyperthermia provides to increase the temperature of tumor area to a degree, where tumor cells are destroyed. In general, obtaining 42 °C is enough to kill majority of diseased cells [38–40]. In such treatment magnetic nanoparticles have the additional advantage that extravasation of particles and their accumulation in tumor area is favored by passive mechanism of enhanced permeability and retention (EPR) [41, 42]. The first use of pure magnetic nanoparticles in hyperthermia treatment dates back to 1957, when Gilchrist et al. [43] heated various samples of tissue with particles of γ-Fe_2O_3 (in the size of diameter 20–100 nm) exposed to a 1.2 MHz magnetic field. Since that time, numerous papers describing various types of magnetic nanoparticles and materials with magnetic nanoparticles inside them, different field strengths and frequencies, and various methods of encapsulation and delivery of those particles have been published. Many efforts have been taken in the last 20 years to improve hyperthermia technique in medical treatment. Nowadays, only local hyperthermia is taking into account as a practical tool against tumor cells. For this purpose, two main approaches are used: (1) magnetic nanoparticles covered by outer layers are injected directly inside tumor or (2) specific antibodies, which are attached to magnetic materials, are recognized and captured by tumor cells, in the presence of external magnetic field. The development of nanotechnology allows to obtain better and better materials for this

purpose. From the practical point of view, magnetic nanoparticles used in such treatment should be covered by materials that satisfy the following requirements [44–46]: (1) avoid agglomeration of MNPs in biological media; (2) ensure the desired surface charge for the MNPs; (3) preserve the functionalities of those materials; (4) prevent the opsonization of MNPs, which can lead to the fast removal of those particles from the blood stream by reticuloendothelial system (RES); and (5) ensure the biocompatibility of MNPs.

The era of medical diagnosis begun in 1895, when Wilhelm Roentgen captured the first X-ray image of his wife's hand. In 1901 he won Nobel Prize for that discovery [47]. Since that date, many developments in this area have been achieved. One of the most popular noninvasive optical imaging methods is magnetic resonance imaging (MRI) [48]. Magnetic nanoparticles have been used as contrast agents in MRI for almost 50 years [22]. MRI does not cause harmful side effects and is a very promising tool for cellular and molecular imaging studies. This noninvasive imaging technique [49, 50] is based on the principle of nuclear magnetic resonance (NMR) [51, 52] and magnetic properties of various materials. The signal in MRI is based on precession of water nuclei of hydrogen within an applied external magnetic field. Due to the application of radiofrequency pulses, the relaxation process (through which the nuclei can return to original aligned state) can generate an image [53]. In order to enhance the difference between healthy and infected tissues, contrast agents are used to shorten the relaxation times (T_1 and T_2) of water. Therefore, the use of magnetically active substances as contrast agents, such as Fe_3O_4 or γ-Fe_2O_3 nanoparticles, can improve sensitivity and resolution of MRI [54–57]. Iron oxide nanoparticles influence two parameters in MRI: (1) T_2 (transverse relaxation time) which describes the energy transfer between adjacent protons and (2) T_2^* almost the same as T_2, but also includes heterogeneities in the environment [58]. Ferromagnetic or superparamagnetic iron oxide nanoparticles reduce value of the relaxation times T_2^* and T_2 by a local disturbance of the uniformity of the magnetic field. Magnetic nanoparticles attached specifically to neoplastic cells allow changing of those parameters in the area of disc tissue and in consequence produce darker images if accumulated in a certain area, allowing better diagnostic specification [59, 60]. Despite the fact that many pharmaceuticals of magnetic colloids or nanomaterials for MRI are available, e.g., superparamagnetic nanoparticles which have been approved by the Food and Drug Administration (FDA) as completely safe for human contrast agents [61], the technology of their use in MRI is still at the initial stage. There are still numerous, so far, unresolved issues, e.g., agglomeration of nanoparticles, difficulty in their targeted and selective orientation onto disc cells, or low efficiency of introduction inside cells those magnetic nanoparticles adsorbed onto their surfaces.

The presence of outer layers provides a reduced rate of magnetic nanoparticle removal from the blood. What is more, the biocompatible shell reduces the absorption of magnetic cores, which minimizes the possible adverse effects on the body.

And finally, using inorganic shells allows the homogeneous distribution of nanoparticles in biological medium, preventing them from agglomeration.

Targeted Drug Delivery Systems

The beginning of the use of magnetic nano- and microparticles as delivery chemotherapeutic agents can be dated back to the 1970s. In 1976 Zimmermann and Pilwat [62] used magnetic erythrocytes for the delivery of cytotoxic drugs. Over the next several years, many investigations had been made in this field [63–65]. However, all these initial applications included the use of particles in micrometer size. For the first time, magnetic nanoparticles were used in 1996 by Lubbe et al. [66] in animal models. Since that time, magnetic nanoparticles have been widely studied as delivery systems of therapeutic agents, using an external magnetic field which allows to drive and locate such systems at the desired organ and tissues [67, 68]. MNPs, used as TDDS, must exhibit specific properties, mainly such as [69] (1) monodispersity, (2) stability, (3) superparamagnetism, and (4) biocompatibility. Monodispersity means that nanoparticles have the same size and shape. Such characteristic possesses the above-mentioned magnetite [70, 71] and maghemite [72] nanoparticles. The stability of MNPs can be achieved by covering those nanoparticles by outer shells, preventing their aggregation. The presence of biocompatible layer covered the magnetic core, ensures permanently biocompatibility of MNPs and may serve as a support for drugs and biomolecules [73]. The third characteristic is superparamagnetism, which describes the behavior of magnetic nanoparticles in the presence and absence of an external magnetic field. Having superparamagnetic properties means that nanoparticles possess them, even after removing the external magnetic field [74]. In TDDS superparamagnetism can be helpful in avoiding the agglomeration, which can induce embolism in blood capillary vessels. As it was mentioned before, this can be also provided by covering such nanoparticles by silica layers.

43.3 Conclusions

The chapter has been devoted to nanomaterials, with the special emphasis to γ-Fe_2O_3 and Fe_3O_4 in nanometer scale, as well as their nanocomposites with silica. The synthesis routes, properties, and the most popular applications in the medical fields were discussed.

Although the described topic is very interesting, but quite new, up to now, it has been well specified in the scientific literature. However, a lot of researches still need to be done, to fulfill a big gap in the area of modern nanotechnology, finding applications in many fields of science and industry. Nanotechnology employing nanomaterials with magnetic core is a very broad field of science, and many of its interesting aspects were omitted in this chapter. It was due to the fact that they were not directly connected with the discussed topic.

This chapter can be treated as a source of collected documents, devoted to the development of modern nanotechnology, and can be useful for people interested in this area, in particular nanomaterials with magnetic core, and their applications in medical fields.

References

1. Bolewski A (1979) Żelazo – Fe. Wyd. Geologiczne, Warszawa, p 9
2. Ślawska-Waniewska A (2004) Wybrane zagadnienia współczesnego biomagnetyzmu. Postęp fizyki 55(4):157–161
3. Zboril R, Mashlan M, Petridis D (2002) Iron(III) oxides from thermal processes synthesis, structural and magnetic properties, Mössbauer spectroscopy characterization, and applications. Chem Mater 14(3):969–982
4. Horak D, Babic M, Mackova H et al (2007) Preparation and properties of magnetic nano- and microsized particles for biological and environmental separations. J Sep Sci 30(11):1751–1772
5. Matijevic E (1986) Science of ceramic chemical processing. In: Hench LL, Ulrich DR (eds). Wiley, New York, p 463–481
6. Tronc E, Chaneac C, Jolivet JP (1998) Structural and magnetic characterization of ε-Fe2O3. J Solid State Chem 139(1):93–104
7. Morales MP, Veintemillas-Verdaguer S, Montero MI et al (1999) Surface and internal spin canting in γ-Fe2O3 nanoparticles. Chem Mater 11(11):3058–3064
8. Massart R (1981) Preparation of aqueous magnetic liquids in alkaline and acidic media. IEEE Trans Magn 17(2):1247–1248
9. Sugimoto T, Matijevic E (1980) Formation of uniform spherical magnetite particles by crystallization from ferrous hydroxide gels. J Colloid Interface Sci 74(1):227–243
10. Liz L, Lopez-Quintela MA, Mira J et al (1994) Preparation of colloidal Fe3O4 ultrafine particles in microemulsions. J Mater Sci 29:3797–3801
11. Tartaj P, Morales MP, Veintemillas-Verdaguer S et al (2006) Synthesis, properties and biomedical applications of magnetic nanoparticles. In: Buschow KHJ (ed) Handbook of magnetic materials. Elsevier, p 403–482 (in press)
12. Xu J, Yang H, Fu W et al (2007) Preparation and magnetic properties of magnetite nanoparticles by sol-gel method. J Magn Magn Mater 309(2):307–311
13. Pascal C, Pascal JL, Favier F et al (1999) Electrochemical synthesis for the control of I-Fe2O3 nanoparticle size. Morphology, microstructure, and magnetic behavior. Chem Mater 11 (1):141–147
14. Abu Mukh-Qasem R, Gedanken A (2005) Sonochemical synthesis of stable hydrosol of Fe3O4 nanoparticles. J Colloid Interface Sci 284(2):489–494
15. Sun S, Zeng H (2002) Size-controlled synthesis of magnetite nanoparticles. J Am Chem Soc 124(28):8204–8205
16. Lowenstam HA (1962) Magnetite in denticle capping in recent chitons (Polyplacophora). Geol Soc Am Bull 73(4):435–438
17. Blakemore R (1975) Magnetotactic bacteria. Science 190(4212):377–379
18. Guerrero-Martinez A, Perez-Juste J, Liz-Marzan LM (2010) Recent progress on silica coating of nanoparticles and related nanomaterials. Adv Mater 22:1182–1195
19. Kumar CSSR (ed) (2009) Magnetic nanomaterials. Nanomaterials for the life sciences, vol 4. Wiley-VCH, Weinheim
20. Yi DK, Selvan ST, Lee SS et al (2005) Silica-coated nanocomposites of magnetic nanoparticles and quantum dots. J Am Chem Soc 127:4990–4991
21. Guo J, Yang W, Deng Y et al (2005) Organic-dye-coupled magnetic nanoparticles encaged inside thermoresponsive PNIPAM microcapsules. Small 7:737–743

22. Gupta AK, Gupta M (2005) Synthesis and surface engineering of iron oxide nanoparticles for biomedical applications. Biomaterials 26:3995–4021
23. Laurent S, Forge D, Port M et al (2008) Magnetic iron oxide nanoparticles: synthesis, stabilization, vectorization, physicochemical characterizations, and biological applications. Chem Rev 108(6):2064–2110
24. Rudzka K, Delgado AV, Viota JL (2012) Maghemite functionalization for antitumor drug vehiculization. Mol Pharm 9:2017–2028
25. Lu AH, Salabas EL, Schuth F (2007) Magnetic nanoparticles: synthesis, protection, functionalization, and application. Angew Chem Int Ed 46:1222–1244
26. Sieben S, Bergemann C, Lubbe A et al (2001) Comparison of different particles and methods for magnetic isolation of circulating tumor cells. J Magn Magn Mater 225:175–179
27. Alam S, Anand C, Logudurai R (2009) Comparative study on the magnetic properties of iron oxide nanoparticles loaded on mesoporous silica and carbon materials with different structure. Microporous Mesoporous Mat 121(1–3):178–184
28. Bourlinos AB, Simopoulos A, Boukos N et al (2002) Magnetic modification of the external surfaces in the MCM-41 porous silica: synthesis, characterization, and functionalization. J Phys Chem B 105:7432–7437
29. Gubin SP, Koksharov YA, Khomutov GB et al (2005) Magnetic nanoparticles: preparation, structure and properties. Russ Chem Rev 74(6):489–520
30. Rosi NL, Mirkin CA (2005) Nanostructures in biodiagnostics. Chem Rev 105(4):1547–1562
31. Iler RK (1979) The chemistry of silica. Wiley, New York
32. Smith PW (2002) Fluorescence emission-based detection and diagnosis of malignancy. J Cell Biochem Suppl 39:54–59
33. Melnik IV, Zub YL, Alonso B et al (2012) Creation of a functional polysiloxane layer on the surface of magnetic nanoparticles using the sol-gel method. Glas Phys Chem 38:96–104
34. Melnyk IV, Zub YL (2012) Preparation and characterization of magnetic nanoparticles with bifunctional surface layer ≡ Si(CH2)3NH2/≡SiCH3 (or ≡ SiC3H7-n). Microporous Mesoporous Mat 154:196–199
35. Rudzka K, Viota JV, Muñoz-Gamez JA (2013) Nanoengineering of doxorubicin delivery systems with functionalized maghemite nanoparticles. Colloids Surf B Biointerfaces 111:88–96
36. Salgueirino-Maceira V, Correa-Duarte MA, Farle M et al (2006) Bifunctional gold-coated magnetic silica spheres. Chem Mater 18(11):2701–2706
37. Maier-Hauff K, Ulrich F, Nestler D et al (2011) Efficacy and safety of intratumoral thermotherapy using magnetic iron-oxide nanoparticles combined with external beam radiotherapy on patients with recurrent glioblastoma multiforme. J Neurooncol 103(2):317–324
38. Dewey WC, Hopwood LE, Sapareto SA et al (1977) Cellular responses to combinations of hyperthermia and radiation. Radiology 123:463–474
39. Hernandez JF, Secrest JA, Hill L et al (2009) Scientific advances in the genetic understanding and diagnosis of malignant hyperthermia. J Perianesth Nurs 24:19–34
40. Hildebrandt B, Wurst P, Ahlers O et al (2002) The cellular and molecular basis of hyperthermia. Crit Rev Oncol Hematol 43:33–56
41. Maeda H (2001) The enhanced permeability and retention (EPR) effect in tumor vasculature: the key role of tumor-selective macromolecular drug targeting. Adv Enzyme Regul 41:189–207
42. Maeda H, Wu J, Sawa T et al (2000) Tumor vascular permeability and the EPR effect in macromolecular therapeutics: a review. J Control Release 65:271–284
43. Gilchrist RK, Shorey WD, Hanselman RC et al (1957) Selective inductive heating of lymph. Ann Surg 146:596–606
44. Laurent S, Dutz S, Hafeli UO et al (2011) Magnetic fluid hyperthermia: focus on superparamagnetic iron oxide nanoparticles. Adv Colloid Interface Sci 166:8–23

45. Mahmoudi M, Milani AS, Stroeve P (2010) Surface architecture of superparamagnetic iron oxide nanoparticles for application in drug delivery and their biological response: a review. Int J Biomed Nanosci Nanotechnol 1(2/3/4):164–201
46. Mahmoudi M, Sant S, Wang B et al (2011) Superparamagnetic iron oxide nanoparticles (SPIONs): development, surface modification and applications in chemotherapy. Adv Drug Deliv Rev 63(1–2):24–46
47. The Official Web Site of the Nobel Prize (2015) http://www.nobelprize.org/nobel_prizes/physics/laureates/1901/. Accessed 10 Dec 2015
48. FDA U.S. Food and Drug Administration (2015) http://www.fda.gov/Radiation-EmittingProducts/RadiationEmittingProductsandProcedures/MedicalImaging/ucm200086.htm. Accessed 14 Dec 2015
49. Lauterbur PC (1973) Image formation by induced local interactions: examples employing nuclear magnetic resonance. Nature 242:190–191
50. Mansfield P (1977) Multi-planar image formation using NMR spin echoes. J Phys C Solid State Phys 10:L55–L58
51. Bloch F, Hansen WW, Packard M (1946) Nuclear induction. Phys Rev 69:127
52. Purcell EM, Torrey HC, Pound RV (1946) Resonance absorption by nuclear magnetic moments in a solid. Phys Rev 69:37–38
53. Richard C, Qle MC, Scherman D (2008) Nanoparticles for imaging and tumor gene delivery. Tumori 94:264–270
54. Choi H, Choi SR, Zhou R et al (2004) Iron oxide nanoparticles as magnetic resonance contrast agent for tumor imaging via folate receptor-targeted delivery. Acad Radiol 11(9):996–1004
55. Sun C, Lee JSH, Zhang M (2008) Magnetic nanoparticles in MR imaging and drug delivery. Adv Drug Deliv Rev 60:1252–1265
56. Wang YX, Hussain SM, Krestin GP (2001) Superparamagnetic iron oxide contrast agents: physicochemical characteristics and applications in MR imaging. Eur Radiol 11:2319–2331
57. Waters EA, Wickline SA (2008) Contrast agents for MRI. Basic Res Cardiol 103:114–121
58. Sharma P, Brown S, Walter G et al (2006) Nanoparticles for bioimaging. Adv Colloid Interface Sci 123–126:471–485
59. Klug G, Kampf T, Bloemer S et al (2010) Intracellular and extracellular T1 and T2 relaxivities of magneto-optical nanoparticles at experimental high fields. Magn Reson Med 64:1607–1615
60. Toboada E, Rodríguez E, Roig A et al (2007) Relaxometric and magnetic characterization of ultrasmall iron oxide nanoparticles with high magnetization. Evaluation as potential T1 magnetic resonance imaging contrast agents for molecular imaging. Langmuir 23:4583–4588
61. Lattuada M, Hatton TA (2007) Functionalization of monodisperse magnetic nanoparticles. Langmuir 23(4):2158–2168
62. Zimmermann U, Pilwat G (1976) Organ specific application of drugs by means of cellular capsule systems. J Biosci 31:732
63. Hafeli UO, Sweeney SM, Beresford BA et al (1994) Magnetically directed poly(lactic acid) 90Y-microspheres: novel agents for targeted intracavitary radiotherapy. J Biomed Mater Res 28(8):901–908
64. Widder KJ, Morris RM, Poore G et al (1981) Tumor remission in Yoshida sarcoma-bearing rats by selective targeting of magnetic albumin microspheres containing doxorubicin. Proc Natl Acad Sci USA 78(1):579–581
65. Widder KJ, Senyel AE, Scarpelli GD (1978) Magnetic microspheres: a model system of site specific drug delivery in vivo. Proc Soc Exp Biol Med 158:141–146
66. Lubbe AS, Bergemann C, Huhnt W et al (1996) Preclinical experiences with magnetic drug targeting: tolerance and efficacy. Cancer Res 56(20):4694–4701
67. Sajja HK, Eest MP, Mao H et al (2009) Development of multifunctional nanoparticles for targeted drug delivery and noninvasive imaging of therapeutic effect. Curr Drug Discov Technol 6(1):43–51
68. Torchilin VP (2007) Targeted pharmaceutical nanocarriers for cancer therapy and imaging. AAPS J 9(2):E128–E147

69. Arruebo M, Fernández-Pacheco R, Ibarra MR et al (2007) Magnetic nanoparticles for drug delivery. Nano Today 2(3):22–32
70. Pileni MP (2003) The role of soft colloidal templates in controlling the size and shape of inorganic nanocrystals. Nat Mater 2:145–150
71. Sun S, Zeng H, Robinson DB et al (2004) Monodisperse MFe2O4 (M = Fe, Co, Mn) nanoparticles. J Am Chem Soc 126(1):273–279
72. Hyeon T, Lee SS, Park J, Chung Y, Na HB (2001) Synthesis of highly crystalline and monodisperse maghemite nanocrystallites without a size-selection process. J Am Chem Soc 123(51):12798–12801
73. Kim JE, Shin JY, Cho MH (2012) Magnetic nanoparticles: an update of application for drug delivery and possible toxic effects. Arch Toxicol 86:685–700
74. Hofmann-Amtenbrink M, Von Rechenberg B, Hofmann H (2009) Superparamagnetic nanoparticles for biomedical application. In: Tan MC (ed) Nanostructured materials for biomedical applications. Trans Research Network, Kerala, pp 119–149
75. Janusz W, Sedłak A (2011) Specific adsorption of carbonate ions at the hematite/aqueous electrolyte solution interface. Physicochem Probl Mi 46:65–72
76. Melnyk IV, Gdula K, Dąbrowski A, YL Zub (2016) Magneto-Sensitive Adsorbents Modified by Functional Nitrogen-Containing Groups. Nanoscale Res Lett 11:61–67
77. K Gdula, A Dąbrowski, E Skwarek (2016) Synthesis, surface characterization and electrokinetic properties of colloidal silica nanoparticles with magnetic core. Adsorption 22:681–688

Chapter 44
Low-Temperature Stage Formation of Interface Composition Systems Cu—Y—Zr—O

O. Gorban, S. Gorban, O. Zarechnaya, M. Kharchenko, and T. Konstantinova

CuO-functionalization zirconia dioxide is a promising material for a wide spectrum of applications. These are in catalysis [1], in the ceramic industry as an active addition at the sintering of ceramics for improving mechanical properties [2], in the field of energy as material for SOFC, and for devices of energy conservation [3]. The highest effectiveness of material in these applications has been achieved due to its high dispersity and homogeneity of the component distribution in the complex system [4]. The coprecipitation method is optimal for synthesis of materials with homogeneous distribution of components in the system [5]. However, in our case the feature of use of this technology is the application of ammonia as a precipitating agent. For CuO-functionalized zirconia synthesis led to the occlusion of copper ions on the surface of the nanoparticle of hydrogel of zirconia hydroxide in the form of copper ammonia complexes $[Cu(NH_3)_m(H_2O)_n]^{2+}$ or hydroxide complexes $[Cu(H_2O)_m(OH)_k]^{2-k}$, where cooper's coordination number $k < 3$ (is equal to 4 or 6), as well as in the form of mixed ammonia hydroxide complexes $[Cu(NH_3)_m(OH)_n]^{2+}$. The structure of the complex depends on synthesis conditions, in particular on pH precipitation. At a high value of pH precipitation, the ammonia complexes are formed; then at pH decrease ammonia groups are substituted on hydroxide groups [6]. Because the radius of the cation of copper (0.73 nm) is closed to the radius of the zirconium cation (0.79 nm), copper ions are easily adsorbed to the cationic vacancies on the surfaces of formed zirconia particles. The maximum capacity to

O. Gorban (✉) • S. Gorban • M. Kharchenko • T. Konstantinova
Donetsk Institute for Physics and Engineering After Named O.O. Galkin NAS of Ukraine, Kiev, Ukraine
e-mail: matscidep@aim.com

O. Zarechnaya
L.M. Litvinenko Institute of Physical-Organic Chemistry and Coal Chemistry, Donetsk, Ukraine
e-mail: olga777_62@mail.ru

O. Fesenko, L. Yatsenko (eds.), *Nanophysics, Nanophotonics, Surface Studies, and Applications*, Springer Proceedings in Physics 183,
DOI 10.1007/978-3-319-30737-4_44

sorption of copper (II) ions has plane (111) of tetragonal zirconia [7], and because amorphous zirconia is an aggregate of planes (111), more homogeneous CuO distribution will be expected in amorphous xerogel and synthesized oxide nanoparticles at further heat treatment. This gives the possibility of controlling the nanoparticle structure and properties in the framework of a unique unified approach to synthesis of modification material for different exploitation uses. However, in using this approach to nanoparticle modification it is necessary to take into account the change of the amorphous xerogel hydrate shell under temperature [8], which as a result will have an appreciable effect on dispersion of the modification material and on the structure of cooper complexes.

In this chapter an influence of modification by cooper-containing is considered at a stage of hydrogel synthesis on the surface state of nanoparticles and their organization in the structure of amorphous xerogel.

44.1 Results and Discussions

The methodology of synthesis of CuO-modified zirconia consists of occlusion of complex composition of Cu(II) ions at the formed amorphous surface of hydrogel particles and following drying of modified hydrogel by the microwave radiation method. The cooper complex formation in this case takes place at the addition of zirconia, yttrium, and cooper salts in the water–ammonia solution with formation of complex hydrogel nanoparticles. Reference [7] showed that in the water–ammonia concentration solutions the cooper ions in solution had different ligand surroundings and formed associations with different structure according to the pH solution and the concentration of components. For a view of the possible structure of the Cu (II) complex it had been synthesized under the conditions of our experiment (pH = 8). The ESR spectrum of the synthesized Cu(II) complex is shown in Fig. 44.1a.

The spectrum is the superposition of two signals, which shows a presence of paramagnetic Cu(II) centers with different ligands in the nearest surroundings. The g-factor values are $g_{\parallel} = 2.25$ and $g_{\perp} = 2.08$ for copper ions in octahedral coordination with a strong tetragonal compression with d_{z^2} base state. The g-factor values of the second ESR signal are $g_{\perp} = 2.17$ and $g_{\parallel} = 2.05$ for copper ions in octahedral coordination with tetragonal distortion with $d_{x^2-y^2}$ base state. That is close to estimate values in Reference [118]: $g_{\parallel} = 2.24$ and $g_{\perp} = 2.1$ and $g_{\parallel} = 2.0$ and $g_{\perp} = 2.25$. The complex behavior of the ESR spectrum shows on different degrees of tetragonal distortion of the octahedral crystal field of the Cu(II) complex as the results of the nonequivalence of kinds of ligands in axial and equatorial positions.

The strong covalence of Cu^{2+} bonds with ligands and nonequivalence of Cu^{2+}-ligand bonds in the *x*- and *y*-axis of the equatorial plane are needed for realization of the spectrum with these parameters. A dimer fragment of the possible structure of the polymer Cu(II) complex is shown in Fig. 44.1b, and calculated parameters

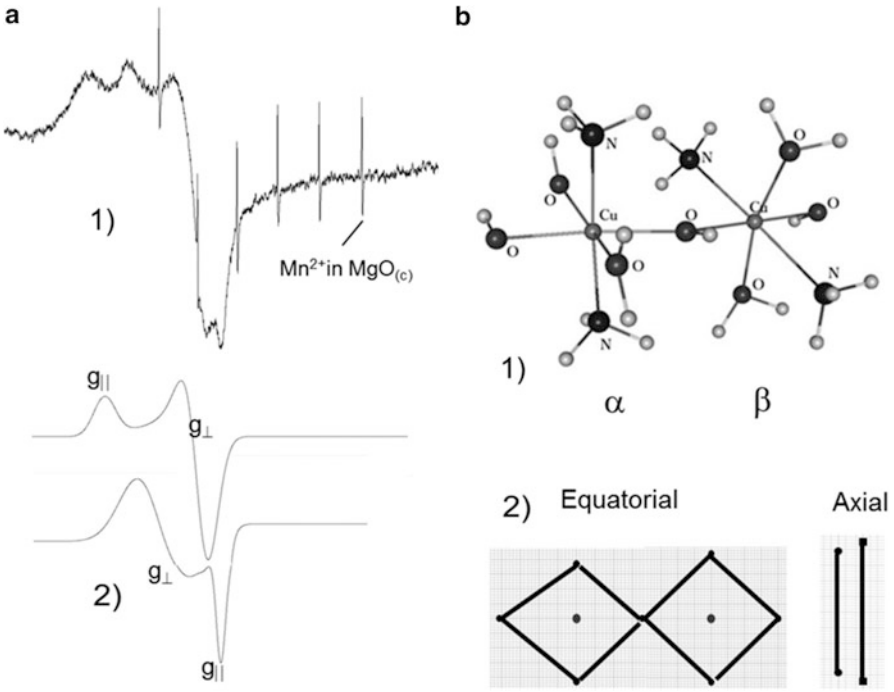

Fig. 44.1 Parameters of cooper (II) (**a**) paramagnetic signal Cu(II) of synthesized complex (ESR spectrum): (*1*) experimental spectra, (*2*) theoretical spectra expansion by WINEPR program, (**b**) possible structure of Cu(II) complex: (*1*) PM6 calculation of structure, (*2*) equatorial and axial projection of ligand positions according Cu(II) centers

of this complex structure are presented in Table 44.1. The structure of the Cu (II) complex was calculated in PM6 of MOPAC 2012 [9].

It is shown that the charge of cooper ion in the complex depends on the ligands in the equatorial and axial positions. The calculated structure confirmed the presence of Cu^{2+} paramagnetic centers in different charge states and with different Cu^{2+}-ligand bonds in the axial and equatorial planes.

The FTIR spectrum of synthesized Cu(II) complex confirmed the ESR and our calculation of the structure of the possible complex; see Fig. 44.2.

In the region of 2800–3600 cm^{-1} there have been observed some absorption bands: 3546 and 3426 cm^{-1}, corresponding to valence oscillations of bond O─H in the OH group, on H_2O molecules, and also 3125 and 3050 cm^{-1}, according to valence oscillations of the N─H bond of NH_3 ligands, which can be found in equatorial and axial positions in a complex, respectively. It is known that the shift of N─H absorption bands in a low-frequency region is due to charge reduction on the nitrogen atom in a complex formation ion; as a consequence, the Cu─N bond becomes shorter and the covalence degree of such a bond is decreased. It has been confirmed by the analysis carried out of structure parameters of the complex (Table 44.1). It is shown for the dimer fragment, where ammonia groups are in

Table 44.1 Calculated parameters of dimer complex structure

Atom (X)	Bond	q in H_2O	R_{Cu-X}	q in Ammonia	R_{Cu-X}
Cu α	–	1.514	–	1.496	
O(central)	Cu—O	−0.779	2.035	−0.724	1.766
N α	Cu—NH_3	−0.433	1.924	−0.449	1.943
N α	Cu—NH_3	−0.422	1.909	−0.425	1.937
O α	Cu—H_2O	−0.655	2.138	−0.649	2.139
O α	Cu—OH	−1.173	2.122	−1.180	2.074
O α	Cu—OH	−1.040	1.832	−1.039	1.855
Cu β	–	0.655	–	0.681	–
O(central)	Cu—O		2.035		2.009
N β	Cu—NH_3	−0.484	2.193	−0.504	2.250
N β	Cu—NH_3	−0.469	2.138	−0.495	2.201
O β	Cu—H_2O	−0.597	2.147	−0.582	2.107
O β	Cu—H_2O	−0.595	2.179	−0.598	2.105
O β	Cu—OH	−1.040	1.832	−1.153	2.079

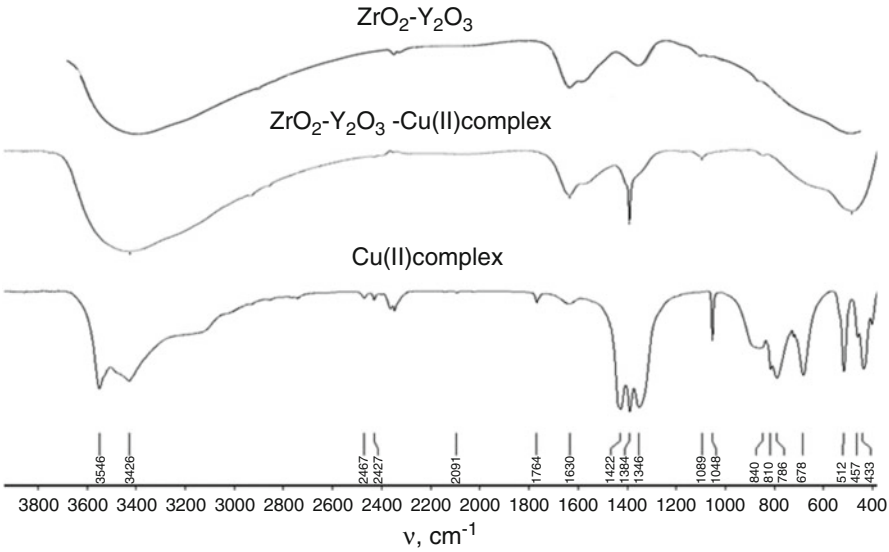

Fig. 44.2 FTIR spectrum of synthesized systems: Cu(II) complex, ZrO_2-3 mol.% Y_2O_3 and precipitated ZrO_2-3 mol% Y_2O_3-8 mol.% Cu(II) complex

axial positions, that the cooper ion has a higher charge and the Cu—N bond is more covalent than for the Cu ion charge and the degree of covalence of the Cu—N bond in the fragment of dimer complex with equatorial positions of ammonia ligands. In the region of 1200–1800 cm^{-1} there have been observed some absorption bands at 1354, 1384, 1422, 1635, and 1763 cm^{-1}, which correspond to deformation

oscillations of the ligand's OH and NH bonds, and also the NO_3 group. The bands at 1354, 1422, and 1635 cm^{-1} correspond to deformation oscillations of NH_3, the band at 1384 cm^{-1} corresponds to oscillations of NO_3 group, and the band at 1763 cm^{-1} is a summary of the adsorption bands of both NH_3 and NO_3 groups. The band at 1048 cm^{-1} corresponds to oscillations of Cu—(OH) or Cu—(OH_2). The band at 858 cm^{-1} corresponds to pendulum oscillations of NH_3. The band at 677 cm^{-1} corresponds to libration oscillations of water's molecules. The band at 511 cm^{-1} corresponds to oscillations of the Cu—O bond, and oscillations of Cu—N occur at 456 and 431 cm^{-1} frequencies.

It was shown, in region 2800–3600 cm^{-1} of valence oscillations, that the wide submaximum at central frequency 3429 cm^{-1} is observed, where the valence oscillations of OH and NH bonds occur. It is noted that the frequencies which make a contribution to the low-frequency shoulder of this band have higher values as compared to the OH and NH bonds for the complex of copper (II). The frequency of the total band of deformation oscillations of H_2O and NH_3 in a composite structure is practically unchanged compared to a clean complex, and also the band of symmetric deformation oscillations of NH_3 or OH terminal groups on the zirconia surface appears at 1574 cm^{-1}. The change of intensities of set peaks in the range of 1300–1400 cm^{-1} frequencies corresponds to N—H deformation vibrations. It can be related to the change of interconnection of ligands with the copper ion in the complex at adsorption of Cu(II) complex on the surface of xerogel nanoparticles. The vibrations of Cu—N and Cu—O bonds of the adsorbed complex had not been divided in a wide submaximum in the area of lattice vibrations of 400–1000 cm^{-1}. The features of the IR spectra of these systems testify to adsorption of complexes of Cu (II) both on oxygen vacancies and on surface oxygen-containing groups (Zr = O or ZrOH).

The ESR spectrum of the modified systems is shown in Fig. 44.3. A spectrum form specifies being on the nanoparticle surface of Cu^{2+} paramagnetic center in octahedral coordination.

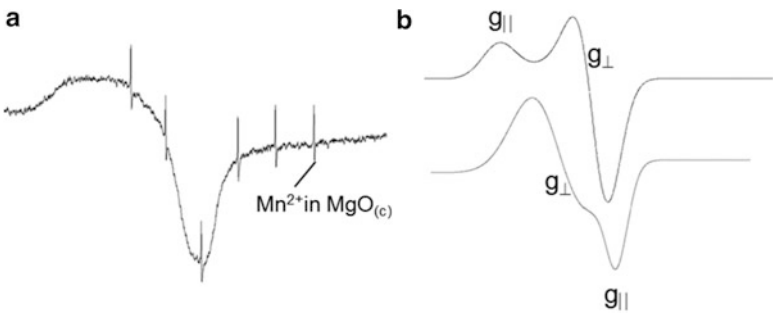

Fig. 44.3 ESR spectra of paramagnetic centers of copper (II) in ZrO_2-3 mol.% Y_2O_3-8 mol.% Cu (II) complex modified systems : (**a**) experimental spectra, (**b**) theoretical spectra expansion by WINEPR program

The spectrum of Cu(II) paramagnetic centers of synthesized ZrO_2-3 mol.% Y_2O_3-8 mol.% Cu(II) complex also shows the presence of two nonequivalent kinds of Cu(II) centers. The estimated g-factor values of the Cu(II) complex that has been coprecipitated with ZrO_2-3 mol.% Y_2O_3 is shifted in a higher range of the magnetic field. There are $g_{\|} = 2.24$, $g_{\perp} = 2.06$ for the first Cu(II) center and inverted signal with $g_{\perp} = 2.15$, $g_{\|} = 2.03$ for the second kind of Cu(II) paramagnetic center. Values of g-factors are for copper ions in octahedral coordination with a strong tetragonal distortion. The shift of g-factors may be connected with the ordering of Cu(II) ions at the adsorption of Cu(II) complexes on the zirconia surface in syntheses. The estimated g-factors of investigated systems are less than the g-factors that had been estimated for Cu(II) complexes on the TiO_2 surface [10]. As in Reference [10], our data suggest that parameters Cu(II) complex which adsorbed on the zirconia surface are determined not only by the Cu (II) base state in complex but also an orbital ordering of octahedral complexes with tetragonal distortion. The tetragonal distortion of octahedral Cu(II) complexes changes at adsorption of the complex on the zirconia surface. The FTIR spectra shows the interaction of the Zr = O and Zr—OH—Zr surface with ammonium ligands of the Cu(II) complex.

44.2 Conclusion

The precipitation of the Cu(II) complex by wet technology led to forming a Cu (II) polymeric complex in octahedral coordination. The nonequivalence of positions of various ligands (NH_3, OH, H_2O) in different octahedral fragments of Cu(II) polymeric complex led to tetragonal distortion of each octahedral of this complex. As result two kinds of paramagnetic Cu(II) centers were present in the investigated polymeric complex. The sorption of the zirconia surface complex led to the change of Cu(II) octahedral coordination due to the interaction between Zr = O or Zr—OH—Zr groups of zirconia surface and ammonium ligands of the Cu (II) complex, and the ordering of Cu(II) paramagnetic centers with different base states was realized.

References

1. Ratnasamy P, Srinivas D, Satyanarayana CVV, Manikandan P, Senthil Kumaran RS, Sachin M, Vasudev N (2004) Shetti Influence of the support on the preferential oxidation of CO in hydrogen-rich steam reformates over the CuO–CeO_2–ZrO_2 system. J Cat 221:455–465
2. Mayo MJ, Seidensticker JR, Hauge DC, Carim AH (1999) Surface chemistry effects on the processing and superplastic properties of nanocrystalline oxide ceramics. Nanostruct Mater 11 (2):271–282
3. Dongare MK, Dongare AM, Tare VB, Kemnitz E (2002) Synthesis and characterization of copper-stabilized zirconia as an anode material for SOFC. Solid State Ion 152–153:455–462

4. Caruso F (2001) Nanoengineering of particle surfaces. Adv Mater 13(1):11–22
5. Ju-Nam Y, Lead JR (2008) Manufactured nanoparticles: an overview of their chemistry, interactions and potential environmental implications. Sci Total Environ 400(1–3):396–414
6. В.Ф. Ануфриенко, Г.А. Зенковец, Р.А. Шутилов. В.Ю. Гаврилов, Н.Т. Васенин, А.А. Шубин, З.Р. Исмагилов, В.Н. Пармон, Особенности ассоциирования ионов Cu2 + в концентрированных водно-аммиачных растворах азотнокислой меди по данным ЭПР. Физическая химия, 440(5), 651–654 (2011)
7. Lemaire L, Scholz SM, Bowen P, Dutta J, Hofmeister H, Hofmann H (1999) Effect of CuO additives on the reversibility of zirconia crystalline phase transitions. J Mater Sci 34:2207–2215
8. Konstantinova T, Danilenko I, Glazunova V, Volkova G, Gorban O (2011) Mesoscopic phenomena in oxide nanoparticles systems: processes of growth. J Nanopart Res 13:4015–4023
9. Maia JDC et al (2012) GPU linear algebra libraries and GPGPU programming for accelerating MOPAC semiempirical quantum chemistry calculations. J Chem Theory Comput 8:3072–3081. doi:10.1021/ct3004645
10. А.А. Алтынников, Л.Т. Цикоза, В.Ф. Ануфриенко Упорядочение ионов Cu(II) в нанесенных медь-титановых оксидных катализаторах, Ж. структ. Химии. 47(6), 1170–1178 (2006)

Chapter 45
Oxidation Resistance of Materials Based on Ti_3AlC_2 Nanolaminate at 600 °C in Air

A.D. Ivasyshyn, O.P. Ostash, T.O. Prikhna, V. Ya. Podhurska, and T.V. Basyuk

45.1 Introduction

Recently, a new classes of materials based on layered carbide Ti_3AlC_2 have attracted a great attention of material scientists due to their exceptional properties. This carbide belongs to so-called MAX phases which have a chemical formula: $M_{n+1}AX_n$—where M is an early transition metal, A is an A-group element, and X is carbon and/or nitrogen. The crystal structure of MAX phases can be described as octahedral ternary metal carbide and/or nitride sandwiched by close-packed layers of A-element. These materials have good thermal and electrical conductivity, low density, high strength and Young's modulus, excellent thermal shock resistance, high chemical resistance, relatively low thermal expansion coefficient, and good machinability [1–3]. Owing to such combination of properties, they have been suggested for various applications, especially as high-temperature structural materials. This requires comprehensive investigations of oxidation resistance of Ti_3AlC_2-based materials. Barsoum et al. [4] had demonstrated that for $Ti_{n+1}AlX_n$ compounds oxidized in the 800–1000 °C temperature range, the scale composed mainly of rutile-based solid solution, $(Ti_{1-y}Al_y)O_{2-y/2}$ where $y < 0.05$, and some Al_2O_3. The oxidation process occurred by the inward diffusion of oxygen and the outward diffusion of Al, Ti, C, and N. It was revealed that the formation of thin layer of Al_2O_3 preceded the nucleation and growth of TiO_2 at the early stages of oxidation [5]. The scale formed at higher temperatures consisted of continuous

A.D. Ivasyshyn (✉) • O.P. Ostash • V.Ya. Podhurska
Karpenko Physico-Mechanical Institute, NAS of Ukraine, 5 Naukova str., Lviv 79060, Ukraine
e-mail: ivasyshyn@ipm.lviv.ua

T.O. Prikhna • T.V. Basyuk
V. Bakul Institute for Superhard Materials, NAS of Ukraine, Avtozavodskaya str., 2, Kiev 04074, Ukraine

O. Fesenko, L. Yatsenko (eds.), *Nanophysics, Nanophotonics, Surface Studies, and Applications*, Springer Proceedings in Physics 183,
DOI 10.1007/978-3-319-30737-4_45

Al_2O_3 inner layer and outer layer changed from rutile TiO_2 at temperatures below 1200 °C to a mixture of Al_2TiO_5 and TiO_2 at 1300 °C [6]. Taotao [7] had reported that the scale of un-dense Ti_3AlC_2 material containing 3 wt.% TiC oxidized at 1000 °C in air consisted of three layers, including an outer un-dense TiO_2 layer adhering to a little Al_2O_3, a thick intermediate $TiO_2 + Al_2O_3$ mixed layer, and a thin inner Al_2O_3 layer with some pores.

In spite of thorough research of oxidation behavior of Ti_3AlC_2-based materials at high temperature, only a few results obtained at intermediate temperatures have been reported [8, 9]. Taking into account the anomalously intense oxidation of Ti_3AlC_2-based material at 500 °C and especially at 600 °C [8], the investigation of oxidation behavior of these materials at intermediate temperatures has a great importance.

In this work the Ti_3AlC_2-based materials have been oxidized at 600 °C in air for 1000 h. The influence of porosity, pre-oxidation treatment, and Nb doping on the oxidation resistance of these materials has been investigated.

45.2 Experimental

The materials used in this work were initially sintered in vacuum from mixture of TiC, TiH_2, and Al powders and then hot pressed at 1350 °C under pressure of 30 MPa for 1 h. The phase composition of the sintered material consisted of 95 wt.% Ti_3AlC_2 and 5 wt.% TiC. Figure 45.1a shows the back-scattered electron image of polished surface of this material. The equiaxed grains of Ti_3AlC_2, fine particles of TiC, and big pores were observed. The porosity of the material was 22 %. After hot pressing refinement of the structure and reduction of the porosity to 1 % have been observed (Fig. 45.1b). The amount of Ti_3AlC_2 was decreased to 92 wt.% and TiC increased to 6 wt.%. Additionally, 2 wt.% Al_2O_3 was revealed in this material. The material doped with 3.5 wt.% Nb fabricated by the same process as the previous material consisted of 56 wt.% $(Ti, Nb)_3AlC_2$, 41 wt.% TiC, and 3 wt.% Al_2O_3. The structure of this material includes equiaxed grains of Ti_3AlC_2 and TiC and uniformly distributed fine particles of Al_2O_3 and small pores (Fig. 45.1c).

The isothermal oxidation tests were carried out at the temperature of 600 °C in static air using rectangular bars with dimensions of 20 × 5 × 3 mm. The specimens were cut by the electrical discharge method, abraded to 1000 grit with SiC paper, and polished by diamond past. The oxidation tests were divided into five stages which had the duration: first stage, 15 h; second stage, 245 h; and the last three stages, 250 h. Each stage consisted of heating to 600 °C in air, exposition for determinated time, and cooling to room temperature. The weight of the specimens was measured before the test and after each stage by analytical balance. The accuracy of the weight measuring was $\pm 10^{-4}$ g. The oxidation resistance of materials tested was characterized by weight gain per unit surface area $\Delta W/S$. Scanning electron microscopy (EVO 40 XVP (Carl Zeiss, Germany)) coupled

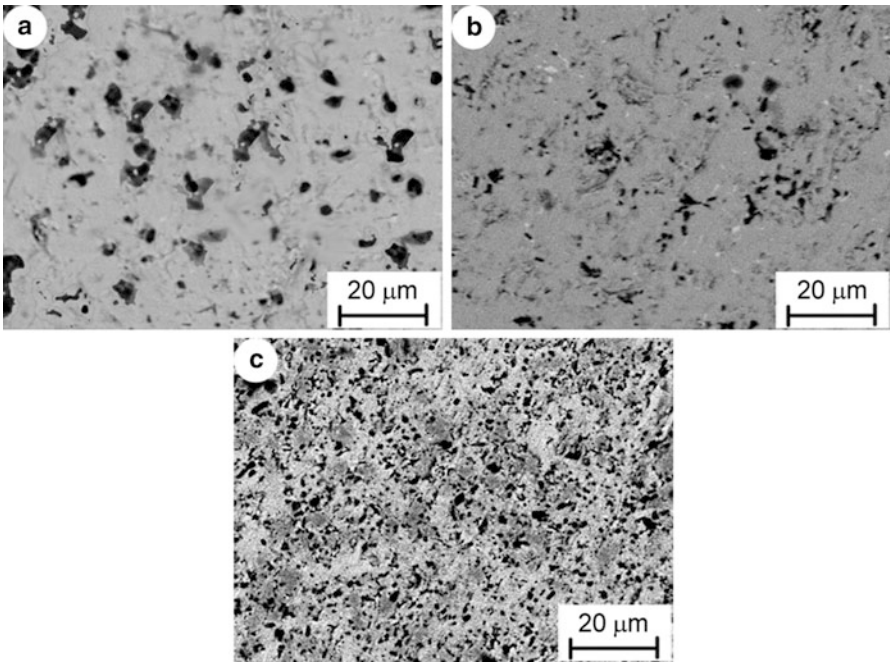

Fig. 45.1 Back-scattered electron images of the polished surfaces: (**a**) Ti_3AlC_2-based material with 22 % porosity, (**b**) Ti_3AlC_2-based material with 1 % porosity, and (**c**) Nb-doped Ti_3AlC_2-based material with 1 % porosity

with energy-dispersive spectroscopy (EDS) (INCA Energy 350 (Oxford Instruments, UK)) were used to study the structure and quantitative elemental content of the bulk material and the oxidized scale.

45.3 Results and Discussion

The dependences of weight gain per unit surface area on oxidation time at 600 °C for Ti_3AlC_2-based materials tested are presented in Fig. 45.2. It can be seen that the $\Delta W/S$ for material with porosity of 22 % monotonically increases and reaches the value of 24 mg/cm^2 after exposition of 437 h. Because of the very high value of the $\Delta W/S$, the test for this material had been stopped. The rapid oxidation of Ti_3AlC_2-based material with porosity of 22 % can be explained by intense penetration of oxygen into the material through the pores. As a result not only outer surface of the specimen but also the surfaces of pores in the bulk material were oxidized (Fig. 45.3a, b).

The oxidation kinetics for Ti_3AlC_2-based material with 1 % porosity at 600 °C remarkably increases on the first stage of the test (Fig. 45.2). After 15 h the weight

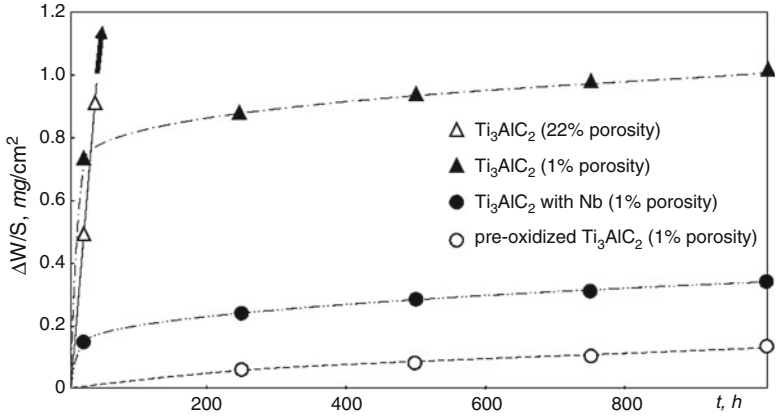

Fig. 45.2 Oxidation kinetics for the Ti_3AlC_2-based materials at 600 °C in air

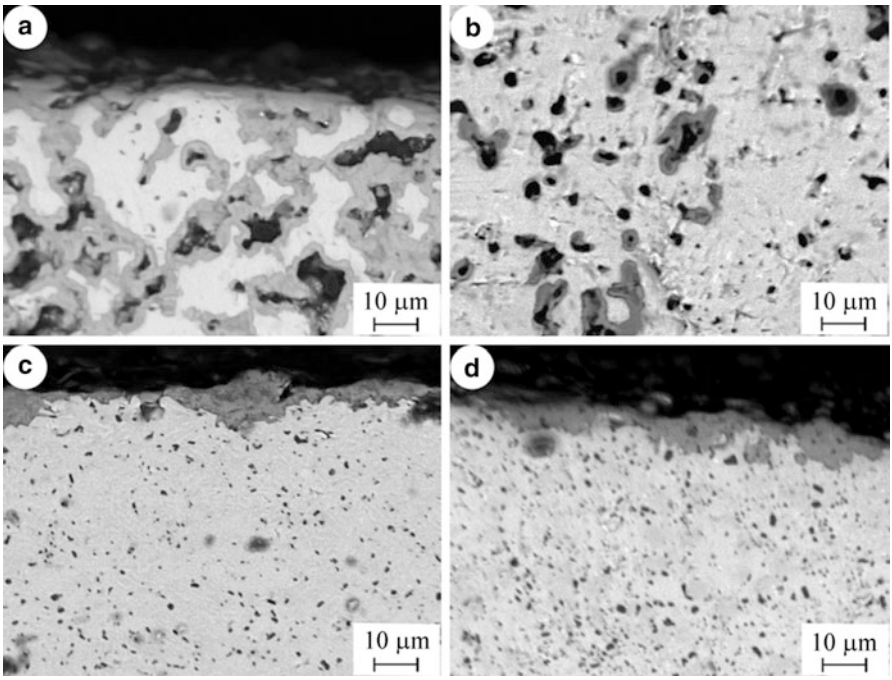

Fig. 45.3 Back-scattered electron images of the scales formed at 600 °C for 1000 h: (**a**) Ti_3AlC_2-based material with 22 % porosity, (**b**) oxidized pores of Ti_3AlC_2-based material with 22 % porosity, (**c**) Ti_3AlC_2-based material with 1 % porosity, and (**d**) Nb-doped Ti_3AlC_2-based material with 1 % porosity

Table 45.1 EDS analysis results of the Ti_3AlC_2-based materials with 1 % porosity (at.%)

	Ti		Al		C		Nb		O	
Materials	Bulk	Scale	Bulk	Scale	Bulk	Scale	Bulk	Scale	Bulk	Scale
Ti_3AlC_2	51.3	23.7	14.8	8.1	34.6	0	0	0	0	68.2
Ti_3AlC_2 with Nb	44.1	25.3	14.9	3.3	42.8	0	1.4	0.6	0	70.1

gain per unit surface area increases more slowly and after 1000 h exposition is 1.0 mg/cm^2. Table 45.1 presents an average quantity of chemical elements in bulk material and scale, obtained by EDS method. It can be seen that carbon misses from the scale and instead of this oxygen presents. This means that the surfaces of Ti_3AlC_2 and TiC particles completely oxidized to TiO_2, Al_2O_3, and gaseous CO or CO_2 phases which volatilized from the scale. The overall equations for the oxidation reactions are:

$$4Ti_3AlC_2 + 23O_2 = 12TiO_2 + 2Al_2O_3 + 8CO_2(g),$$
$$TiC + 2O_2 = TiO_2 + CO_2(g).$$

Wang and Zhou [8] had demonstrated that the scale formed at 600 °C on the surface of the Ti_3AlC_2 material with 5 val.% TiC consisted of amorphous Al_2O_3, anatase, and rutile TiO_2. The formation of anatase from Ti_3AlC_2 led to the increase of stress due to the difference of their volume expansion. Therefore, the rapid increase of $\Delta W/S$ value for Ti_3AlC_2-based material with 1 % porosity on the first stage of the test can be associated with intense scale formation as well as with low protective property of the thin scale due to microcracks and also with penetration of oxygen through micropores into the bulk material. After a long-term exposition, when micropores were covered with oxides and the scale thickness was increased (Fig. 45.3c), the inward diffusion of oxygen and outward diffusion of Ti and Al became slow. As a result the oxidation kinetics was decreased. Based on these results, it can be assumed that the preliminary oxidation to form the protective layer of oxides would increase the oxidation resistance of Ti_3AlC_2-based materials. The pre-oxidation at 1000–1300 °C for 2 h provides the formation of dense scale which consists of Al_2O_3 and rutile TiO_2 without anatase TiO_2 [10]. In the present study, the pre-oxidation of Ti_3AlC_2-based material with 1 % porosity was performed at 1200 °C in air for 2 h. The long-term oxidation resistance was investigated at 600 °C in air for 1000 h. As can be seen in Fig. 45.2, the pre-oxidized material demonstrates the negligible increase of weight gain per unit surface area during all test. The value of $\Delta W/S$ for this material not exceeds a 0.11 mg/cm^2 after 1000 h exposition.

The influence of Nb on the oxidation resistance of Ti_3AlC_2-based material with 1 % porosity had been investigated. Despite a greater content of TiC, the weight gain per unit surface area for this material increases more slowly as compared with material without Nb (Fig. 45.2). The $\Delta W/S$ is 0.34 mg/cm^2 after exposition at 600 °C for 1000 h. This value is approximately three times smaller than that for Ti_3AlC_2-based material without Nb. Barsoum et al. [11] had shown that TiC has a

deleterious effect on the oxidation kinetics of Ti_3SiC_2-based materials which also belong to isotypic structure $M_{n+1}AX_n$. The contradiction of this conclusion with the results obtained in the present work can be explained by the positive effect of Nb on the oxidation resistance of Ti_3AlC_2-based material. The EDS analysis shows that content of Ti, Al, and Nb in the scale of Ti_3AlC_2-based material with Nb is less than that in the bulk material (Table 45.1). On the other hand, the content of Al in the scale of this material is significantly less than that of the material without Nb. Therefore, it is reasonable to assume that the scale of Ti_3AlC_2-based material with Nb consists mainly of TiO_2 and minor quantity of Al_2O_3 (Fig. 45.3d). According to [6], the formation of dense Al_2O_3 layer is responsible for high oxidation resistance of Ti_3AlC_2-based materials. Thus, the material with Nb ought to be less oxidation resistant than the material without Nb. Jiang et al. [12] had concluded that Nb in solid solution with TiO_2 improves the oxidation resistance of Ti–Al–Nb alloys by impeding mass transformation in TiO_2. Evidently in the case of Ti_3AlC_2-based materials, the positive effect of Nb manifests in the same manner.

45.4 Conclusions

The investigation of oxidation resistance of Ti_3AlC_2-based materials had been carried out at 600 °C in static air for 1000 h. The results showed that the weight gain per unit surface area for sintered Ti_3AlC_2-based material with porosity of 22 % monolithically increased and after 437 h reached the value of 24 mg/cm^2. The drastic increase of oxidation kinetics of this material is caused by intense oxidation of not only the outer surface of specimen but also the surfaces of pores. The weight gain per unit surface area for hot-pressed Ti_3AlC_2-based material with 1 % porosity intensively increased for the first 15 h of oxidation, and then the oxidation kinetics slowly decreased. The pre-oxidation at 1200 °C for 2 h eliminated the initial oxidation of this material at 600 °C. It was revealed that the additional doping with Nb significantly improves the oxidation resistance of Ti_3AlC_2-based material.

References

1. Radovic M, Barsoum MW (2013) MAX phases: bridging the gap between metals and ceramics. Am Ceram Soc Bull 92(3):20–27
2. Barsoum MW, Yoo H-I, Polushina IK et al (2000) Electrical conductivity, thermopower, and Hall effect of Ti_3AlC_2, Ti_4AlN_3, and Ti_3SiC_2. Phys Rev 62(15):1094–1098
3. Prikhna T, Cabioc'h T, Gawalek W et al (2014) Study of thermal stability and mechanical characteristics of MAX-phases of Ti–Al–C(N) system and their solid solutions. Adv Sci Technol 89:123–128
4. Barsoum MW, Tzenov N, Procopio A et al (2001) Oxidation of $Ti_{n+1}AlX_n$ (n = 1-3 and X = C, N): II. Experimental results. J Electrochem Soc 148(8):551–562. doi:10.1149/1.1380256

5. Song GM, Pei YT, Sloof WG et al (2008) Early stages of oxidation of Ti_3AlC_2 ceramics. Mater Chem Phys 112:762–768
6. Wang XH, Zhou YC (2003) Oxidation behavior of Ti_3AlC_2 at 1000–1400 °C in air. Corros Sci 45:891–907
7. Taotao A (2012) High-temperature oxidation behavior of un-dense Ti_3AlC_2 material at 1000 °C in air. Ceram Int 38:2537–2541
8. Wang XH, Zhou YC (2003) Oxidation behavior of TiC-containing Ti_3AlC_2 based material at 500–900 °C in air. Mat Res Innov 7:381–390. doi:10.1007/s10019-003-0278-7
9. Pang WK, Low IM, O'Connor BH et al (2009) Oxidation characteristics of Ti_3AlC_2 over the temperature range 500–900 °C. Mater Chem Phys 117:384–389
10. Wang XH, Zhou YC (2003) Improvement of intermediate-temperature oxidation resistance of Ti_3AlC_2 by pre-oxidation at high temperatures. Mat Res Innov 7:205–211. doi:10.1007/s10019-033-0252-4
11. Barsoum MW, El-Raghy T, Ogbuji LUJT (1997) Oxidation of Ti_3SiC_2 in air. J Electrochem Soc 144:2508–2516. doi:10.1149/1.1837846
12. Jiang H, Hirohasi M, Lu Y et al (2002) Effect of Nb on the high temperature oxidation of Ti–(0–50 at.%)Al. Scr Mater 46:639–643

Chapter 46
Self-Propagating High-Temperature Synthesis (SHS): A Simple Route to Carbon-Related Nanomaterials

Magdalena Kurcz, Michał Soszyński, and Andrzej Huczko

46.1 Introduction

The production of nanomaterials is at the core issue of nanotechnology. Following the famous Feynman's proposition of the imitation of Nature [1], two approaches have been developed to produce nanomaterials: (1) "top-down" (miniaturization) and (2) "bottom-up." The latter one involves the rearrangement and the growth of small species (atoms, ions, particles, etc.) into larger objects, accordingly below 100 nm (in one direction). Different techniques of matter atomization can be used to produce these starting building blocks. The self-propagating high-temperature synthesis (SHS), often referred to as the combustion synthesis (CS), has long been used not only as a commercial technique (e.g., as a thermite welding or in "emergency oxygen" generation aboard the plane) but also in fireworks and in a production of special ceramics [2]. It is based on self-sustained, highly exothermic reactions [3]. We propose here the use of this approach to synthesize carbon-related nanomaterials.

Carbon is one of the most important elements in the world. Even though it is not the most common, its significance is obvious as it builds organic matter. People have always been interested in this element, but until the twentieth century, only two allotropes of carbon were known: graphite and diamond (in addition to amorphous carbon, i.e., soot or carbon black).

The last two decades of the twentieth century brought into the daylight, however, new carbon allotropes. Firstly, in 1985, the fullerenes were discovered, the importance of the discovery was honored with the Nobel Prize (1996), and carbon

M. Kurcz • M. Soszyński • A. Huczko (✉)
Laboratory of Nanomaterials Physics and Chemistry, Department of Chemistry
Warsaw University, 1 Pasteur Street, Warsaw 02-093, Poland
e-mail: ahuczko@chem.uw.edu.pl

O. Fesenko, L. Yatsenko (eds.), *Nanophysics, Nanophotonics, Surface Studies, and Applications*, Springer Proceedings in Physics 183,
DOI 10.1007/978-3-319-30737-4_46

nanotubes were introduced to the world in 1991. The latter were even called the black diamonds of the twentieth century. But the era of carbon discoveries is not over yet. The very beginning of the twenty-first century brought one more very important discovery of carbon allotrope—graphene.

Here we show how the SHS route can be used to produce different carbon-related nanomaterials: silicon carbide nanowires and few-layered graphene.

46.2 Self-Propagating High-Temperature Synthesis: Experimental

The combustion synthesis was carried out in a modified calorimeter bomb (Fig. 46.1), using three stainless steel reactors with different volumes of 340, 550, and 2700 cm^3. The reactors were pretested at the pressure of up to 10 MPa and are resistant to extreme process parameters: very high temperature, pressure gradients, and chemically aggressive reaction environment. The reactors were modified with:

- The attachment of the observation port for spectroscopic and optical monitoring of the combustion process
- The pressure-controlling system allowing recording of combustion pressure online

Before the combustion, the reactants were loaded into the quartz crucible and moved into the reactor, then the reactor was filled with combustion gas (Ar, CO, CO_2, air, O_2), and the combustion pressure was adjusted as preplanned. The reaction was started by resistive heating of the crucible content with the igniter (carbon, kanthal, or tungsten tape) as shown in Fig. 46.2.

The reaction was usually terminated within a fraction of a second. The solid products were collected and analyzed using different methods:

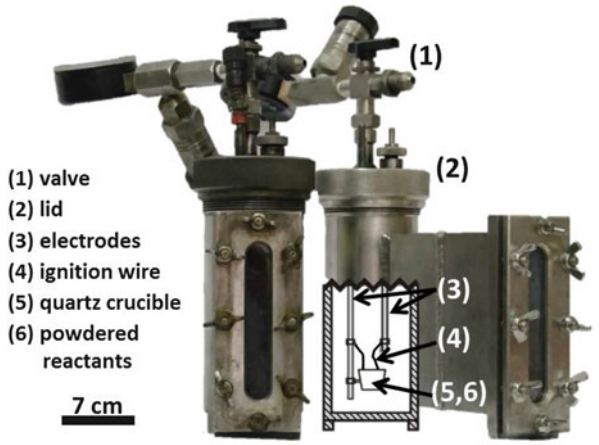

Fig. 46.1 Modified bomb calorimeter: volume 340 cm^3 (*left*) and 550 cm^3 (*right*)

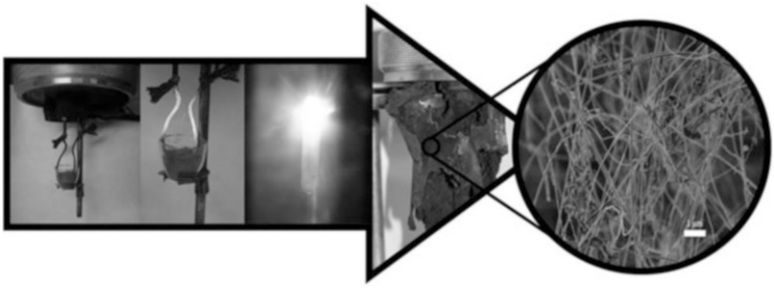

Fig. 46.2 Combustion synthesis of SiC nanowires

- Chemical analysis (determination of unreacted silicon and carbon formed) [4]
- Electron microscopy (SEM/TEM/EDX) observation (morphology and composition) [5]
- XRD (phase identification) [6]
- Raman spectroscopy (C and SiC characterization) [6]

46.3 Production of Silicon Carbide Nanowires

We found earlier [7] that the redox reaction between solid elemental silicon and powdered poly(tetra)fluoroethylene (PTFE, Teflon®) following the equation

$$\mathrm{Si} + \left(-\mathrm{CF_2} - \mathrm{CF_2}\right)_n \rightarrow \mathrm{SiC} + \mathrm{C} + \mathrm{SiF_4}$$

efficiently yielded one-dimensional SiC nanostructures. We successfully carried out the experiments using both pure and waste (Si from recycled solar cells) reactants [8]. An initiation of the combustion leads to a rapid (usually less than 1 s) reaction during which the SiC nanowires (with diameters in the range of 10–100 and length up to tens of microns; Fig. 46.3) grow efficiently.

The solid spongelike products (Fig. 46.4) contain also some unreacted Si, soot, and silica (in the case of a reaction carried out under oxygen-containing combustion atmosphere), while the off-gas is dominated by SiF_4 along with some fluorocarbon gases (CF_4, C_2F_6). These are the components which give rise to the final pressure built-up.

In order to isolate the SiCNWs, the purification protocol was elaborated as follows (Fig. 46.5):

– 0.5 h boiling in 30 % KOH solution: removal of unreacted Si and SiO_2 (SiC does not react with KOH)
– Calcination of the product at 873 K for 3.5 h in air: oxidation of carbon

This relatively simple purification process allows for the isolation of SiCNWs up to 95 % purity. From the mass balance of the purification process, the total Si conversion degree and extent of Si conversion into SiC can be calculated.

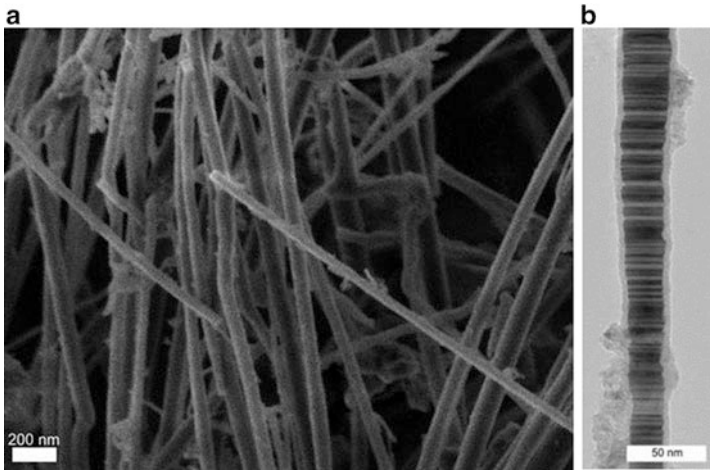

Fig. 46.3 Morphology (SEM image, (**a**); TEM, (**b**)) of purified nanofiber SiC

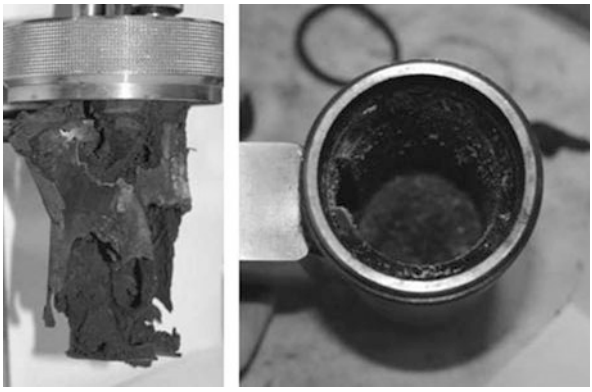

Fig. 46.4 The morphology of the raw product

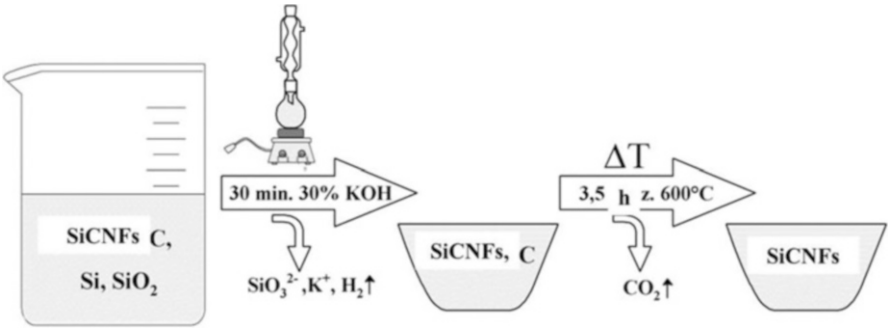

Fig. 46.5 Scheme for isolation of pure SiC nanowires

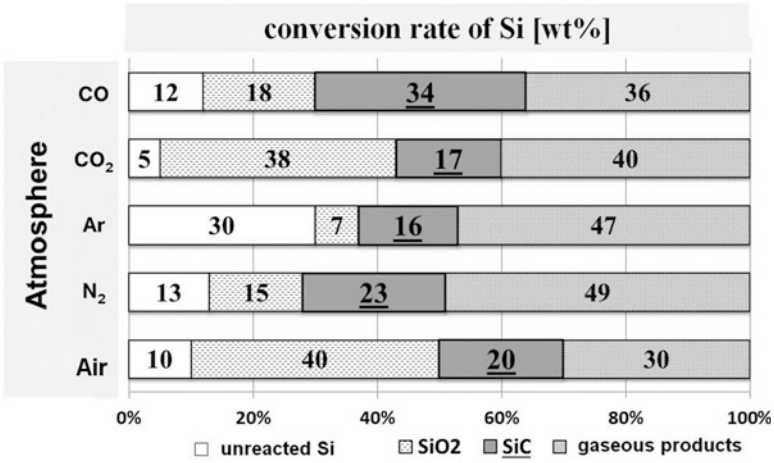

Fig. 46.6 Si conversion degree vs. combustion atmosphere

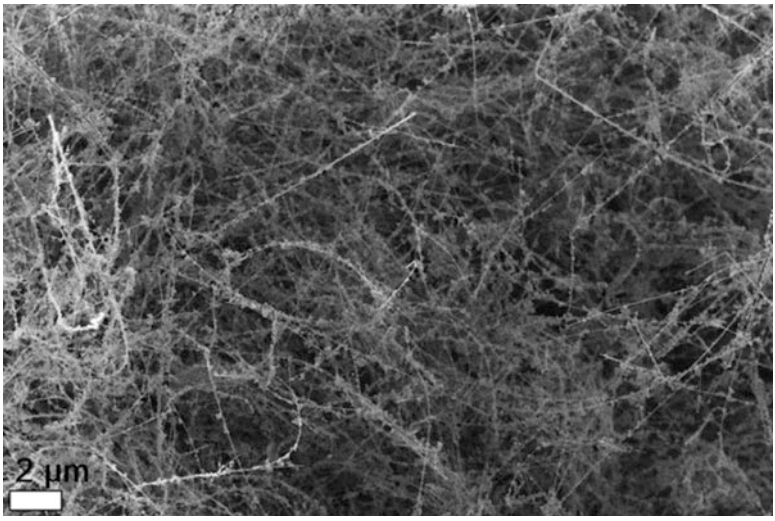

Fig. 46.7 SEM image of the morphology of the raw product (Si/PTFE combusted in CO)

The combustion atmosphere is the main operational parameter strongly influencing the process yield [9]. This clearly indicates that the reaction takes place partially in the gas phase. The results of systematic studies of combustion atmosphere for the stoichiometric Si/PTFE (36/64 wt.%) ratio are shown in Fig. 46.6.

The highest conversion was found for CO atmosphere suggesting not only that the presence of oxygen can be important for Si mass transport (gaseous SiO) but also that the formed gaseous carbon can also participate in SiC growth. The high yield for such atmosphere is confirmed by SEM observation with very high content of SiC nanowires in raw product picture (Fig. 46.7).

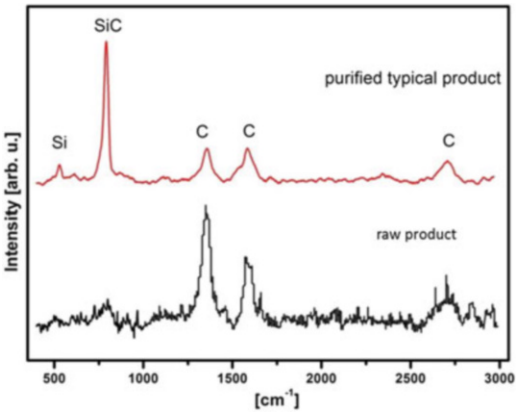

Fig. 46.8 Raman spectra of raw and purified products (Si/PTFE combustion in air)

Raman spectroscopy helped to identify the main components of products (Fig. 46.8).

The raw product is dominated by partially amorphous carbon nanostructures with the bands at 1354 and 1587 cm^{-1}. The band found at 2696 cm^{-1} can be assigned as a secondary carbon D band (1354 cm^{-1}). The band at 510 cm^{-1} is assigned to Si and is observed both in raw and purified product. Its intensity decreases as a result of the purification process. The characteristic strong band at a wave number 790 cm^{-1} corresponds to β-SiC.

XRD measurements (not presented here) also confirmed the presence of main components in raw product as shown above.

46.3.1 Reaction Silicides/PTFE

The reaction of elemental silicon with PTFE proved to proceed rapidly and efficiently, yielding solid products containing relatively high concentration of SiC nanowires. Its mechanism, however, still remains rather mysterious. The conditions of SiCNW formation and product morphology show that the growth process can occur partially under thermodynamic nonequilibrium, while the final product composition is the result of many parallel intermediate reactions and is governed by its kinetics. Some measurements point out also the fact that self-catalytic effect, related to Si nanocrystallites and V-L-S mechanism, can be considered as one of the possible reaction channels. To explore more in depth that subject, several runs were carried out with different Si-bearing reducers (silicides, alloys) to test whether other elements existing in SiCNW growth zone can influence somehow its formation and composition of final solid products. The stoichiometric ratio of starting reactants was calculated according to the general equation as follows:

$$\mathrm{MeSi} + (\mathrm{CF_2})_n \rightarrow \mathrm{SiC} + \mathrm{SiF_4} + \mathrm{MeC} + \mathrm{MeF} + \mathrm{Si} + \mathrm{Me} + \mathrm{C}$$

Obviously, the scheme of such reaction in the case of oxygen-containing combustion atmosphere is probably much more complicated.

Twenty different silicides and Si-related reducers were tested altogether. The combustion atmosphere was either Ar or CO_2, while the initial reaction pressure was set at ca. 1.0 MPa following our former results [10]. We also showed earlier [11] that in the case of combustion in CO_2 atmosphere, one can expect its partial reduction resulting in elemental carbon which can then participate either in formation of carbides or graphene-related nanostructures.

All combustions were successful (with one exception of Cu_5Si). The operational parameters of all runs are collected in Table 46.1.

All combustions were highly exothermic, and due to relatively high temperatures (ca. 2000 K) [10], the reactions were accompanied by a sharp, two- to threefold pressure increase in the growth zone. The distinct mass decrease of reactants is related to the evolution of gaseous products, mostly SiF_4 but also CF_4 and C_2F_6 (as confirmed by GCMS analyses of off-gases).

The collected products were characterized using wet chemistry analyses, SEM observations, and XRD measurements (Table 46.2).

The raw products have the morphology of either black sootlike or grayish spongelike material, with different content of fiber components (SiCNWs). The products contain low amount of free silicon. Thus, the total conversion/decomposition of starting silicides reaches 100 %, with higher conversion in runs carried out under CO_2 atmosphere. Metal carbides and fluorides, containing metal from the respective silicides, usually accompany the main components of solid products (SiC and carbon). Carbon dioxide combustion atmosphere clearly favores the formation of SiC nanowires along with silica nanoparticles, thus confirming the possible participation of oxygen (resulting from CO_2 reduction) in the growth process, probably through the mass transport of silicon (gaseous SiO). This conclusion was confirmed by SEM observations showing the high content of fibrous components in several combustion products—examples of images in Fig. 46.9.

XRD measurements (examples in Fig. 46.10, also Table 46.2) confirm the presence of SiC, unreacted Si, carbon, and respective fluorides and carbides.

In summary, the SiC nanowires can be efficiently produced not only via the direct reduction of PTFE with Si elemental but also with the use of other Si-bearing reactants, i.e., silicides. It confirms that the combustion temperatures are high enough to dissociate silicides yielding silicon. The high content of SiCNWs in several products may indicate a kind of catalytic action of the metals (resulting from silicide decomposition), but the complex composition of products (XRD) indicate many parallel intermediate reaction occurring in the SiC nanowire growth zone.

Table 46.1 SiCNW synthesis: operational parameters of combustion

Run #	Reactants	Combustion atmosphere	Initial pressure, MPa	Final pressure, MPa	Mass of reactants, g	Mass of raw product, g
1	Si/PTFE	Ar	1.00	2.21	3.60	1.02
2	Si/PTFE	CO_2	1.03	1.97	3.48	1.46
3	$CaSi_2$/PTFE	Ar	1.03	3.62	4.68	2.33
4	$CaSi_2$/PTFE	CO_2	0.95	2.45	3.15	1.51
5	$MgSi_2$/PTFE	Ar	1.05	1.99	2.22	1.47
6	$MgSi_2$/PTFE	CO_2	1.09	2.31	2.75	1.87
7	Si_2Sr/PTFE	Ar	1.06	2.96	3.20	1.54
8	Si_2Sr/PTFE	CO_2	1.05	2.75	3.27	2.46
9	$NbSi_2$/PTFE	Ar	1.05	1.76	3.33	1.22
10	$NbSi_2$/PTFE	CO_2	1.07	1.67	3.08	1.02
11	$MoSi_2$/PTFE	Ar	1.06	1.59	3.00	1.05
12	$MoSi_2$/PTFE	CO_2	1.09	1.56	2.69	0.82
13	$Mn_{15}Si_{26}$/PTFE	Ar	1.06	1.62	2.78	1.34
14	$Mn_{15}Si_{26}$/PTFE	CO_2	1.08	1.53	2.77	1.61
15	Si_2Zr/PTFE	Ar	1.05	1.85	2.98	1.21
16	Si_2Zr/PTFE	CO_2	1.08	1.82	2.89	1.13
17	WSi_2/PTFE	Ar	1.06	1.64	3.38	1.34
18	WSi_2/PTFE	CO_2	1.07	1.53	2.77	1.30
19	$FeSi_2$/PTFE	Ar	1.09	1.35	3.24	1.33
20	$FeSi_2$/PTFE	CO_2	1.08	1.23	3.08	1.28
21	$CrSi_2$/PTFE	Ar	1.08	1.86	3.15	1.10
22	$CrSi_2$/PTFE	CO_2	1.08	1.80	3.20	0.97
23	Si_2Ti/PTFE	Ar	1.05	2.20	4.77	1.34
24	Si_2Ti/PTFE	CO_2	1.08	2.16	4.23	0.98
25	VSi_2/PTFE	Ar	1.05	2.12	4.25	0.95
26	VSi_2/PTFE	CO_2	1.05	2.21	4.00	1.08
27	$HfSi_2$/PTFE	Ar	1.02	1.61	2.11	0.84
28	$HfSi_2$/PTFE	CO_2	1.06	1.45	1.45	0.53
29	$Co_{0,5}Fe_{0,5}Si_2$/PTFE	Ar	1.06	2.27	6.09	1.94
30	$Co_{0,5}Fe_{0,5}Si_2$/PTFE	CO_2	1.12	2.07	6.36	2.16
31	$Ni_{0,5}Fe_{0,5}Si_2$/PTFE	Ar	1.05	1.71	6.21	2.34
32	$Ni_{0,5}Fe_{0,5}Si_2$/PTFE	CO_2	1.06	2.09	5.86	1.98
33	$Co_{0,5}Ni_{0,5}Si_2$/PTFE	Ar	1.06	1.32	4.37	2.46
34	$Co_{0,5}Ni_{0,5}Si_2$/PTFE	CO_2	1.03	1.97	5.46	2.34
35	$TaSi_2$/PTFE	Ar	1.03	2.16	6.19	2.37
36	$TaSi_2$/PTFE	CO_2	1.08	1.57	2.57	0.96
37	$FeSi_2$/PTFE	Ar	1.06	1.94	5.51	1.73
38	$FeSi_2$/PTFE	CO_2	1.06	1.87	4.36	1.83
39	Fe-Si/PTFE	Ar	1.00	2.13	5.06	2.13
40	Fe-Si/PTFE	CO_2	1.00	1.95	4.76	2.31

Table 46.2 SiCNW synthesis: results of combustion

Run #	Reactants	Raw product morphology	Free Si content, wt %	Total conversion degree of silicide, %	SEM observation	XRD
1	Si/PTFE	Sootlike	14.8	70.0	Mostly sootlike particles with scattered SiCNWs	SiC: s.; Si-s.; C-w.
2	Si/PTFE	Partially spongelike	7.2	95	Mostly sootlike particles with scattered SiCNWs and silica nanoparticles	SiC: v.s.; Si-m.; C-w.
3	$CaSi_2$/PTFE	Partially spongelike	8.5	65.7	Plenty of SiCNWs with some sootlike particles	CaF_2: v.s.; Si-m.; SiC-w.; Si-w.; C-w.
4	$CaSi_2$/PTFE	Partially spongelike	5.9	75.9	Plenty of SiCNWs with some sootlike particles and silica nanoparticles	CaF_2: v.s.; Si-m.; SiC-w.; Si-w.; C-w.
5	$MgSi_2$/PTFE	Sootlike	5.9	37.7	Plenty of SiCNWs with some sootlike particles	MgF_2-v.s.; SiC-m.; Si-m.; C-w.
6	$MgSi_2$/PTFE	Sootlike	4.9	46.9	Plenty of SiCNWs with some sootlike particles and silica nanoparticles	MgF_2-v.s.; SiC-m.; Si-m.; C-w.
7	Si_2Sr/PTFE	Sootlike	10.2	69.1	Plenty of SiCNWs with some sootlike particles and silica nanoparticles	SrF_2-v.s.; Si-m.; SiC-w.
8	Si_2Sr/PTFE	Sootlike	6.7	80.2	Sootlike and silica nanoparticles with few SiCNWs	SrF_2-v.s.; Si-m.; SiC-w.
9	$NbSi_2$/PTFE	Partially spongelike	1.3	94.5	Mostly sootlike particles with very few short nanorods	NbC-m.

(continued)

Table 46.2 (continued)

Run #	Reactants	Raw product morphology	Free Si content, wt %	Total conversion degree of silicide, %	SEM observation	XRD
10	$NbSi_2$/PTFE	Sootlike	2.5	90.1	Mostly sootlike particles with few short nanorods	NbC-m.
11	$MoSi_2$/PTFE	Partially spongelike	1.6	81.6	Mostly sootlike particles	MoC-m.
12	$MoSi_2$/PTFE	Spongelike	0	100	Mostly sootlike particles	MoC-m.
13	$Mn_{15}Si_{26}$/PTFE	Partially spongelike	6.6	65.1	Mostly sootlike particles with few SiCNWs	SiC-m.
14	$Mn_{15}Si_{26}$/PTFE	Partially spongelike	6.5	65.6	Sootlike particles with SiCNWs	SiC-m.
15	Si_2Zr/PTFE	Spongelike	3.2	62.3	Mostly sootlike particles with many short nanorods	ZrC-m.
16	Si_2Zr/PTFE	Partially spongelike	1.6	81.2	Mostly sootlike particles with many short nanorods	ZrC-m., ZrO_2-m.; C-m.; SiO_2-w.
17	WSi_2/PTFE	Spongelike	0.6	93.2	Mostly sootlike particles with few short nanorods	W_2C-m.; WC-m.; WSi_2-w.
18	WSi_2/PTFE	Spongelike	0	100	Mostly sootlike particles with few short nanorods	W_2C-m.; WC-m.; WSi_2-w.
19	$FeSi_2$/PTFE	Sootlike	n.a.	n.a.	Mostly sootlike particles with few SiCNWs	Fe_3Si-w.; Fe-w.; SiC-w.
20	$FeSi_2$/PTFE	Sootlike	n.a.	n.a.	Sootlike particles with few SiCNWs and silica nanoparticles	Fe_3Si-w.; Fe-w.; SiC-w.
21	$CrSi_2$/PTFE	Spongelike	1.8	95.6	Plenty of SiCNWs with some sootlike particles	$Cr_xC_yN_z$-w.
22	$CrSi_2$/PTFE	Spongelike	1.4	97.8	Plenty of SiCNWs with some sootlike and silica particles	$Cr_xC_yN_z$-w.

(continued)

Table 46.2 (continued)

Run #	Reactants	Raw product morphology	Free Si content, wt %	Total conversion degree of silicide, %	SEM observation	XRD
23	Si_2Ti/PTFE	Sootlike	2.8	92.0	Mostly sootlike particles with many TiC nanocrystallites	TiC-s.; TiF_3-m.; C-w.; Si-w.
24	Si_2Ti/PTFE	Sootlike	2.9	92.0	Mostly sootlike particles with many TiC nanocrystallites	TiC-s.; TiF_3-m.; C-w.; Si-w.
25	Vsi_2/PTFE	Sootlike	2.0	91.2	Mostly sootlike particles with nanocrystallites	V_4C_3-s.; VF_3-m.; VSi_2-w.; C-w.
26	Vsi_2/PTFE	Sootlike	2.2	92.1	Mostly sootlike particles	V_4C_3-s.; VF_3-m.; VSi_2-w.; C-w.
27	$HfSi_2$/PTFE	Sootlike	2.8	94.5	Mostly sootlike particles with few SiCNWs and nanocrystallites	HfC-s.; Si-w.; C-w.; HfF_4-w.; $HfSi_2$-w.
28	$HfSi_2$/PTFE	Sootlike	3.1	91.1	Mostly sootlike particles with few SiCNWs and nanocrystallites	V_4C_3-s.; VF_3-m.; VSi_2-w.; C-w.
29	$Co_{0,5}Fe_{0,5}Si_2$/PTFE	Sootlike	1.9	76.5	Sootlike particles with bundles of SiCNWs	$CoSi_2$-m.; SiC-w.
30	$Co_{0,5}Fe_{0,5}Si_2$/PTFE	Sootlike	2.4	70.4	Sootlike particles with scattered SiCNWs	$CoSi_2$-m.; SiC-w.
31	$Ni_{0,5}Fe_{0,5}Si_2$/PTFE	Sootlike	1.8	74.2	Mostly sootlike particles with scattered SiCNWs	Fe_3Si-m.; Fe_2Si-m.; SiC-w.
32	$Ni_{0,5}Fe_{0,5}Si_2$/PTFE	Sootlike	2.3	70.7	Mostly sootlike particles with scattered SiCNWs	Fe_3Si-m.; Fe_2Si-m.; SiC-w.
33	$Co_{0,5}Ni_{0,5}Si_2$/PTFE	Sootlike	6.7	69.3	Mostly sootlike particles with very few SiCNWs	$CoSi_2$-m.; $NiSi_2$-w.; SiC-w.

(continued)

Table 46.2 (continued)

Run #	Reactants	Raw product morphology	Free Si content, wt %	Total conversion degree of silicide, %	SEM observation	XRD
34	$Co_{0,5}Ni_{0,5}Si_2$/PTFE	Sootlike	2.6	88.2	Sootlike particles with few SiCNWs and silica nanoparticles	$CoSi_2$-m.; $NiSi_2$-w.; SiC-w.
35	$TaSi_2$/PTFE	Sootlike	2.8	78.9	Mostly sootlike particles with few SiCNWs and TaC nanocrystallites	TaC-s.; TaF_3-m.; SiC-m.
36	$TaSi_2$/PTFE	Sootlike	2.1	84.1	Mostly sootlike particles with few SiCNWs and TaC nanocrystallites	TaC-s.; TaF_3-m.; SiC-m.
37	$FeSi_2$/PTFE	Sootlike			Mostly sootlike particles with few SiCNWs	Fe_2Si-m.; Fe-w.; C-m.
38	$FeSi_2$/PTFE	Sootlike	2.9	71.6	Mostly sootlike particles with few SiCNWs and silica nanoparticles	Fe_2Si-m.; Fe-w.; C-m.
39	Fe-Si/PTFE	Sootlike	2.5	76.0	Sootlike particles with few SiCNWs	SiC-s.; FeSi-m.; $FeSi_2$-m.; C-m.; Si-w.
40	Fe-Si/PTFE	Spongelike	0	100	Sootlike particles with few SiCNWs and silica nanoparticles	SiC-s.; FeSi-m.; $FeSi_2$-w.; C-m.; Si-w

n.a. non-analyzed, *v.s.* very strong, *s.* strong, *m.* medium, w. weak

46.4 Production of Graphene-Related Nanostructures

In 2004 [12] Novoselov and Geim isolated, using a rather simple approach (Scotch tape exfoliation), graphene—2D honeycomb carbon structure. Since then graphene, with its unique electron and mechanical properties [13], has become a wonder material, opening new applications and possibilities especially in electronics. In the light of wide possibilities of graphene's applications [14–17], a vivid aspect is its production. Graphene can be obtained using many different methods; however,

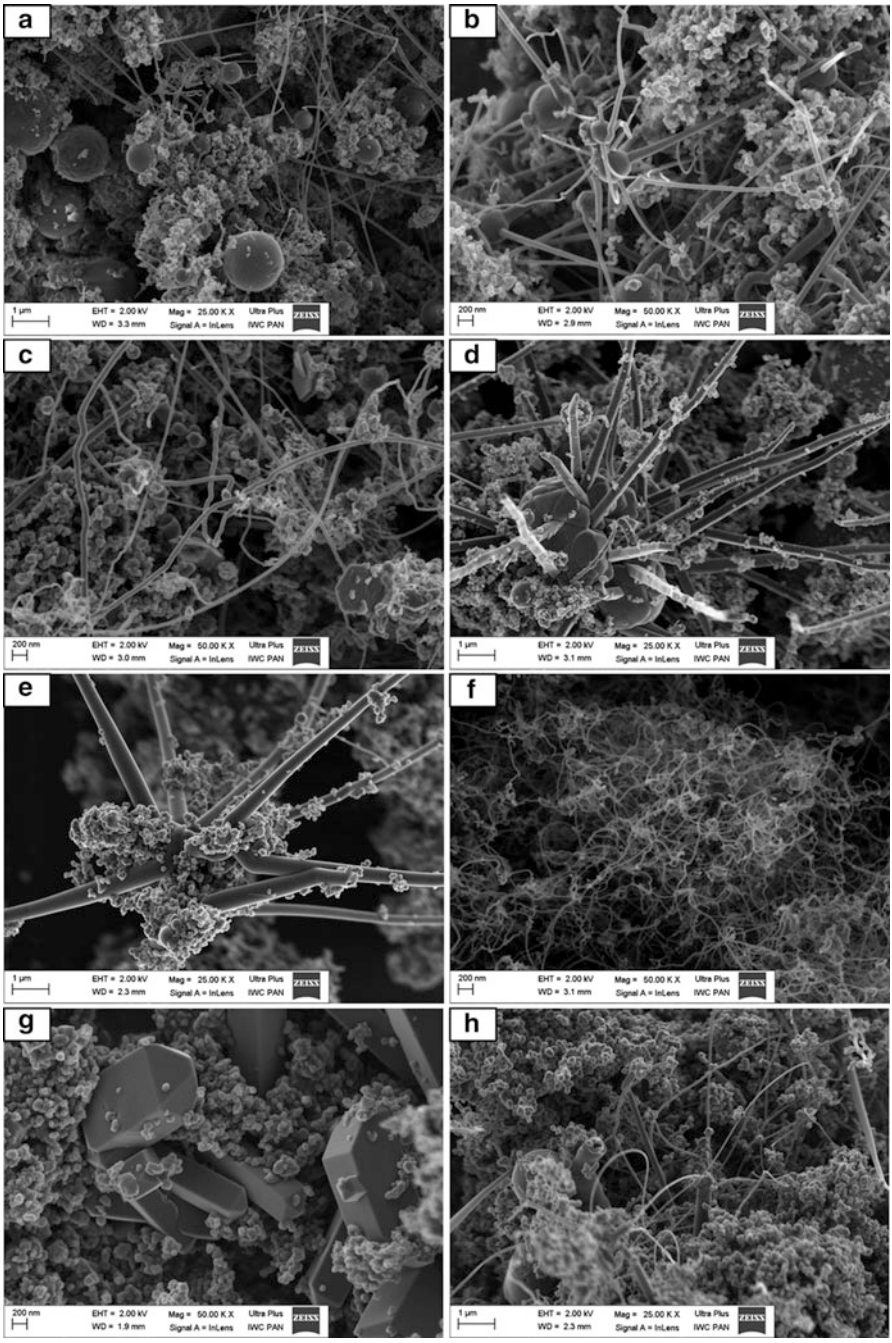

Fig. 46.9 SEM images of raw products: run 4 (**a**), run 7 (**b**), run 14 (**c**), run 16 (**d**), run 19 (**e**), run 21 (**f**), run 23 (**g**), run 29 (**h**), run 35 (**i**), run 39 (**j**)

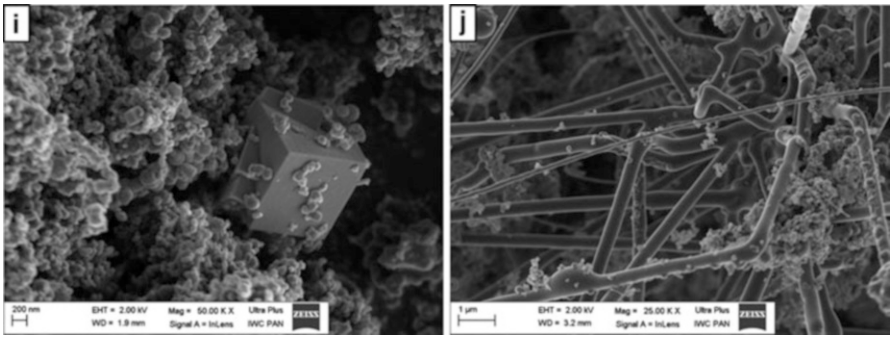

Fig. 46.9 (continued)

each method has its own advantages and drawbacks, and only few are acceptable for electronics applications. Exfoliation of graphene can be performed via different approaches [18], i.e., chemical, mechanical, and thermal, but each has some restrictions: it is hard to be scaled up, tedious, and time-consuming or involves wet chemistry with all its pros and cons (environmental issue). The most promising technique from an electronics point of view is *chemical vapor deposition* (CVD) that can work even in a continuous mode and also epitaxial growth on SiC. Although these methods allow the synthesis of low-defected high-quality material, the limit is a cost of the production. So the production of graphene is on one hand limited with potentially dangerous methods, involving hazardous, environment unfriendly chemicals, and on the other hand with high costs.

We propose here an alternative method for graphene-like material production. Combustion synthesis, opposite to previously mentioned ones, is exothermic, hence cheap, fast (lasts usually within a fraction of a second), one pot, and "green" (hazardous or waste materials such as CO and CO_2 can be utilized, and new, graphene-like materials can be synthesized) method. As SHS is a redox reaction, it demands a mixture of a strong oxidant and a reducer. We use here Mg (as a reducer) and gaseous carbon oxides CO_x (as oxidants). In such a system, an autothermal, highly exothermic, partially nonequilibrium reduction reaction takes place. Thanks to high temperatures (up to 2000 K), high pressures during the reaction, and fast quenching after the synthesis, a deep reduction of carbon oxides toward petal-like/few-layered graphene product is accomplished. A simplified scheme of the reaction is as follows:

$$x\,\mathrm{Mg} + \mathrm{CO}_x \rightarrow x\,\mathrm{MgO} + \mathrm{C}$$

We carried out the parametric studies. We examined the influence of operating parameters (type of oxidant: CO, CO_2, Mg grain size, reactants stoichiometry, and CO_x initial pressure) on final product yield and morphology. Two series of experiments were performed, one with CO and the other with CO_2 as an oxidant. In both series, a wide range of pressures was studied (from 1 MPa up to 5.6/7.5 MPa). Because of magnesium mass limit (the amount of magnesium was limited to 1 g only), as it is a very reactive metal and we did not want the reaction to be too violent

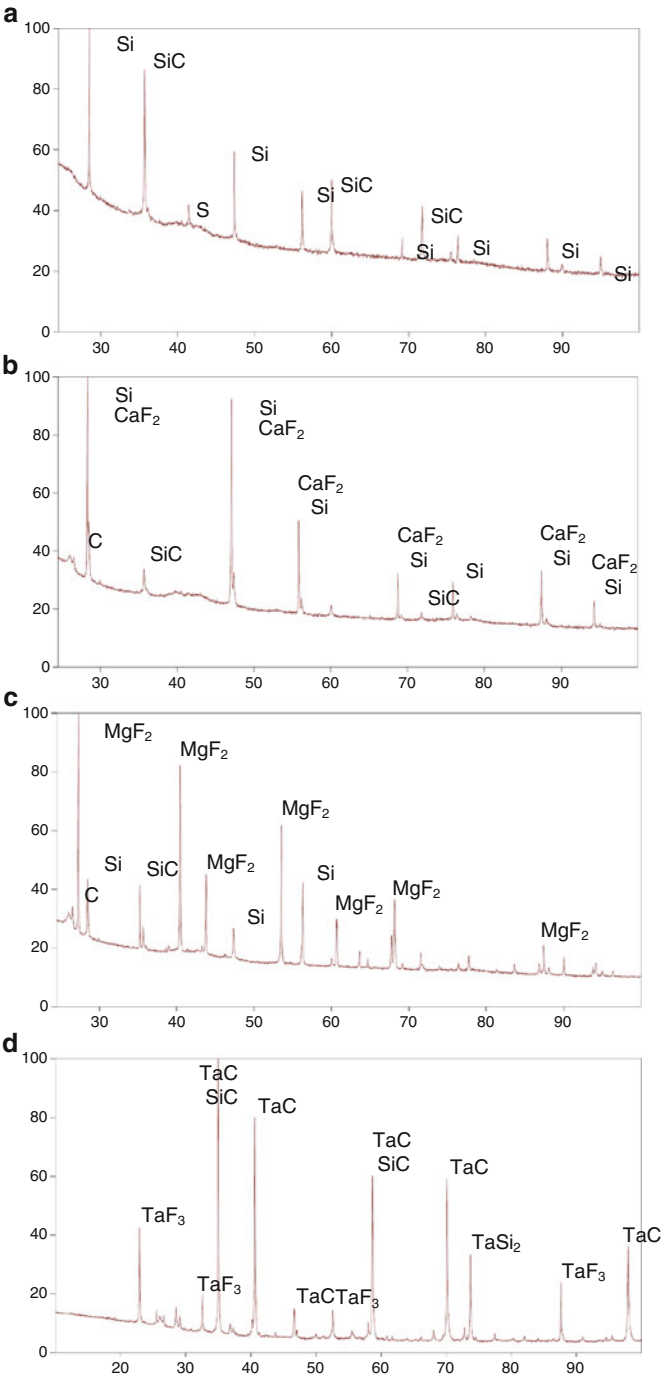

Fig. 46.10 XRD spectra of selected raw products: run 2 (**a**); run 3 (**b**); run 5 (**c**); run 35 (**d**)

Table 46.3 Graphene-related nanostructure synthesis: operational parameters and results of combustion in CO

Reactants stoichiometry	Mass of Mg, g	CO initial pressure, MPa	Mass of raw product, g	C content in product %	Yield %
Mg excess	1.01	0.14	No reaction		
CO excess	1.02	0.57	1.44	12.2	67.0
CO excess	1.02	1.05	1.58	22.1	73.5
CO excess	1.00[a]	2.04	1.83	21.5	85.1
CO excess large Si grains	1,01[a]	2.07	1.34	13.1	62.4
CO excess	1.00	3.62	1.67	20.5	77.7
CO excess	1.00	5.00	1.52	18.3	71.0
CO excess	1.00	5.65	1.27	17.4	59.3
CO excess	1.02[b]	7.55	1.24	12.0	57.9
CO excess	1.01[b]	7.55	1.24	10.2	57.8

[a]Experiments repeated with different Mg grain size
[b]Repeated experiments

Table 46.4 Graphene-related nanostructure synthesis: operational parameters and results of combustion in CO_2

Reactants stoichiometry	Mass of Mg, g	CO_2 initial pressure, MPa	Mass of raw product, g	C content in product %	Yield %
Mg excess	1.00	0.14	1.04	2.3	54.5
CO_2 excess	1.00	0.49	1.10	8.4	57.7
CO_2 excess	1.00	1.00	1.59	14.3	83.2
CO_2 excess	1.01	2.10	1.62	19.2	84.6
CO_2 excess	1.01	3.50	1.63	14.7	85.4
CO_2 excess	1.00	5.01	1.46	12.7	76.4
CO_2 excess	1.01	5.62	1.08	10.5	56.5

(safety reasons), only the exploratory experiments with the lowest gas pressure had an excess of magnesium. The influence of magnesium grain size on the combustion was studied only in CO system. The products were analyzed with XRD and SEM techniques to identify products and to study their morphology.

All syntheses were conducted in the reactor presented above. Magnesium (about 1 g) was loaded to the quartz crucible and placed in the reactor; then, the reaction gas (CO or CO_2) was introduced. The reaction was initiated with ohmic heating. During combustion, no "explosion" was observed, while the fast reaction took place in the crucible, which was almost white-hot. Tables 46.3 and 46.4 present reaction parameters and results, respectively.

As expected from the reaction scheme, the products were solid, remaining in the crucible only. An increase of raw product mass (from several to several tens of percent) in comparison with the starting solid Mg was, as expected, observed due to oxidation. The products were hard, blackish, or grayish materials. After removing from the crucible, the products were crushed and grinded in a mortar. Powdered

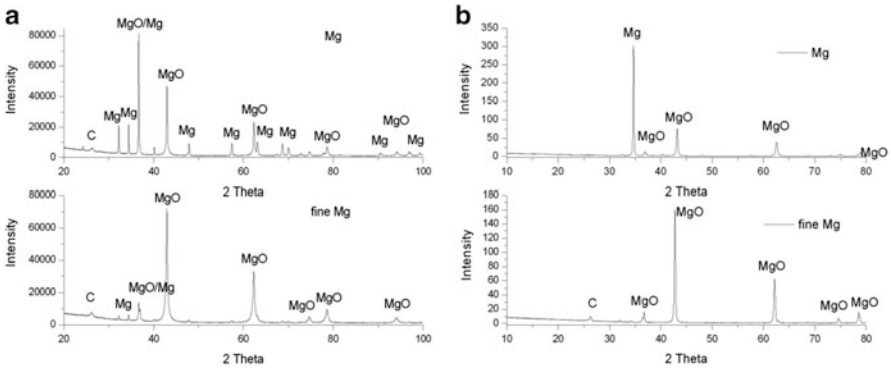

Fig. 46.11 XRD spectra of raw products for fine and coarse Mg powder: CO system (**a**); CO_2 system (**b**)

products were purified via a wet chemistry protocol (boiling in 3 M HCl for 1.5 h) to remove residual Mg and unwanted product—MgO.

The experiment showed that the size of magnesium powder influences the reaction. Smaller grains have higher surface area and so are in better contact with the other reactant (CO_x) which accelerates reaction toward higher conversion rates. XRD patterns (Fig. 46.11) prove that finer Mg powder ensures complete reaction, as almost no traces of Mg were found. In contrary, some residual Mg is still present in sample when larger grain size is used. This indicates that diffusion and reactant transport are not a limiting factor at higher pressures. However, at lower pressure (about 0.1 MPa), an availability of reactants is the key factor (see Tables 46.3 and 46.4). In CO system, the reaction did not start at all; there was only some small amount of product on the carbon tape, which might indicate that there was not enough heat or there was not enough contact between Mg and CO (low CO pressure). In CO_2 system, the conversion was low when Mg was in excess, which might be also explained with the lack of gaseous reactant or poor diffusion/contact.

Regarding the pressure effect, in the whole pressure range, petal-like product was produced, and no connection can be found between pressure and sample morphology (SEM) (Fig. 46.12). The changes in pressure in both systems influence, however, the hardness of the material. The higher the pressure, the harder the material. At 2 MPa, the highest yield of carbon product is obtained in both systems. That may indicate an optimum.

One can notice (Fig. 46.13) that higher pressure improves graphitization of product, while at lower pressure, turbostratic carbon is mostly formed. There are also traces of Si and SiC in products (XRD patterns) coming from the partial reduction of crucible material (SiO_2).

The comparison of CO and CO_2 systems shows that CO atmosphere gives slightly higher content of layered carbon in a product for a whole range of pressures.

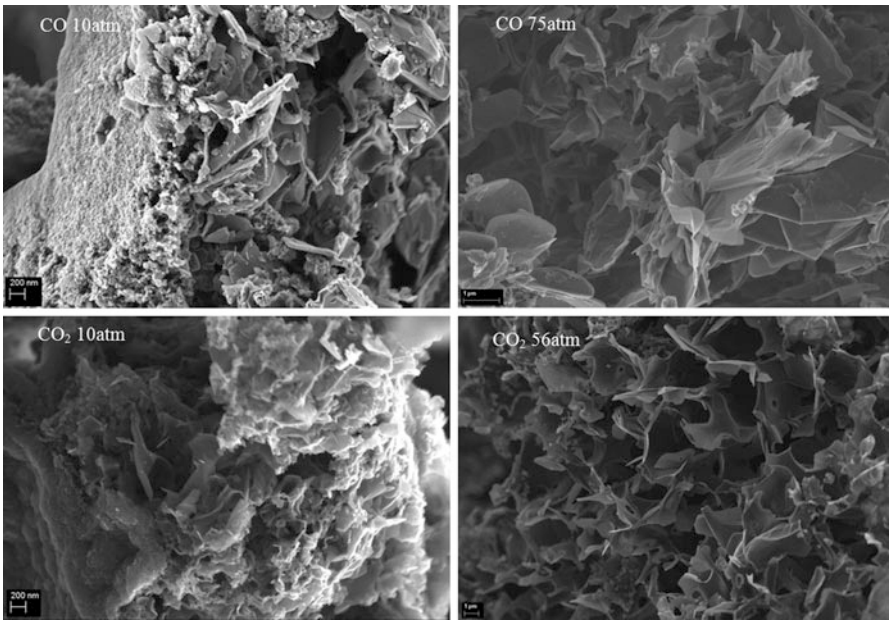

Fig. 46.12 SEM images of selected products

In summary, SHS is a very fast and cheap method, which provides conditions for petal-like carbon production. A direct and deep reduction of carbon oxides with magnesium produces carbon material containing few-layered graphene, applicable for composites. It is also worth mentioning that the process utilizes CO_2 considered to be a greenhouse gas and transforms it into a new, promising graphene-related nanomaterial, so it could also be seen as recycling method.

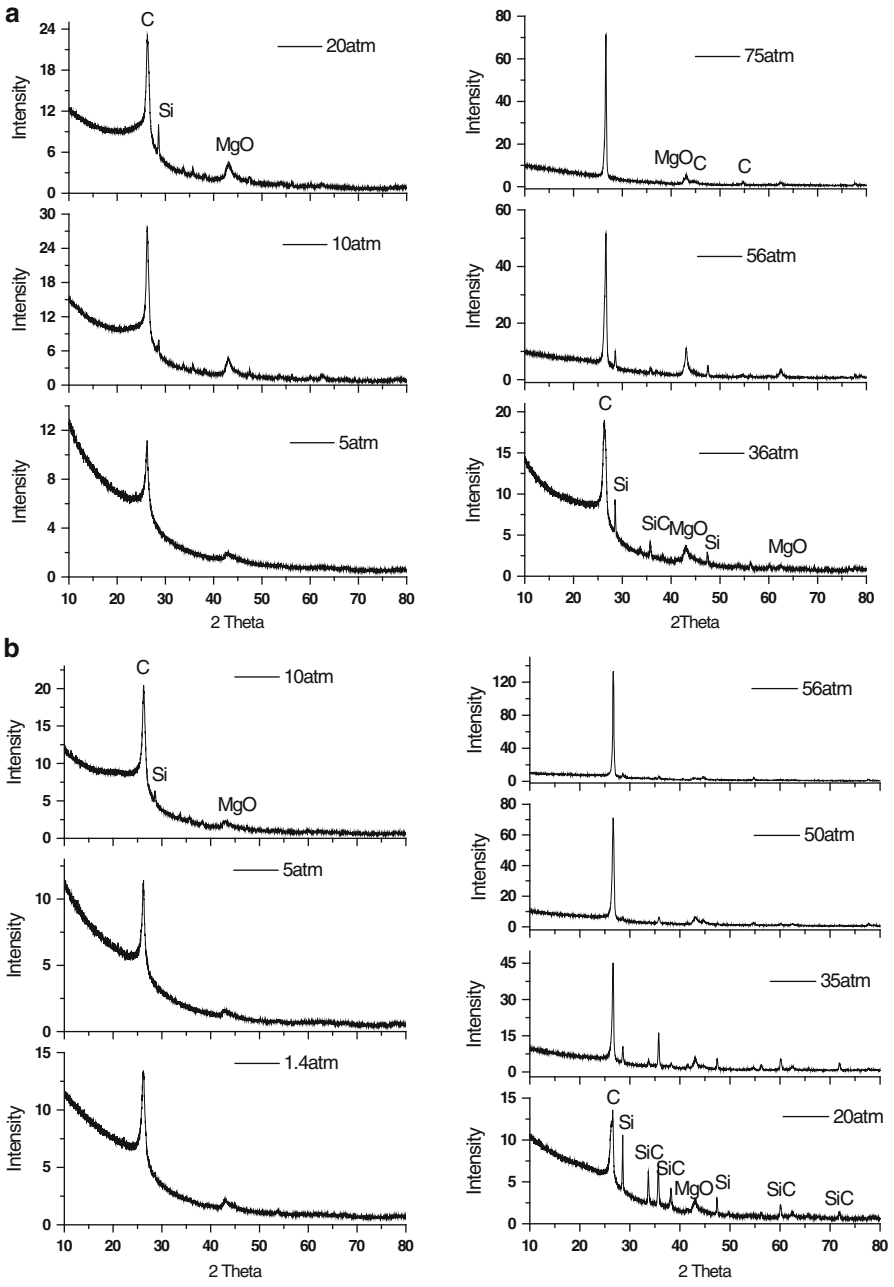

Fig. 46.13 Pressure vs. graphitization degree: CO system (**a**); CO_2 system (**b**)

References

1. Feynman RP (1960) There's plenty of room at the bottom. Eng Sci 23:22–36
2. Lackner M (ed) (2010) Combustion synthesis: novel routes to novel materials. Bentham Science Publishers, Sharjah
3. Merzhanov A (2004) The chemistry of self-propagating high-temperature synthesis. J Mater Chem 14:192–200
4. Soszyński M, Dąbrowska A, Bystrzejewski M, Huczko A (2010) Combustion synthesis of one-dimensional nanocrystalline silicon. Carbide Cryst Res Technol 12:1241–1244
5. Soszyński M, Łabędź O, Huczko A (2014) Combustion synthesis of Si-related crystalline nanostructures. J Cryst Growth 401:445–448
6. Huczko A, Dąbrowska A, Soszyński M et al (2011) Ultra-fast self-catalytic growth of silicon carbide nanowires. J Mater Res 26(24):3065–3071
7. Huczko A, Lange H, Chojecki G et al (2003) Synthesis of novel nanostructures by metal–polytetrafluoroethene thermolysis. J Phys Chem B 107:2519–2524
8. Dąbrowska A, Soszyński M, Huczko A (2013) Towards green chemistry: a new approach to the synthesis of semiconducting SiC nanowires. Phys Status Solidi B 250(12):2713–2716
9. Soszyński M, Dąbrowska A, Huczko A (2011) Spontaneous formation and characterization of silicon carbide nanowires produced via thermolysis. Phys Status Solidi 248(11):2708–2711
10. Huczko A, Osica M, Rutkowska A et al (2007) A self assembly SHS approach to form silicon carbide nanofibres. J Phys Condens Matter 19:395022–395033
11. Dąbrowska A, Huczko A, Dyjak S (2012) Fast and efficient combustion synthesis route to produce novel nanocarbons. Phys Status Solidi B 249:2373–2377
12. Novoselov KS, Geim AK, Morozov SV et al (2004) Electric field effect in atomically thin carbon films. Science 306:666–669
13. Geim AK, Novoselov KS (2007) The rise of graphene. Nat Mater 6:183–191
14. Avouris P, Dimitrakopoulos C (2012) Graphene: synthesis and applications. Mater Today 15:86–97
15. Bonaccorso F, Lombardo A, Hasan T et al (2012) Production and processing of graphene and 2d crystals. Mater Today 15:564–589
16. Wu YH, Yu T, Shen ZX (2010) Two-dimensional carbon nanostructures: fundamental properties, synthesis, characterization, and potential applications. J Appl Phys 108:071301–071336
17. Choi W, Lee JW (2012) Graphene: synthesis and application. CRC Press/Taylor & Francis Group, Boca Raton
18. Cai M, Thorpe D, Adamsonb DH et al (2012) Methods of graphite exfoliation. J Mater Chem 22:24992–25002

Chapter 47
Influence of Treatment Temperature on Microstructure and Properties of YSZ–NiO Anode Materials

V. Ya. Podhurska, B.D. Vasyliv, O.P. Ostash, Ye. M. Brodnikovskyi, and O.D. Vasylyev

47.1 Introduction

There exists a number of publications announcing dual influence of operating temperature on resulting physical and mechanical properties of the Ni-containing anode material for solid oxide fuel cells (SOFCs) after its cyclic reduction–oxidation (redox) treatment [1–3]. It is well known that electrical conductivity of metallic Ni (of about 1.4×10^7 S/m) is much higher than that of YSZ–Ni cermet. According to our data, after exposition of the ceramics sintered of NiO powder, for 4 h or more in pure hydrogen at 600 °C, complete reduction can be achieved [4]. Resulting electrical conductivity of the material is about $(1–5) \times 10^6$ S/m. However, exposition of NiO ceramics at this regime in Ar–5 vol.%H_2 mixture that is operating environment for SOFC anode causes partial reduction of the NiO particles forming thin edgings (of thickness of 0.1–0.4 μm) around them. Thus, electrical conductivity of the material treated is in the range of $(1–5) \times 10^5$ S/m depending on the average particle size, porosity and resulting contacts between Ni edgings. During redox treatment of NiO ceramics, structural transformation of boundaries of contacting nickel phase particles occurs causing an increase in strength.

In our previous works, it was revealed for ScCeSZ–NiO anode ceramics that at selected redox treatment regimes when the material is heated in vacuum and intermediate degassing between reduction and oxidation stages is performed,

V.Y. Podhurska (✉) • B.D. Vasyliv • O.P. Ostash
H.V. Karpenko Physico-Mechanical Institute of the NAS of Ukraine, 5 Naukova Str., Lviv 79060, Ukraine
e-mail: podhurskavika@gmail.com

Y.M. Brodnikovskyi • O.D. Vasylyev
I.M. Frantsevich Institute for Problems of Materials Science of the NAS of Ukraine, 3 Krzhyzhanovsky Str., Kyiv 03680, Ukraine

O. Fesenko, L. Yatsenko (eds.), *Nanophysics, Nanophotonics, Surface Studies, and Applications*, Springer Proceedings in Physics 183,
DOI 10.1007/978-3-319-30737-4_47

substantial improvements in strength (up to 112 %) and electrical conductivity can be reached at the treatment temperature of 600 °C [5, 6].

The aim of this work is to study the physical and mechanical behaviours of the SOFC anode material during the cyclic redox treatment depending on the treatment temperature and also to find out microstructural changes causing resulting properties of the material.

47.2 Experimental

Anode ceramics of YSZ–NiO system sintered at Forschungszentrum Jülich (Germany) of zirconium oxide powder stabilized with 8 mol.% Y_2O_3, with addition of 50 wt.% NiO, has been investigated. A series of specimens of the size of $1 \times 5 \times 25$ mm were singly reduced at 600 or 800 °C in hydrogenous environment (the Ar–5 vol.%H_2 mixture or hydrogen of 99.99 vol.%H_2 purity) under the pressure of 0.15 MPa (Fig. 47.1a) or subjected to redox cycling (see Table 47.1). The redox treatment of ceramics was performed for five cycles according to the scheme [4]: heating in vacuum from 20 to 600 °C, reduction in hydrogenous environment at 600 or 800 °C under the pressure of 0.15 MPa, degassing, oxidation in air at 600 °C and cooling down to 20 °C in air (Fig. 47.1b). Reduction–oxidation stage duration was chosen taking into account literature data on complete or partial reduction of the material [7]. After the redox cycling, reduction of materials in hydrogenous environment for 4 h at 600 °C or for 1 h at 800 °C under the pressure of 0.15 MPa with cooling in argon was performed (see a scheme in Fig. 47.1a). The heating–cooling rate was 20 °C/min.

Ultimate fracture stresses of materials in the initial state, σ_{f0}, and after corresponding treatment, σ_f, were determined during the three-point bending test

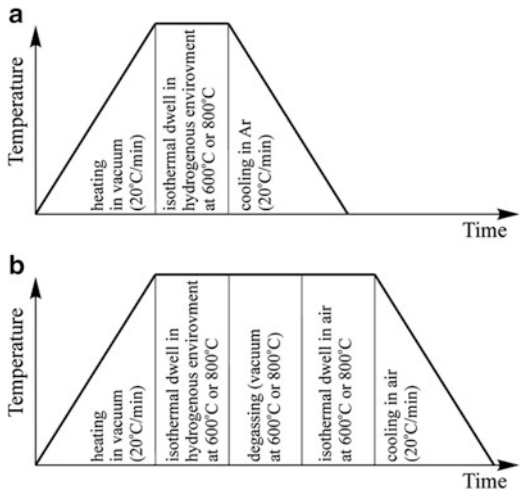

Fig. 47.1 The treatment schemes applied for YSZ–NiO ceramics: (**a**) single reduction in hydrogenous environment; (**b**) a cycle of redox treatment

Table 47.1 The treatment regimes for the materials tested

No. of version	Environment	Treatment temperature (°C)	Reduction/oxidation stage duration (h)	Variant of treatment
1	Ar–H_2 mixture	600	4	R
2	H_2	600	4	R
3	Ar–H_2 mixture/air	600	4	RO
4	H_2/air	600	4	RO
5	Ar–H_2 mixture	800	1	R
6	Ar–H_2 mixture/air	800	1	RO

R single reduction, *RO* redox cycling

of the specimens in air at 20 °C. Based on these data, relative strength, σ_f/σ_{f0}, of the material treated was evaluated.

The specific electrical conductivity of material, σ, was determined in air at 20 °C using the Van der Pauw method. SEM microstructures and microfractographs of the versions of specimens were investigated using the electron microscope Carl Zeiss EVO-40 XVP.

The X-ray analysis was carried out using X-ray diffractometer (Cu $K\alpha$) with Bragg–Brentano-type geometry. The average size of coherent dispersion areas of nickel phase, D, was calculated using Win CSD programme [8].

The spacing between the planes in the atomic lattice, d, of zirconia phase (line (220)) was estimated using the Rietveld method [8], and the residual stresses, σ_r, were evaluated using the equation

$$\sigma_r = -\frac{E}{\nu} \cdot \frac{d - d_0}{d_0} \tag{47.1}$$

where E is the Young's modulus and ν is the Poisson's ratio; the values of these parameters were selected according to [9]; d_0 is the spacing between the planes in the atomic lattice of zirconia phase ((220) line) for the as-received material.

Thermodynamics of reactions of nickel phase reduction and oxidation was analyzed by calculating the changes in Gibbs free energy, ΔG, using standard data [10].

47.3 Results and Discussions

47.3.1 Thermodynamics of the Reduction and Oxidation Stages

It is known [11] that in the temperature range 630–680 °C, a transition from diffusion to kinetic mechanism of oxidation occurs. Additionally, by analyzing

Table 47.2 The data of thermodynamics of reduction and oxidation stages for the material tested

Reaction	Gibbs free energy, ΔG (kJ/mol), at 600 °C	Equilibrium constant, K, at 600 °C	Gibbs free energy, ΔG (kJ/mol), at 800 °C	Equilibrium constant, K, at 800 °C
Reduction	−41	2.7×10^2	−43	1.3×10^2
Oxidation	−159	3×10^9	−145	1×10^7

the thermodynamics of reduction and oxidation stages, it was revealed that in the temperature range 600–800 °C, the change in Gibbs free energy, ΔG, is more negative, and the equilibrium constant, K, is higher considerably for the reaction of nickel oxidation than of its reduction (see Table 47.2). According to this we concluded that during redox cycling at higher temperature, the Ni oxidation stage becomes more intensive than the NiO reduction, one which probably can result in increase of unreduced particles amount into the bulk of the material treated. In such a case, the resulting structure does not meet the requirements on uniformity and, finally, efficiency of an anode substrate.

47.3.2 The Treatment Temperature of 600 °C

Exposition of YSZ–NiO ceramics at the temperature 600 °C for 4 h in Ar–5 vol.% H_2 mixture that is operating environment for SOFC anode (version 1 in Table 47.1) causes partial reduction of the NiO particles by diffusion mechanism. Thin Ni edgings (of thickness of 0.1–0.3 μm) are formed around NiO particles (Fig. 47.2a).

The substructure of these edgings was evaluated using X-ray data on average size of coherent dispersion areas of nickel phase, D (Fig. 47.3a). This parameter was measured as 45 nm.

Reduction in strength to 84 % of the value for the as-received YSZ–NiO ceramics (Fig. 47.3c) is possibly caused by partial structural transformation of nickel phase followed by a little volume decrease. It is displayed in the mixed fracture micromechanism (Fig. 47.2b). However, no noticeable change of zirconia skeleton was found for this variant of the treatment. As compared with as-received material, residual stresses did not change as well (Fig. 47.3b). Electrical conductivity of the material of 2.7×10^5 S/m is provided by thin films of Ni around NiO particles united into the network (Fig. 47.3d).

More intensive reduction of YSZ–NiO ceramics by the same diffusion mechanism occurs in pure hydrogen (version 2 in Table 47.1). During 4 h the structure of completely reduced Ni particles is formed (Fig. 47.2c). The substructure parameter (average size D) of these particles was measured as 41 nm that is less than for version 1 (Fig. 47.3a). Simultaneously, the volume decrease of the initial NiO particles of 41.6 % occurs [12]. Nanopores on Ni particles formed due to their shrinkage as well as the pores between the particles prevent the rise of residual tensile stresses (Fig. 47.3b). Nickel phase transformation followed by volume

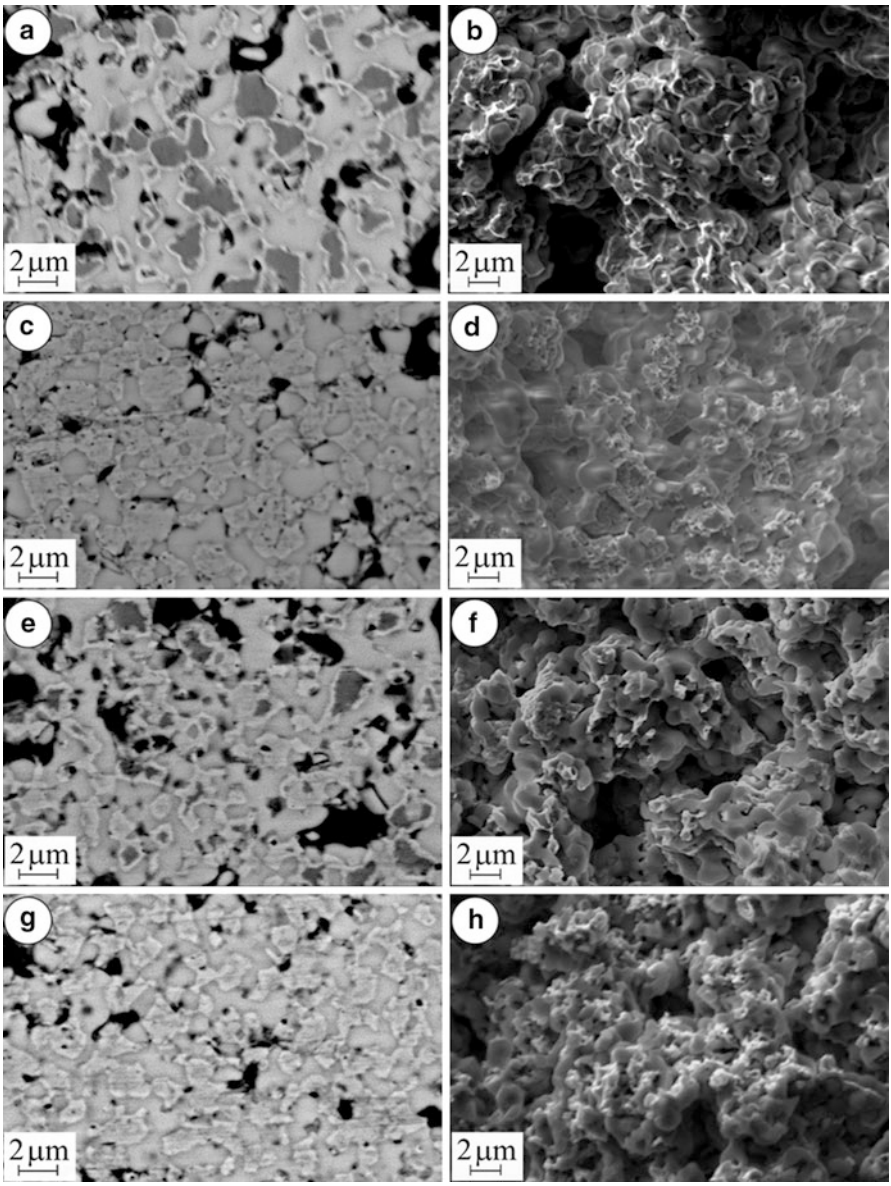

Fig. 47.2 SEM microstructures (**a**, **c**, **e**, **g**) and microfractographs (**b**, **d**, **f**, **h**) for the material in versions 1 (**a**, **b**), 2 (**c**, **d**), 3 (**e**, **f**) and 4 (**g**, **h**) (see Table 47.1)

change and formation of pores causes the losses of significant percentage of particle bonds and violate material integrity which is displayed in predominantly intergranular fracture micromechanism (Fig. 47.2d). Reduction in strength to 48 % of the value for the as-received YSZ–NiO ceramics is recognized

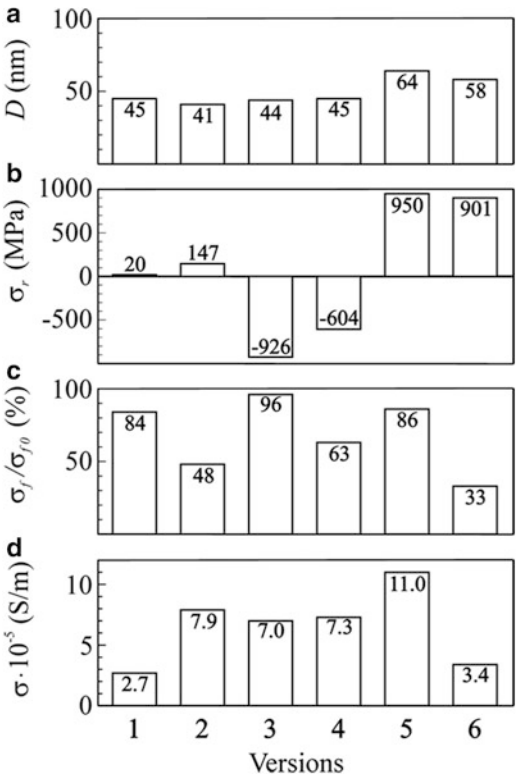

Fig. 47.3 Average size of coherent dispersion area, D (**a**); residual stresses, σ_r, in zirconia phase (**b**); relative strength, σ_f/σ_{f0}, (**c**); and specific electrical conductivity, σ, (**d**) for material in versions 1–6 (see Table 47.1); numbers on the bars indicate values of corresponding parameters

(Fig. 47.3c). Thanks to complete reduction of nickel phase, the high electrical conductivity (Fig. 47.3d) of the material is achieved compared to the similar functional materials [13].

According to our data [4], there exists substantial difference in mechanical behaviour of NiO ceramics after redox treatment as compared with that of the singly reduced material, at the treatment temperature of 600 °C. During the treatment, structural transformation of boundaries of contacting nickel phase particles occurs, causing an increase in strength.

The cleavage fracture micromechanism was noted in the specimens tested. This micromechanism corresponds to higher cohesive strength of nickel phase particles as compared with ultimate cleavage stress of the particles themselves.

Such treatment technique has been used in this work for improvement of strength and electrical conductivity of YSZ–NiO ceramics. Upon redox cycling, exposition of the material at the temperature 600 °C for 4 h in air resulted in complete oxidation of preliminary reduced Ni edgings on NiO particles (version 3 in Table 47.1, Fig. 47.2e) as well as of preliminary reduced Ni particles (version 4, Fig. 47.2g) by diffusion mechanism. After five cycles of the redox treatment at 600 °C with the final reduction stage (version 3), most of NiO particles were reduced completely, forming continuous network of electrically conducting

material in zirconia skeleton (Fig. 47.2e) which resulted in the value of specific electrical conductivity of the material of 7×10^5 S/m (Fig. 47.3d). Fragmentation of coarse grains of nickel phase resulted in more fine structure of the material treated. The substructure parameter, D, of reduced particles for version 3 was measured as 44 nm what is similar to that for version 1 (Fig. 47.3a). Thus, no distinct change of substructure of nickel particles was found.

The X-ray data displayed reduction of 2Θ angle for cyclically treated materials. In accordance with the Wolf–Bragg's law

$$2d \sin \Theta = n\lambda \tag{47.2}$$

where n is a positive integer and λ is the wavelength of incident wave, the spacing between the planes in the atomic lattice, d, of zirconia phase increases resulting (see (1)) in considerable relaxation of residual stresses, σ_r, in material of versions 3 and 4 as compared with as-received material (Fig. 47.3b). This affects positively the mechanical behaviour of material, especially of version 3 (Fig. 47.3c).

The mixed fracture micromechanism was noted in tested specimens of versions 3 (Fig. 47.2f) and 4 (Fig. 47.2h). The fracture surfaces comprise brittle cleavage areas of ceramic matrix neighbouring to ductile fracture ones of reduced nickel (Fig. 47.2f). Like for the NiO ceramics treated [4], this corresponds to higher cohesive strength between the particles of zirconia and nickel phase as compared with the singly reduced material.

47.3.3 The Treatment Temperature of 800 °C

In order to reduce the redox treatment duration, the behaviour of YSZ–NiO ceramics was estimated under redox cycling at 800 °C. During single exposition of the material in Ar–5 vol.%H_2 mixture at this temperature (version 5 in Table 47.1), NiO particles are reduced completely within 1 h (Fig. 47.4a) by diffusion mechanism of much higher intensity as compared with version 1. Reduced Ni particles are dotted with nanopores. The NiO-to-Ni transformation is carried out rapidly with formation of comparatively coarse substructure (parameter D of reduced particles was measured as 64 nm; see Fig. 47.3a).

The X-ray data displayed increase of 2Θ angle for the material singly reduced at 800 °C. Consequently, the spacing between the planes in the atomic lattice, d, of zirconia phase decreases, resulting in considerable growth of residual stresses, σ_r, in material of version 5 as compared with as-received material (Fig. 47.3b).

The singly reduced material has somewhat lower strength as compared with as-received ceramics (Fig. 47.3c, version 5) but substantially higher electrical conductivity as compared with the material treated at 600 °C (Fig. 47.3d, versions 5 and 1, respectively). The mixed fracture micromechanism is recognized in the specimens tested (Fig. 47.4b). It is similar to the one after redox treatment of YSZ–NiO ceramics at 600 °C. It also evidences that single reduction at 800 °C does

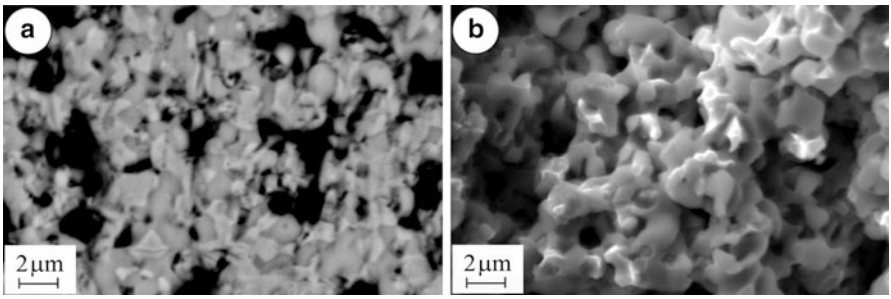

Fig. 47.4 SEM microstructure (**a**) and microfractograph (**b**) for the material in version 5 (see Table 47.1)

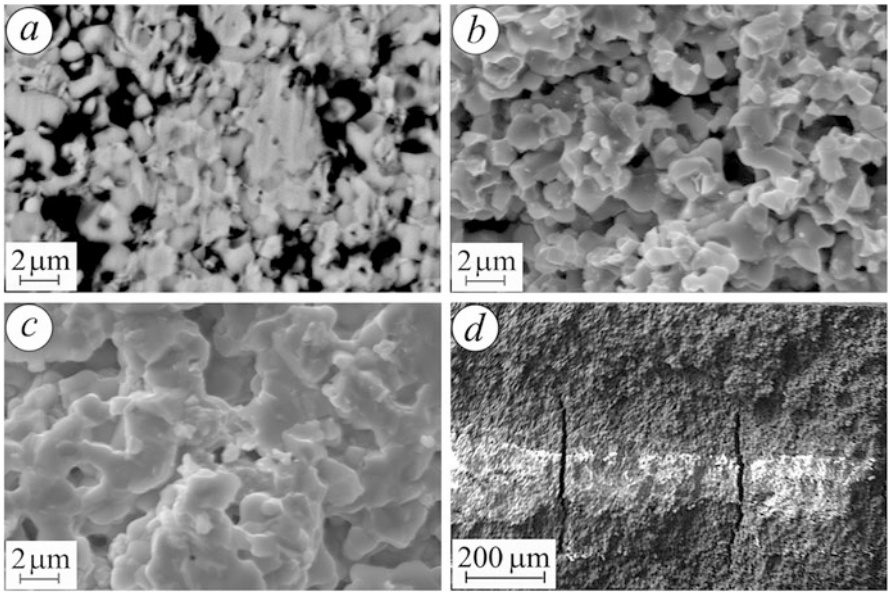

Fig. 47.5 SEM microstructure (**a**) and microfractographs (**b–d**) for the material in version 6 (see Table 47.1)

not violate the integrity of zirconia skeleton, and a partial decrease in strength is caused by nickel phase transformation.

Contrary to the positive effect of redox treatment of YSZ–NiO ceramics at 600 °C, a negative tendency for strength of YSZ–NiO ceramics during the treatment at 800 °C is noted (Fig. 47.3c, version 6). In both cases of the treatment of YSZ–NiO ceramics, the resulting structures are similar (Fig. 47.5a as compared with Fig. 47.2e) except for the peculiar (of green colour) inner part of specimens after the treatment at 800 °C (Fig. 47.5d). As stated above a kinetic mechanism of

oxidation at this temperature intensifies the growth of unreduced volume of the anode during redox cycling.

Two different areas on the fracture surface picture of a specimen treated at 800 °C are observed. In the reduced layer, mixed fracture micromechanism comprising transgranular cleavage of zirconia particles and intergranular fracture along the boundaries of contacting nickel phase particles dominates (Fig. 47.5b). The nickel particles of smaller sizes had possibly agglomerated on zirconia particles. Being intact, they are separated by a network of the pores formed during redox treatment. Thus, this fracture micromechanism is as energy expensive as the one revealed for the material after redox treatment at 600 °C (Fig. 47.2f).

In unreduced inner layer of the anode transgranular cleavage, a fracture of coarse zirconia and nickel oxide agglomerates dominates, and occasionally the signs of intergranular fracture along the boundaries of particles of smaller size are observed (Fig. 47.5c).

In spite of similar levels of residual stresses in the zirconia phase that were estimated for the entire reduced volume (Fig. 47.3b, version 5) and outer reduced layer (version 6), respectively, different structural factors affect the integrity of these materials.

The total strength of the material after redox treatment at 800 °C is decreased considerably with the array of microcracks into the bulk of the specimen (Fig. 47.5d) that have been formed during the treatment normally to its surface. These microcracks are nucleated following a stress gradient on the boundaries between reduced and unreduced layers as a result of thermal expansion (thermal expansion coefficients for YSZ, NiO and Ni phases are 10.9×10^{-6}, 14.1×10^{-6} and 16.4×10^{-6} K^{-1}, respectively [14]). The reduced layer showed the value of specific electrical conductivity 3.4×10^5 S/m (Fig. 47.3d, version 6) which is satisfactory for SOFC anode. However, this value is lower than that of the material singly reduced at 800 °C (version 5). Besides, the unreduced layer having very low electrical conductivity becomes a substantial obstacle in achieving required electrochemical performance of the fuel cell.

Thus, contrary to the positive effect of redox treatment at 600 °C on strength and electrical conductivity of YSZ–NiO ceramics, such treatment at 800 °C causes formation of anode structure with reduced outer and unreduced inner layers as well as the array of microcracks in the bulk of an anode initiated normally to its surface, which causes the loss of its integrity. The unreduced inner layer of the anode has unsatisfactory electrical conductivity.

47.4 Conclusions

A cyclic treatment technique (redox cycling) comprising stages of material exposition in reducing and oxidizing high-temperature gas environments and intermediate degassing between these stages has been developed to improve the strength and electrical conductivity of YSZ–NiO ceramic anode substrates for solid oxide fuel cells.

Using the treatment temperature 600 °C, the structure providing improved physical and mechanical properties of the material was formed. However, at the treatment temperature 800 °C, the anode structure with the array of microcracks was formed that reduced significantly the strength and electrical conductivity of the material. Based on the data of thermodynamics and X-ray analysis, the obtained results were related with influence of temperature rise on intensification of nickel oxidation and increase of residual stresses.

References

1. Sarantaridis D, Atkinson A (2007) Redox cycling of Ni-based solid oxide fuel cell anodes: a review. Fuel Cells 3:246–258
2. Ettler M, Timmermann H, Malzbender J et al (2010) Durability of Ni anodes during reoxidation cycles. J Power Sources 195:5452–5467
3. Wood A, Waldbillig D (2011) Preconditioning treatment to enhance redox tolerance of solid oxide fuel cells. US Patent 8,029,946 B2, 4 Oct 2011
4. Podhurs'ka VY, Vasyliv BD, Ostash OP et al (2014) Structural transformations in the NiO-containing anode of ceramic fuel cells in the course of its reduction and oxidation. Mater Sci 49(6):805–811
5. Ostash OP, Vasyliv BD, Podhurs'ka VY et al (2011) Optimization of the properties of 10Sc1CeSZ–NiO composite by the redox treatment. Mater Sci 46(5):653–658
6. Vasyliv BD, Podhurs'ka VY, Ostash OP et al (2013) Influence of reducing and oxidizing media on the physicomechanical properties of ScCeSZ–NiO and YSZ–NiO ceramics. Mater Sci 49(2):135–144
7. Tikekar N, Armstrong T, Virkar A (2006) Reduction and reoxidation kinetics of nickel-based SOFC anodes. J Electrochem Soc 153:A654–A663
8. Akselrud LG, Zavalii PY, Grin YN et al (1993) Use of the CSD program package for structure determination from powder data. Mater Sci Forum 133:335–342. doi:10.4028/www.scientific.net/MSF.133-136.335
9. Sun B, Rudkin RA, Atkinson A (2009) Effect of thermal cycling on residual stress and curvature of anode-supported SOFCs. Fuel Cells 6:805–813
10. Mills I, Cvitas T, Homann K et al (1993) Quantities, units and symbols in physical chemistry. Blackwell, London
11. Peraldi R, Monceau D, Pieraggi B (2002) Correlations between growth kinetics and microstructure for scales formed by high-temperature oxidation of pure nickel. I. Morphologies and microstructures. Oxid Met 58:249–273
12. Faes A, Nakajo A, Hessler-Wyser A et al (2009) RedOx study of anode-supported solid oxide fuel cell. J Power Sources 193:55–64
13. Zhang Y, Liu B, Tu B et al (2005) Redox cycling of Ni–YSZ anode investigated by TRP technique. Solid State Ion 176:2193–2199
14. Mori M, Yamamoto T, Itoh H et al (1998) Thermal expansion of nickel-zirconia anodes in solid oxide fuel cells during fabrication and operation. J Electrochem Soc 145:1374–1381

Index

O. Fesenko, L. Yatsenko (eds.), *Nanophysics, Nanophotonics, Surface Studies, and Applications*, Springer Proceedings in Physics 183,
DOI 10.1007/978-3-319-30737-4